

# **DEVELOPING AN INTEGRATED APPROACH TO PREDICTING THE WATER USE OF RIPARIAN VEGETATION**

Report to the Water Research Commission

by

A.L. Birkhead<sup>1</sup>, B.W. Olbrich<sup>2</sup>, C.S. James<sup>1</sup> and K.H. Rogers<sup>1</sup>

<sup>1</sup>Centre for Water in the Environment  
University of the Witwatersrand  
Private Bag 3, WITS 2050  
Johannesburg  
South Africa

<sup>2</sup>Environmentek  
CSIR  
Private Bag X11227  
Nelspruit, 1200  
South Africa

Report to the Water Research Commission on the Project "Developing an  
Integrated Approach to Predicting the Water Use of Riparian Vegetation"

Project Leaders: Prof CS James and Prof KH Rogers

WRC Report No. 474/1/97

ISBN 1 86845 269 7

## EXTENDED EXECUTIVE SUMMARY

---

### 1 Introduction and Objectives

There is an ever increasing demand for South Africa's limited water resources, primarily due to population growth and continued agricultural and industrial development. As a result, the pressure on river systems is steadily increasing, and this has resulted in declining flows and a decrease in the capacity of the rivers to meet the demands they face. The objective of this study was to focus on one of these rivers, the Sabie River, and to examine the water requirements of one component of the riverine system which is often overlooked, the riparian vegetation within the Kruger National Park.

Seven major rivers flow through the Kruger National Park (KNP) in the Mpumalanga and Northern Provinces and are critical for both the existence of unique biota within their riparian zones and for the survival of animal wildlife during the dry season. All seven rivers rise west of the KNP in catchment areas subjected to increasing anthropogenic pressure for the available land and water resources. As a result, the flow regimes of several of these rivers have been affected and a number have changed from perennial to seasonal and even ephemeral systems, as has occurred with the Letaba River.

The historically perennial Sabie River has also been affected, and the reduced winter base flows are resulting in increased stress levels amongst the natural river biota. Consequently, there is an urgent need to manage the water resources within the catchment effectively to ensure the viability of riverine ecosystems. In particular, adequate water must be supplied to meet the consumptive or transpirational demands of the riparian vegetation, not only for its own maintenance, but also for its contribution to the habitat of invertebrates, fish, reptiles, amphibians, birds and mammals.

The specific objective of this investigation was to

***develop the means to predict transpiration by riparian vegetation under different river flow and meteorological conditions for the Sabie River in the Kruger National Park.***

The Sabie River in the KNP was selected for study because of its ecological importance, and the potential impacts that further flow modifications could have on the riparian vegetation and related ecosystems. It is the focus of an integrated research thrust funded under the Kruger National Park Rivers Research Programme. The majority of the field data collection for this study was conducted on an alluvial section of the river near the Narina camp site located approximately 5 km upstream of Skukuza.

Several quantitative models were developed and integrated to describe the various components of the riparian water balance, as illustrated in Figure 1. The rationale for pursuing an integrated study of the riparian water balance is that all processes defining fluxes between surface water, subsurface storage and movement, and riparian transpiration are intrinsically linked in the riparian system under investigation. Three main models were developed to simulate the movement of water through the system. The supply of water was addressed in a river hydraulics model describing surface flow in the river. Subsurface flow in the alluvial bank zone adjacent to the river and availability of soil moisture for transpiration was modelled in a bank storage dynamics model, and the consumptive water use by riparian vegetation accounted for by a transpiration model. The riparian water balance is defined by the interactions between these component models.

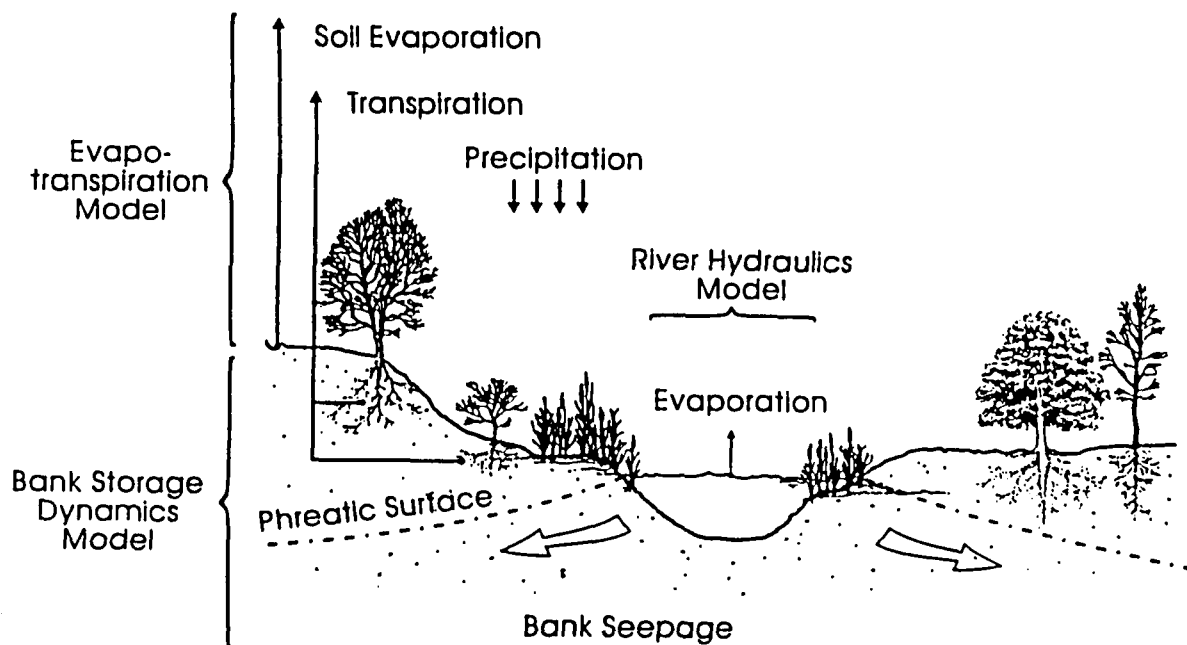


**Figure 1** Water balance along a two-dimensional vertical section through the riparian zone, showing component models.

## 2 River Hydraulics

The river hydraulics component of the riparian water balance (Figure 1) provides the means to translate discharge into local hydraulic conditions such as river stage (water level) and flow velocity. The temporal variation of river stage is the primary determinant governing the interaction between

surface and subsurface flows. The output from the river hydraulics model for this study is the ability to synthesize rating (stage-discharge) relationships. This has been achieved by determining flow resistance from field measurements as well as developing a technique for synthesizing approximate steady-state rating curves using modified nonlinear Muskingum routing.

## 2.1 Flow Resistance

The Manning's resistance coefficients determined within this study are in the range 0.021 to 0.10, and compare well with those of Broadhurst *et al.* (in press) for a typically braided morphological channel type. The data of Broadhurst *et al.* (Table 1) include the other four major channel types along the Sabie River as identified by Heritage *et al.* (in press). A comparison of the rating curve fitted to measured data from the Narina site and synthesized using Manning's flow equation (Figure 2) confirm that the resistance data are transferable within the Sabie River, and should also be applicable to other river systems with similar resistance characteristics.

**Table 1** Manning's flow resistance coefficient at a reach scale for the major channel types along the Sabie River (after Broadhurst *et al.*, in press)

Discharge (m <sup>3</sup> /s)	Channel Type				
	Single Thread	Braided	Pool Rapid	Mixed Anastomosing	Bedrock Anastomosing
0	0.170	0.077	0.300	0.310	1.940
5	0.074	0.055	0.120	0.140	0.710
10	0.058	0.045	0.120	0.110	0.610
20	0.041	0.036	0.110	0.089	0.420
30	0.081	0.033	0.098	0.076	0.370
40	0.077		0.091	0.070	0.390
60				0.064	
80				0.062	
1000				0.078	

## 2.2 Muskingum Routing

A technique has been developed for synthesizing the approximate steady state rating curve for a river cross-section using remotely gauged discharge and local stage hydrographs. The modest data requirements include a short-term stage hydrograph and cross-sectional survey at the section of interest, the corresponding discharge hydrograph at the remote location, and an estimate of the distance along the river between the section and discharge monitoring location. Three models are presented for optimising



the parameters of the rating curve, expressed as a simple power function using the hydrograph data. All three methods were verified by comparison with rigorous flood routing in a hypothetical channel.

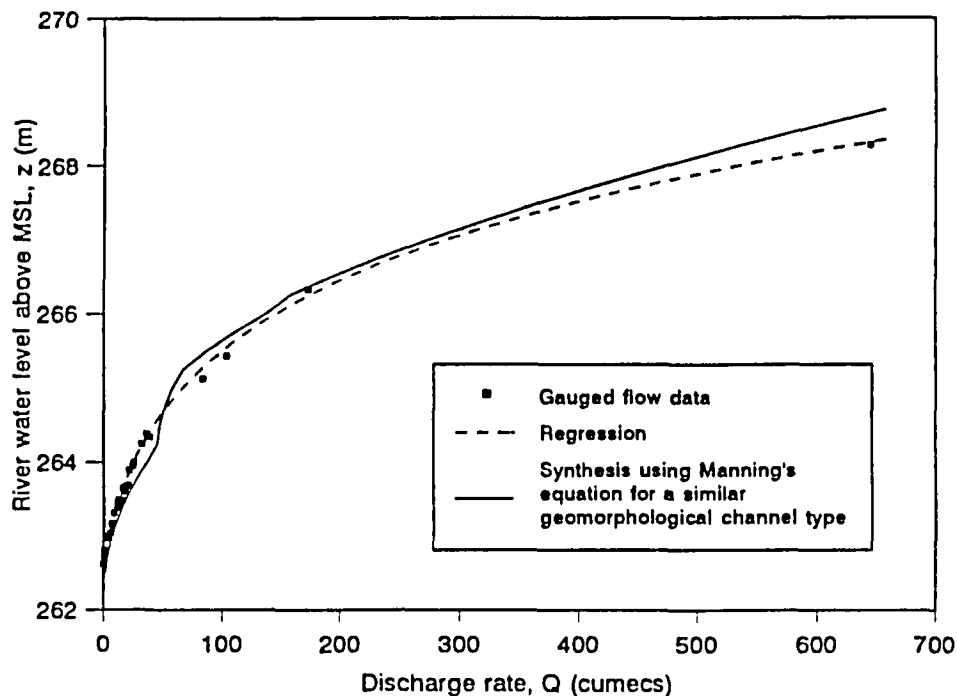


**Figure 2** Synthesized and gauged rating curves data for a cross-section through a typically braided morphological channel type.

The application of these procedures to the reach upstream of the study site showed that neglecting bank storage led to unrealistic estimates of the Muskingum storage weighting factor and unreliable rating curve parameter values. The procedure was successfully modified to account for bank storage by estimating the extent and the porosity of bank alluvium and assuming an instantaneous bank storage response. The synthesized rating curve was compared with point data consisting of clearly identifiable points on the remote discharge and local stage hydrographs that could be correlated between the stations. The field data were collected over the duration of the project and agree closely with the synthesized curve, as shown in Figure 3 for two of the models.

### 3 Bank Storage Dynamics

The dynamics in the bank storage are determined by the interaction between surface flow, groundwater and soil moisture in the saturated and unsaturated regions of the alluvial bank zone, respectively, and losses to

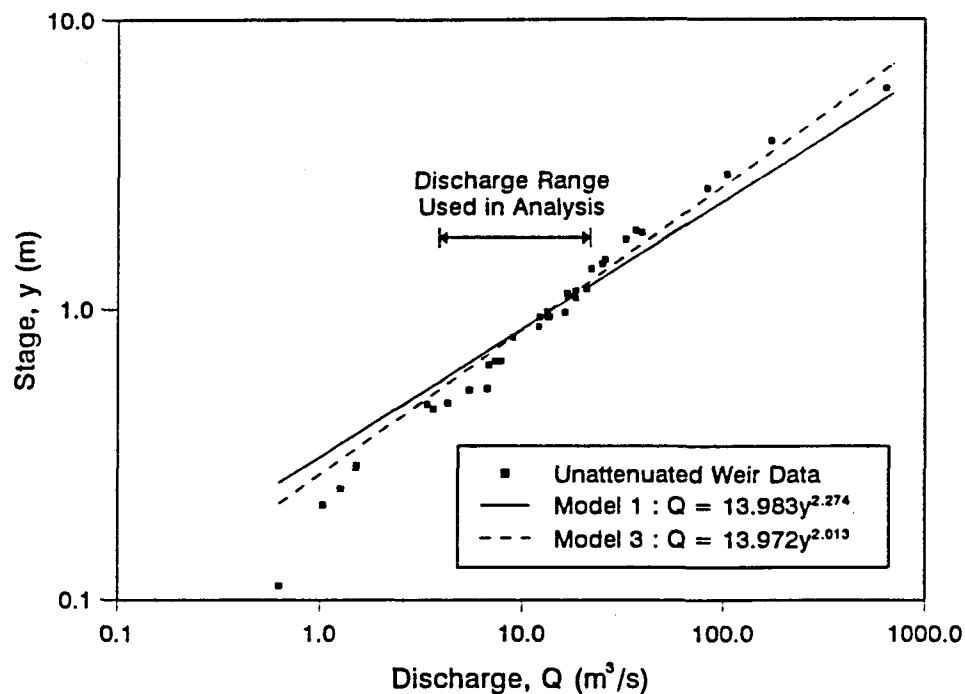


**Figure 3** Comparison of the synthesized rating curve and unrouted flow data for a cross-section on the Sabie River.

evapotranspiration (Figure 1). The bank storage component of the riparian water balance was described using a generalised finite-difference model which was validated using analytical and numerical models from the literature, as well as experimental data. The bank storage response was predicted acceptably in a deterministic application of a saturated two-dimensional form of the model at the Narina site.

Improved replication was achieved by extending the model to quasi three-dimensions to account for local hydraulic conditions, and calibrating the bulk alluvial-hydraulic parameter values. The modelled (quasi-three dimensional) and measured groundwater level hydrographs along a cross-section through the study site are plotted in Figure 4a, and the change in temporal bank storage volumes are plotted in Figure 4b. The predictive potential of the calibrated model was established by excellent correlation with field data, as illustrated in Figure 5. The value of the deterministic modelling approach is that generality is assured, but a major disadvantage is the large data requirement which may be difficult and expensive to acquire. These data include the temporal distribution of river stage, macro-channel surface and bedrock topography, spatial distribution of alluvial-hydraulic characteristics, and meteorological conditions (e.g. rainfall and evaporative demand). Incorporating vegetation water use in the model

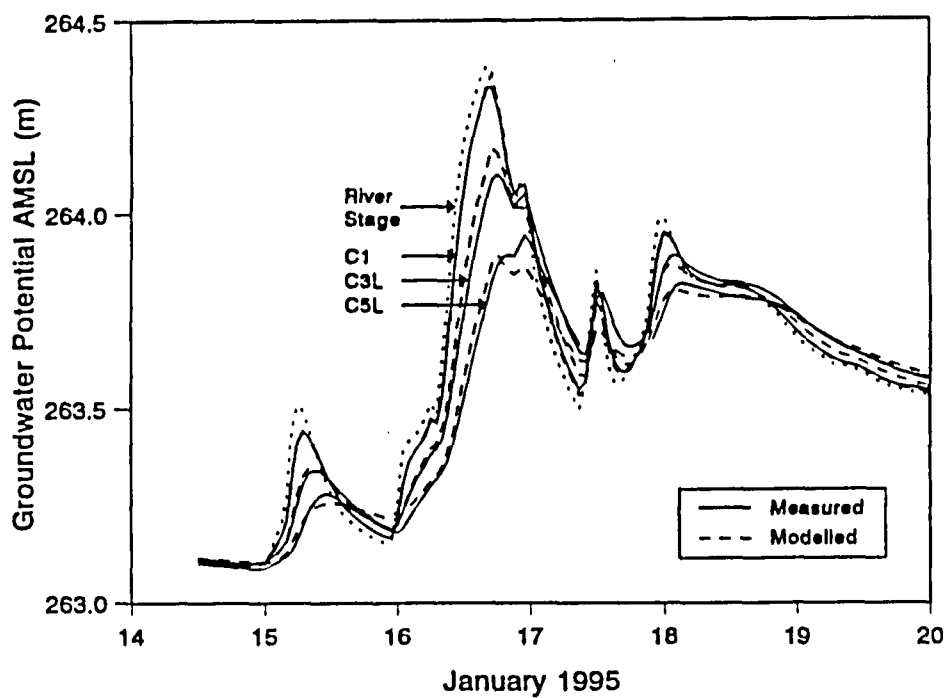


Figure 4a Measured and modelled groundwater responses along a cross-section through the study site.

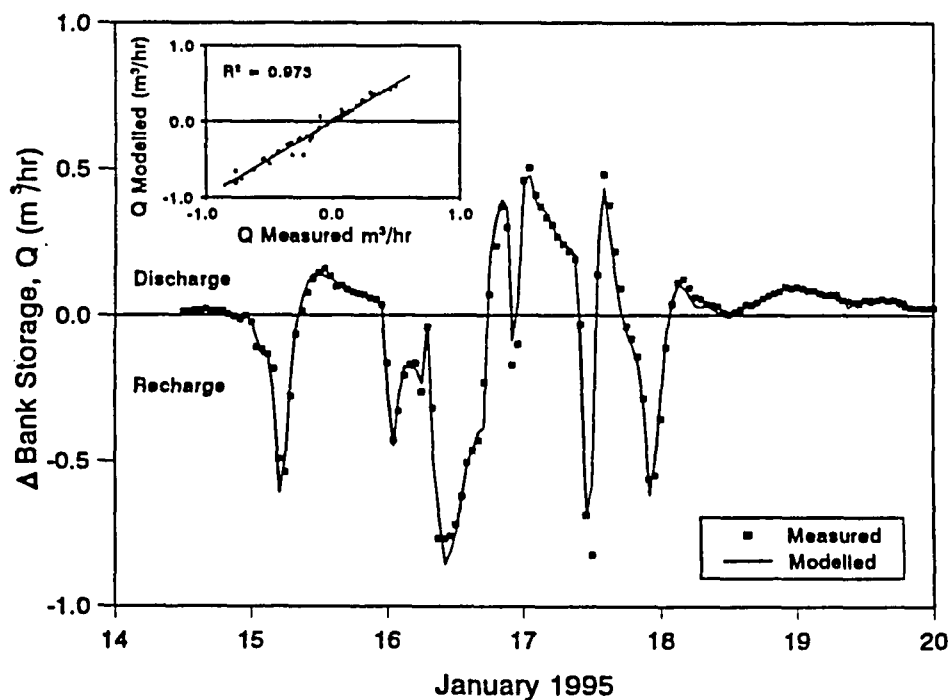
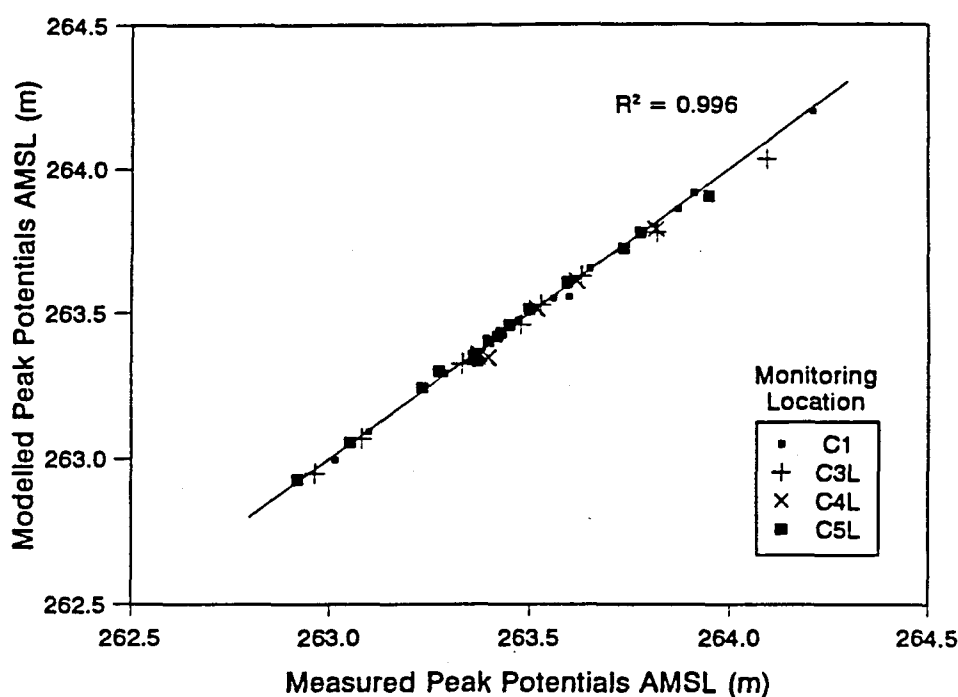


Figure 4b Change in volumetric bank storage along a cross-section through the study site.



**Figure 5** Correlation between measured and modelled peak groundwater potentials over the period December 1992 to January 1995.

requires additional data, including actual transpiration (a function of evaporative demand, water availability and vegetation type), and the spatial distribution of plant roots. Nevertheless, deterministic application of the saturated two-dimensional (uncalibrated) model demonstrated that the general response of the alluvial groundwater to changes in river stage may be acceptably predicted with moderate data requirements.

The bank storage model was also applied deterministically to simulate the temporal water content distribution in a profile through the unsaturated zone. The modelling was conducted using measured transpiration data from a *Ficus sycomorus* tree to determine the relative importance of bank seepage in providing water to the riparian vegetation. Good agreement between predicted and observed water contents was obtained (Figure 6), despite the necessary approximations required to characterise the highly stratified deposit, distribution of plant roots, and rainfall at the site. Soil water contents in the unsaturated zone were monitored using a neutron probe, and these data were calibrated using gravimetrically determined soil water contents. The results of the simulation clearly emphasize the importance of lateral seepage from the river as the mechanism recharging subsurface water to support transpiration, as illustrated by the cumulative fluxes in Figure 7. As a consequence of the good lateral hydraulic connectivity at the study site, the vegetation showed no symptoms of

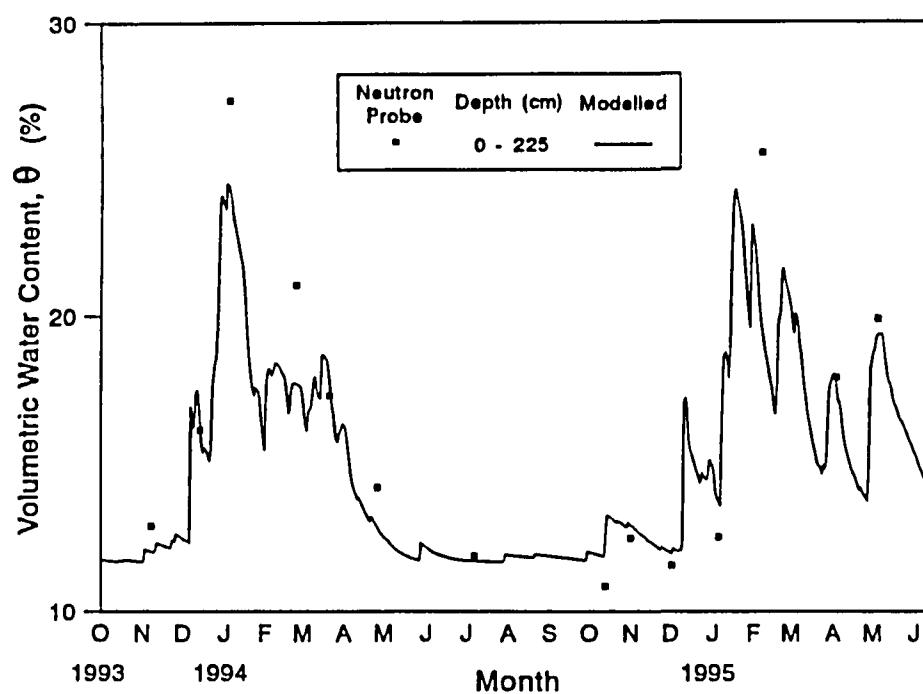


Figure 6 Measured and modelled changes in water content for a profile through the unsaturated zone at the study site.

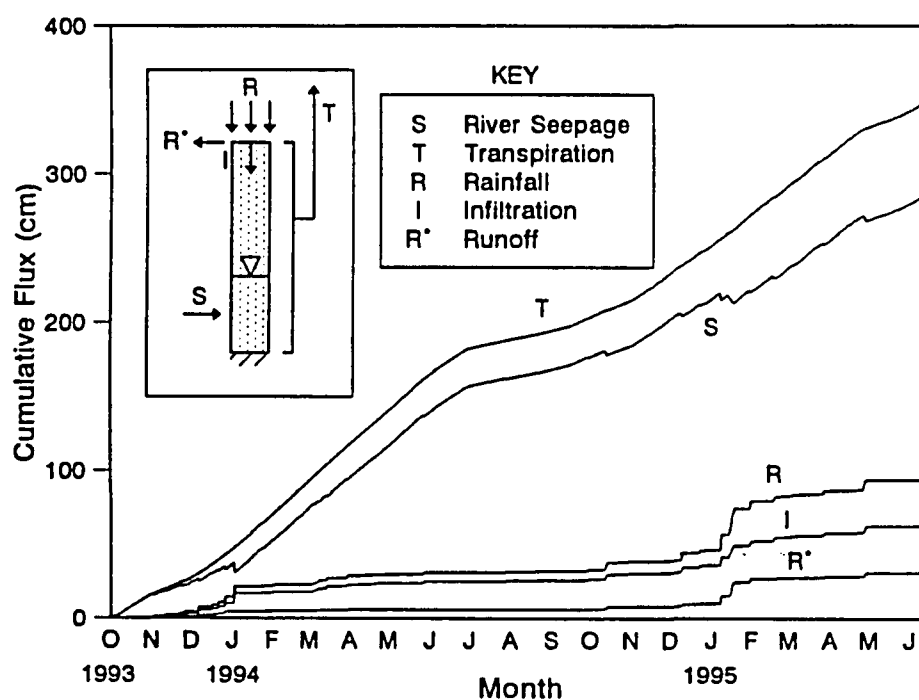


Figure 7 Cumulative fluxes defining the water balance for the soil column below a *F. sycomorus* tree at the study site.

water stress even during low flow conditions, and it was concluded that the vegetation at the site would transpire at near potential rates provided there was flow in the active channel.

Bank seepage provided for 95% of the water use during the winter of 1994, and 74% and 80% of the water use during the summers of 1993/94 and 1994/95, respectively. These results show the modest contribution that rainfall infiltration makes to transpiration during summer (20% to 25%), and the almost total dependence of vegetation transpiration on surface flow during winter. It is therefore quite clear that adequate base flows should be maintained to ensure that the consumptive water requirements of the riparian vegetation are met.

#### 4 Transpiration by Riparian Vegetation

The transpiration component of the riparian water balance was modelled empirically because this approach has previously been used successfully for trees growing under circumstances of non-limiting water availability, and because it was necessary to develop a model whose input data requirements are easily satisfied. Consequently, a simple regression modelling approach was used, since a more process-based approach would require data such as stomatal conductance or aerodynamic roughness of the canopy which would be very difficult to collect for the whole 114 km section of the river. As a result, a simpler route was followed, and two models were developed, one for riparian trees and the other for the abundant reed species, *Phragmites mauritianus*.

##### 4.1 Transpiration by Trees

The strategy used to model the transpiration by trees was first to concentrate data collection at the Narina study site. This was achieved by monitoring a *Ficus sycomorus* tree continuously over a two and a half year period and comparing its transpiration rates to other trees (*Berchemia zeyheri*, *Diospiros mespiliformis*, *Trichilia emetica*, *Spirostachys africana*) at the site during four intensive water use sampling surveys. Further research was also conducted to determine whether there were significant differences between the dominant riparian species in a survey of transpiration rates along the Sabie River. This survey also included the species *Combretum erythrophyllum*, *Acacia robusta*, *Breonadia salicina* and *Syzgium guineense*.

The transpiration rates of the trees at the study site were found to be strongly correlated (Figure 8), as were the rates for the broader spectrum of riparian trees. This correlation indicated that all the trees were responding to the same environmental stimuli, and had continual access to phreatic water. The relative ranking in the daily transpiration of the trees

sampled at the Narina site also remained relatively constant through the course of the study despite large changes in transpiration from one sample period to the next. The species comparison revealed that there were no significant differences in transpiration between the various riparian tree species, suggesting that in the riparian habitat, the absolute transpiration rate depended more on tree size than the species concerned. This also indicated that tree size could be used for extrapolating transpiration rates from one site to the river.

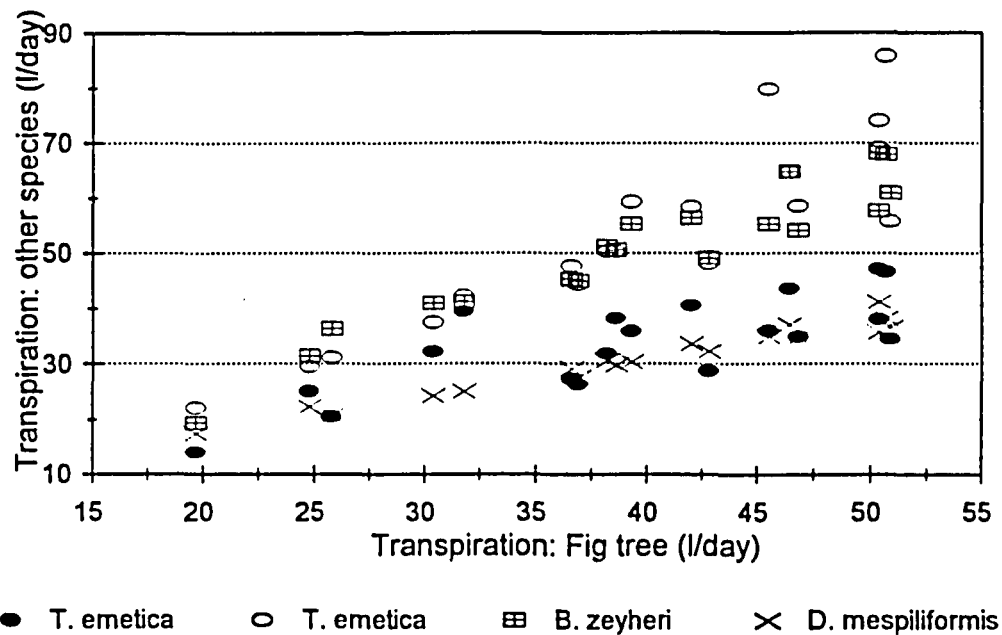


**Figure 8** Daily total transpiration rates recorded on five sample trees at the Narina study site over a period of 19 days during October 1994 showing the good correlation recorded between the reference fig tree and the remaining four species sampled.

Transpiration at the Narina site was found to vary strongly with season and between years of study. Peak transpiration rates were recorded in the latter half of summer, while the lowest transpiration rates were recorded prior to the onset of the summer rains towards the end of winter. The variability in transpiration corresponded approximately with that recorded in leaf area index (LAI) at the site (Figure 9), but it is not clear to what extent the changes in LAI were causative, or merely indicated a change in the phenology of the plants. Importantly, none of the trees at the Narina site showed any symptoms of water stress, even at the end of the dry winter season when streamflow was at its lowest. This suggests that the changing LAI was not a result of stress-induced leaf abscission, but rather reflected the natural phenology of the trees at the site.

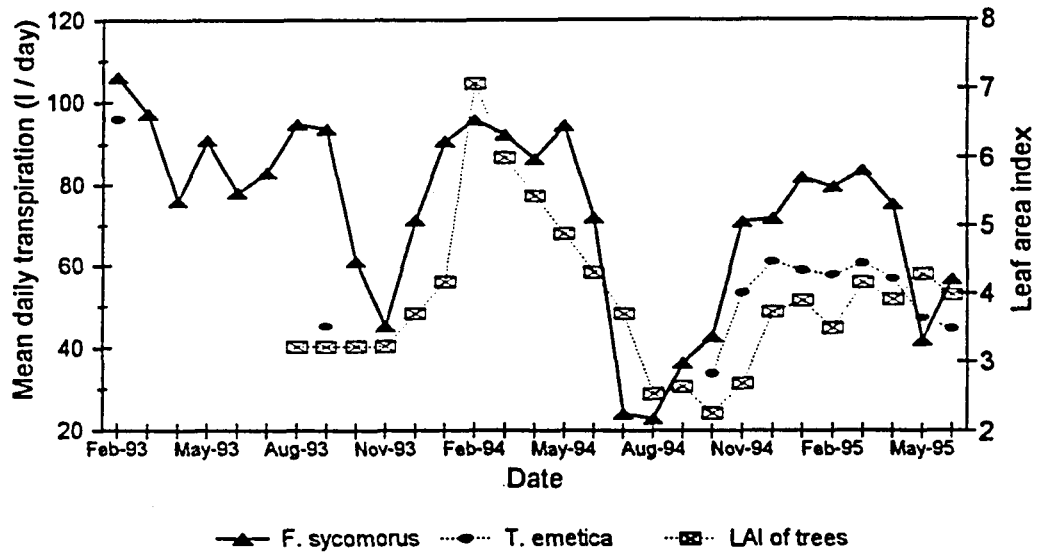


**Figure 9** Variation in the monthly, mean daily transpiration rates recorded for a *F. sycomorus* and *T. emetica* tree, and the corresponding variation in LAI recorded in the riparian forest at the Narina study site over the course of the study.

The generalised transpiration model developed for the *F. sycomorus* tree and *P. mauritianus* is given by

$$T = c_1LAI + c_2(1 - e^{-VPD}) + c_3z_{ps} + c_4$$

1

where

$T$  is the transpiration rate (litres/day)

$c_i$  is the  $i^{th}$  regression coefficient

$LAI$  is the leaf area index

$VPD$  is the mean daytime vapour pressure deficit (kPa)

$z_{ps}$  is the relative phreatic surface elevation (m)

The strong seasonal variation in the transpiration from the fig tree necessitated that the parameter values in Equation 1 change over the course of the study, resulting in different coefficients corresponding to months (Table 2). Despite the variation observed, a satisfactory model was developed ( $R^2 = 0.78$ ) with a particularly pleasing fit between observed and predicted transpiration rates for the period November 1993 to November 1994 (Figure 10). The transpiration model developed only requires one meteorological parameter ( $VPD$ ) which is non-linearly correlated with transpiration, and one vegetation parameter ( $LAI$ ). In addition, the model requires phreatic surface level data, indicating that transpiration is a function of river stage as determined by bank storage dynamics.



**Table 2** Parameter values for the *F. sycomorus* tree transpiration model (Equation 1)

Month	Regression coefficient			
	$c_1$	$c_2$	$c_3$	$c_4$
Jan	15.276	61.992	22.493	-83.416
Feb	-1.476	61.992	22.493	-12.182
Mar to Jun	21.052	61.992	22.493	-83.416
Jul	40.566	61.992	22.493	-143.773
Aug to Sep	21.052	61.992	22.493	-83.416
Oct	16.446	61.992	22.493	-83.416
Nov	13.499	61.992	22.493	-83.416
Dec	21.052	61.992	9.022	-83.416

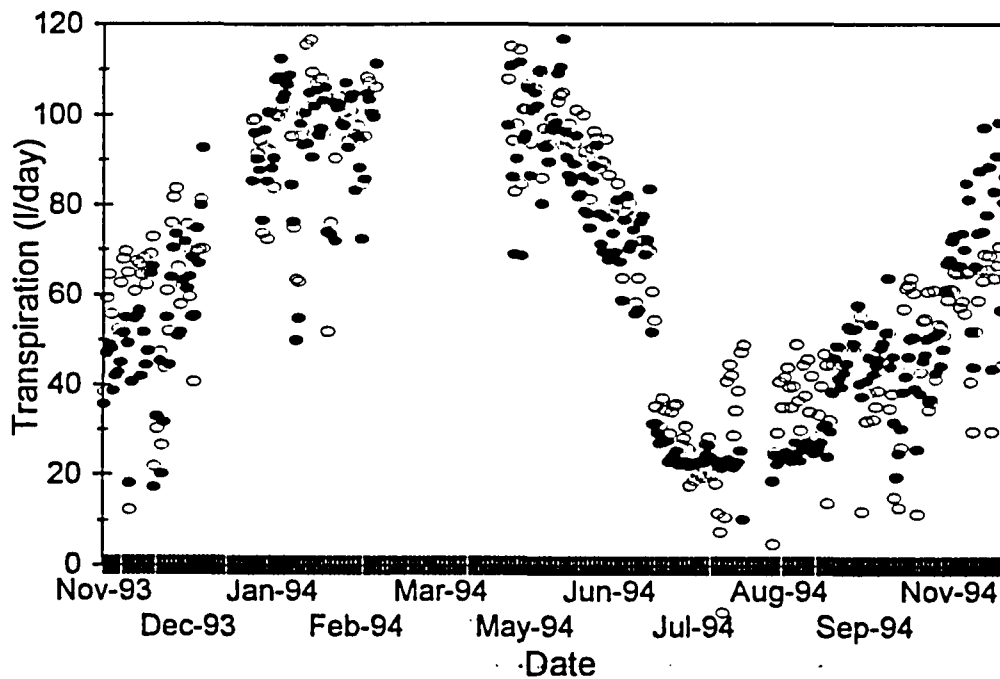


**Figure 10** Comparison between the observed transpiration recorded in the fig tree (●) and that predicted by the model (○) for the period November 1993 to November 1994.

The fact that water level is one of the parameters in the model is anomalous given the earlier statement that the trees at the Narina site were not found to suffer from water stress even during the height of the dry season (as shown by pre-dawn xylem pressure potential data). This suggests that the water level may be present as a surrogate for some other parameter which influences tree water use. One possibility is that the trees at the Narina site may well be nutrient limited, and the higher transpiration recorded during periods of high flow may be a result of the introduction of nutrients into the system.

#### **4.2 Transpiration by Reeds**

Transpiration measurements from the reed bed at Narina were made during three discrete periods ranging from 9 to 23 days in duration. Two of the surveys took place at the end of the dry season (September 1993 and October 1994), while the third survey was timed to coincide with a high-flow period in February 1995. In September 1993 the reed bed consisted predominantly of young, vigorously growing reeds, while those sampled in the subsequent surveys were progressively older with relatively more dead material in the reed bed. During each survey 16 reeds were sampled using heat balance technology which resulted in hourly and daily estimates of transpiration from the individual reeds. Following the survey the sample reeds were harvested to determine their leaf areas. These data were used to determine the transpiration per unit leaf area for each reed. The median transpiration per unit leaf area was then multiplied by the LAI measured in the reed bed to estimate transpiration in millimetres.

As was the case in the trees, the variation in transpiration rates recorded in individual reeds was highly correlated. The absolute transpiration rates were high averaging 12 mm/day in summer and 7 mm/day in winter, indicating that reeds are significant water users. While these rates are high, they are reasonable given the evaporative demand and free access to groundwater water at the site.

There was considerable variation in the absolute transpiration rates recorded both between individual reeds, and over the three survey periods. The highest transpiration rates were recorded during the September 1993 and February 1995 surveys, while the rates recorded during October 1994 were about only half that recorded in the other surveys. It is not clear what caused this difference, although it is possible that both reed age and season may play a role.

Two empirical transpiration models were developed for the reeds by categorising the data according firstly by age class (young and mature), and secondly by season (winter and summer). The parameter values for the alternate models are given in Table 3. Note that the output from the

models presented in Table 3 must be multiplied by an estimate of the LAI of the reed bed to estimate transpiration in mm/day.

**Table 3** Parameter values (Equation 1) for the two models that predict transpiration in litres per square centimetre of foliage per day from a *P. mauritanus* reed bed

Model	Age class and season	Regression coefficient			
		$C_1$	$C_2$	$C_3$	$C_4$
Model 1	Young	0	2.200	0	2.822
	Mature	0	2.200	0	0.849
Model 2	Young	0	3.431	0	2.223
	Mature Winter	0	3.431	0	-0.214
	Summer	0	3.431	0	0.899

### 4.3 Transpiration Losses from the Study Site

Transpiration losses from the trees at the study site were determined by applying the transpiration model (Equation 1 and Table 2), taking into account the linear relationship between the transpiration rate (per unit basal area) of the reference *F. sycomorus* tree and the other trees sampled at the Narina site. This resulted in an estimate of the total transpiration per unit basal area of trees at the site, and was multiplied by the total basal areas of each of the dominant species to estimate the total daily transpiration of trees rooted in the study area.

Transpiration from the trees was found to be conservative, averaging 2.8 mm/day and 1.6 mm/day for summer and winter respectively (Figure 11). The rates are considered conservative given the free availability of water at the site, and high evaporative demand in the semi-arid environment. It was felt that the conservative rates may be a consequence of the age of the trees, older trees having been shown to have reduced transpiration rates per unit leaf area as a consequence of an obstructed hydraulic architecture. The above estimate does not include transpiration from all the species at the site, as some were either structurally unsuitable (multi-stemmed shrubs) for measurement, or too ephemeral as was the case for sub-canopy grasses and forbes. It was estimated that these species may have comprised as much as 30% of the foliage at the site, resulting in an equivalent under-estimation in transpiration.

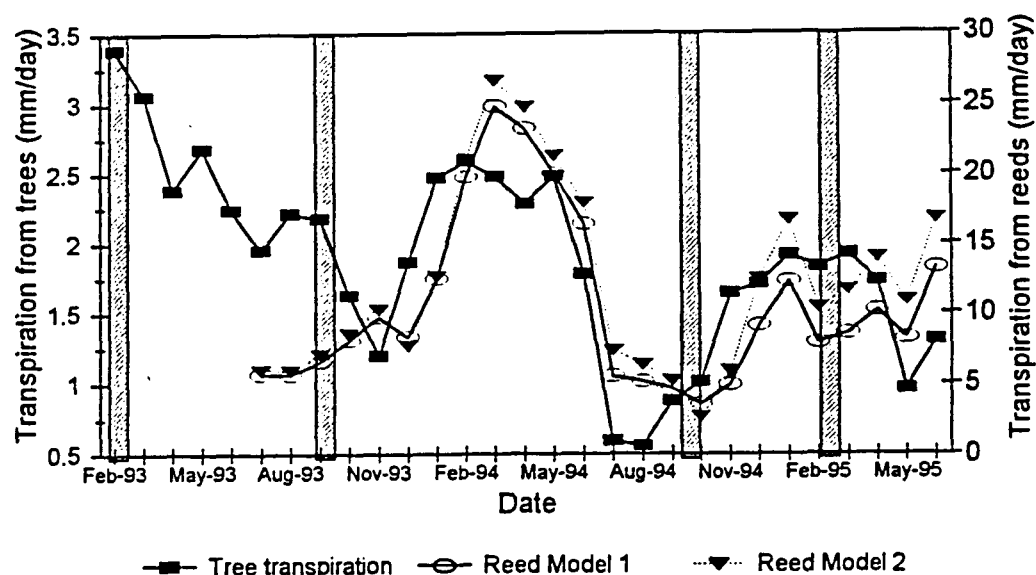


**Figure 11** Monthly, mean daily transpiration rates estimated for all the trees at the Narina study site, and the output from the two reed model simulations for February 1993 to June 1995. The cross-hatched areas indicate those periods of intensive measurements of transpiration from the tree species.

There was also a clear seasonal trend in transpiration peak rates being recorded during the latter part of summer, and lower rates during the latter part of the winter (Figure 11). This trend is consistent with those illustrated for the fig tree transpiration and riparian forest LAI illustrated in Figure 9.

Transpiration from the *P. mauritianus* reed bed was calculated by applying the generalised model (Equation 1) to the area colonised by reeds, with appropriate coefficients from Table 3 to account for the age class and time of year. The modelled rates for the period January 1994 to June 1994 consistently averaged more than 15 mm/day (Figure 11) and are considered unrealistically high and require further verification.

#### 4.4 Transpiration Losses from the Sabie River

The consumptive water use of the riparian vegetation along the Sabie River in the KNP was estimated using three methods. Firstly, the mean monthly modelled transpiration from trees at the Narina site was extrapolated to the extent of the river in the KNP. Secondly, the long-term mean Symons pan evaporation estimate was multiplied by the total area of the riverine forest on the Sabie River. Thirdly, the data from a low flow weir gauging study

were interpreted. A summary of these results, together with the transpiration losses for trees and reeds from the study site is given in Table 4.

**Table 4** Summary of transpiration losses for trees and reeds at the study site, and extrapolation to the Sabie River, KNP

Study Site	Winter	Summer	Annual
Trees	1.6 mm/day ‡	2.8 mm/day ‡	2.0 mm/day ‡
Reeds	7 mm/day ‡	12 mm/day ‡ 25 mm/day ↑	9.2 mm/day ‡
<b>Sabie River, KNP</b>			
Transpiration Modelling	0.25 m <sup>3</sup> /s ↓	1.51 m <sup>3</sup> /s ↑	0.84 m <sup>3</sup> /s ‡
Symons pan			1.54 m <sup>3</sup> /s ‡
Weir gauging	0.46 m <sup>3</sup> /s ‡		

↓ minimum, ↑ maximum, ‡ average

The results of the above methods were all in good agreement, with the Symons pan estimate giving the highest mean annual evaporation rate of 1.54 m<sup>3</sup>/s. The highest mean monthly results from the site-specific transpiration extrapolation was 1.51 m<sup>3</sup>/s and the lowest 0.25 m<sup>3</sup>/s, for February 1993 and August 1994, respectively. The water balance determined from weir discharge gauging resulted in an average low flow loss for winter of 0.46 m<sup>3</sup>/s.

The relative seasonal demand of the riverine vegetation for water was determined by comparing the total transpiration for the vegetation against the discharge recorded at the Narina site. It was found that the proportion of the river discharge required to meet the consumptive use of the riparian forest increases steadily through the winter months (Figure 12), and the vegetation was estimated to consume up to 41% (August 1993) of the river discharge recorded at the study site. The importance of this is that the relative demand for water is highest during that period when the supply is at its lowest.

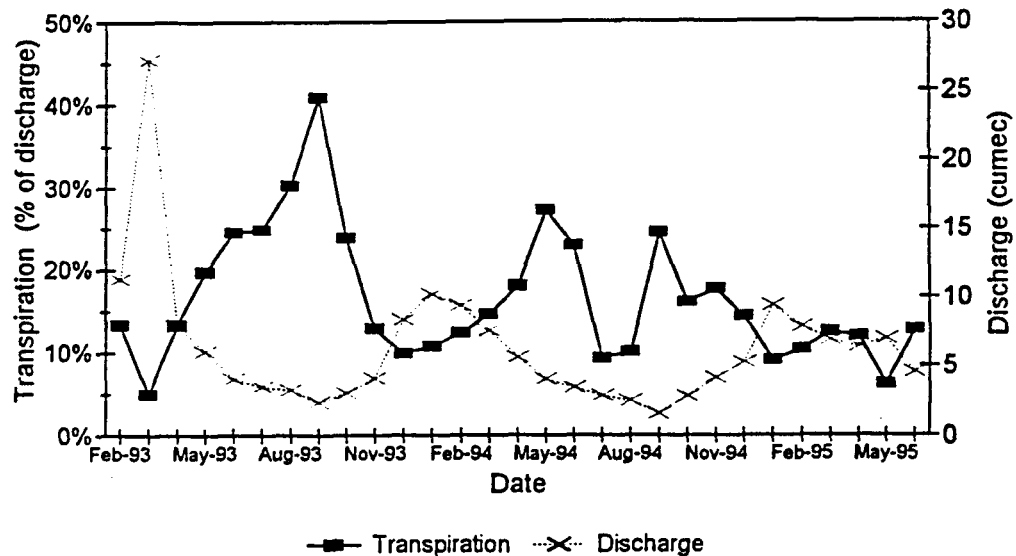


**Figure 12** Estimated consumptive water use from the riverine vegetation on the Sabie River as a percentage of the recorded discharge from February 1993 to June 1995.

## **5 Recommendations for Further Research**

### **5.1 Flow Requirements for the Vegetation in the Anastomosing Geomorphological Channel Types**

The extensive influence of bedrock in the Sabie River system has important implications for estimating the consumptive water use of riparian vegetation, since irregular bedrock topography obstructs seepage from surface flow. Flow variability (resulting in surface flooding) is a fundamental process recharging subsurface storage and local riparian vegetation in variable source supply areas of the river. This was demonstrated by the extensive riparian tree mortalities observed in 1991/92, which were strongly correlated with bedrock influence. The areas with bedrock influence also coincide with the sections of the river where the riparian forest is best developed and at its widest. It is therefore imperative that the flow regimes be tailored to suit the rehydration of the isolated alluvial deposits to ensure the survival of the forest that has developed in these areas:—There is consequently an urgent need to determine the water use by riparian vegetation in bedrock dominated morphologies. These data can then be used to optimise the delivery of water to the river to ensure that at least the consumptive needs of the riparian forest in the anastomosing sections of the river are met. If this is achieved, the results of this study suggest that the needs of the trees situated on alluvial substrate such as that at Narina, will also automatically be met.

## **5.2                      Developing Early Warning Systems to Prevent Mortality of the Riparian Forest**

It is important to develop techniques that can be used to monitor the response of vegetation in these bedrock influenced sections of the river to the altered flow regimes and also to develop methods that will serve as an early warning system so that unnecessary mortality can be prevented. This is particularly relevant given the future ability to regulate flows through releases from the Injaka Dam. Two techniques should be considered here, including growth increment measurements and the development of techniques to measure the spatial distribution of LAI. Since LAI reflects the integrated soil moisture status of the site, trees on sites experiencing water stress will drop leaves and therefore the change in LAI on these sites will be out of phase with those on parts of the system adequately supplied with water. This measurement is likely to be particularly useful as it will allow the sections of the river most sensitive to changes in the flow regime to be identified. It may also be of value to establish long-term monitoring of tree growth, population density, and LAI.

## **5.3                      Verification of Tree and Reed Transpiration Data**

It is important to stress that further research should also focus on verifying the consumptive water use estimates produced by this study and validating the model outputs. It is suggested that accurate manual flow gauging would provide a suitable test of the transmission losses for low flow periods determined in this study. In addition, further measurements need be made on the water use of reed beds, as the estimates based on results from the application of the heat balance technique on individual reeds in this study were not entirely satisfactory. It is also necessary to validate and verify the transpiration rates estimated by the two reed models presented in this study, particularly as reeds are a dominant vegetation type in the Sabie River system. It is suggested that a more integrative method such as the Bowen Ratio technique be used to derive independent estimates of transpiration to compare to those derived using the heat balance technique. A project, which will commence in 1997, has been initiated by the Water Research Commission to address this need.

## **5.4                      General**

The interaction between river and subsurface flow is important in seasonal and ephemeral river systems (e.g. Letaba River), where upstream flows must be specified to satisfy ecological requirements downstream. The need to address the interaction between alluvial storage and flow activation in these infrequently active river systems has arisen in numerous workshops conducted to establish the ecological instream flow requirements (IFR's) of rivers across Southern Africa.

Continued data collection (biotic and abiotic) along the Sabie River and meteorological data collection at the Narina site initiated within this project and other projects is required to improve the knowledge base and provide data for future simulations and models generated by projects within the KNP Rivers Research Programme.

## 6 Conclusions

Models describing river hydraulics, dynamic bank storage and transpiration by riparian vegetation have been developed and verified, based on intensive data collection at the Narina site on the Sabie River. Integrated transpiration, bank storage, and river hydraulics modelling at the study site shows average seasonal daily consumptive water use by the riparian trees to be 1.6 mm/day and 2.8 mm/day during winter and summer, respectively. Reeds exhibit significantly higher water demands, estimated during winter and summer at 7 mm/day and 12 mm/day, respectively. These rates represent near potential consumptive losses. Predictions from the reed transpiration model were unrealistically high ( $> 15$  mm/day), and the model requires further validation.

The results of the integrated modelling emphasize the need to maintain adequate base flows during winter for alluvial sections of the historically perennial river. This was particularly the case as the data showed transpiration accounted for up to 41% of the winter base flow at the end of the dry season. The results of the three methods used to estimate the consumptive water use by the riparian vegetation along the Sabie River (KNP) over the course of the study compare well. Transpiration losses account for a range of the river's flows, from a minimum of  $0.25 \text{ m}^3/\text{s}$  in winter to a maximum of  $1.54 \text{ m}^3/\text{s}$  in summer.

## 7 Bibliography

Birkhead, A.L., Olbrich, B.W., James, C.S. and Rogers, K.H., in press. Developing an Integrated Approach to Predicting the Water Use of Riparian Vegetation. *Water Research Commission Report No. 474/1/96, Volume 1*. Water Research Commission, South Africa.

Broadhurst, L.J., Heritage, G.L., van Niekerk, A.W., James, C.S. and Rogers, K.H., in press. Translating Hydrological Output into Local Hydraulic Conditions on the Sabie River, Kruger National Park. *Water Research Commission Report No. 474/2/96, Volume 2*. Water Research Commission, South Africa.

Heritage, G.L., van Niekerk, A.W., Moon, B.P., Rogers, K.H. and James, C.S., in press. Geomorphological Responses of the Sabie and Letaba Rivers to Changing Flow and Sediment Regimes. *Water Research Commission Report No. 376/1/96, Volume 1*. Water Research Commission, South Africa.



## **ACKNOWLEDGEMENTS**

---

The funding of this project by the Water Research Commission is gratefully acknowledged, as are contributions by the steering committee consisting of the following members:

Dr P.C.M. Reid	Water Research Commission (Chairman 1992 to 1994)
Dr S. Mitchell	Water Research Commission (Chairman 1995)
Mr D.S. van der Merwe	Water Research Commission
Mr D. Huyser	Water Research Commission (Committee Secretary)
Mr J.M. Bosch	Enviromentek, CSIR
Mr C. Bruwer	Department of Water Affairs and Forestry
Prof J.M. de Jager	University of the Free State

The study was supported financially and materially by the Mazda Wildlife Fund and ISS International Ltd., and logistically by the National Parks Board.

The field work support provided by M. Oelofse (Department of Civil Engineering, University of the Witwatersrand); G. Heritage and L. Broadhurst (Centre for Water in the Environment, University of the Witwatersrand); P. Frost (King's College, London University); G. Strydom, P. Mdlomo, G. Mauleke and J. Mabosa (Kruger National Park); T. Poulter, D. Mapanga, S. Soko and K. Hudson (Environmentek, CSIR) contributed significantly to this project, and it is appreciated.

## CONTENTS

---

Title Page	
Extended Executive Summary	i
Acknowledgements	xx
Contents	xxi
List of Acronyms	xxv
List of Figures	xxvi
List of Tables	xxxv
1 Introduction	1.1
1.1 Background	1.1
1.2 Project Objectives	1.2
1.3 Interdisciplinary Study	1.3
1.4 Conceptual Model of the Riparian Water Balance	1.3
2 Data Collection	2.1
2.1 Study Site Locality	2.1
2.2 Groundwater Model Data Collection	2.3
2.2.1 Monitoring System for Groundwater and River Stage	2.3
2.2.2 Monitoring Soil Moisture in the Unsaturated Zone	2.10
2.2.3 Delineating Groundwater Flow Boundaries	2.20
2.2.4 Fluvial Sediment Characteristics	2.22
2.3 Transpiration Model Data Collection	2.28
2.3.1 Meteorological Conditions	2.28
2.3.2 Leaf Area Surveys	2.36
2.3.3 Pre-Dawn Xylem Pressure Potentials	2.40
2.3.4 Transpiration from Trees	2.41
2.3.5 Reed Transpiration	2.58
3 Modelling River Hydraulics	3.1
3.1 Scope	3.1
3.2 River Hydraulics Pilot Study	3.1
3.2.1 Study Reach Morphology, Riparian Vegetation and Location of Cross-Sections	3.1

3.2.2	Hydraulics Data Collection . . . . .	3.5
3.2.3	Rating Curves . . . . .	3.5
3.2.4	Total Flow Resistance . . . . .	3.8
3.2.5	Synthesis of Rating Curves Using Flow Resistance Data for Similar Morphological Channel Types . . . . .	3.12
3.3	Synthesis of Rating Curves from Local Stage and Remote Discharge Monitoring Using Nonlinear Muskingum Routing . . . . .	3.17
3.3.1	Scope . . . . .	3.17
3.3.2	Muskingum Models . . . . .	3.18
3.3.3	Parameter Evaluation . . . . .	3.21
3.3.4	Model Verification . . . . .	3.26
3.3.5	Model Application . . . . .	3.30
4	Modelling Bank Storage Dynamics . . . . .	4.1
4.1	Model Development . . . . .	4.1
4.1.1	Groundwater Flow in the Saturated Zone . . . . .	4.1
4.1.2	Soil Water in the Unsaturated Zone . . . . .	4.29
4.1.3	Coupling Saturated and Unsaturated Flow Models . . . . .	4.36
4.1.4	Modelling Soil-Hydraulic Characteristics . . . . .	4.40
4.2	Bank Storage Model Code Validation . . . . .	4.43
4.2.1	Scope . . . . .	4.43
4.2.2	Groundwater Flow in the Saturated Zone . . . . .	4.45
4.2.3	Soil Water in the Unsaturated Zone . . . . .	4.69
4.2.4	Coupled Saturated and Unsaturated Models . . . . .	4.76
4.3	Bank Storage Dynamics Model Verification . . . . .	4.85
4.3.1	Scope . . . . .	4.85
4.3.2	Saturated Flow . . . . .	4.86
4.3.3	Unsaturated Flow . . . . .	4.95
5	Transpiration Modelling . . . . .	5.1
5.1	Introduction . . . . .	5.1
5.1.1	The Data Sets and Time Step of the Transpiration Models . . . . .	5.1

5.2	Methodology	5.1
5.2.1	Identifying Outliers/Influential Points	5.2
5.2.2	Model Selection	5.2
5.2.3	Random and Normal Residuals and Regression Adequacy	5.3
5.2.4	Collinear Predictors and Significant Coefficients	5.3
5.3	Modelling Transpiration from the Fig Tree.	5.4
5.3.1	Monthly Indicators and Slope Variables	5.4
5.3.2	The Predictive Model for Transpiration from the Reference Fig Tree	5.5
5.4	Modelling Transpiration from the Reeds	5.12
5.4.1	Season/Age Indicators and Slope Variables	5.12
5.4.2	What is the Most Appropriate Measure of the Mean Water Use of the Reed Bed?	5.13
5.4.3	Transformation of Vapour Pressure Deficit	5.14
5.4.4	Models Derived for the Mean Daily Transpiration of the Reed Bed	5.15
5.4.5	The Distribution of Residuals for the Reed Models	5.16
6	Sabie River Riparian Water Balance	6.1
6.1	Potential Transpiration Losses	6.1
6.1.1	Transpiration from the Narina Site	6.1
6.1.2	Scaling the Transpiration Model from Narina to the Sabie River	6.9
6.1.3	Seasonal and Long Term Trends in Transpiration	6.11
6.2	The Sabie River Riparian Water Balance in the Kruger National Park in Perspective	6.13
6.3	Water Balance Between Gauging Stations	6.14
6.3.1	Transmission Losses	6.14
6.3.2	Water Supply to Rest Camps	6.15
6.3.3	Losses to Evapotranspiration, Animal Consumption and Regional Aquifers	6.16
6.4	Water Balance in the Unsaturated Zone at the Narina Study Site from Neutron Probe Measurements	6.17

6.5	Diurnal River Stage Fluctuations . . . . .	6.18
7	Discussion, Conclusions and Recommendations . . . . .	7.1
7.1	Scope . . . . .	7.1
7.2	Intensive Data Collection and Integrated Modelling . . . . .	7.1
7.2.1	The Need for an Integrated Modelling Approach in Semi-Arid River Systems . . . . .	7.1
7.2.2	River Hydraulics . . . . .	7.1
7.2.3	Bank Storage Dynamics . . . . .	7.3
7.2.4	Transpiration by Riparian Vegetation . . . . .	7.4
7.2.5	Extending the Integrated Modelling Approach . . . . .	7.6
7.3	Riparian Water Balance at the Study Site . . . . .	7.7
7.3.1	Distribution of Subsurface Water in the Saturated and Unsaturated Zones . . . . .	7.7
7.3.2	Transpiration . . . . .	7.8
7.4	Riparian Water Balance Along the Sabie River in the KNP in Relation to Water Demands in the Catchment . . . . .	7.9
7.5	Recommendations . . . . .	7.10
7.5.1	Data Archiving . . . . .	7.10
7.5.2	Technology Transfer and Research Priorities . . . . .	7.12
8	References . . . . .	8.1
9	Appendices . . . . .	9.1
	Chapter 2 Data Collection . . . . .	9.1
	Chapter 3 Modelling River Hydraulics . . . . .	9.10
	Chapter 4 Modelling Bank Storage Dynamics . . . . .	9.16

## **LIST OF ACRONYMS**

---

AMSL	Above mean sea level
cumec/s	cubic metre/s per second
DF	Dupuit-Forcheimer
HPV	Heat pulse velocity
KNP	Kruger National Park
KNPRRP	Kruger National Park rivers research programme
LAI	Leaf area index
MAR	Mean annual runoff
PAR	Photosynthetically active radiation
RH	Relative humidity
VPD	Vapour pressure deficit

## LIST OF FIGURES

---

### Chapter 1 Introduction

- 1.1 Water balance across a two-dimensional vertical section through the riparian zone, showing component models . . . . . 1.4
- 1.2 Data required for development and application of the riparian water balance model, with the fundamental interactions between components of the system . . . . . 1.5

### Chapter 2 Data Collection

- 2.1 Location of study site along the Sabie River in the Kruger National Park . . . . . 2.2
- 2.2 Layout of the groundwater monitoring system at the study site 2.4
- 2.3 Design of two nested piezometers at a monitoring location, showing piezometer tip detail . . . . . 2.6
- 2.4 Cable network for connecting the pressure transmitters, data recorders, power supply and laptop link . . . . . 2.7
- 2.5 Plot of daily variations in the battery potential difference and solar charge from 15 to 20 January 1994 . . . . . 2.9
- 2.6 Design of river stage monitoring system . . . . . 2.10
- 2.7a Relative changes in neutron probe count ratios at location 5C-D (Fig. 2.2) over the seasons (i)1993/94 and (ii)1994/95 . 2.12
- 2.7b Relative changes in neutron probe count ratios at location 4C-D (Fig. 2.2) over the seasons (i)1993/94 and (ii)1994/95 . 2.13
- 2.7c Relative changes in neutron probe count ratios at location 3C-D (Fig. 2.2) over the seasons (i)1993/94 and (ii)1994/95 . 2.14
- 2.7d Relative changes in neutron probe count ratios at location 3U-C (Fig. 2.2) over the seasons (i)1993/94 and (ii)1994/95 . 2.15
- 2.7e Relative changes in neutron probe count ratios at location 4U-C (Fig. 2.2) over the seasons (i)1993/94 and (ii)1994/95 . 2.16
- 2.7f Relative changes in neutron probe count ratios at location 5U-C (Fig. 2.2) over the seasons (i)1993/94 and (ii)1994/95 . 2.17
- 2.7g Relative changes in neutron probe count ratios at location C3-4 (Fig. 2.2) over the seasons (i)1993/94 and (ii)1994/95 . 2.18
- 2.8 (a) Neutron probe and (b) gravimetrically determined water content profiles . . . . . 2.19
- 2.9 Calibration of the neutron probe using volumetric water content data from location C3-4 . . . . . 2.20
- 2.10 Cross-section through the central monitoring line (Fig. 2.2) showing the bedrock profile and stratified fluvial deposit . . . . 2.21
- 2.11 Groundwater flow boundaries encompassing the macro-channel infill deposit at the Narina study site (Fig. 3.1) . . . . . 2.22
- 2.12 Sediment size distributions along vertical profiles at locations (a) C3 and (b) C5 of Fig. 2.2 . . . . . 2.23

2.13	Stratified profile at C3-4 . . . . .	2.25
2.14	Equation 4.73 (after van Genuchten, 1978) fitted to water retention data for the four characteristic sediment types in Table 2.4 . . . . .	2.27
2.15	Total monthly rainfall recorded at Skukuza from December 1992 to June 1995 . . . . .	2.30
2.16	A summary of monthly daytime temperature (a), relative humidity (b), VPD (c), PAR (d) and wind speed (e) recorded at the Narina site from December 1992 to June 1995 . . . . .	2.32
2.17	Hourly temperatures recorded at Narina from 25 June to 5 July 1994 . . . . .	2.33
2.18	A frequency distribution of mean hourly, daytime wind speeds recorded for four periods during the year in 1993 . . . . .	2.34
2.19	A frequency analysis of mean hourly daytime wind speeds analysed by time of day for the year 1993 . . . . .	2.35
2.20	Wind roses illustrating the frequencies with which wind was recorded from each of the various wind directions for the years 1993 and 1994 . . . . .	2.36
2.21	The spatial variation in the leaf area index over the study site. The x axis represents the distance (m) along a transect which runs perpendicularly towards the river. Position 0 on the x axis is situated on the fringe of the riparian forest away from the river and position 80 is situated very close to the open river channel . . . . .	2.37
2.22	The leaf area index distribution of <i>F. sycomorus</i> across the study site . . . . .	2.37
2.23	The leaf area index distribution of the reed <i>P. mauritianus</i> across the study site . . . . .	2.37
2.24	The change in LAI recorded at the Narina study site in the trees, reeds and the site as a whole from September 1993 to June 1995 . . . . .	2.39
2.25	Pre-dawn xylem pressure potentials recorded on six species at the Narina study site. The species names have been abbreviated to: B. zey ( <i>Berchemia zeyheri</i> ), D. mesp ( <i>Diospiros mespiliformis</i> ), F. syc ( <i>Ficus sycomorus</i> ), T. emet ( <i>Trichilia emetica</i> ), and S. afr ( <i>Spirostachys africana</i> ) . . . . .	2.40
2.26	A schematic diagram illustrating a cross-section through a stem and the probe implantation strategy used on the sample trees. d1 to d4 represent the increasing depths to which the single thermistor bead in each probe is implanted beneath the cambium . . . . .	2.44



2.27	Daily transpiration rates recorded in the reference <i>F. sycomorus</i> tree for the period 11 February 1993 to 5 June 1995. The figure also illustrates the transpiration rates recorded by a <i>T. emetica</i> tree at the site for the periods when it was monitored . . . . .	2.46
2.28	Variation in the monthly mean daily transpiration recorded in the reference <i>F. sycomorus</i> and the <i>T. emetica</i> (river) tree, and the variation in LAI recorded in the riparian forest over the course of the study . . . . .	2.47
2.29	Trends in the monthly mean daily transpiration from the <i>F. sycomorus</i> tree, discharge measured at the Narina site, and monthly rainfall recorded over the course of the study. In the figure the rainfall data have been divided by ten to facilitate comparison with the other data presented . . . . .	2.48
2.30	Mean daily total transpiration recorded for the six tree species sampled at the Narina site for the four intensive transpiration sampling surveys conducted . . . . .	2.51
2.31	Transpiration rates recorded in the five sample trees over the course of a cloudless day (14 February 1993). The recorded transpiration rates have been scaled by expressing the actual rate as a proportion of the maximum rate achieved by each individual on the particular day . . . . .	2.52
2.32	The relationship between the transpiration rate recorded in the reference <i>F. sycomorus</i> tree and the other four tree species sampled at the Narina site. The data in the figure were taken from a two week sample period in October 1994 . . . . .	2.53
2.33	Box and whisker plots illustrating the daily transpiration recorded for each of the trees sampled in the species comparison. The mean (-), median (...), 90th, 75th, 25th and 10th percentiles of the recorded transpiration rates are illustrated. The extremes are also illustrated ( ) where these fall beyond the 90th and 10th percentiles . . . . .	2.56
2.34	Box and whisker plots illustrating daily transpiration recorded for each of the trees sampled in the species comparison. These data have been adjusted for differences in stem cross-sectional area (a proxy for tree size). The mean (-), median (...), 90th, 75th, 25th and 10th percentiles of the recorded transpiration rates are illustrated. The extremes are also illustrated ( ) where these fall beyond the 90th and 10th percentiles . . . . .	2.57

2.35	i. (Left) Illustration of the stem steady state heat energy balance. Heat energy flux components are represented by arrows. Terms <i>Eheater</i> , <i>Eup</i> , <i>Edown</i> , and <i>Eradiat</i> are determined directly using sensors and <i>Esap</i> is determined by subtraction of the latter three terms from <i>Eheater</i> , ie. $Esap = Eheater - Eup - Edown - Eradiat$ . ii. (Right) Diagram showing the conceptual components of the SSHEB technique gauge and the terms used in discussing the computational theory associated with its sensing components . . . . .	2.59
2.36	The mean daily transpiration of sixteen reeds sampled at each of three field survey sessions at the Narina study site . . . . .	2.62
2.37	The mean daily transpiration of sixteen reeds assessed at each of three field surveys at the Narina study site. The transpiration rates have been adjusted for differences in leaf area between the sample reeds to derive estimates of transpiration per unit leaf area . . . . .	2.62

### Chapter 3 Modelling River Hydraulics

3.1	Location of cross-sections along the study reach (1986 aerial photograph) . . . . .	3.2
3.2	Longitudinal river profile and cross-sectional morphology . . . . .	3.4
3.3	Peak flow level recorders installed at cross-section 6 . . . . .	3.6
3.4	Measured and fitted rating curve for the Narina study site (cross-section 3) . . . . .	3.7
3.5	Rating curves for cross-sections 1 to 9 . . . . .	3.7
3.6	Variation in Manning's $n$ with discharge rate . . . . .	3.11
3.7	Variation in Manning's $n$ with Discharge rate for different geomorphological channel types (after Broadhurst <i>et al.</i> , in press) . . . . .	3.11
3.8	Synthesized rating curve for cross-section 3 using Manning's resistance coefficient for a similar morphological type . . . . .	3.15
3.9	Variability of the friction slope-resistance coefficient term in equation 3.2 over the discharge range 5 m <sup>3</sup> /s to 655 m <sup>3</sup> /s . . . . .	3.16
3.10	Sensitivity of the synthesized rating relationship to changes in friction slope and Manning's resistance coefficient . . . . .	3.16
3.11	Error in maximum flow depth for $n = 0.050$ and $S_f = 0.00033$ . . . . .	3.17
3.12	Upstream discharge and downstream stage hydrographs for a complete flood event . . . . .	3.25
3.13	Upstream discharge hydrograph and routed downstream stage hydrograph for Event 1 in rectangular channel . . . . .	3.27

3.14	Model 1 optimised storage data for Event 1 in rectangular channel . . . . .	3.29
3.15	Model 1 synthesized rating curves for three flood events in rectangular channel compared with Manning's uniform flow relationship . . . . .	3.30
3.16	Rating curves produced by Koutitas (1983) model for rectangular channel . . . . .	3.31
3.17	Monitored discharge and stage hydrographs at the upstream gauging weir and downstream site on the Sabie River . . . . .	3.32
3.18	Optimised storage data plotted using the coefficients produced by applying Model 1 (a) and Model 3 (b) to the Sabie River flood data . . . . .	3.34
3.19	Monitored and estimated bank storage variations at the Sabie River site during the flood event analyzed . . . . .	3.35
3.20	Optimised storage data plotted using the coefficients produced by applying Model 1 to the Sabie River flood data, including bank storage dynamics . . . . .	3.36
3.21	Comparison of the synthesized rating curve and unrouted flow data, for the Sabie River site . . . . .	3.37

#### Chapter 4 Modelling Bank Storage Dynamics

4.1	Convention for the numbering and position of nodes: (a) Orientation of axes within the river bank; (b) space mesh (y,z); (c) space-time mesh (x,t) . . . . .	4.4
4.2	Flow boundaries encompassing the saturated and unsaturated flow domains in the x-z plane . . . . .	4.5
4.3	Flow through an elementary volume directly below the phreatic surface . . . . .	4.7
4.4	Approximating the phreatic surface boundary . . . . .	4.9
4.5	Geometry for computing the phreatic surface elevation . . . . .	4.17
4.6	Procedure for computing steady state groundwater potentials and phreatic surface position . . . . .	4.19
4.7	Procedure for computing transient groundwater potentials and phreatic surface profiles . . . . .	4.20
4.8	Zero-value groundwater potentials at nodes between successive phreatic surface boundary positions . . . . .	4.21
4.9	Flow boundaries encompassing the saturated flow domains in the x-y and x-z planes . . . . .	4.23
4.10	Vertical flow model in the x-z plane imbedded within horizontal flow model on x-y plane . . . . .	4.26
4.11	Orientation of groundwater potential coefficients for (a) a node in the vertical modelling plane; (b) a node in the horizontal modelling plane located immediately upstream of the imbedded vertical model . . . . .	4.27

4.12	Structure of the array of coefficients, $A^*$ for the coupled vertical and horizontal two-dimensional flow models . . . . .	4.29
4.13	Diagrammatic definitions of soil water potential, soil suction and elevation head measured using a tensiometer (after Bear and Verruijt, 1992) . . . . .	4.30
4.14	Convention for the numbering and position of nodes: (a) space region ( $z$ ); (b) space-time region ( $z,t$ ) . . . . .	4.34
4.15	Coupling the saturated and unsaturated flow models in a vertical cross-section through the riparian bank zone . . . . .	4.36
4.16	Location of the coefficients of groundwater potential and soil suction for the nodes directly below and above the phreatic surface, respectively . . . . .	4.40
4.17	Water retention relationships using the model of van Genuchten (1980) . . . . .	4.42
4.18	Hysteresis in the water retention relationship . . . . .	4.44
4.19	Steady seepage from rectangular channel section with constant phreatic surface level at lateral boundary . . . . .	4.47
4.20	Phreatic surface profile and geometry for uniform vertical infiltration . . . . .	4.49
4.21	Bank geometry for the one-dimensional saturated transient flow analysis . . . . .	4.50
4.22	Experimental sand flume apparatus . . . . .	4.52
4.23	Boundary configurations and soil-hydraulic conditions for the flume tests in Table 4.3 . . . . .	4.54
4.24a	Experimentally, numerically and analytically determined piezometric potentials for flume test 1 . . . . .	4.55
4.24b	Experimentally, numerically and analytically determined seepage rates for flume test 1 . . . . .	4.55
4.25	Experimentally and numerically determined piezometric potentials for flume test 2 . . . . .	4.56
4.26	Analytically and numerically determined phreatic surface profiles for uniform vertical infiltration . . . . .	4.59
4.27	Bank seepage responses predicted analytically and numerically	4.61
4.28a	Spatial distribution of total flow gradient at $t = 5.0$ days . . .	4.62
4.28b	Spatial distribution of the ratio vertical to total flow gradient at $t = 5.0$ days . . . . .	4.62
4.29	Sensitivity of bank storage to the selection of finite-difference spatial and temporal parameter values . . . .	4.63
4.30	Bank seepage responses predicted analytically and numerically	4.65
4.31a	Spatial distribution of total flow gradient at $t = 0.5$ days . . .	4.66
4.31b	Spatial distribution of the ratio vertical to total flow gradient at $t = 0.5$ days . . . . .	4.66
4.32	Sensitivity of bank storage to the selection of finite-difference spatial parameter values . . . . .	4.67
4.33	Cross-sectional bank geometry and boundary conditions . . . .	4.68
4.34	Bank seepage responses predicted analytically and numerically	4.70

4.35	Bank storage responses predicted analytically and numerically	4.70
4.36a	Temporal distribution of soil water potential predicted analytically and numerically for drainage from a soil column . .	4.74
4.36b	Temporal distribution of water content predicted analytically and numerically for drainage from a soil column . .	4.74
4.37a	Sensitivity of outflow to selection of finite-difference spatial parameter values . . . . .	4.75
4.37b	Sensitivity of outflow to selection of finite-difference temporal parameter values . . . . .	4.75
4.38	Temporal distribution of water content predicted analytically and numerically for infiltration into a soil column . . . . .	4.77
4.39	Outflow at the phreatic surface predicted analytically and numerically . . . . .	4.77
4.40	Bank seepage responses predicted analytically and numerically	4.79
4.41	Phreatic surface responses predicted numerically . . . . .	4.79
4.42	Water content profile responses predicted numerically . . . . .	4.80
4.43	Bank seepage responses predicted numerically . . . . .	4.81
4.44	Phreatic surface responses predicted numerically . . . . .	4.81
4.45	Water content profile responses predicted numerically . . . . .	4.82
4.46	Measured and modelled phreatic surface response at the Hulsart Well . . . . .	4.84
4.47	Measured and modelled (two-dimensional deterministic) groundwater potential hydrographs . . . . .	4.87
4.48	Measured and modelled (two-dimensional calibrated) groundwater potential hydrographs . . . . .	4.88
4.49a	Measured and modelled (three-dimensional calibrated) groundwater potential responses along the central line . . . . .	4.90
4.49b	Measured and modelled (three-dimensional calibrated) groundwater potential responses along monitoring line 3 . . . . .	4.90
4.49c	Measured and modelled (three-dimensional calibrated) groundwater potential responses along monitoring line 5 . . . . .	4.91
4.50	Measured and modelled lateral ( $i_x$ ) and longitudinal ( $i_y$ ) flow gradients . . . . .	4.92
4.51	Modelled groundwater potential and phreatic surface responses along the central monitoring line . . . . .	4.92
4.52a	Change in bank storage along a cross-section through the central monitoring line . . . . .	4.93
4.52b	Relative bank storage within a cross-section through the central monitoring line . . . . .	4.93
4.53	Modelled groundwater potential and phreatic surface responses along the central monitoring line . . . . .	4.94
4.54	Correlation between measured and modelled peak groundwater potentials over the period December 1992 to January 1995 . . . . .	4.95
4.55a	Measured and modelled changes in water content for upper, intermediate and lower layers in the unsaturated zone . . . . .	4.99

4.55b	Measured and modelled changes in water content for the aggregated layers in Fig. 4.55a . . . . .	4.99
4.56	Cumulative fluxes defining the water balance for the soil column at location C3-4 from October 1993 to June 1995 . .	4.101
4.57	Contribution of the unsaturated and saturated zones to transpiration at location C3-4 . . . . .	4.101

## Chapter 5 Modelling Transpiration Losses

5.1	A comparison of the observed transpiration rates recorded for the fig tree against those predicted by the model . . . . .	5.5
5.2	The distribution of residuals for the model. The cross-hatched area represents that period where the model performs best (November 1993 to November 1994) . . . . .	5.7
5.3	The distribution of residuals ( ), and the river level (□) expressed in meters above the minimum level recorded during the study, for the period 11 February to 8 May 1993 . .	5.8
5.4	A comparison of the observed transpiration recorded in the fig tree (●) and that predicted by the model (○) for the period November 1993 to November 1994 . . . . .	5.9
5.5	A comparison of the observed mean daily transpiration per unit leaf area recorded for the reed bed (●) with that predicted by Model 1 (○), and the corresponding distribution of residuals (□) . . . . .	5.17
5.6	A comparison of the observed mean daily transpiration per unit leaf area recorded for the reed bed (●) with that predicted by the Model 2 (○), and the corresponding distribution of residuals (□). The location of the two outliers (Δ) omitted from the analysis . . . . .	5.17

## Chapter 6 Sabie River Riparian Water Balance

6.1	The basal area recorded for the tree species at the Narina site, and relative proportion they contribute to the total . . . . .	6.2
6.2	Simulated daily transpiration rates from the reed bed at the Narina study site for the period 1 July 1993 to 5 June 1995. The vertical cross-hatched rectangles correspond to those periods where the estimates are based on actual field data . . . . .	6.7
6.3	Monthly mean daily transpiration rates estimated for all the trees at the Narina study site, and the output of the two reed model simulations from February 1993 to June 1995. The cross-hatched areas indicate those periods where intensive measurements were made of transpiration from the tree species . . . . .	6.9

6.4	Variation in the consumptive water use of riverine vegetation along the entire length of the Sabie River in the Kruger National Park in m <sup>3</sup> /s, and the discharge of the Sabie River measured at the Narina site . . . . .	6.10
6.5	Estimated consumptive water use from the riverine vegetation on the Sabie River as a percentage of the recorded discharge from February 1993 to June 1995 . . . . .	6.12
6.6	Mean monthly transmission losses between gauging stations .	6.16
6.7	Daily fluctuations of river stage and piezometric potentials . .	6.18
6.8	Frequency distribution of river stage fluctuations arising from evapotranspiration . . . . .	6.19

## Chapter 7 Discussion, Conclusions and Recommendations

7.1	Water demands at 1990 (Olifants River), 1985 (Sabie and Letaba Rivers) and 2010 (Sabie and Olifants Rivers) as a percentage of the MAR for the respective catchments . . . . .	7.10
-----	--	------

## LIST OF TABLES

---

### Chapter 2 Data Collection

2.1	Instrumentation used for the measurement and recording of water levels and for powering the monitoring system . . . . .	2.8
2.2	Sampling depths at C3 and C5 . . . . .	2.24
2.3	Saturated hydraulic conductivities . . . . .	2.26
2.4	Parameter values in the van Genuchten models . . . . .	2.27
2.5	Sensors connected to the MCS 120.02 EX automatic data logger installed at the weather station at the selected study site on the Sabie River in the Kruger National Park . . . . .	2.28
2.6	A summary of the meteorological conditions recorded at the Narina site for the duration of the study . . . . .	2.29
2.7	The diameter at cambium, sapwood thickness, moisture content and wood density of the species sampled at the Narina site . . . . .	2.50
2.8	The diameters of each of the sample trees selected for the species comparison . . . . .	2.54
2.9	The mean diameter, height and leaf area of the sixteen <i>P. mauritanus</i> reeds sampled at each of the three sample periods, and the mean LAI for the reed bed . . . . .	2.61

### Chapter 3 Modelling River Hydraulics

3.1	Study reach morphology . . . . .	3.3
3.2	Regression coefficients in equation 3.1 . . . . .	3.6
3.3	Resistance coefficients for the sub-reaches . . . . .	3.9
3.4	Coefficients in equation 3.5 . . . . .	3.10
3.5	River stage and friction slopes . . . . .	3.13
3.6	Manning's $n$ for a braided channel type . . . . .	3.14
3.7	Data for unsteady flow computations . . . . .	3.27
3.8	Optimised rating curve parameters for rectangular channel . . . . .	3.28
3.9	Errors in parameter estimation . . . . .	3.28
3.10	Channel and hydraulic characteristics for the Sabie River analysis . . . . .	3.32
3.11	Optimised rating coefficients for the Sabie River site . . . . .	3.33

### Chapter 4 Modelling Bank Storage Dynamics

4.1	Time-step restrictions for various finite-difference formulations (Rushton and Redshaw, 1979) . . . . .	4.12
4.2	Criteria for computing the phreatic surface elevation . . . . .	4.19
4.3	Sand flume tests . . . . .	4.52
4.4	Finite-difference parameter values . . . . .	4.53
4.5	Finite-difference parameter values . . . . .	4.56



4.6	Seepage rates . . . . .	4.57
4.7	Finite-difference parameter values . . . . .	4.57
4.8	Seepage rates . . . . .	4.58
4.9	Finite-difference parameter values . . . . .	4.58
4.10	Physical and alluvial data . . . . .	4.60
4.11	Hydraulic data . . . . .	4.60
4.12	Finite-difference parameter values . . . . .	4.60
4.13	Finite-difference parameter values . . . . .	4.63
4.14	Physical and alluvial data . . . . .	4.64
4.15	Hydraulic data . . . . .	4.64
4.16	Finite-difference parameter values . . . . .	4.65
4.17	Finite-difference parameter values . . . . .	4.67
4.18	Physical and alluvial data . . . . .	4.69
4.19	Soil-hydraulic data . . . . .	4.73
4.20	Finite-difference parameter values . . . . .	4.73
4.21	Finite-difference parameter values . . . . .	4.76
4.22	Alluvial-hydraulic data . . . . .	4.78
4.23	Alluvial-hydraulic data . . . . .	4.80
4.24	Hulsart watershed profile . . . . .	4.83
4.25	Percolation rates . . . . .	4.83
4.26	Soil-hydraulic data . . . . .	4.84
4.27	Finite-difference parameter values . . . . .	4.85
4.28	Calibrated alluvial-hydraulic parameter values . . . . .	4.87
4.29	Calibrated alluvial-hydraulic parameter values . . . . .	4.89

## Chapter 5 Modelling Transpiration Losses

5.1	The fig tree transpiration model ( $R^2=0.779$ ). This model was developed with a daily time step and requires data on the leaf area index, river level at the Narina site, and vapour pressure deficit. The model predicts transpiration in litres per day. . . . .	5.11
5.2	Predicting the mean water use of the reed bed with a model in which VPD has been transformed to reflect the nature of the relationship between transpiration and VPD. . . .	5.15
5.3	The coefficients for the two best models developed to predict the median daily transpiration per unit leaf area from the reed bed at the Narina study site. . . . .	5.16

## Chapter 6 Sabie River Riparian Water Balance

6.1	The mean daily transpiration per unit sapwood area ( $l\text{ cm}^{-2}\text{ day}^{-1}$ ) calculated for each of trees sampled during the intensive HPV surveys carried out at the Narina study site . . . . .	6.3
-----	--	-----

6.2	The periods into which the transpiration simulation for the Narina site was divided up, and the relationships used to extrapolate from the reference tree data to the data for the whole Narina site . . . . .	6.4
6.3	The periods for which the various reed sub-models were applied in the simulation exercise to estimate yearlong transpiration rates from the reed bed. The model notation refers to the models presented in Chapter 5 . . . . .	6.5
6.4	Abstractions at pumping stations . . . . .	6.16
6.5	Water usage at rest camps . . . . .	6.16

## Chapter 7 Discussion, Conclusions and Recommendations

7.1	Projected water demands and land use for the Sabie River catchment (Chunnet <i>et al.</i> , 1990a; 1990b) . . . . .	7.11
-----	---	------

## Chapter 9 Appendices

### Chapter 3 Modelling River Hydraulics

A3.1	Cross-section chainage . . . . .	9.10
A3.2	Elevations of cross-section bench marks relative to MSL . . . . .	9.11
A3.3	Elevation to the top of the PFLR's relative to MSL . . . . .	9.10
A3.4	Discharge and stage levels recorded over the period June 1993 to January 1995 . . . . .	9.12
A3.5.1	Hydraulic data : cross-section 1 . . . . .	9.13
A3.5.2	Hydraulic data : cross-section 2 . . . . .	9.13
A3.5.3	Hydraulic data : cross-section 3 . . . . .	9.14
A3.5.4	Hydraulic data : cross-section 4 . . . . .	9.13
A3.5.5	Hydraulic data : cross-section 5 . . . . .	9.13
A3.5.6	Hydraulic data : cross-section 6 . . . . .	9.15
A3.5.7	Hydraulic data : cross-section 7 . . . . .	9.15
A3.5.8	Hydraulic data : cross-section 8 . . . . .	9.15

### Chapter 4 Modelling Bank Storage Dynamics

A4.1	Flume Tests : Saturated hydraulic conductivities . . . . .	9.18
A4.2	Flume Test 1 : Piezometric potentials . . . . .	9.19
A4.3	Flume Test 1 : Seepage rates . . . . .	9.19
A4.4	Flume Test 2 : Piezometric potentials . . . . .	9.20
A4.5	Flume Test 2 : Seepage rates . . . . .	9.20
A4.6	Flume Test 3 : Piezometric potentials . . . . .	9.21
A4.7	Flume Test 3 : Seepage rates . . . . .	9.21

## CHAPTER 1

### INTRODUCTION

---

#### 1.1 Background

The seven major rivers flowing through the Kruger National Park (Crocodile, Sabie, Olifants, Letaba, Shingwedzi, Levuvhu and Limpopo Rivers) all rise beyond the western border of the Kruger National Park (KNP) and drain catchments that are being subjected to increasing pressure for their available land and water resources. This pressure results from the escalating human population growth in the rural areas immediately west of the KNP, coupled with afforestation and agricultural development in the upper catchments. The projected increase in the human population in these rural areas is from 2.7 m. in 1985 to 4.7 m. by the year 2000 (Urban Foundation, 1990). The associated increase in the domestic, mining, municipal and industrial water consumption within the Sabie River catchment is estimated at 659%, from  $7.4 \times 10^6 \text{ m}^3/\text{a}$  in 1985 to  $56.2 \times 10^6 \text{ m}^3/\text{a}$  by the year 2010 (Chunnet *et al.*, 1990a). Afforestation in the Sabie River catchment has resulted in an estimated 17% reduction in the mean annual runoff, with no further significant reduction expected under current permit restrictions. The estimated increase in water consumption by irrigation is 130%, from  $99.3 \times 10^6 \text{ m}^3/\text{a}$  in 1985 to  $228.1 \times 10^6 \text{ m}^3/\text{a}$  by the year 2010 (Chunnet *et al.*, 1990a, 1990b).

This increasing development has resulted in the rivers flowing through the KNP in the Mpumalanga Province having become progressively depleted and contaminated. Previously perennial rivers now flow as seasonal and even ephemeral systems (e.g. Letaba River, Venter and Deacon, 1994). Denudation of the catchment landscape is also resulting in increased sediment production (van Niekerk and Heritage, 1994). These changes in the flow and sediment regimes of the rivers are leading to morphological adjustments, with associated changes in habitat and water availability for aquatic and riparian biota. Concerns for the impacts of upstream development on the ecological functioning of the riverine ecosystems within the KNP's rivers led to the formation of the multidisciplinary KNP Rivers Research Programme (KNPRRP) (see Reid, 1990 and Deacon, 1991). The programme was initiated to establish the ecological water requirements of the rivers flowing through the KNP, so that they may be given due consideration in the planning and management of future resources developments. In a situation of competition between various sectors for the limited water resource, it is important for environmental requirements to be established reliably, so that these claims can be substantiated and allocations made equitably. Environmental requirements are both consumptive (transpiration and animal consumption) and non-consumptive (habitat-related) in nature.

Attention has focused mainly on the Sabie River as the most natural, but imminently threatened perennial river flowing through the KNP. The Sabie River is characterised by a wide fringe of riparian vegetation colonising the river banks, where more than 130 indigenous species of shrubs and trees occur. The riverine vegetation is not only an essential refuge for fish, reptiles, amphibians, invertebrates and hippopotami, but also provides important habitat for birdlife and browsers that utilise the riparian zone. In the Sabie River, this vegetation is susceptible to widespread fatalities and re-distribution resulting from inadequate water supply and morphological changes due to modified flow and sediment regimes. The future viability of the whole riparian ecosystem therefore depends on ensuring a water supply sufficient for the maintenance of riparian vegetation.

## **1.2 Project Objectives**

There are three main issues which need attention to effectively manage the water requirements of riparian vegetation (Rogers, 1991).

- 1 The need for non-consumptive flows such as flooding to provide seed germination opportunities and a disturbance regime which maintains species diversity.**
- 2 The minimum water supply which will permit persistence of the vegetation during times of drought.**
- 3 The need to model consumptive water use by vegetation (transpiration) under different river flow and climatological conditions.**

The first two issues require detailed physiological and ecological studies of riparian plant species and are not the direct concern of this project. This project focuses on the third issue and thus aims to provide the means to predict the water use by the riparian zone under different riverine and atmospheric conditions.

The objective was achieved by pursuing the following specific objectives described in the project proposal (Rogers, 1991). The chapter reference where each of the objectives is addressed is indicated in parentheses.

- 1 Using a bank storage dynamics model, develop a series of conceptual models which clearly define the project information needs, output potential and the interactions required to obtain them (Chapter 1.3).**
- 2 Develop a river hydraulics model which will provide the ability to predict rating curves for single and multiple channel rivers (Chapter 3).**

- 3      Develop a vegetation transpiration model which provides the ability to predict transpiration losses for a given leaf area, water supply, season and meteorological conditions (Chapter 5).
- 4      Refine the bank storage dynamics model to link river hydraulics and vegetation transpiration models (Chapter 4).
- 5      Collect the appropriate field data to parameterise and or calibrate these models (Chapter 2).
- 6      Apply the theory and techniques developed to the Sabie River (KNP) to
  - 6.1      estimate seasonal changes in consumptive water use by riparian vegetation (Chapter 6), and
  - 6.2      assess the strengths and limitations of the overall technique and its component models (Chapter 7).

### **1.3                      Interdisciplinary Study**

The occurrence and transfer of water between the systems described in 3, 4 and 5 above need to be described quantitatively. The range of specialities involved requires an interdisciplinary approach, and this project is consequently a collaborative effort between the Centre for Water in the Environment (University of the Witwatersrand) and the Division for Water, Environment and Forestry Technology in the CSIR.

### **1.4                      Conceptual Model of the Riparian Water Balance**

The partitioning of the riparian water balance into three component models, including, river hydraulics; bank storage dynamics; and evapotranspiration and the basic patterns of water movement into and out of a two-dimensional cross-section through the riparian zone, are illustrated in Fig. 1.1.

The data requirements for developing and verifying the component models, and for practical application of the water balance model, are shown in Fig. 1.2. The interactions between the three basic components of the water balance are also indicated. River discharge and climatic conditions are the two fundamental input variables that drive the water balance. The river discharge is the primary management variable, with no direct control being administered over the prevailing climate. The physical and biological systems respond to regulated river flows, with a feedback resulting from changes in bank storage dynamics, vegetation water extraction patterns, geomorphological response and riparian forest structure (species

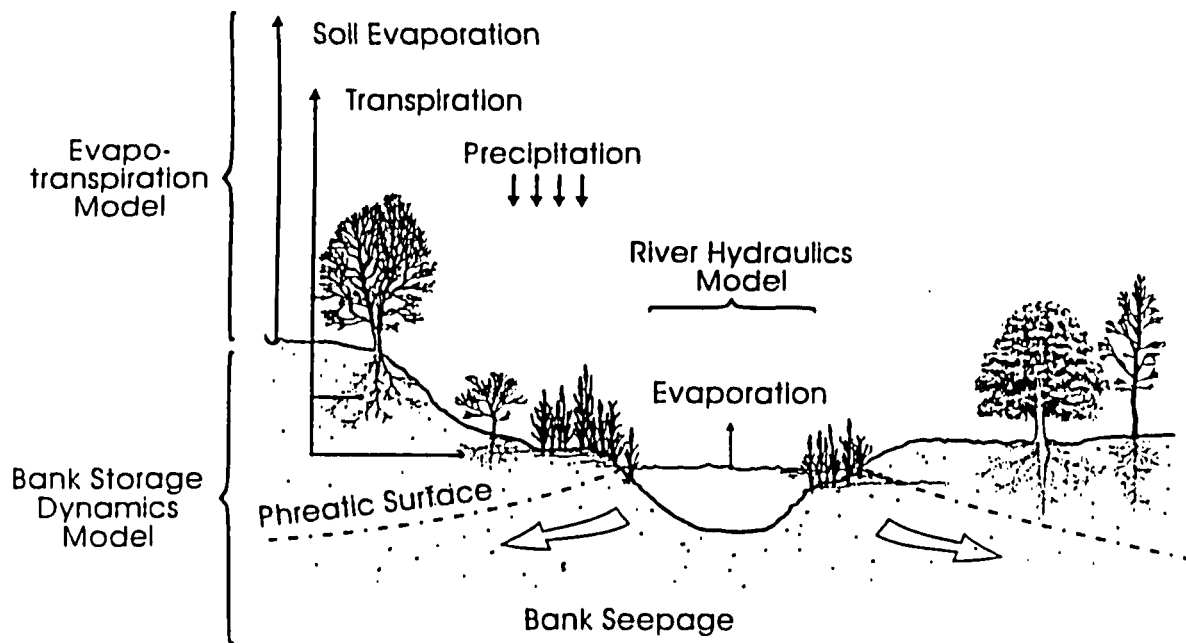


**Figure 1.1** Water balance across a two-dimensional vertical section through the riparian zone, showing component models.

composition and distribution).

The Sabie River is characterised by well developed mature riparian forest and further flow modifications could have severe impacts on the riparian vegetation. The Sabie River is also the focus the interdisciplinary KNP Rivers Research Programme, and consequently, model development, verification and application (Fig 1.2) are based on intensive data collection (Chapter 2) at a site on the Sabie River near the Narina camp, located approximately 5 km upstream of Skukuza.

The river hydraulics component involves the determination of river stage corresponding to the primary input variable: *river discharge rate* (Fig 1.2). River hydraulics along the Sabie River is addressed in Chapter 3. A study of the resistance characteristics of the geomorphological channel types identified by Heritage *et al.* (in press) is reported in volume 2 of this report by Broadhurst *et al.* (in press). A hydrological routing methodology for synthesizing rating relationships from short term flow data is also developed (Chapter 3.3).

Bank storage dynamics involves the interaction between in-bank groundwater, surface flow in the river channel and evapotranspiration. This component of the riparian water balance is described in Chapter 4 by a generalised finite-difference simulation model for the movement of

subsurface water in the river banks adjacent to the active channel. Phreatic surface responses to event related fluctuations of river stage are modelled deterministically, as is the daily variation in soil water content along a profile through the unsaturated zone below the canopy of a *Ficus sycomorus* tree.

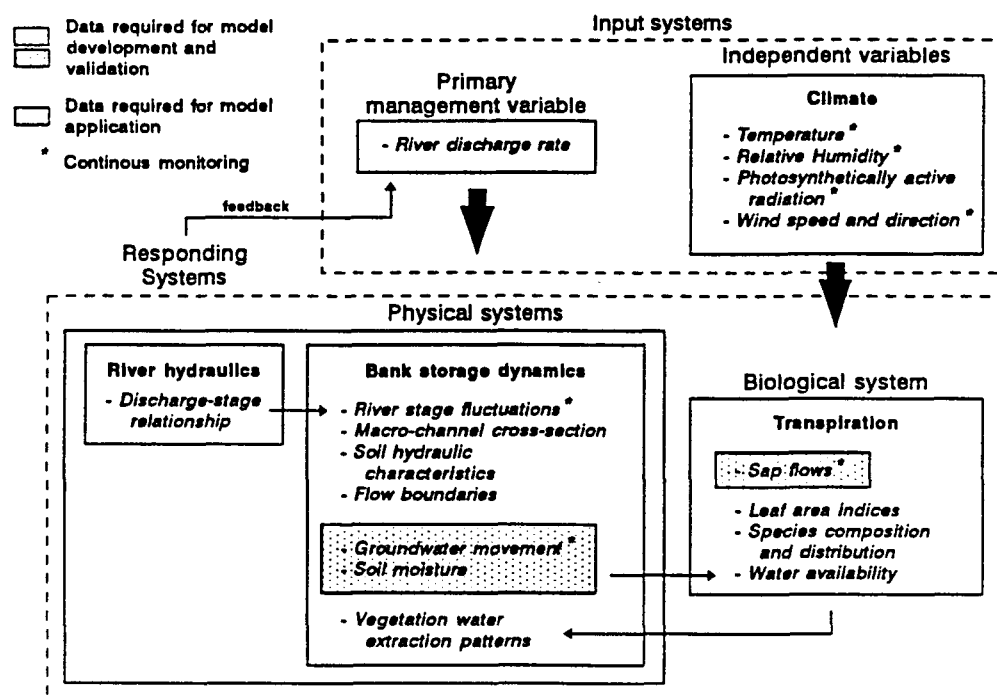


Figure 1.2 Data required for development and application of the riparian water balance model, with the fundamental interactions between components of the system.

The transpiration component of the riparian water balance is modelled in Chapter 5 using an empirically-based methodology, owing to the morphological heterogeneity, species diversity and spatial distribution of riparian vegetation along the Sabie River system. Seasonal transpiration losses from the Narina site are quantified in Chapter 6, as is the scaling of transpiration from Narina to the Sabie River. An approximate water balance between gauged sections along the river is also presented.

The intensive data collection, integrated modelling approach, water balance at the Narina study site, and transmission losses along the Sabie River in the KNP in relation to water demands in the catchment, are discussed in Chapter 7. Recommendations for the transfer of technology developed within this project, further research and the archiving of data are also provided.

## CHAPTER 2 DATA COLLECTION

---

### 2.1 Study Site Locality

The study site was selected to meet accessibility, security, and physical and biological suitability criteria. The Sabie River within the KNP was examined using 1:10 000 scale aerial photographs taken in 1982, ground photographs, macro-channel cross-section surveys and ground reconnaissance.

Accessibility to the study site from Skukuza rest camp, preferably using non-tourist roads, was an important practical consideration influencing site selection. The reach of the Sabie River upstream of the Kruger Gate entrance to the Park was not considered as it forms the border between the KNP and farming communities, and consequently presents potential problems for the security of expensive monitoring equipment.

A study site with simplified flow boundaries would reduce complexities in bank storage dynamics model development. Such sites are limited along the Sabie River, which has a mixed bedrock-alluvial channel with a complex morphology (van Niekerk and Heritage, 1994). Bedrock outcrops occur in the river channel in areas displaying local change in bedrock resistance as a result of lithological and structural variability (Cheshire, 1994). Deposition of alluvial sediments occurs upstream of such bedrock controls in the active channel as a result of the reduced energy gradient and associated channel competence. To facilitate groundwater data monitoring and modelling, the study location should ideally have a simple macro-channel geometry (single-thread channel) and relatively deep alluvial deposits with a zone of saturation above the bedrock. Once a generalised deterministic model of the physical processes governing groundwater movement has been developed and tested, it may then be applied to the more complex geomorphological and biological systems found along the Sabie River (bedrock anastomosing, braided channels and vegetated channel bars) and to other rivers.

The biological characteristics required of the study site include the presence of a suite of the large woody riparian species commonly found along the Sabie River, as well as the reed species *Phragmites mauritianus*.

Based on the above practical, physical and biological considerations, a study site on the Sabie River was selected, approximately 5 km upstream of Skukuza rest camp (Fig. 2.1). Access to the study site is by means of a well-maintained non-tourist gravel road. The study area is characterised by a single-thread active channel and lateral bar deposit, densely colonised with reeds. The lateral bar deposit within the study area has existed since



the earliest aerial photographs taken in 1940. Results of a ground-penetrating radar and surface surveys suggest that the lateral bar is aggrading, with preferential deposition having taken place on the upstream section of the bar (Birkhead *et al.*, 1996a). The site was viewed as being particularly suitable as the stability of the active channel bank affords protection during floods. Furthermore, the wide riparian zone allowed the investigation of groundwater movement across a broad macro-channel. The tree species at the study site include *Trichilia emetica*; *Diospyros mespiliformis*; *Spirostachys africana*; *Ficus sycomorus* and *Berchemia zeyheri*.

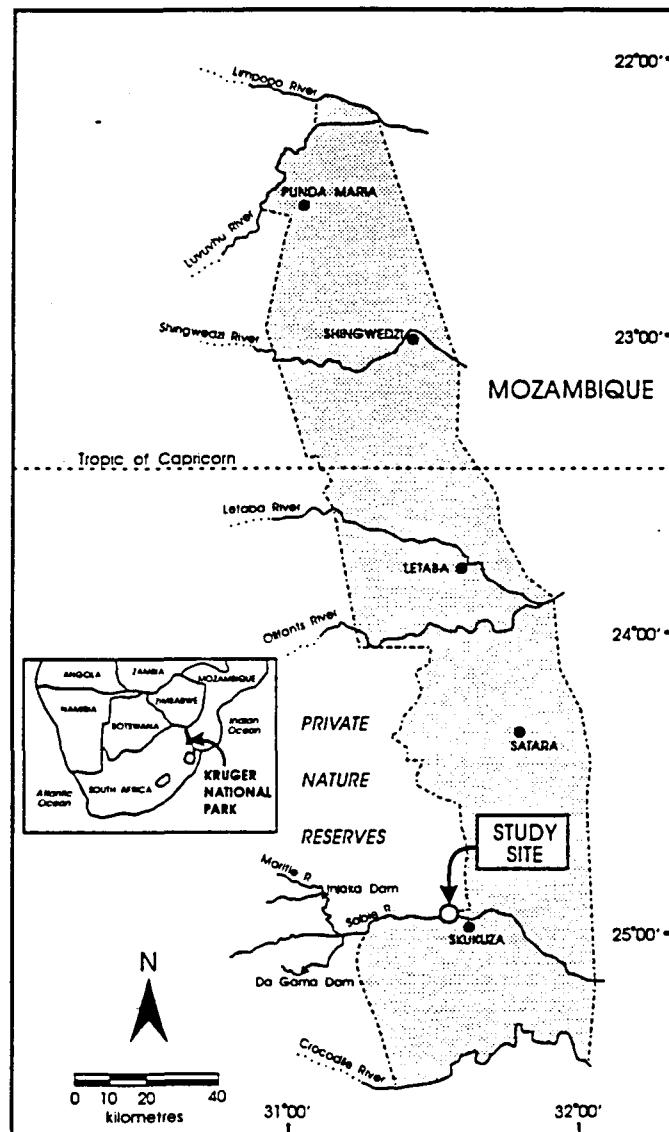


Figure 2.1 Location of the study site along the Sabie River in the Kruger National Park.

## **2.2 Groundwater Model Data Collection**

Data required for development of the bank storage dynamics model include the continuous time variation of the groundwater potentials and river stage, periodic values of soil moisture in the unsaturated zone, and delineation of the permeable and impermeable boundaries.

### **2.2.1 Monitoring System for Groundwater and River Stage**

The finite-difference groundwater model (Chapter 4) predicts the unsteady phreatic surface profile, groundwater potentials and soil-water contents along a macro-channel cross-section through the riparian zone. These predictions are used to compute the direction of groundwater movement and bank seepage rates. The groundwater responds to changes in river stage, which is one of the basic input variables that drives the two-dimensional groundwater model (Fig. 1.2). It is therefore necessary to monitor the temporal variation of river stage at the study site to provide model input data, and also to record the responding groundwater potentials for comparison with modelled predictions.

Electronic pressure transmitters were installed for groundwater and river stage levels. Other systems, such as float systems linked to chart recorders or shaft encoders and indirect electronic ultrasound depth measurement devices, were considered unsuitable for multiple location monitoring in this ecologically sensitive environment because of inappropriate installation requirements and high costs. Pressure transmitters were favoured over other electronic instruments, such as vibrating wire transducers, because of their wide use locally, favourable installation requirements, ability to tolerate severe environmental conditions, and suitability to the application of monitoring fluid pressure at multiple locations with a single recorder. The type of pressure transmitter used consists of a stainless steel body and a length of cable lead housing a three-wire system and a venting core that maintains atmospheric pressure at the instrument. The transmitter utilises a semiconductor pressure sensor, the specific resistance of which varies proportionally to the pressure applied by the fluid to the silicon membrane of the sensor.

The groundwater monitoring system installed within the study area covers a two-dimensional horizontal grid of measuring points (Fig. 2.2). The central (C) monitoring line consists of a set of five measuring points, spaced at 12.5 m intervals from the low-flow active channel bank to the foot of the macro-channel bank. Monitoring points on the central line measure the groundwater potentials in a lateral (transverse) direction. Three of the measuring points on the central line (3, 4 and 5) consist of two nested piezometers positioned at different elevations to measure the vertical components of flow within the bank. The upstream (U) and

downstream (D) lines of three measuring points each are set 20 m off the central line, constituting a grid of measuring locations. The system also allows any local depressions in the groundwater potential arising from localised water extractions by large trees to be measured. The majority of the system's components are installed below ground level to prevent animal disturbance and visual detection.

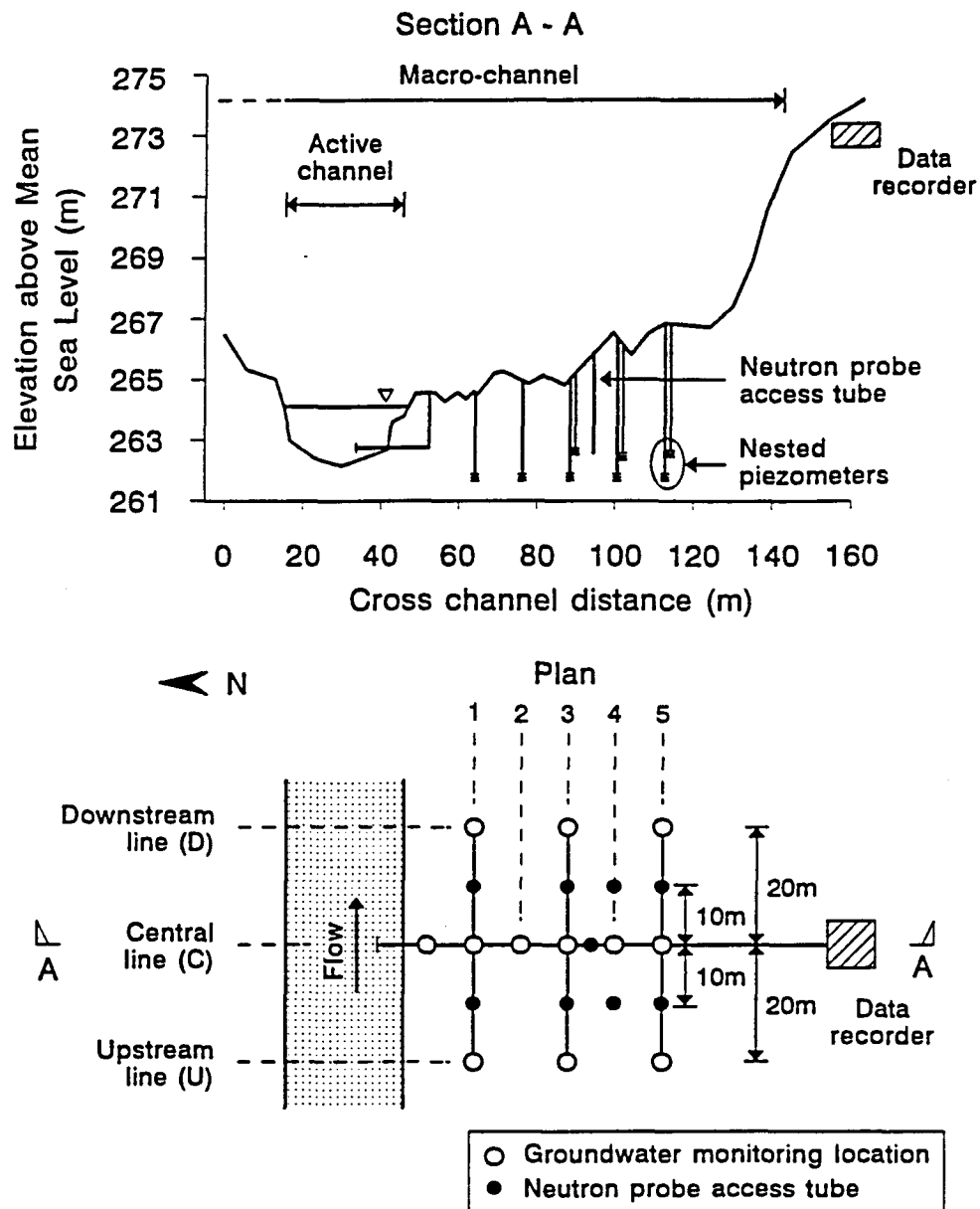


**Figure 2.2** Layout of the groundwater monitoring system at the study site.

The height difference between two nested piezometers must be maximised to detect vertical flow gradients. The observation hole should therefore extend to bedrock for placement of the lower piezometer tube.

Observation holes for piezometer placement were hand-augered with a 75 mm dia. auger head. This method gave good sample recovery of sediments up to 40 mm dia. The sides of the augered observation holes were self-supporting to the depth of the phreatic surface. The change from cohesive to non-cohesive sands occurred in the vicinity of the phreatic surface, resulting in collapse of the observation hole with no additional increase in depth. To prevent collapse in the zone of saturation a temporary casing was driven ahead of the auger head. This enabled sediment recovery to a maximum depth of 0.75 m below the phreatic surface, which was insufficient for extension of the observation holes to bedrock level.

The piezometer tubes were constructed from galvanised steel conduit rather than polyvinyl chloride (PVC) conduit to provide protection against lightning for the pressure transmitters suspended in the piezometers. The lightning protection to the pressure transmitters provided by the conducting sheath is a more important consideration than the non-corrosive qualities of PVC. The pressure transmitters contribute a considerable proportion of the overall costs of the monitoring equipment (nine pressure transmitters constitute 50% of the total expenditure on equipment for the monitoring system), and it is therefore imperative to incorporate protective features in the design.

A piezometer consists of a length of conduit with a tip connection at the base and the upper end protected with a steel access cap at the ground surface (Fig. 2.3). The cap provides access to the piezometer for installation of pressure transmitters, on-site calibration and general maintenance requirements. The access cap is cast into concrete with a small section of the cap protruding above ground level. This design feature prevents interference by large animals utilising the riparian zone, particularly elephants and hippopotami, and also limits flooding disturbance. The function of the tip placed at the bottom of the piezometer is to allow the free flow of groundwater between the alluvium and the piezometer tube. The design of the tip is based on the Casagrande-type piezometer tip described by Clark (1988). The piezometer tip is a 40 mm dia. conduit with 3 mm wide slots cut into opposite sides over a length of 200 mm. The tip is covered with a stainless steel mesh (200  $\mu$ m aperture) which is clamped onto the slotted end (Fig. 2.3). Gravel packs were placed around the piezometer tip in the observation hole to ensure good connectivity with the surrounding alluvial groundwater reservoir. Bentonite clay seals were used above and below the piezometer tips to prevent vertical flow in the packed and backfilled observation hole. The level of water in the piezometer therefore represents an averaged piezometric potential over the height of the piezometer tip.

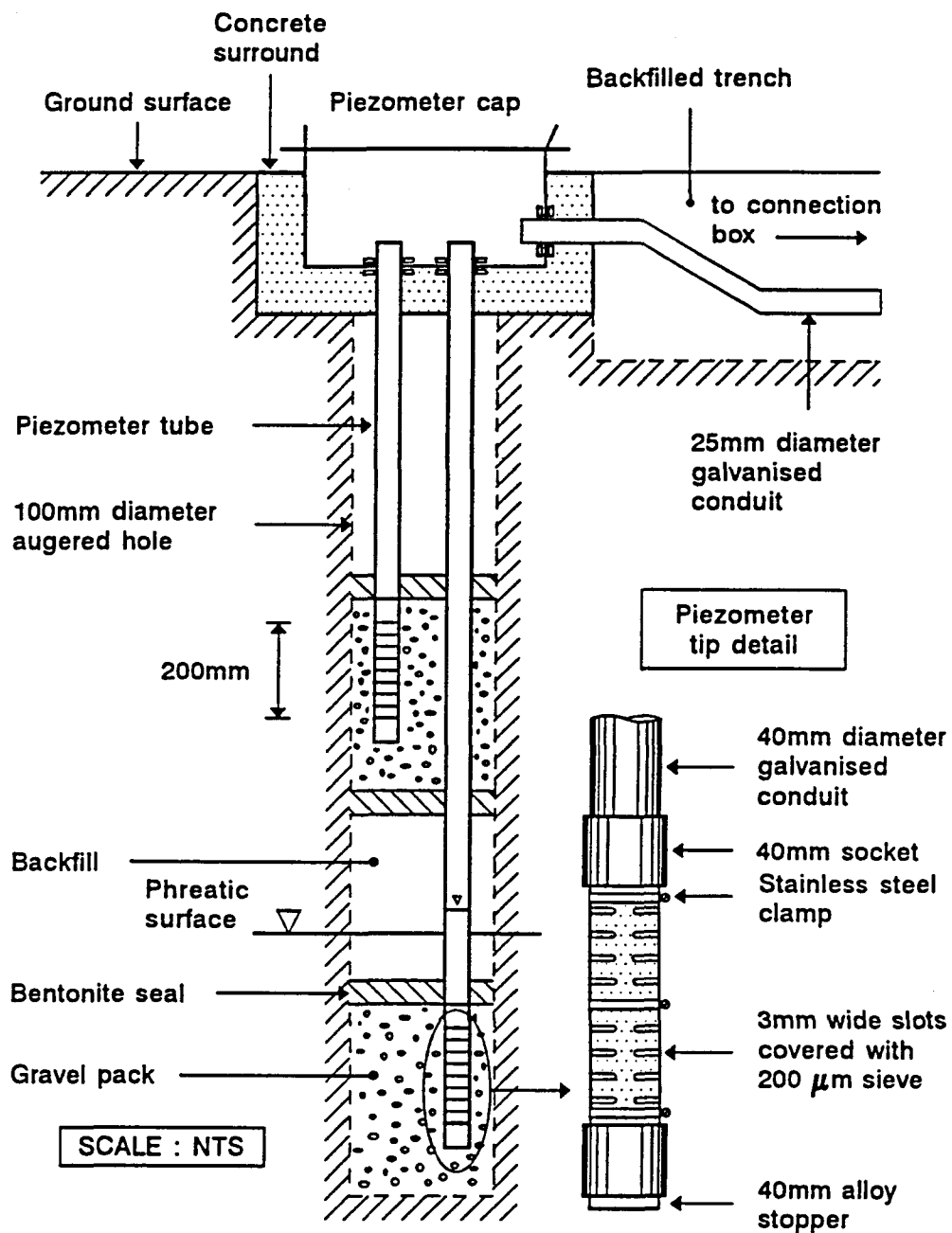


**Figure 2.3** Design of two nested piezometers at a monitoring location, showing piezometer tip detail.

The cables from the transmitters are connected at a series of junctions to a cable network that connects the transmitters to the data recorder (Fig. 2.4). The cable network also carries venting access to each of the transmitter venting tubes. The cable and venting network is a modular system, which facilitates the relocation of pressure transmitters at different monitoring locations within the study area. Steel conduit and junction

boxes are used throughout the network to provide lightning protection and are installed below ground level to deter animal disturbance. The automatic recorders (loggers) are housed in a robust steel box above the macro-channel bank (Fig. 2.2).

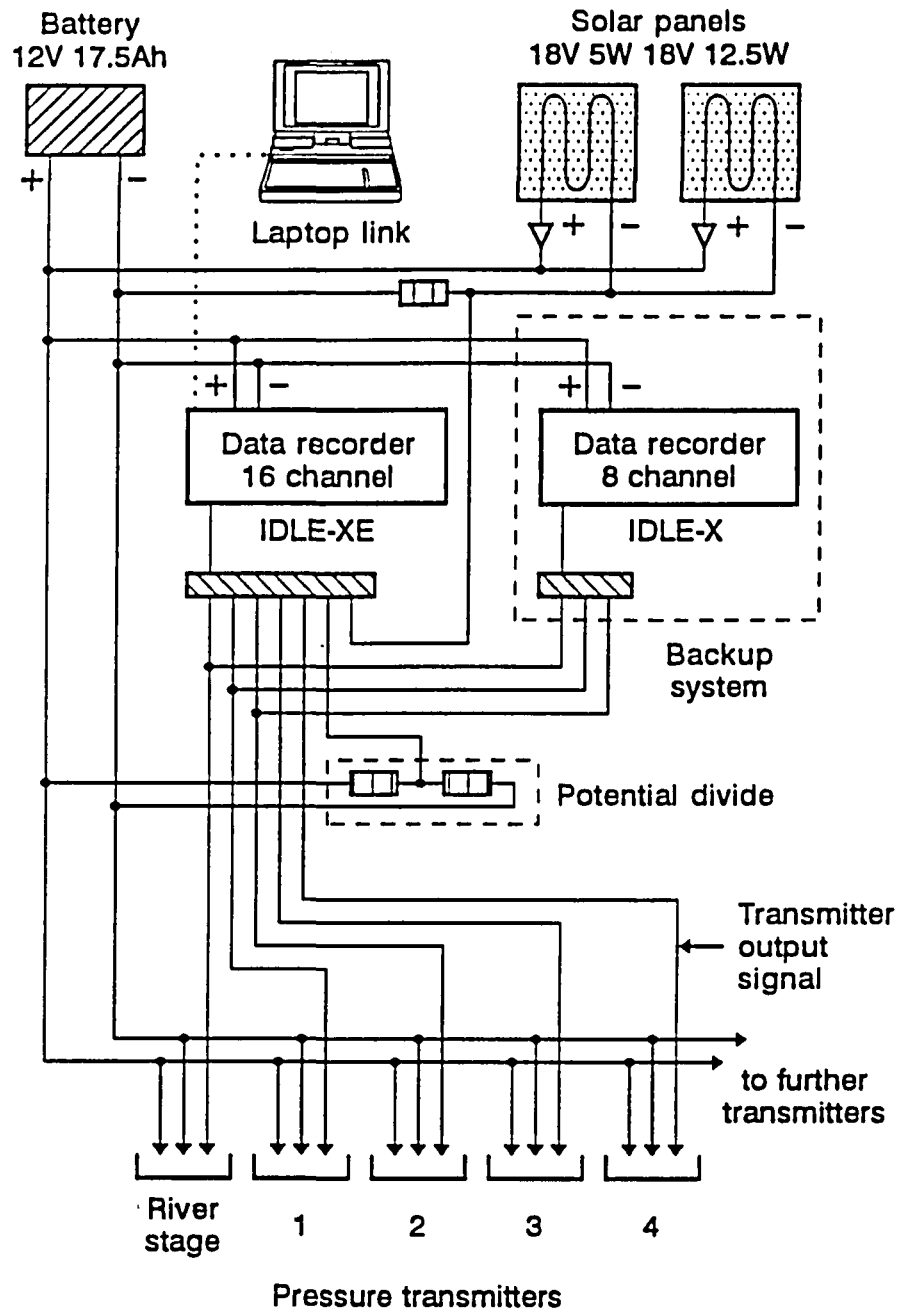


**Figure 2.4** Cable network for connecting the pressure transmitters, data recorders, power supply and laptop link.

The main components of the automatic water level measurement, recording and power supply systems are given in Table 2.1.<sup>1</sup>

**Table 2.1** Instrumentation used for the measurement and recording of water levels and for powering the monitoring system

	Units	Instrumentation <sup>1</sup>
Water level measurement	9	WIKA model 891.13.530 0-20 mA 0-40 kPa pressure transmitter
Automatic water level recording system	1	16 channel (analog & digital) DDS IDLE-XE data recorder
	1	8 channel (analog & digital) DDS IDLE-X data recorder
Power supply to monitoring system	1	12 V 17 Ah/20 h lead acid battery
	1	18 V 5 W solar panel
	1	18V 12.5 W solar panel

A compromise must be made between range and accuracy when selecting a pressure transmitter, as accuracy decreases with increased range of measurement. The selected transmitter has a range of 0 m to 4 m water head (0 kPa to 40 kPa), with a corresponding accuracy of 0.25% of the full-scale range (8 mm water head). The transmitter has a pressure safety limit of 8 bar, allowing it to be subjected to water levels of up to 8 m before any permanent damage results. This represents a flow discharge at the study site of approximately 1 500 m<sup>3</sup>/s, which is an extreme flood event.

The pressure transmitters require a power supply in the range 10 V to 30 V. This is supplied by the external battery which is charged by two solar panels (Fig. 2.4). The solar panels are positioned beyond the riparian forest canopy to prevent shading, particularly during winter. In addition to the transmitter outputs (piezometric potentials), the potential difference across the battery and the current produced by the solar panels are also recorded.

The potential difference is measured using a potential divide, and the solar current is calculated by measuring the voltage drop across a resistor. This allows the adequacy of the power supply to the measuring and recording systems to be monitored, and provides useful information for diagnosing

---

<sup>1</sup> Trade names have been supplied to provide specific information on the instrumentation used and do not constitute endorsement by the authors, their respective organisations, or funding agencies.

the periods and causes of electronic malfunctions. Typical plots of the hourly recordings of the battery potential difference and solar current are presented in Fig. 2.5. The battery is fully charged at 12.8 V, with the increase above this level representing the static voltage produced by solar charge. This static charge falls rapidly when the battery discharges through the monitoring circuits at night. In the absence of solar power, the monitoring system will operate for a minimum of four days with each of the nine transmitters drawing the maximum current (20 mA per transmitter) at the pressure limit of the instruments (4 m water head). The solar panels are designed to produce 0.97 A when operating under optimal climatic conditions.

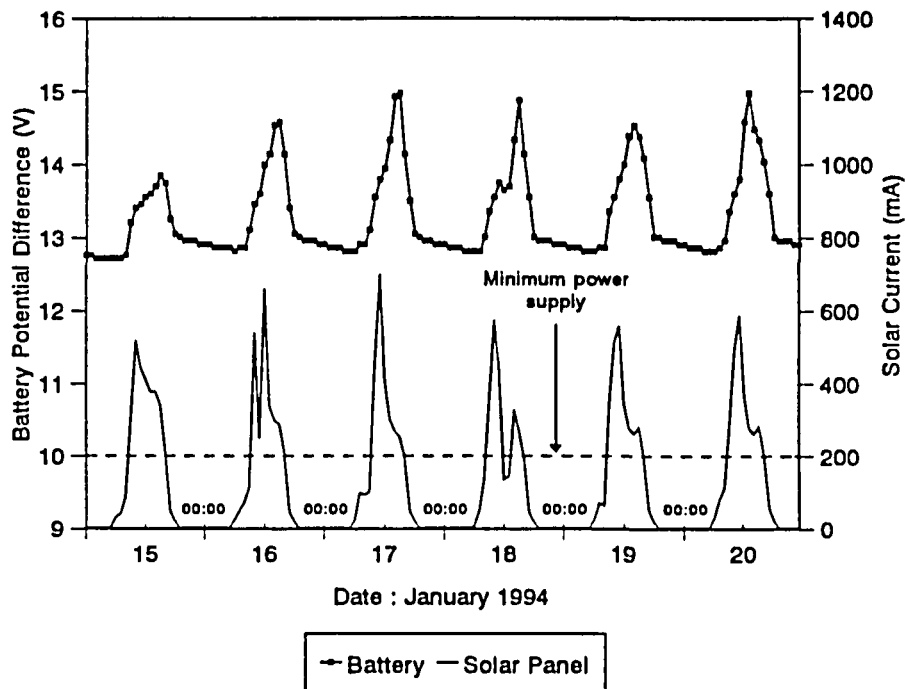


**Figure 2.5** Plot of daily variations in the battery potential difference and solar charge from 15 to 20 January 1994.

The data recorders can be linked to a computer, providing an efficient method of programming the recorder parameters and downloading data. The parameters and recorded data are stored on a removable random access memory (RAM) pack, which may be exchanged in the field or downloaded on site onto disk storage using a laptop computer (Fig. 2.4).

The river stage monitoring facility consists of a horizontal inlet pipe connected to a vertical stilling well, which is protected at the surface with an access cap (Fig. 2.6). The inlet is covered with a 200  $\mu\text{m}$  aperture sieve to prevent silt intrusion, while allowing rapid response of water in the



stilling well to stage fluctuations. The access pipe is positioned directly above the active channel bed to allow the measurement of shallow flow depths. A pressure transmitter is suspended in the stilling well and connected to the wiring and venting network in the same way as those for the groundwater monitoring system (Fig. 2.4). The deposition of sediment over the lateral channel bar during flood events in November 1992 and March 1993 prompted the installation of manhole pipes to gain access to the buried stage access cap (Fig. 2.6).

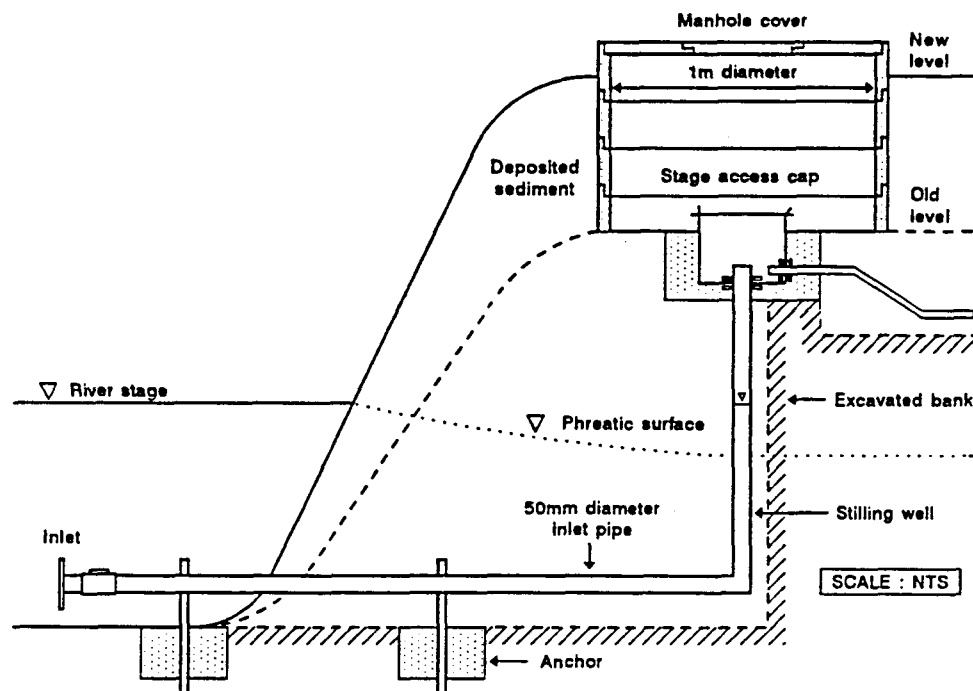


Figure 2.6 Design of the river stage monitoring system.

### 2.2.2 Monitoring Soil Moisture in the Unsaturated Zone

Soil moisture contents in the unsaturated zone were monitored using a neutron probe. This has been shown to be an effective and convenient means of measuring soil moisture at various depths in a soil profile (Cuenca, 1988). Eight aluminium access tubes were installed within the study area for this purpose, on either side of the central groundwater monitoring line at locations 1, 3, 4 and 5 (Fig. 2.2). An additional access tube was installed midway between groundwater monitoring locations C3 and C4 (C3-4) for comparison of neutron probe data with gravimetrically determined soil water contents of augered samples. This comparison is necessary to establish the accuracy of neutron probe data at the study site, where the fluvial deposits are highly stratified and variable, ranging from

clays and silts to coarse sands and fine gravels. Because of the time and difficulty involved in extracting samples for water content measurements in non-cohesive dry sands, only this one location (C3-4) was used for comparison. The results obtained have provided sufficient information for calibration of the neutron probe and given indications of the temporal and spatial intensity of data collection required for this purpose.

The neutron probe data are conveniently presented as neutron count ratios which is the ratio between the observed count when the neutron source has been lowered into the neutron probe access tube, and the standard count recorded while the source is retained in the housing of the apparatus. In Fig. 2.7, the data are presented as the change in count ratio relative to a reference level, which is taken as the lowest count ratio observed the previous season. For both data sets in Fig. 2.7 ((i) November 1993 to July 1994, and (ii) November 1994 to July 1995), the reference level selected is the count ratio recorded during November 1993 and October 1994, respectively. Positive changes in the count ratio therefore reflect an increase in soil water content, while negative changes, such as those observed at location 5C-D from January 1994 to February 1994, indicate a reduction in soil water content.

Neutron probe measurements were taken at 25 cm intervals up to depth of 200 cm. (Fig. 2.7 and Fig. 2.8). The neutron probe data (Fig. 2.8a) exhibit the same spatial and temporal variations in soil water status as the gravimetrically determined water content profiles (Fig. 2.8b). The probe data provide a more averaged measure of the spatial variability due to the larger spherical zone of measurement inherent in the technique. Limited data were collected at volumetric water contents above 30%, primarily because flows were confined to the active channel since March 1993. Additional data at high moisture contents were derived by artificially saturating the bank and collecting the required water content and neutron probe data. Figure 2.9 is a plot of the neutron probe data against the water contents measured from sampled sediments. The water contents are expressed per unit volume of soil sample and are averaged over 25 cm depths to coincide with the neutron probe measurement positions. The data correlate well, with measurements at 100, 200 and 225 cm plotting lower. The sediment types at these depths are relatively homogeneous coarse-grained sands (Fig. 2.13), and different linear calibration functions are fitted. The calibration equations are significant in describing soil moisture contents ( $R^2=0.88$ ,  $p<0.001$  and  $R^2=0.93$ ,  $p<0.001$ ) and gives standard errors of 2.20% and 1.67% in the prediction of the spatially averaged volumetric water content from neutron measurements for the fine and coarse textured sediments, respectively. These results support the use of the neutron probe to estimate the volumetric water content within the stratified fluvial deposit.

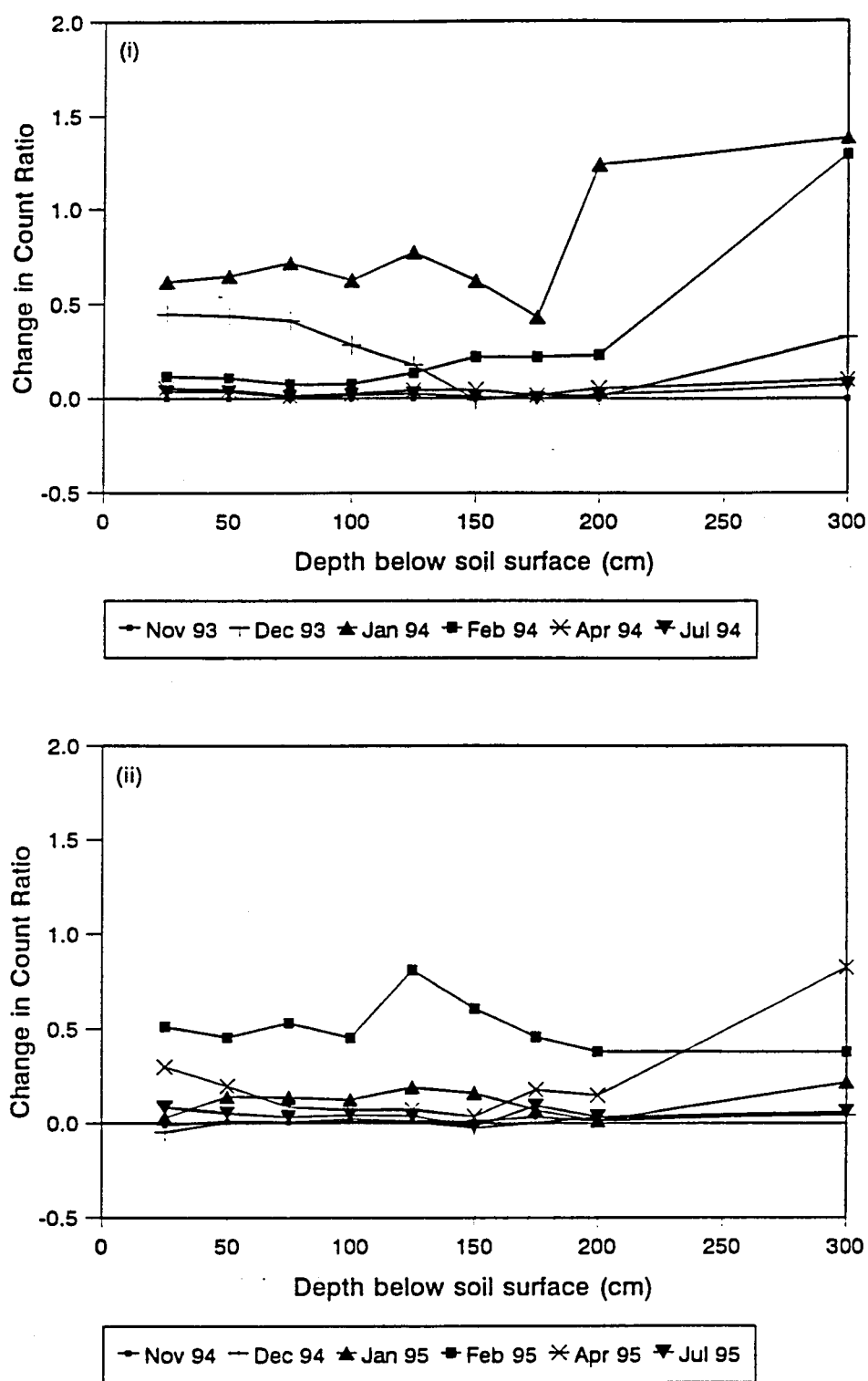


**Figure 2.7a** Relative changes in neutron probe count ratios at location 5C-D (Fig. 2.2) over the seasons (i) 1993/94 and (ii) 1994/95.

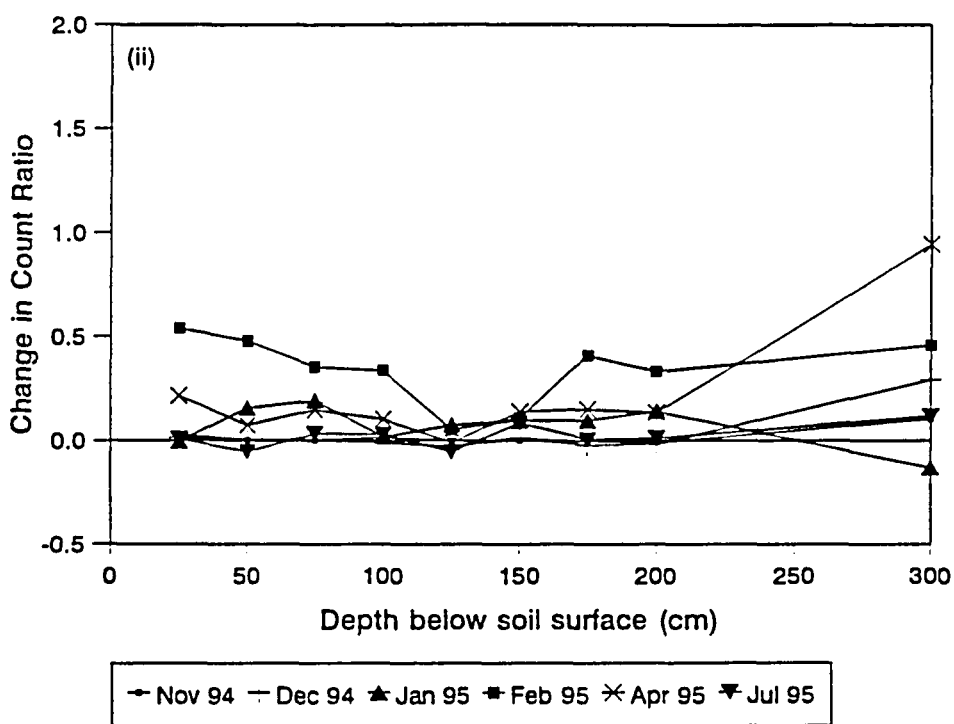
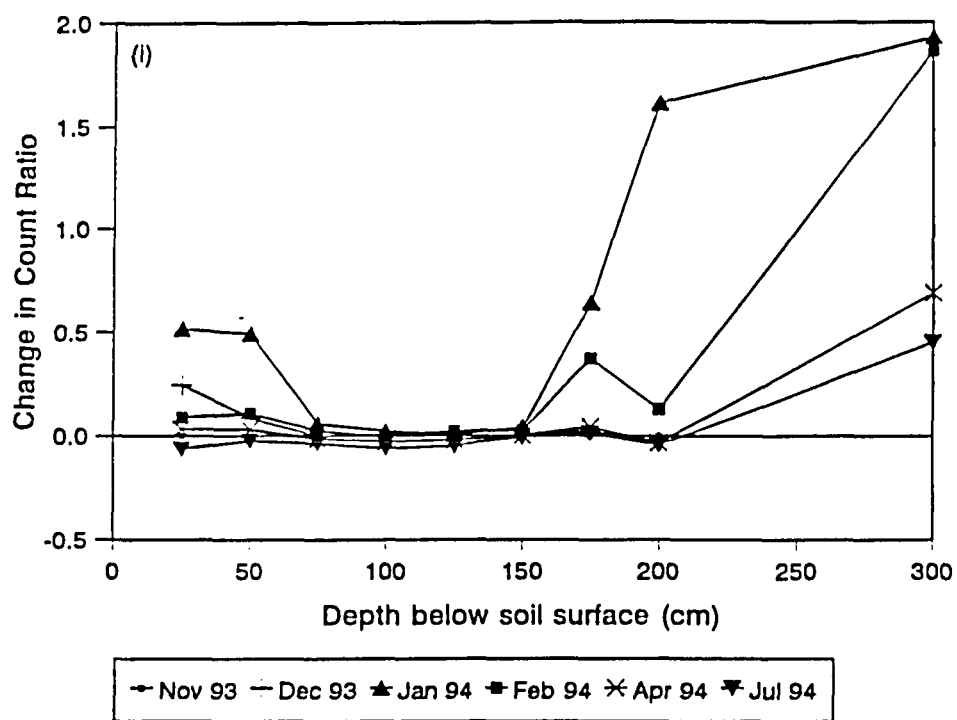


**Figure 2.7b** Relative changes in neutron probe count ratios at location 4C-D (Fig. 2.2) over the seasons (i) 1993/94 and (ii) 1994/95.

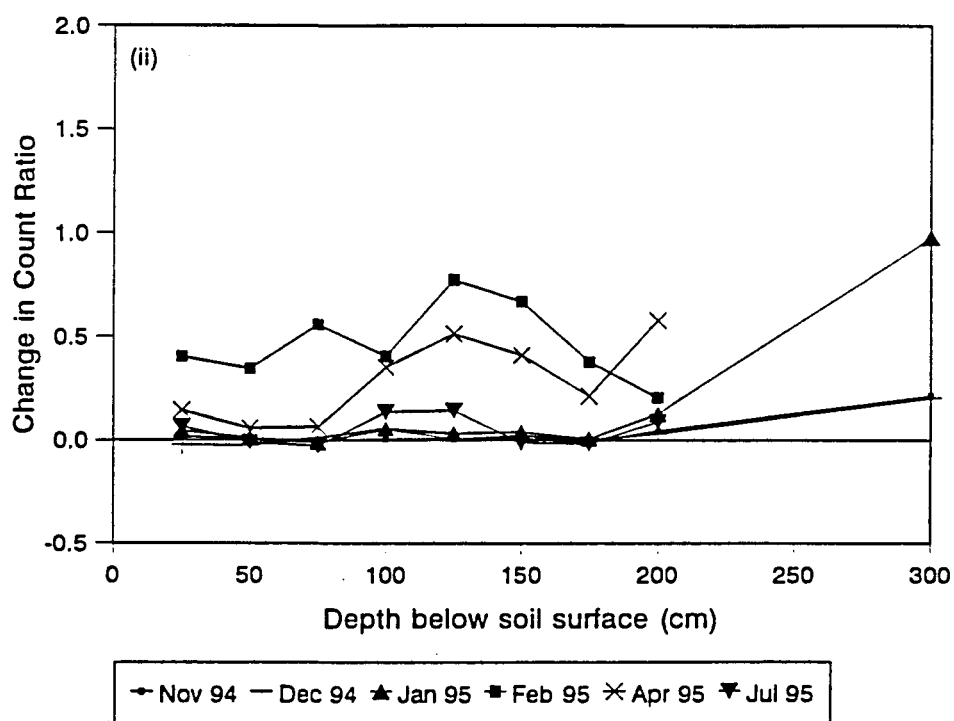
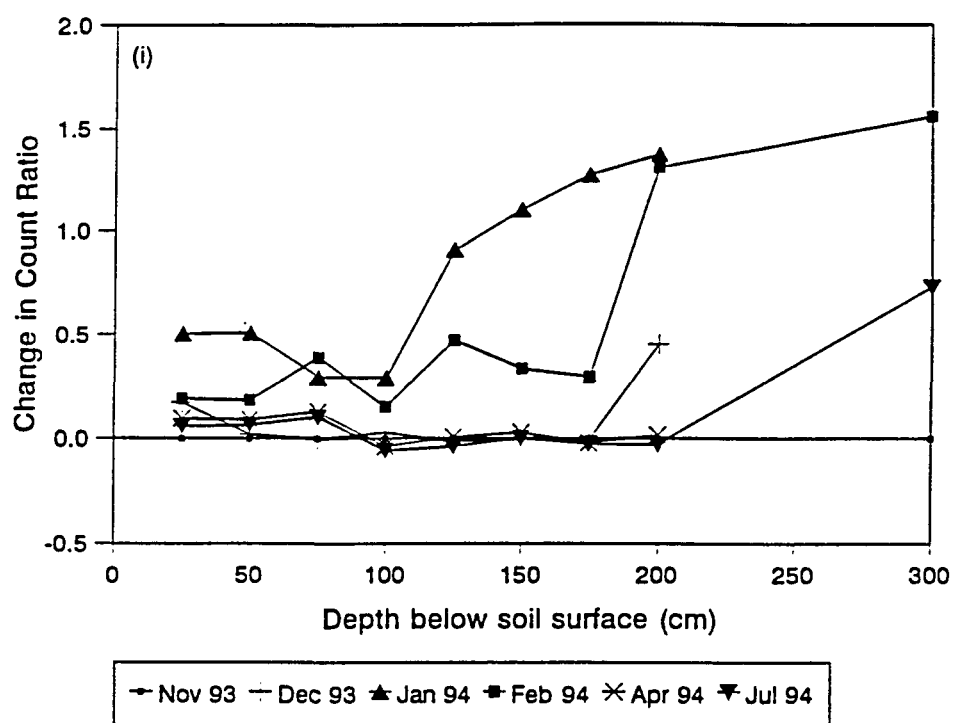


**Figure 2.7c** Relative changes in neutron probe count ratios at location 3C-D (Fig. 2.2) over the seasons (i) 1993/94 and (ii) 1994/95.

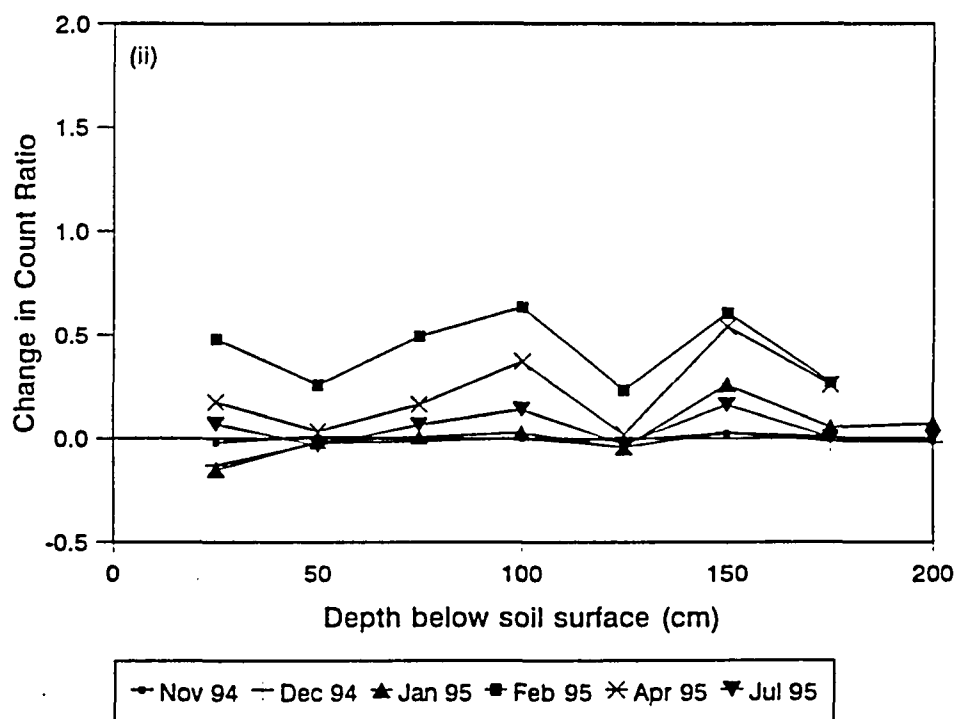
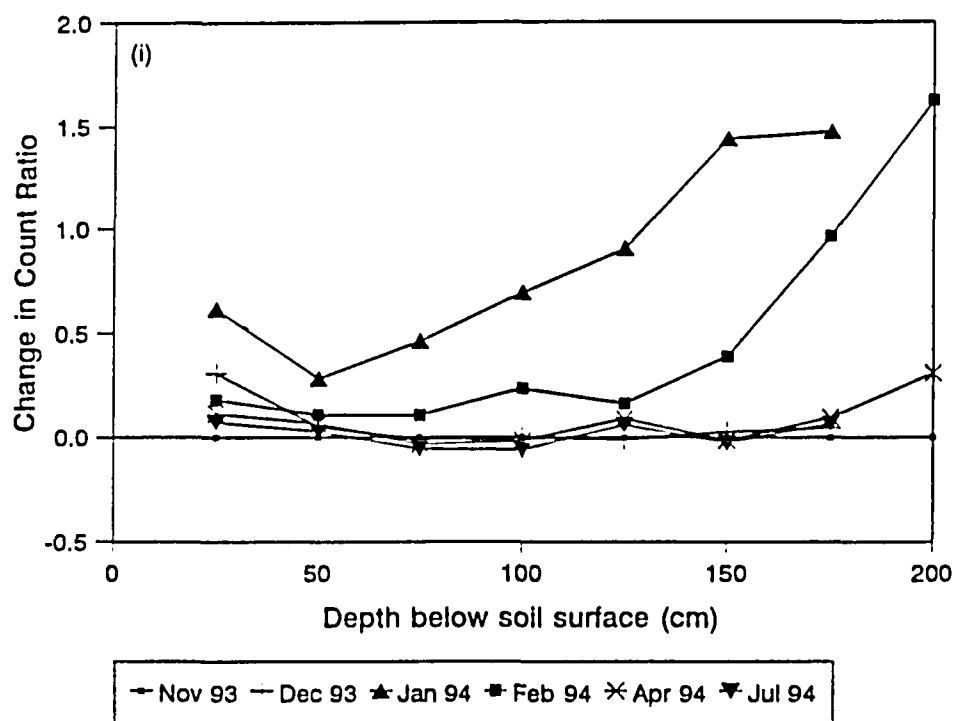


Figure 2.7d Relative changes in neutron probe count ratios at location 3U-C (Fig. 2.2) over the seasons (i) 1993/94 and (ii) 1994/95.

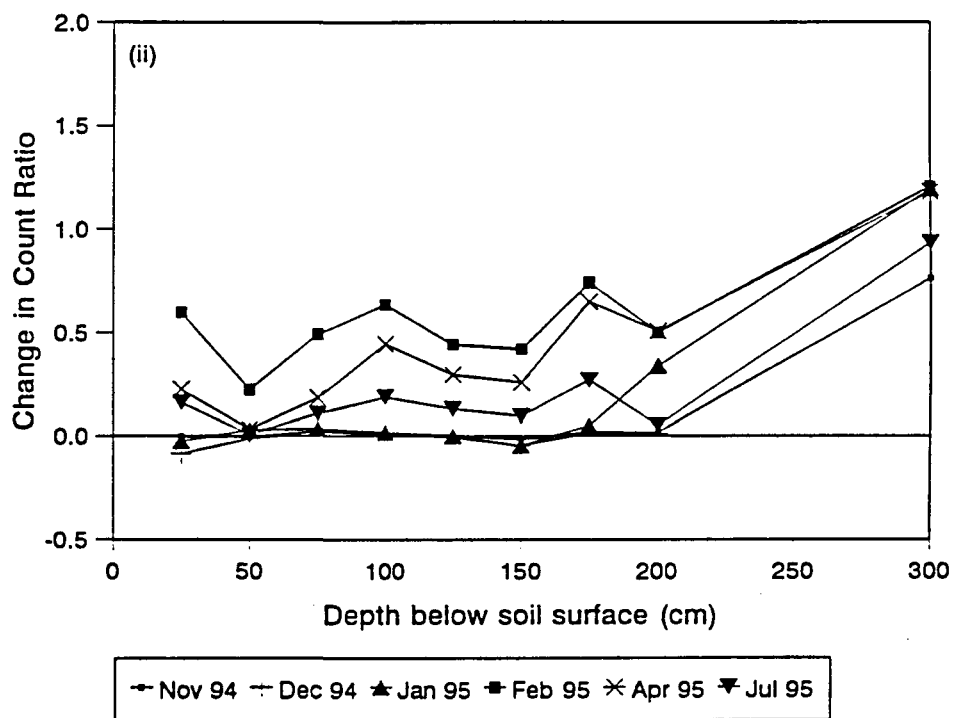
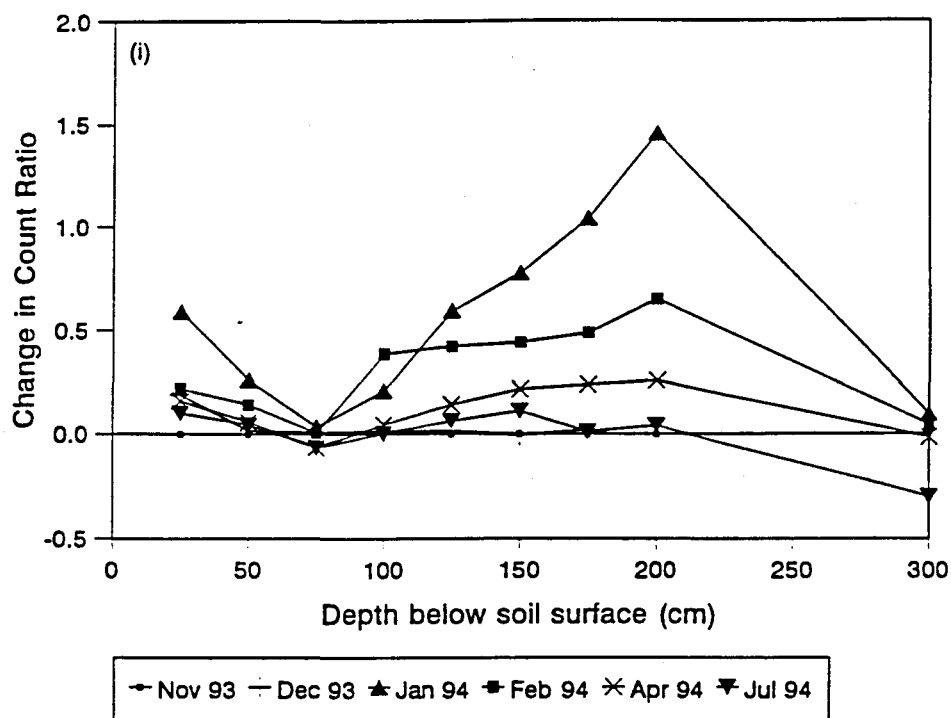
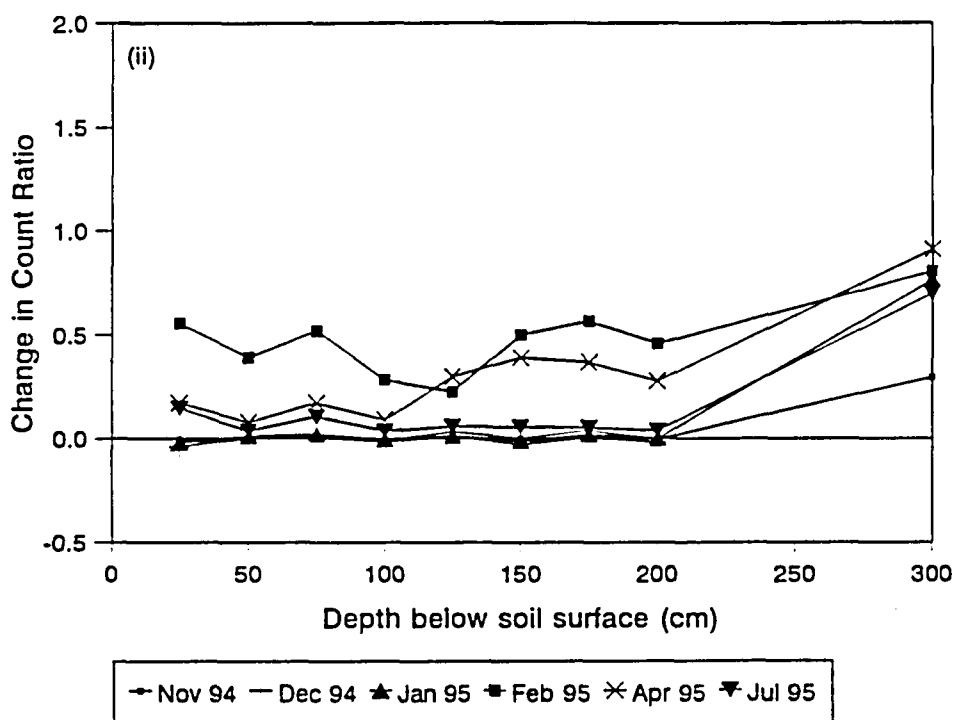
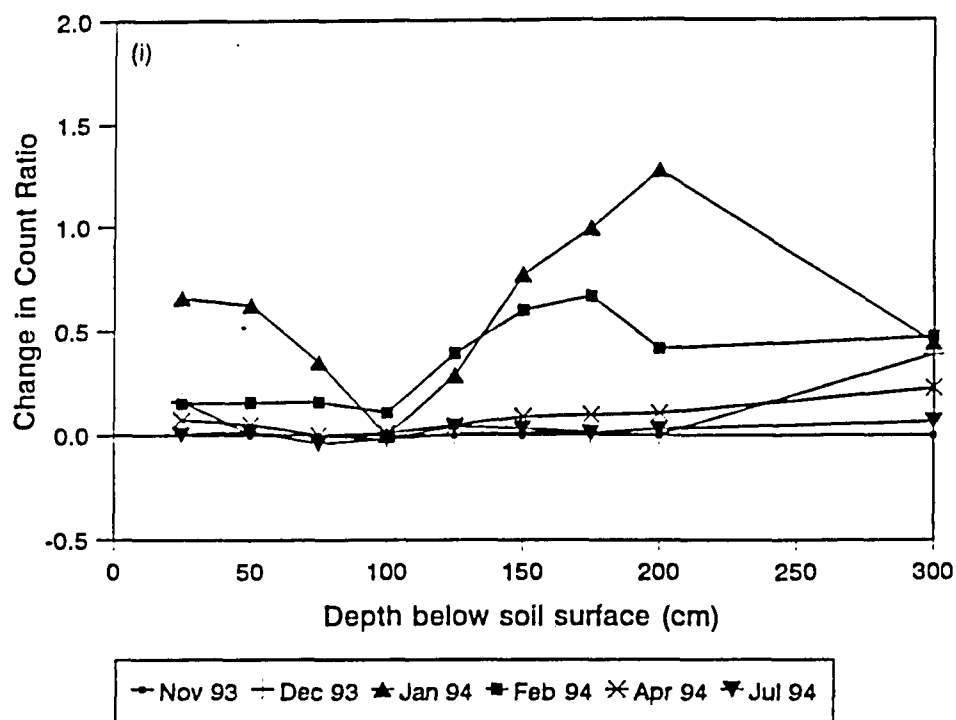


Figure 2.7e Relative changes in neutron probe count ratios at location 4U-C (Fig. 2.2) over the seasons (i) 1993/94 and (ii) 1994/95.



**Figure 2.7f** Relative changes in neutron probe count ratios at location 5U-C (Fig. 2.2) over the seasons (i) 1993/94 and (ii) 1994/95.



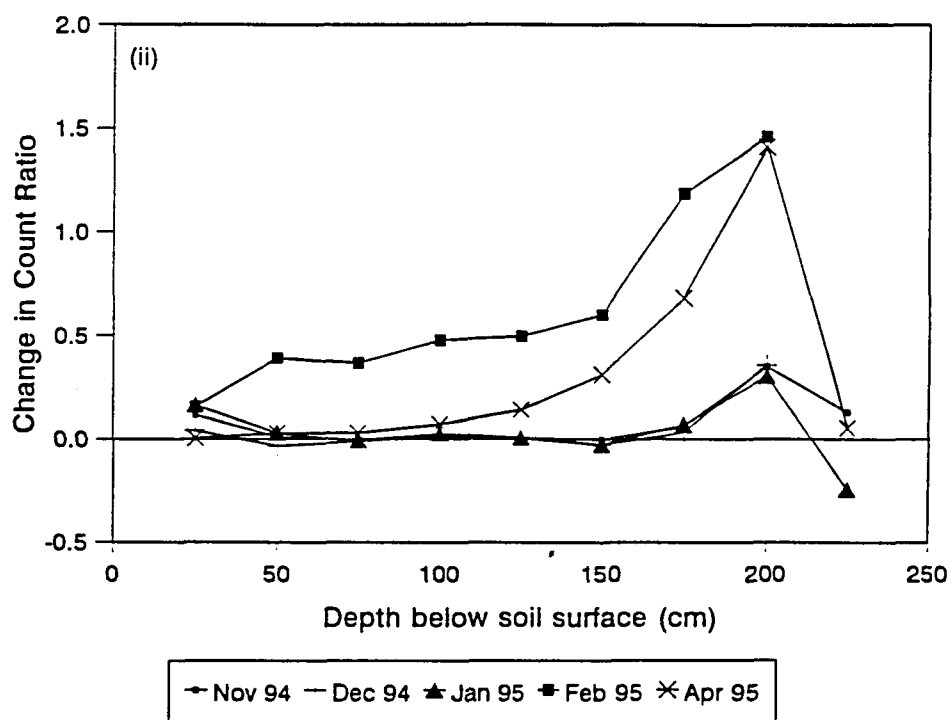
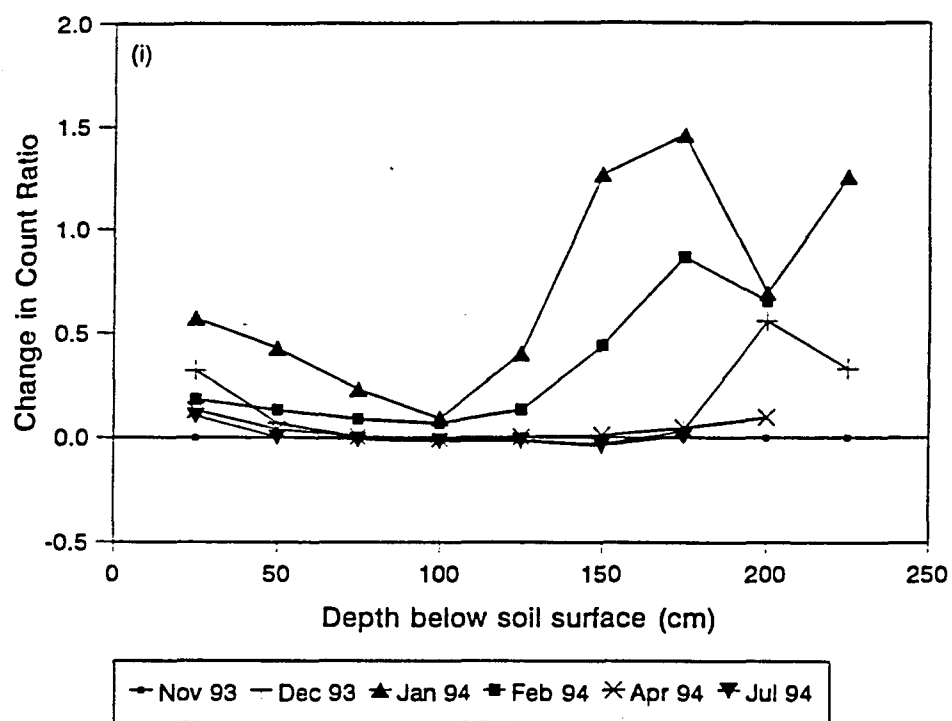
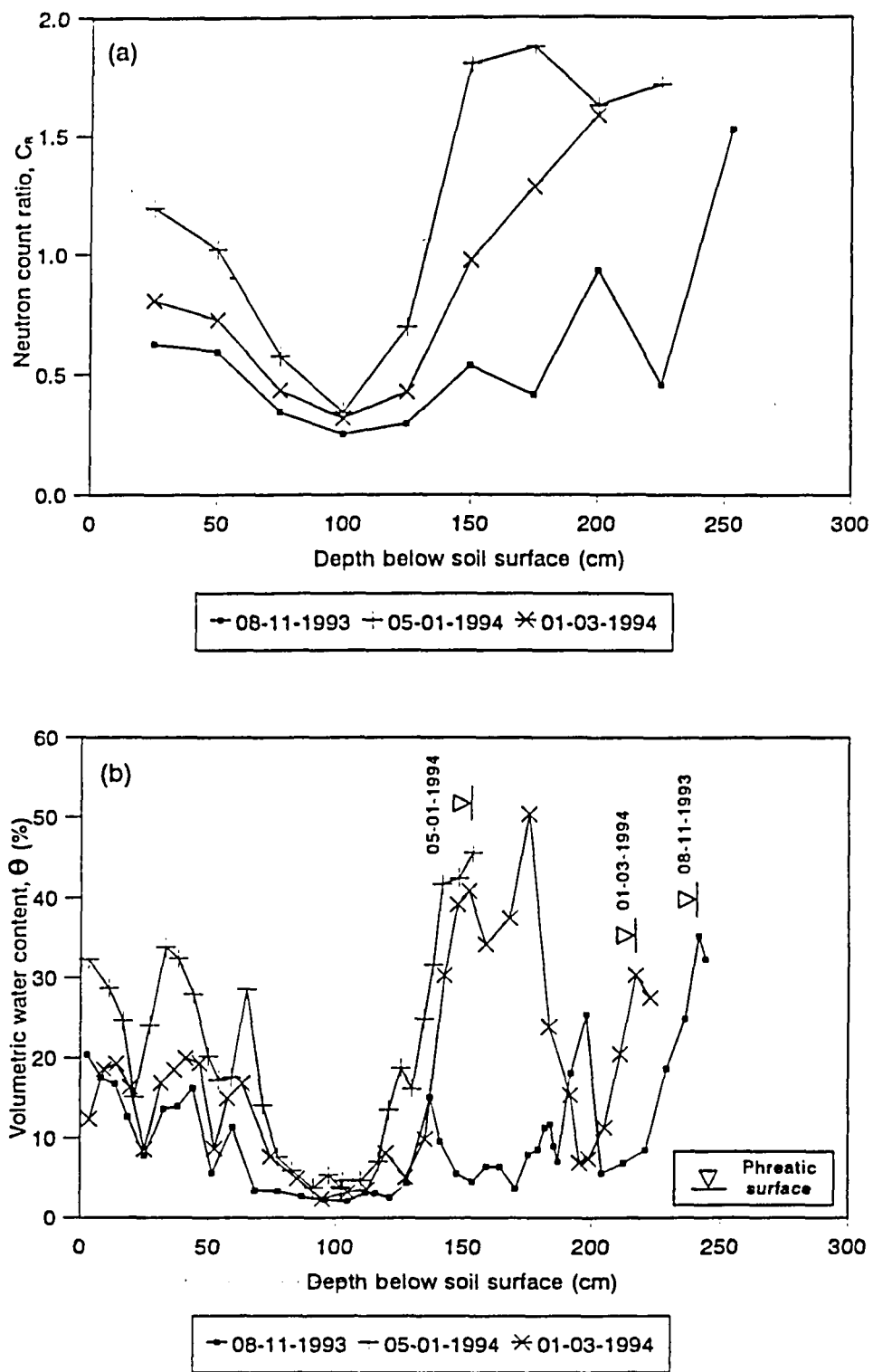
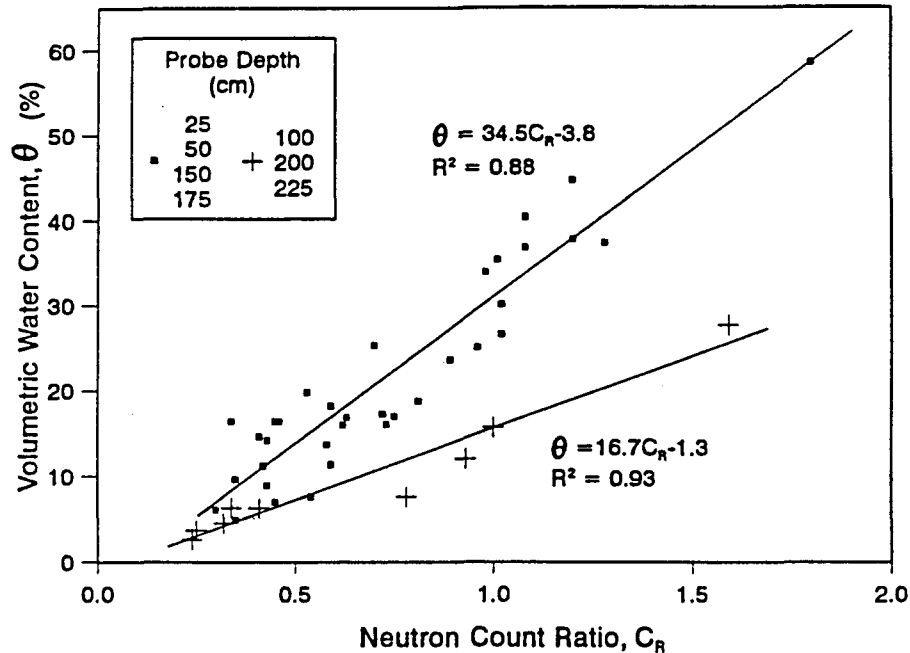


Figure 2.7g Relative changes in neutron probe count ratios at location C3-4 (Fig. 2.2) over the seasons (i) 1993/94 and (ii) 1994/95.



**Figure 2.8** (a) Neutron probe and (b) gravimetrically determined water content profiles.



**Figure 2.9** Calibration of the neutron probe using volumetric water content data from location C3-4.

### 2.2.3 Delineating Groundwater Flow Boundaries

To model the groundwater flow it is necessary to map the spatial variability and the types of flow boundaries present in the macro-channel. The fluvial sediments at the study site are deposited over gneiss bedrock, which forms the lower groundwater flow boundary. This lower boundary is considered impervious relative to the high saturated hydraulic conductivities of the coarse fluvial sands ( $K_s \sim 10$  m/hr, Table 2.3). Physical probing techniques and ground-penetrating radar (GPR) surveys were conducted to establish the bedrock profile below the coarse sandy sediments constituting the lateral channel bar deposit (Birkhead *et al.*, 1996a, Appendix 2). The survey demonstrated that GPR is an effective sedimentological tool for accurately delineating bedrock topography underlying coarse fluvial sediments.

The bedrock profile determined using a 90 MHz centre frequency GPR survey and physical probing are plotted on a cross-section through the central monitoring line in Fig. 2.10. The probing data and continuous GPR profile agree satisfactorily, yielding a regression coefficient  $R^2 = 0.79$  and an average error of 0.37 m for the limited data set consisting of nine independent observations. The radar data are calibrated using dielectric constant,  $\epsilon = 7$  (dry silt) and  $\epsilon = 25$  (saturated sand) for below and above

the phreatic surface, respectively (refer to equation 1 and Table 1 in Appendix 2). The phreatic surface profile is provided by the groundwater monitoring system. The GRP imagery became difficult to interpret beyond the active channel bar due to severe signal dissipation associated with the sediment types constituting the macro-channel infill (stratified clay, silt and sand deposits). The GPR survey deviated from the central monitoring line for  $80 \text{ m} < x < 110 \text{ m}$  to avoid large trees (Fig. 2 in Appendix 2), resulting in an "patched" profile in this region (Fig. 2.10).

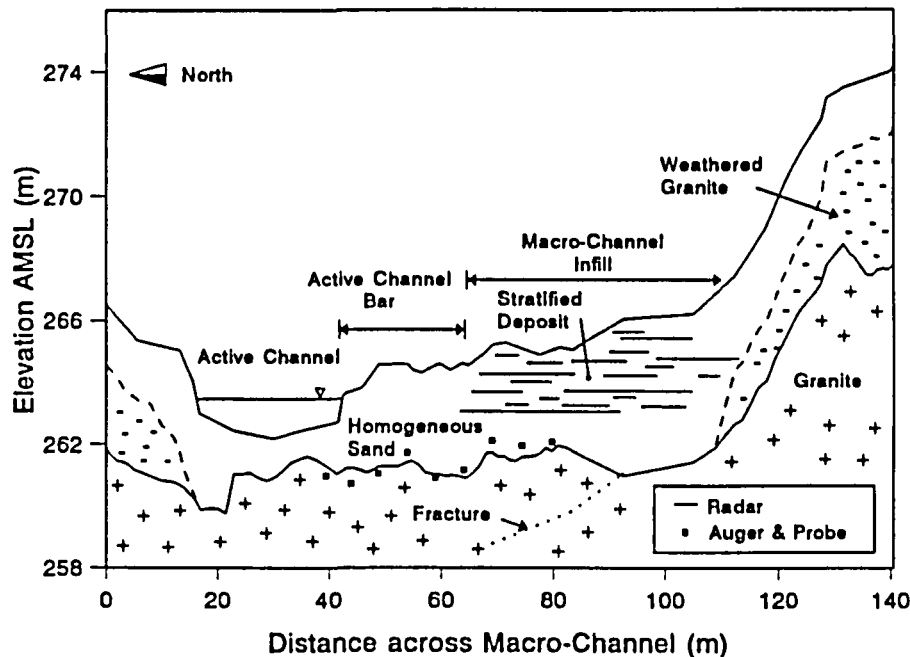


**Figure 2.10** Cross-section through the central monitoring line (Fig. 2.2) showing the bedrock profile and stratified fluvial deposit.

The flow boundaries encompassing the macro-channel lateral bar from cross-section 1 (downstream) to cross-section 4 (upstream) (Fig. 3.1 and Fig. 3.2) are plotted in Fig. 2.11. An impervious boundary is delineated at the macro-channel bank (extent of the riparian zone) and river stages are specified along the active channel bank. For discharges below  $50 \text{ m}^3/\text{s}$ , surface flow is confined to the active channel. Gneiss outcrops (Fig. 4 in Appendix 2) in the active channel immediately downstream of cross-section 2 result in an abrupt reduction in stage (Fig. 2.11, Section A-A). Isolated physical probing was used to establish the depth to bedrock across the macro-channel infill deposit. The location of the groundwater monitoring system, and position of longitudinal (Fig. 1 in Appendix 2) and lateral (Fig. 2.11) GPR survey profiles are also indicated.

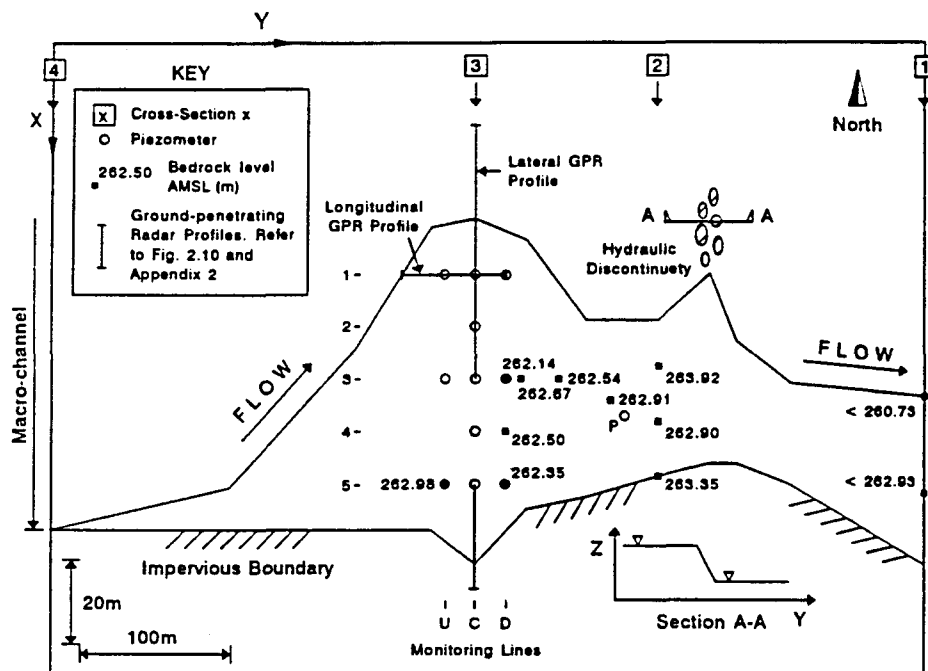


Figure 2.11 Groundwater flow boundaries encompassing the macro-channel infill deposit at the Narina study site (Fig. 3.1).

## 2.2.4 Fluvial Sediment Characteristics

### 2.2.4.1 Spatial Variability

The sedimentary composition of the active channel lateral bar (Fig. 2.10) was established by Birkhead *et al.* (1996a), using a GPR survey combined with dynamic cone penetration tests and sediment size classification. The fluvial deposit consists mainly of medium grain-sized sands to gravels, with isolated clay lenses (Fig. 6 in Appendix 2).

Sediment extracted for placement of observation holes at locations C3 and C5 were used to determine the vertical distribution of sediment sizes (Fig. 2.12). Mechanical grain-size analyses were combined with hydrometer tests for samples containing appreciable quantities (5%) with grain diameters less than 0.075 mm. Sediment size distributions at C3 and C5 are plotted in Fig. 2.12, and the sampling depths are given in Table 2.2. Both locations show general increases in textural composition with depth. The vertical variability in sediment size distributions at C3 may be used to broadly define three distinct layers, including an upper and lower layer consisting of stratified deposits of varying composition, and an intermediate layer composed of homogeneous coarse sand (Fig. 2.13). The coarse sand deposits at the base of profiles C3 and C5 were observed (from the

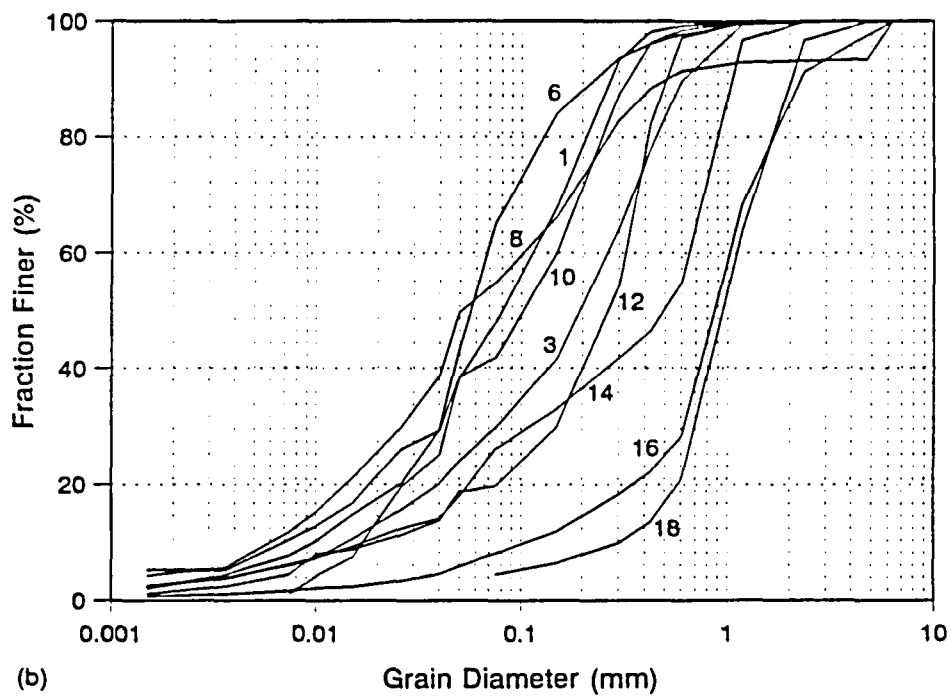
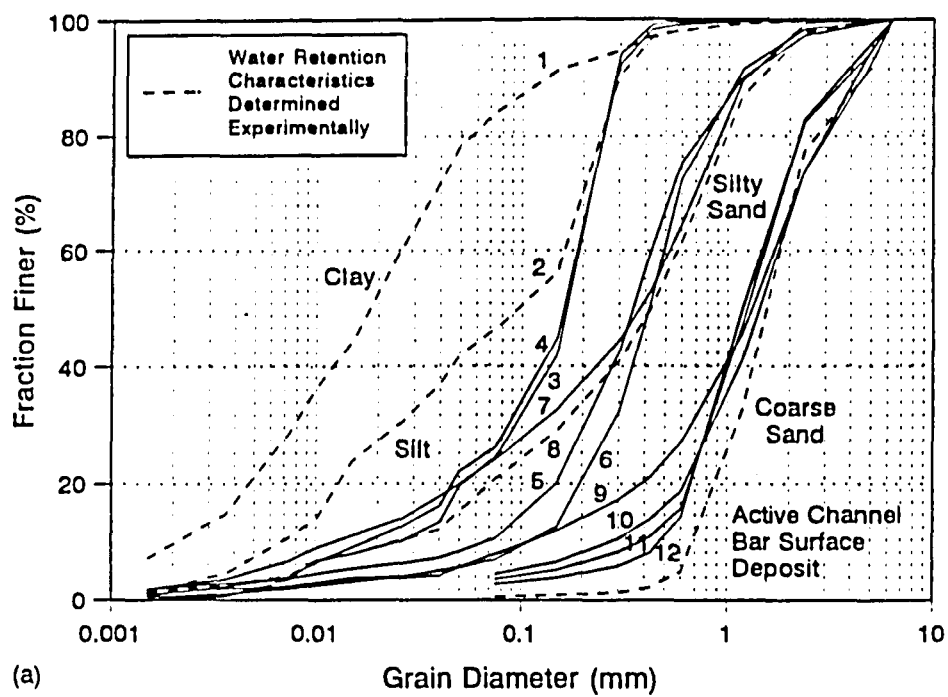


**Figure 2.12** Sediment size distributions along vertical profiles at locations (a) C3 and (b) C5 of Fig. 2.2.

placement of observation holes) to be laterally extensive across the site. The underlying layer is of similar composition to the active channel bar surface deposit (Fig. 2.12a). Four sediment samples were selected (clay, silt, silty sand and coarse sand) to describe broadly the range of sediments at the site (Fig. 2.12a and Table 2.2).

**Table 2.2** Sampling depths at C3 and C5

Sample No.		Location	
		C3	C5
		Surface Elevation AMSL (m)	
		265.08	266.17
		Depth (m)	
1	clay	0.10 - 0.25	0.00 - 0.20
2	silt	0.25 - 0.44	
3		0.44 - 0.50	0.44 - 0.57
4		0.50 - 0.67	
5		0.67 - 0.86	
6		0.86 - 0.94	1.02 - 1.40
7		0.94 - 1.17	
8	silty sand	1.17 - 1.30	1.70 - 1.93
9		1.30 - 1.70	
10		1.70 - 1.84	2.07 - 2.32
11		1.84 - 2.17	
12	coarse sand	2.17 - 2.25	2.60 - 2.73
14			2.73 - 2.90
16			3.06 - 3.20
18			3.35 - 3.50

The vertical profile at C3-4 (Fig. 2.2) is divided into layers using the four characteristic sediment types (Fig. 2.13). The specific densities and porosities required to calculate gravimetric water contents per unit volume from extracted samples were determined using standard laboratory testing procedures.

#### **2.2.4.2 Hydraulic Characteristics**

##### **2.2.4.2.1 Field Measurements**

The Guelph permeameter described by Fourie and Strayton (1996) was used to determine the saturated hydraulic conductivity of surface sediments across the study site. The application of this insitu testing was

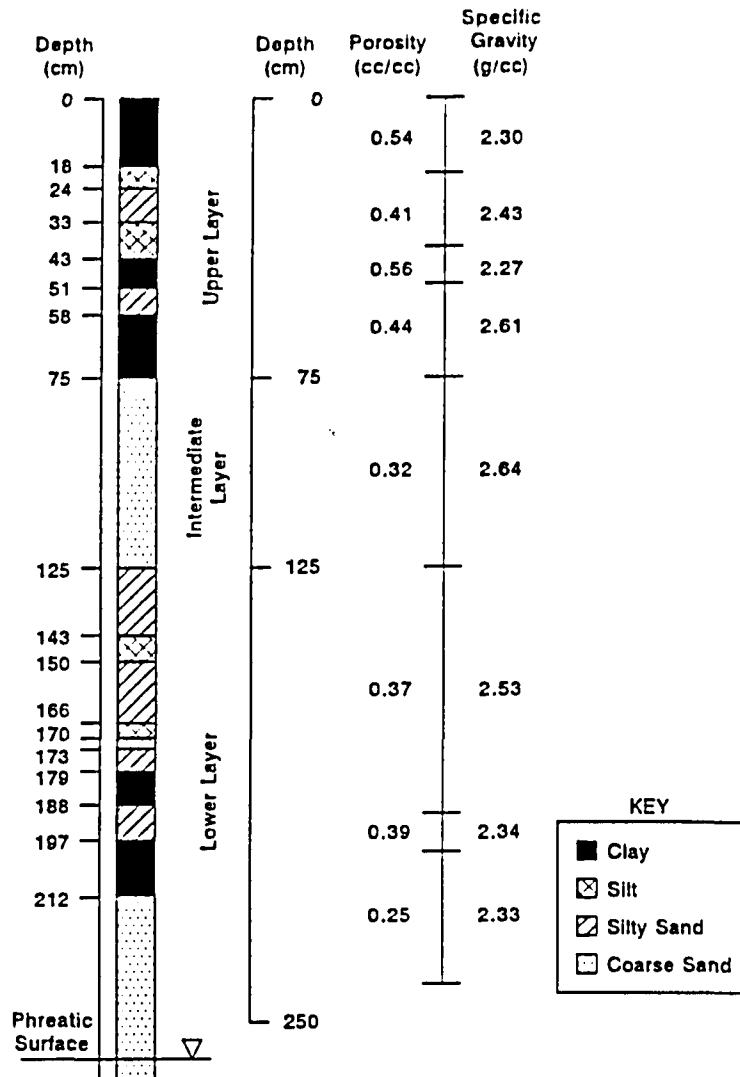


Figure 2.13 Stratified profile at C3-4.

unsuccessful due to the inability to obtain equilibrium infiltration resulting from sedimentary stratification (Fig. 2.13). Heterogeneity is a difficulty with field testing of hydraulic conductivity, and resulted in the use of laboratory methods of analysis.

#### 2.2.4.2.2 Laboratory Testing

##### *Saturated Hydraulic Conductivity*

Saturated hydraulic conductivities of the four characteristic sediments (Fig. 2.13) were determined using constant head permeability tests. The disturbed clay and silt samples were reconstituted in flexible wall membranes and placed in a triaxial cell apparatus. The cell pressures were



varied to determine the sensitivity to changes in void ratio. A rigid wall apparatus for larger specimens was used for the more conductive silty sand and coarse sand samples, and the test results are given in Table 2.3. Approximate linear reductions in saturated hydraulic conductivity with increasing cell pressures may be noted.

**Table 2.3** Saturated hydraulic conductivities

Sediment Type	Specimen Dimensions		Cell Pressure (kPa)	$K_s$ (m/hr)
	Length (mm)	Diameter (mm)		
Clay	74.4	33.9	50	$1.56 \times 10^{-4}$
			100	$8.03 \times 10^{-5}$
			300	$2.25 \times 10^{-5}$
Silt	79.0	36.0	50	$2.92 \times 10^{-3}$
			100	$1.75 \times 10^{-3}$
			300	$4.97 \times 10^{-4}$
Silty Sand	205.0	76.2	-	$3.51 \times 10^{-2}$
Coarse Sand	205.0	76.2	-	21.85

### *Water Retention Data*

Water retention data for desorption from reconstituted samples of the clay, silt and silty sand sediments were determined using the controlled outflow apparatus described by Papageorgiou (1994). Volumetric water contents corresponding to soil suctions in the range 5.6 kPa to 143.4 kPa (0.56 m to 14.34 m) were measured (Fig. 2.14). The soil suction vs. water content data for the coarse sand was determined by incrementally draining water under gravity from a soil column, and observing the corresponding drop in phreatic surface level. Water retention data are required up to the soil suction corresponding to the wilting point (150 m), beyond the range that may be determined in the laboratory using the controlled outflow apparatus. To facilitate extension of the water retention relationships, water contents derived from field samples extracted at the end of the dry seasons are incorporated in the data sets. The closed form analytical model of van Genuchten (1978) (equation 4.73) is fitted by regression to the water retention data, and the parameter values for each sediment type are given in Table 2.4. The expression derived by van Genuchten (1980) (equation 4.74) is used to synthesize the unsaturated hydraulic conductivity, with  $\lambda = 0.5$  (Table 2.4).

**Table 2.4** Parameter values in the van Genuchten models

Parameter Values	Sediment Types			
	Clay	Silt	Silty Sand	Coarse Sand
$\theta_s$	0.47	0.36	0.27	0.37
$\theta_r$	0.00	0.00	0.00	0.03
$\alpha$ (cm <sup>-1</sup> )	$1.26 \times 10^{-2}$	$5.63 \times 10^{-1}$	2.75	25
$n$	1.92	1.19	1.20	5.00
$m = 1-1/n$	0.48	0.16	0.17	0.8
$l$	0.5	0.5	0.5	0.5

The regression water retention relationships of van Genuchten (1978) (Fig. 2.14) and synthesized hydraulic conductivities are only valid over the soil suction range 0 to 150 m. The reduced range of applicability may be observed by the unrealistic zero values for the residual water contents for the clay, silt and silty sand sediments (Table 2.4) which apply at soil suctions well above the wilting point.

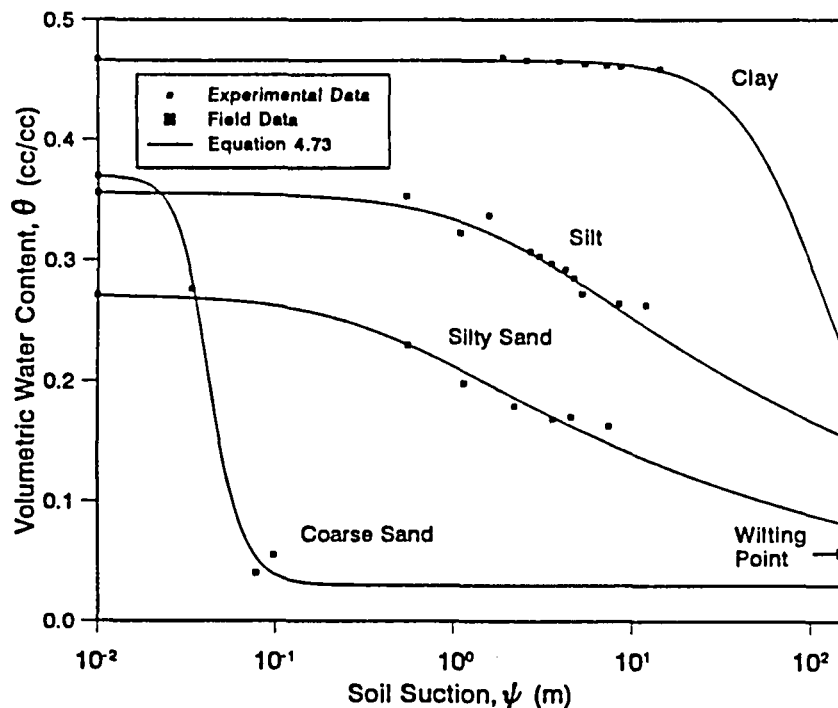


**Figure 2.14** Equation 4.73 (after van Genuchten, 1978) fitted to the water retention data for the four characteristic sediments types in Table 2.4.

## 2.3 Transpiration Model Data Collection

### 2.3.1 Meteorological Conditions

One of the objectives of this research was to gain an adequate understanding of the main meteorological factors governing the water use of the riparian vegetation. The prevailing weather conditions were recorded for the duration of the study by a standard MC Systems<sup>1</sup> automatic weather station erected adjacent to the Narina site in December 1992. At this station, photosynthetically active radiation (PAR), relative humidity (RH), temperature, wind direction and wind speed were recorded. RH and temperature were recorded hourly. VPD was calculated from the RH and temperature data. The logger was programmed to calculate hourly averages of minutely data for each of the above parameters. Table 2.5 summarises the sensors installed at the automatic weather station. Rainfall was recorded at the weather station located at Skukuza, approximately 3 km from the Narina site. These data, in conjunction with the vegetation transpiration data, were used to develop the riparian transpiration models.

**Table 2.5** Sensors connected to the MCS 120.02 EX automatic data logger installed at the weather station at the selected study site on the Sabie River in the Kruger National Park

Sensor	Parameter being measured	Log period
Licor quantum	Photosynthetically active radiation (PAR)	Hourly average
MCS 174	Temperature and relative humidity	Hourly average
MCS 177	Wind speed	Hourly average
MCS 176	Wind direction	Hourly average

The meteorological data collected at the Narina site was collated and screened using appropriate procedures to identify areas of poor data. The data set begins on the 16th December 1992 and ends on the 6th of June 1995. The hourly data collected by the weather station have been summarised to produce daily, weekly, monthly and annual totals, means, maxima and minima where appropriate. The daily data set was used in the development of the transpiration models for the *Ficus sycomorus* tree and the reeds. Monthly and annual data summaries were used mainly to describe conditions pertaining at the time of the study.

---

<sup>1</sup> Mike Cotton Systems, P.O. Box 73, Steenberg 7947, South Africa

### 2.3.1.1 Annual Profile of the Meteorological Conditions Recorded at the Narina Study Site

Table 2.6 summarises the annual trend in meteorological conditions recorded at the Narina site over the duration of the study. The data illustrate that there was considerable variation in climate from year to year. For example the extremes in temperature recorded in 1994 showed a larger range than the other two years on record with a maximum of 49°C and a minimum of -3.7°C. The relative humidity was also lowest during that year, with an average daytime value of 59.2%. These two factors combined resulted in the highest levels of evaporative demand during that year with a VPD of 1.56 kPa. By contrast to 1994, the conditions recorded during the first half of 1995 were milder, with lower temperatures, higher humidities and consequently also the lowest average daytime VPDs. These conditions were due to the increased incidence of cloudiness during the first half of 1995, as indicated by the lower levels of PAR.

The year-to-year variation recorded in the primary meteorological conditions driving the transpiration process underscores the necessity of recording evaporation over periods of longer than one year, and also of developing techniques that allow one to predict the rates under conditions other than those governing during the period when the data were collected.

**Table 2.6** A summary of the meteorological conditions recorded at the Narina site for the duration of the study.

	YEAR	MEAN $\pm$ STD	MAX	MIN
Temperature	1993	25.9 $\pm$ 7.5	45.8	-1.0
	1994	27.5 $\pm$ 7.8	49.0	-3.7
	1995	25.9 $\pm$ 6.7	41.9	1.2
Relative humidity	1993	63.1 $\pm$ 25.7	100	7.0
	1994	59.2 $\pm$ 27.4	100	8.9
	1995	74.2 $\pm$ 24.5	100	14.2
VPD	1993	1.28 $\pm$ 1.12	5.80	0
	1994	1.56 $\pm$ 1.32	7.24	0
	1995	0.93 $\pm$ 1.02	5.08	0
PAR	1993	659.1 $\pm$ 533.2		0
	1994	681.4 $\pm$ 532.3		0
	1995	586.6 $\pm$ 518.8		0
WIND SPEED	1993	1.3 $\pm$ 0.5		0
	1994	1.5 $\pm$ 0.8		0
	1995	1.2 $\pm$ 0.5		0

### 2.3.1.2 Monthly Trends in the Meteorological Conditions Recorded at the Narina Study Site

#### *Rainfall*

The initial hypothesis of this study assumed that the bulk of the supply of water to the riverine vegetation originates from the Sabie River. However, rainfall is potentially an important additional source of water, particularly during the rainy season. The annual total rainfall recorded varied from 331 mm in the 1993/94 season to 626 mm in the 1994/95 season. The 1992/93 season was intermediate, although on the dry end, at 387 mm.

The monthly rainfall recorded at Skukuza over the three years of this study (Figure 2.15) has the distribution one would expect in the summer rainfall region. The bulk of the rain was received between December and April. The maximum monthly total received was 323 mm during January in the 1994/95 season, while the typical average monthly total received during the rainy season was 60 mm per month.

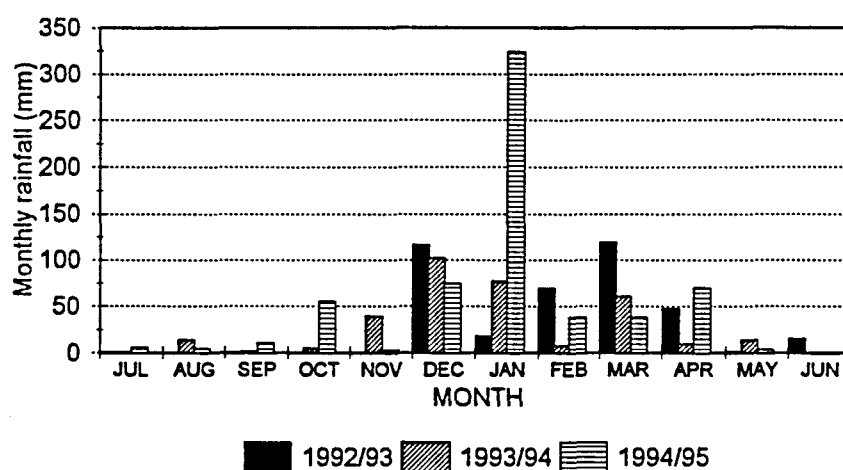


**Figure 2.15** Total monthly rainfall recorded at Skukuza from December 1992 to June 1995.

The trend in monthly rainfall was slightly different for each season (Figure 2.15). Peaks were recorded early and late in the rainy season during the first season (1992/93), with very low rainfall recorded for January. The first rain in the 1993/94 season was recorded in November, with significant amounts in December and January, followed by a decline to April. By contrast to the above two seasons, large quantities of rain fell during January in the 1994/95 season, again with hints of a mid-summer dry period, and relatively high rainfall being recorded for April. The above data illustrate that rainfall in this area is typically very variable, and is likely to play a varied role in the direct supply of water to the riverine vegetation.

## *Temperature*

Trends in the mean monthly maximum mean and minimum temperatures, humidity and PAR recorded at Narina (Figure 2.16 a, b, and d) all illustrate the expected seasonal trends. Maximum temperatures were recorded during the summer months, while the minimum temperatures were recorded during the late winter months. Mean daytime temperatures were approximately 8°C higher during the winter months than during the summer months. There was also a considerable range in the absolute temperatures (Fig 2.16a). This range was approximately 25°C during summer and increased to approximately 35°C during the cold winter months.

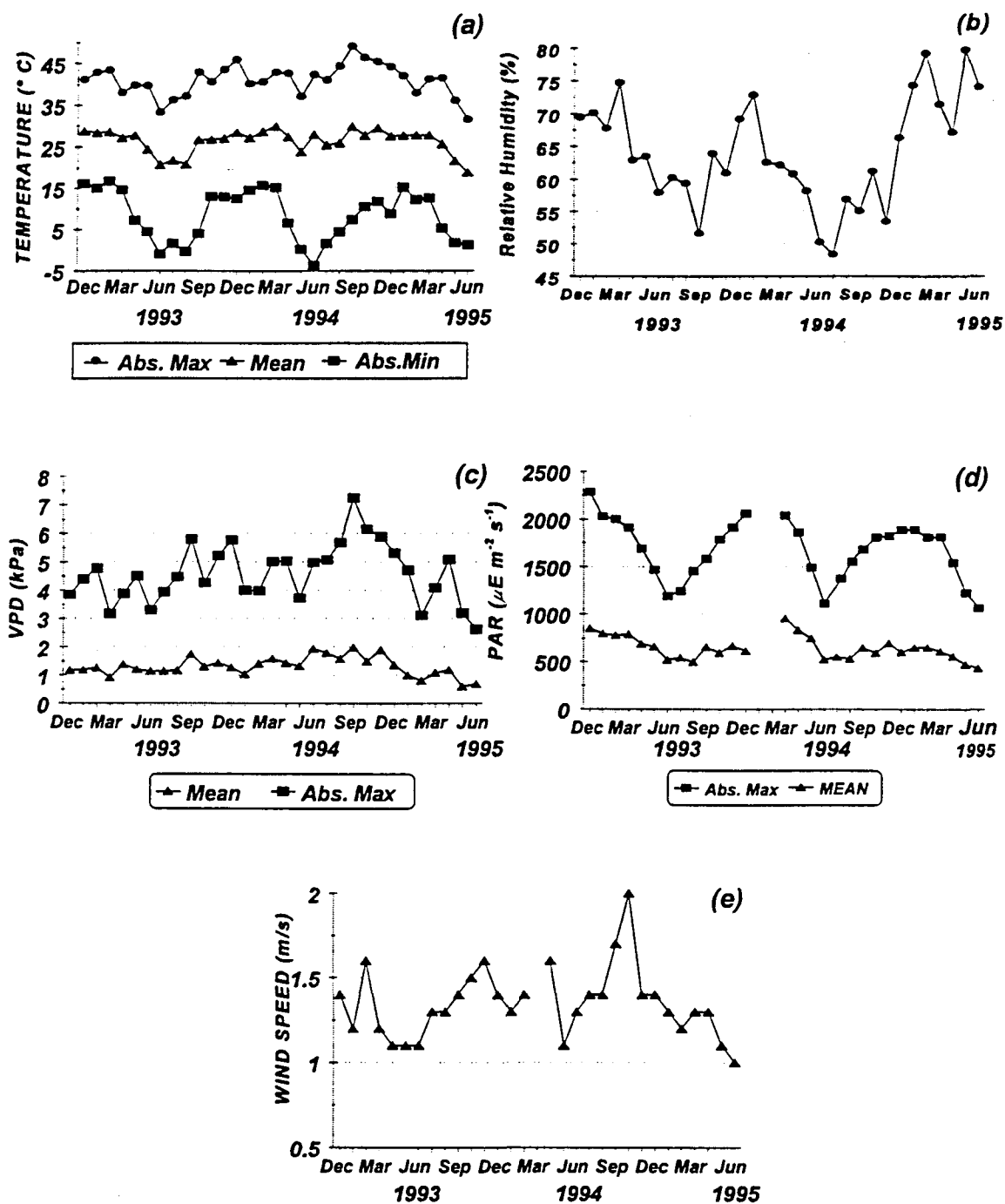


**Figure 2.16** A summary of monthly daytime temperature (a), relative humidity, (b), VPD (c), PAR (d) and wind speed (e) recorded at the Narina site from December 1992 to June 1995.

A particularly low minimum temperature of  $-3.7^{\circ}\text{C}$  (verified by the temperature recorded at Skukuza's manual weather station) was recorded on the morning of 30 June 1994 (Figure 2.17). This cold snap is believed to have caused the large-scale die off observed in the *Ficus sycomorus* trees along the Sabie River. The reference fig tree was also severely affected - severe die-back was observed on along the secondary branches and many of the leaves were lost. The impact of this event on the research strategy will be discussed in section 3.2.4

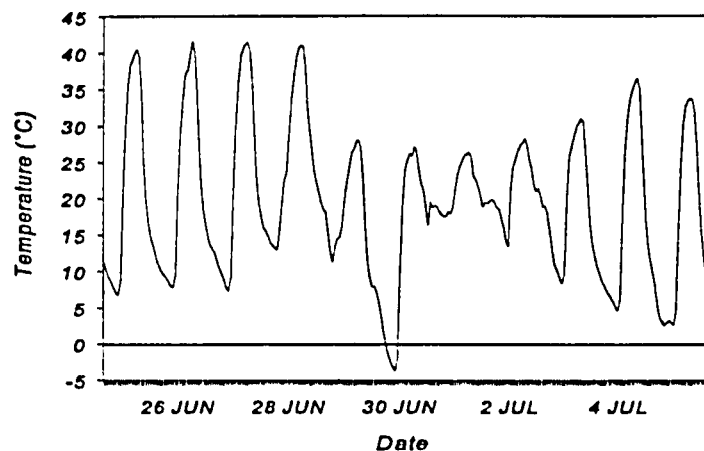


**Figure 2.17** Hourly temperatures recorded at Narina from 25 June to 5 July 1994

The expected seasonal trend in humidity was also recorded with the late winter months being considerably drier than those conditions recorded during the rainy season (Fig 2.16b). The highest mean monthly humidities recorded during the three summers on record all occurred during the late summer months of February and March. Despite the general annual cycle recorded in humidity, there was considerable year-to-year variation, such as the high humidities recorded in June during 1995.

The trend in vapour pressure deficit (Figure 2.16c) was less clear than was the case with either temperature, or relative humidity. Absolute monthly maximum values were consistently high throughout the study period reaching peak values in September and October of 1994. Mean monthly daytime values illustrate that while the VPD fluctuates considerably from month to month, the highest values were generally recorded in the months from June to December, coinciding with the latter section of the dry season, prior to the onset of the summer rains.

The mean monthly PAR data are affected by both the changing azimuth through the course of the year, and the incidence of cloudy weather. The trend illustrated by the absolute mean monthly maximum PAR curve clearly demonstrates the effect of the changing azimuth: low maximum PAR values are recorded when the sun angle is at its lowest during the winter solstice, while the highest PAR values are recorded during the summer solstice (Figure 2.16d). The monthly mean



daytime PAR levels varied between 480 in June 1995 and almost 1000 in April 1994. While the interaction between azimuth and the incidence of cloudy condition resulted in no really clear annual trend, the highest levels were usually recorded on cloudless days. This accounts for the relatively high mean daytime levels of PAR recorded during April, May and June in 1994, despite the relatively low azimuth at that time of year.

In general, mean daytime windspeeds were low, with a maximum mean monthly daytime value of only  $1.95 \text{ m sec}^{-1}$ , and a mean of  $1.33 \text{ m sec}^{-1}$  over the duration of the study (Figure 2.16e). No clear trend was evident in the mean monthly wind speed recorded at Narina. In general, however, the data indicate a trend of increasing wind speeds after mid winter during the months of September, October, and November, and generally low wind speeds for April, May and June.

The wind speed frequency distribution (Figure 2.18) confirms that high wind speeds are uncommon. The period April to June also stands out as being the period during which wind speeds were lowest. The observed pattern was repeated for both complete years on record (1993 and 1994).

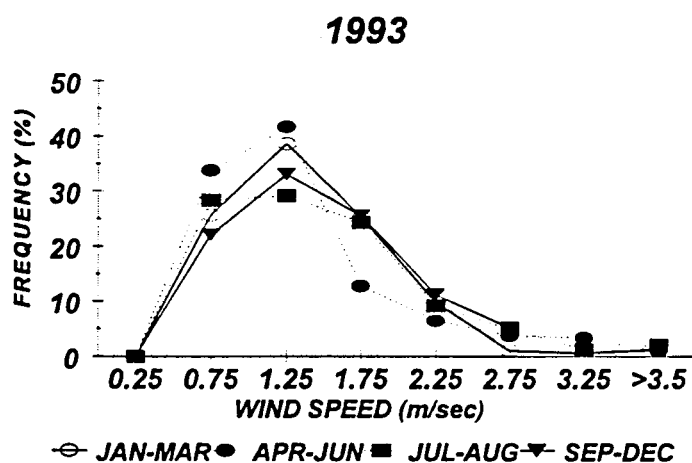


**Figure 2.18** A frequency distribution of mean hourly, daytime wind speeds recorded for four periods during the year in 1993.

Further analysis of the wind speed data illustrates that the highest wind speeds were generally recorded over the mid day period (Figure 2.19). More importantly, low wind speeds (between  $0.5$  and  $1.0 \text{ m sec}^{-1}$ ) were very uncommon during the mid day period. This is significant as it ensures that the tree canopies are well ventilated, minimising the extent to which the boundary layer restricts evaporation of water from the tree canopy over that time of day during which evaporation rates are highest.

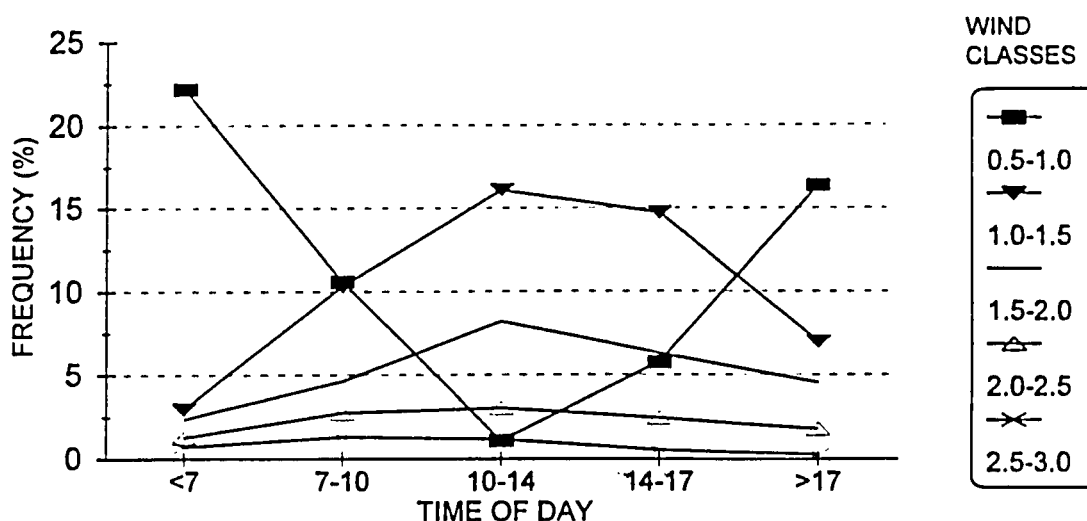


**Figure 2.19** A frequency analysis of mean hourly daytime wind speeds analysed by time of day for the year 1993

A matter of some initial concern was that the location of the weather station adjacent to the riparian zone (rather than within the zone) would result in an aberration in the data under those conditions when the wind direction incident on the weather station originated over the riparian zone. As a result, the relative humidities recorded under conditions of a northerly wind would be higher as a result of the riparian zone, rather than reflecting a change in the ambient meteorological conditions. This would be most evident during the dry winter period when the terrestrial conditions were at their driest.

An analysis of the wind direction for the two full years on record illustrates that the prevailing wind directions were the north and south east (Figure 2.20). Westerly and south westerly winds were found to be very rare. In general, the south easterly wind direction was most common during the summer months. However, from April through to August the northerly and south-easterly wind directions were approximately equally common. The northerly wind direction was only recorded between 25 and 10% of the time and was found to have no significant influence on the humidities and temperatures recorded at the weather station. This indicates that the weather data recorded at the weather station was not significantly affected by the proximity of the adjacent riparian zone, and as a consequence it was not necessary to edit out those sections of the data for which the wind was blowing from a northerly direction prior to developing the transpiration model for the riparian vegetation.

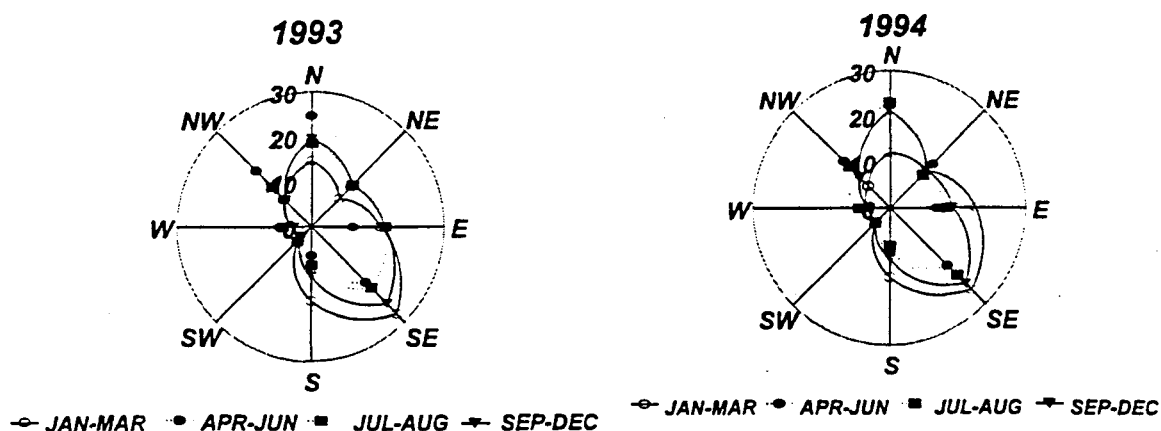


**Figure 2.20** Wind roses illustrating the frequencies with which wind was recorded from each of the various wind directions for years 1993 and 1994.

## 2.3.2 Leaf Area Surveys

### 2.3.2.1 Changes in Leaf Area Index at the Narina Site

The canopy dynamics were monitored at monthly intervals from November 1993 using a Licor LI 2000 Leaf Area Metre. Three transects were established at the Narina site corresponding with the lines of piezimeters running perpendicularly to the river. Wooden stakes were used to mark five metre intervals on each transect to ensure that readings were made at precisely the same point. Monthly readings were taken at each stake on each of the three transects. These readings corresponded to the times at which the neutron probe measurements were taken. Each transect was sub-divided into sections corresponding to reeds and woody vegetation, and these data were analysed to determine the change in leaf area index (LAI) in reeds and the forest canopy at the Narina site (Figs 2.21 - 2.23).

The Licor instrument requires two measurements to estimate leaf area index. Firstly an 'above canopy' light reading that is used to determine the intensity of the radiation without the influence of the canopy. The intensity of the radiation is measured in five concentric hemispheres varying in angle from the vertical. Secondly, it requires a 'below canopy' reading that measures the attenuation of light through the canopy - again measured in five hemispheres. The 'above canopy' reading was taken in the road immediately adjacent to the weather station as this was the area least affected by surrounding vegetation. The below canopy readings were taken along each of the above transects. As the surrounding vegetation was judged to have an influence in the above canopy reading, the Licor Li1600 software was used to edit out the two outermost hemispheres - the leaf area index estimates presented are therefore based on the three inner hemispheres which provided the most reliable data. As recommended by the manufacturers of the instrument, readings were consistently taken early in the morning, or under overcast conditions.

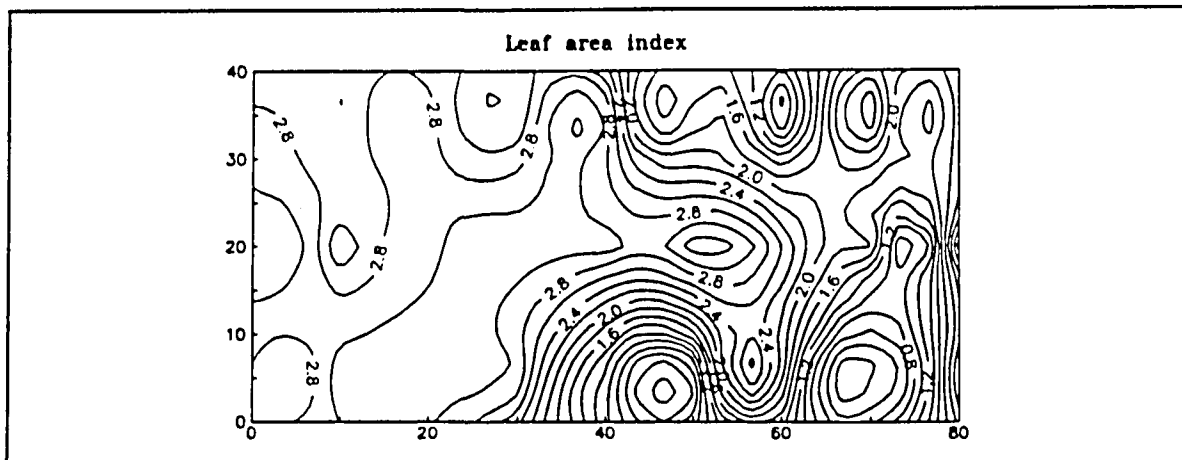


**Figure 2.21** The spatial variation in the leaf area index over the study site. The x axis represents the distance (m) along a transect which runs perpendicularly towards the river. Position 0 on the x axis is situated on the fringe of the riparian forest away from the river and position 80 is situated very close to the open river channel.

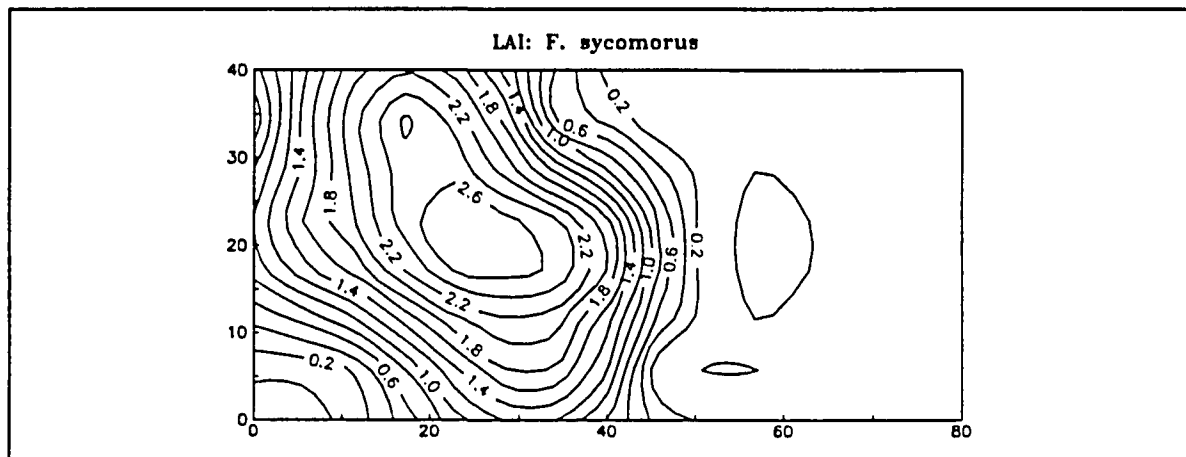


**Figure 2.22** The leaf area index distribution of *F. sycomorus* across the study site.

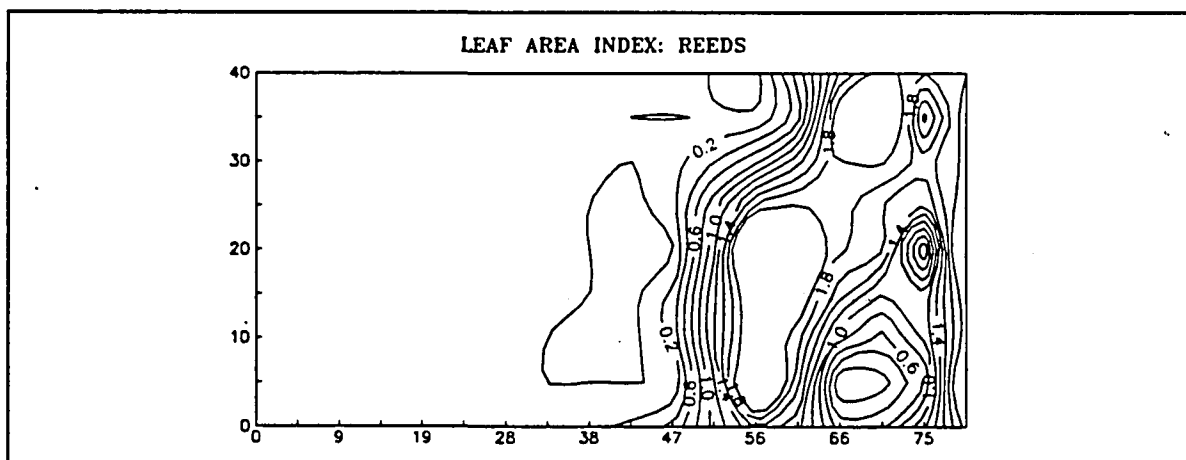


**Figure 2.23** The leaf area index distribution of the reed *P. mauritianus* across the study site.

As it was necessary to cut a path through the reed vegetation, a 180° mask was used on the leaf area metre to screen out the area affected by the path. While readings were taken, the metre was orientated to exclude the area disturbed by cutting the access path. As an additional precaution, the metre was held approximately 50 cm off the path. In the reed bed readings were taken 30 cm above the ground, while the metre was held at waist height in the riparian forest.

In addition to the LAI measurements, a visual estimate was made of the relative contribution of the various species to the leaf area index (LAI) at each point on the three transects. A kriging function was then used to develop a spatial representation of how the total LAI varied over the site (Fig 2.21) and how the LAI of the various species varied over the site (Fig 2.22 and Fig 2.23). These figures illustrate the situation as recorded during February 1993 at the start of the study, and no major changes occurred in the distribution of the species over the course of this study.

Fig 2.22 illustrates that *F. sycomorus* accounts for a large proportion of the leaf area within the riparian forest while Fig 2.23 illustrates the position and LAI of the reed bed. These measurements of leaf area index will be used to extrapolate from the estimates of transpiration per unit leaf area to the estimate of the total transpiration from the study site. There is, however, some concern that the leaf area index measurements for the site are lower than expected, raising the possibility that the LI-2000 underestimated the actual leaf area index on the site.

While the diagrams above are well suited to illustrating the variations in canopy density at the site, and also the relative location of the riparian forest to the reed bed, they do not lend themselves to demonstrating trends in LAI over the course of the study. For this purpose all those readings taken under the riparian forest and in the reed bed have been grouped separately to illustrate changes in these two broad vegetation categories over time.

The data show a very strong seasonal trend in leaf area index, with peaks in leaf area index being recorded in late summer, and the lowest levels being recorded in both vegetation types just prior to the onset of the summer rainy season (Figure 2.24). The highest levels recorded in the riverine forest were approximately seven, while the peak recorded in the reedbed was marginally lower at six. The peak levels in LAI for both vegetation types were recorded in February and March, presumably in response to the cumulative effect of both rising river levels and rainfall. The development of the young reed bed into an older and more dense stand can also clearly be seen, with low LAI's being recorded for an extended period (July 1994 to January 1995), followed by considerably higher values for the remainder of the period.

The contrast in the leaf area recorded during the 1993/94 season to that recorded during the 1994/95 season was also noteworthy. During the 1993/94 season there was a sharp peak in the LAI of both the reed bed and the riverine forest. In the 1994/95 season, however, high levels in the LAI of the reed bed were maintained through to June, while the LAI in the riparian forest also remained high

for a much longer period, but at a slightly lower level than the peak recorded during the previous season.

The dynamic behaviour of the riparian canopy poses significant challenges to the prediction of the consumptive water use of the riparian vegetation, as the LAI is a key variable in determining the quantity of water transpired by the vegetation. Any changes in LAI are likely to have a direct influence on evaporation as it reflects a direct change in the evaporative surface. Predicting the consumptive water use of the vegetation therefore requires accurate measurements of LAI in the riparian vegetation. While the Licor instrument has been shown to be useful in measuring changes in LAI at selected sites on the Sabie River, it does not provide an adequate estimate of the spatial distribution of LAI in the river system. Further technological development is necessary to test techniques that would allow the rapid assessment of LAI through means such as remote sensing.

The Licor LI200 measuring device offers the only feasible, non-destructive and cost effective means of documenting changes in the LAI of riverine vegetation, its results are generally considered conservative. This is consistent with the experience of Dye and Olbrich (1992) who found that LAI measured using the Licor LI200 was consistently lower than that estimated by leaf stripping in Eucalyptus trees. This is most likely a consequence of the non-random distribution of leaves in the canopies of riverine trees - a violation of the criteria required for the use of the apparatus. Under the current application in a riparian habitat, it was of some concern that the abundance of aerial plant parts such as stems and branches may have compromised the reliability of the results. This became a concern in the reed bed as it grew older, and in the *Ficus capreifolia* stand at the site. Despite the reservations expressed above, the instrument proved a valuable tool particularly in documenting the seasonal changes in LAI.

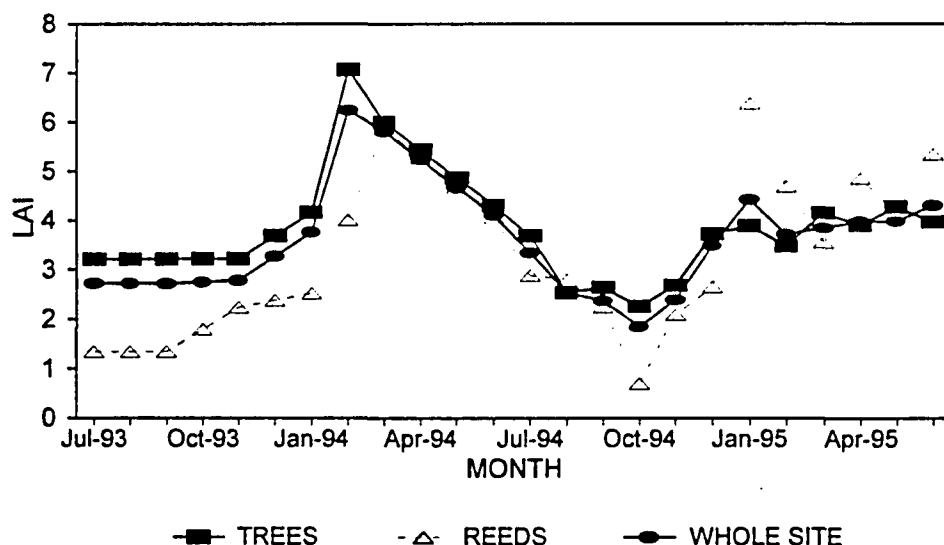


**Figure 2.24** The change in LAI recorded at the Narina study site in the trees, reeds and the site as a whole from September 1993 to June 1995.

### 2.3.3 Pre-dawn Xylem Pressure Potentials

Pre-dawn xylem pressure potential data were collected during each of the intensive field measurements on the species at Narina. They are therefore available for February 1993, September 1993, October 1994, and February 1995 (Fig 2.25). This was necessary to document the water status of the five reference trees at Narina. The data illustrates that water stress was not evident in any of the trees measured at Narina, even at the height of the dry season. The only tree which showed symptoms of water stress was a *Spirostachys africana* situated at the edge of the riparian fringe. It was clear that this individual was not 'riparian' and more representative of terrestrial trees than of the riparian zone. For this reason, this tree was not selected for further analysis.

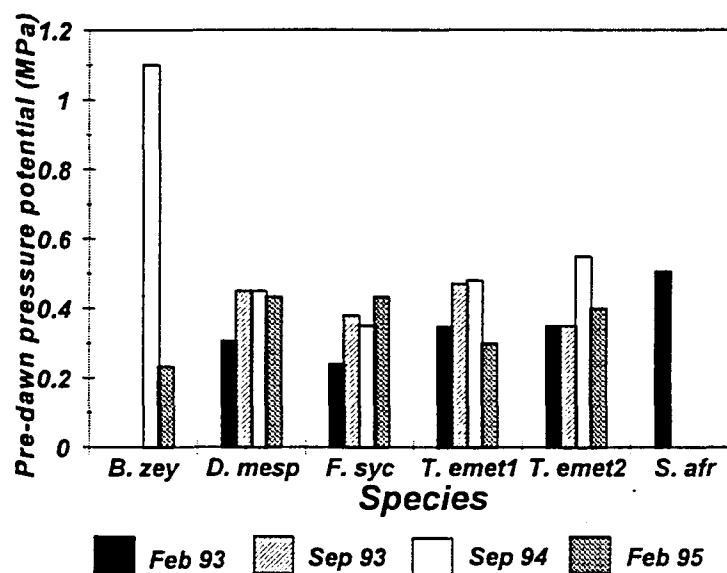


**Figure 2.25** Pre-dawn xylem pressure potentials recorded on six species at the Narina study site. The species names have been abbreviated to: B. zey (*Berchemia zeyheri*), D. mesp (*Diospiros mespiliformis*), F. syc (*Ficus sycomorus*), T. emet (*Trichilia emetica*), and S. afr (*Spirostachys africana*).

The conclusion drawn above has a significant impact on the modelling of transpiration from the riparian zone and particularly on the necessity of linking the transpiration model to the soil water model. Essentially, the above paragraph suggests that the riparian trees on the Narina site were found to transpire at potential rates and that water supply was found not to be limiting even at the height of the dry season. For this reason, it should be anticipated that transpiration from the riverine zone is a function of the ambient meteorological conditions and the amount of foliage in the riverine vegetation (so long as water supply is not limiting).

It is believed that the layers of highly conductive, coarse sand in the alluvial bank at Narina are central to the observed results. The high conductivity of the coarse sand layers ensure that so long as there is water in the stream channel, it is quickly distributed to the trees growing on the alluvial bank, including those that are located some distance from the channel itself. It is important to bear in mind that serious errors could be incurred should the transpiration model developed on the above data set, be applied to sites where there is poor connectivity between the roots of the vegetation and the water in the stream channel.

During the low-flow period in October and November 1992 drought related mortalities were recorded at sections of the Sabie River. Trees in these sections were clearly not well connected to water in the stream channel, and it is believed that bedrock intrusions isolated trees from the water in the stream channel. The challenge is to identify such sites and to realise that the above assumption of 'no water stress' is not always valid for these sites, especially under low-flow conditions.

#### **2.3.4 Transpiration from Trees**

##### **2.3.4.1 Strategy**

The initial aim of this project was to determine the consumptive water use of the riverine trees and reeds growing at the Narina site so that these data could be used to determine whether closure was achieved in the water budget for the site. To achieve this, year-long water use data were required for all the vegetation on the site. Two sampling strategies were used to meet this aim: The first, was to carry out periods of intensive field measurements to characterise the relationship between species at the Narina site and to determine whether this was affected by season. The second was to gather continuous measurements on a single "reference" fig tree which would be used to determine the relationship between transpiration and the most important driving climatic variables. This data set would also be used to extrapolate the transpiration record through time using the relationships established between the species, as determined during the intensive field measurements.

##### **2.3.4.2 Methodology**

The most suitable technique for measuring transpiration from trees is the heat pulse velocity technique (HPV). It is widely used both in South Africa (Dye and Olbrich, 1993) and internationally, especially in forest hydrology studies (Swanson, 1983). While techniques such as the Bowen Ratio technique would have been attractive as it provides an integrated estimate of total evaporation from the riparian zone, its requirements for fetch could not be met along the Sabie River. Essentially, the HPV technique measures the rate of water flow up the stem of trees, which is then multiplied by the total area of the conducting sapwood to derive a measure of transpiration from the foliage which that stem supports.



## *HPV Data Collection and Analysis*

In this study we have followed the method of Marshall (1958) and Swanson (1983), and applied the necessary correction for wounding (Swanson and Whitfield, 1981). This approach is process-based and does not require the calibration of the technique on the species on which it is to be used.

The study was carried out using five Forestek HPV loggers, each with a capacity to log twelve channels, which equates to twelve point estimates of sap flow within the sapwood of the selected sample trees. The measurements were made with sets of HPV probes comprising a pair of 1.8 mm thick Teflon probes each containing a single thermistor, and a line heater element. The probes are inserted into three vertically-aligned parallel holes drilled through a 20 mm thick drill jig along the radius of the stem. As the compensation technique was used, the holes were unevenly spaced: 5 mm between the lower thermistor and the heater and 10 mm between the heater and the upper thermistor. The thermistors were connected in a Wheatstone bridge configuration. The heat pulse was generated by supplying a current to the line heaters for 0.7 seconds, and the time taken for the bridge to return to the initial balance point after the heater was pulsed was then recorded. The number of probes used per sample tree depended on the tree size. In stems of diameter less than 20 cm four probe sets were used, while eight sets of probes were used in larger stems.

The loggers were programmed to pulse all connected probes simultaneously at hourly intervals throughout the day. As sap flow ceases at night, and the technique is unable to resolve very slow flow rates, the loggers were programmed not to record any data between the hours of 21h00 and 04h00. The loggers have the capacity to store up to two months of data, which is down-loaded via a conventional RS232 port dump to a laptop PC.

All data were processed using the formulae below:

The heat pulse velocity ( $u$ ) can then be calculated using the following formula (Swanson, 1983):

$$u = (X_u + X_d)/2t \quad (\text{m s}^{-1}) \dots\dots\dots [1]$$

where:  $X_u$  and  $X_d$  are distances (m) from the line heater to the upstream and downstream thermistors respectively. Both  $X_u$  and  $X_d$  are regarded as positive quantities.  $(X_u + X_d)/2$  is referred to as the probe separation in the remainder of this chapter. 't' is the time taken in seconds for the bridge to return to the initial balance point after the heater is pulsed.

Early HPV studies found that the technique consistently under-estimated actual sap flow by approximately half (Doley and Grieve, 1966; Cohen, Fuchs and Green, 1981). Swanson (1983) investigated the source of the under-estimation by simulating the effect of the non-conducting, wounded tissue, which develops as a

result of probe implantation, on the transfer of heat to and from the sapwood. The result of the work was the publication of wound-correction co-efficients for a range of wound widths, and a selection of probe materials and espacements (Swanson and Whitfield, 1981). These were all found to influence the measurements of heat pulse velocity. The heat pulse velocity ( $u'$ ) was therefore corrected for the effect of wounding using Swanson and Whitfield's (1981) wound correction co-efficients for Teflon probes.

The correction takes the form:

$$u' = p + qu + r(u)^2 \dots\dots\dots [2]$$

where: p,q and r are the correction coefficients derived for the measured wound size and Teflon probes in the (-0.5,0,1.0) configuration.

The corrected heat pulse velocities are converted to sap flux density using the formula of Marshall (1958):

$$v = \rho_b(m_c + 0.33)u' \text{ (kg m}^{-2} \text{ s}^{-1}) \dots\dots\dots [3]$$

where:  $v$  = sap flux density  
 $\rho_b$  = wood density  
 $m_c$  = moisture fraction, dry weight basis  
0.33 = specific heat of dry wood

The sap flow rate was calculated by multiplying the mean sap flux density [3] by the sapwood area:

$$\text{Sap flow} = vA \text{ (kg s}^{-1}) \dots\dots\dots [4]$$

where:  $A$  = sapwood area

The moisture fraction in equation [3] was calculated using:

$$m_c = (\text{fresh weight} - \text{dry weight})/\text{dry weight} \dots\dots\dots [5]$$

In this study the moisture content was measured in four sapwood samples from each tree which were first weighed fresh and subsequently dried in an oven at approximately 80°C until no further weight loss was recorded.

The wood density,  $\rho_b$ , in equation [3] was calculated using:

$$\rho_b = \text{dry weight/volume of fresh wood} \dots\dots\dots [6]$$

Archimedes' principle was used to determine the volume of the wood samples. This entailed recording the change in mass on the immersion of the wood sample in a beaker of water placed on a scale.

Because radial differences in sap flux do occur (Swanson 1983, Olbrich 1994), each of the four probes was implanted to a different depth within the sapwood to ensure that the variation in the sapwood was covered. The depths were selected so that the entire sapwood area was approximately evenly sampled (Figure 2.26). Where eight probes were used per tree, each of the sample depths was replicated twice, replicates being placed approximately diametrically opposite to one another on the stem. The mean sap flux density recorded by each of the sample probes was used in equation [4] to calculate the sap flow or transpiration rate.

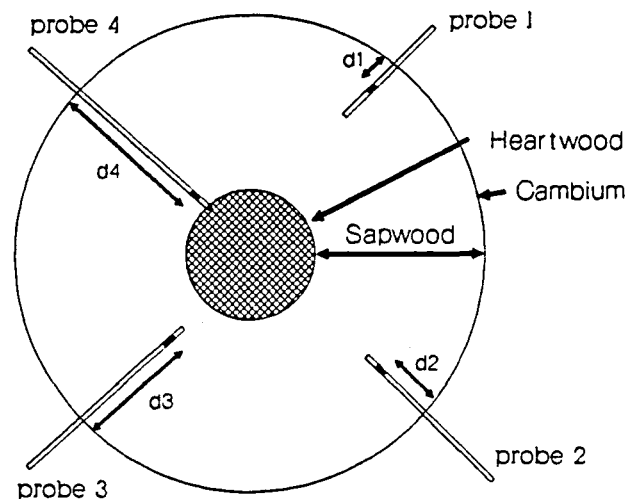


**Figure 2.26** A schematic diagram illustrating a cross-section through a stem and the probe implantation strategy used on the sample trees. d1 to d4 represent the increasing depths to which the single thermistor bead in each probe is implanted beneath the cambium.

To accommodate the sensitivity surrounding the destructive sampling of vegetation in the Kruger National Park, trees were sub-sampled where possible, with probes implanted in branches rather than at the base of the stem. In addition it was necessary to build a platform in one of the *F. sycomorus* trees to gain access to the branches and for the data logging equipment to be well out of reach of any potential flood events.

#### 2.3.4.3 Transpiration from the Reference Fig Tree

One of the research strategies used in this study was to collect long term measurements on a single "reference" fig tree which would be used to determine the relationship between transpiration and the most important driving climatic variables. This data set would also be used to extrapolate the transpiration record through time. Hourly transpiration data were available for the reference *F. sycomorus* tree at the Narina site from February 1993 to June 1995. The data set was, however, not entirely complete due to occasional instrument malfunction

which has led to the loss of data. As the HPV logger recorded hourly transpiration rates, these were summed on a daily basis to derive total daily transpiration estimates. It was also decided to monitor the transpiration rates of a second tree, a *T. emetica* at the Narina site following the severe frost event recorded during June 1994. It was of some concern that the *F. sycomorus* tree would not recover from the frost, and therefore not adequately represent the rates recorded by the other trees at the site.

The daily transpiration rates recorded on the two trees show considerable day-to-day variation (Figure 2.27) illustrating the effect daily changes in meteorological conditions have on the water use of trees. In addition, there is a fairly clear seasonal trend with the highest transpiration rates being recorded during the latter half of summer and the lowest rates during the months August to October (Figure 2.27). The impact of the severe frost recorded in June 1994 was also clear with the transpiration rates of the fig tree declining to a very stable and low level during that period. The recovery was, however, fairly rapid and the transpiration rates increased during the ensuing summer almost to the level recorded during the previous summer. This was quite fortuitous, as there was some mortality amongst fig trees at the Narina site, and should the reference tree have died it would have compromised the study considerably. Figure 2.27 also illustrates the high degree of correlation in the daily transpiration rates between the *T. emetica* and the *F. sycomorus* trees, illustrating that transpiration in the two species is controlled by the same environmental stimuli. Also evident is that the difference in the transpiration rates between the two species decreases from the earlier measurements made, such as those in February and September 1993, to those made after October 1994 (Figure 2.27). It is likely that this reflects both the impact of the frost on the fig tree and the growth in the *T. emetica* tree. It was clear from the repeated field observations that the *T. emetica* tree especially was growing very rapidly.

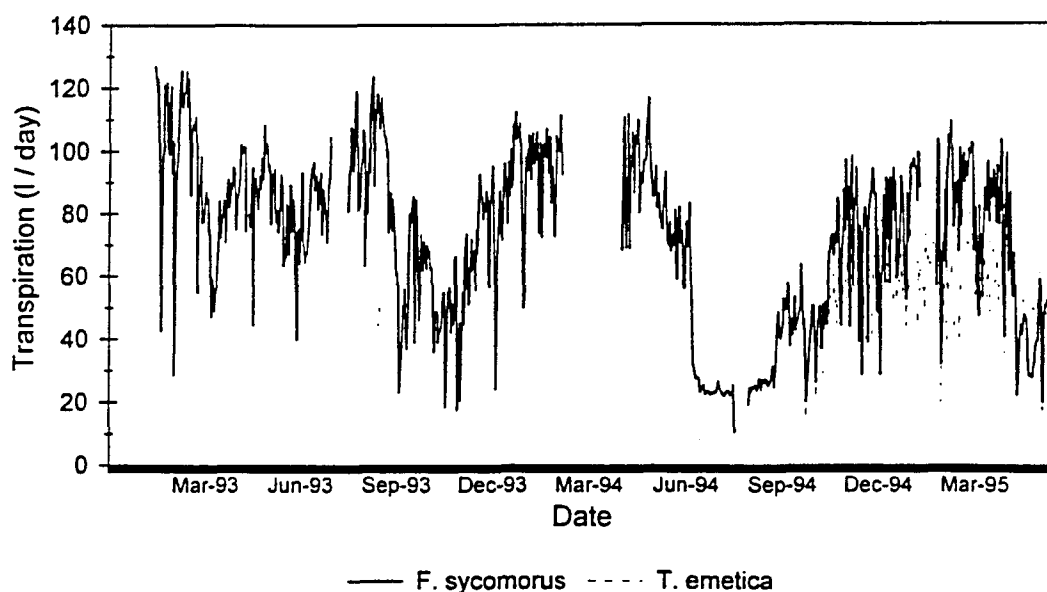


**Figure 2.27** Daily transpiration rates recorded in the reference *F. sycomorus* tree for the period 11 February 1993 to 5 June 1995. The figure also illustrates the transpiration rates recorded by a *T. emetica* tree at the site for the periods when it was monitored.

The seasonal trends in the data are most clearly illustrated when monthly mean daily transpiration data are plotted over the course of the study (Figure 2.28). This figure suggests that LAI is one of the variables causing the seasonal fluctuation in water use. It is significant that the transpiration rate increased in the fig and *T. emetica* trees prior to any increase in the LAI in the spring of 1993 and 1994. Similarly transpiration declined more sharply during autumn than did the LAI. This suggests that transpiration is under physiological control as well as being affected by changes in the canopy area. The lag observed in autumn may also be a result of the inability of the LAI metre to distinguish between live and dead foliage.

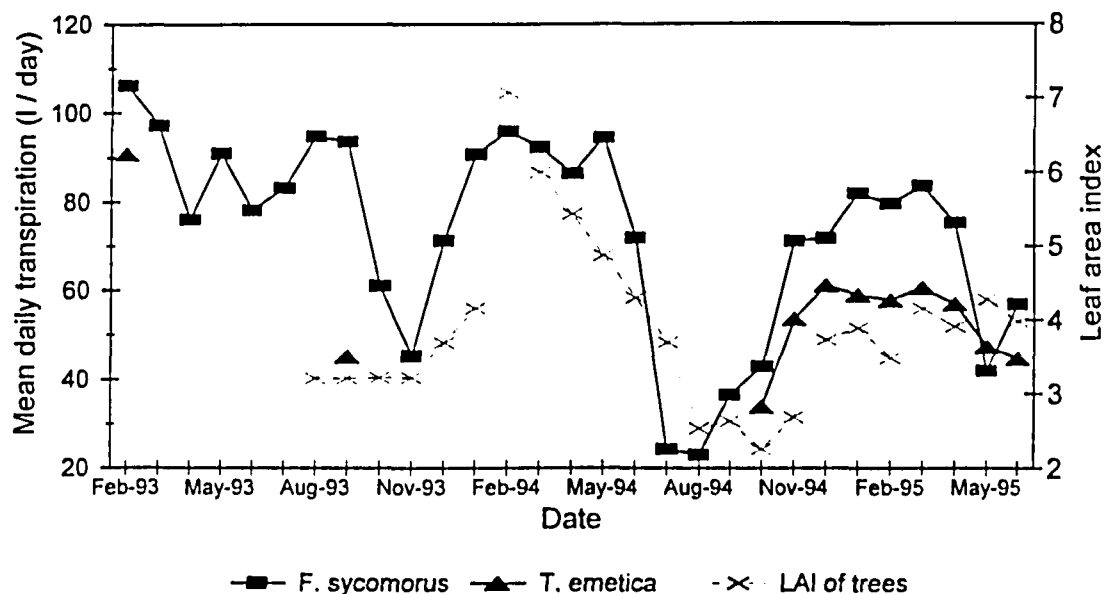


**Figure 2.28** Variation in the monthly mean daily transpiration recorded in the reference *F. sycomorus* and the *T. emetica* (river) tree, and the variation in LAI recorded in the riparian forest over the course of the study

It is not entirely clear what stimulates the seasonal changes in transpiration rates. Examining the two variables that affect water availability at the site, rainfall and river discharge (Figure 2.29) illustrates that both these show a similar seasonal trend. Examining these trends in detail shows, for example, that while the discharge increased steadily from September to November 1993, this coincided with a sharp decline in the transpiration rate recorded in the reference tree. The rainfall recorded during November and December 1993 coincides with the sharp rise in transpiration - suggesting that rainfall triggers the rise in transpiration. This is, however contradicted during the early summer of 1994, where transpiration was found to rise one month before any significant rainfall event (Figure 2.29). While it is clear that water availability at the site must influence the transpirational behaviour of the trees, it is not entirely clear to what extent it acts as a trigger mechanism to stimulate the seasonal trends observed in the transpiration data. No evidence was found to suggest that the trees were experiencing stress at the Narina site, even at the time when water availability was at its lowest (section 2.3.3). It should also be emphasised that although there was a seasonal fluctuation in the discharge, this did not have a major effect on the water table - for example, even when the river was at its lowest the water table was only 3 to 4 m below the ground and within easy reach of mature riverine trees. This suggests that the trees at the site exhibit a natural seasonal oscillation in transpiration, the amplitude of which is moderated should water availability become limiting at the site.

The above data also illustrate very contrasting transpiration patterns for each of the replicate years. In 1993, the transpiration rate fluctuated at a fairly elevated

level of about 90 l per day from February to September whereafter it declined sharply to November (Figure 2.29). In the following season, the mean daily rate of 90 l per day was only maintained for five months until May, whereafter it declined sharply to the low levels recorded in June and July (Figure 2.29). Bear in mind that the severe frost only occurred at the end of June, indicating that it was not the frost that resulted in the very low rates recorded during June. It is possible that the large flood event recorded during March 1993 caused this difference between the two years. Further, as water availability has been shown not to be limiting (as long as there was still flowing water in the river), this suggests that the flood event had an impact on a resource other than water. One possibility is that large flood events may introduce new nutrients to the site, stimulating growth and foliar development, and hence increasing transpiration. This would suggest that the riverine systems may suffer nutrient limitations in the absence of flood events - further physiological investigations are required to test this hypothesis.

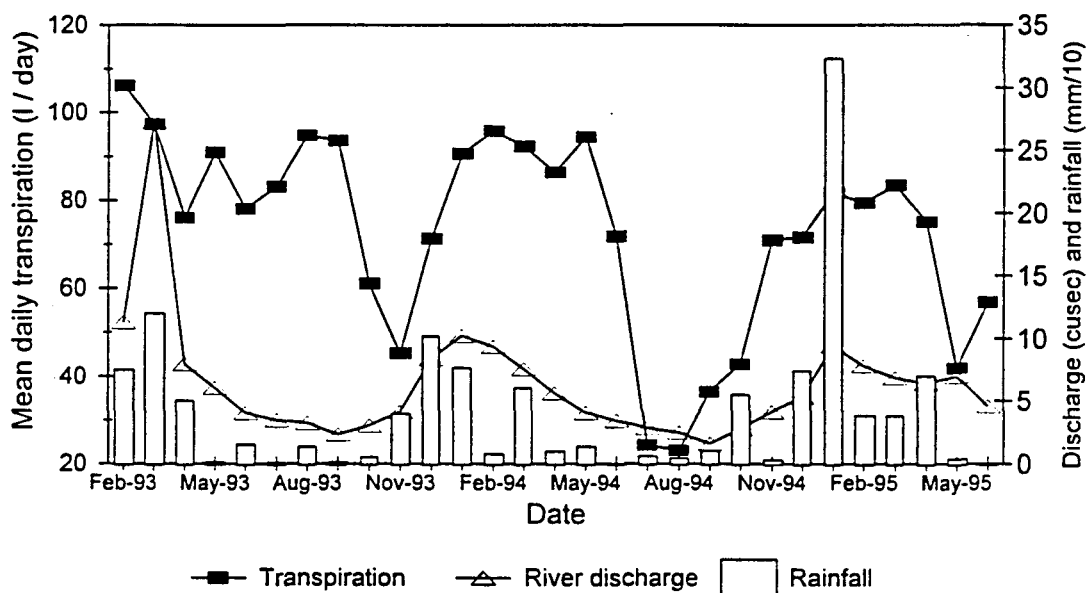


**Figure 2.29** Trends in the monthly mean daily transpiration from the *F. sycomorus* tree, discharge measured at the Narina site, and monthly rainfall recorded over the course of the study. In the figure the rainfall data have been divided by ten to facilitate comparison with the other data presented.

#### 2.3.4.4 Transpiration Rates Recorded During Seasonal Sampling Sessions at the Narina Site

The Narina study site is dominated by large trees, particularly *Ficus sycomorus* and *Trichilia emetica*. Other tree species also present, include *Diospiros mespiliformis*, *Spirostachys africana*, *Combretum erythrophyllum* and *Berchemia zeyheri*. It was decided to concentrate on those species which comprise the largest proportion of the leaf area on the selected study site, and were generally

most widely spread in the Sabie River system. For this reason, the comparisons presented below were made between *F. sycomorus*, two *T. emetica* trees, *D. mespiliformis*, *B. zeyheri* and *S. africana*. The *S. africana* tree growing at the top of the riparian bank was only sampled during the first two surveys. The reason for this was that the water relations of the tree indicated that it was not connected to the water table in the riparian zone, and was therefore more representative of a terrestrial tree than a riparian one. It is also important to note that *Bretonadia salicina* and *Syzgium guineense*, common elsewhere on the river system, were not present at the study site and therefore not included in the surveys.

To distinguish between the two *T. emetica* trees they will be referred to as *T. emetica* (river), and *T. emetica* (bank). The tree denoted 'river' was situated approximately 40 m from the open stream channel on the edge of the reed bed, while the 'bank' tree was situated approximately 25 m further away from the stream near the steep primary channel bank.

Four periods of intensive HPV sampling were carried out at the Narina site to establish the relationship between the reference fig tree and the other dominant trees on the site. These were carried out in February 1993, September 1993, October 1994 and February 1995. The two February assessments were carried out to coincide with the high-flow periods and maximum canopy development, while the September and October assessments represent measurements taken when the LAI, soil moisture and river flow was at near minimum levels.

These measurements were then be used to derive regression equations relating the transpiration recorded by the reference fig tree and each of the other selected individuals. These regression equations were used to estimate what the transpiration was for each of the selected individuals during the periods between the intensive measurements. In this way it was possible to build up a record of the total transpiration from the Narina site.

Table 2.7 lists the diameter at cambium, sapwood thickness, moisture content, and wood density used in processing the HPV data to derive the estimates of hourly transpiration rates of the trees sampled at Narina. As wound development was in some instances indistinct, and it was not possible to destructively sample the trees to gather better data on wound size, it was necessary to use the same wound size estimate, 3.17 mm, for all the trees. This value represents the mean of those samples on which wound size was discernable.

Table 2.7 shows that some of the trees grew actively over the two and a half year study. For example, the diameter of the fig branch increased by 3.9 cm, while the stem diameter of the *T. emetica* (river) increased by 2.9 cm. The change in diameter of *T. emetica* (bank) and the *D. mespiliformis* tree are not reliable estimates of growth as successive measurements were not made at the same level on the stem. This was because it was necessary to implant the HPV probes away from the influence of previous probe-implantation sites.



**Table 2.7** The diameter at cambium, sapwood thickness, moisture content and wood density of the species sampled at the Narina site.

Tree	Diameter at cambium (cm)				Sapwood thickness (cm)	Moisture content (g g <sup>-1</sup> dry weight)	Wood density (g cm <sup>-3</sup> )
	Feb '93	Sep '93	Oct '94	Feb 95			
<i>F. sycomorus</i>	27.7	28.2	30.4	31.6	4.5	1.26	0.48
<i>T. emetica</i> (bank)	41.8	43.15	46.35	47.12	5.0	0.71	0.51
<i>T. emetica</i> (river)	30.6	30.1	31.8	33.5	5.0	0.76	0.48
<i>B. zeyheri</i>	-	48.7	52.1	52.1	4.5	0.29	0.74
<i>D. mespiliformis</i>	29.9	29.9	31.31	35.1	6.0	0.65	0.65
<i>S. africana</i>	18.84	18.85	-	-	3.0	0.28	0.71

#### *General Trends in the Data*

Contrasting transpiration rates were recorded for the species sampled during the four surveys at Narina. The transpiration rates recorded during the second high-flow survey were all generally depressed by comparison to those recorded during the first high-flow survey with the mean daily transpiration declining from 138.9 to 88.6 l per tree per day. Similarly, lower rates were recorded for the second low-flow survey than during the first with the mean rate declining from 81.4 to 41.6 l per tree per day. It is noteworthy that the transpiration rates recorded in the *F. sycomorus* showed the least change from the high-flow to the low-flow survey. In fact, higher transpiration rates were recorded for the fig tree during the September 1993 low-flow survey than were recorded during the February 1995 high-flow survey (Figure 2.30). It is likely that this result reflects the impact of the severe frost experienced during the winter of 1994 on the vigour of the tree during the following summer. For the other riparian trees, the low flow transpiration rates were consistently lower than those recorded during the two high-flow surveys.

The relative ranking of the two *T. emetica* trees, the *D. mespiliformis* and the *B. zeyheri* tree remained remarkably consistent. The highest transpiration rates were consistently recorded for the *T. emetica* (bank), followed by the *B. zeyheri* (when it was sampled) and the *D. mespiliformis*. The lowest transpiration rates were generally recorded in the *T. emetica* (river), with the exception of the October 1994 sampling period where it ranked second last to the *D. mespiliformis* tree (Figure 2.30).

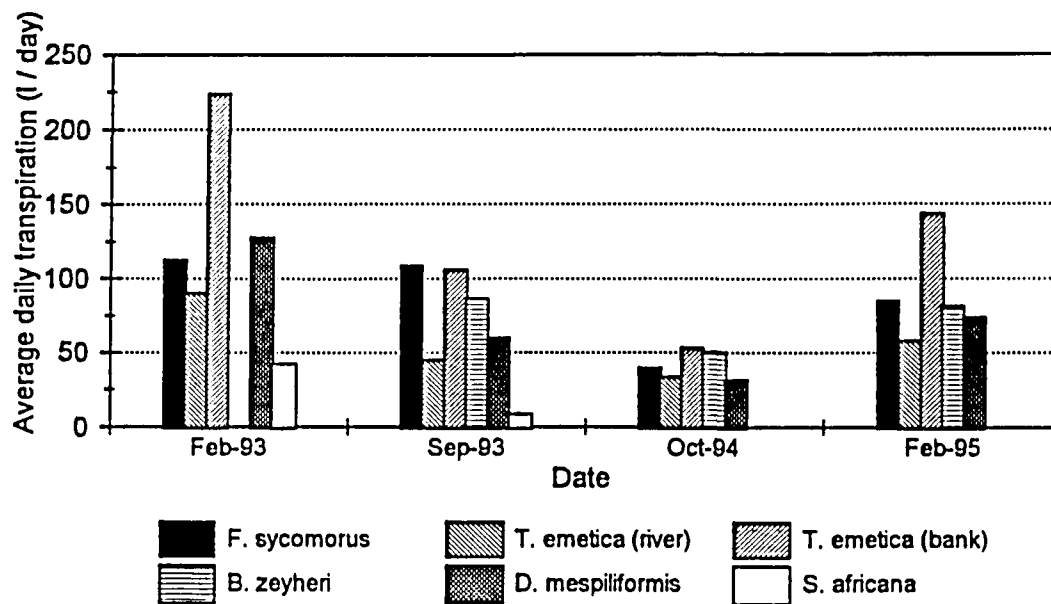


**Figure 2.30** Mean daily total transpiration recorded for the six tree species sampled at the Narina site for the four intensive transpiration sampling surveys conducted.

#### 2.3.4.5 The Relationship in Transpiration Rates between the Tree Species Sampled at Narina

Measurements made on the five sample trees at half-hourly intervals revealed that the individuals responded synchronously to the changing climate (Figure 2.30). The recorded transpiration rates of all five sample trees showed a dramatic increase between 6h30 and 7h00 and four of the five sample trees achieved their maximum transpiration rates over the mid-day period. *S. africana* responded differently in that its maximum transpiration rate was recorded between 9h00 and 10h00 in the morning. Isolated clouds passed over the site at 10h00 and 12h00 resulting in the lower transpiration estimates for those times.

The difference in the behaviour between *S. africana* and the other four sample trees is more apparent when the transpiration rates are normalised (scaled) by expressing the recorded transpiration rate as a proportion of the maximum recorded by the individual on that particular day (Figure 2.31). A completely cloudless day (14 February 1993) was used to illustrate this point. The curve charted by *S. africana* stands out as being completely different to the other four sample trees. *S. africana* achieves a maximum transpiration rate at approximately 8h30. It maintains this rate for about two hours whereafter transpiration declines over the mid-day period despite rising evaporative demand. A slight recovery is recorded in the late afternoon. This is typical of plants experiencing water stress and suggests that *S. africana* does not have free access to the water table in the riparian zone, and represents the behaviour of a terrestrial rather than a riparian

tree. For this reason it was decided to exclude this tree from further transpiration surveys at Narina.

Figure 2.31 also illustrates that *D. mespiliformis* and *F. sycomorus* show deviations from the other species in the late afternoon. *F. sycomorus* maintained a high transpiration rate for longer, while the reduction in transpiration in *D. mespiliformis* was more abrupt. This was most probably due to differences in the exposure of the two canopies to sunlight at low azimuths. The *D. mespiliformis* tree was situated on the southern side of the riparian forest amongst several other large trees, while the *F. sycomorus* branch being sampled was on the northern side of the riparian forest and would have been completely exposed to sunlight even late in the afternoon, resulting in higher transpiration rates.

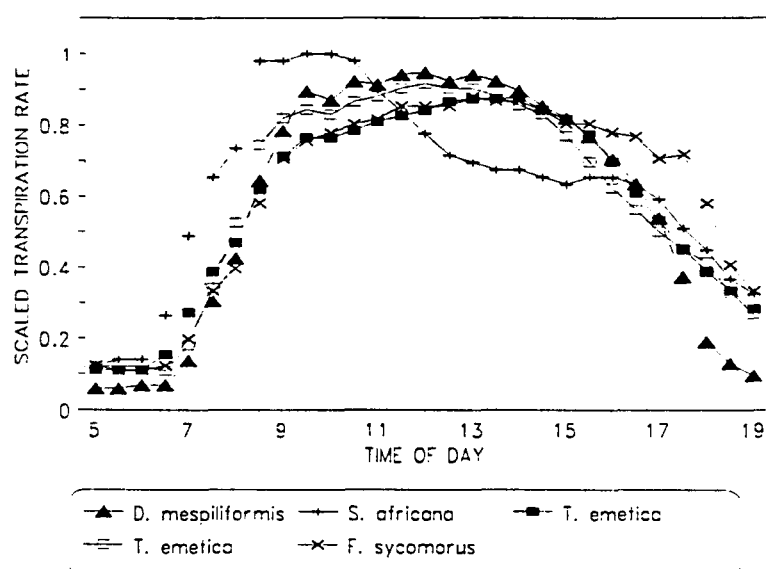


**Figure 2.31** Transpiration rates recorded in the five sample trees over the course of a cloudless day (14 February 1993). The recorded transpiration rates have been scaled by expressing the actual rate as a proportion of the maximum rate achieved by each individual on the particular day

A more important consideration is to examine the relationship between the reference fig tree and the trees sampled during the four 'seasonal' visits to the Narina site. A sample data set containing hourly data for each of the trees collected over a two week period in October 1994 was extracted to illustrate the very high linear correlation in the hourly transpiration data (Figure 2.32). The  $R^2$  values for the correlations illustrated in the figure range from 0.87 to 0.95. The figure confirms that the relationships are linear over a large range of transpiration values and the regressions have near zero intercepts. As the daily transpiration rates are merely an aggregation of the component hourly data, these will also have a linear relationship with near zero intercepts. The high correlation in hourly and daily total transpiration between trees growing on the same site has also been recorded in several other previous studies (Dye *et al.*, 1994, Olbrich *et al.*,

1993), and deviations are only expected should there be differences in water availability between sample trees.

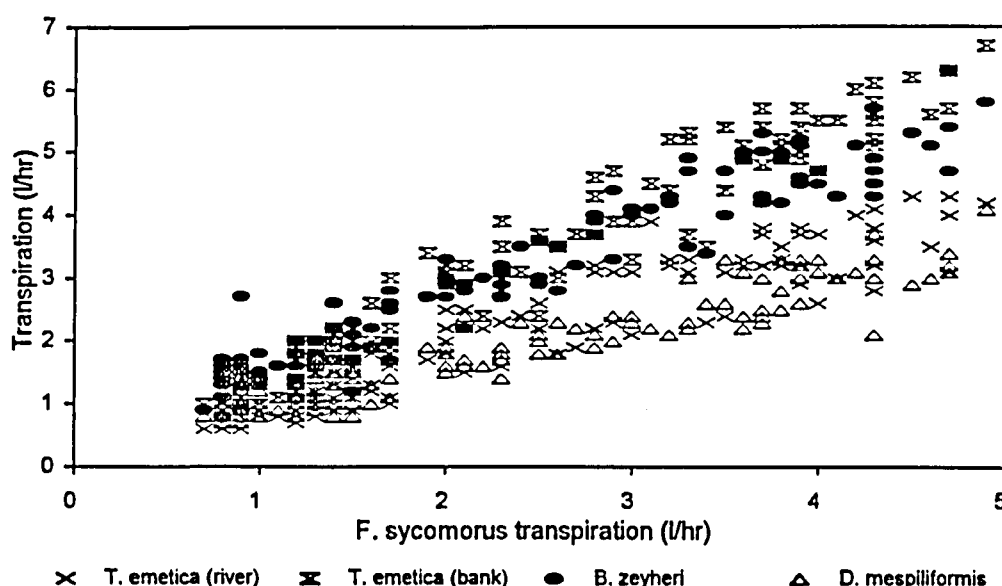


**Figure 2.32** The relationship between the transpiration rate recorded in the reference *F. sycomorus* tree and the other four tree species sampled at the Narina site. The data in the figure were taken from a two week sample period in October 1994.

#### 2.3.4.6 Transpiration from a Broader Range of Species

As only a limited range of the tree species were present at the Narina site, it was necessary to determine whether there were significant differences in transpiration between species. Water use was measured for a period of at least two days on a total of 35 trees comprising nine tree species commonly found along the banks of the Sabie River in the Kruger National Park. Measurements were made over as short a period as possible to ensure that climatic and seasonal variation had the minimum effect on confounding the results. At least two full days of transpiration data were collected from each of the sample trees. In addition, it was decided to make the measurements at a time of year when water was freely available. For this reason, this study was conducted during the high-flow period from the 8th of February to the 10th of March 1995.

The climate during this period was generally partly cloudy and sunny, with a brief spell during late February and March where light showers were recorded. During the heaviest of these falls 18.3 mm was recorded on the 18th of February, the remainder of the showers were very light with an average of only 2.2 mm being recorded. Rainfall during the preceding month of January totalled 323.4 mm. The mean flow recorded in the river this period was  $7.58 \text{ m}^3 \text{ sec}^{-1}$  with a minimum of

3.8 and a maximum of 20.1 m<sup>3</sup> sec<sup>-1</sup> respectively. These values are considerably higher than the mean wintertime discharge levels of 2.96 m<sup>3</sup> sec<sup>-1</sup>. Given the above climatic and flow conditions it is likely that the criterium of soil moisture being non-limiting to transpiration was met, and that the climate was consistent enough to enable an adequate comparison between the various species monitored over the period.

Table 2.8 lists the diameters at breast height of the sample trees selected for this study. Every effort was made to restrict the size of the selected sample trees to the range 25 to 35 cm in diameter, and to have the trees growing on as similar a substrate as possible to ensure an adequate level of comparability between the sample trees. Table 2.8 illustrates that the sample fig trees selected had the largest diameters, followed by the *D. mespiliformis* trees. This reflects the demographics of the riverine forest where these species appear to establish episodically. As a consequence, young individuals are relatively uncommon. All the selected trees were located between the Narina study site and Heritage *et al.* (1996) site 17, approximately 9 km downstream of Skukuza. Twenty of the trees selected were located in the well developed riparian forest on the northern bank of the Sabie on what is known as the fishing road immediately downstream of Skukuza, ten were located in the vicinity of the Narina site, and the remaining five trees on the southern bank opposite the fishing road. Trees on which the stem had been damaged by elephants or floods were not selected as it is uncertain what effect this would have on the flow of water in the sapwood. This would cause problems in the application of the HPV measuring technique.

**Table 2.8** The diameters of each of the sample trees selected for the species comparison.

Species	Diameter (cm)						Average
	Tree 1	Tree 2	Tree 3	Tree 4	Tree 5	Tree 6	
<i>C. erythrophyllum</i>	34.9	33.2	25.4	45.9			34.9
<i>A. robusta</i>	30.0	26.2	30.0	30.6	27.3		28.8
<i>B. salicina</i>	17.2	16.9	16.9	35.4	32.1	29.9	24.7
<i>D. mespiliformis</i>	50.4	29.0	23.6	45.4	36.7		37.0
<i>S. guineense</i>	21.0	27.8	41.9	16.7			26.9
<i>S. africana</i>	19.9	18.4					19.2
<i>T. emetica</i>	18.7	22.3	18.3	27.3	48.5	34.0	28.2
<i>F. sycomorus</i>	46.0	68.8	29.8				48.2
<i>B. zeyheri</i>	52.1						52.1

Following HPV sampling, four 60 mm long, 30 mm-diameter cores of sapwood were extracted from each of the sample trees. Two of the cores were extracted over the holes in which the HPV probes had been inserted - these were then used

to measure the wound widths for each of the trees. The other two cores were removed away from the influence of the HPV probes and used to determine the moisture content, wood density and sapwood thickness.

Problems were, however, encountered in measuring the sapwood thickness in all the species except *S. africana*, due to the failure of the methyl orange stain which is a commonly used to distinguish sapwood from heartwood. A broader range of stains was then tested, also without result. A series of densitometry tests were then conducted on the stem cores which showed no systematic trend in wood density along the radius of the tree. A technique was then applied in which dye is infused into an oblique 5mm hole drilled along the radius of the tree, and a core removed from immediately above the point of infusion to determine the zone in which the dye was being transported. This zone was then assumed to constitute the sapwood. This technique was only partially successful, and revealed that the sapwood of the riparian trees was considerably thicker than that of terrestrial forest species previously worked on. As it is important to determine the sapwood thickness accurately, the final technique applied to each of the sample trees was to do four radial HPV profiles on each of the sample trees. Four sets of HPV probes were inserted (away from the influence of any of the previous sample points) to a depth 60 mm beneath the cambium. Sequential readings were then taken withdrawing the probes 5mm at a time. These data were collected between 10h00 and 16h00 when sap flow rates are at their highest, resulting in the clearest distinction between the heat pulse times recorded in the sapwood and those recorded in the heartwood where no water transport is occurring.

The transpiration data show that there was considerable variation in the daily water use of the individual trees both within and between the various tree species sampled (Figure 2.33). The daily water use of the individual trees was found to vary from as little as 20.4 l per day recorded on a *Spirostachys africana* tree to as much as 396.5 litres per day in a *Diospiros mespiliformis* tree. This is likely to be partly due to differences in tree size - large trees are likely to use substantially more water than small trees. The large variation between replicate samples of each species resulted in no significant difference between trees (Table 2.8) in their total daily water use ( $P=0.69$ ).

A measure was therefore required that could be used to adjust the water use estimates recorded above for differences in tree size. The most appropriate estimate of tree size would be an estimate of the total canopy area as this reflects the surface area from which evaporation takes place. It was, however, not possible to derive this measure as the trees could not be destructively sampled. It was also not possible to use an instrument such as the Licor Li-200 to measure leaf area non-destructively as the trees were located in a riparian forest, and the instrument would be unable to discriminate between the foliage of the sample tree and that of neighbouring individuals. The only remaining measure was to use the stem cross-sectional area as an estimate of tree size. This remains a relevant measure of tree size as it is directly related to leaf area. Research on forest species has established that there is a relationship between the leaf area and the sapwood area (Olbrich 1994, Waring and Schlesinger, 1985).

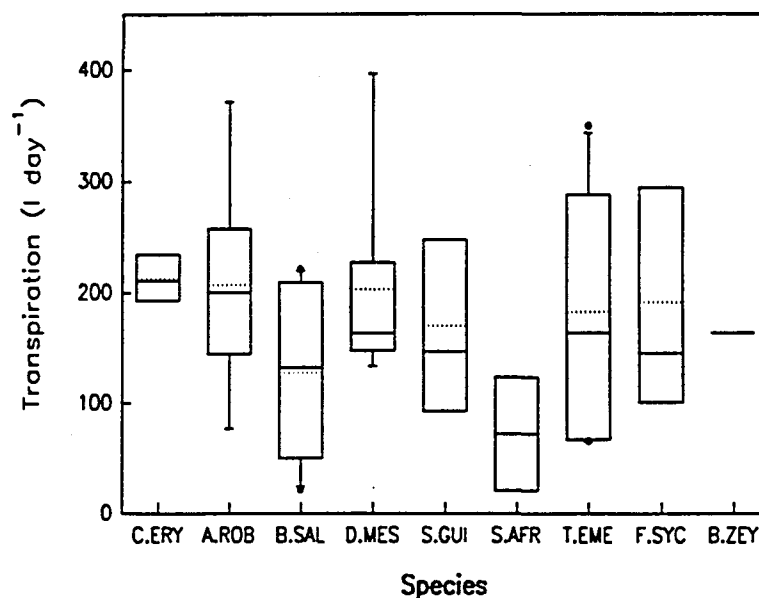


**Figure 2.33** Daily transpiration recorded for each of the trees sampled in the species comparison illustrated in a box and whisker plot. The mean (-), median (...), 90th, 75th, 25th and 10th percentiles of the recorded transpiration rates are illustrated. Where transpiration The extremes are also illustrated (●) where these fall beyond the 90th and 10th percentiles.

Adjusting the daily water use data for differences in stem cross-sectional area resulted in a measure of water use with the units  $\text{l m}^{-2} \text{ day}^{-1}$ . In certain instances this resulted in increased variation recorded within species, such as in *C. erythrophyllum*, and *S. africana*, (Figure 2.34). In most instances, however, this resulted in a reduction of variation observed within a species, most notably *S. guineense* and *F. sycomorus* (Figure 2.34). This suggests that differences in cross-sectional area, a proxy for tree size, does account for some of the variation observed. It was disturbing that this was not consistently expressed. A possible explanation for this is that in some cases, although the stem was large at the base, the upper parts of the tree had been damaged (either by floods or elephants) resulting in a distorted relationship between canopy and stem size.

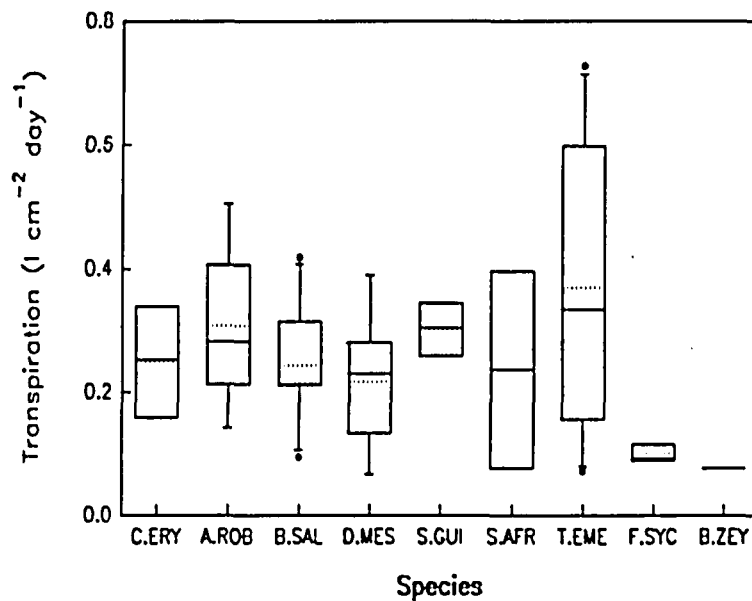


**Figure 2.34** Daily transpiration recorded for each of the trees sampled in the species comparison illustrated in a box and whisker plot. These data have been adjusted for differences in stem cross-sectional area (a proxy for tree size). The mean (-), median (...), 90th, 75th, 25th and 10th percentiles of the recorded transpiration rates are illustrated. The extremes are also illustrated (●) where these fall beyond the 90th and 10th percentiles.

A Duncan's multiple range test was conducted on the adjusted data to test whether there were significant differences between species after adjustments had been made for differences in tree size. This revealed that there were no significant differences in daily water use between species ( $P=0.45$ ). The implication of this result is that tree size rather than species is the dominant variable determining water use. This result probably reflects the fact that species occurring in riparian habitats have not evolved strategies to conserve water use as it is generally freely available within that habitat.

It should also be stressed that although considerable effort in manpower and equipment was committed to this study, the above result was derived from a total of only 159 transpiration days from a total of 35 trees during a one-month survey. Relative to the sources of possible variation, such as season, species, tree age and tree size, this does not represent a very large data set, and considerably more effort need be invested should the significance of the above sources of variation on the water use of riparian forest be determined.

The implication of this result on determining the water use of the riverine forest is that, for the purposes of this study, there is no strong indication of a need to discriminate between species in the forest. The total water use of the forest is therefore determined by the number and size of the trees present rather than their constituent species.



## 2.3.5 Reed Transpiration

### 2.3.5.1 Introduction

Reeds are one of the dominant vegetation types in the Sabie River system, particularly east of Lower Sabie camp. The reed *Phragmites mauritianus* plays an important role in the river system - not only in colonising and stabilising interfluvial sand banks, but also in providing fodder to elephants and buffalo during the dry season. Approximately a fifth of the macro-channel at the Narina site was colonised by reeds, and these were sampled to determine daily water use rates, and develop a transpiration model to predict the water use of a reed bed. This vegetation type was undoubtedly the most dynamic on the site and it developed from a sparse reed bed in February 1993 to a tall, dense, vigorously growing bed in February 1995.

### 2.3.5.2 Methods

The transpiration rates of the reeds were measured using the stem steady state heat energy balance technique (SSHEB). Measurements were made three times in the reed bed at the Narina site. Two of the assessments were carried out during September 1993 and September 1994 - corresponding to low flow periods. One assessment was made during the February 1995, corresponding to a high flow period.

The SSHEB technique uses the continuous application of heat as a tracer to determine the vertical sap flow rate in plants with entire stems up to 130 mm in diameter. By supplying a heat energy flux,  $E_{heater}$  ( $J s^{-1}$ ) to a section of stem (using a surrounding heater) and accounting for its assumed component losses (Figure 2.35) by conduction,  $E_{axial}$  ( $= E_{up} + E_{down}$ ) &  $E_{radial}$ , both vertically through and radially from the stem (determined using a set of strategically placed thermocouples and a thermopile (Figure 2.35) respectively, and (ii) sap convection,  $E_{sap}$  (determined as the difference between the heater produced heat flux and that lost in (i) above) - the rate of sap flux ( $g s^{-1}$ ) can be calculated from the quotient of the sap convection energy component ( $J s^{-1}$ ) and a related temperature variable ( $J g^{-1}$ ) (the latter calculated as the product of sap specific heat capacity ( $J g^{-1} K^{-1}$ ) and temperature difference (K) between above and below the heater) (Equation 7). The SSHEB is a non-intrusive, non-invasive alternative *in situ* technique for determination of sap flux in small plants, without the limitations often posed by aerodynamic techniques.

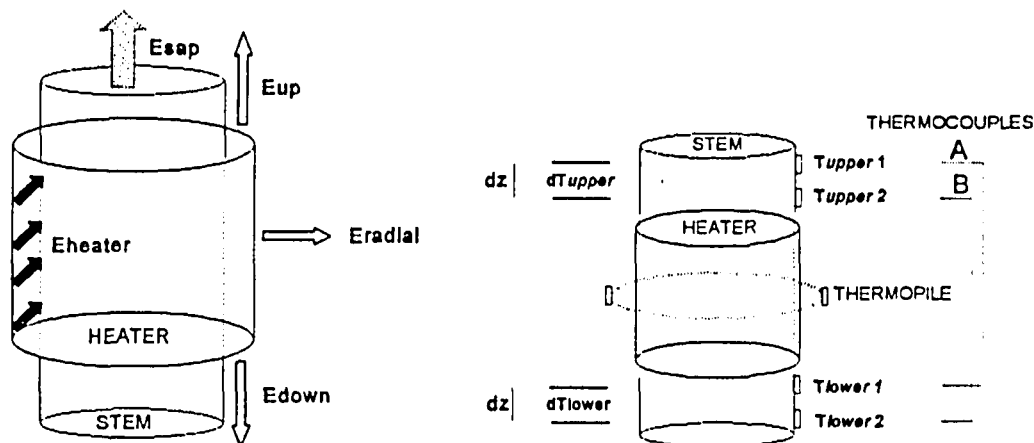


**Figure 2.35** i. (Left) Illustration of the stem steady state heat energy balance. Heat energy flux components are represented by arrows. Terms  $E_{heater}$ ,  $E_{up}$ ,  $E_{down}$ , and  $E_{radial}$  are determined directly using sensors and  $E_{sap}$  is determined by subtraction of the latter three terms from  $E_{heater}$ , ie.  $E_{sap} = E_{heater} - E_{up} - E_{down} - E_{radial}$ . ii. (Right) Diagram showing the conceptual components of the SSHEB technique gauge and the terms used in discussing the computational theory associated with its sensing components.

$$Sap\ Flow(g) = \frac{E_{heater} - E_{axial} - E_{radial}}{C_w \times dT_{stem}} \dots\dots\dots [7]$$

where:  $E_{heater} - E_{axial} - E_{radial} = E_{sap}$  (W);  $C^w$  is the specific heat of water ( $4.186\ J\ g^{-1}\ K^{-1}$ ),  $dT_{stem}$  (K) is mean temperature difference between two fixed points either side of the heater.

The precision of the technique has been assessed by Sakuratani (1981). He recorded maximum transpiration rates of  $60\ g\ 30\ min^{-1}$  in potted soybean (*Glycine max*) and sunflower (*Helianthus annuus*) plants with stem diameters of 4.3 to 14.8 mm in diameter. He showed that the water flow rate determined by the SSHEB technique in these plants agreed well ( $\pm 10\ \%$ ) with their transpiration rate as determined by mass balance, particularly when the transpiration rate was higher than  $10\ g\ 30\ min^{-1}$ . When transpiration rates were less than  $10\ g\ 30\ min^{-1}$  the sap flow rate determined by SSHEB technique deviated systematically from the transpiration rate by a magnitude of 1.2 to 2.2 times. He suggested that this may have been mainly due to disregard of influences of heat conduction in the stem on the heat transport.

### *Gauge Application*

Sixteen reeds were selected in four size classes from two parts of the reed bed at the Narina site. Every effort was made to select reeds that were as representative of the reed bed as possible. The reeds were wiped with a moist cloth at the base of the culm where the SSHEB collars were to be attached, and the precise diameter of the stems measured. Regression equations developed for reeds were then used to estimate the sap conducting areas and thermal conductivities for inclusion in the logger program. A thin film of Dow Corning electrical insulating compound was applied to the stem, and these areas covered by a layer of cling wrap. A second film of electrical compound was then applied, and the gauges fitted onto the culm over these areas. Three layers of 7mm -thick insulation foam were then wrapped over the gauges. A further layer of reflective aluminium foil was then wrapped over the entire gauge, and made water proof with a last layer of plastic. The data were recorded on two Campbell CR21X loggers, each accommodating a total of eight gauges via an AM416 multiplexer. Power was supplied by a bank of five twelve volt car batteries (connected in parallel). The loggers were programmed to collect data at one minutely intervals and record fifteen minute averages of these data to SM192/716 storage modules.

The data logger was initially programmed with  $K_{\text{gauge}}$  values for each of the gauges as determined in the laboratory. It was, however, necessary to adjust these values during the data editing procedure as temperature gradients in the stem result in violations of the basic assumptions in this technique. As a result non-zero flow was measured at night. The following adjustment procedure was therefore followed: The heat flux components ( $E_{\text{heater}}$ ,  $E_{\text{axial}}$ ,  $E_{\text{radial}}$  and  $E_{\text{sap}}$ ) that comprise the energy balance were plotted against time.  $E_{\text{radial}}$  was adjusted iteratively until  $E_{\text{sap}}$  under no-flow conditions was zero. This is justified by the principle assumption of steady state heat balance, which implies that the difference between  $E_{\text{heater}}$  and the remaining components is zero. In other words,  $E_{\text{sap}}$  is adjusted to zero by iteratively adjusting  $E_{\text{radial}}$  for no-flow conditions which is effected by adjusting  $K_{\text{gauge}}$ . This was necessary because the nature of the insulation was changed between determining  $K_{\text{gauge}}$  values in the laboratory and in the field.

The above fifteen minutely data were further edited to remove erroneous data which resulted from limitations in the technique in measuring the flows early in the morning, and late in the evening accurately. These errors arise due to violations of assumptions in the technique, limitations the thermocouples, cables and data logger impose on precision, and temperature gradients in the culms of the plants. The fifteen minutely data were then aggregated to derive hourly estimates, and further to daily total transpiration.

### **2.3.5.3 Results and Discussion**

The mean stem diameter of the reeds sampled during the three sampling sessions was very similar, ranging from 14.9 to 15.1 mm (Table 2.9). The most

significant differences between the reeds sampled during the three field sessions was in the mean leaf area and height. The reeds sampled during February 1995 had the lowest leaf area, followed by those sampled during the first visit, with the October 1994 reeds having the largest leaf area (Table 2.9). The reeds sampled during the first session were also the shortest. The change in LAI relative to the change in the mean leaf area per reed sampled suggests that the main change from September 1994 to September 1995 was that the individual leaf area per reed increased, while the data for February 1995 suggests that there was an increase in the number of reeds in the reed bed - resulting in the increased LAI. This is consistent with our field experience, as considerable effort was required to keep the transect paths open during the 1994/95 summer period, and the overall impression was that the reed bed had become extremely tall and dense. Over the course of the study the reed bed developed from a young, relatively short sparse bed in September 1993 to a considerably denser and taller stand in February 1995.

**Table 2.9** The mean diameter, height and leaf area of the sixteen *P. mauritanus* reeds sampled at each of the three sample periods, and the mean LAI for the reed bed.

	Diameter (mm)	Height (m)	Leaf area (cm <sup>2</sup> )	LAI of reed bed
September 1993	15.0	2.71	1091	1.40
September 1994	14.9	3.53	1330	2.24
February 1995	15.1	3.41	958	4.13

The average daily water use of the sixteen sample reeds fluctuated during each of the three sample periods as a consequence of varying evaporative demand (Figure 2.36).

There are, however, clear differences over the three sample periods. The reeds sampled during the September 1993 visit had the highest transpiration rates, averaging 0.61 litres per reed per day, while the average rate recorded in the two latter sample periods was only approximately half that at 0.31 and 0.28 l per reed per day.

As it is conventional to adjust transpiration rates for differences in leaf area, the daily transpiration was divided by the leaf area of each of the respective reeds (Figure 2.37). The data confirms that the differences in the daily transpiration of the reeds was not a consequence of differences in leaf area, rather it suggests that the transpiration rate of the reeds changed over the course of the study, perhaps as a consequence of the reeds ageing.

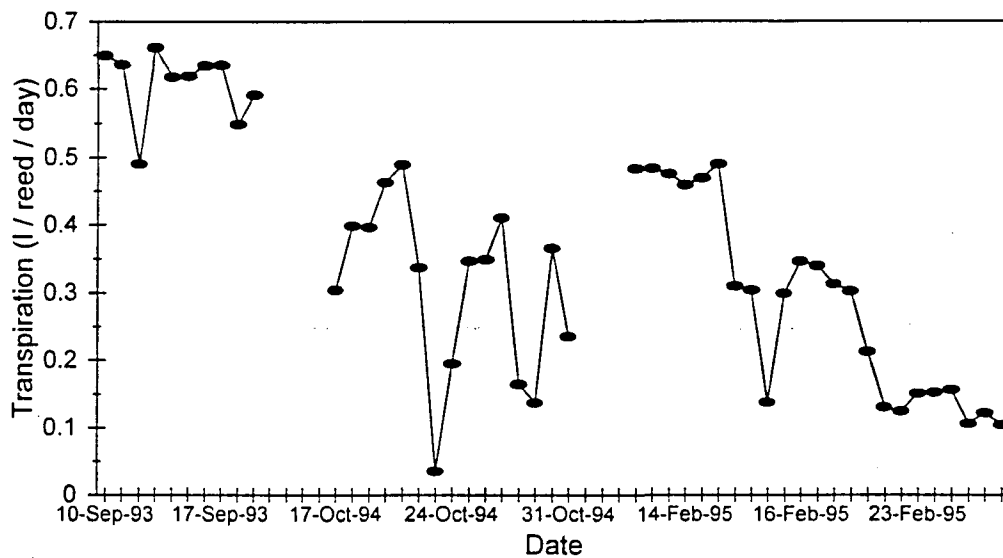


**Figure 2.36** The mean daily transpiration of sixteen reeds sampled at each of three field survey sessions at the Narina study site.

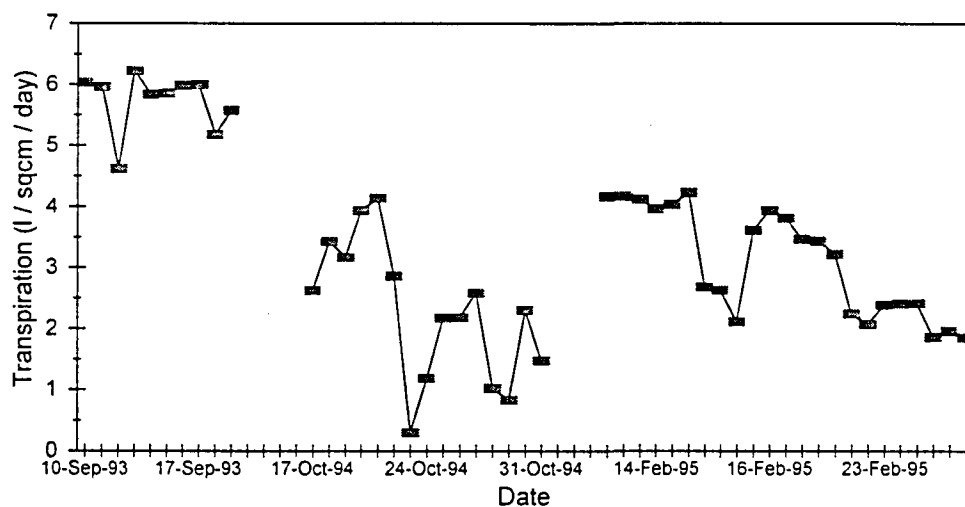


**Figure 2.37** The mean daily transpiration of sixteen reeds assessed at each of three field surveys at the Narina study site. The transpiration rates have been adjusted for differences in leaf area between the sample reeds to derive estimates of transpiration per unit leaf area..

Two options were considered in scaling up transpiration estimates from individual reed based measurements to those representing reed beds. The first was to consider scaling up using the daily water use per reed data. This would then require estimates of the population density of the reeds at the study site. While it may be feasible to derive this data for small areas, it would most probably require a degree of destructive sampling, and would also be arduous and time

consuming. The second option was to use leaf area index data to scale up transpiration. This option was considered more practical, as it is possible to conduct leaf area index surveys using an instrument such as the Licor 2000, and also to determine the seasonal changes in LAI as was done in section 2.3.2 of this report. In addition, further technological development may make it possible to conduct remote sensing surveys to derive spatial LAI data for large areas (such as the Sabie River system). For these reasons the transpiration estimates were adjusted for differences in leaf area to present data on the transpiration per unit leaf area. Deriving spatial estimates then only requires estimates for LAI, which were already available for this study. The reed model development therefore focussed on developing a model to predict transpiration per unit leaf area for a reed bed. This model is presented in Chapter 5.

## **CHAPTER 3**

### **MODELLING RIVER HYDRAULICS**

---

#### **3.1 Scope**

The required output from the river hydraulics study is the ability to synthesize stage-discharge relationships (rating curves) at selected locations along the Sabie River where the riparian bank storage and transpiration models are to be applied. A study of river hydraulics may be undertaken at various levels of intensity, ranging from coarse estimates of total flow resistance using values from river channels displaying similar frictional characteristics (eg. Barnes, 1967), to a more rigorous study of the various components contributing to total flow resistance for the specific system (eg. skin friction, channel form and vegetational resistance).

A reach along the Sabie River was selected for a pilot hydraulics study. The primary objective of the study was to provide initial estimates of total flow resistance and to assess the accuracy with which water surface level data must be collected to produce reliable flow resistance data. The pilot study assisted with the initiation of a more intensive and extensive river hydraulics study. The latter quantifies the roughness components (morphological, sedimentological and vegetational) for a range of channel types (braided, bedrock anastomosing, mixed anastomosing, pool-rapid, and single thread) identified along the Sabie River by van Niekerk and Heritage (1995). A description and results of the pilot hydraulics study are provided in 3.2. The broader hydraulics study is reported separately by Broadhurst *et al.* (in press), since it is integral to any study involving river hydraulic variables (eg. flow depth and velocity) along the Sabie River and for similar river systems.

A technique has been developed for synthesizing the approximate steady-state rating curve for a river cross-section using gauged discharge and stage hydrographs. The methodology involves the optimisation of a modified non-linear form of the Muskingum hydrological storage routing equation, and is described in 3.3

#### **3.2 River Hydraulics Pilot Study**

##### **3.2.1 Study Reach Morphology, Riparian Vegetation and Location of Cross-Sections**

A study reach 1182 m in length, incorporating the Narina study site (where continuous stage, groundwater level, transpiration and meteorological data has been collected), was selected for hydraulics data collection and analysis (Fig. 3.1 and Fig 3.2, Chapter 3 Appendix Table A3.1). The Sabie River in the vicinity of the study reach is incised into the underlying

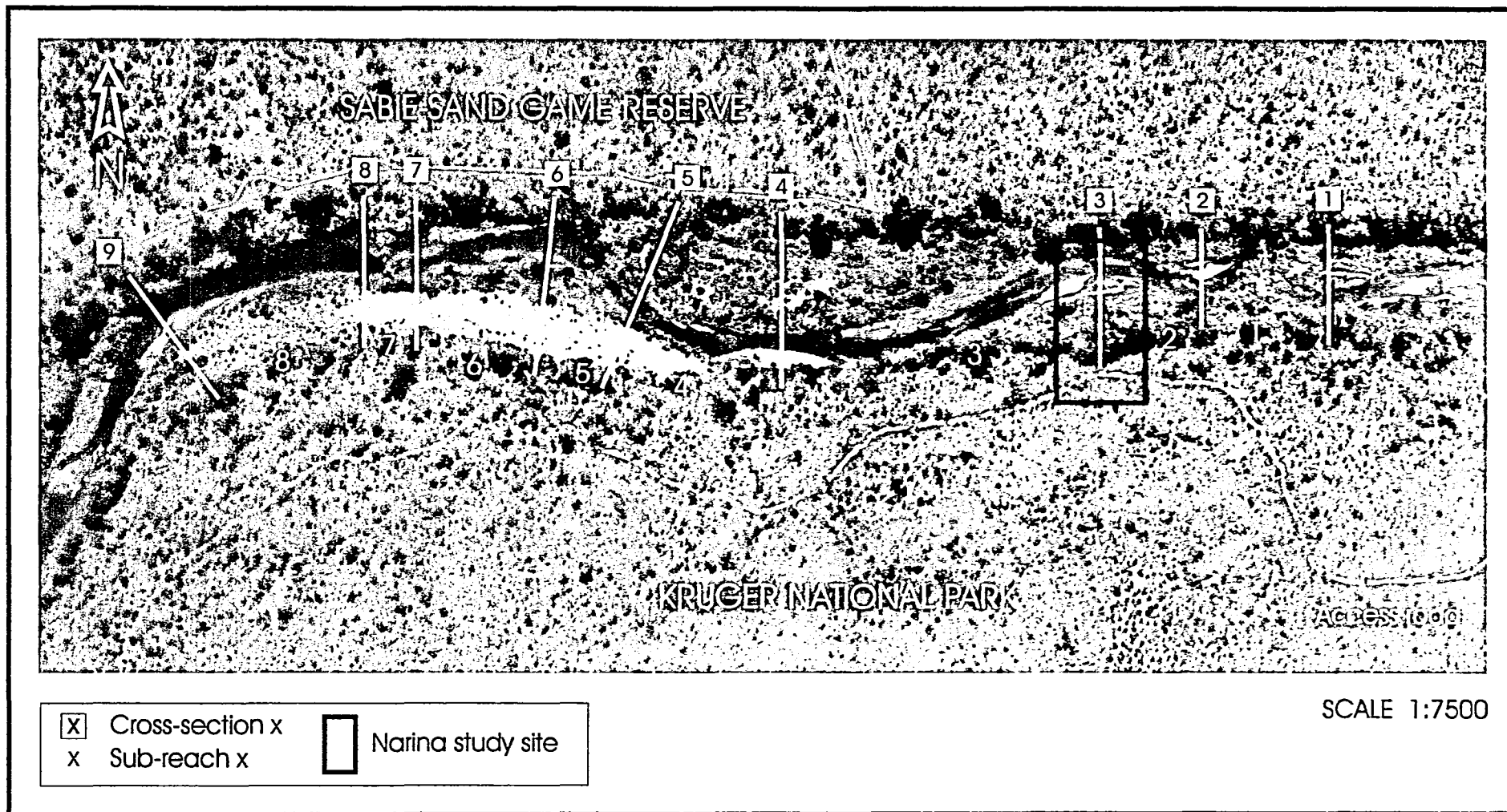


Figure 3.1 Location of Cross-sections along the Study Reach (1986 Aerial Photograph).



gneisses and granites of the basement complex, forming a 150 to 200 m wide macro channel that is influenced by seasonal and ephemeral flow events. Perennial flow is maintained in a smaller active channel displaying bedrock and alluvial geomorphological features. The study reach displays a braided river morphology, incorporating pool-rapid sequences (Table 3.1).

**Table 3.1** Study reach morphology

Sub-Reach	River Morphology	
	Morphological Type	Morphological Unit
1	Pool-Rapid	Rapid, MCBB, ACBB
2	Braided	MCLB, ACBB
3	Braided	MCLB, ACBB
4	Braided	MCLB, ACBB
5	Pool-Rapid	Rapid, MCLB
6	Pool-Rapid	Pool, MCLB
7	Pool-Rapid	Rapid, MCLB
8	Pool-Rapid	Pool, MCLB

MCBB Macro Channel Braid Bar  
MCLB Macro Channel Lateral Bar  
ACBB Active Channel Braid Bar

Bedrock outcrops occur in the river channel in areas displaying local change in bedrock resistance as a result of lithological and structural variability (Cheshire, 1994). Cross-sections were surveyed immediately upstream and downstream of the major hydraulic controls formed by bedrock outcrops, isolating these units that result in abrupt drops in the river water surface level (sub-reaches 1,5 and 7). The cross-sectional channel morphology was also surveyed at changes in the active channel planform and channel slope (cross-sections 2, 3 and 4). A total of eight macro-channel cross-sections were surveyed along the pilot study reach, with cross-section 9 corresponding to cross-section 14, having been previously surveyed for a Geomorphology study (Heritage *et al.*, in press).

The distribution of riparian vegetation includes large trees along the macro channel banks, with individuals located on the macro channel lateral bar deposits. The lateral (macro and active channel) and braid bars are also vegetated with herbaceous cover and phragmites. Increased colonisation of the fluvial deposits by phragmites over the study period has been noted, with rapid recovery and increased growth experienced following flood events in December 1992 and March 1993.

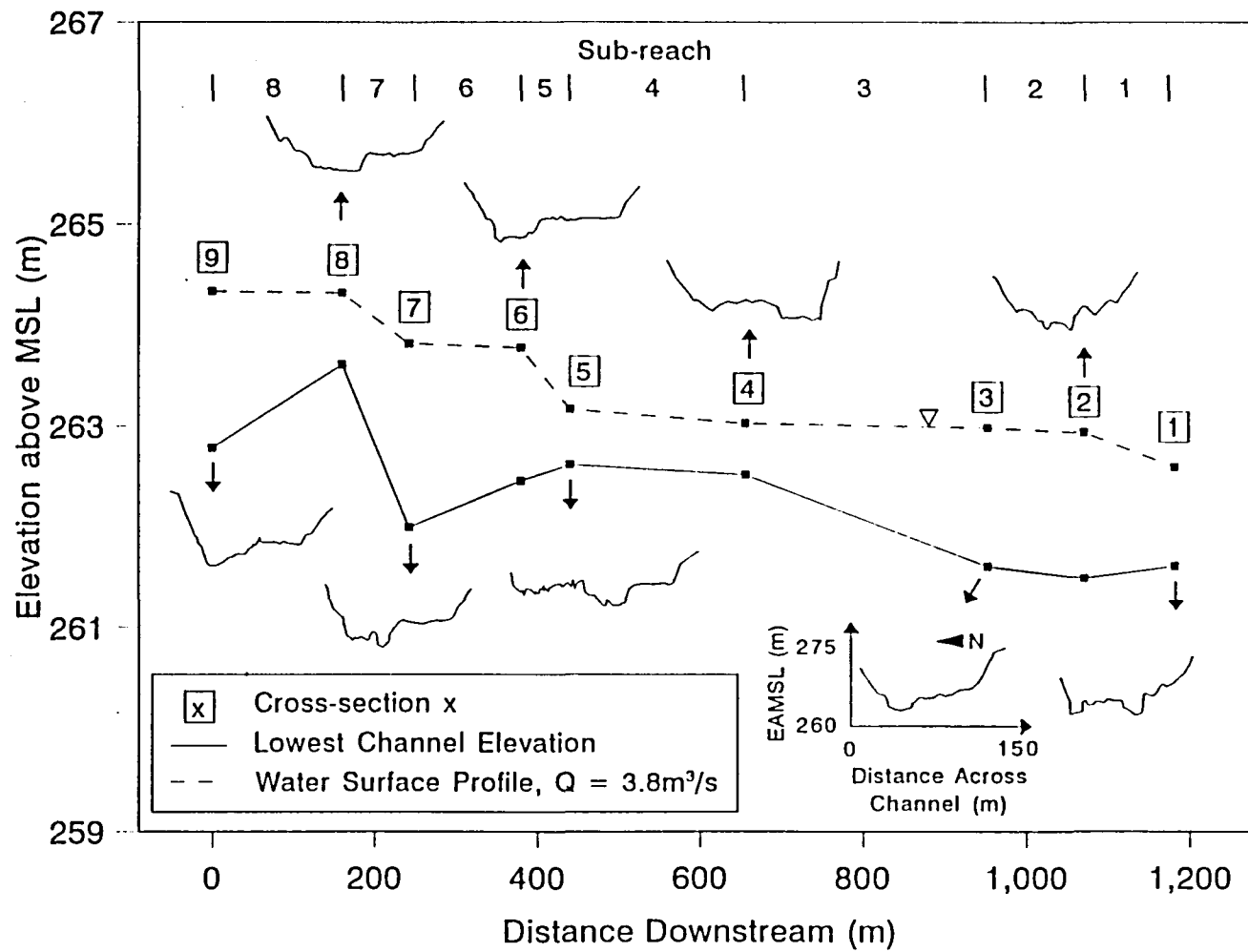


Figure 3.2 Longitudinal River Profile and Cross-sectional Morphology.

### 3.2.2 Hydraulics Data Collection

Stage levels were manually surveyed during the low-flow periods at each of the cross-sections (Chapter 3 Appendix Table A3.3). A series of 2 or 3 peak stage level recorders (poles coated with water soluble paint) were installed along the channel banks at each of the cross-sections to provide stage data for intermediate and high flows (Fig. 3.3). The peak stage was determined by the highest level to which paint washoff occurred on the recording poles. Strand lines produced by small particles of floating debris (mainly vegetation) were also used to provide a record of the peak flow levels. A Crump weir (DWAf gauging station X3H021) is located 4600 m upstream of the Narina study site (cross-section 3), and no major tributaries join the Sabie River in the intervening reach. The peak stage for a flow event is assumed to correspond to the peak discharge monitored at the upstream weir. The unsteady effects of flow attenuation and looped rating curves, and influent flow to the river between the study reach and weir are neglected in the study.

During the data collection period (June 1993 to January 1995), discharges in the range 2 m<sup>3</sup>/s to 45 m<sup>3</sup>/s were recorded at the gauging weir. Within this limited flow range, five accurately surveyed stage levels in the low-flow range 2.05 m<sup>3</sup>/s to 6.31 m<sup>3</sup>/s were measured. Peak flow level recorder and strand line data were used to measure peak flow levels corresponding to higher flow discharges. Washoff levels were often indistinct, and the peak flow level recorders seldom provided sufficiently accurate data that could be used to calculate resistance coefficients. Tabulated discharge and corresponding stage level data are included in the Appendix (Table A3.4).

Due to the limited flow data collected, the influence of vegetational resistance is confined to the interaction of low and intermediate flows with fringe communities (predominantly phragmites) along the active channel banks.

### 3.2.3 Rating Curves

Stage levels have been recorded at the Narina study site (cross-section 3) at hourly intervals over the monitoring period October 1992 to June 1995. Peaks and troughs on the stage (Narina) and discharge (upstream gauging weir) hydrographs have been used to construct a rating curve (Fig. 3.4). Adequate data are available up to a discharge of 50 m<sup>3</sup>/s, with sparse data recorded at higher flows due to logger malfunctions and limited high flows. A relationship of the form given by equation 3.1 is fitted to the data, and the regression coefficients are listed in Table 3.2.

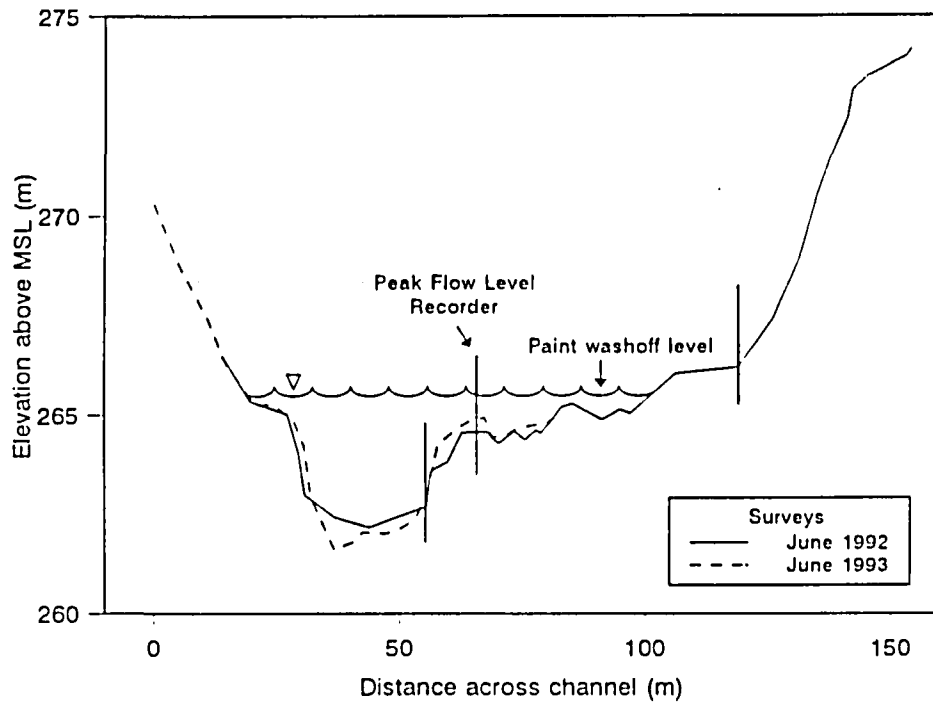


Figure 3.3 Peak Flow Level Recorders Installed at Cross-section 6.

$$z = a(Q+b)^c + d$$

3.1

where  $z$  is the stage level above MSL (m)

$Q$  is the discharge rate ( $\text{m}^3/\text{s}$ )

The rating data for the river cross-sections (excluding section 3) are plotted in Fig. 3.5. Regression relationships are fitted to the data where sufficient data are available, and the regression coefficients in equation 3.1 are given in Table 3.2.

Table 3.2 Regression coefficients in equation 3.1

Cross-section	$a$	$b$	$c$	$d$
1	9.296	6.250	0.080	251.47
3*	7.488	9.902	0.112	252.83
4	8.236	45.080	0.166	247.33
5	6.451	44.545	0.180	250.21
6	19.655	18.231	0.053	240.61
7	8.287	53.461	0.155	248.26

\* Narina Study Site

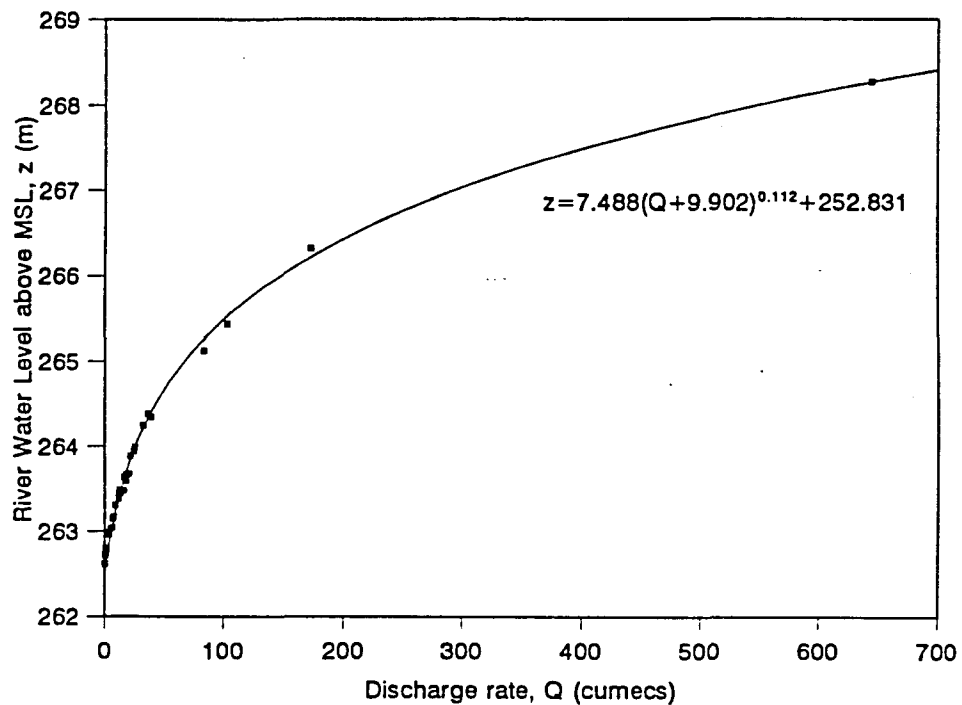


Figure 3.4 Measured and Fitted Rating Curve for the Narina Study Site (Cross-section 3).

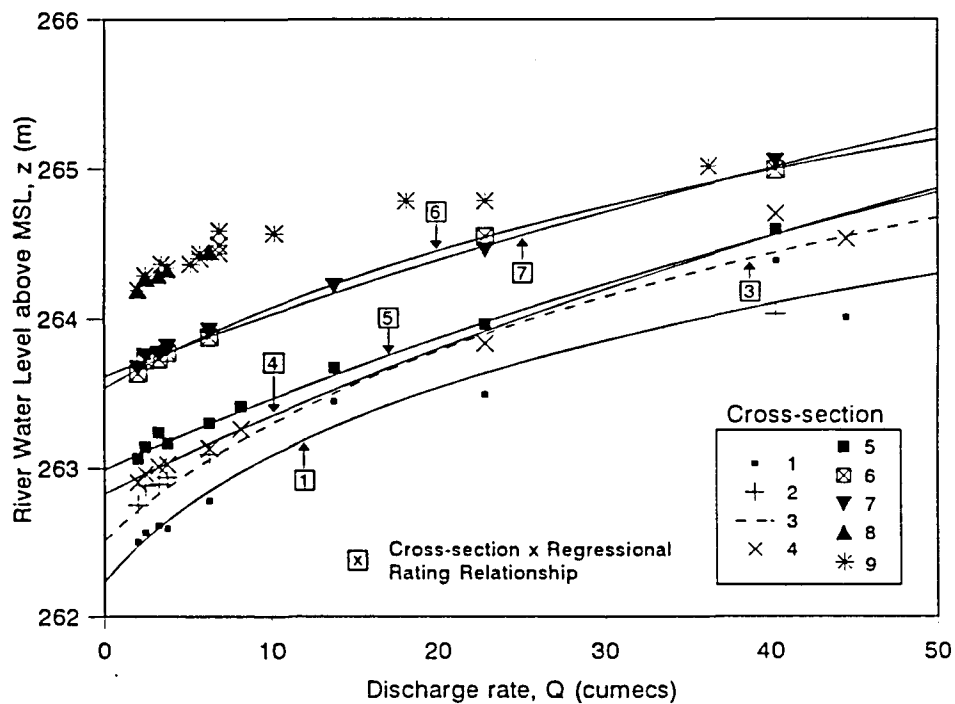


Figure 3.5 Rating Curves for Cross-sections 1 to 9.

### 3.2.4 Total Flow Resistance

Two relationships that are commonly applied to estimate total flow resistance of a river channel are according to Manning and Darcy-Weisbach.

#### 3.2.4.1 Manning's Relationship

Manning's relationship for total flow resistance is given by

$$v = \frac{1}{n} R^{2/3} S_f^{1/2} \quad 3.2$$

where  $v$  is the average flow velocity (m/s)

$R$  is the hydraulic radius (m)

$S_f$  is the energy gradient

$n$  is Manning's empirical resistance coefficient (s/m<sup>1/3</sup>)

#### 3.2.4.2 Darcy-Weisbach Relationship

The Darcy-Weisbach equation is given by

$$v = \left( \frac{1}{f} 8gRS_f \right)^{1/2} \quad 3.3$$

where  $g$  is the gravitational acceleration constant (m/s<sup>2</sup>)

$f$  is a dimensionless frictional factor

Expressing the friction factor,  $f$  in terms of Manning's  $n$ ,

$$f = n^2 \frac{8g}{R^{1/3}} \quad 3.4$$

#### 3.2.4.3 Calculation of Sub-reach Resistance Coefficients

The resistance coefficients for the sub-reaches are calculated by applying equations 3.2 and 3.4 between cross-sections, assuming linear energy gradients. The validity of this assumption was confirmed by computing non-uniform flow profiles using a backwaters programme. The resistance coefficients for sub-reaches 2 to 6 are given in Table 3.3, and Manning's  $n$

is plotted against discharge in Fig. 3.6.

Relationships of the form

$$n = eQ^i + hQ + j$$

3.5

are fitted to the resistance data for sub-reaches 3 to 6, and the regression coefficients are given in Table 3.4.

**Table 3.3** Resistance coefficients for the sub-reaches

Discharge (m <sup>3</sup> /s)	Sub-reach				
	2	3	4	5	6
	Manning's $n$ Friction factor $f$				
2.05	0.108	0.032	0.021	0.232	0.082
	0.937	0.103	0.056	5.796	0.674
2.49	0.070	0.030	0.027	0.257	0.086
	0.430	0.089	0.091	6.800	0.680
3.28	0.079	0.032	0.032	0.218	0.068
	0.544	0.105	0.129	4.773	0.433
3.80	0.075	0.025	0.021	0.192	0.068
	0.484	0.061	0.054	3.451	0.426
6.31	0.036	0.018	0.021	0.162	0.053
	0.109	0.029	0.050	2.484	0.255
8.20			0.026		
			0.069		
22.83		0.035	0.034	0.162	
		0.091	0.095	2.110	
40.29				0.146	0.044
				1.490	0.134
44.51		0.046			
		0.142			

**Table 3.4** Coefficients in equation 3.5

Sub-Reach	<i>e</i>	<i>i</i>	<i>h</i>	<i>j</i>
3	0.579	-0.018	0.0011	-0.543
4	-0.336	0.998	0.3337	-0.028
5	0.223	-1.016	0.0	0.143
6	0.089	-0.917	0.0	0.040

Sub-reaches 1 and 7 are characterised by large rapids and the resistance coefficients for these morphological units are not included in Table 3.4 and Fig. 3.6. It is not appropriate to calibrate these sub-reaches using the resistance relationships in equations 3.2 or 3.3, because large energy gradients result from abrupt drops in river stage associated with hydraulic controls (bedrock outcrops) in the active channel. The influence of bedrock outcrops in the active channel will reduce with increasing discharge as hydraulic controls confined to the active channel/s become drowned out. Sub-reach 5 is included in the analysis since it is a small rapid section.

The friction coefficients for sub-reaches 2, 5 and 6 reduce with increasing flow up to 10 m<sup>3</sup>/s, thereafter remaining constant over the data range presented. The initial reduction in resistance is due to a rapid increase in flow velocity corresponding with a small rise in stage. Sub-reaches 2 and 6 are morphologically similar, situated in depositional zones upstream of bedrock outcrops in the active channel. The Manning's resistance coefficients for these sub-reaches agree closely, ranging from 0.11 (2 m<sup>3</sup>/s) to 0.04 (40 m<sup>3</sup>/s).

Sub-reaches 3 and 4 are characterised by an alluvial active channel, with incipient braid bars at low flows. The resistance coefficients for this section of the study reach show a gradual increase from 0.02 (2 m<sup>3</sup>/s) to 0.05 (40 m<sup>3</sup>/s) (Fig. 3.6). Flows in this range remain within a well-defined active channel, and rising stages result in substantial increases in cross-sectional flow area with only small increases in wetted perimeter.

Fig. 3.7 shows the change in Manning's *n* with discharge rate for the different morphological types encountered along the Sabie River (Broadhurst *et al.*, in press). The resistance factors are reach averaged values, calculated from data collected at a number of cross-sections located within the particular morphological type. The range of resistance coefficients for the braided river morphology (0.06 to 0.03, Fig. 3.7) agree well with those calculated in the pilot study (0.05 to 0.02) for sub-reaches 2,3,4 and 6, which are typically braided sections.



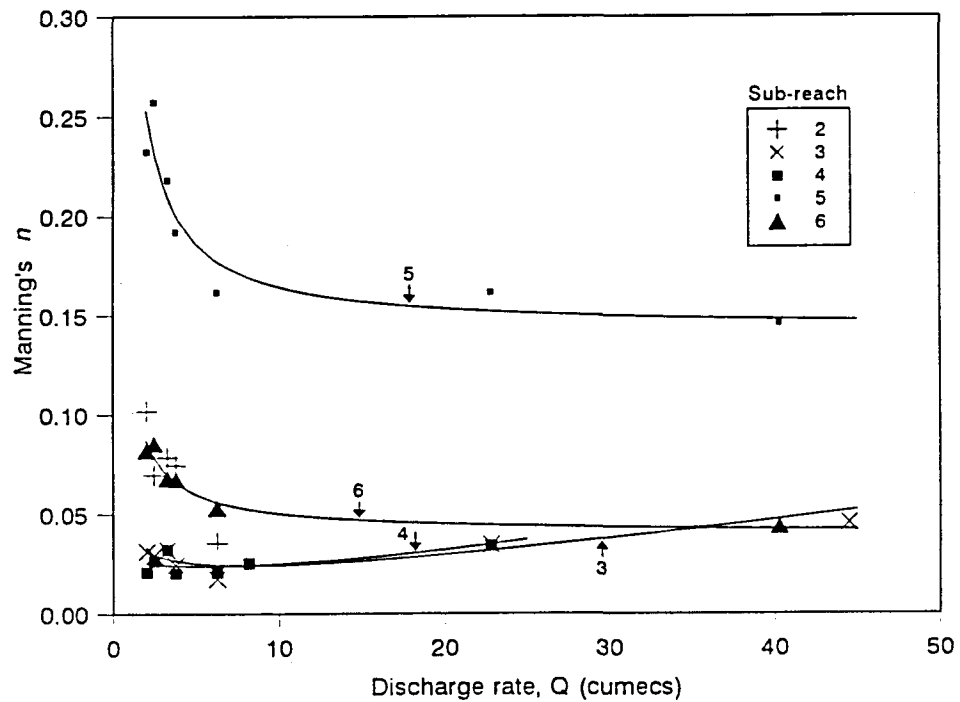


Figure 3.6 Variation in Manning's  $n$  with Discharge Rate.

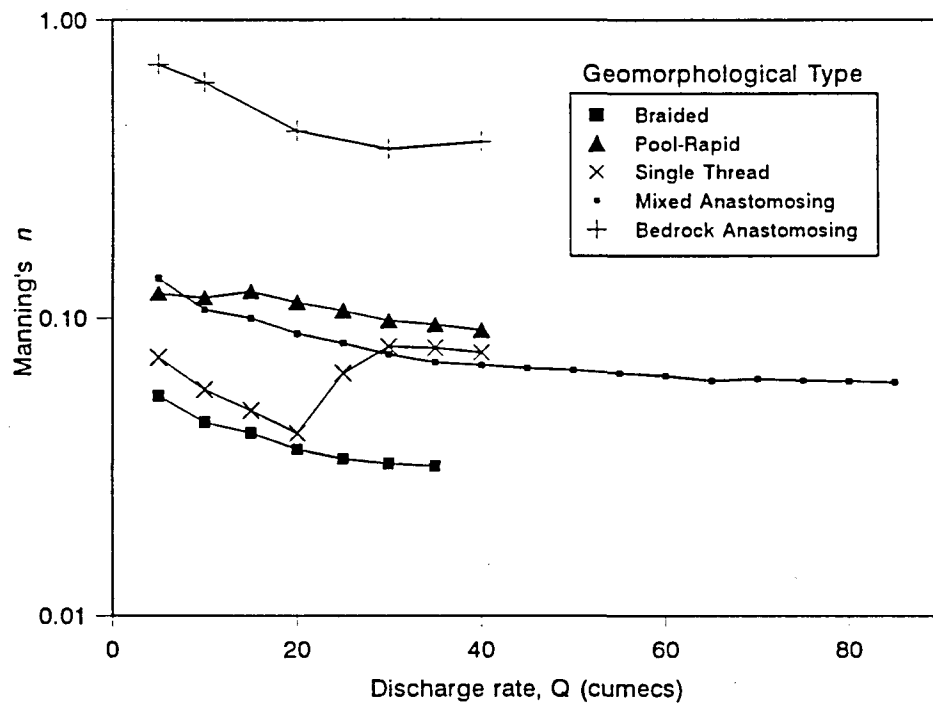


Figure 3.7 Variation in Manning's  $n$  with Discharge Rate for Different Geomorphological Types (Broadhurst *et al.*, in press).

Calculated values of selected hydraulic parameters (average flow velocity ( $v$ ), maximum flow depth ( $D_{max}$ ), cross-sectional flow area ( $A$ ), wetted perimeter ( $P$ ), and hydraulic radius ( $R$ )) obtained from measured discharge rates and stages are tabulated for each cross-section in the Appendix to Chapter 3 (Tables A3.5.1 to A3.5.8).

### **3.2.5            Synthesis of Rating Curves using Flow Resistance Data for Similar Morphological Channel Types**

The prediction of rating relationships using total flow resistance as determined by Broadhurst *et al.* (in press) is illustrated by synthesizing stage-discharge data for cross-section 3 at the Narina study site (Fig. 3.1). Cross-section 3 is selected due to the availability of gauged rating data up to 650 m<sup>3</sup>/s (Fig. 3.4).

#### **3.2.5.1            Data Requirements**

The prediction of stage levels from resistance type relationships requires the following data :

- *Cross-sectional geometry*
- *Friction slope/s*
- *Flow resistance data*

##### **1    *Cross-sectional Geometry***

Cross-sectional geometry may be routinely determined by conventional survey techniques. Alternatively, photogrammetric analysis may be employed. The latter method, however, requires surveyed photographic control with the disadvantage of reduced accuracy over a conventional cross-sectional survey.

The cross-sectional shape is required to compute the flow area ( $A$ ) and wetted perimeter ( $P$ ), corresponding to river stage.

##### **2    *Friction Slope/s***

The friction slope or flow energy gradient should ideally be determined for a range of flow discharges (low, intermediate and high), as a consequence of changes in cross-sectional shape, hydraulic controls and flow resistance with discharge. The water surface slope may be used instead of the energy gradient within an approximately uniform (geometrically and flow resistivity) reach, since the gradient of velocity head may be neglected. This alleviates the necessity to survey cross-sectional profiles upstream and downstream of the section to compute changes in velocity head.

The measured water surface and friction slopes for sub-reaches 2 and 3 are tabulated in Table 3.5. The slopes agree well in sub-reach 2, with larger differences occurring in sub-reach 3. The energy-water surface slope discrepancy in sub-reach 3 at a discharge of 6.31 m<sup>3</sup>/s is attributed to an inaccurate stage measurement at cross-section 4. The friction slopes for the sub-reaches upstream and downstream of cross-section 3 are in the range 0.00015 to 0.00059, with no clear trend detected. The general scatter is attributed to measurement inaccuracies in the low energy slope environment due to the backing-up of flow. An average value of 0.00033 is adopted. With increasing discharge, the energy gradient will tend towards the regional channel slope ( $\pm 0.0015$ ) as local hydraulic controls, particularly bedrock outcrops in the active channel, become drowned out.

**Table 3.5** River stage and friction slopes

Discharge m <sup>3</sup> /s	Sub-reach			
	2		3	
	Stage slope	$S_f$	Stage slope	$S_f$
2.05	0.00038	0.00038	0.00036	0.00043
2.49	0.00017	0.00017	0.00020	0.00024
3.28	0.00035	0.00034	0.00026	0.00030
3.80	0.00037	0.00036	0.00014	0.00018
6.31	0.00015	0.00014	0.00007	0.00015
22.83			0.00034	0.00034
44.51			0.00063	0.00059

### 3 Flow Resistance Data

Cross-section 3 is located in a braided channel type with active channel and macro channel braided bars (Table 3.1). For this channel type and morphological units present, the Manning's resistance coefficients calculated by Broadhurst *et al.* (in press) are given in Table 3.6.

The Manning's resistance coefficient shows a general decline over the flow range. Since no data is available for discharges above 35 m<sup>3</sup>/s for this channel type (Fig. 3.7), an asymptotic value of 0.033 is assumed.

#### 3.2.5.2 Results and Discussion

Manning's resistance relationship (equation 3.2) is applied to synthesize the rating curve at cross-section 3 up to a discharge of 650 m<sup>3</sup>/s. An iterative solution is initially required ( $n$  is a function of  $Q$  up to 35 m<sup>3</sup>/s), whereafter the discharge rate corresponding to a given stage may be obtain explicitly.

**Table 3.6** Manning's  $n$  for a braided channel type

Discharge $\text{m}^3/\text{s}$	Manning's $n$
5	0.054
10	0.032
15	0.043
20	0.038
25	0.034
30	0.031
35	0.035

The synthesized and gauged rating data are plotted in Fig. 3.8. The predicted and actual relationships compare extremely well. Over the discharge range 5 to 35  $\text{m}^3/\text{s}$  (for which friction slope and energy gradient data are available) the maximum error in stage is 0.033 m, and 0.041 m for the extrapolated curve.

The positive correlation achieved between the gauged and synthesized rating curves is attributed to the approximately constant value of the

term  $\frac{\sqrt{S_f}}{n}$  over the extrapolated flow range. Over the range 50  $\text{m}^3/\text{s}$  to 650

$\text{m}^3/\text{s}$ , 80% of the data lies within one standard deviation of the mean. This is graphically illustrated in Fig. 3.9, where the friction slope-resistance term is plotted against discharge using the rating curve function fitted to the gauged data for cross-section 3 (Fig. 3.4). It is unlikely, however, that either the friction slope or resistance coefficient will remain constant with discharge.

For example, the friction slope will tend towards the regional macro-channel slope at high discharges when local active channel hydraulic controls become drowned out. Assuming that the friction slope may be approximated by the regional channel gradient at the peak flood discharge of 650  $\text{m}^3/\text{s}$  (recorded in March 1993), results in a Manning's  $n$  of 0.056 which is 70% higher than the extrapolated value of 0.033 applied in the synthesis. The low variability in the friction slope-resistance term in equation 3.2 is a characteristic of the study site, and may not be assumed in general.

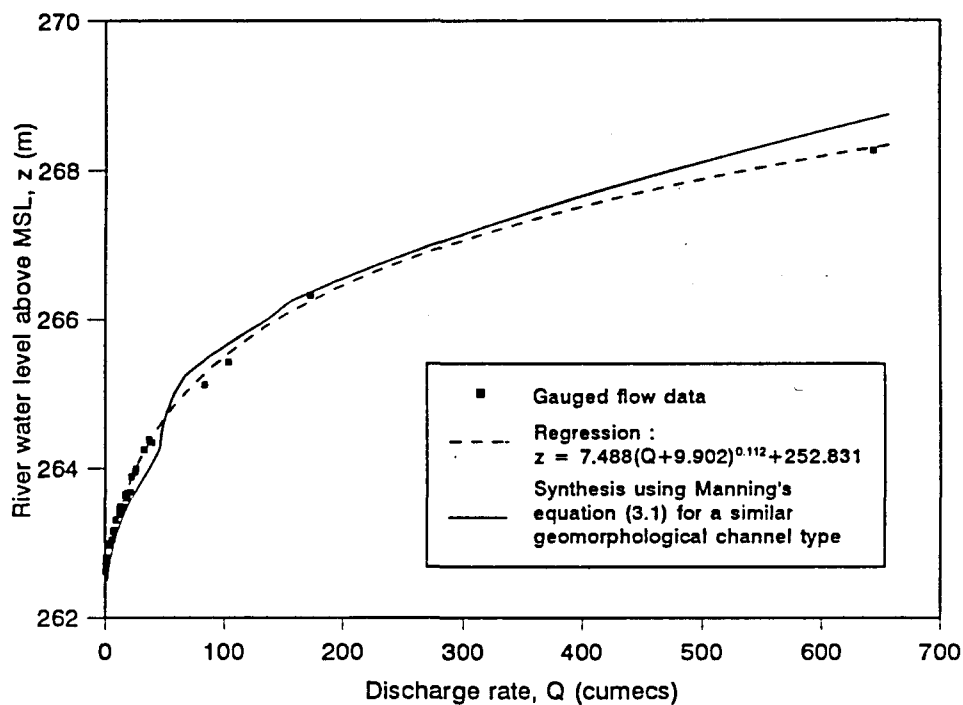
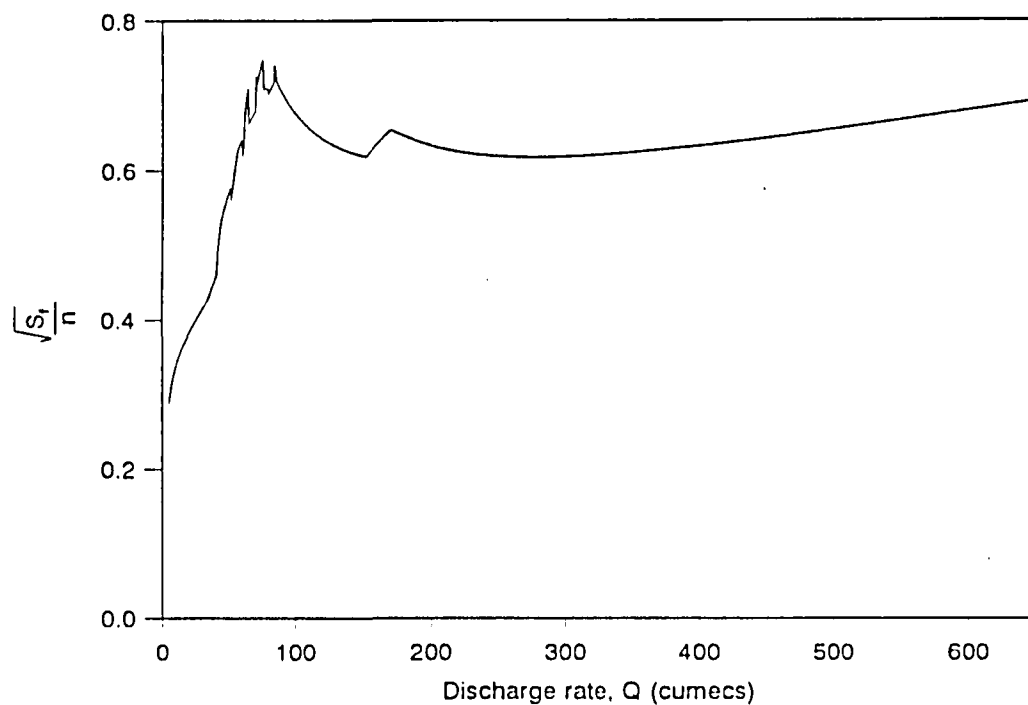
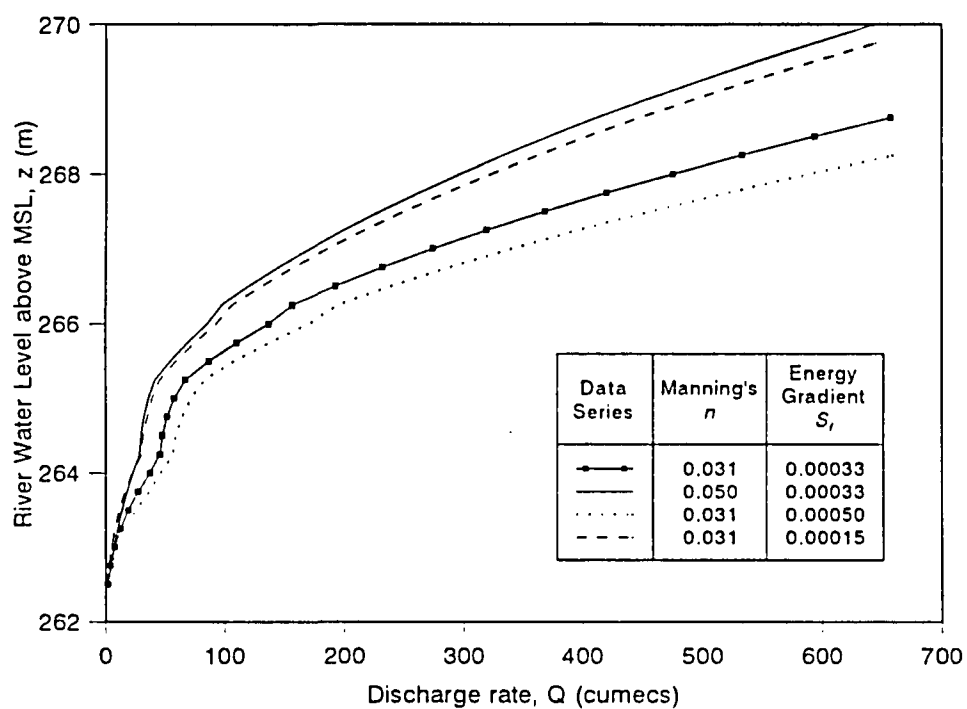


Figure 3.8 Synthesized Rating Curve for Cross-section 3 using Manning's Resistance Coefficient for a Similar Morphological Type.

The sensitivity of the synthesized rating curve to changes in friction slope and resistance coefficient within the range of uncertainty in these parameters over the limited input data range (5 m<sup>3</sup>/s to 35 m<sup>3</sup>/s for Manning's resistance coefficient, and 2 m<sup>3</sup>/s to 45 m<sup>3</sup>/s for the friction slope) is illustrated in Fig. 3.10. The error in maximum flow depth is plotted against discharge rate in Fig. 3.11. The average maximum flow depth error is 17% over the full discharge range, with a maximum error of 45% at a discharge of 50 m<sup>3</sup>/s. The maximum error corresponds to a localised increase in the rating curve gradient, resulting from a reduction in hydraulic radius as flow overtops the active channel banks (see Chapter 3 Appendix Table A3.5.3). This change in slope is not apparent in the gauged flow data (Fig. 3.4), most likely due to associated adjustments in the flow resistance and energy slopes.



**Figure 3.9** Variability of the Friction Slope-Resistance Coefficient Term in Equation 3.2 over the Discharge Range 5 m<sup>3</sup>/s to 655 m<sup>3</sup>/s.



**Figure 3.10** Sensitivity of the Synthesized Rating Relationship to Changes in Friction Slope and Manning's Resistance Coefficient.

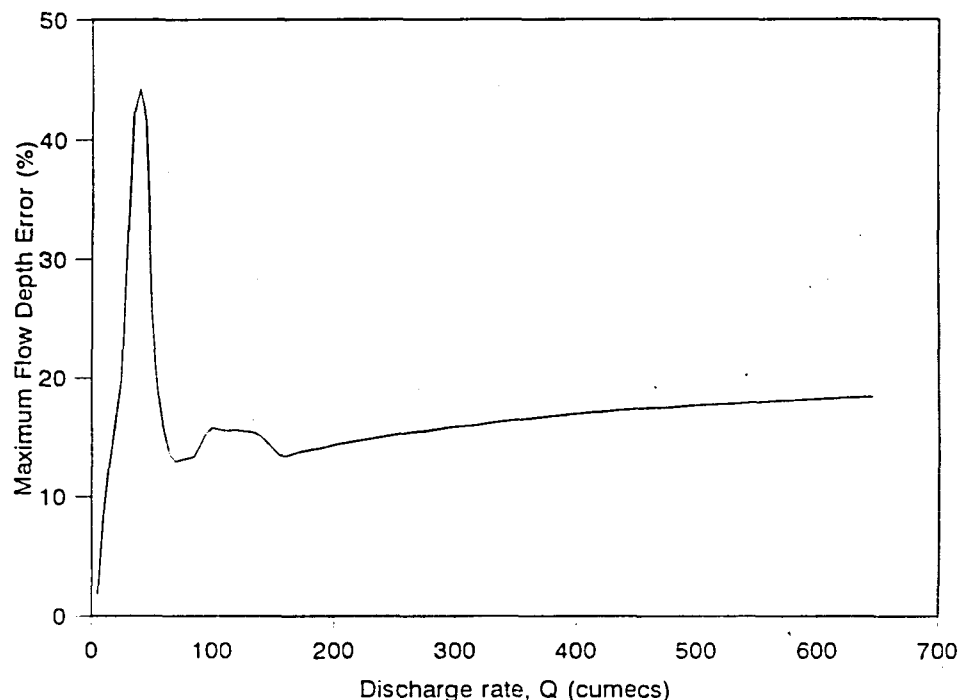


Figure 3.11 Error in Maximum Flow Depth For  $n=0.050$  and  $S_f=0.00033$ .

### 3.3 Synthesis of Rating Curves from Local Stage and Remote Discharge Monitoring using Nonlinear Muskingum Routing

#### 3.3.1 Scope

The discharges at local and remote sites can be related by a variety of flood routing procedures ranging in simplicity from Muskingum-type models to solution of the full dynamic flow (Saint-Venant) equations. If the local stage-discharge relationship can be expressed as a simple mathematical function, then the local discharge can be expressed in terms of local stage and a routing model used to relate local stage to remote discharge, accounting for lag and attenuation effects. If the form, but not the parameter values, of the stage-discharge relationship can be assumed and simultaneous local stage and remote discharge data are available, then the routing procedure can be adapted to infer the parameter values and hence synthesize the stage-discharge relationship.

This approach is developed here, using nonlinear Muskingum routing principles to relate flow conditions at the site of interest to discharges recorded at a location some distance upstream. The local stage-discharge relationship is assumed to be described by a simple power function, enabling the local flow conditions to be expressed in terms of stage. Using local stage measurements in the routing model enables the power function

parameters to be estimated by an optimization technique. The method is tested against results obtained by explicit solution of the Saint-Venant equations for a rectangular, prismatic channel, and then demonstrated by synthesizing a rating curve for the Narina study site on the Sabie River in the Kruger National Park (Fig. 3.1).

### 3.3.2 Muskingum Models

The flow conditions at two locations on a river can be related through the continuity equation

$$\frac{dS}{dt} = I - O \quad 3.6$$

in which  $I$  and  $O$  represent the inflow and outflow discharges to the river reach between the two locations,  $S$  represents the storage volume within the reach, and  $t$  is time. This equation can be expressed in finite difference form as

$$\frac{S_t - S_{t-1}}{\Delta t} = \frac{I_t + I_{t-1}}{2} - \frac{O_t + O_{t-1}}{2} \quad 3.7$$

in which  $\Delta t$  is the period between times  $t$  and  $t-1$ .

Generally, stage-discharge relationships are continuous and monotonic, and can be described by simple mathematical expressions, such as

$$Q_t = a_1 y_t^{m_1} \quad 3.8$$

in which  $Q_t$  is the discharge and  $y_t$  is the stage at time  $t$ . Stage will be considered here to be measured from the bed of the channel, and therefore to be synonymous with flow depth.

Substitution of equation 3.8 for  $O$  in equation 3.7 gives the relationship between time-varying discharge at the upstream end of a reach and the time-varying stage at the downstream end,

$$S_t - S_{t-1} = \left[ \frac{I_t + I_{t-1}}{2} - \frac{a_1 y_t^{m_1} + a_1 y_{t-1}^{m_1}}{2} \right] \Delta t \quad 3.9$$



This can also be written as

$$S_t - S_{t-1} = \left[ T_t - \frac{a_1}{2} (y_t^{m_1} + y_{t-1}^{m_1}) \right] \Delta t \quad 3.10$$

in which

$$T_t = \frac{I_t + I_{t-1}}{2} \quad 3.11$$

The storage within the reach at any time  $t > 1$  during an event beginning with steady flow at  $t = 1$  can then be determined as

$$S_t = \left[ \sum_{i=2}^t T_i - \frac{a_1}{2} \sum_{i=2}^t (y_i^{m_1} + y_{i-1}^{m_1}) \right] \Delta t + S_1 \quad 3.12$$

in which  $S_1$  is the storage (assumed here to be prismatic) in the channel at  $t = 1$ .

$S_t$  can also be estimated using the Muskingum approximations (as originally proposed by McCarthy, 1938), developed from equation 3.8 and the relationship between prismatic storage and flow depth

$$S_t = a_2 y_t^{m_2} \quad 3.13$$

By combining equations 3.8 and 3.13 the prismatic storage can be expressed in terms of discharge, i.e.

$$S_t = \frac{a_2}{a_1^{m_2/m_1}} Q_t^{m_2/m_1} \quad 3.14$$

During an unsteady flow event the reach storage is not prismatic and is estimated as a weighted average of the prismatic storages calculated using the upstream and downstream flow conditions, represented by  $I$  and  $O$  respectively,

$$S_t = \frac{a_2}{a_1^{m_2/m_1}} (x I_t^{m_2/m_1} + (1 - x) O_t^{m_2/m_1}) \quad 3.15$$

Equation 3.15 can be approximated by

$$S_t = \frac{a_2}{a_1^{m_2/m_1}} (x I_t + (1 - x) O_t)^{m_2/m_1} \quad 3.16$$

which is a simplification of the rigorous form (equation 3.15) since addition and exponentiation are not commutative operations (Meehan, 1979). However, this form has the advantage of being easily linearized through logarithmic transformation.

Either equation 3.15 or equation 3.16 can be solved conjunctively with equation 3.7 for flood routing. For example, Gill (1978) and Tung (1985) have used the form of equation 3.17 and Yoon and Padmanabhan (1993) describe the use of both in the software package MUPERS (MUSkingum Parameter Estimation and flood Routing System). Gill (1979) and Yoon and Padmanabhan (1993) have shown that the simpler equation 3.16 actually produces more accurate results than the more rigorous equation 3.15.

Equations 3.15 and 3.16 can also be expressed in terms of the downstream stage by substituting equation 3.8 for  $O_t$ . Equation 3.15 then becomes

$$S_t = a_2 \left[ x \left( \frac{I_t}{a_1} \right)^{m_2/m_1} + (1 - x) y_t^{m_2} \right] \quad 3.17$$

and equation 3.16 becomes

$$S_t = \frac{a_2}{a_1^{m_2/m_1}} (x I_t + (1 - x) a_1 y_t^{m_1})^{m_2/m_1} \quad 3.18$$

Either equation 3.17 or equation 3.18 can then be solved with equation 3.10 to route a flood hydrograph in terms of upstream discharge and downstream stage.

The values of  $a_2$  and  $m_2$  can be estimated from the cross-sectional geometry of the river, since prismatic storage can be expressed as

$$S_t = l A_t \quad 3.19$$

in which  $l$  is the length of the river reach and  $A_t$  is the cross-sectional area at time  $t$ . Equating equations 3.13 and 3.19 gives

$$A_t = \frac{a_2}{J} y_t^{m_2} \quad 3.20$$

Values for  $a_2$  and  $m_2$  can therefore be determined by fitting a power relationship to area and stage data obtained from a cross-section survey.

If the upstream discharge and downstream stage are known, then the routing procedure can be inverted to determine the parameters  $a_1$  and  $m_1$ , which define the downstream stage-discharge relationship. This can be achieved by finding the values of  $a_1$ ,  $m_1$ , and  $x$  which minimize the difference between the left and right hand sides of the nonlinear routing equation (the continuity equation (equation 3.10) with  $S_t$  defined by either of the weighted discharge relationships (equations 3.17 or 3.18) through a routed event.

### 3.3.3 Parameter Evaluation

The parameters to be evaluated appear on both sides of the nonlinear routing equation and the minimization requires an advanced parameter estimation technique. The unconstrained optimization method of Fletcher and Reeves (1964) for arbitrary differentiable functions is appropriate in this case and has been applied.

The objective function ( $E$ ) is defined as the sum of the squares of differences between the reach storage as calculated from the measured data (equation 3.12) and as estimated from either equation 3.17 or equation 3.18. This is minimized in terms of the variables  $a_1$ ,  $m_1$ , and  $x$  by applying the following steps (Tung, 1985; Minoux, 1986).

1. Select initial values for the decision variables, i.e.

$$z^k = (a_1^k; m_1^k; x^k) \quad 3.21$$

with  $k = 1$ .

2. Compute the gradient vector

$$g^k = \left[ \frac{\partial E}{\partial a_1^k}; \frac{\partial E}{\partial m_1^k}; \frac{\partial E}{\partial x^k} \right] \quad 3.22$$

and set the search direction vector  $d^k = -g^k$ .

3. Evaluate  $\gamma^k$  which minimizes the objective function

$$E(z^k + \gamma^k d^k) = E \left[ a_1^k - \gamma^k \frac{\partial E}{\partial a_1^k}; m_1^k - \gamma^k \frac{\partial E}{\partial m_1^k}; x^k - \gamma^k \frac{\partial E}{\partial x^k} \right] \quad 3.23$$

4. Compute the gradient vector  $g^k$  at the improved position, given by

$$z^{k+1} = z^k + \gamma^k d^k \quad 3.24$$

5. Redefine the search direction vector as

$$d^{k+1} = -g^{k+1} + \beta^k d^k, \beta^k = \frac{\|g^{k+1}\|^2}{\|g^k\|^2} \quad 3.25$$

6. Set  $k = k + 1$  and return to step 3 until convergence is achieved to the required tolerance.

This method reduces optimization in three dimensions to an iterative one-dimensional procedure. Due to the implicit nature of the derivative  $\frac{\partial E}{\partial \gamma}$ , the

Dichotomy method without derivatives (Minoux, 1986) is applied to numerically minimize the objective function in step 3 of the algorithm.

This procedure has been applied using equation 3.18 (Model 1) and equation 3.17 (Model 2) to define the weighted discharge estimate of storage.

### 3.3.3.1 Model 1

The objective function ( $E$ ) is defined as the sum of the squares of differences between the reach storage as calculated from the measured data (equation 3.12) and as estimated from equation 3.18, i.e.

$$E = \sum_{t=2}^{nt} \left[ \Delta t \sum_{i=2}^t T_i - \frac{a_1}{2} \Delta t \sum_{i=2}^t (y_i^{m_1} + y_{i-1}^{m_1}) + S_1 - \frac{a_2}{a_1^{m_2/m_1}} \left\{ x I_t + (1-x) a_1 y_t^{m_1} \right\}^{m_2/m_1} \right]^2 \quad 3.26$$

Time  $t=1$  is the when the flood flow first enters the reach and time  $t=nt$  is when the flood flow exits the reach.

The gradients of the objective function with respect to the calibration parameters  $a_1$ ,  $m_1$  and  $x$  are

$$\frac{\partial E}{\partial a_1} = \sum_{t=2}^{nt} \left\{ -2 E_t \left[ \frac{\Delta t}{2} \sum_{i=2}^t (y_i^{m_1} + y_{i-1}^{m_1}) + \frac{a_2 m_2}{a_1^{m_2/m_1} m_1} wQ_t^{(m_2 - m_1)/m_1} (1 - x) y_t^{m_1} - \frac{a_2 m_2}{a_1^{(m_1 + m_2)/m_1} m_1} wQ_t^{m_2/m_1} \right] \right\} \quad 3.27$$

$$\begin{aligned} \frac{\partial E}{\partial m_1} = \sum_{t=2}^{nt} \left\{ -2 E_t \left[ \frac{a_1 \Delta t}{2} \sum_{i=2}^t (y_{i-1}^{m_1} \ln y_{i-1} + y_i^{m_1} \ln y_i) - \frac{a_2 \ln a_1^{-m_2}}{a_1^{m_2/m_1} m_1^2} wQ_t^{m_2/m_1} \right. \right. \\ \left. \left. + \frac{a_2}{a_1^{m_2/m_1}} wQ_t^{m_2/m_1} \left\{ \frac{m_2}{m_1 wQ_t} (1 - x) a_1 y_t^{m_1} \ln y_t - \frac{m_2}{m_1^2} \ln wQ_t \right\} \right] \right\} \end{aligned} \quad 3.28$$

$$\frac{\partial E}{\partial x} = \sum_{t=2}^{nt} \left\{ -2 E_t \left[ \frac{a_2 m_2}{a_1^{m_2/m_1} m_1} wQ_t^{(m_2 - m_1)/m_1} (I_t - a_1 y_t^{m_1}) \right] \right\} \quad 3.29$$

where

$$wQ_t = x I_t + (1 - x) a_1 y_t^{m_1} \quad 3.30$$

and

$$E_t = \left\{ \sum_{i=2}^t [I_i - \frac{a_1}{2} \sum_{i=2}^t (y_i^{m_1} + y_{i-1}^{m_1})] \Delta t + S_1 - \frac{a_2}{a_1^{m_2/m_1}} wQ_t^{m_2/m_1} \right\}^2 \quad 3.31$$

are the weighted discharge estimate of  $S_t$  and objective function value at time  $t$  respectively.

### 3.3.3.2 Model 2

The objective function ( $E$ ) is defined as the sum of the squares of differences between the reach storage as calculated from the measured data (equation 3.12) and as estimated from equation 3.17, i.e.

$$\begin{aligned} E = \sum_{t=2}^{nt} \left[ \Delta t \sum_{i=2}^t I_i - \frac{a_1}{2} \Delta t \sum_{i=2}^t (y_i^{m_1} + y_{i-1}^{m_1}) + S_1 \right. \\ \left. - a_2 \left\{ x \left( \frac{I_t}{a_1} \right)^{m_2/m_1} + (1 - x) y_t^{m_1} \right\}^2 \right] \end{aligned} \quad 3.32$$

The gradients of the objective function with respect to the calibration parameters  $a_1$ ,  $m_1$ , and  $x$  are

$$\frac{\partial E}{\partial a_1} = \sum_{t=2}^{nt} \left\{ -2 E_t \left[ \frac{\Delta t}{2} \sum_{i=2}^t (y_i^{m_1} + y_{i-1}^{m_1}) - \frac{m_2 a_2}{m_1 a_1^{(m_2+m_1)/m_1}} I_t^{m_2/m_1} \right] \right\} \quad 3.33$$

$$\begin{aligned} \frac{\partial E}{\partial m_1} = \sum_{t=2}^{nt} \left\{ -2 E_t \left[ \frac{a_1 \Delta t}{2} \sum_{i=2}^t (y_{i-1}^{m_1} \ln y_{i-1} + y_i^{m_1} \ln y_i) \right. \right. \\ \left. \left. - \frac{a_2 m_2}{m_1^2} \left( \frac{I_t}{a_1} \right)^{m_2/m_1} \ln \left( \frac{I_t}{a_1} \right) \right] \right\} \end{aligned} \quad 3.34$$

$$\frac{\partial E}{\partial x} = \sum_{t=2}^{nt} \left\{ -2 E_t \left[ a_2 \left( \frac{I_t}{a_1} \right)^{m_2/m_1} - a_2 y_t^{m_1} \right] \right\} \quad 3.35$$

with

$$\begin{aligned} E_t = \left\{ \sum_{i=2}^t T_i \Delta t - \frac{a_1 \Delta t}{2} \sum_{i=2}^t (y_i^{m_1} + y_{i-1}^{m_1}) + S_1 \right. \\ \left. - a_2 \left[ x \left( \frac{I_t}{a_1} \right)^{m_2/m_1} + (1-x) y_t^{m_1} \right]^2 \right\} \end{aligned} \quad 3.36$$

### 3.3.3.3 Model 3

If steady flow is reestablished rapidly after a flood event the analysis can be simplified by considering only one time step which includes the passage of the entire flood event through the reach, i.e.  $\Delta t = t_f$  as shown in Fig.

3.12. The objective function for Model 1 can then be written as

$$\begin{aligned} E = \{ (I_1 - a_1 y_1^{m_1}) \Delta t + S_1 - \frac{a_2}{a_1^{m_2/m_1}} [x I_1 + (1-x) a_1 y_1^{m_1}]^{m_2/m_1} \}^2 \\ + \left\{ \left[ \sum_{t=2}^{nt} T_t - \frac{a_1}{2} \sum_{t=2}^{nt} (y_t^{m_1} + y_{t-1}^{m_1}) \right] \Delta t + S_1 \right. \\ \left. - \frac{a_2}{a_1^{m_2/m_1}} [x I_{nt} + (1-x) a_1 y_{nt}^{m_1}]^{m_2/m_1} \right\}^2 \end{aligned} \quad 3.37$$

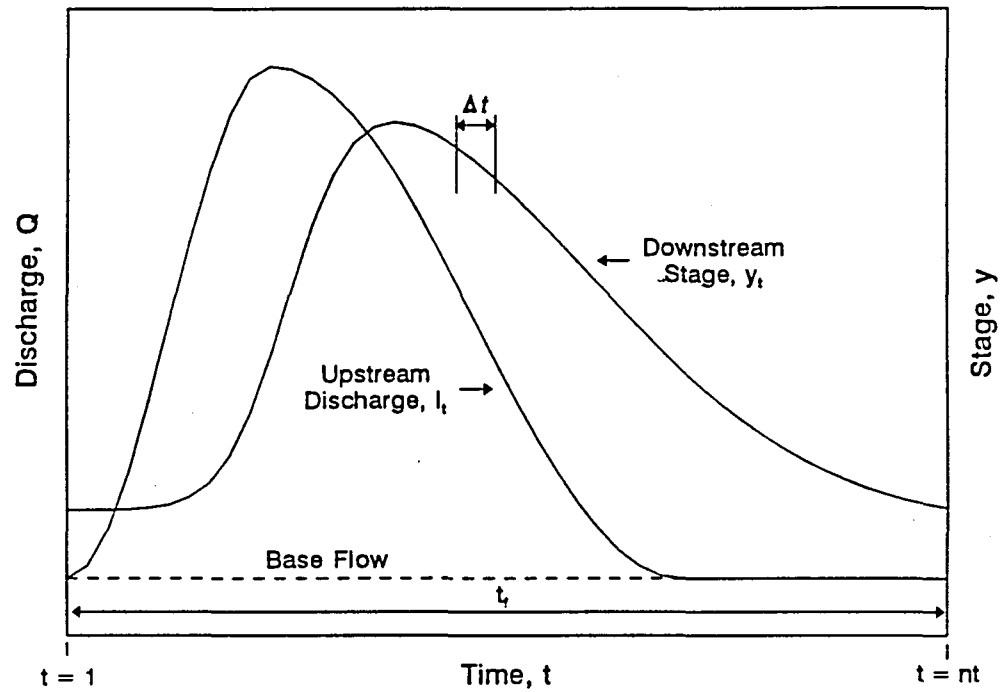


Figure 3.12 Upstream discharge and downstream stage hydrographs for a complete flood event.

This can be simplified by substituting the rating curve boundary conditions

$$I_1 = a_1 y_1^{m_1} \quad 3.38$$

and

$$I_{nt} = a_1 y_{nt}^{m_1} \quad 3.39$$

and the initial prism storage

$$S_1 = a_2 y_1^{m_2} \quad 3.40$$

to obtain

$$E = \left\{ \left[ \sum_{t=2}^{nt} T_t - \frac{a_1}{2} \sum_{t=2}^{nt} (y_t^{m_1} + y_{t-1}^{m_1}) \right] \Delta t - a_2 (y_{nt}^{m_2} - y_1^{m_2}) \right\}^2 \quad 3.41$$

If  $E$  is set to zero then equations 3.39 and 3.41 can be solved directly for the unknown  $a_1$  and  $m_1$ , and the optimization procedure is unnecessary. This is identical to equation 3.12, with  $S_t$  given by equation 3.13, which was derived directly from the continuity equation. As the entire flood

hydrograph is considered, lag and attenuation need not be accounted for and the Muskingum parameter  $x$  does not feature in this model.

Model 3 is simpler to apply than Models 1 and 2, but requires data for a full hydrograph between steady state conditions. In natural rivers the receding limb of the hydrograph reduces exponentially and effectively steady conditions are not reestablished for a long time. In such cases Models 1 and 2 are more applicable and can be applied to less than the full hydrograph.

### 3.3.4 Model Verification

The performances of the three models have been assessed by applying them to resynthesize a stage-discharge relationship from information generated by rigorous routing in a hypothetical situation.

Three flood events with different magnitudes and durations were routed along a prismatic rectangular channel section, using the explicit finite difference solution scheme for the unsteady flow equations proposed by Koutitas (1983) and presented by Chadwick and Morfett (1993). Each flood event was defined by a complex sinusoidal discharge hydrograph specified at the upstream end of the reach (as shown in Fig. 3.13, for example), and Manning's equation was specified as the downstream boundary condition. The channel characteristics, hydraulic data for each event, and the finite-difference routing parameters used in the unsteady flow computations are listed in Table 3.7 ( $Q_p$ ,  $Q_b$ ,  $t_p$ , and  $t_b$  are defined in Fig. 3.13).

The outflow stage hydrograph for each of the events defined in Table 3.7 was determined by applying the finite difference model (results are shown in Fig. 3.13 for Event 1). The inflow discharge hydrograph and the routed outflow stage hydrograph were then used to synthesize the downstream rating curve by applying the parameter estimation techniques described above. The optimized rating curve parameters obtained for each of the events using each of the parameter estimation models are presented in Table 3.8, as well as the implied values of Manning's  $n$ . Also presented in Table 3.8 are the parameter values corresponding to Manning's equation, expressed in the form of equation 3.8.

Figure 3.14 illustrates the optimization procedure of Model 1 applied to Event 1. The weighted discharge estimate of storage defined by equation 3.31 is plotted against the data-based estimate defined by equation 3.17. The curve indicates equality of these estimates and the points are plotted using the optimal parameters which minimize deviation from the curve over the whole range of the data, in accordance with the objective function defined by equation 3.27.



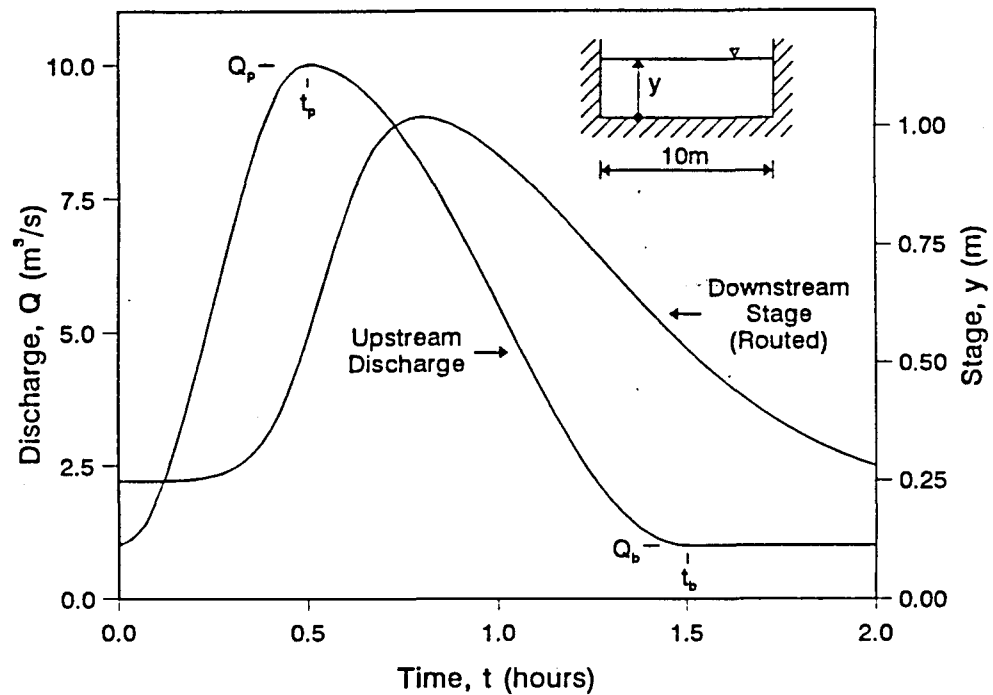


Figure 3.13 Upstream discharge hydrograph and routed downstream stage hydrograph for Event 1 in rectangular channel.

Table 3.7 Data for unsteady flow computations in rectangular channel

Channel Characteristics			
Width = 10 m			
Reach length = 1250 m			
Gradient = 0.001			
Manning's $n$ = 0.030			
Hydraulic Data			
	Event 1	Event 2	Event 3
$Q_p$ (m³/s)	10	50	100
$Q_b$ (m³/s)	1	5	10
$t_p$ (hr)	0.5	1.5	0.5
$t_b$ (hr)	1.5	3.0	1.5
Finite Difference Routing Parameters			
$\Delta x$ = 250 m			
$\Delta t$ = 20 s			

**Table 3.8** Optimized rating curve parameters for rectangular channel

Optimized Rating Curve Parameters									
	Event 1			Event 2			Event 3		
	Model 1	Model 2	Model 3	Model 1	Model 2	Model 3	Model 1	Model 2	Model 3
$a_1$	8.636	8.751	9.397	9.313	9.260	9.153	9.821	9.702	9.370
$m_1$	1.356	1.385	1.608	1.501	1.508	1.524	1.430	1.440	1.468
$x$	0.278	0.314	-	0.286	0.317	-	0.195	0.220	-
$n$	0.031	0.031	0.030	0.030	0.030	0.030	0.030	0.030	0.030
Parameters Derived from Manning's Equation ( $n = 0.030$ )									
$a_1$	9.477			9.293			9.653		
$m_1$	1.619			1.512			1.449		

**Table 3.9** Errors in parameter estimation

Error (%)									
	Event 1			Event 2			Event 3		
	Model 1	Model 2	Model 3	Model 1	Model 2	Model 3	Model 1	Model 2	Model 3
$a_1$	-8.87	-7.66	-0.84	-0.22	-0.36	-1.51	1.74	0.51	-2.93
$m_1$	-16.24	-14.45	-0.68	-0.73	-0.26	0.79	-1.31	-0.62	1.31

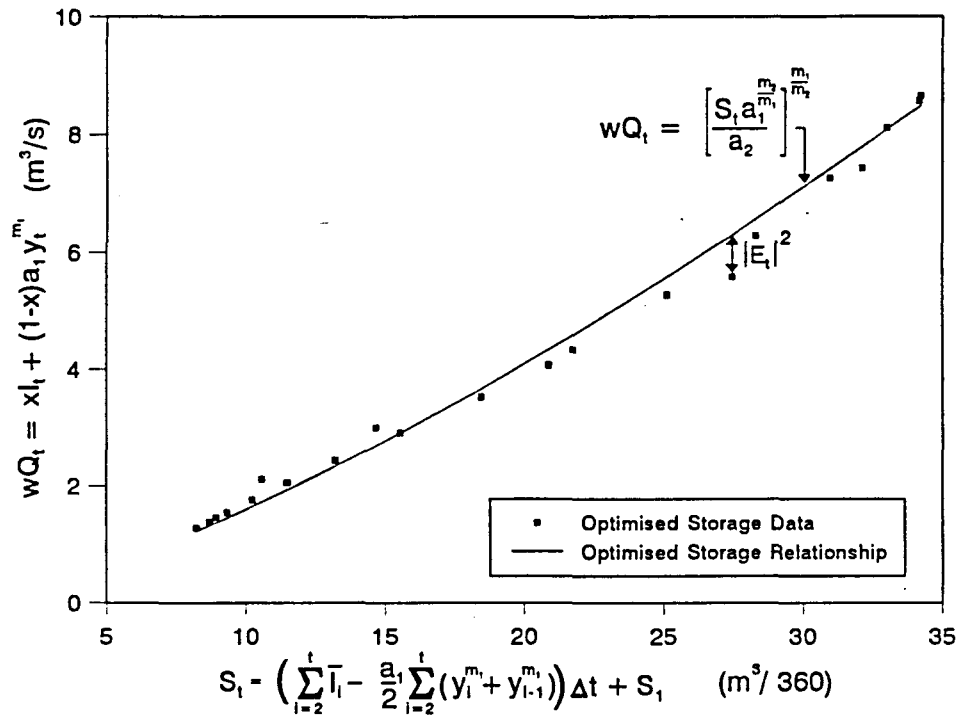


Figure 3.14 Model 1 optimised storage data for Event 1 in rectangular channel.

The predicted values of Manning's  $n$ , obtained by fitting the synthesized rating curves to Manning's equation, agree closely with the specified value in all cases. The errors in prediction of  $a_t$ , and  $m_t$ , relative to the values implied by the specified Manning's equation are summarized in Table 3.9. This shows that the performances of Models 1 and 2 in predicting values of  $a_t$ , and  $m_t$ , are almost identical. Model 3 performed better than the others for Event 1, but slightly worse for Events 2 and 3.

The synthesized rating curves, using the Model 1 parameters, are plotted in Fig. 3.15 together with Manning's rating curve for uniform flow. The synthesized rating curve for the range of flows in each event compares well with the Manning curve. The rating curve produced using Event 1 has been extrapolated beyond the peak discharge of 10 m<sup>3</sup>/s to demonstrate the uncertainty in predictions of the synthesized rating curves beyond the range of the data used in the analysis. The underprediction of discharge increases with rising stage to approximately 20% at 100 m<sup>3</sup>/s. Considering that the extrapolation is over an order of magnitude this predictive error is not unacceptable, however.

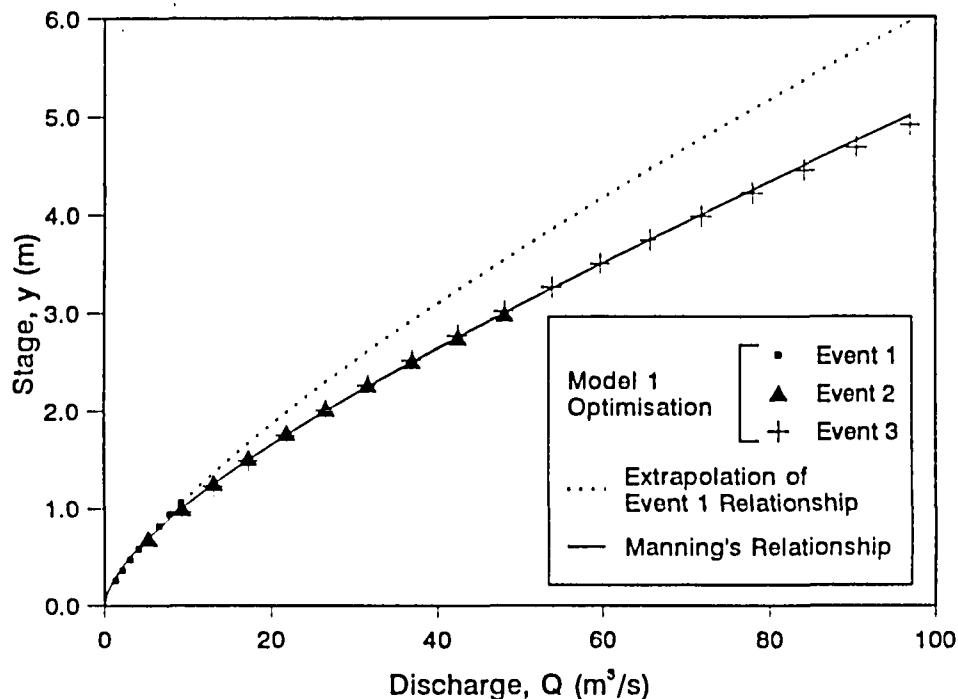
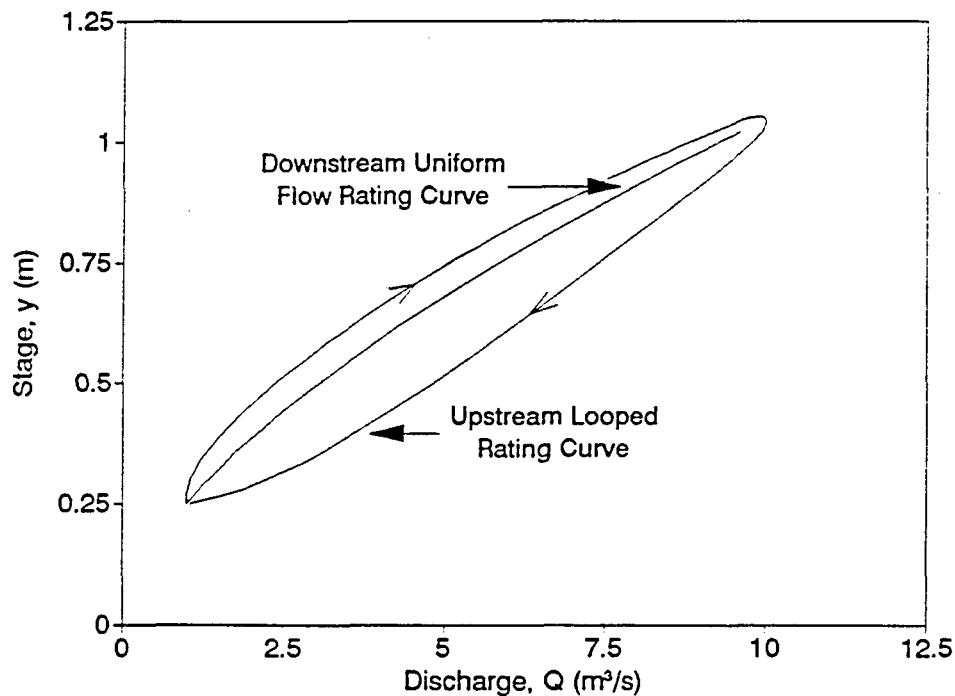


Figure 3.15 Model 1 synthesized rating curves for three flood events in rectangular channel compared with Manning's uniform flow relationship.

The synthesized rating curves approximate the uniform flow rating curve, since the assumed rating function (equation 3.8) is independent of the energy gradient. Under unsteady flow conditions rating curves are actually looped, as a consequence of the difference in energy gradient for corresponding stages on the rising and falling limbs of a hydrograph. Figure 3.16 shows the upstream and downstream rating curves for Event 1, produced by the explicit solution of the unsteady flow equations. The upstream rating curve shows significant hysteresis introduced by unsteady flow conditions, whilst the downstream curve is Manning's uniform flow relationship, specified as a boundary condition.

### 3.3.5 Model Application

The three parameter estimation models have been applied to synthesize the uniform flow rating curve for a site on the Sabie River in the Kruger National Park, South Africa. Stage and phreatic surface levels in the river bank are being monitored continuously at hourly intervals at this site as part of a study of the surface-subsurface water interactions (Birkhead *et al.*, 1995). The site is located 4.6 km downstream of a gauging weir, from which a continuous record of discharge rate is available.



**Figure 3.16** Rating curves produced by Koutitas (1983) model for rectangular channel.

The flood event shown in Fig. 3.17 was selected from the record for the analysis. The necessary channel characteristics and hydraulic information are summarized in Table 3.10. The values of  $a_2$  and  $m_2$  were determined by fitting equation 3.20 to the channel cross section within the range of flow depths recorded. The site is situated directly upstream of a bedrock outcrop which retains water at zero flow and this level has therefore been used as the stage datum rather than the alluvial channel bed, as shown in Fig. 3.17 (inset). The value of  $m_2$  is close to unity, suggesting an approximately rectangular active channel for the range of flow depths considered, which was corroborated by field observations. Aerial photographs indicate an average active channel width over the length of the reach of 23 m. The calibration of the channel storage relationship (equation 3.20) using the downstream site morphology therefore gives parameter values that are representative of the reach for the selected flow event.

The optimized rating parameters for each of the three models are given in Table 3.11 (neglecting bank storage), and the relationship between the two estimates of storage produced by Model 1 is plotted in Fig. 3.18a. The wide discrepancy from the curve indicating equality of the estimates shows that the final value of the objective function is far from zero, which implies that the model is not representing the reach storage correctly. The

optimized values of  $x$  produced by Models 1 and 2 support this :  $x$  is generally expected to be between 0 and 0.5 (e.g. Tung, 1985).

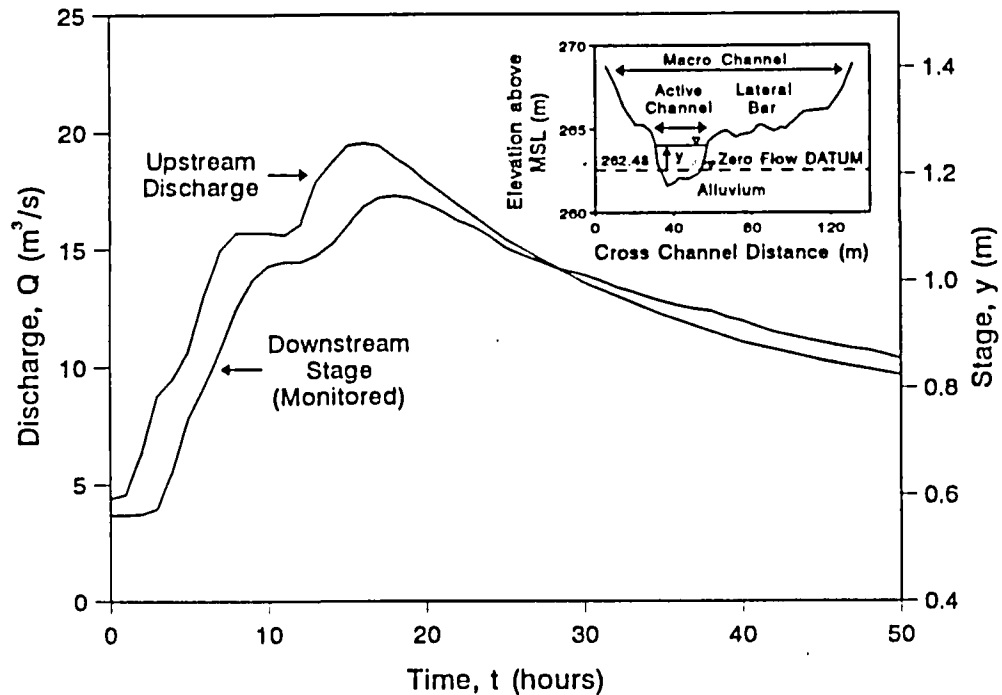


Figure 3.17 Monitored discharge and stage hydrographs at the upstream gauging weir and downstream site on the Sabie River.

Table 3.10 Channel and hydraulic characteristics for the Sabie River analysis

Channel Characteristics
$a_2/l = 22.66$ $m_2 = 1.021$ $l = 4600 \text{ m}$
Hydraulic Data
$Q = 4.39 \text{ to } 19.51 \text{ m}^3/\text{s}$ $\Delta t = 3600 \text{ s}$

The results of Model 3 also indicate incorrect representation of reach storage. In this application the portion of the hydrograph up to  $t = 50$  hours was used (Fig. 3.17), at which time flow was assumed to be steady. The storage relationship for this analysis is shown in Fig. 3.18b. The close

agreement at the end point indicates the exact solution at this time. However, the wide discrepancy for all points between the beginning and end of the event illustrates that the model takes no account of intermediate prismatic channel storage.

**Table 3.11** Optimised rating coefficients for the Sabie River site.

	Model 1	Model 2	Model 3
<b>Neglecting Bank Storage (<math>a_2/l = 22.66</math>)</b>			
$a_1$	14.551	14.541	14.206
$m_1$	1.713	1.711	2.043
$x$	1.699	1.517	-
<b>Including Bank Storage</b>			
$a_2^*/l$	51.0	50.9	53.0
$a_1$	13.983	13.983	13.972
$m_1$	2.274	2.278	2.013
$x$	0.262	0.297	-

It is clear from these results that representation of the reach storage by equation 3.13 or estimation of its parameters through equation 3.20 is unreliable in this case, i.e. the reach storage cannot be related simply to the channel geometry. A potentially significant component of storage that would be neglected by this treatment is that within the channel banks. The Sabie River is a mixed bedrock-alluvial channel system (van Niekerk and Heritage, 1994), with fluvial deposits within a bedrock macro-channel (Fig. 3.17 inset). A significant proportion of the fluvial deposits consists of coarse-grained material (medium sands to fine gravels), which have high hydraulic conductivities. Phreatic level monitoring in the river bank has confirmed very rapid response of bank storage to channel flow variations (Birkhead *et al.*, 1995). Bank storage in the alluvium adjacent to the active channel must therefore contribute significantly to reach storage, and should be accounted for. There is therefore justification for adding bank storage to equation 3.13, i.e.

$$S_t = a_2 y_t^{m_1} + \text{Bank Storage}_t \quad 3.42$$

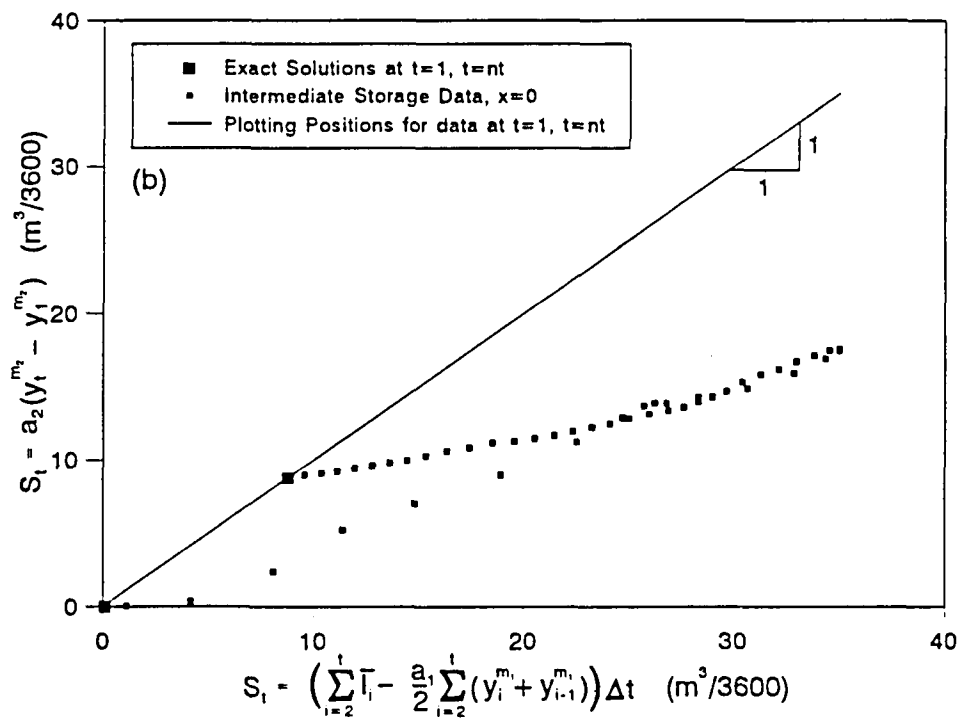
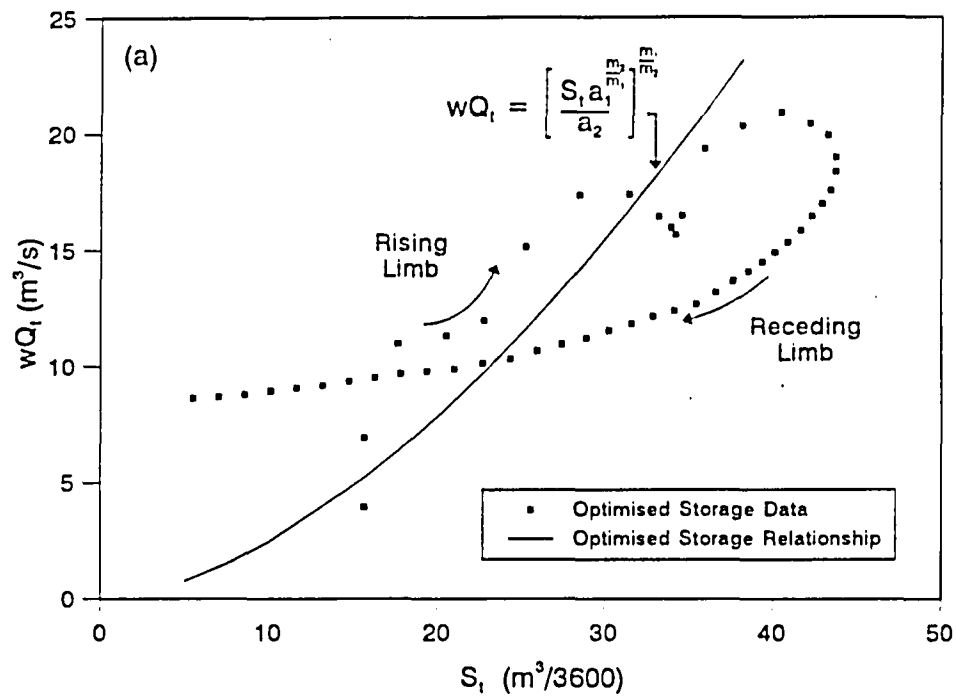


**Figure 3.18** Optimised storage data plotted using the coefficients produced by applying Model 1 (a) and Model 2 (b) to the Sabie River flood data.



Assuming instantaneous response of bank storage to changes in river stage, the reach storage can be approximated by

$$S_t = (a_2 + a_3 / \eta) y_t^{m_2} = a_2^* y_t^{m_2} \quad 3.43$$

where  $a_3$  is the average width of alluvium in the macro-channel, for an approximately rectangular change in the area of saturated alluvium (i.e.  $m_2 \approx 1.021 \approx 1$ ), and  $\eta$  is the porosity of the bank material.

The validity of treating the bank storage cross-sectional area as rectangular can be confirmed by comparing bank storage volumes determined by using this assumption with actual volumes obtained by integration of the monitored phreatic surface at the study site. The variations of actual and estimated volumes (using a measured porosity value of 0.25) during the recorded event (Fig. 3.17) are compared in Fig. 3.19. The correspondence between the two variations is acceptable overall and good during recession of the flood. The accuracy of the approximation for a particular system will depend on the width of alluvium constituting the banks, the pattern of sediment deposition (as lateral or mid channel bars), local hydraulic conductivity, and the rate of rise and fall of river stage.

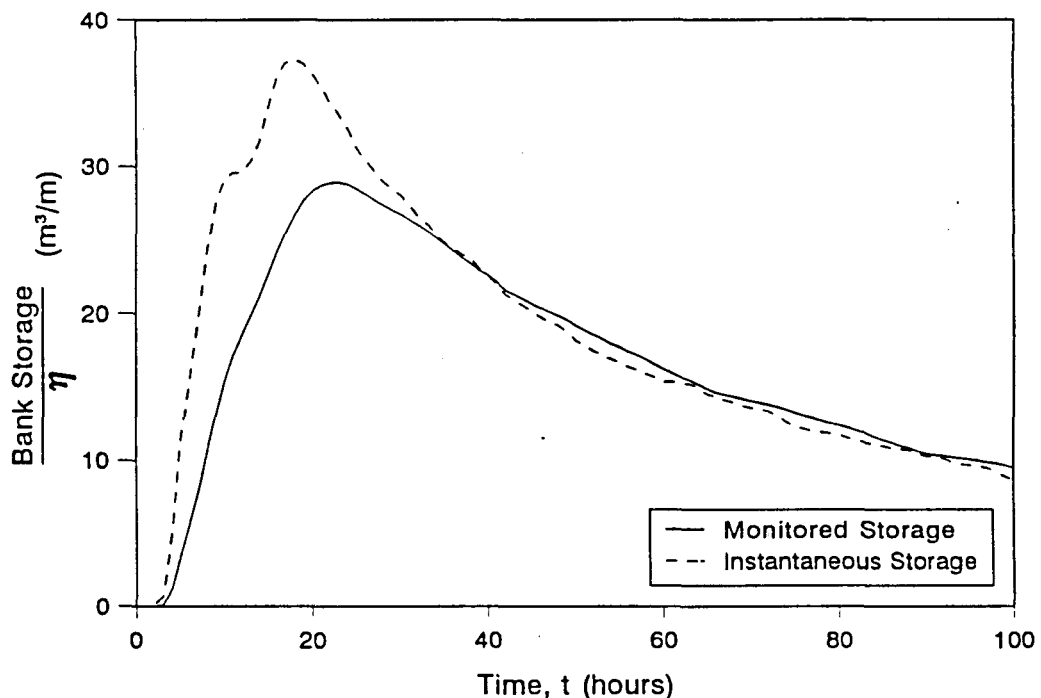


Figure 3.19 Monitored and estimated bank storage variations at the Sabie River site during the flood event analyzed.

The parameter estimation procedures were repeated using the modified storage function (equation 3.43), and treating the coefficient  $a_2^*$  in the reach storage relationship (equation 3.43) as an additional unknown. The revised results are given in the lower part of Table 3.11. The new relationship between the two estimates of storage (Fig. 3.20) confirms that the storage description is now realistic.

From an analysis of scale 1:10 000 aerial photographs, the average width of the macro-channel over the reach is 146 m. The measured sediment porosity at the downstream site is 0.25. The effective bank storage width

$(a_3\eta)$  is therefore 30.8 m, and the effective reach storage width  $\frac{a_2^*}{I}$  is 53.5 m, which agrees closely with the optimised values in Table 3.11 (51.0, 50.9 and 53.0 for Models 1, 2 and 3, respectively).

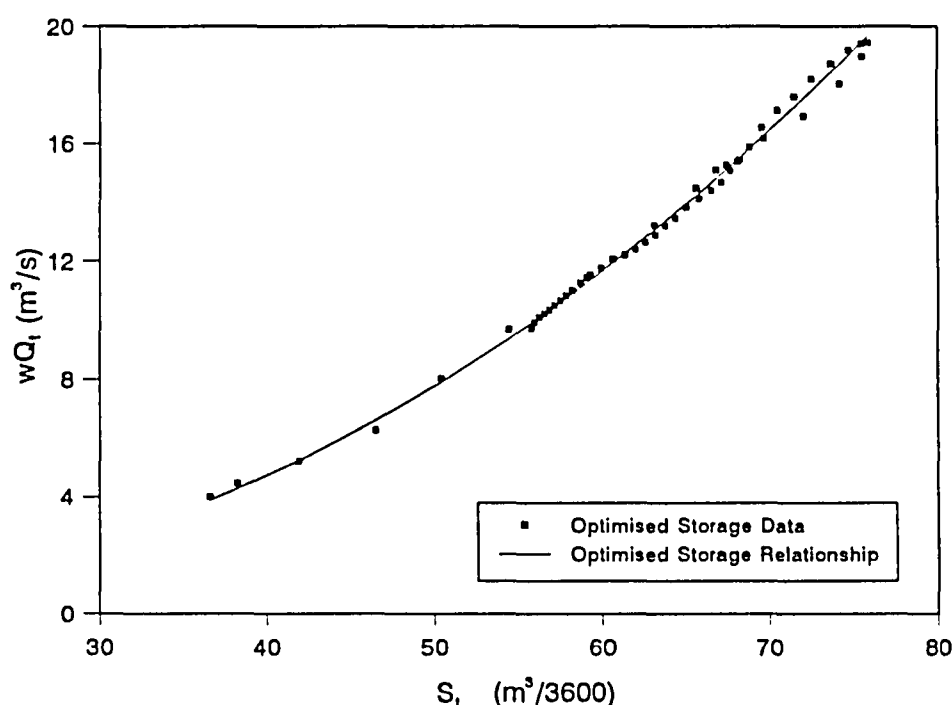
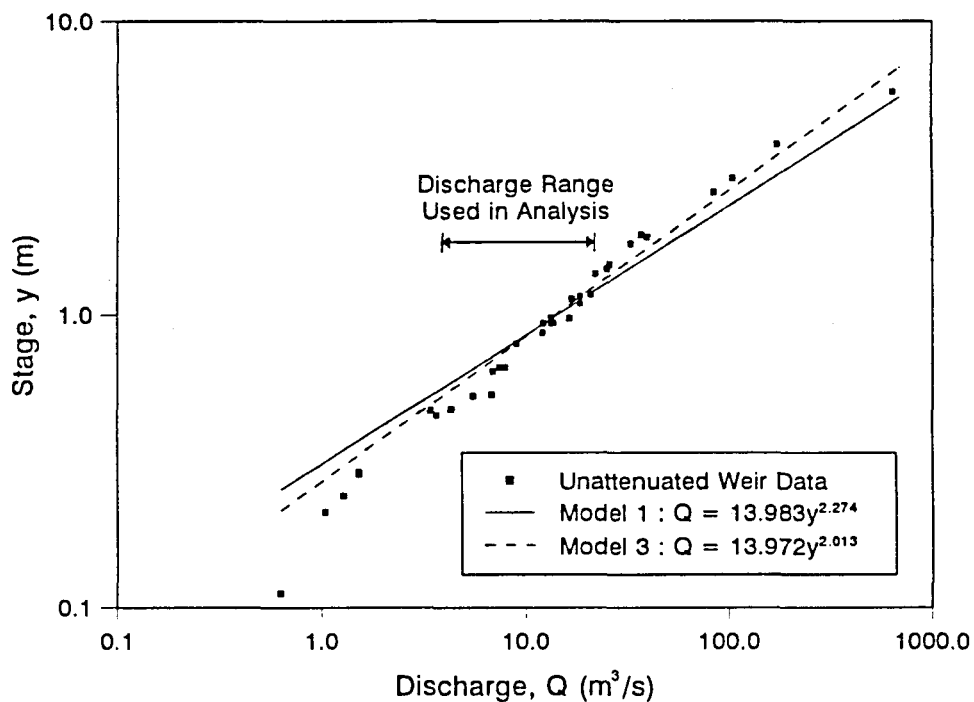


Figure 3.20 Optimised storage data plotted using the coefficients produced by applying Model 1 to the Sabie River flood data, including bank storage dynamics.

The synthesized (Model 1) rating curve for the downstream site on the Sabie River is presented in Fig. 3.21. Local discharges have not been gauged at this site, and so no direct assessment of the results is possible. However, values of local stage and corresponding (unattenuated) weir discharge measured during the period 1993 to 1995 have also been plotted

on Fig. 3.21 to give an indication of the validity of the synthesized rating curve. These points represent peak values or other clearly identifiable points on the hydrograph that can be correlated between the two stations. Using such data to define the rating curve does not account for attenuation and requires protracted field work. The synthesized curve is derived from continuous monitoring at both stations for a single event, and is therefore much more data efficient. The close agreement between the data and the synthesized curve over the range of discharges used in the analysis indicates that attenuation is not significant in this case, although it would undoubtedly be so in others. The apparent overestimation of discharge by the extrapolated curve indicates that the relationship changes with stage, and could also reflect greater attenuation of larger peaks. The event used for analysis should therefore be as large as possible, and caution exercised in extrapolation of the results.



**Figure 3.21** Comparison of the synthesized rating curve and unrouted flow data, for the Sabie River site.

## CHAPTER 4

### MODELLING BANK STORAGE DYNAMICS

---

#### 4.1 Model Development

##### 4.1.1 Groundwater Flow in the Saturated Zone

##### 4.1.1.1 Flow Equations

A relationship for flow rate through porous media is given by Darcy's law, which may be stated in the form (Cernica, 1982)

$$Q = KiA \quad 4.1$$

where

$Q$  is the discharge rate ( $\text{m}^3/\text{s}$ )

$K$  is the saturated hydraulic conductivity ( $\text{m/s}$ )

$A$  is the cross-sectional flow area normal to the flow direction ( $\text{m}^2$ )

$i$  is the hydraulic gradient normal to the direction of flow

Darcy's law accounts for mass (gravitational) forces and surface (pressure) forces to overcome viscous resistance within the medium, but neglects inertial forces (Zarandy, 1993). The relationship also ignores the internal structure of the soil skeleton, and assumes an evenly distributed flow within a homogeneous medium.

The conditions under which Darcy's law is applicable are discussed by Zarandy (1993). Zarandy contends that for the majority of soil types, Darcy's linear relationship is valid. For coarse materials and in the vicinity of point sources the application of equation 4.1 may lead to significant errors if the hydraulic gradient is sufficiently high to induce turbulent flow. The hydraulic gradients in natural systems are generally sufficiently low to allow inertial forces to be neglected, and Darcy's linear law may consequently be applied in the practical solution of the majority of groundwater flow problems, without significant errors (Bear and Verruijt, 1992; Zarandy, 1993). Darcy's law is a special case of the more general non-linear Navier-Stokes equations. Numerous simplified non-linear flow rate relationships for groundwater systems with high hydraulic gradients have been proposed. There is, however, no universally accepted simplified non-linear motion equation (Bear and Verruijt, 1992).

The specific discharge,  $q_s$  ( $\text{m/s}$ ), is defined as

$$q_s = Ki = \frac{Q}{A} \quad 4.2$$

Flow takes place through only the part of the cross-sectional area occupied by void spaces. The portion of the total area available to flow is  $\eta A$ , where

$\eta$  is the volumetric porosity of the medium. It can be shown that the average areal porosity is equal to the volumetric porosity (Bear and Verruijt, 1992). The volumetric porosity is given by

$$\eta = \frac{V_v}{V} \quad 4.3$$

where

$V_v$  is the volume of the voids ( $\text{m}^3$ )

$V$  is the total volume occupied by the medium ( $\text{m}^3$ )

The average flow velocity,  $v$  (m/s) through the medium is then given by

$$v = \frac{Q}{\eta A} = \frac{q_s}{\eta} \quad 4.4$$

The hydraulic conductivity,  $K$ , is a function of fluid and porous medium properties according to the relationship (Bear and Verruijt, 1992)

$$K = k \frac{\rho g}{\mu} = k \frac{g}{v} \quad 4.5$$

where

$k$  is the matrix intrinsic permeability ( $\text{m}^2$ )

$\rho$  is the fluid density ( $\text{kg}/\text{m}^3$ )

$g$  is the gravitational acceleration ( $\text{m}/\text{s}^2$ )

$\mu$  is the fluid absolute viscosity ( $\text{kg}/\text{m.s}$ )

$v$  is the fluid kinematic viscosity ( $\text{kg.s}/\text{m}^2$ )

The intrinsic permeability is dependent only on the properties of the solid matrix, and may be related to physical soil characteristics such as grain-size composition (e.g. Vuković and Soro, 1992).

The hydraulic gradient,  $i$ , in equation 4.1 results from a differential groundwater potential across an element within the medium. If  $\Delta h$  represents the total reduction in potential of the fluid over a distance  $\Delta s$ , then, in the limit (Rushton and Redshaw, 1979)

$$i = -\frac{\partial h}{\partial s} \quad 4.6$$

The negative sign in equation 4.6 signifies that flow takes place in the direction of decreasing potential. The groundwater potential represents an average potential of the fluid over a representative elementary volume of the medium, as defined by Bear and Verruijt (1992) in the continuum approach to flow through porous media. The groundwater potential at any point in the fluid is the sum of the kinetic, pressure and elevation components, given by

$$h = \frac{v^2}{2g} + \frac{p}{\rho g} + z \quad 4.7$$

where

$p$  is the pressure intensity (kg/m.s<sup>2</sup>)

$z$  is the elevation potential (m)

The term representing the kinetic potential in equation 4.7 has been found to be less significant than the groundwater potential (Bear and Verruijt, 1992), and is generally neglected in seepage studies. If the fluid density remains constant, then groundwater potential may replace pressure intensity in equation 4.7. This is a good approximation for shallow flow systems where the compressibility of water is negligible.

The general three-dimensional mass balance (or continuity) equation describing flow through a saturated porous medium under unsteady conditions is given by (Bear and Verruijt, 1992; Rushton and Redshaw, 1979)

$$\frac{\partial}{\partial x}(K_x \frac{\partial h}{\partial x}) + \frac{\partial}{\partial y}(K_y \frac{\partial h}{\partial y}) + \frac{\partial}{\partial z}(K_z \frac{\partial h}{\partial z}) = S_s \frac{\partial h}{\partial t} + q_v \quad 4.8$$

where

$x$ ,  $y$ , and  $z$  are the three orthogonal directions (m)

$K_x$ ,  $K_y$ , and  $K_z$  are the hydraulic conductivities in the  $x$ ,  $y$ , and  $z$  directions respectively (m/s)

$S_s$  is the specific storativity (m<sup>-1</sup>)

$t$  is time (s)

$q_v$  is the extraction rate per unit volume of soil (s<sup>-1</sup>)

The orientation of axes within the bank adjacent to a river channel, are illustrated in Fig. 4.1. The lateral (transverse), longitudinal, and vertical directions are represented by the  $x$ ,  $y$ , and  $z$  cartesian ordinate systems, respectively.

A change in the groundwater potential results in a change in pressure due to the compressibility of water and the change in pore volume arising from the compressibility of the soil skeleton. The volume of water released or taken into elastic storage per unit volume of soil per unit change in potential, is termed the specific storativity,  $S_s$ . The specific storativity applies uniformly throughout the saturated zone. The sink or source function,  $q_v$ , in equation 4.8 accounts for water extracted from or recharged to the groundwater system. This external flux may vary spatially and temporally, and represents water extracted by plant roots in a natural riparian system in the absence of artificial extractions or recharge.

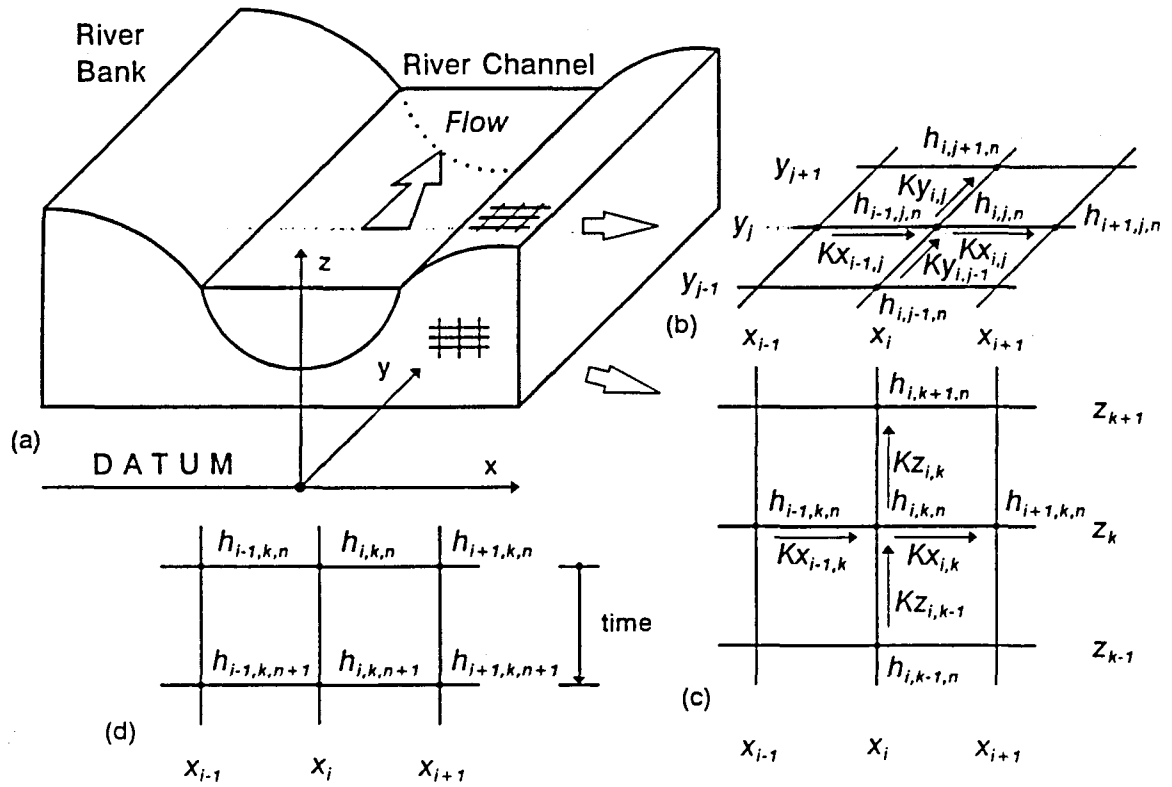


**Figure 4.1** Convention for the numbering and position of nodes: (a) Orientation of axes within the river bank; (b) space mesh  $(y, z)$ ; (c) space mesh  $(x, z)$ ; (d) space-time mesh  $(x, t)$ .

#### 4.1.1.2 Two-dimensional Vertical Flow Model

##### 4.1.1.2.1 Mass Balance Equation

The mass balance equation for two-dimensional transient flow through a vertical cross-section of unit width is obtained by substituting  $\partial h / \partial y = 0$  in equation 4.8, yielding

$$\frac{\partial}{\partial x} (K_x \frac{\partial h}{\partial x}) + \frac{\partial}{\partial z} (K_z \frac{\partial h}{\partial z}) = S_s \frac{\partial h}{\partial t} + q_v \quad 4.9$$

##### 4.1.1.2.2 Boundary Conditions

The mass balance equation describes mathematically the flow through the medium, but contains no information relating to the specific system or the shape of the flow domain. Supplementary information in the form of

boundary conditions is required to express the way in which the flow domain interacts with its adjacent environment. In the model, boundary conditions are mathematical expressions of the physical conditions imposed by the external side of the boundary on the flow domain. Boundaries to the saturated zone may include impervious (e.g. bedrock), semi-pervious and pervious boundaries (e.g. contact with free water body), and a phreatic surface.

The boundaries encompassing the saturated domain in the riparian zone are illustrated in Fig. 4.2. An impervious interface is stipulated as the lower boundary, physically representing the bedrock topography at the study site (refer to Chapter 2: Data Collection). The condition that applies at the lower boundary is that no flow may occur normal to the bedrock surface. Expressed mathematically,  $\partial h / \partial n = 0$ , where  $n$  is the direction normal to the boundary. This condition is modelled by setting the hydraulic conductivities on the external side of the boundary to zero, ie.  $K_x = K_z = 0$ .

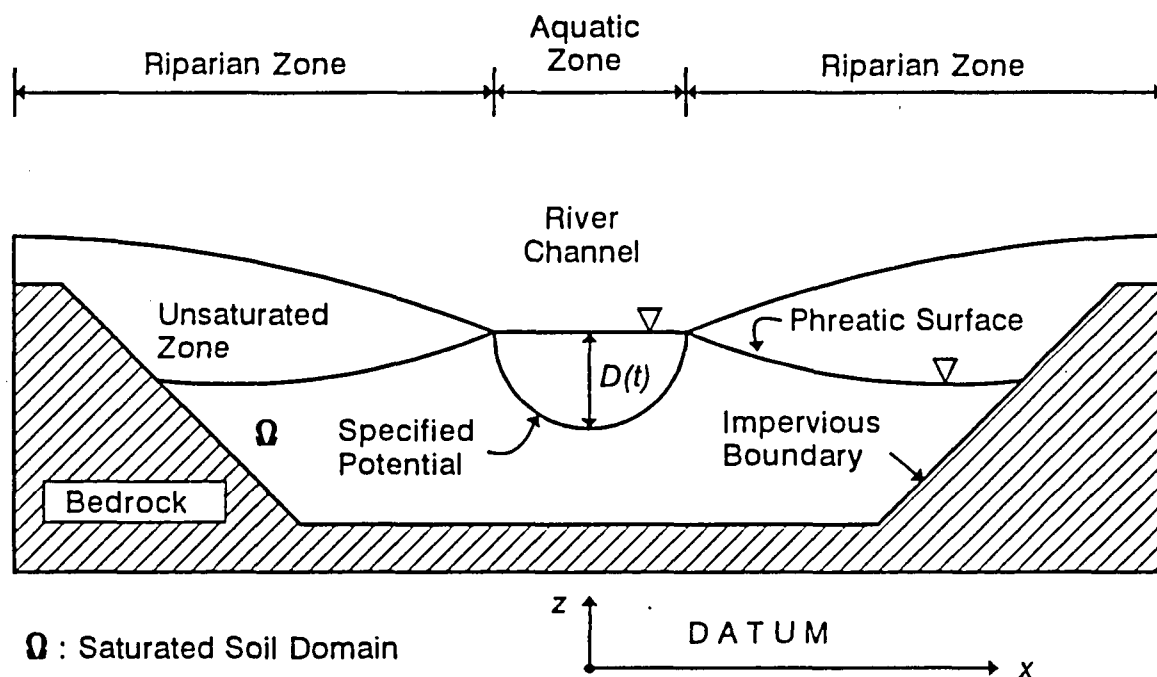


**Figure 4.2** Flow boundaries encompassing the saturated and unsaturated flow domains in the x-z plane.

A constant or variable potential or a flux may be expressed along the contact of a saturated domain with a body of water. Constant water potentials imply that there is an unlimited supply of water upon which the system may draw, such as a lake. The perimeter of the river channel is



represented by a variable potential, since changes in river discharge result in stage fluctuations. This boundary condition is expressed as  $h = D(t)$ , where  $D(t)$  is the temporal river stage.

Groundwater flows will continuously adjust to changing boundary conditions (river stage fluctuations, capillary rise or percolation from the unsaturated zone, and plant root extractions), resulting in a transient phreatic surface profile. The mass balance equation (equation 4.9) is modified for the phreatic surface to account for unsteady boundary behaviour.

The following formulation for the mass balance equation directly below the phreatic surface is based on the derivation by Rushton and Redshaw (1979) for steady-state flow. The analysis is extended to include transient conditions, the extraction of soil-water, and a moving phreatic surface.

Consider three-dimensional transient flow through an element of soil of dimensions  $dx$ ,  $dy$  and  $dz$ , directly below a moving phreatic surface (Fig. 4.3). Assuming that the soil matrix constituting the elementary volume is incompressible, the conservation of mass requires that the total flow entering the element equals the flow leaving the element plus the increase in the rate of volumetric water storage.

At the centroid of the element  $C(x = y = z = 0)$ , the specific discharges are  $q_{sx}$ ,  $q_{sy}$  and  $q_{sz}$  in the  $x$ ,  $y$  and  $z$  directions respectively. Therefore, on the plane  $x = -0.5dx$ , the velocity in the  $x$ -direction is

$$q_{sx} - \frac{\partial q_{sx}}{\partial x} \frac{dx}{2} \quad 4.10$$

The flow entering the element across this plane is given by

$$(q_{sx} - \frac{\partial q_{sx}}{\partial x} \frac{dx}{2}) dy dz \quad 4.11$$

Similarly, the flow leaving the element across the plane  $x = 0.5dx$  is given by

$$(q_{sx} + \frac{\partial q_{sx}}{\partial x} \frac{dx}{2}) dy dz \quad 4.12$$

Similar expressions hold for the flows in the  $y$  and  $z$  directions and the net flow out of the element is therefore given by

$$(\frac{\partial q_{sx}}{\partial x} + \frac{\partial q_{sy}}{\partial y} + \frac{\partial q_{sz}}{\partial z}) dx dy dz \quad 4.13$$

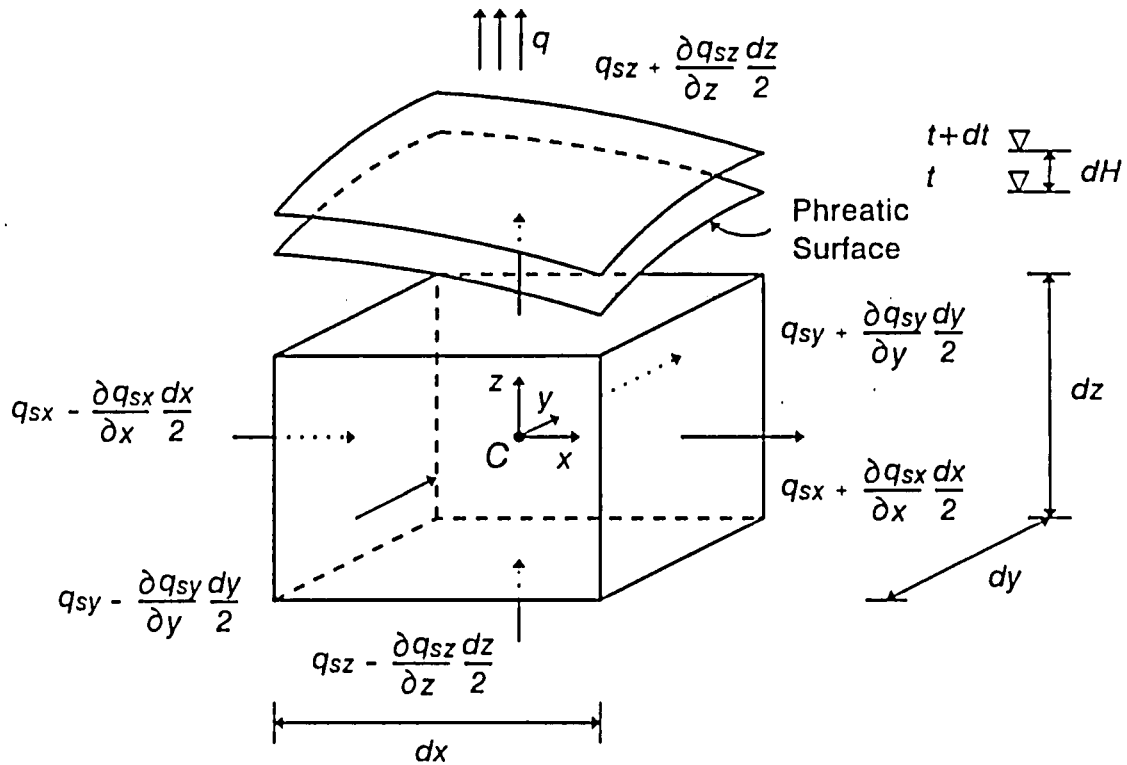


Figure 4.3 Flow through an elementary volume directly below the phreatic surface.

Over a discrete time interval  $dt$ , the element experiences an outflow (extraction) per unit volume,  $q_v$  (Fig. 4.3). The volumetric rate of extraction is given by

$$q_v dx dy dz \quad 4.14$$

In addition to the extractions to support transpiration losses and saturated-unsaturated flow interaction, a rise in the phreatic surface by  $dH$  results in a sink as water is taken up by elastic and void storage within voids of the soil matrix. The void storage is assumed to apply to a dimensionally fixed volume directly below the phreatic surface, whereas the elastic storage applies uniformly throughout the depth of saturation (equation 4.8).

The partially saturated flow concept of specific yield accounts for water taken up by or released from void storage, resulting from the filling or draining of void spaces, respectively. The specific yield is defined as the volume of water released per unit plan area from storage due to a unit fall in the elevation of the phreatic surface.

The rate at which water is taken into elastic and void storage over the time interval  $dt$ , due to a rise in the phreatic surface is given by

$$S_s \frac{\partial h}{\partial t} dx dy dz + S_v \frac{\partial H}{\partial t} dx dy \quad 4.15$$

where

$S_v$  is the specific yield

$dH$  is the vertical displacement of the phreatic surface over the time interval  $dt$  (m)

The change in groundwater potential at the centroid of the elementary volume is assumed to be approximately equal to the vertical displacement of the phreatic surface. The displacement of the phreatic surface,  $dH$ , in equation 4.15 may consequently be replaced by the change in groundwater potential at the centroid of the volume,  $dh$ .

By the conservation of mass (or mass balance), the net flow rate out of the element must equal the decrease in the rate of volumetric storage, yielding

$$\left( \frac{\partial q_{sx}}{\partial x} + \frac{\partial q_{sy}}{\partial y} + \frac{\partial q_{sz}}{\partial z} \right) dx dy dz = S_s \frac{\partial h}{\partial t} dx dy dz + S_v \frac{\partial h}{\partial t} dx dy + q_v dx dy dz \quad 4.16$$

The components of the specific discharge,  $q_s$ , are given by Darcy's law (equation 4.1) as

$$\begin{aligned} q_{sx} &= -K_x \frac{\partial h}{\partial x} \\ q_{sy} &= -K_y \frac{\partial h}{\partial y} \\ q_{sz} &= -K_z \frac{\partial h}{\partial z} \end{aligned} \quad 4.17$$

Differentiating each of the equations in 4.17 with respect to  $x$ ,  $y$  and  $z$  respectively, and substituting in equation 4.16 gives the mass balance equation for an element of fluid directly below a transient phreatic surface

$$\frac{\partial}{\partial x} (K_x \frac{\partial h}{\partial x}) + \frac{\partial}{\partial y} (K_y \frac{\partial h}{\partial y}) + \frac{\partial}{\partial z} (K_z \frac{\partial h}{\partial z}) = S_s \frac{\partial h}{\partial t} + \frac{S_v}{dz} \frac{\partial h}{\partial t} + q_v \quad 4.18$$

It is convenient to express the extraction term,  $q_v$ , as an outflow per unit plan area, physically representing transpiration losses, capillarity or percolation. For two-dimensional vertical flow, equation 4.18 reduces to

$$\frac{\partial}{\partial x} (K_x \frac{\partial h}{\partial x}) + \frac{\partial}{\partial z} (K_z \frac{\partial h}{\partial z}) = S_s \frac{\partial h}{\partial t} + \frac{S_v}{dz} \frac{\partial h}{\partial t} + \frac{q}{dz} \quad 4.19$$

where

$q$  is the extraction rate per unit plan area (m/s)

An additional boundary condition that applies at the phreatic surface is that the pressure is atmospheric ( $p = 0$ ), hence  $h = z$  in equation 4.7.

The position of the phreatic surface is not known a-priori, and must be determined as part of the solution by simultaneously satisfying the boundary condition and governing mass balance (equation 4.19) for a given surface geometry. In the model, the phreatic surface is treated as a solid upper boundary by setting the hydraulic conductivities on the external side of the surface to zero, ie.  $K_x = K_z = 0$  (Fig. 4.4).

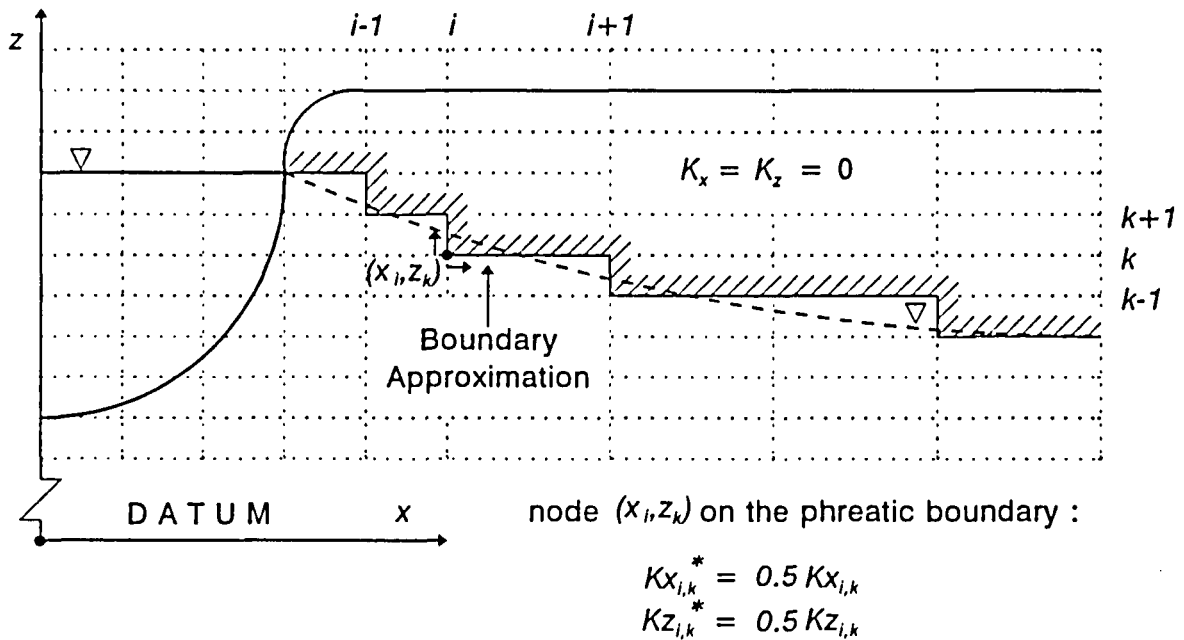


Figure 4.4 Approximating the phreatic surface boundary.

In shallow phreatic systems, the changes in elastic storage are less significant than the changes in void storage resulting from transient phreatic surface behaviour. The specific storage coefficient is usually within range  $10^{-5}$  to  $10^{-7} \text{ m}^{-1}$  (Rushton and Redshaw, 1979), whereas the specific yield is usually taken equal to the effective porosity. The effective porosity is defined as

$$\eta_e = \frac{V_v - V_w}{V} \quad 4.20$$

where

$\eta_e$  is the effective porosity

$V_w$  is the volume of the water remaining after downward gravity drainage has materially ceased ( $\text{m}^3$ )

The contribution to the change in volumetric storage by specific storativity may consequently be neglected in equations 4.9 and 4.19. The transient behaviour of the system is consequently included in the model by the unsteady boundary conditions (river stage, moving phreatic surface, and time-dependent extractions).

#### 4.1.1.2.3 Finite-difference Model

A finite-difference model is used to obtain solution to the governing mass balance and boundary equations.

##### 4.1.1.2.3.1 Finite-difference Grid

The saturated domain is divided into discrete spatial elements using a grid or mesh. In this way, the continuous function of groundwater potential is described by values at the intersection of grid lines (nodes) at distinct times. The convention for the numbering and position of nodes is illustrated in Fig. 4.1. Subscripts  $i, j$  and  $k$  are used to denote the grids lines in the  $x, y$  and  $z$  directions respectively, and subscript  $n$  denotes time. The storage coefficient and flux are defined spatially, and the groundwater potential is defined spatially and temporally. The hydraulic conductivities are specified at the midpoints between nodes using geometric means as proposed by Haverkamp and Vauclin (1979).

In the  $x$ - $z$  plane:

$$\begin{aligned}\overline{Kx}_{i,k} &= \sqrt{Kx_{i,k}Kx_{i+1,k}} \\ \overline{Kz}_{i,k} &= \sqrt{Kz_{i,k}Kz_{i,k+1}}\end{aligned}\tag{4.21}$$

where

$\overline{Kx}_{i,k}$  is the hydraulic conductivity in the  $x$  direction between nodes  $(x_i, z_k)$  and  $x_{i+1}, z_k$  (m/s)  
 $Kx_{i,k}$  is the hydraulic conductivity in the  $x$  direction at node  $(x_i, z_k)$  (m/s)  
 $Kx_{i+1,k}$  is the hydraulic conductivity in the  $x$  direction at node  $(x_{i+1}, z_k)$  (m/s)

The bar denoting spatially averaged hydraulic conductivities in each of the equations in 4.21 is suppressed in Fig. 4.1 and Fig. 4.4, and in subsequent equations.

##### 4.1.1.2.3.2 Boundary Approximations

Irregular boundaries are approximated by straight line segments of the finite-difference mesh (Fig. 4.4). The grid spacings may be irregular, allowing smaller mesh sizes to be used to approximate curved boundaries and in areas where the hydraulic gradients are high. Boundary coefficients

are applied between nodes situated on the approximated boundaries to reduce the cross-sectional flow area. In the model, this is achieved by reducing the hydraulic conductivity between nodes (Fig. 4.4), which is equivalent to reducing the flow area in equation 4.1.

#### 4.1.1.2.3.3 Finite-difference Formulation

Finite-difference approximations are used to express the partial differential mass balance equations 4.9 and 4.19 as finite-difference equations. The fundamental difference between the various finite-difference approximations is the characterisation of the time-dependent term  $S\partial h/\partial t$  in the mass balance equations, where  $S$  is the appropriate storage coefficient.

##### *Selection of a Finite-difference Approximation*

Rushton and Redshaw (1979) present the solution of backward, central, and forward-difference approximations for the case of abstraction from a square aquifer in the x-y plane, with regular mesh spacings and homogeneous soil-hydraulic properties. A two-dimensional horizontal form of the mass balance equation is used, neglecting vertical flow components. Both confined and unconfined systems are modelled. Each of the different solution methods are discussed with reference to the required computational programming and effort, stability and convergence, and the representation of boundaries. The suggested time-step restrictions required to achieve stable and convergent solutions are summarised in Table 4.1.

The transmissivity,  $T$ , is defined as the product of the hydraulic conductivity and the vertical depth of saturation,  $m$ , and applies to a two-dimensional model in the x-y plane. For variable grid spacings and heterogeneous soil-hydraulic characteristics, the smallest value of the time-step in Table 4.1 is the critical condition.

The analysis shows the backward-difference formulation to be an unconditionally stable approximation. Furthermore, the representation of system boundaries is straightforward, not requiring the modifications necessary in the central-difference method. Rushton and Redshaw (1979) suggest that the only valid reason for selecting an alternative finite-difference scheme is to achieve economy in computing effort. Advancement in the processing and operating capabilities of digital computers has made it possible to process large systems of simultaneous equations that previously required considerable computing effort (time and memory allocation). The computing effort required is therefore a less consequential issue compared with stability and convergence criteria. The backward-difference formulation is consequently selected as the approximation to the mass-balance equation.

**Table 4.1** Time-step restrictions for various finite-difference formulations (Rushton and Redshaw, 1979)

Method of Solution	Finite-difference Approximation	Time-step Restriction
Direct	Forward-difference explicit	$\Delta t \leq 0.25 \Delta x^2 S/T$
Successive Over Relaxation (SOR)	Backward-difference implicit	no restriction
Alternating-direction Implicit (ADI)	Central-difference implicit	$\Delta t \leq 0.05 b^2 S/T$
Alternating-direction Explicit (ADE)	Central-difference explicit	$\Delta t \leq 5.0 \Delta x^2 S/T$
Modified Iterative Alternating-direction Implicit (MIADI)	Backward-difference implicit	no restriction

where

$\Delta t$  is the time-step (s)

$\Delta x$  is the grid spacing in the x direction (m)

$b$  is the shortest distance between opposite boundaries (m)

$S$  is the appropriate storage coefficient

$T$  is the aquifer transmissivity (m<sup>2</sup>/s)

#### *Backward-difference Formulation*

Selecting equation 4.19 as an example of the backward-difference time approximation

$$\frac{\partial}{\partial x} (Kx \frac{\partial h_{n+1}}{\partial x}) + \frac{\partial}{\partial z} (Kz \frac{\partial h_{n+1}}{\partial z}) = \frac{S_y}{dz} \frac{h_{n+1} - h_n}{\Delta t} + \frac{q}{dz} \quad 4.22$$

Writing equation 4.22 in finite-difference form using a central-difference spatial approximation and the notation of Fig. 4.1,

$$\begin{aligned} & \frac{1}{\Delta x_c} (Kx_{i,k} \frac{h_{i+1,k,n+1} - h_{i,k,n+1}}{\Delta x_f} - Kx_{i-1,k} \frac{h_{i,k,n+1} - h_{i-1,k,n+1}}{\Delta x_b}) \\ & + \frac{1}{\Delta z_c} (Kz_{i,k} \frac{h_{i,k+1,n+1} - h_{i,k,n+1}}{\Delta z_f} - Kz_{i,k-1} \frac{h_{i,k,n+1} - h_{i,k-1,n+1}}{\Delta z_b}) \\ & = \frac{S_{y,i,k}}{\Delta z_c} \frac{h_{i,k,n+1} - h_{i,k,n}}{\Delta t} + \frac{q_{i,k,n+1}}{\Delta z_c} \end{aligned} \quad 4.23$$

where in the x direction

$\Delta x_f = x_{i+1,k} - x_{i,k}$  is the forward-difference spatial approximation

$\Delta x_c = \frac{(x_{i+1,k} - x_{i-1,k})}{2}$  is the central-difference spatial approximation

$\Delta x_b = x_{i,k} - x_{i-1,k}$  is the backward-difference spatial approximation

and in the z direction

$\Delta z_f = z_{i+1,k} - z_{i,k}$

$\Delta z_c = \frac{(z_{i+1,k} - z_{i-1,k})}{2}$

$\Delta z_b = z_{i,k} - z_{i-1,k}$

The structure of fluvial sediments may be highly variable (Reading, 1986), reflecting the ensuing processes of erosion and deposition that result from changes in the discharge and sediment regime in rivers. Expression 4.23 allows for spatial variability (heterogeneity) in hydraulic conductivity, specific yield (effective porosity) and soil-water extractions.

#### 4.1.1.2.3.4 Solution Procedure

##### *Solution of Simultaneous Equations*

Equation 4.23 is the finite-difference approximation to the continuous mass balance function (equation 4.19), for a node positioned at  $(x_i, z_k)$  on the finite-difference grid covering the domain. If  $ni$  and  $nk$  are the number of nodes in the x and z directions respectively in a rectangular domain, then the number of equations is given by  $ni.nk$ , and the number of unknowns is  $ni.nk + 2(ni + nk)$ . The boundary conditions provide the remaining  $2(ni + nk)$  equations that are required to solve the system.

Rewriting equation 4.23 with all the unknowns on the left hand side of the equality sign, gives

$$\begin{aligned}
 & \left( \frac{Kz_{i,k-1}}{\Delta z_c \Delta z_b} \right) h_{i,k-1,n+1} + \left( \frac{Kx_{i-1,k}}{\Delta x_c \Delta x_b} \right) h_{i-1,k,n+1} \\
 & - \left( \frac{Kz_{i,k}}{\Delta z_c \Delta z_f} + \frac{Kx_{i-1,k}}{\Delta x_c \Delta x_b} + \frac{Kx_{i,k}}{\Delta x_c \Delta x_f} + \frac{Kz_{i,k-1}}{\Delta z_c \Delta z_b} + \frac{S_{y_{i,k}}}{\Delta z_c \Delta t} \right) h_{i,k,n+1} \\
 & + \left( \frac{Kx_{i,k}}{\Delta x_c \Delta x_f} \right) h_{i+1,k,n+1} + \left( \frac{Kz_{i,k}}{\Delta z_c \Delta z_f} \right) h_{i,k+1,n+1} \\
 & = - \left( \frac{S_{y_{i,k}}}{\Delta z_c \Delta t} \right) h_{i,k,n} + \frac{q_{i,k,n}}{\Delta z_c}
 \end{aligned} \tag{4.24}$$



It is convenient to write equation 4.24 in the form

$$A_{i,k}h_{i,k-1,n+1} + B_{i,k}h_{i-1,k,n+1} + C_{i,k}h_{i,k,n+1} + D_{i,k}h_{i+1,k,n+1} + E_{i,k}h_{i,k+1,n+1} = F_{i,k} \quad 4.25$$

where

$$A_{i,k} = \frac{Kz_{i,k-1}}{\Delta z_c \Delta z_b} ; B_{i,k} = \frac{Kx_{i-1,k}}{\Delta x_c \Delta x_b}$$

$$D_{i,k} = \frac{Kx_{i,k}}{\Delta x_c \Delta x_f} ; E_{i,k} = \frac{Kz_{i,k}}{\Delta z_c \Delta z_f}$$

$$C_{i,k} = -A_{i,k} - B_{i,k} - D_{i,k} - E_{i,k} - \frac{S_{yi,k}}{\Delta z_c \Delta t}$$

$$F_{i,k} = - \left( \frac{S_{yi,k}}{\Delta z_c \Delta t} \right) h_{i,k,n} + \frac{q_{i,k,n}}{\Delta z_c} \quad 4.26$$

A set of simultaneous finite-difference equations for the domain is assembled by writing equation 4.25 for each node of the grid. These simultaneous equations have the form

$$A^* h = B^* \quad 4.27$$

where

$A^*$  is the two-dimensional array of coefficients

$h$  is the one-dimensional array of groundwater potentials

$B^*$  is the one-dimensional array of constants

and are given by

$$\begin{pmatrix} C_{1,1} & D_{1,1} & & E_{1,1} & & & & \\ B_{2,1} & C_{2,1} & D_{2,1} & & E_{2,1} & & & \\ & \cdot & \cdot & \cdot & & \cdot & & \\ A_{i,k} & & B_{i,k} & C_{i,k} & D_{i,k} & & E_{i,k} & \\ & \cdot & & \cdot & \cdot & \cdot & & \\ & & A_{ni-1,nk} & & B_{ni-1,nk} & C_{ni-1,nk} & D_{ni-1,nk} & \\ & & & A_{ni,nk} & & B_{ni,nk} & C_{ni,nk} & \end{pmatrix} \begin{pmatrix} h_{1,1,n+1} \\ h_{2,1,n+1} \\ \cdot \\ h_{i,k,n+1} \\ \cdot \\ h_{ni-1,nk,n+1} \\ h_{ni,nk,n+1} \end{pmatrix} = \begin{pmatrix} F_{1,1,n} \\ F_{2,1,n} \\ \cdot \\ F_{i,k,n} \\ \cdot \\ F_{ni-1,nk,n} \\ F_{ni,nk,n} \end{pmatrix} \quad 4.28$$

It is necessary to write equation 4.28 only for computational nodes falling within the domain of interest where the groundwater potentials are required. The computational nodes falling within the domain are numbered consecutively, in columnwise followed by rowwise order, in the direction of the axes (Fig. 4.4). The coefficients in equations 4.26 are computed for each of the nodes and are assembled into the two-dimensional array of coefficients,  $A^*$ . The coefficient for the node under consideration,  $C$ , falls on the main diagonal, with the  $B$  and  $D$  coefficients adjacently positioned (equation 4.28). The  $A$  and  $E$  coefficients are generally positioned further from the main diagonal, representing the interaction between nodes on adjacent rows of the grid.

The array of coefficients is symmetric about the main diagonal in terms of non-zero elements. The system of equations is, however, non-symmetric in terms of the parameter values of elements for a variable finite-difference grid. This is due to the central-difference spatial approximations ( $\Delta x_c$  and  $\Delta z_c$ ) in the coefficients of the equations in 4.26. The coefficients between computational nodes and nodes containing prescribed groundwater potentials are included in the array of constants,  $B^*$ . Coefficients between computational nodes and nodes on the external side of an impervious boundary are zero.

Various methods of solution are available for solving large sets of simultaneous equations generated by groundwater flow problems, including iterative and direct solution procedures. The iterative techniques generally reduce multi-dimension spatial systems to equation solving in one spatial dimension by incorporating iterative procedures. The methods used most frequently are Successive Over Relation (SOR), Gauss-Seidel, Alternating Direction Implicit (ADI), and Iterative ADI (Prickett, 1975). Iterative methods are generally incorporated in the solution procedures to alleviate the necessity of solving large systems of simultaneous equations. These methods are, however, susceptible to producing serious errors with certain combinations of boundary conditions (Rushton and Redshaw, 1979), and consequently a direct solution of equation 4.28 is adopted here. Furthermore, the solution of the set of equation represented by 4.27 using SOR and ADI was found to be computationally inefficient.

The array,  $A^*$ , is sparse (only a relatively small number of its elements are non-zero) and represents a variably banded diagonal system. Methods have been developed for solving sparse systems of equations with reduced computational effort resulting from the large number of zero elements. These methods depend on the precise pattern of sparsity of the system. The structure of  $A^*$  clearly depends on the shape of the domain, the type of boundary conditions, and the finite-difference grid (Fig. 4.4). For complex patterns of sparsity, software packages have been developed to automate the procedure of computing how fill-ins (zero elements which

become non-zero during the solution process) are to be minimised (Press *et al.*, 1989). The methods for sparse systems generally act to decrease the method's numerical stability, as compared to for example regular lower and upper (*LU*) decomposition with pivoting.

The *LU* decomposition with forward and backward-substitution as discussed by Press *et al.* (1989) is used to solve 4.28. The principal advantage of this technique over Gauss-Jordan or Gaussian elimination with backsubstitution lies in the reduced computing effort. The method utilises Crout's algorithm with partial and implicit pivoting to decompose the array of coefficients into lower and upper triangular systems. A routine for forward and backwardsubstitution is implemented on the *LU* decomposed array of coefficients ( $A^*$ ) and the array of constants ( $B^*$ ), to return the solution of groundwater potentials ( $h$ ).

#### *Phreatic Surface Position*

The phreatic surface is an internal boundary delineating saturated and unsaturated flow states. When flow in these domains is considered separately, the phreatic surface is treated as a physical boundary to each zone, with a flux across the surface maintaining saturated-unsaturated flow continuity.

Figure 4.5 is a plot of the potentials (groundwater ( $h$ ), pressure ( $p/\gamma$ ), and elevation ( $z$ )) at the nodes directly above and below the phreatic surface. The phreatic surface is located at the intersection of the groundwater and elevation potentials, or where the pressure potential relative to atmospheric pressure is zero.

The phreatic surface elevation is given by

$$z_{ps} = z_k + z^* \quad 4.29$$

where

$z_{ps}$  is the elevation of the phreatic surface (m)

$z_k$  is the elevation of the  $k^{th}$  node (m)

$z^*$  is the vertical height difference between  $z_k$  and the phreatic surface(m)

The phreatic surface elevation is computed at each vertical grid line. The nodes along each vertical are scanned from bottom to top ( $k = 1$  to  $nk$ , respectively) and the node is found where one of the following three criteria (in the order prescribed) is satisfied :

1. The previous phreatic surface boundary node,  $k_{ps}$ , is reached.

- 
- The graph plots Height above Datum (m) on the vertical axis against Potential (m) on the horizontal axis. A horizontal line represents the Phreatic Surface at a constant pressure  $p=0$ . Three diagonal lines represent different potential types: Groundwater Potential (decreasing), Elevation Potential (increasing), and Pressure Potential (decreasing). The intersection of the Phreatic Surface and Elevation Potential lines defines the elevation  $z_k$ . The intersection of the Phreatic Surface and Groundwater Potential lines defines the head  $h_{i,k}$ . The vertical distance between the Phreatic Surface and the Groundwater Potential line at a specific point is labeled  $z^*$ . The horizontal distance between the vertical lines through  $h_{i,k}$  and  $h_{i,k-1}$  is labeled  $z^*_i$ . A slope triangle in the bottom left corner indicates a 1:1 ratio between the horizontal and vertical axes. The datum is marked at the origin (0,0).

The above criteria are given in Table 4.2, together with the corresponding mathematical conditions, the nodes used to compute the phreatic surface elevation, and an explanation of the applicable boundary conditions. The significant computational differences between the criteria lie in an interpolation or extrapolation of the groundwater potentials. The need to extrapolate arises from zero-values on the external side of the boundary for a rising phreatic surface (Fig. 4.8).

## 4.17

The procedure for computing transient behaviour is illustrated in Fig. 4.7. The phreatic surface is spatially fixed during time-steps, and the change in profile is determined at the end of time-steps from groundwater potentials using the procedure in Figure 4.7. In this way, groundwater flows and phreatic surface profiles continually adjust to time-dependant boundary conditions.

The expressions for computing the vertical height difference  $z^*$  (equation 4.29) referred to in Fig. 4.6 for each of the three criteria in Table 4.2, are

$$z^* = h_{i,k} \quad 4.30a$$

$$z^* = \frac{z_k - h_{i,k}}{h_{i,k} - h_{i,k-1} - (z_k - z_{k-1})} \quad 4.30b$$

$$z^* = \frac{z_k - h_{i,k}}{h_{i,k+1} - h_{i,k} - (z_{k+1} - z_k)} \quad 4.30c$$

For a rising phreatic surface, zero-value groundwater potentials at nodes on the external side of the boundary at the previous time-step may fall on the internal side of the updated boundary position (Fig. 4.8). The groundwater potentials at the nodes approximating the phreatic surface boundary are required at each time-step to compute the water uptake by voids (equation 4.14).

**Table 4.2** Criteria for computing the phreatic surface elevation

Criterion	Mathematical condition	Nodes	Explanation
1. A	$k = k_{ps}, h_{i,k-1} = 0$	$k$	Shallow saturated depth
B	$k = k_{ps}$	$k, k-1$	Boundary extrapolation
2.	$h_{i,k} > 0, h_{i,k+1} = 0$	$k, k-1$	Seepage face, extrapolation
3.	$h_{i,k} \geq z_k, h_{i,k+1} < z_{k+1}$	$k, k+1$	Boundary interpolation

Groundwater potentials at nodes between successive rising phreatic surface profiles are estimated by linear extrapolation, i.e.

$$h_{i,k,n+1} = \frac{h_{i,k-1,n} - h_{i,k-2,n}(z_k - z_{k-1})}{z_{k-1} - z_{k-2}} + h_{i,k-1,n} \quad 4.31$$

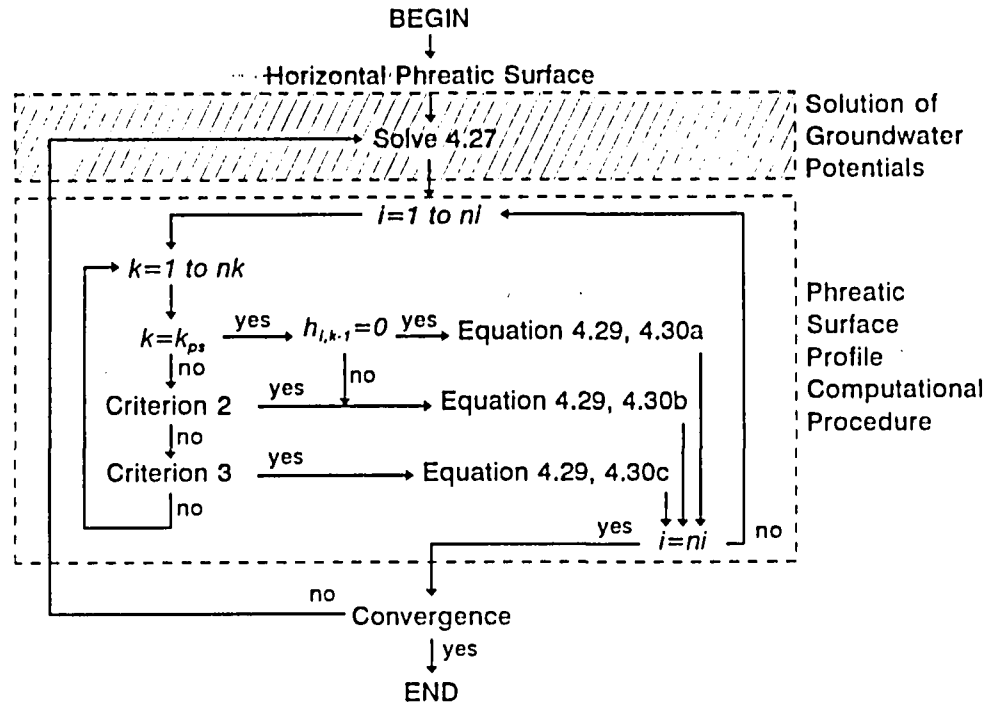


Figure 4.6 Procedure for computing steady state groundwater potentials and phreatic surface position.

#### 4.1.1.3 Two-dimensional Horizontal Flow Model

##### 4.1.1.3.1 Mass Balance Equation

The mass balance equation describing unsteady flow through a two-dimensional, horizontal, phreatic system is given by (Rushton and Redshaw, 1979)

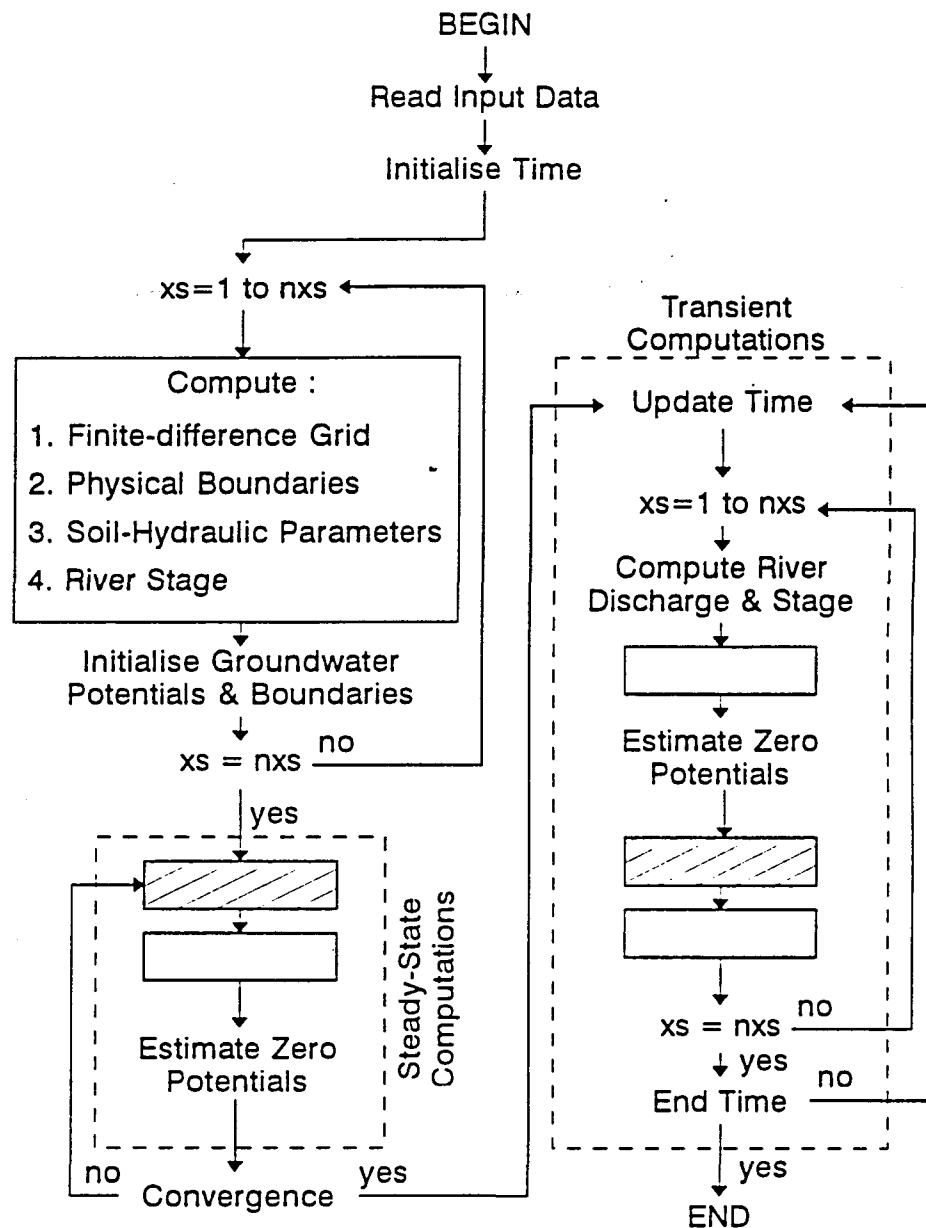
$$\frac{\partial}{\partial x}(mK_x \frac{\partial \bar{h}}{\partial x}) + \frac{\partial}{\partial y}(mK_y \frac{\partial \bar{h}}{\partial y}) = S_s m \frac{\partial \bar{h}}{\partial t} + S_y \frac{\partial \bar{h}}{\partial t} + q \quad 4.32$$



where

$\bar{h}$  is the depth averaged groundwater potential (m)

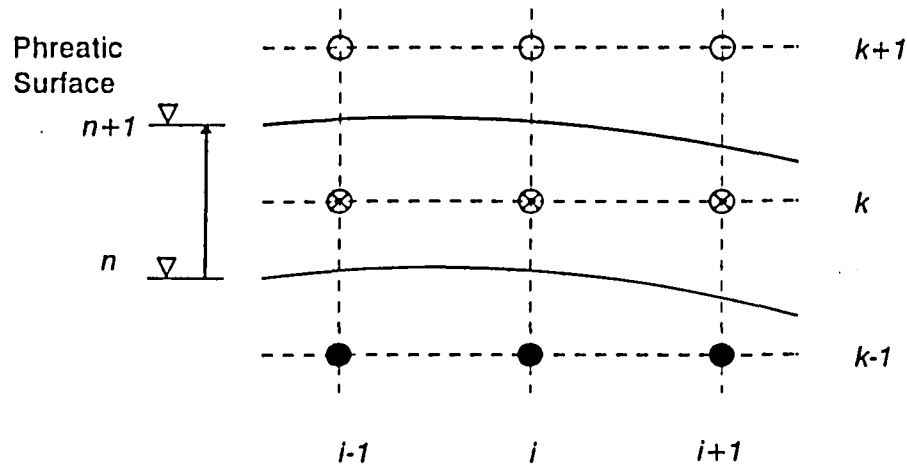
$m$  is the depth of saturation (m)

$q$  is the extraction rate per unit plan area (m/s)



- nxs    Number of Cross-Sections  
    Solution of Groundwater Potentials (Fig. 4.6)  
    Phreatic Surface & Boundary Computations (Fig. 4.6)

**Figure 4.7** Procedure for computing transient groundwater potentials and phreatic surface profiles.



- nodes on the external side of the boundary at  $n$  and  $n+1$
- ⊗ nodes on the external side of the boundary at  $n$ , but on the internal side at  $n+1$
- nodes on the internal side of the boundary at  $n$  and  $n+1$

**Figure 4.8** Zero-value groundwater potentials at nodes between successive phreatic surface boundary positions.

Equation 4.32 may be derived directly from equation 4.18 by substituting  $dz = m$  in the mass balance equation (i.e. the height of the elementary volume in Fig. 4.3 is increased to represent the depth of saturation).

The groundwater potential represents an average potential over the depth of saturation and is given by (Rushton and Redshaw, 1979)

$$\bar{h} = \frac{1}{m} \int h_{x,y,z,t} dz \quad 4.33$$

The bar in equation 4.33 is subsequently suppressed in equations relating to two-dimensional horizontal flow.

In two-dimensional horizontal flow, transmissivities replace the saturated depth-hydraulic conductivity parameters, and the confined storage coefficient replaces the saturated depth-specific storage coefficient according to equations 4.34 and 4.35, respectively.



$$\begin{aligned} T_x &= mK_x \\ T_y &= mK_y \end{aligned} \quad 4.34$$

$$S_c = mS_s \quad 4.35$$

Neglecting the contribution of changes in confined storage compared to the overall change in the volumetric storage within a shallow phreatic system (as for the two-dimensional vertical flow model, 4.1.1.2), the mass balance equation for flow in the x-y plane (Fig. 4.1) is given by

$$\frac{\partial}{\partial x} (T_x \frac{\partial h}{\partial x}) + \frac{\partial}{\partial y} (T_y \frac{\partial h}{\partial y}) = S_y \frac{\partial h}{\partial t} + q \quad 4.36$$

#### 4.1.1.3.2 Boundary Conditions

Boundaries to the saturated domain include prescribed potentials (river stages) along the active channel bank, and impervious boundaries at bedrock-sediment interfaces (Fig. 4.9). The plan location of the impervious (macro channel bank) and pervious (active channel bank) boundaries will vary temporally as a function of saturated depth,  $m_{x,y}$ , for non-vertical interfaces. Temporal variations in the location of flow boundaries are not considered significant at the study site (Fig. 2.11) for flows confined to the active channel. Transient water-sediment and sediment-bedrock boundaries may be treated similarly to the phreatic surface boundary (see 4.1.1.2.2).

In a two-dimensional horizontal model the groundwater potentials are averaged over the depth of saturation, and therefore also represent the elevation of the phreatic surface. Fluxes across the phreatic surface are included in the mass balance equation (equation 4.36) to account for flow interaction between the saturated and unsaturated zones.

To reduce the spatial extent of the domain being modelled, it may be necessary to isolate a river reach by imposing artificial impervious flow boundaries upstream and downstream of the reach (Fig. 4.9). These limits to the domain will result in inaccuracies in the vicinity of the artificial boundaries, the significance of which will depend on the extent of longitudinal groundwater flow. In the absence of longitudinal flow these transverse boundaries represent streamlines, rationalising the use of a two-dimensional vertical model in the x-z plane.

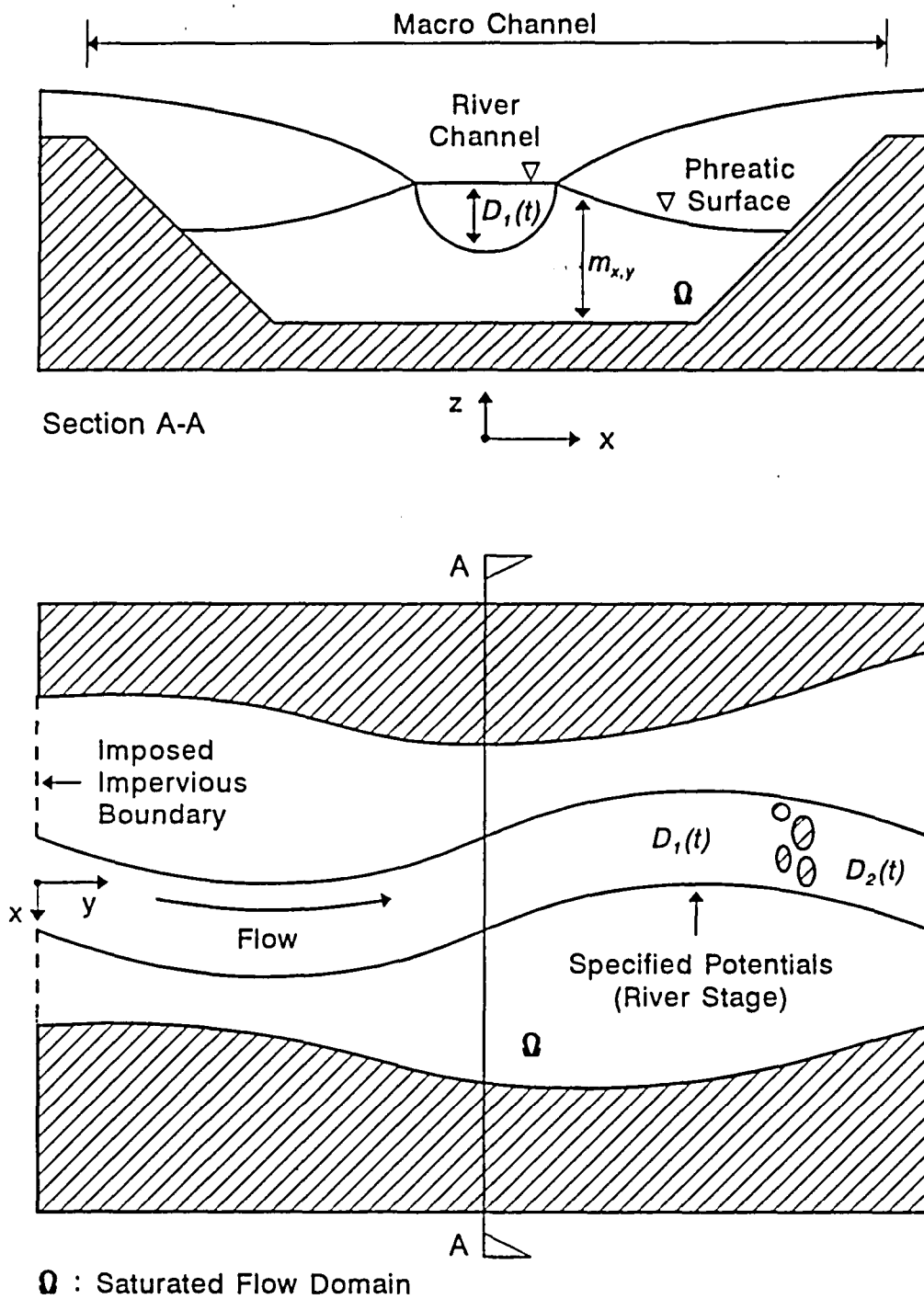


Figure 4.9 Flow boundaries encompassing the saturated flow domains in the  $x$ - $y$  and  $x$ - $z$  planes.

#### 4.1.1.3.3 Finite-difference Model

##### 4.1.1.3.3.1 Linearisation of Mass Balance Equation

In confined groundwater systems, the saturated depth represents a constant thickness through which flow takes place. For a phreatic system, the saturated depth is a function of the groundwater potential and is therefore time-dependant. The saturated depth in each of the equations in 4.34 is given by

$$m = h - z_b \quad 4.37$$

where

$z_b$  is the bedrock elevation (m)

Substituting equation 4.37 into 4.36 results in a non-linear mass balance equation. The system is linearised by using the groundwater potentials computed during the preceding time-step to determine the saturated depth, and maintaining this value for the subsequent computation. i.e.

$$m_{n+1} = h_n - z_b \quad 4.38$$

This linearisation is identical to the step-wise procedure used to model transient phreatic surface profiles in the two-dimensional vertical model (4.1.1.2.3.4).

##### 4.1.1.3.3.2 Finite-difference Formulation

Backward-difference time and central-difference spatial approximations are used to express equation 4.36 in finite-difference form. Using the notation of Fig. 4.1,

$$\begin{aligned} & \frac{1}{\Delta x_c} (Tx_{ij,n+1} \frac{h_{i+1,j,n+1} - h_{ij,n+1}}{\Delta x_f} - Tx_{i-1,j,n+1} \frac{h_{ij,n+1} - h_{i-1,j,n+1}}{\Delta x_b}) \\ & + \frac{1}{\Delta y_c} (Ty_{ij,n+1} \frac{h_{ij+1,n+1} - h_{ij,n+1}}{\Delta y_f} - Ty_{ij-1,n+1} \frac{h_{ij,n+1} - h_{ij-1,n+1}}{\Delta y_b}) \\ & = S_{vij} \frac{h_{ij,n+1} - h_{ij,n}}{\Delta t} + q_{ij,n} \end{aligned} \quad 4.39$$

#### 4.1.1.3.3.3 Solution Procedure

Rewriting equation 4.39 in the form equivalent to equation 4.25 for two-dimensional vertical flow,

$$A_{ij,n+1}h_{ij-1,n+1} + B_{ij,n+1}h_{i-1,j,n+1} + C_{ij,n+1}h_{ij,n+1} + D_{ij,n+1}h_{i+1,j,n+1} + E_{ij,n+1}h_{ij+1,n+1} = F_{ij,n+1} \quad 4.40$$

where

$$\begin{aligned} A_{ij,n+1} &= \frac{Ty_{ij-1,n}}{\Delta y_c \Delta y_b} \\ B_{ij,n+1} &= \frac{Tx_{i-1,j,n}}{\Delta x_c \Delta x_b} \\ D_{ij,n+1} &= \frac{Tx_{i,j,n}}{\Delta x_c \Delta x_f} \\ E_{ij,n+1} &= \frac{Ty_{ij,n}}{\Delta y_c \Delta y_f} \\ C_{ij,n+1} &= -A_{ij,n+1} - B_{ij,n+1} - D_{ij,n+1} - E_{ij,n+1} - \frac{S_{y,i}}{\Delta t} \\ F_{ij,n+1} &= -\left(\frac{S_{y,i}}{\Delta t}\right)h_{ij,n} + q_{ij,n} \end{aligned} \quad 4.41$$

The time-dependence of the groundwater potential coefficients in equation 4.40 results from temporal variations in saturated depth. A set of simultaneous finite-difference equations for the domain is assembled by writing equation 4.40 for each node of the grid. This set of equations is of identical form to that for two-dimensional vertical flow, viz.

$$A \cdot h = B \quad 4.42$$

and may be solved using LU decomposition with forward and backward-substitution.

#### 4.1.1.4 Coupling Vertical and Horizontal Flow Models

The spatially isolated two-dimensional vertical and horizontal flow models illustrated in Fig. 4.1 are coupled to produce a quasi three-dimensional model. The vertical flow model developed in 4.1.1.2 is imbedded within the horizontal flow model developed in 4.1.1.3 (Fig. 4.10). This allows flow conditions in the vertical and lateral directions to be examined in greater detail within a cross-section through the riparian zone.

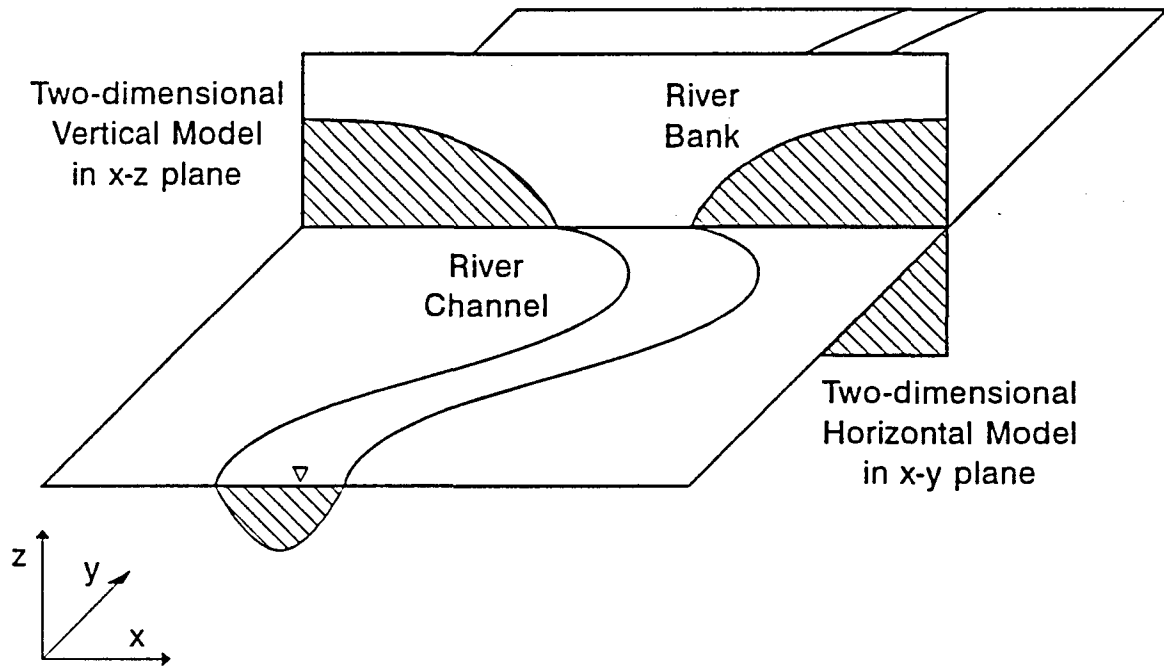


Figure 4.10 Vertical flow model in x-z plane imbedded within horizontal flow model in x-y plane.

Figure 4.11 shows the spatial orientation of groundwater potential coefficients (coefficients in equations 4.25 and 4.40) for nodes in the vertical and horizontal planes located immediately upstream of the imbedded vertical model.

#### 4.1.1.4.1 Modifications to Finite-Difference Equations

##### 4.1.1.4.1.1 Vertical Flow Model

Equation 4.25 is modified for a node in the vertical modelling plane to give

$$A_{i,k}h_{i,k-1,n+1} + B_{i,k}h_{i-1,k,n+1} + C_{i,k}h_{i,k,n+1} + D_{i,k}h_{i+1,k,n+1} + E_{i,k}h_{i,k+1,n+1} + G_{i,k}h_{ij-1,n+1} + H_{i,k}h_{ij+1,n+1} = F_{i,k} \quad 4.43$$

where  $G_{i,k}$  and  $H_{i,k}$  are the coefficients of groundwater potential that account for flow interactions in the upstream and downstream longitudinal directions, respectively, (Fig. 4.11(a)) and are given in equation 4.44. The expression for the groundwater potential coefficient at the node under consideration,  $C_{i,k}$ , is extended to include longitudinal flow interaction (equation 4.44).

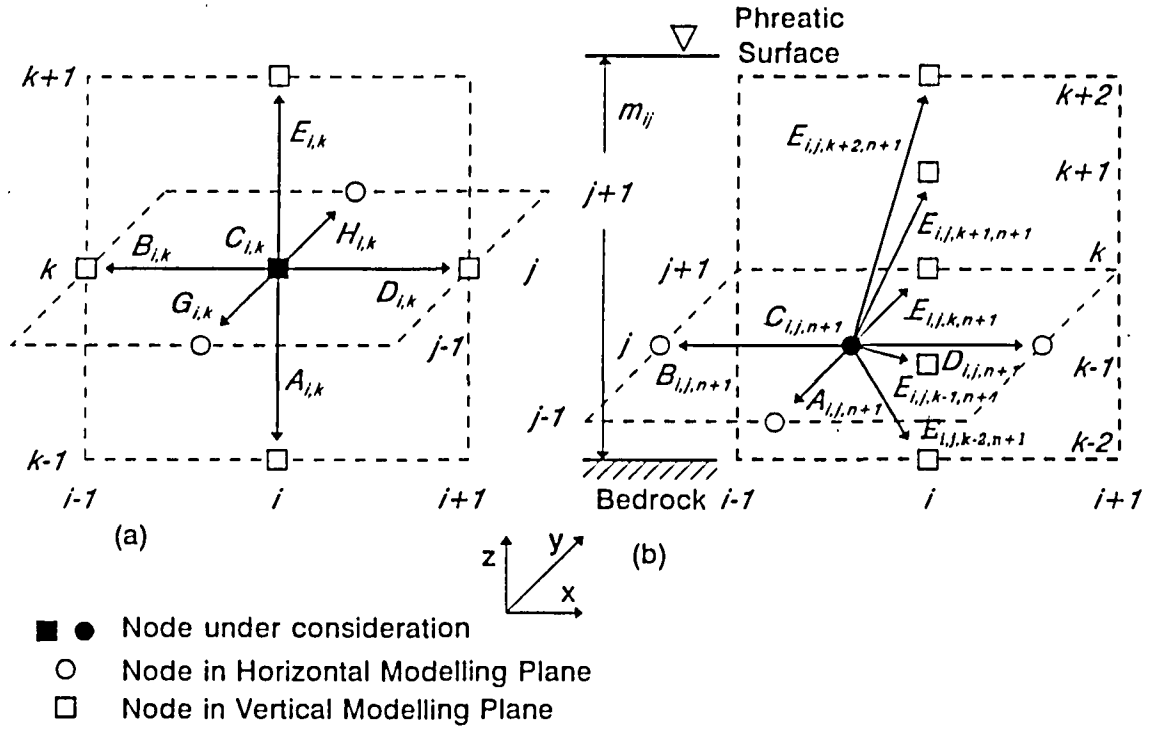


Figure 4.11 Orientation of groundwater potential coefficients for (a) a node in the vertical modelling plane; (b) a node in the horizontal modelling plane located immediately upstream of the imbedded vertical model.

$$\begin{aligned}
 G_{i,k} &= \frac{Ky_{ij-1}}{\Delta y_c \Delta y_b} \\
 H_{i,k} &= \frac{Ky_{ij}}{\Delta y_c \Delta y_f} \\
 C_{i,k} &= -A_{i,k} - B_{i,k} - D_{i,k} - E_{i,k} - H_{i,k} - G_{i,k} - \frac{S_{y_{i,k}}}{\Delta Z_c \Delta t}
 \end{aligned}
 \tag{4.44}$$

#### 4.1.1.4.1.2 Horizontal Flow Model

Equation 4.40 describing flow interaction between nodes in the horizontal plane is modified for the nodes adjacent to the imbedded vertical model. Using a node located immediately upstream of the intersection of the horizontal and vertical modelling plane to illustrate the modification (Fig. 4.11(b)),

$$\begin{aligned}
 A_{i,j,n+1}h_{ij-1,n+1} + B_{i,j,n+1}h_{i-1,j,n+1} + C_{i,j,n+1}h_{ij,n+1} + D_{i,j,n+1}h_{i+1,j,n+1} \\
 + \sum_{k=1}^{nk} (E_{i,j,k,n+1}h_{ij+1,k,n+1}) = F_{i,j,n+1}
 \end{aligned}
 \tag{4.45}$$

where

$$E_{ij,k,n+1} = \frac{Ky_{ij}\Delta z_c}{\Delta y_c \Delta y_f} \quad 4.46$$

$$C_{ij,n+1} = -A_{ij,n+1} - B_{ij,n+1} - D_{ij,n+1} - \frac{Ty_{ij,n}}{\Delta y_c \Delta y_f} - \frac{S_{y,i}}{\Delta t}$$

and the remaining coefficients are given by the expressions in 4.41.

The summation term in equation 4.45 replaces the single corresponding term in equation 4.40, and represents the interaction between the flow in a column extending over the full saturated depth in the horizontal model, and vertically compartmentalised flow elements in the imbedded vertical model (Fig. 4.11(b)). For a node located immediately downstream of the intersection of the horizontal and vertical modelling planes, the summation term will apply to the first term ( $Ah$ ) in equation 4.45.

#### 4.1.1.4.2 Matrix of Simultaneous Equations

The matrix of simultaneous equations for the coupled horizontal and vertical saturated flow models is assembled by writing the flow equations (4.40, 4.43 and 4.45) for each computational node of the horizontal and vertical grids. The computational nodes are numbered consecutively in the lateral direction, followed by the longitudinal and vertical directions for the horizontal and vertical models, respectively.

The array of coefficients,  $A^*$ , consists of five distinct belts (Fig. 4.12), representing

1. Nodes within the horizontal flow model upstream and downstream of the imbedded vertical model (equation 4.40),
2. Nodes within the horizontal flow model adjacent to the imbedded vertical flow model (e.g. equation 4.45),
3. Nodes within the vertical flow model (equation 4.43).

The array of coefficients (Fig. 4.12) is a variably banded diagonal system. The specific structure of the array depends on the shape of the horizontal and vertical flow domains and the boundary conditions. LU decomposition as described previously (4.1.1.2.3.4) is used to solve the set of coupled flow equations.

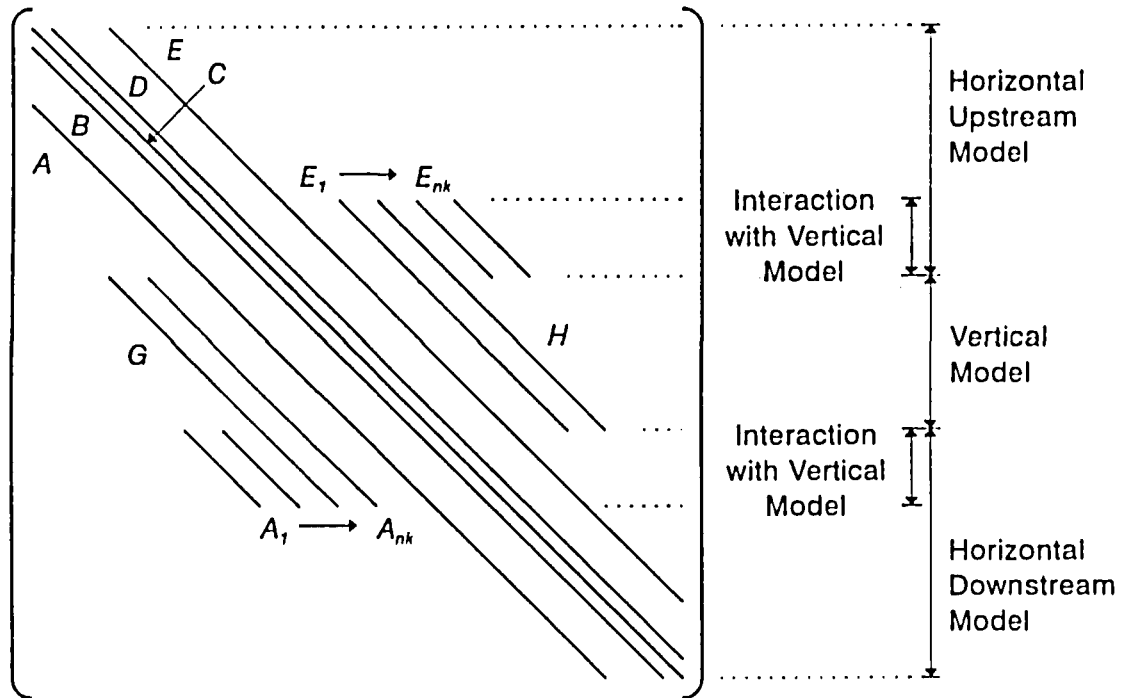


Figure 4.12 Structure of the array of coefficients,  $A^*$  for the coupled vertical and horizontal two-dimensional flow models.

#### 4.1.2 Soil Water in the Unsaturated Zone

##### 4.1.2.1 Flow Equations

The capillary pressure exerted by a fluid is the pressure difference between the phases on the air-fluid interface, and is given by

$$p_c = p_{air} - p_{fluid} \quad 4.47$$

where

$p_c$  is the capillary pressure ( $\text{kg/m.s}^2$ )

$p_{air}$  is the pressure in the air ( $\text{kg/m.s}^2$ )

$p_{fluid}$  is the pressure in the fluid ( $\text{kg/m.s}^2$ )

Assuming the air pressure in the void spaces is at atmospheric pressure ( $p_{air} = 0$ ), then

$$p_{fluid} = -p_c \quad 4.48$$



Neglecting the kinetic potential (c.f. equation 4.7), the soil-water potential (piezometric head) at any point in the fluid of the two phase flow is given by

$$h = \frac{p_{fluid}}{\rho g} + z \quad 4.49$$

Substituting from equation 4.49 and assuming a constant fluid density  $\rho$ ,

$$\begin{aligned} h &= -\frac{p_c}{\rho g} + z \\ &= -h_c + z \\ &= -\psi + z \end{aligned} \quad 4.50$$

where

$h_c$  is capillary pressure head (m)

$\psi$  is the soil suction (m)

The diagrammatic definition for soil water potential, soil suction and elevation head, measured using a tensiometer, are given in Fig. 4.13.

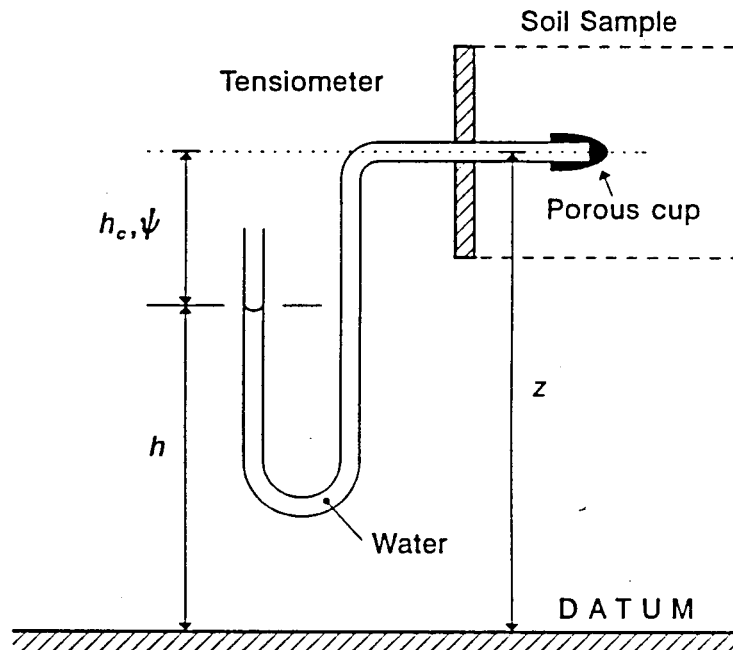


**Figure 4.13** Diagrammatic definitions of soil water potential, soil suction and elevation head measured using a tensiometer (after Bear and Verruijt, 1992).

The soil suction for every soil is related to the volumetric water content,  $\theta$ , i.e.

$$\psi = f^n(\theta) \quad 4.51$$

Darcy's relationship for flow rate through saturated porous media (equation 4.1) is a special case of the more general relationship for an unsaturated state containing air and fluid phases, which is given by

$$Q = K(\psi)iA = K(\theta)iA \quad 4.52$$

where

$K(\psi)$  is the unsaturated hydraulic conductivity (m/s)

#### 4.1.2.1.1 Three-dimensional Mass Balance Equation

Consider three-dimensional transient flow through an element of unsaturated porous media of dimensions  $dx$ ,  $dy$  and  $dz$ . By the conservation of mass, the net flow rate out of the element must equal the decrease in the rate of volumetric water storage, i.e.

$$\frac{d\theta}{dt}dxdydz = -\left(\frac{\partial q_{sx}}{\partial x} + \frac{\partial q_{sy}}{\partial y} + \frac{\partial q_{sz}}{\partial z}\right)dxdydz - q_vdxdydz \quad 4.53$$

where

$q_v$  is the extraction rate per unit volume of soil ( $s^{-1}$ )

The components of the specific discharge,  $q_s$ , are given by Darcy's law (equation 4.52) as

$$\begin{aligned} q_{sx} &= -K_x(\psi)\frac{\partial h}{\partial x} \\ q_{sy} &= -K_y(\psi)\frac{\partial h}{\partial y} \\ q_{sz} &= -K_z(\psi)\frac{\partial h}{\partial z} \end{aligned} \quad 4.54$$

Differentiating each of the equations in 4.54 with respect to  $x$ ,  $y$  and  $z$  respectively, and substituting in equation 4.53 gives the general three-dimensional mass balance equation for transient flow through an unsaturated porous medium

$$\frac{d\psi}{dt} = -\frac{1}{C} \left[ \frac{\partial}{\partial x} K_x(\psi) \frac{\partial \psi}{\partial x} + \frac{\partial}{\partial y} K_y(\psi) \frac{\partial \psi}{\partial y} + \frac{\partial}{\partial z} K_z(\psi) \left( \frac{\partial \psi}{\partial z} - 1 \right) \right] - \frac{q_v}{C} \quad 4.55$$

where

$C$  is the differential soil water capacity ( $m^{-1}$ ), given by

$$C = \frac{d\theta}{d\psi} \quad 4.56$$

For an isotropic material and neglecting the soil water sink, equation 4.55 is equivalent to the relationship given by Bear and Verruijt (1992) in grad notation

$$\frac{d\psi}{dt} + \frac{1}{d\theta/d\psi} [\nabla \cdot K(\psi) \nabla \psi - \frac{\partial K(\psi)}{\partial z}] = 0 \quad 4.57$$

Saturated flow is a special case of flow in an unsaturated state with  $C = 0$  and  $K(\psi) = \text{constant}$ . For example, the three-dimensional unsteady equation for *saturated* flow may be obtained directly from equation 4.55 by substituting  $\psi = z - h$ , to obtain

$$\frac{\partial}{\partial x} (K_x \frac{\partial h}{\partial x}) + \frac{\partial}{\partial y} (K_y \frac{\partial h}{\partial y}) + \frac{\partial}{\partial z} (K_z \frac{\partial h}{\partial z}) = q_v \quad 4.58$$

The right-hand side of equation 4.58 may be extended to include transient storage due to water compressibility (as in equation 4.8).

#### 4.1.2.2 One-dimensional Vertical Flow Model

##### 4.1.2.2.1 Mass Balance Equation

The mass balance equation for one-dimensional transient flow is obtained by substituting  $\partial\psi/\partial x = \partial\psi/\partial y = 0$  in equation 4.55, giving

$$\frac{d\psi}{dt} = -\frac{1}{C} \left[ \frac{\partial}{\partial z} K_z(\psi) \left( \frac{\partial \psi}{\partial z} - 1 \right) \right] - \frac{q_v}{C} \quad 4.59$$

This is the well known Richard's equation, which has received considerable attention in the literature (e.g. Freeze, 1969; Haverkamp *et al.*, 1977; Feddes *et al.*, 1988 and Babajimopoulos, 1991).

Equation 4.59 is often expressed in the form

$$\frac{d\psi^*}{dt} = \frac{1}{C} \left[ \frac{\partial}{\partial z} K_z(\psi^*) \left( \frac{\partial \psi^*}{\partial z} + 1 \right) \right] - \frac{q_v}{C} \quad 4.60$$

where

$\psi^*$  is the soil water potential (m), with  $\psi^* \equiv -\psi$

#### 4.1.2.2.2 Boundary Conditions

Boundaries to the unsaturated domain may include those encompassing the saturated domain (4.1.1.2.2), with the addition of the atmospheric-soil interface at the soil surface (Fig. 4.2). In the riparian zone, lower flow boundary conditions include either zero flux normal to a bedrock interface, or a specified zero soil water suction at the phreatic surface. The atmosphere influences the unsaturated zone at the soil surface through infiltration and evaporation. The maximum possible (potential) flux across the soil surface depends on atmospheric conditions, while the actual flux is limited by the ability of the soil to transport water. At the upper boundary, a flux is prescribed that is limited by the Darcian absorption or exfiltration capacity of the soil.

#### 4.1.2.2.3 Finite-difference Model

##### 4.1.2.2.3.1 Finite-difference Grid

The one-dimensional space and space-time region occupied by the spatial variable  $z$  (index  $l$ ), and temporal variable  $t$  (index  $n$ ) are illustrated in Fig. 4.14. The vertical axis is divided into compartments extending from the soil surface to bedrock. The soil suction, soil water capacity and hydraulic conductivity are defined spatially and temporally. The hydraulic conductivities are specified at the midpoints between nodes using geometric means (Haverkamp and Vauclin, 1979).

##### 4.1.2.2.3.2 Finite-difference Formulation

Equation 4.59 is approximated using a backward-difference time formulation, with implicit linearisation. This implies that the soil water capacity and hydraulic conductivity are taken at an intermediate time between  $t$  and  $t + \Delta t$ , corresponding to the arithmetic mean soil suctions between times. Implicit linearisation is applied by Belmans *et al.* (1983) in the Simulation model of the WAter balance of a CROPPed soil (SWACROP). This is a modification of the method proposed by Haverkamp *et al.* (1977), which applies explicit linearisation by evaluating the soil-hydraulic parameters at time  $t$ .

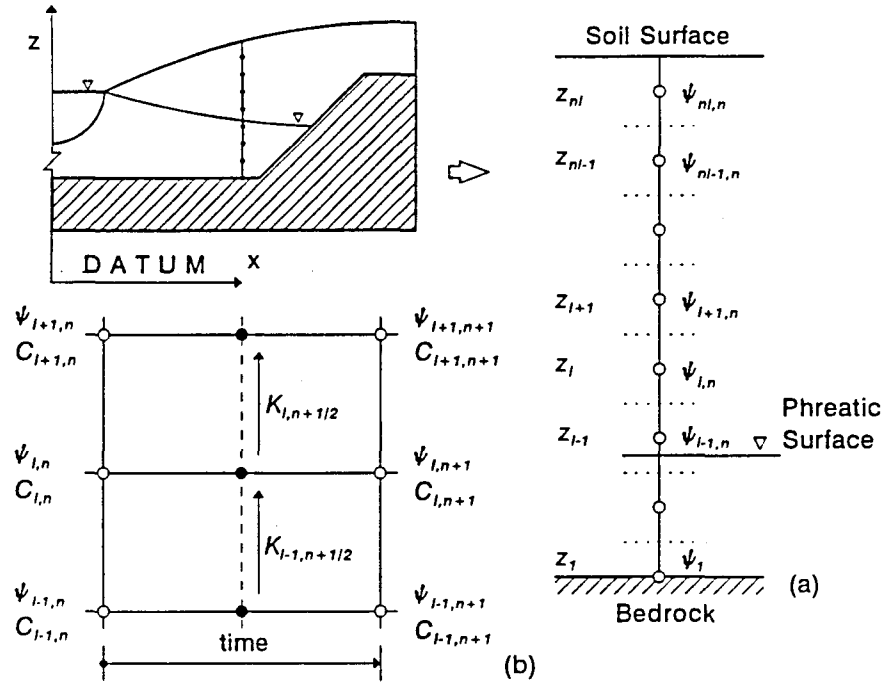


Figure 4.14 Convention for the numbering and position of nodes : (a) space region ( $z$ ); (b) space-time region ( $z, t$ ).

A backward-difference time approximation of equation 4.55 leads to

$$C_{n+\frac{1}{2}} \frac{\psi_{n+1} - \psi_n}{\Delta t} = -\frac{\partial}{\partial z} \left\{ Kz(\psi)_{n+\frac{1}{2}} \left( \frac{\partial \psi_{n+1}}{\partial z} - 1 \right) \right\} - \frac{q}{dz} \quad 4.61$$

where

$q$  is the extraction rate per unit plan area (m/s)

Writing equation 4.61 in finite-difference form using a central-difference spatial approximation and the notation of Fig. 4.14,

$$C_{i,n+\frac{1}{2}} \frac{\psi_{i,n+1} - \psi_{i,n}}{\Delta t} = -\frac{1}{\Delta z_c} \left\{ Kz(\psi)_{i,n+\frac{1}{2}} \left( \frac{\psi_{i+1,n+1} - \psi_{i,n+1}}{\Delta z_f} - 1 \right) - Kz(\psi)_{i-1,n+\frac{1}{2}} \left( \frac{\psi_{i,n+1} - \psi_{i-1,n+1}}{\Delta z_b} - 1 \right) \right\} - \frac{q_{i,n+1}}{\Delta z_c} \quad 4.62$$

#### 4.1.2.2.4 Solution Procedure

##### *Solution of Simultaneous Equations*

Rewriting equation 4.62 for each node of the unsaturated depth region, results in a set of simultaneous equations of the form

$$A_l \psi_{l-1,n+1} + B_l \psi_{l,n+1} + D_l \psi_{l+1,n+1} = E_l \quad 4.63$$

where

$$A_l = \frac{Kz(\psi)_{l-1,n+\frac{1}{2}}}{\Delta z_c \Delta z_b}$$

$$D_l = \frac{Kz(\psi)_{l,n+\frac{1}{2}}}{\Delta z_c \Delta z_f}$$

$$B_l = -A_l - D_l + \frac{C_{l,n+\frac{1}{2}}}{\Delta t}$$

$$E_l = \left( \frac{C_{l,n+\frac{1}{2}}}{\Delta t} \right) \psi_{l,n} + \frac{1}{\Delta z_c} (Kz(\psi)_{l,n+\frac{1}{2}} - Kz(\psi)_{l-1,n+\frac{1}{2}} - q_{l,n+1}) \quad 4.64$$

Once again, (see sections 4.1.1.2.3.4 and 4.1.1.3.3.3) a set of simultaneous equations of the form  $A^* \psi = B^*$  is assembled by writing equation 4.63 for each node of the one-dimensional spatial domain.

The equation for the node directly below the soil surface ( $l = n$ ) is modified to include the atmospheric-soil surface interface flux boundary condition.

The nodal coefficients in equation 4.63 become

$$D_{nl} = 0$$

$$E_{nl} = \left( \frac{C_{nl,n+\frac{1}{2}}}{\Delta t} \right) \psi_{l,n} + \frac{1}{\Delta z_c} (-q_s - Kz(\psi)_{nl-1,n+\frac{1}{2}} - q_{nl,n+1}) \quad 4.65$$

where  $q_s$  is the flux across the atmospheric-soil surface interface.

The coefficients  $A_{nl}$  and  $B_{nl}$  remain unchanged.

#### 4.1.3 Coupling Saturated and Unsaturated Flow Models

The connection between the saturated and unsaturated flow is made possible by considering the phreatic surface as an internal transient boundary that responds to flow from both flow systems. The spatial linkage between the two-dimensional vertical saturated and several one-dimensional vertical unsaturated flow models is illustrated in Fig. 4.15.

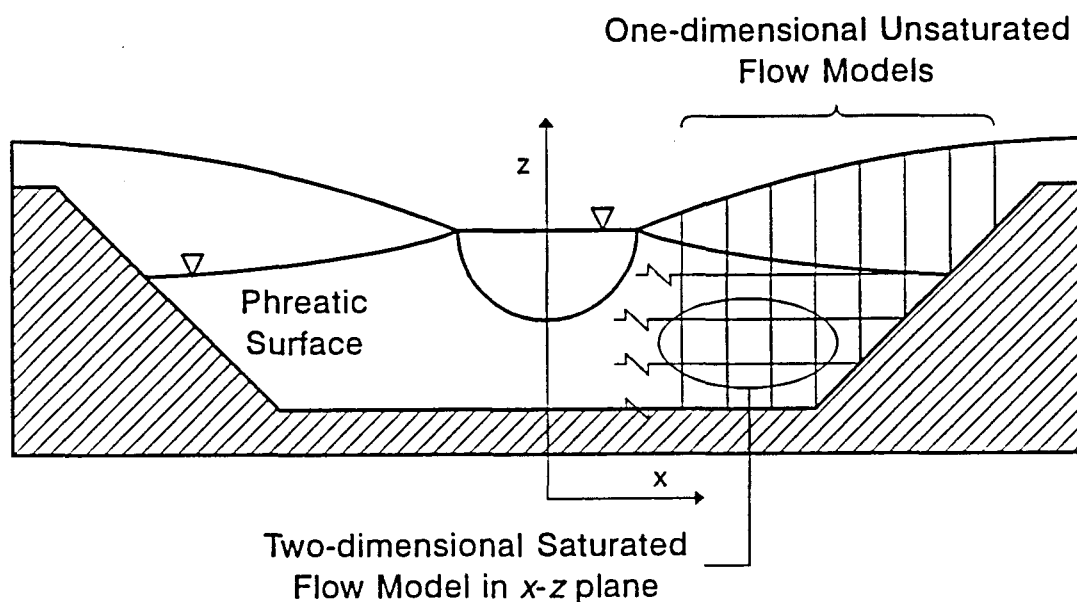


Figure 4.15 Coupling the saturated and unsaturated flow models in a vertical cross-section through the riparian bank zone.

The unsaturated concept of specific yield or effective porosity (4.1.1.2.2), is applied in saturated flow modelling to account for the interaction with the unsaturated zone above a transient phreatic surface. A spatially averaged specific yield is used widely in hydrogeological investigations of subsurface aquifers, and may be considered an appropriate approximation for long-term groundwater studies. The assumption of instantaneous response in the unsaturated zone may, however, be inadequate under certain conditions.

Contemporary investigations show that the specific yield can vary with depth to and rise or fall of the phreatic surface (Zarandy, 1993). The inadequacy of assuming a constant specific yield is discussed by Childs and Poulouvasilis (1962), where temporal soil-moisture profiles above a

transient phreatic surface are predicted and compared with experimental observations.

The concept of delayed yield was introduced by Boulton (1963) to account for the time-dependant nature of drainage during pumping tests. The delayed yield model assumes that a drop in the phreatic surface leads to an instantaneous release of soil-water, plus a delayed yield which decreases exponentially (Rushton and Redshaw, 1979). This description is an improvement on the constant yield analysis for a extraction from groundwater storage.

Various alternatives exist for connecting the saturated and unsaturated flow systems to maintain flow continuity across the phreatic surface. The entire subsurface domain (saturated and unsaturated regions) may be modelled by applying the general unsaturated flow equation (e.g. equation 4.55 for three-dimensional flow). The saturated region consequently becomes a simplification of the entire subsurface flow, where the hydraulic conductivities are invariant with water content. This approach allows the phreatic surface to be disregarded as a transient boundary, and its position may be found by locating the points where the groundwater pressure potentials are zero (Fig. 4.5). The above methodology, however, requires that a full three-dimensional model be developed (for flow in the riparian zone at the study site). The use of fictitious input data are then necessary to reduce the spatial dimensions to produce an appropriate model for the specific flow system being analyzed.

Iterative and direct solution procedures are presented for coupling the quasi three-dimensional saturated and one-dimensional unsaturated flow models developed.

#### 4.1.3.1 Iterative Solution Procedures

Pikul *et al.* (1974) present a numerical model based on the coupled one-dimensional horizontal and one-dimensional vertical unsaturated flow equations. The solution procedure used is as follows:

1. Solve for the groundwater potentials and the phreatic surface position at time  $t_n$ , using the specific yield  $S_{yn-1}$  at time  $t_{n-1}$ .
2. Using the predicted change in phreatic surface position between  $t_{n-1}$  and  $t_n$  as input boundary conditions, solve for the soil suctions along each of the unsaturated vertical flow models.
3. Perform water balances over the unsaturated soil columns to define an effective specific yield, given by



$$S_{yn} = \theta_s - \theta_{mn} \quad 4.66$$

where

$\theta_s$  is the volumetric water content at saturation

$\theta_{mn}$  is the minimum volumetric water content below the depth from which moisture may be removed directly by evapotranspiration

#### 4. Advance the time-step.

To maintain an adequate flow balance between the coupled systems, Pikul *et al.* (1974) found that it may be necessary to iterate until convergence is achieved, with iteration cycles being required when the time step exceeded a limit unique to the problem. The linkage between the saturated and unsaturated zones adopted by Pikul *et al.* (1974), although representing an improvement of the constant specific yield concept, does not establish flow continuity over the saturated-unsaturated regions.

Flow continuity across the phreatic surface may be achieved by modifying step 3. of the above procedure, to give

$$S_{yn} = \frac{\sum_{i=1}^{l=nl} (\theta_n - \theta_{n-1})}{z_{ps_n} - z_{ps_{n-1}}} - q_v \Delta t \quad 4.67$$

where

$z_{ps_n}$  is the phreatic surface elevation predicted from the saturated flow model at time  $t_n$

Application of the modified procedure was found to perform satisfactorily for groundwater flow response to a fluctuation (rise and subsequent fall) of river stage. Convergence, however, was difficult to attain for small changes in phreatic surface position, and when the flux across the phreatic surface is in the opposite direction to the phreatic surface movement.

The following saturated-unsaturated coupling procedure is described by Zarandy (1993):

The flux across the phreatic surface predicted from the saturated flow model is prescribed as the lower boundary condition to the vertical unsaturated flow profile, and the convergence criteria is given by

$$1 - \epsilon < \frac{z_{ps_i}^*}{z_{ps_j}} < 1 + \epsilon \quad 4.68$$

where

$i$  is the iteration index

$z_{ps_i}^*$  is the phreatic surface elevation predicted from the unsaturated flow model

$z_{ps_i}$  is the phreatic surface elevation predicted from the saturated flow model

$\epsilon$  is the accuracy of the phreatic surface predictions ( $\epsilon \ll 1$ )

If the condition represented by equation 4.68 is not satisfied, then the saturated flow computation is repeated using an improved estimate of the specific yield, according to the equation:

$$S_{y_{i+1}} = S_{y_i} \left( 1 - \frac{z_{ps_i}^* - z_{ps_i}}{2z_{ps_i}} \right) \quad 4.69$$

Iterations continue until the convergence criteria is satisfied.

#### 4.1.3.2 Simultaneous Solution Procedure

A direct solution procedure is adopted here for linking the saturated and unsaturated flow models due to the obvious advantages over approximate iterative methods. The simultaneous solution of the saturated and unsaturated flow equations is achieved by considering the flow interaction between the upper and lower nodes of the saturated and unsaturated regions, respectively (Fig. 4.16), and modifying the finite-difference flow equations.

##### 4.1.3.2.1 Modifications to Finite-Difference Equations

Applying the relationship between soil-water or groundwater potential and soil suction (equation 4.50), the linkage between the saturated and unsaturated finite-difference flow equations is developed.

##### 4.1.3.2.1.1 Saturated Two-Dimensional Vertical Flow Model

Equation 4.43 is modified for the node directly below the phreatic surface in the vertical modelling plane to read

$$A_{i,k}h_{i,k-1,n+1} + B_{i,k}h_{i-1,k,n+1} + C_{i,k}h_{i,k,n+1} + D_{i,k}h_{i+1,k,n+1} + E_{i,k}(z_l - \psi_{l,n+1}) + G_{i,k}h_{ij-1,n+1} + H_{i,k}h_{ij+1,n+1} = F_{i,k} \quad 4.70$$

where  $k$  and  $l$  are the nodes in the saturated and unsaturated regions directly below and above the phreatic surface, respectively.



unsaturated hydraulic conductivity are probably the single most important factor limiting the successful application of unsaturated flow models. Direct methods to estimate unsaturated hydraulic conductivity (laboratory and field) are difficult to implement, expensive and time consuming. For these reasons, indirect methods have been developed to predict soil hydraulic properties from more easily measurable data, such as soil water retention data and soil texture.

A comprehensive review and comparative analysis of empirical formulas for determining saturated hydraulic conductivity from grain-size composition are given by Vuković and Soro (1992). Zarandy (1993) provides an extensive bibliography of models for computing unsaturated hydraulic conductivity and gives the more widely used expressions.

#### 4.1.4.1 Prediction of Hydraulic Conductivity from Soil Water Retention Data

The closed form analytical model proposed by van Genuchten (1978) has received application in numerical modelling of unsaturated flow dynamics (e.g. Feddes *et al.*, 1988), and provides a good description of soil water retention and hydraulic characteristics (Papageorgiou, 1994).

The volumetric water content is described empirically by van Genuchten (1980) as a function of soil suction (water retention relationship)

$$\theta = \theta_r + \frac{\theta_s - \theta_r}{(1 + |\alpha\psi|^n)^m} \quad (\theta_r \leq \theta \leq \theta_s) \quad 4.73$$

where

$\theta_r$  is the residual volumetric water content

$\theta_s$  is the saturated volumetric water content

$\alpha, n$  are parameters determining the shape of the water retention curve

$m = 1 - 1/n$

Soil water retention curves for three different soil types, fitted by van Genuchten (1980) using equation 4.73, are illustrated in Fig 4.17.

The residual water content refers to the water content where the gradient  $d\theta/d\psi$  becomes zero ( $\psi \rightarrow \infty$ ). For practical purposes the residual water content may be defined as the water content at some large negative value of the pressure head, for example, at the permanent wilting point ( $\psi = -15\,000$  cm, Harr (1962)). The dimensionless parameter  $n$  determines the rate at which the S-shaped retention curve turns toward the ordinate for large values of soil suction, while  $\alpha$  equals approximately the inverse of the pressure head at the inflection point where  $d\theta/d\psi$  is a maximum.

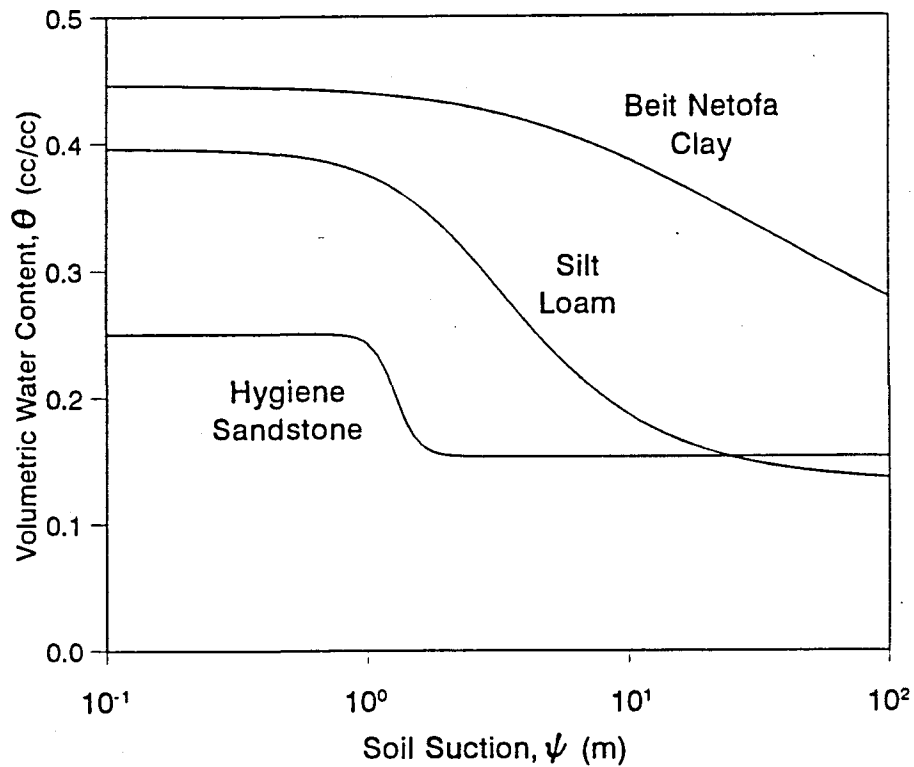


Figure 4.17 Water retention relationships using the model of van Genuchten (1980).

A closed form analytical expression describing the unsaturated hydraulic conductivity in terms of soil suction was derived by van Genuchten (1980) by combining equation 3.73 with the pore-size distribution theory of Mualem (1976), giving (Wösten and van Genuchten, 1988)

$$K(\psi) = K_s \frac{[(1 + |\alpha\psi|^n)^m - |\alpha\psi|^{n-1}]^2}{(1 + |\alpha\psi|^n)^{m(l+2)}} \quad 4.74$$

where

$K_s$  is the saturated hydraulic conductivity (m/s)

$l$  is a soil specific parameter

Although  $l$  is a soil specific parameter, Mualem (1976) concluded from an analysis of a number of soil hydraulic data sets that  $l$  is on average approximately 0.5. Wösten and van Genuchten (1988) found the hydraulic properties of coarse-textured soils were independent of  $l$ , yielding a constant value of 0.22, which agreed well with Mualem's (1976) average of 0.5. For medium and fine-textured soils, however,  $l$  could clearly be related to percent silt, bulk density, and topsoil or subsoil. Fixing  $l$  at 0.5 in these cases did not result in acceptable fits of the experimental data.

The soil water capacity may be determined from the continuous expression for the soil water content-suction relationship. Differentiating equation 4.73 with respect to soil suction,

$$C(\psi) = \frac{d\theta}{d\psi} = -amn |\alpha\psi|^{n-1} \frac{\theta_s - \theta_r}{(1 + |\alpha\psi|^n)^{m+1}} \quad 4.75$$

Van Genuchten (1986, unpublished) developed software to fit the analytical models to measured soil-hydraulic data and to predict conductivity data from observed water retention curves. Kabat and Neeffjes (1988) extended this program and developed a user-friendly software package.

#### 4.1.4.2 Hysteresis

The water retention curve for a soil is usually obtained by removing water from an initially saturated soil sample (desorption). If water is added to an initially drier sample (adsorption), the moisture content in the soil will be different at equivalent soil suctions, as illustrated in Fig. 4.18. This hysteresis phenomenon results from the ink-bottle and raindrop effects, and entrapped air (Bear and Verruijt, 1992).

The model of van Genuchten is valid for monotonic wetting and drying cycles only (Hack-ten Broeke and Kabat, 1988). Kool and Parker (1987) extended the model for hysteresis in water retention curves and hydraulic conductivity functions. Hysteresis curves are rarely applied in practise when modelling unsaturated flow. The effects of hysteresis are considered insignificant compared to the difficulty of adequately describing the necessary input data including soil heterogeneity and boundary conditions (refer to Chapter 2: Data Collection). Consequently, hysteresis is neglected in the riparian bank storage model, although the occurrence of wetting and drying cycles resulting from river stage fluctuations are inherent.

### 4.2 Bank Storage Model Code Validation

#### 4.2.1 Scope

Code validation describes the process whereby the integrity of a model code is tested by comparing modelled results with data typically derived from independent analytical and numerical models, and experimental tests. Validation is distinguished from model verification which assess the ability of a model to characterise a specific field or experimental system. Model verification is addressed in 4.3 for a study site on the Sabie River in the Kruger National Park.

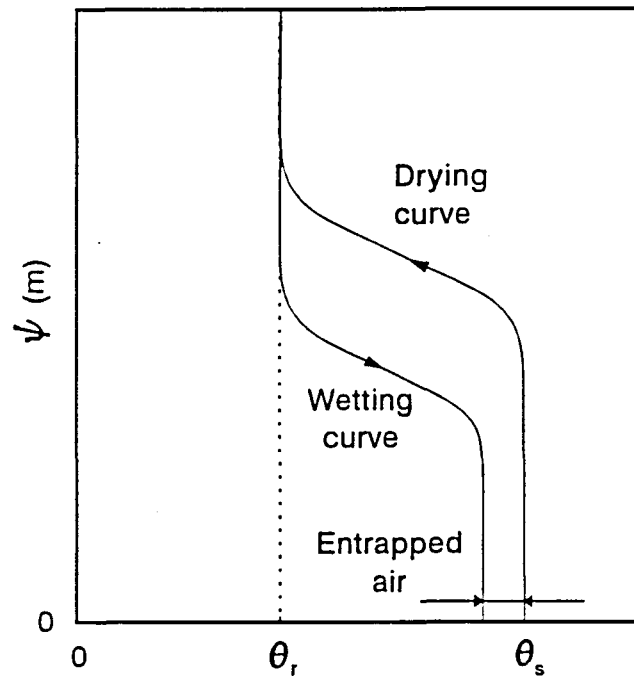


Figure 4.18 Hysteresis in the water retention relationship.

The use of analytical solutions for validation is most desirable since these are exact solutions. Analytical models are limited in application to simplified geometric, soil and hydraulic conditions, but nevertheless provide valuable tools for validating saturated (e.g. Cooper and Rorabaugh (1963); Abdulrazzak and Morel-Seytoux (1983); Zhang (1992)) and unsaturated (e.g. Grant *et al.* (1991); Srivastava and Yeh (1991); Warrick *et al.* (1991)) flow models.

Numerous numerical models based on various approximating forms of the general partial-differential flow equations are available in the literature for saturated (e.g. Bruch (1973); Gureghian (1978); Hornberger *et al.* (1970); Pinder and Sauer (1970); Verma and Bratsaert (1971); Zitta and Wiggert (1970); and Zucker *et al.* (1973)), unsaturated (Belmans *et al.* (1983); Freeze (1969, 1972); and Zhang and Berndtsson (1991)), and saturated-unsaturated (eg. Binley and Bevan (1992); Freeze (1972); Pikul *et al.* (1974); and Verma and Brutsaert (1970)) flows. Although numerical models are approximate, they nevertheless provide useful comparative solutions provided account is taken of the spatial, temporal and mass-balance approximations, convergence and stability considerations.

Viscous fluid models (e.g. Ibrahim and Brutsaert (1965)), sand flume models (e.g. Abdulrazzak and Morel-Seytoux (1983)), and soil column tests (e.g. Childs and Poulouvasilis (1962); Kastanek (1971); Watson (1967)) have been extensively used to study bank storage dynamics and vertical infiltration and drainage, providing appropriate data for validating model codes. The viscous fluid model is an analog model resulting from the similarity between relationships describing two-dimensional flow of a viscous fluid between parallel plates and saturated flow through porous media. The first use of such a model was by Hele-Shaw in 1898 (Pricket, 1975). Pricket (1975) presents selected applications of the Hele-Shaw and sand flume models.

Physical models are being used less widely due to the increasing number of analytical and numerical solutions schemes available for a range of flow situations. Experimental tests are also subject to observational inaccuracies, particularly in the determination of soil-hydraulic parameters. Physical models, nevertheless, provide useful means of validating codes for which no comparative analytical or numerical models exist.

Bank storage dynamics models are typically numerically based solutions of finite-difference (as applied here) or finite-element approximations to governing partial differential flow equations. The use of numerical solution techniques arises from the need to incorporate complex morphological, soil-hydraulic, hydraulic, biotic and climatic conditions. Code validation provides the ability to assess the sensitivity of numerical models to the selection of temporal and spatial parameters inherent in the solution procedure.

A combination of analytical, numerical, and physical sand flume models are used to validate the saturated, unsaturated and coupled saturated-unsaturated model codes.

#### **4.2.2 Groundwater Flow in the Saturated Zone**

##### **4.2.2.1 Review of Models from the Literature**

###### **4.2.2.1.1 Steady-State Conditions**

Numerous analytical and numerical groundwater models make use of the well known Dupuit-Forcheimer approximations to simplify the governing flow equations, and thereby simplify the solution procedure.



### *Dupuit-Forcheimer Theory of Unconfined Flow*

The Dupuit-Forcheimer (DF) theory is based on two assumptions (Harr, 1962):

1. For small flow gradients the streamlines are considered horizontal, and consequently equipotentials are assumed to be vertical.
2. The hydraulic gradient is equal to the gradient of the phreatic surface and is invariant with depth.

In many groundwater studies, application of the DF approximations produce results that compare favourably with those of more rigorous approaches, experimental and field data (eg. Pikul *et al.* (1974); Verma and Brutsaert (1971)).

The loss of water from storage reservoirs and en transport to regions of utilisation have received considerable attention in the literature due to its importance for the management of water resources. Approximate steady-state analytical solutions based on the DF approximations have therefore been developed for simplified conditions to identify the factors influencing losses and enable seepage rates to be calculated theoretically (e.g. Bouwer, 1969) and graphically (e.g. Zhang, 1992).

#### **4.2.2.1.1.1 Uniform Lateral Seepage**

Seepage rate formulae have been derived for the situation where the stage is maintained at a constant level in the reservoir or stream, and the phreatic surface elevation is prescribed laterally (Fig. 4.19).

#### *Rectangular Channel*

For a rectangular channel with the channel bed extending to the impermeable layer (Fig. 4.19), the elevation of any point on an assumed parabolic phreatic surface profile is given by

$$h = \left( \frac{h_1^2 - h_2^2}{L} x + h_2^2 \right)^{1/2} \quad 4.76a$$

where

$h_1$  is the stage level (m)

$h_2$  is the elevation of the phreatic surface at a distance  $L$  from  $h_1$  (m)

$h$  is the elevation of the phreatic surface at a distance  $x$  from  $h_1$  (m)

$L$  is the lateral distance between  $h_1$  and  $h_2$  (m)

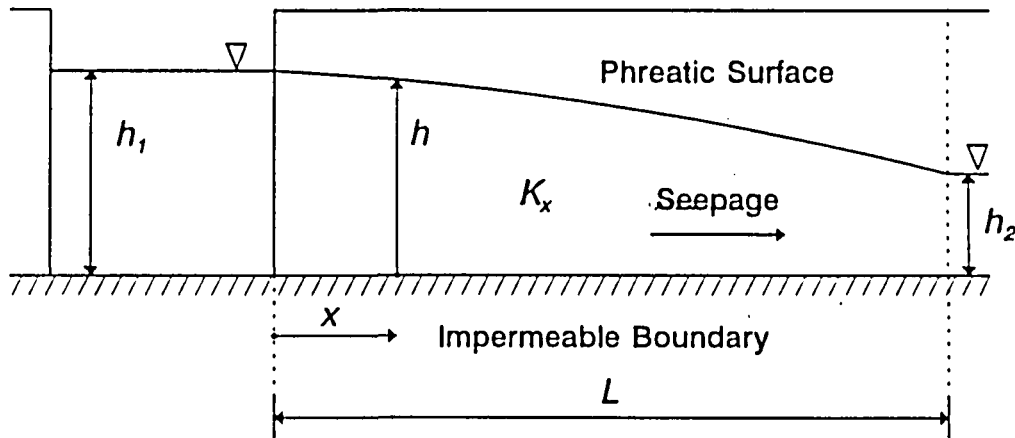


Figure 4.19 Steady seepage from rectangular channel section with constant phreatic surface level at lateral boundary.

Applying the DF approximations, the seepage rate is given by

$$Q = -K_x \frac{dh}{dx} h = -K_x \frac{h_1^2 - h_2^2}{2L} \quad 4.76b$$

#### *Trapezoidal Channel*

Equation 4.76b may be extended to a trapezoidal channel with the channel bed elevated above the impermeable layer to give the approximate seepage rate (Bouwer, 1969)

$$Q = K_x \frac{(h_1 - h_2 + d)(h_1 + h_2 + d)}{2L - w + ah_1} \quad 4.77$$

where

$a^{-1}$  is the slope of the channel bank

$w$  is the width of the channel bed (m)

$d$  is the vertical height between the channel bed and the impermeable layer (m)

Bouwer (1969) used an electrical analog model to show that the error in seepage rate increases with increased ratio of  $d/w$ .

#### 4.2.2.1.1.2 Uniform Vertical Infiltration

##### *Rectangular Channel*

The phreatic surface profile developed for horizontal seepage resulting from uniform vertical infiltration (Fig. 4.20) may be derived theoretically. Applying the DF approximations, the rate of lateral seepage is given by Darcy's law as

$$q(L-x) = K_x \frac{dh}{dx} h \quad 4.78a$$

Separating differential terms and applying integrals leads to

$$q \int (L-x) dx = K_x \int h dh \quad 4.78b$$

Applying the boundary condition ( $h = h_1$  at  $x = 0$ ) to evaluate the integration constants, the solution of equation 4.78b results in the following phreatic surface profile

$$h = \left( \frac{2qLx}{K_x} - \frac{qx^2}{K_x} + h_1^2 \right)^{1/2} \quad 4.78c$$

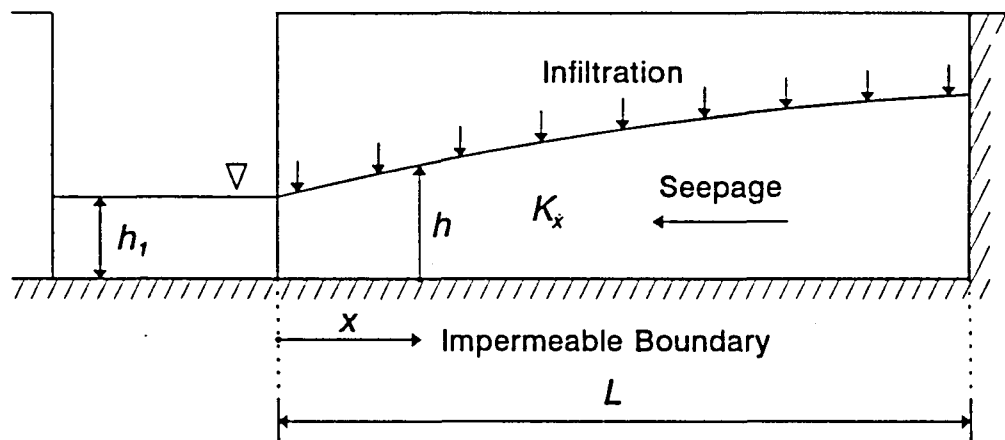


Figure 4.20 Phreatic surface profile and geometry for uniform vertical infiltration.

#### 4.2.2.1.2 Transient Conditions

Analytic solutions for dynamic stream-bank storage interaction are difficult to obtain due to the unconfined nature of the flow and need to characterise temporal variations of river stage. Analytic solutions for the changes in groundwater potential, seepage rate, and dynamic bank storage volume that result from the passing of a flood wave in a rectangular surface stream were developed by Cooper and Rorabaugh (1963). The model of Cooper and Rorabaugh (1963) is the only known available analytical solution in the literature for transient stream-bank storage interaction, and has been used elsewhere to validate numerical model codes (e.g. Hornberger *et al.* (1970); Moench *et al.* (1974); and Dillon (1983)).

##### 4.2.2.1.2.1 Analytical Model of Cooper and Rorabaugh (1963)

###### *Characterisation of the Stage Hydrograph*

Cooper and Rorabaugh (1963) approximated the stage hydrograph by one of the family of curves defined by

$$D_t = \begin{cases} ND_o e^{-\delta t} (1 - \cos \omega t), & 0 \leq t \leq \tau \\ 0, & t \geq \tau \end{cases} \quad 4.79$$

where

$D_o$  is the maximum rise in stage (m)

$\tau$  is the duration of the flood wave (s)

$\omega = 2\pi/\tau$

$\delta$  is a constant determining the degree of asymmetry of the stage hydrograph ( $\delta = 0$  for a symmetric hydrograph)

$$N = \frac{\delta^2 + \omega^2}{2\omega^2} e^{\frac{2\delta}{\omega} \arctan \frac{\omega}{\delta}} \quad 4.80$$

###### *Mass Balance Equation*

The flow system is modelled using the following approximate form of the general mass balance equation,

$$\frac{\partial^2 h}{\partial x^2} = \frac{S}{T} \frac{\partial h}{\partial t} \quad 4.81$$

Equation 4.81 makes use of the DF approximations (one-dimensional flow) and assumes confined flow (constant transmissibility). The confined flow representation assumes that changes in groundwater potential and hence

phreatic surface fluctuations are small compared with the saturated flow depth. Solutions are derived for the case of a laterally finite (Fig. 4.21) and a semi-infinite flow system ( $L = \infty$ ). For the case of a finite flow system, the boundary and initial conditions on  $h$  are given by

$$\begin{aligned} h_{x,0} &= 0, \quad 0 \leq x \leq L \\ \frac{\partial h_{L,t}}{\partial x} &= 0, \quad t \geq 0 \\ h_{0,t} &= D_t \end{aligned} \quad 4.82$$

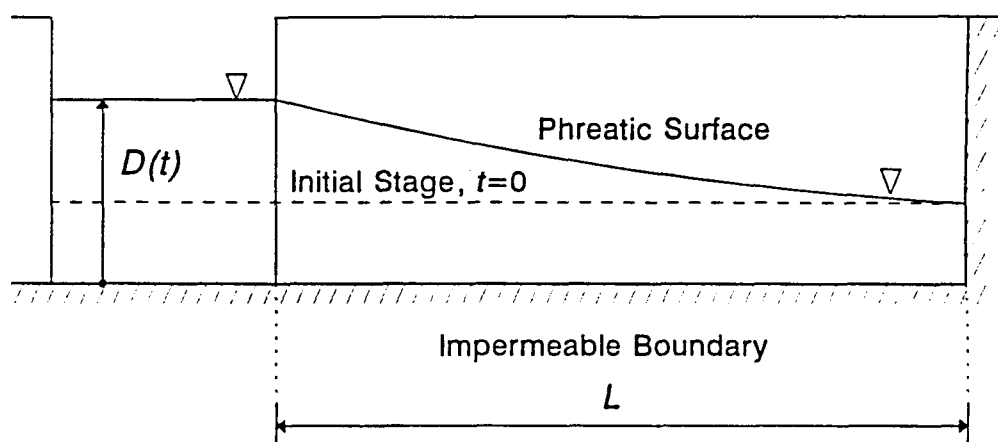


Figure 4.21 Bank geometry for the one-dimensional saturated transient flow analysis.

### *Solution Scheme*

The expressions for groundwater potentials, seepage rates and bank storage volumes derived by Cooper and Rorabaugh are given in Appendix 4.1.

The solution of equations A4.1, A4.2 and A4.3 (Appendix 4.1) for groundwater potentials, seepage rates and bank storage volumes, respectively, requires the sum of an infinite number of terms. The summation term was found to converge rapidly, allowing truncation of the higher order terms.

#### 4.2.2.1.2.2 Numerical Model of Hornberger *et al.* (1970)

Hornberger *et al.* (1970) used a one-dimensional saturated horizontal (DF approximations) groundwater model to study the response of bank storage to fluctuations of river stage within a homogeneous isotropic medium. The physical description of the flow system is identical to that considered by Cooper and Rorabaugh (1963) (Fig. 4.21).

##### *Mass Balance Equation*

The mass balance equation used is given by

$$\frac{\partial^2 h^2}{\partial x^2} = 2 \frac{S}{K} \frac{\partial h}{\partial t} \quad 4.83$$

##### *Solution Scheme*

Hornberger *et al.* (1970) non-dimensionalise equation 4.83 using the following dimensionless parameters

$$\begin{aligned} \xi &= \frac{x}{L} \\ \tau &= \frac{Kt}{LS} \\ H &= \frac{h}{L} \end{aligned} \quad 4.84$$

The finite-difference predictor-corrector scheme suggested by Douglas and Jones (1963) is used to develop a set of linear tridiagonal equations, which are solved using the Thomas (1949) algorithm.

#### 4.2.2.2 Physical Modelling Using a Sand Flume

A sand flume is a scaled down version of a full scale system, including its boundary configurations and soil-hydraulic properties. A 1.71 m long, 0.3 m wide sand flume facility was designed to physically simulate two-dimensional steady-state seepage between two constant head reservoirs (Fig. 4.22). A constant head reservoir on the right hand side of the flume provides a fixed stage level in the river channel cross-section ( $h_1$ ), whilst the reservoir on the left hand side acts as a laterally prescribed phreatic surface level ( $h_2$ ). A set of piezometers are set 50 mm above the base of the flume bed, and are connected to a manometer board to measure the piezometric potentials.

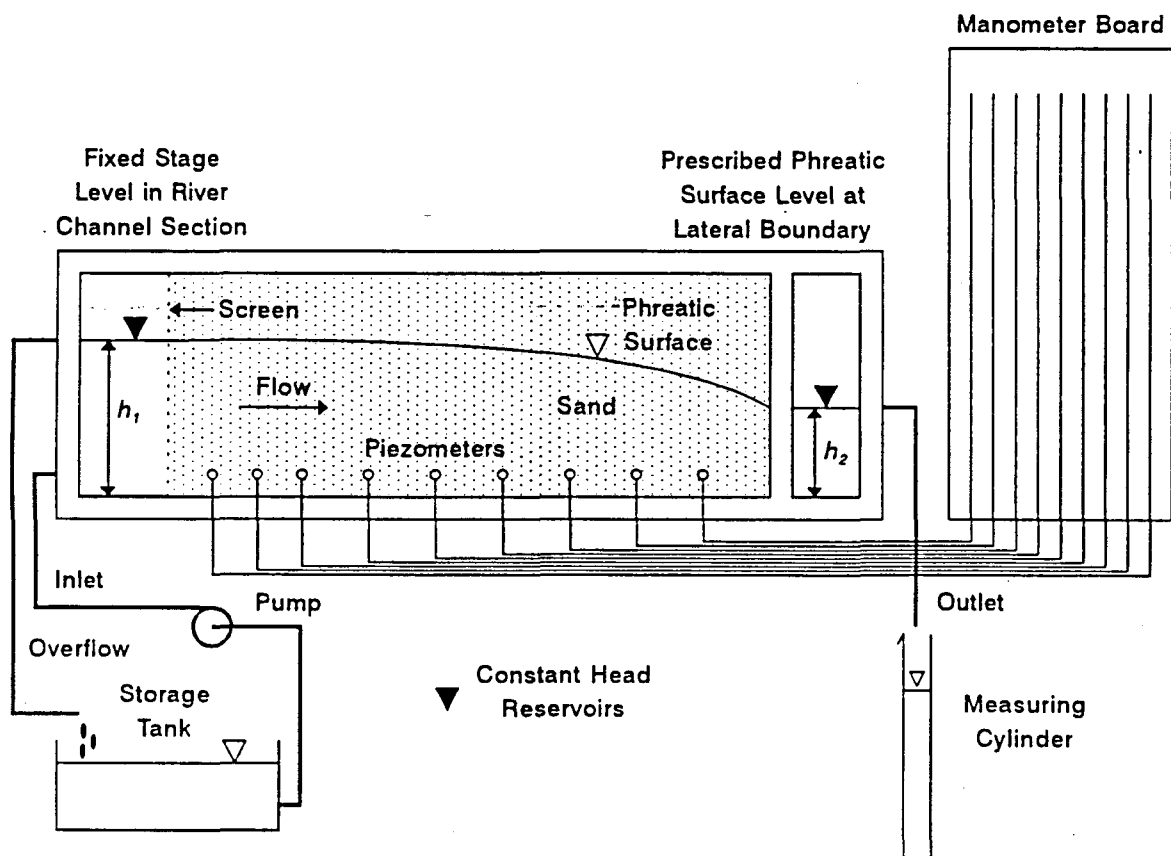


Figure 4.22 Experimental sand flume apparatus.

#### 4.2.2.2.1 Flume Tests

A series of three model tests were performed with different boundary configurations and soil-hydraulic conditions (Table 4.3 and Fig. 4.23). Industrially graded crushed silica sands were used in the flume and saturated hydraulic conductivities were determined using a constant head apparatus (e.g. Cernica, 1982).

Table 4.3 Sand flume tests

Flume Test	Hydraulic Conductivity	Channel Shape	Impervious Boundary
1	Uniform	Rectangular	Horizontal
2	Seven-Layered	Rectangular	Horizontal
3	Uniform	Trapezoidal	Irregular

The hydraulic conductivities of the flume material and test results (piezometric potentials and seepage rates) are tabulated in Appendix 4.2.

#### 4.2.2.3 Model Code Validation

##### 4.2.2.3.1 Steady-State Conditions

##### 4.2.2.3.1.1 Steady-State Lateral Seepage

#### *Rectangular Channel*

##### Flume Test 1

The piezometric potentials of three selected profiles for the flow system illustrated in Fig. 4.23a are plotted in Fig. 4.24a. The numerical model finite-difference parameters are listed in Table 4.4. The profiles obtained from the analytical, numerical and experimental models correlate well, with the numerical model performing slightly better than the analytical approximation. Both models, however, display larger deviations with increased hydraulics gradients. The discrepancies are attributed to the assumed parabolic profile in the analytical model (equation 4.76a) and neglecting unsaturated flow in both the analytical and numerical models.

Table 4.4 Finite-difference parameters

$\Delta x$	=	0.10 (0.0 m to 0.3 m)
	=	0.20 (0.3 m to 1.7 m)
$\Delta z$	=	0.05 (0.0 m to 0.3 m)

The seepage rates are plotted in Fig. 4.24b. The analytical expression and numerical model data show exceptional agreement. The flume data also correlate well with the analytical solution, yielding a regression coefficient  $R^2=0.96$ . The scatter in the flume data are attributed to experimental inaccuracies (measurement errors, changes in water level, and uneven compaction resulting in heterogenous hydraulic conditions).

##### Flume Test 2

The homogeneous soil profile of Fig. 4.23a is replaced with a stratified profile (Table 4.3, Fig. 4.23b, Table A4.1). The flow system is modelled numerically, and the results are compared with the flume data (Appendix Table A4.4 and Table A4.5). The finite-difference parameters used in the numerical simulation are given in Table 4.5.



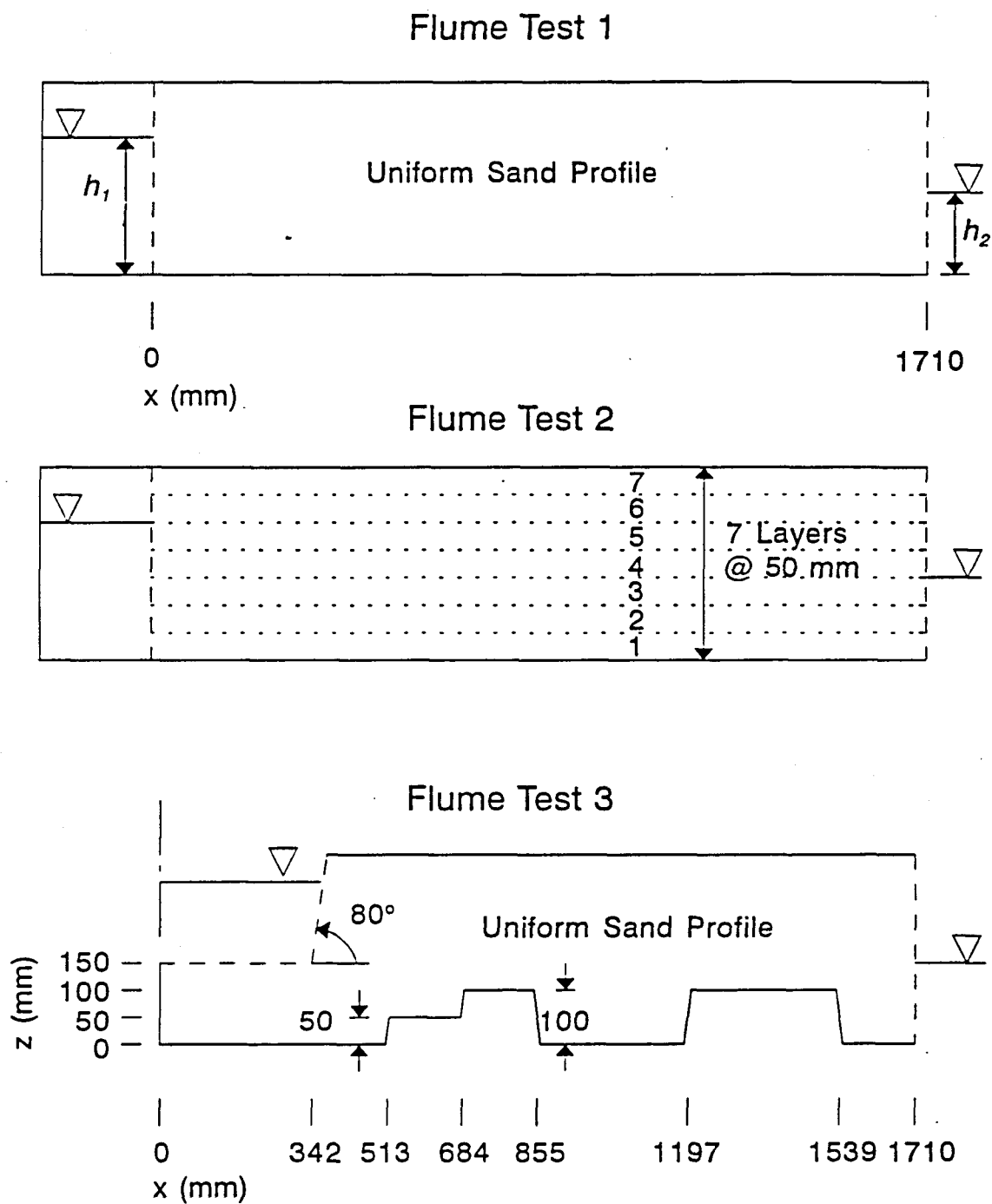


**Figure 4.23** Boundary configurations and soil-hydraulic conditions for the flume tests in Table 4.3.

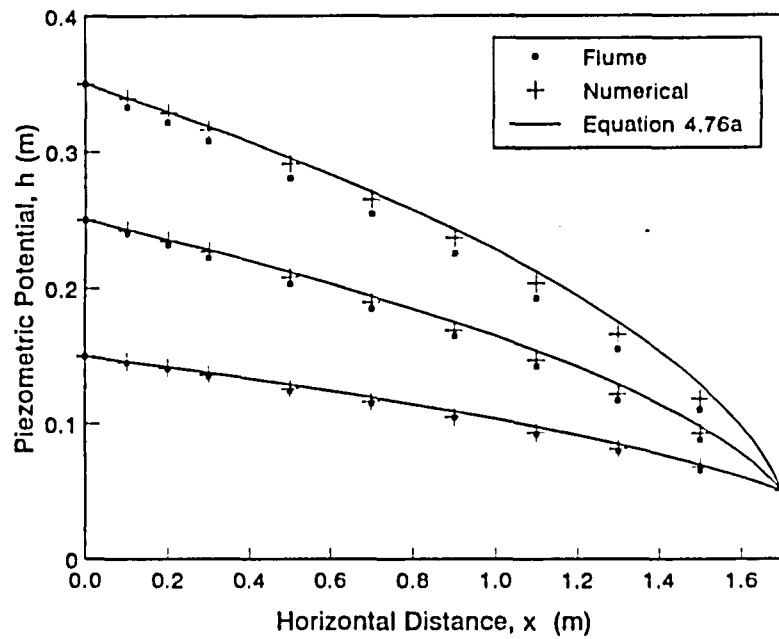


Figure 4.24a Experimentally, numerically and analytically determined piezometric potentials for flume test 1.

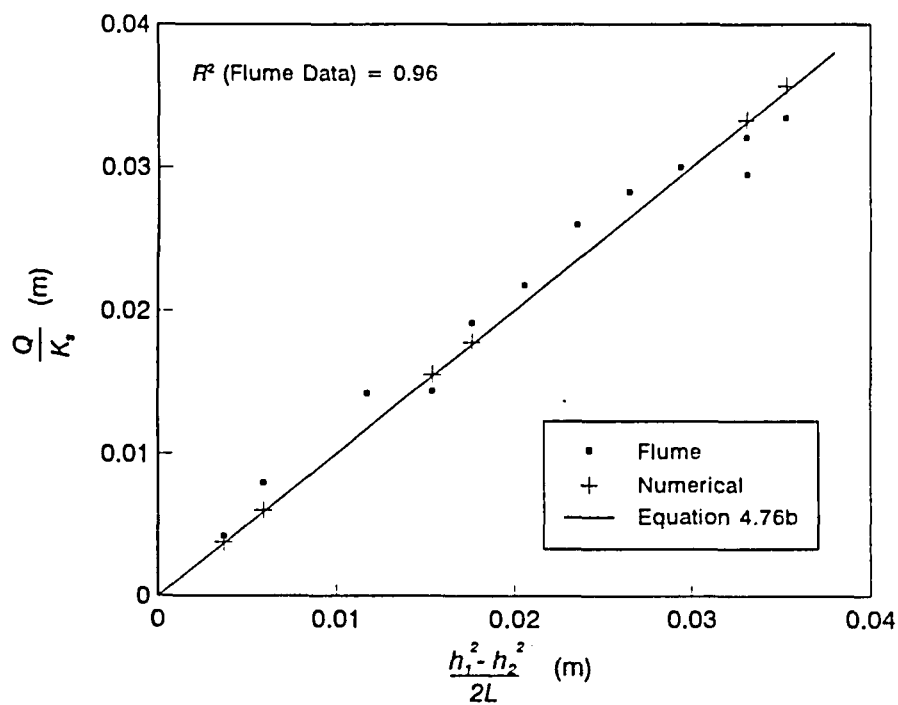
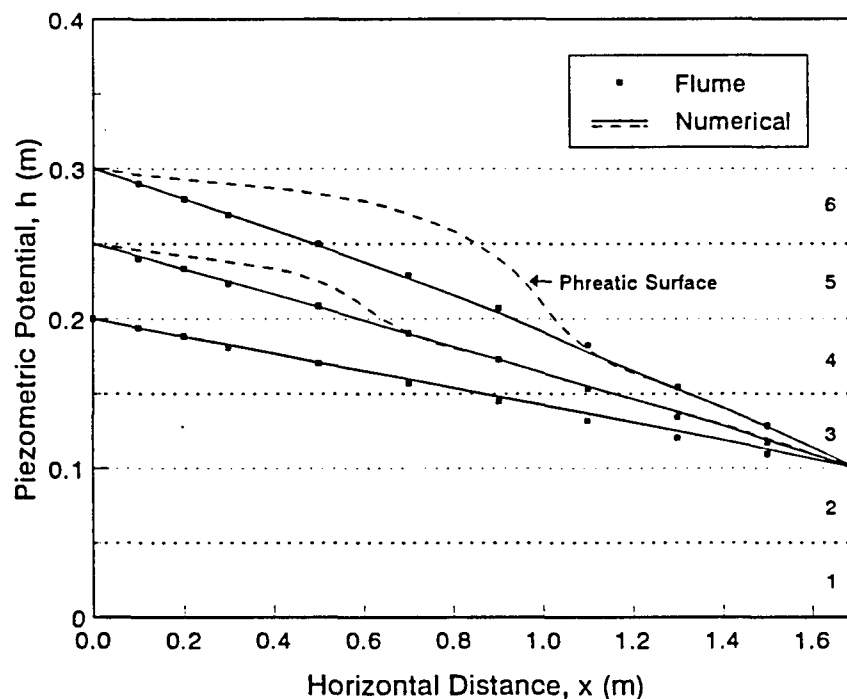


Figure 4.24b Experimentally, numerically and analytically determined seepage rates for flume test 1.

**Table 4.5** Finite-difference parameter values

$\Delta x$ (m)	=	0.10 (0.0 to 0.3)
	=	0.20 (0.3 to 1.7)
$\Delta z$ (m)	=	0.049 (0.0 to 0.049)
	=	0.001 (0.049 + 0.05n to 0.051 + 0.05n); n = 0,1,2,3
	=	0.049 (0.051 + 0.05n to 0.099 + 0.05n); n = 0,1,2,3

The piezometric potentials (as determined experimentally and numerically) and phreatic surface profiles (determined numerically) are plotted in Fig. 4.25. The potentials correlate well, showing an approximately linear reduction along the length of the flume, resembling a confined flow system. This is a consequence of the high relative hydraulic conductivity of layer 2 (Fig. 4.23b, Table A4.1), which accounts for 76% and 89% of the total seepage at the inflow and outflow boundaries respectively, when  $h_i = 0.25$  m. The effect of the low relative hydraulic conductivity of layer 4 (Fig. 4.23b, Table A4.1) is to increase the vertical flow gradients across the layer. This is illustrated in Fig. 4.25 by the difference between the numerically determined piezometric potentials and phreatic surface profiles for stage (inflow) levels greater than 0.20 m.



**Figure 4.25** Experimentally and numerically determined piezometric potentials for flume test 2.

The measured and modelled seepage rates are given in Table 4.6. The flows predicted numerically are approximately 10% higher than the measured values. This suggests that the hydraulic conductivity of the profile, particularly layer 2 which contributes the most flow, is overestimated.

The structure of fluvial sediments may be highly variable (Reading, 1986), reflecting the ensuing processes of erosion and deposition that results from changes in the flow discharge and sediment regime in rivers. The experimental stratified profile illustrates the significant effects layering may have on the distribution of groundwater potential, phreatic surface profiles and seepage rates.

**Table 4.6 Seepage rates**

$h_1$ (m)	$h_2$ (m)	Seepage Rate (ml/min)		Error (%)
		Flume	Numerical	
0.30	0.10	1592	1768	10
0.25	0.10	1081	1173	8
0.20	0.10	676	770	12
0.15	0.10	335	374	10

### *Trapezoidal Channel*

#### Flume Test 3

A trapezoidal channel cross-section and irregular flow boundaries were constructed in the sand flume with a uniform sand profile (Fig. 4.23c). The flow system is modelled numerically using the finite-difference parameter values in Table 4.7, and the measured and modelled seepage rates are given in Table 4.8. The experimental and numerical rates compare well, with an average error of 8%.

**Table 4.7 Finite-difference parameter values**

$\Delta x$ (m)	=	0.086 (0.000 to 0.342)
	=	0.008 (0.342 to 0.376)
	=	0.137 (0.376 to 0.513)
	=	0.171 (0.513 to 1.700)
$\Delta z$ (m)	=	0.050 (0.000 to 0.350)

**Table 4.8 Seepage rates**

$h_1$ (m)	$h_2$ (m)	Seepage Rate (ml/min)		Error (%)
		Flume	Numerical	
0.20	0.10	341	350	+3
0.20	0.15	317	275	-13
0.15	0.10	247	262	+6
0.15	0.15	198	182	-8
0.10	0.10	124	139	+12

The system is also modelled numerically with a horizontal flume base,  $h_1 = 0.20$  m and  $h_2 = 0.15$  m. The increased sectional flow area reduces the phreatic surface elevation by up to 0.011 m and increases the seepage rate by 50% to 412 ml/min (c.f. 275 ml/min in Table 4.8). Equation 4.77 gives an approximate seepage rate of 423 ml/min for a horizontal lower boundary (3% difference).

#### 4.2.2.3.1.2 Uniform Vertical Infiltration

Analytically and numerically determined phreatic surface profiles for the flow system illustrated Fig. 4.20 are computed for uniform infiltration rates of 0.5, 1 and 2 cm/day (Fig. 4.26). The physical and alluvial-hydraulic data used in the analysis are given in Table 4.10, and the numerical finite-difference parameters are listed in Table 4.9. In the numerical (saturated flow) model, infiltration is applied at the phreatic surface boundary.

**Table 4.9 Finite-difference parameter values**

$\Delta x$ (m)	=	1.0 (0 to 5.0)
	=	5.0 (5.0 to 10.0)
	=	10.0 (10.0 to 100.0)
$\Delta z$ (m)	=	0.25 (0 to 5.0)

The computed phreatic surface profiles agree well (Fig. 4.26), with the numerical model predicting a marginally elevated profile. The higher profile results from larger relative vertical flow gradients that arise with an increased rate of infiltration.

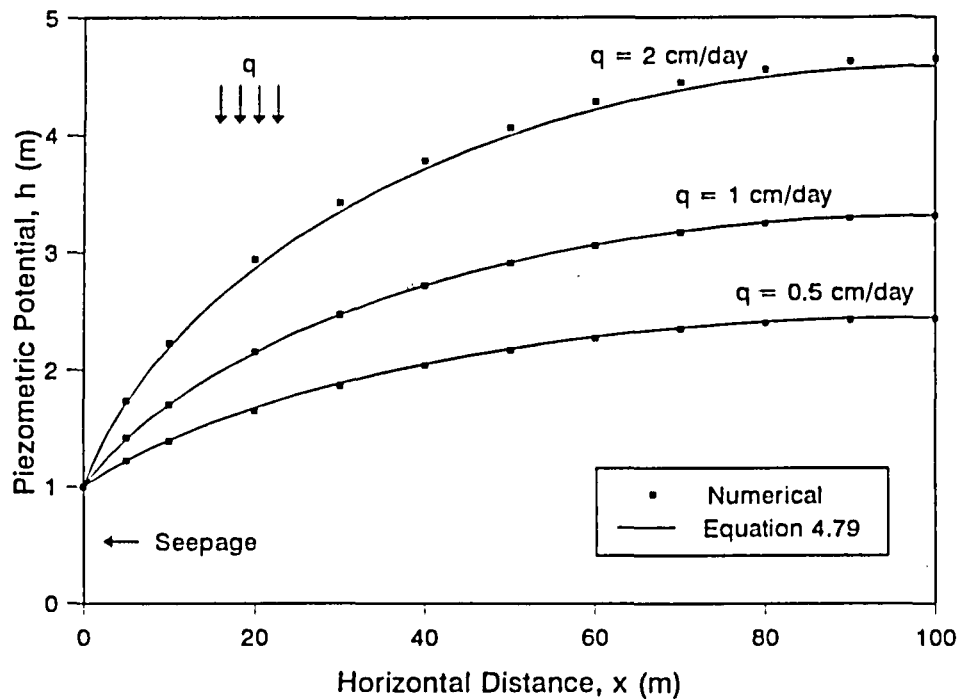


Figure 4.26 Analytically and numerically determined phreatic surface profiles for uniform vertical infiltration.

#### 4.2.2.3.2 Transient Conditions

Validation of the saturated two-dimensional vertical flow model developed in 4.1.1.2 is addressed by comparing solutions with the analytical linear model of Cooper and Rorabaugh (1963) and numerical one-dimensional model Hornberger *et al.* (1970). Symmetric stage hydrographs (equation 4.80,  $\delta = 0$ ) are prescribed; the bank storage zone is homogeneous and isotropic and the flow system is confined laterally by an impervious boundary (Fig. 4.21). The phreatic surface profile is initially horizontal and at the stream stage level.

##### 4.2.2.3.2.1 Rectangular Channel Section

###### Small Relative Vertical Flow Gradients

The physical and alluvial-hydraulic characteristics, hydraulic data, and finite-difference parameters used in the validation are given in Tables 4.10, 4.11 and 4.12, respectively.

Table 4.10 Physical and alluvial data

Physical Characteristics
$L = 100 \text{ m}$
Alluvial-Hydraulic Data
$K_s = 10 \text{ m/day}$ $\theta_s = 0.35$ $\theta_r = 0.05$

Table 4.11 Hydraulic data

Parameter	Event 1	Event 2
$h_o$	1.0	1.0
$h_p$	1.5	3.0
$t_d$	10.0	10.0

where

$h_o$  is the initial stage (m)

$h_p$  is the peak stage (m)

$t_d$  is the duration of the flood wave (days)

Table 4.12 Finite-difference parameter values

Event	Numerical Model				
	Two-dimensional			Hornberger <i>et al.</i> (1970)	
	$\Delta t$ (day)	$\Delta x$ (m)	$\Delta z$ (m)	$\Delta t$ (day)	$\Delta x$ (m)
1	0.1	5.0	0.1	0.1	5.0
2	0.1	5.0	0.2	0.1	5.0

Bank seepage rates for event 1 in Table 4.11 are plotted in Fig. 4.27 using the dimensionless parameters (equations 4.84) proposed by Hornberger *et al.* (1970). The dimensionless stage hydrograph is plotted as an inset, and refers to ratio of river stage ( $h$ ) to initial stage ( $h_o$ ). The spatial distribution of total flow gradient and ratio of vertical to total flow gradient, produced with the two-dimensional model, are plotted in Fig. 4.28a and Fig. 4.28b, respectively, at  $t = 5.0$  days.

The seepage rates from the non-linear numerical models are almost identical, substantiating the validity of the DF approximations inherent in the one-dimensional model for the particular conditions (physical, alluvial and hydraulic) considered in the analysis. This is confirmed by the low

relative vertical flow gradients that arise during the event (Fig. 4.28b). The non-linear model of Cooper and Rorabaugh (1963) produces underestimates due to the approximation of constant transmissibility necessary to derive the analytical solution. Hornberger *et al.* (1970) demonstrate that the linear model produces acceptable results for peak to initial stage ratios of up to 1.5.

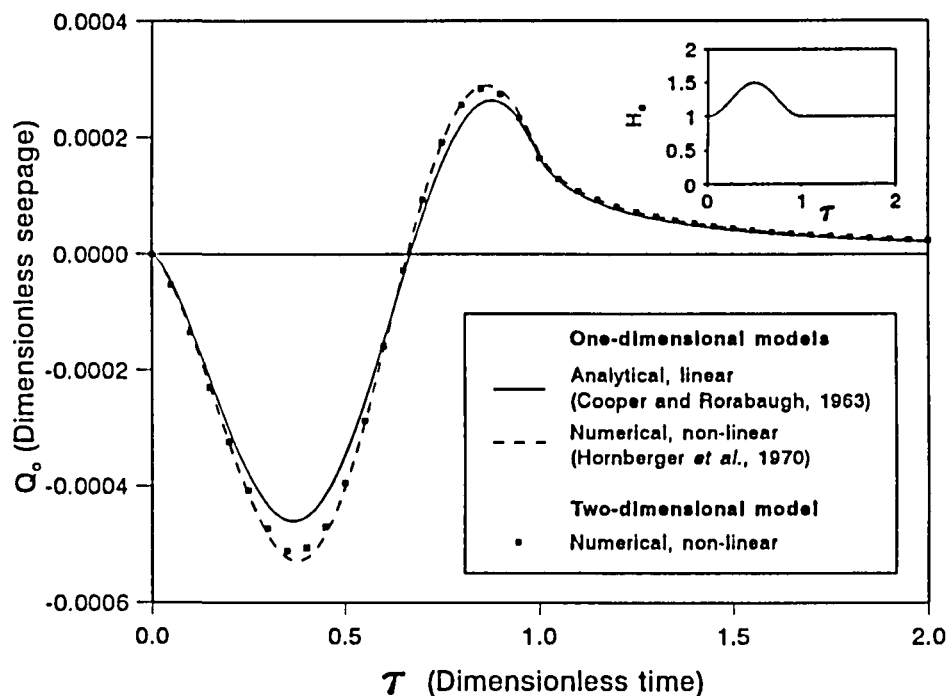


Figure 4.27 Bank seepage responses predicted analytically and numerically.

Sensitivity of the two-dimensional model to selection of finite-difference parameters is assessed using the event 1 hydrological data (Table 4.11). The finite-difference parameters used in the analysis are given in Table 4.13, and the results are plotted in Fig. 4.29 using bank storage responses for ease of comparison.

For the one-dimensional model of Hornberger *et al.* (1970), no discernable improvement in accuracy was noted to be achieved by further reducing the finite-difference parameter values given in Table 4.13. The one-dimensional numerical model may be used in the comparative analysis since the contribution of vertical flow has been shown to be small (Fig. 4.28). Nevertheless, the sensitivity to selection of the discrete vertical dimension,  $\Delta z$ , needs to be addressed. This is because the one-dimensional non-linear model uses a continuous lateral variation of pressure potential (or flow depth) to compute transmissibility, whereas the two-dimensional model uses a spatial flow depth approximation.



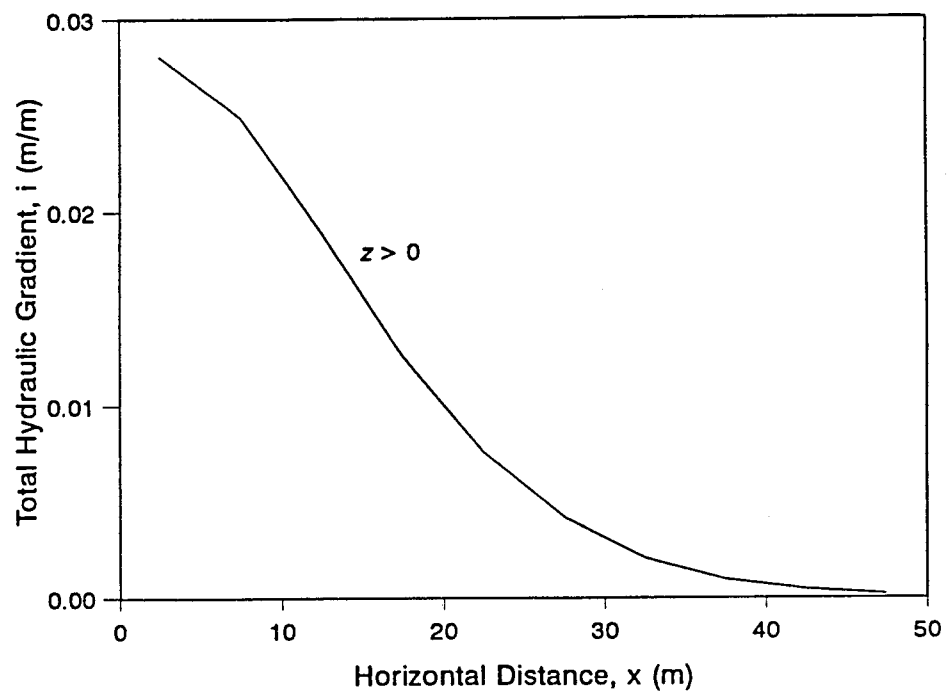


Figure 4.28a Spatial distribution of total flow gradient at  $t = 5.0$  days.

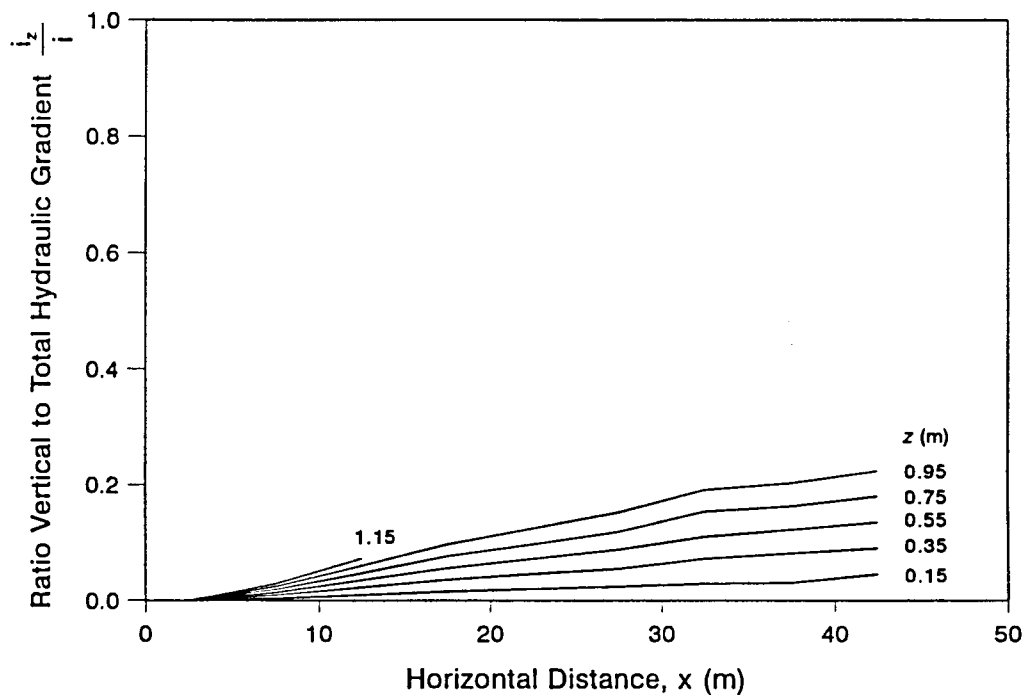


Figure 4.28b Spatial distribution of the ratio vertical to total flow gradient at  $t = 5.0$  days.

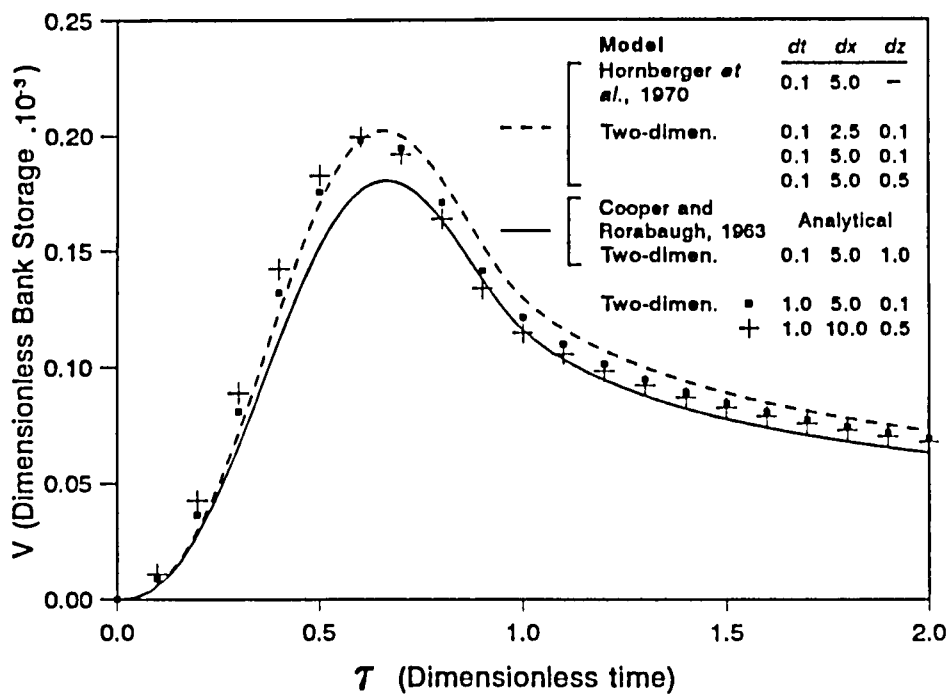


Figure 4.29 Sensitivity of bank storage to the selection of finite-difference spatial and temporal parameter values.

Table 4.13 Finite-difference parameter values

Numerical Model				
Two-dimensional			Hornberger <i>et al.</i> (1970)	
$\Delta t$ (day)	$\Delta x$ (m)	$\Delta z$ (m)	$\Delta t$ (day)	$\Delta x$ (m)
0.1	2.5	0.1	0.1	5.0
0.1	5.0	0.1		
0.1	5.0	0.5		
0.1	5.0	1.0		
1.0	5.0	0.1		
1.0	10.0	0.5		

For  $\Delta t = 0.1$  day,  $\Delta x \leq 5.0$  m and  $\Delta z \leq 0.1$  day, the two-dimensional model produces results that are practically indistinguishable from the one-dimensional numerical model of Hornberger *et al.* (1970). As expected, increasing  $\Delta z$  to 1.0 m produces results equivalent to those of the linear analytical model of Cooper and Rorabaugh (1963). This is due to the finite-difference flow depth approximation in the two-dimensional model being

equivalent to the constant transmissivity applied in the analytical solution. Increasing the time-step and spatial increments further results in the responses shown in Fig. 4.29.

With the exception of  $\Delta z = 1.0$  m (which was chosen to illustrate the significance of flow depth approximation), the results are fairly insensitive to the selected finite-difference parameters. This should however be verified for each particular flow system by choosing different finite-difference parameter values and assessing the modelled results.

#### Large Relative Vertical Flow Gradients

The hydraulic characteristics of the alluvium and hydrological data are modified to induce significant vertical flow gradients. The physical and alluvial-hydraulic characteristics, hydrological data and finite-difference parameter values used in the analysis are specified in Tables 4.14, 4.15 and 4.16, respectively.

**Table 4.14** Physical and alluvial data

<b>Physical Characteristics</b>
$L = 10$ m
<b>Alluvial-Hydraulic Data</b>
$K_s = 0.5$ m/day $\theta_s = 0.35$ $\theta_r = 0.05$

**Table 4.15** Hydraulic data

Parameter	Event 3
$h_o$	0.5
$h_p$	1.0
$t_d$	1.0

The results of the analysis are plotted in Fig. 4.30. The two-dimensional model predictions show larger deviations from the one-dimensional non-linear model results than previously noted (Fig. 4.27). This is due to the larger relative vertical flow gradients developed within the bank zone, illustrated by the spatial distribution of total flow gradient (Fig. 4.31a), and ratio of vertical to total flow gradient (Fig. 4.31b) at  $t = 0.5$  days.

Table 4.16 Finite-difference parameter values

Numerical Model				
Two-dimensional			Hornberger <i>et al.</i> (1970)	
$\Delta t$ (day)	$\Delta x$ (m)	$\Delta z$ (m)	$\Delta t$ (day)	$\Delta x$ (m)
0.01	0.1 (0.0 to 5.0) 0.5 (5.0 to 10.0)	0.1	0.01	0.1

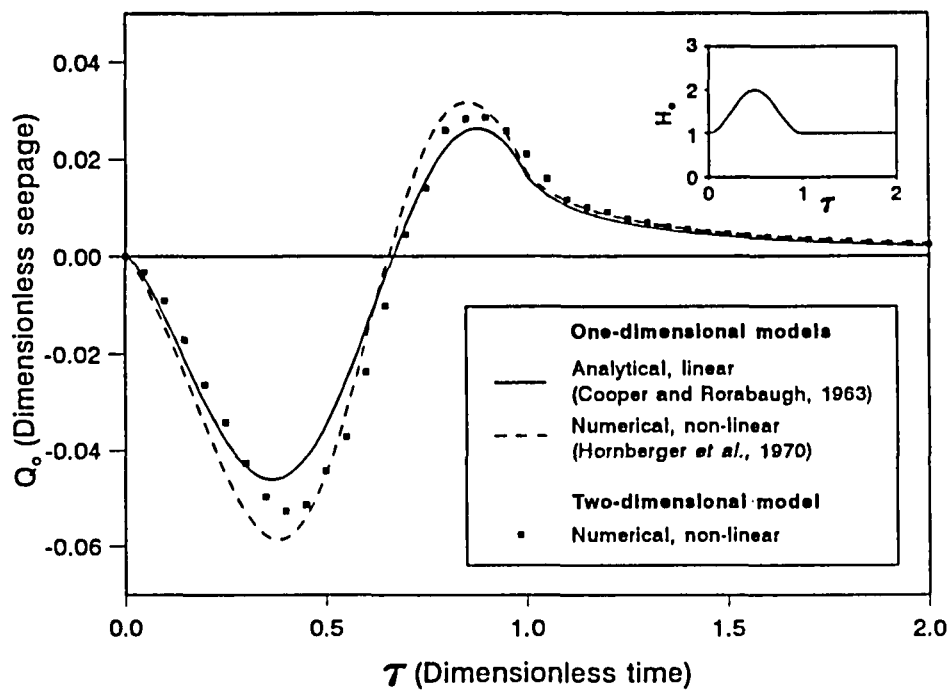


Figure 4.30 Bank seepage responses predicted analytically and numerically.

Sensitivity to selection of the vertical spatial increment  $\Delta z$  (Table 4.17) is assessed to elucidate the importance this parameter value in a flow system with significant vertical flow gradients. The time-step,  $\Delta t$ , and horizontal spatial increment,  $\Delta x$ , remain unchanged from the values given in Table 4.16. Reducing  $\Delta t$  and  $\Delta x$  further has been shown to produce no significant improvement in the accuracy of the solution.

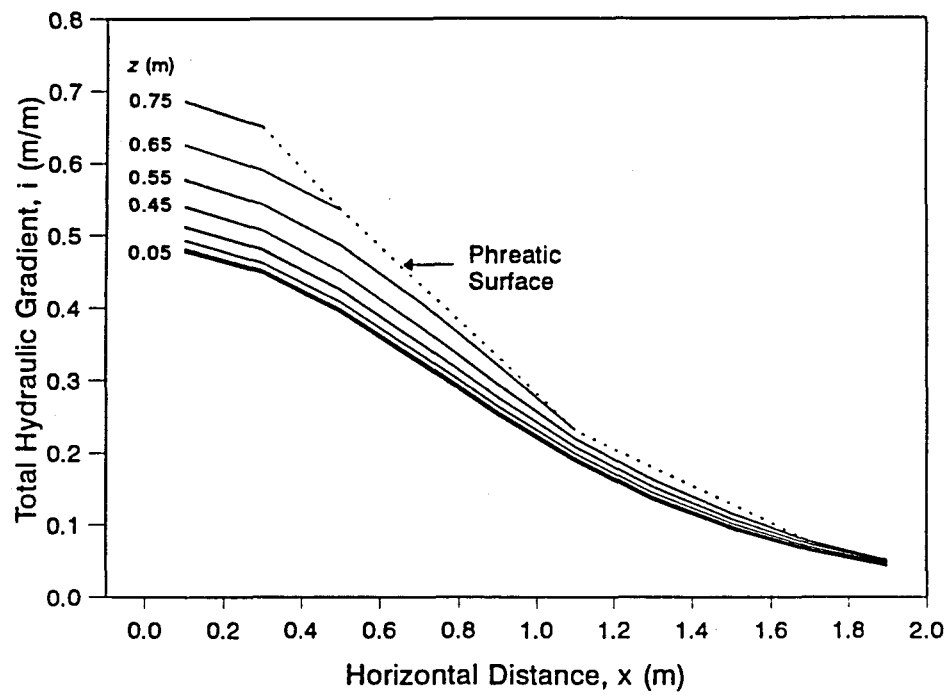


Figure 4.31a Spatial distribution of total flow gradient at  $t = 0.5$  days.

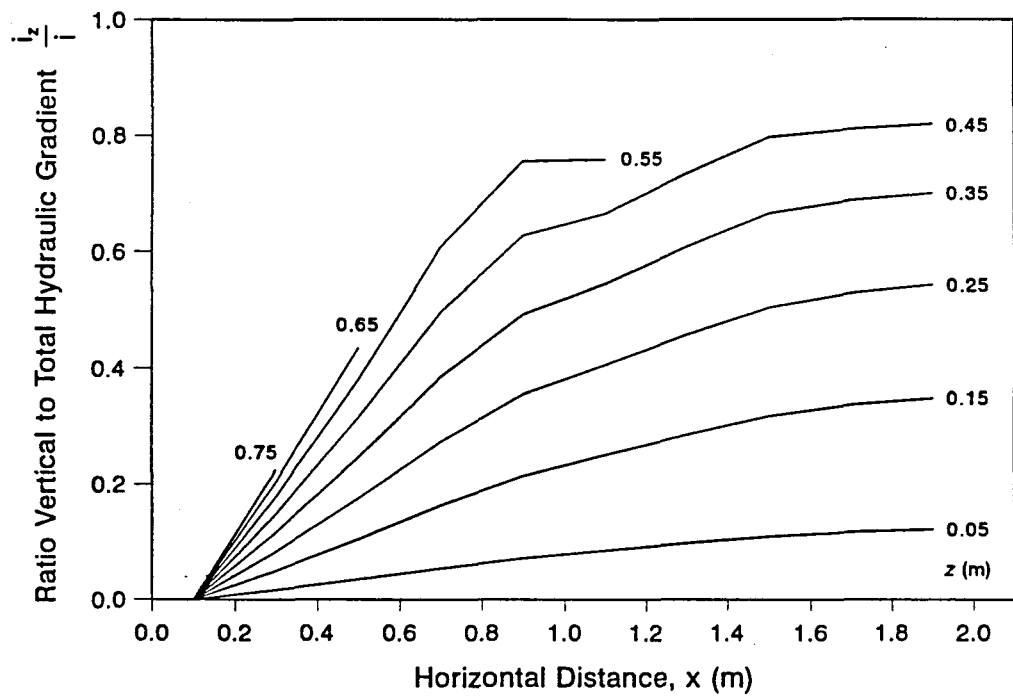
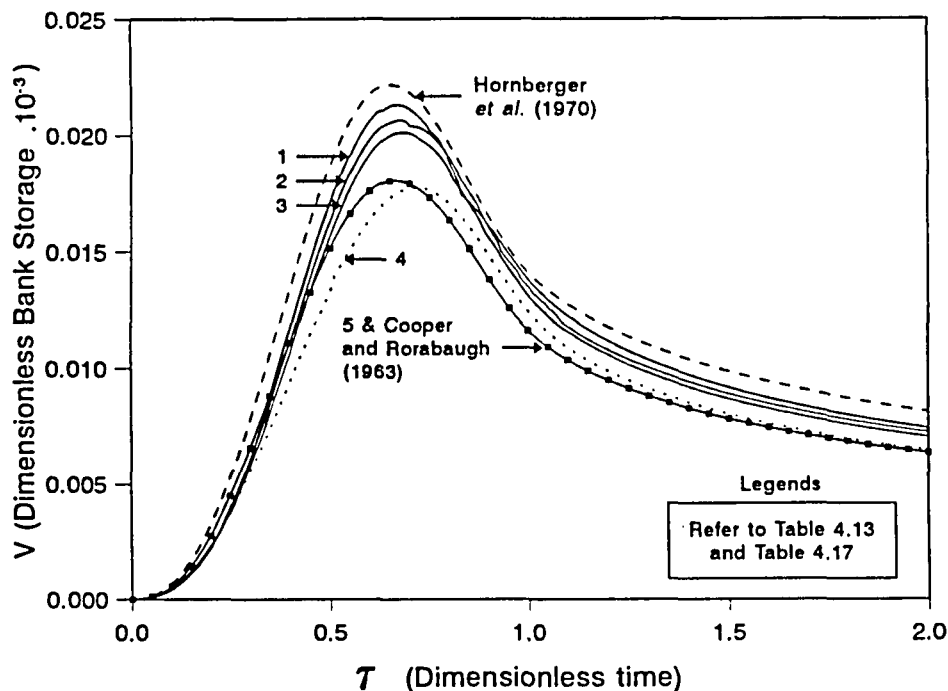


Figure 4.31b Spatial distribution of the ratio vertical to total flow gradient at  $t = 0.5$  days.

**Table 4.17** Finite-difference parameter values

Two-dimensional Model			
Sensitivity Analysis	$\Delta z$ (m)	$z$ range (m)	$K_z$ (m/day)
1	0.50	0.0 to 1.5	0.5
2	0.25	0.0 to 1.5	0.5
3	0.10	0.0 to 1.5	0.5
4	0.50	0.0 to 0.5	0.5
	1.00	0.5 to 1.5	
5	1.00	0.0 to 2.0	0.0

The results of the sensitivity analysis are plotted using temporal bank storage values (Fig. 4.32). Reducing  $\Delta z$  decreases the seepage rates, with bank storage volumes plotting progressively lower than the one-dimensional non-linear model results. The reduction in seepage rates and bank storage volumes are a consequence of the non-horizontal streamlines that arise with significant vertical flow gradients. For  $\tau > 0.4$ , the one-dimensional non-linear (numerical) and linear (analytical) models provide upper and lower bounds to the most accurate prediction of the change in storage volume by the two-dimensional numerical model.



**Figure 4.32** Sensitivity of bank storage to the selection of finite-difference spatial parameter values.

The results using the analysis 4 parameter values in Table 4.17 (Fig. 4.32) are compared with the analytical solution to determine the influence of modelling vertical flow distributions across two nodes and exercising confined flow conditions. Preventing vertical flow entirely (analysis 5, Table 4.17), whilst maintaining confined flow conditions, produces results equivalent those of the analytical linear model, as expected.

#### 4.2.2.3.2 Trapezoidal Channel Section

##### Large Relative Vertical Flow Gradients

The cross-sectional channel morphology is modified to a trapezoidal channel shape with the bed elevated above the horizontal impervious boundary (Fig. 4.33, Table 4.18). The hydrological event 3 data are used (Table 4.15), and the finite-difference parameters are given in Table 4.16.

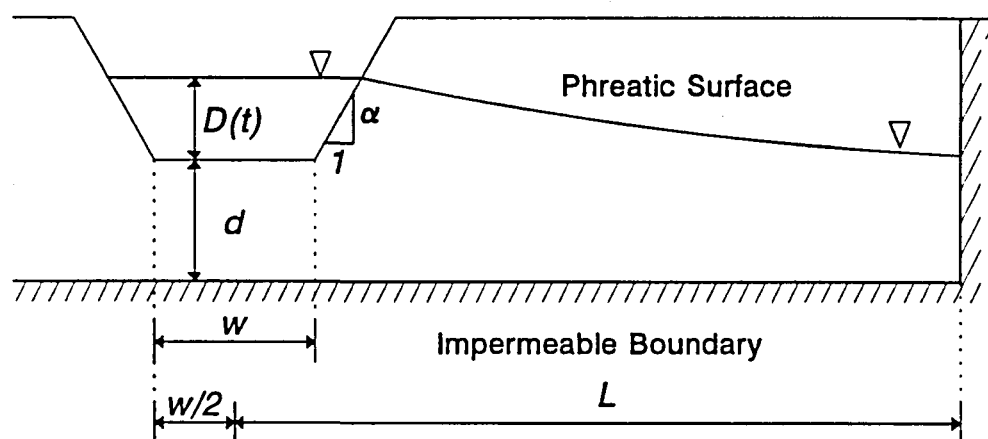


Figure 4.33 Cross-sectional bank geometry and boundary conditions.

The flow system is also modelled one-dimensionally assuming a rectangular channel extending to the impervious layer. The seepage rate and bank storage results are plotted in Fig. 4.34 and Fig. 4.35, respectively. For  $\tau < 1$ , the two-dimensional model results are significantly lower than the one-dimensional approximations. This illustrates the influence of cross-sectional geometry and the inaccuracies that may be introduced by assuming one-dimensional flow conditions.

**Table 4.18** Physical and alluvial data

Physical Characteristics
$w = 2 \text{ m}$ $\alpha = 1.0$ $d = 1.0 \text{ m}$ $L = 11 \text{ m}$
Alluvial-Hydraulic Data
$K_s = 0.5 \text{ m/day}$ $\theta_s = 0.35$ $\theta_r = 0.05$

The conditions under which it is appropriate to apply two-dimensional modelling depends not only on channel geometry and alluvial-hydraulic characteristics, but also on the interdependence between saturated hydraulic conductivity and the rate of change of river stage. This has been illustrated by modelling flow responses within different bank geometries using different alluvial-hydraulic characteristics and flow events

#### **4.2.3 Soil Water in the Unsaturated Zone**

Numerical models are widely used for predicting moisture movement in unsaturated soils (see Feddes *et al.*, 1988). Numerical models are, however, susceptible to convergence and mass balance problems (Srivastava and Yeh, 1991), and it is therefore desirable to test numerical model codes against analytical solutions. Analytical models describing unsaturated flow are difficult to obtain, however, because of the non-linear governing equation. Solutions have been developed, nevertheless, by applying the exponential hydraulic parameter model proposed by Gardner (1958), which allows the governing flow equation to be linearised. Analytical models are generally limited to steady-state semi-infinite flow systems (Srivastava and Yeh, 1991)

The numerical one-dimensional unsaturated model described in 4.1.2.2 has as its lower boundary condition a transient phreatic surface. Analytical models with this boundary condition are scarce or do not exist. Srivastava and Yeh (1991) developed analytical solutions to a linearised form of the one-dimensional unsaturated mass balance equation in homogeneous and two-layered profiles. Boundary conditions include constant vertical infiltration rate toward a steady phreatic surface positioned at the base of the profile. The model of Srivastava and Yeh (1991) is applied here to validate the numerical model code using analyses of drainage and wetting phenomena.



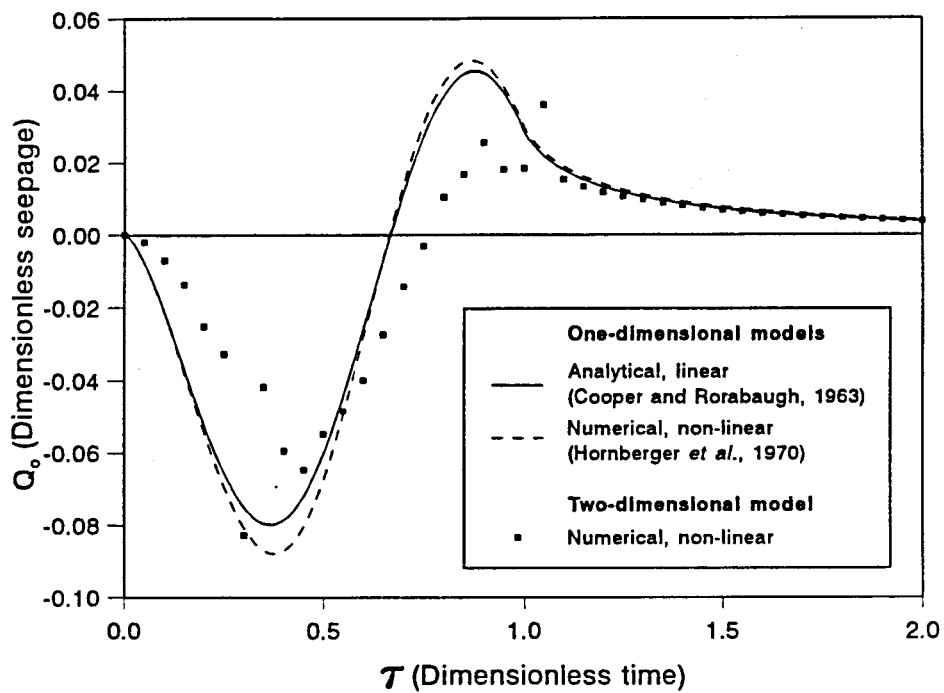


Figure 4.34 Bank seepage responses predicted analytically and numerically.

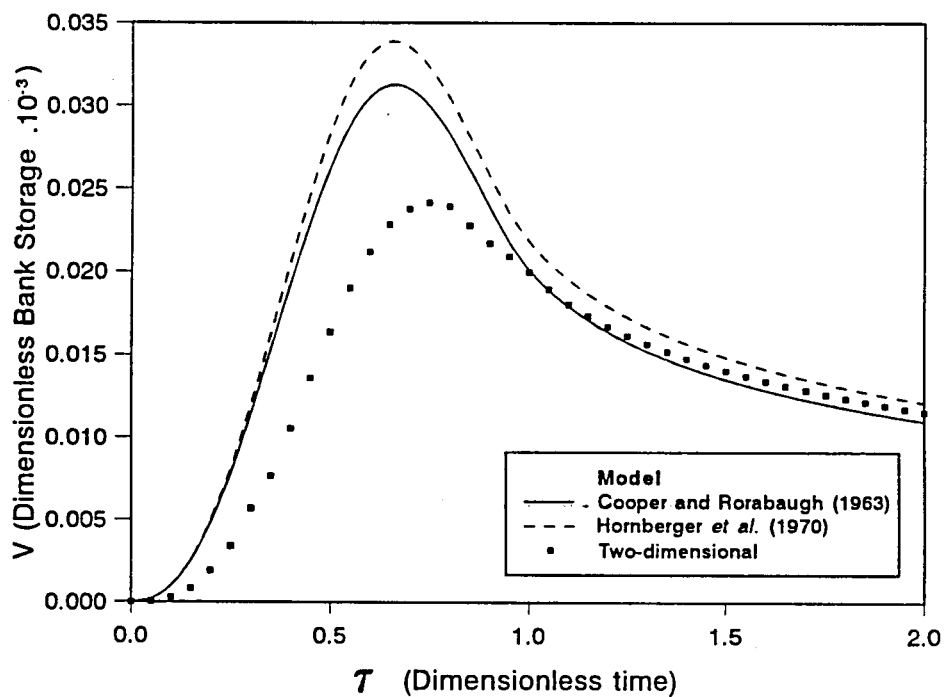


Figure 4.35 Bank storage responses predicted analytically and numerically.

#### 4.2.3.1 Analytical Model of Srivastava and Yeh (1991)

##### *Characterisation of Soil-Hydraulic Relationships*

Srivastava and Yeh (1991) describe the water retention and hydraulic conductivity relations using the following constitutive relations

$$\begin{aligned} K(\psi^*) &= K_s e^{\alpha \psi^*} \\ \theta &= \theta_r + (\theta_s - \theta_r) e^{\alpha \psi^*} \end{aligned} \quad 4.85$$

where  $\alpha$  is a soil pore-size distribution parameter

##### *Mass Balance Equation*

The relationships in equation 4.85 assume hydraulic conductivity varies linearly with water content, and do not accurately characterise soil-hydraulic relations near saturation. Nevertheless, they provide the means to derive useful comparative analytical solutions by linearising the one-dimensional mass balance equation 4.60, to give

$$\frac{\partial^2 K_s}{\partial z_s^2} + \alpha \frac{\partial K_s}{\partial z_s} = \alpha \frac{(\theta_s - \theta_r)}{K_s} \frac{\partial K_s}{\partial t_s} \quad 4.86$$

where  $K_s = K(\psi^*)$

##### *Solution Scheme*

For the case of a homogeneous profile, Srivastava and Yeh (1991) nondimensionlise equation 4.86, using the following dimensionless parameters

$$z = \alpha z_s$$

$$K = \frac{K_s}{K_s}$$

$$q_A = \frac{q_A^*}{K_s}, \quad q_B = \frac{q_B^*}{K_s}$$

$$t = \frac{\alpha K_s t_s}{\theta_s - \theta_r} \quad 4.87$$

where

$q_A$  is the initial flux at the soil surface (m/s)

$q_B$  is the flux at the soil surface for  $t > 0$  (m/s)

The dimensionless linear mass balance equation may then be written as

$$\frac{\partial^2 K}{\partial z^2} + \frac{\partial K}{\partial z} = \frac{\partial K}{\partial t} \quad 4.88$$

subject to the boundary and initial conditions

$$\begin{aligned} K_{z,0} &= q_A - (q_B - e^{a\psi_0})e^{-z} \\ K_{0,t} &= e^{a\psi_0} \\ \left[ \frac{\partial K}{\partial z} + K \right]_{z=L} &= q_B \end{aligned} \quad 4.89$$

where

$\psi_0$  is the pressure potential at the lower boundary  
( $\psi_0 = 0$  for phreatic surface boundary)

Solutions are derived by applying the residue theorem (Özisik, 1980) to the Laplace transformation of equation 4.91. The solutions for hydraulic conductivity and outflow at the phreatic surface are given in Appendix 4.3.

### Computations

The solution of equations 4.88 and 4.89 requires the sum of an infinite number of terms, which include the parameter  $\lambda_n$ , to be evaluated. The summation term (Appendix equations A4.4a and A4.4b) was found to converge fairly rapidly, permitting truncation of high order terms. The values of  $\lambda$  are given by the positive roots of the characteristic equation

$$\tan(\lambda L) + 2\lambda = 0 \quad 4.90$$

Srivastava and Yeh (1991) observed that equation 4.88 subject to the boundary conditions (equation in 4.89) converges well for a variety of problems analyzed, but convergence was found to be slow for certain cases at small times. Under these conditions, an alternative solution scheme to equation 4.88, subject to the conditions in equation 4.89, was proposed.

#### 4.2.3.2 Model Code Validation

##### 4.2.3.2.1 Soil-Hydraulic Characteristics

The soil-hydraulic data used in equation 4.89 are given in Table 4.19.

**Table 4.19** Soil-hydraulic data

$K_s = 1.0 \text{ cm/hr}$
$\theta_s = 0.35$
$\theta_r = 0.05$
$\alpha = 0.1 \text{ cm}^{-1}$

##### 4.2.3.2.1.1 Drainage from an Initially Saturated Profile

Drainage from an initially saturated 100 cm deep profile is modelled analytically (Srivastava and Yeh, 1991) and numerically (one-dimensional model described in 4.1.2.2). To generate an initially saturated profile, the initial infiltration rate at the soil surface ( $q_A$ ) is taken equal to the saturated hydraulic conductivity ( $K_s$ ). For  $t > 0$ , infiltration ceases, and a zero pressure potential is prescribed at the base of the profile. These boundary conditions are equivalent to an instantaneous drop in phreatic surface level.

The modelled soil water potentials and volumetric water content profiles are plotted in Figs. 4.36a and 4.36b, respectively. The analytical and numerical solutions agree exceptionally well at all times, with drainage having materially ceased after  $t = 100 \text{ hr}$ . The finite-difference parameters used in the numerical analysis are given in Table 4.20.

**Table 4.20** Finite-difference parameter values

$\Delta t = 0.167 \text{ hours}$
$\Delta z = 2.5 \text{ cm}$

Numerical sensitivity to selection of finite-difference temporal and spatial increments is assessed using the values of Table 4.21. The results are plotted in Figs. 4.37a and 4.37b, using outflow rate (flux) at the phreatic surface for ease of comparison. The numerical solution is relatively insensitive to changes in  $\Delta z$ , with under and overpredictions for  $t < 25 \text{ hr}$ , and  $25 \text{ hr} < t < 80 \text{ hr}$ , respectively. Increasing  $\Delta t$  beyond 1.0 hr results in more substantial overestimates for  $15 \text{ hr} < t < 80 \text{ hr}$ .

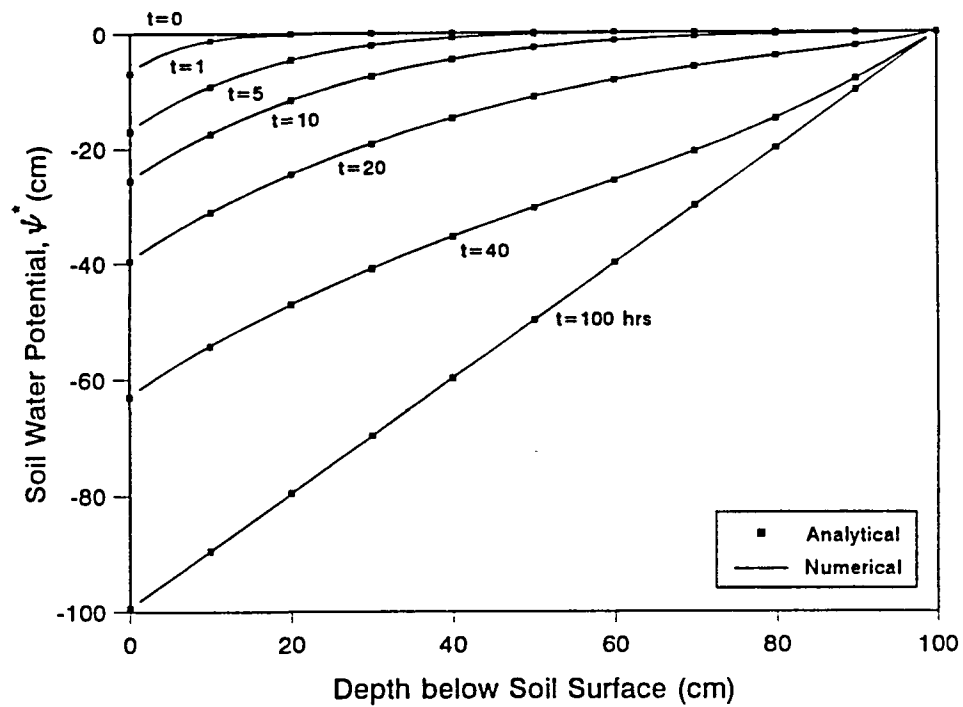


**Figure 4.36a** Temporal distribution of soil water potential predicted analytically and numerically for drainage from a soil column.

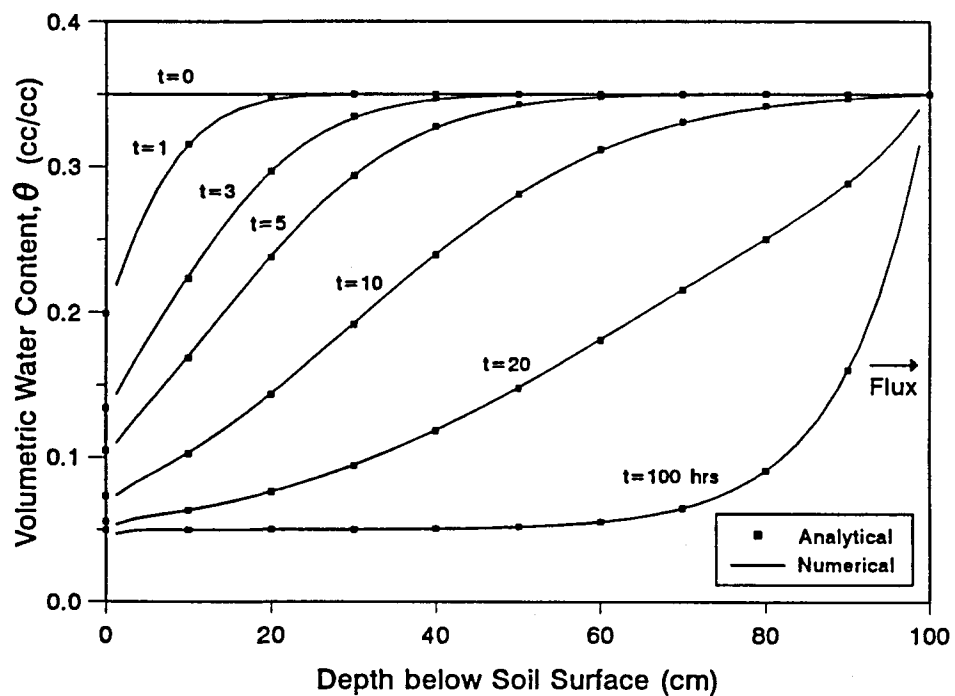


**Figure 4.36b** Temporal distribution of water content predicted analytically and numerically for drainage from a soil column.

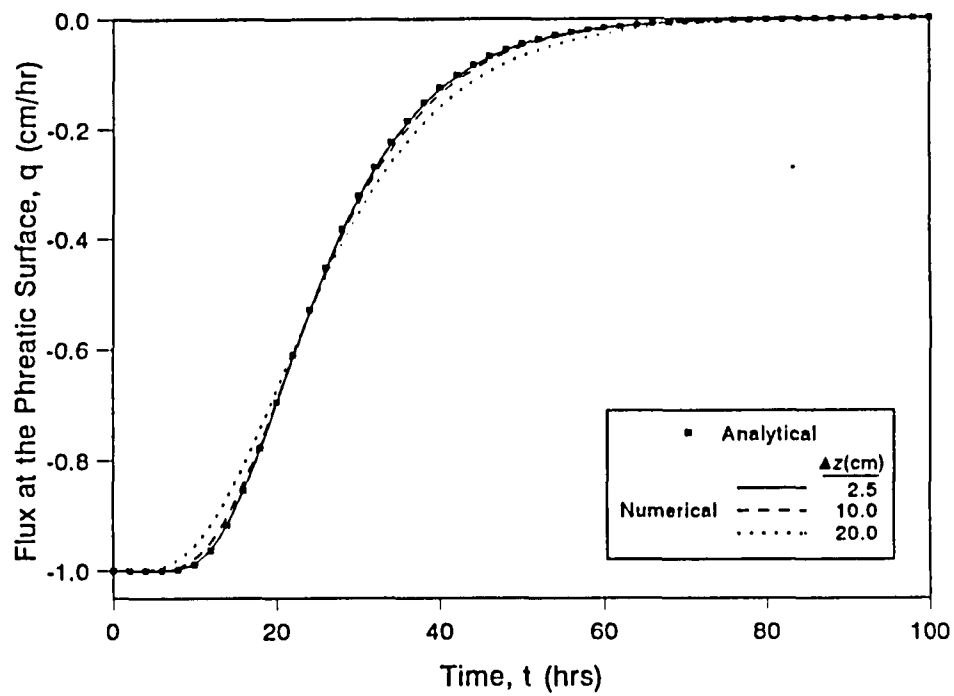


**Figure 4.37a** Sensitivity of outflow to selection of finite-difference spatial parameter values.

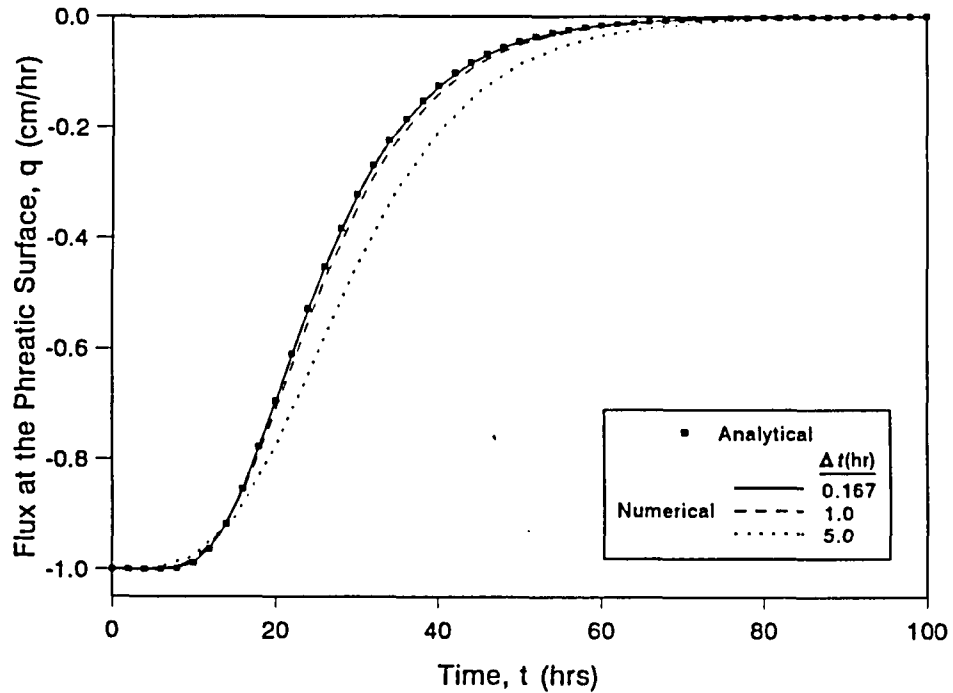


**Figure 4.37b** Sensitivity of outflow to selection of finite-difference temporal parameter values.

**Table 4.21** Finite-difference parameter values

$\Delta t$ (hour)	$\Delta z$ (cm)
0.167	2.5
0.167	10.0
0.167	20.0
1.0	2.5
5.0	2.5

#### **4.2.3.2.1.2 Steady Rate of Infiltration**

The progression of a wetting front is modelled using a constant infiltration rate ( $q_b = 0.5$  cm/hr). The profile is initially at equilibrium with the phreatic surface, which is positioned at a depth of 100 cm. The finite-difference parameter values used in the numerical analysis are as for the drainage from an initially saturated profile (Table 4.20).

The analytical and numerical solutions again compare exceptionally well at all times (Figs. 4.38 and 4.39), with equilibrium conditions materially re-established by  $t = 100$  hr.

#### **4.2.4 Coupled Saturated and Unsaturated Models**

Coupled saturated-unsaturated flow models such as the quasi two-dimensional model developed by Pikul *et al.* (1974), are rare. Saturated flow is most often treated as a special case of unsaturated flow, for which single equation models have been developed (e.g. Binley and Bevan (1992); Freeze (1972); and Verma and Brutsaert (1970)). The valuable of a coupled model is that it may readily be used to assess the contribution of flow in the unsaturated zone. This is achieved by applying the model separately for both saturated and coupled flow states.

Research is presently being directed to simultaneous solutions of two-dimensional horizontal saturated and one-dimensional vertical unsaturated models, to develop a quasi three-dimensional models (Zarandy, 1993). This approach alleviates the need to apply a full three-dimensional unsaturated flow model, conditional to the predominance of vertical flow in the unsaturated zone. The complexity of coupling models, however, lies in achieving flow continuity across the internal phreatic surface boundary. This linkage is complicated further when the vertical distribution of flow in the saturated zone is considered, since the spatial discretisation of a transient phreatic surface boundary is required.

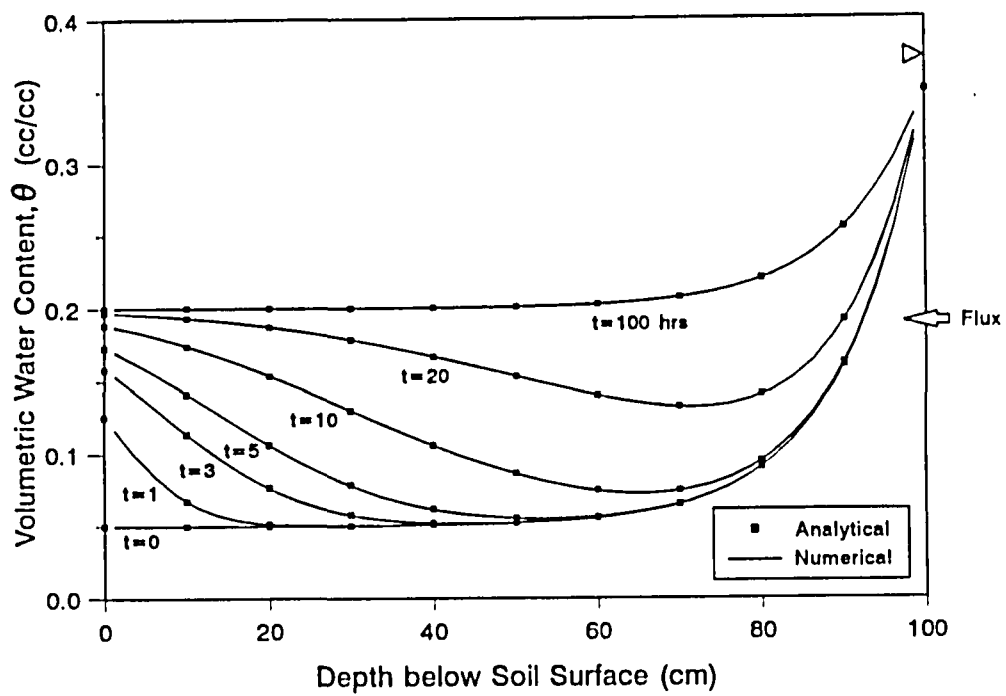


Figure 4.38 Temporal distribution of water content predicted analytically and numerically for infiltration into a soil column.

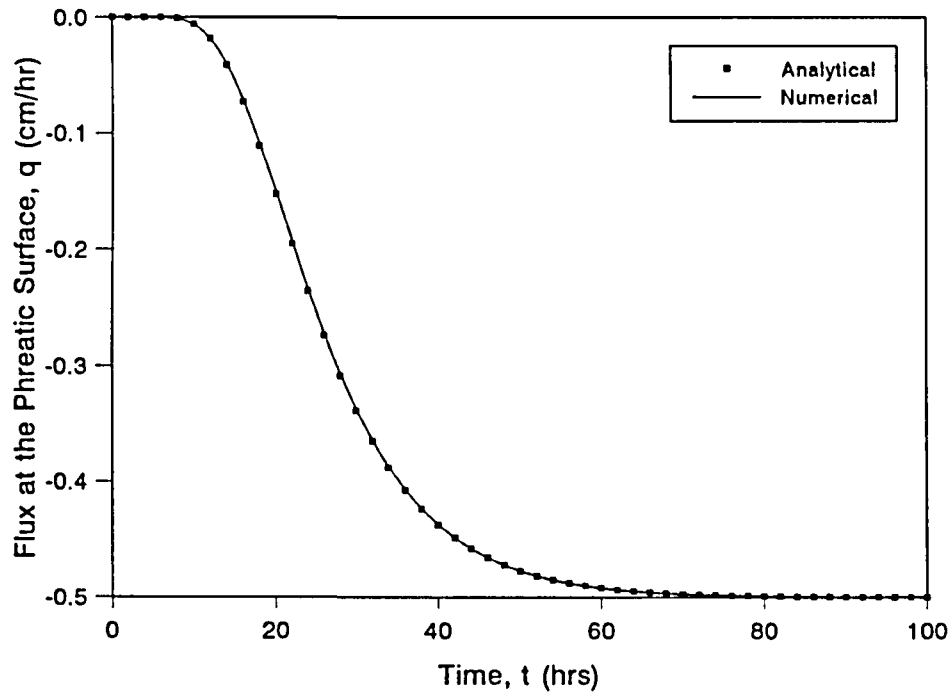


Figure 4.39 Outflow at the phreatic surface predicted analytically and numerically.



The coupled saturated-unsaturated model developed in 4.1 is used to obtain solutions for bank storage response to fluctuations of river stage, and results are compared with saturated model solutions presented in 4.2.2.3.2.

Unsaturated alluvial-hydraulic characteristics are characterised using the van Genuchten analytical soil water retention (equation 4.73) and hydraulic conductivity (equation 4.74) models.

#### 4.2.4.1 Rectangular Channel

##### Small Relative Vertical Flow Gradients

The physical and finite-difference parameter values used in the analysis are given in Tables 4.10 and 4.12, respectively. The effects on seepage rate and response of the phreatic surface of characteristically different water retention profiles are modelled (Table 4.22, Fig. 4.42 at  $\tau = 0$ ). The unsaturated hydraulic conductivity is synthesized using equation 4.74, with  $l = 0.5$ . The stage hydrograph described by event 2 data (Table 4.11) is routed past the channel section.

**Table 4.22** Alluvial-hydraulic data

Parameter	Profile 1	Profile 2
$K_s$ (m/day)	10	10
$\theta_s$	0.35	0.35
$\theta_r$	0.05	0.05
$\alpha$ ( $m^{-1}$ )	0.5	1.5
$n$	5.0	5.0
$m$ ( $1-1/n$ )	0.8	0.8
$l$	0.5	0.5

The seepage rates, phreatic surface and water content profiles ( $x = 5$  m) are plotted in Fig. 4.40, Fig. 4.41 and Fig. 4.42, respectively. The seepage rates predicted using profile 2 data are marginally lower than the two-dimensional saturated results, with profile 1 displaying larger reductions in flow rate. The phreatic surface elevations are generally slightly lower than those for the saturated flow model (Fig. 4.41). The water contents for both profiles adjust continuously to the fluctuating phreatic surfaces, demonstrated by the coincident equilibrium and modelled water content data at the peak phreatic surface elevations at  $\tau = 0.56$  (Fig. 4.42). The reduced seepage rates (Fig. 4.40) are attributed to decreased volumetric water uptake within the unsaturated zone, arising from changes in water content at the soil surface (Fig. 4.42), and are therefore more noticeable for the profile 1 data.

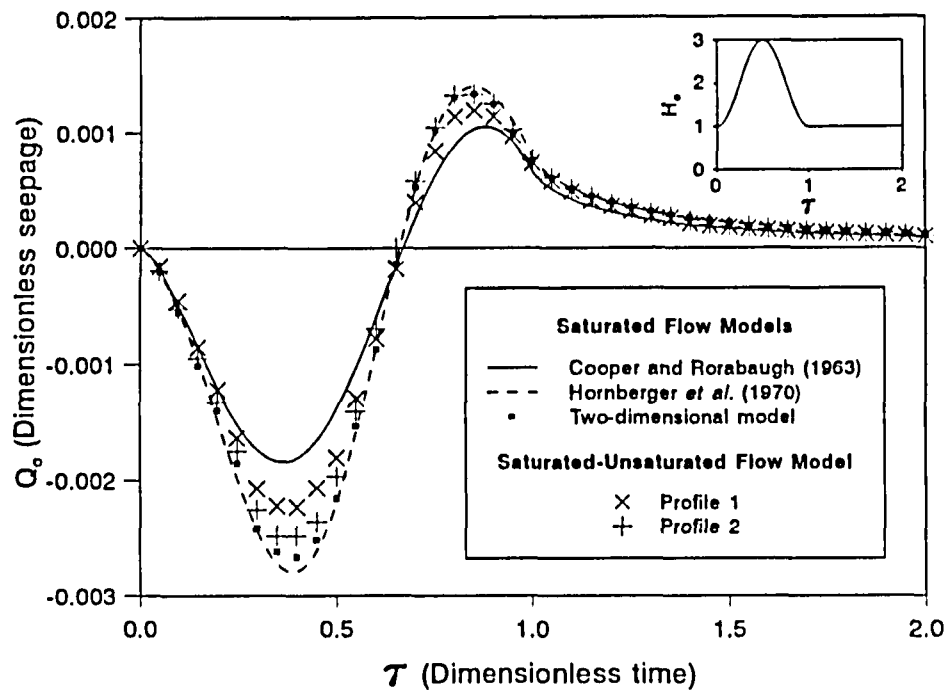


Figure 4.40 Bank seepage response predicted analytically and numerically.

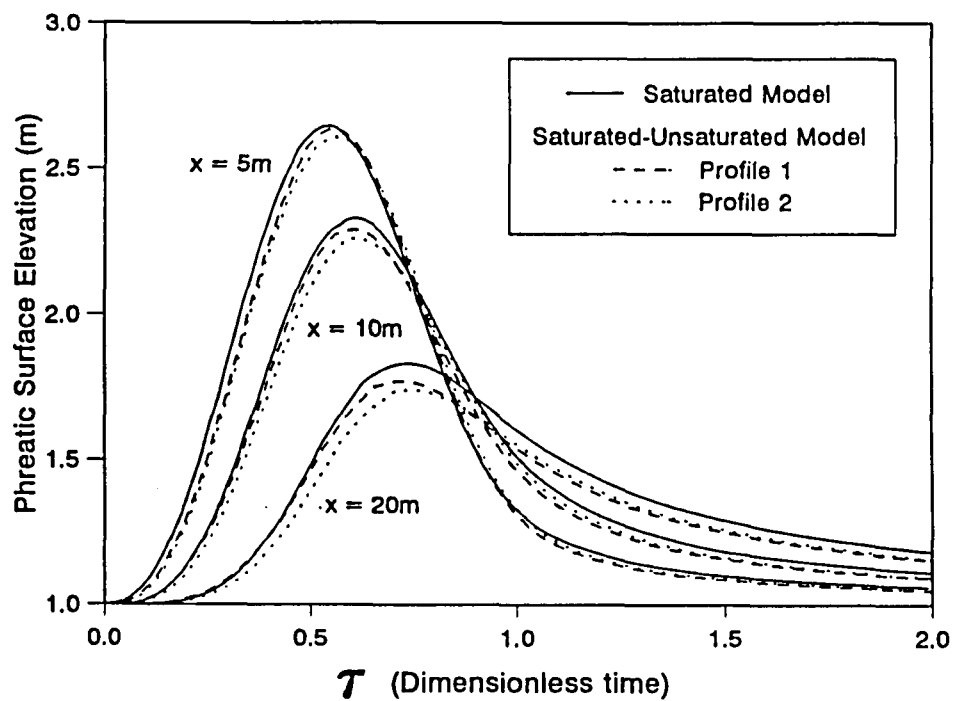


Figure 4.41 Phreatic surface responses predicted numerically.

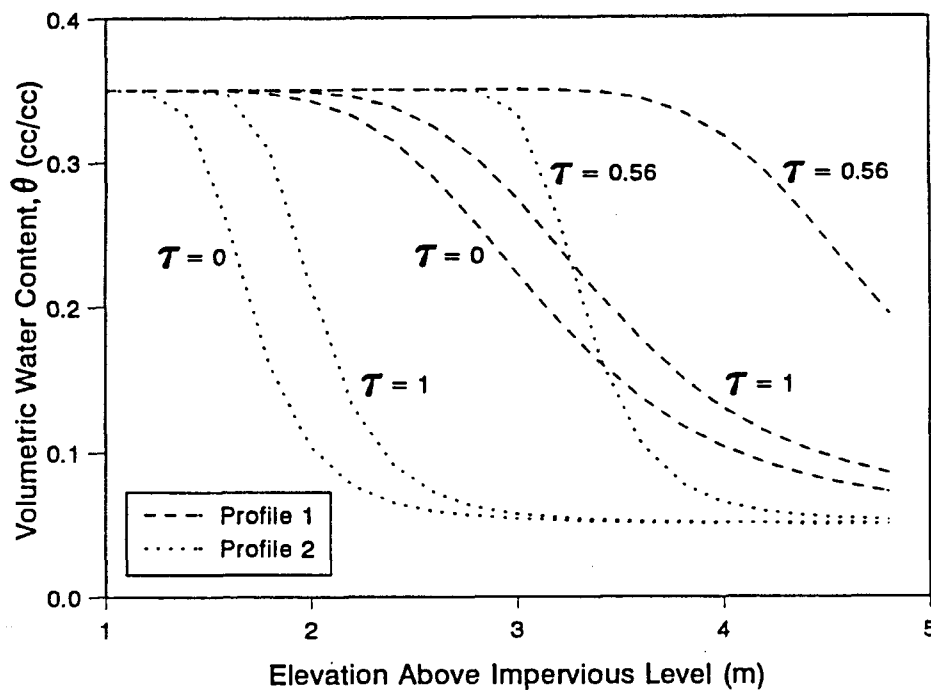


Figure 4.42 Water content profile responses predicted numerically.

#### Large Relative Vertical Flow Gradients

The bank storage response of Fig. 4.30 is analyzed using the coupled saturated-unsaturated solution, with the unsaturated alluvial-hydraulic parameters listed in Table 4.23.

Table 4.23 Alluvial-hydraulic data

$K_s = 0.5$ m/day
$\theta_s = 0.35$
$\theta_r = 0.05$
$\alpha = 2.0$ m <sup>-1</sup>
$n = 5.0$
$m = (1-1/n) = 0.8$
$l = 0.5$

Including unsaturated flow in the analysis reduces the predicted maximum seepage rates (Fig. 4.43) and phreatic surface levels (Fig. 4.44). The reasons for lower seepage rates are provided by an analysis of the temporal water content profiles (Fig. 4.45). During the rising stage, the water content profile is unable to generate a vertical translation of the initial equilibrium profile. The water content profile therefore becomes

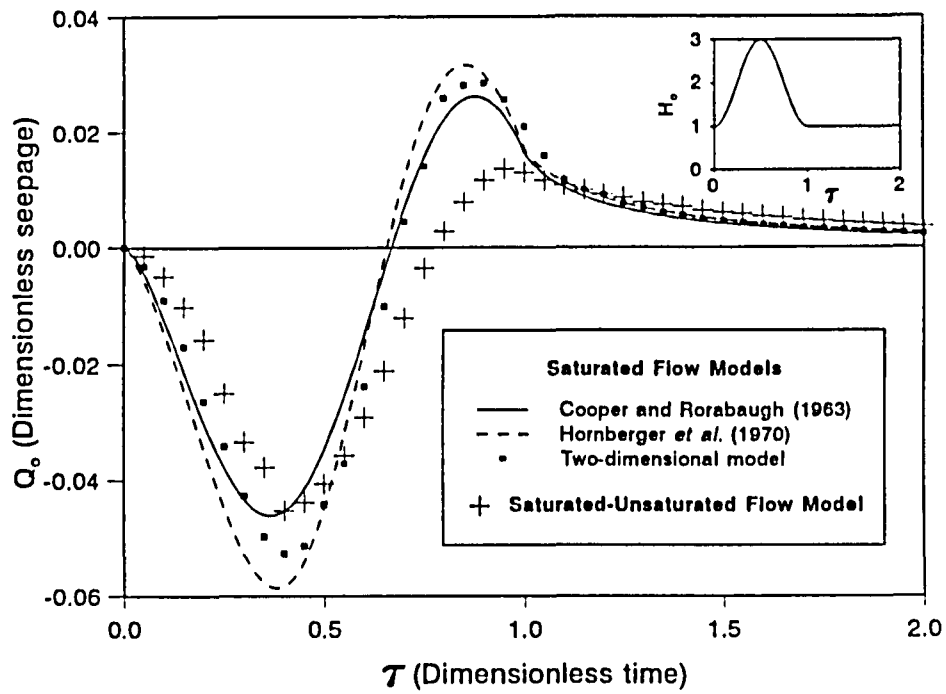


Figure 4.43 Bank seepage responses predicted numerically.

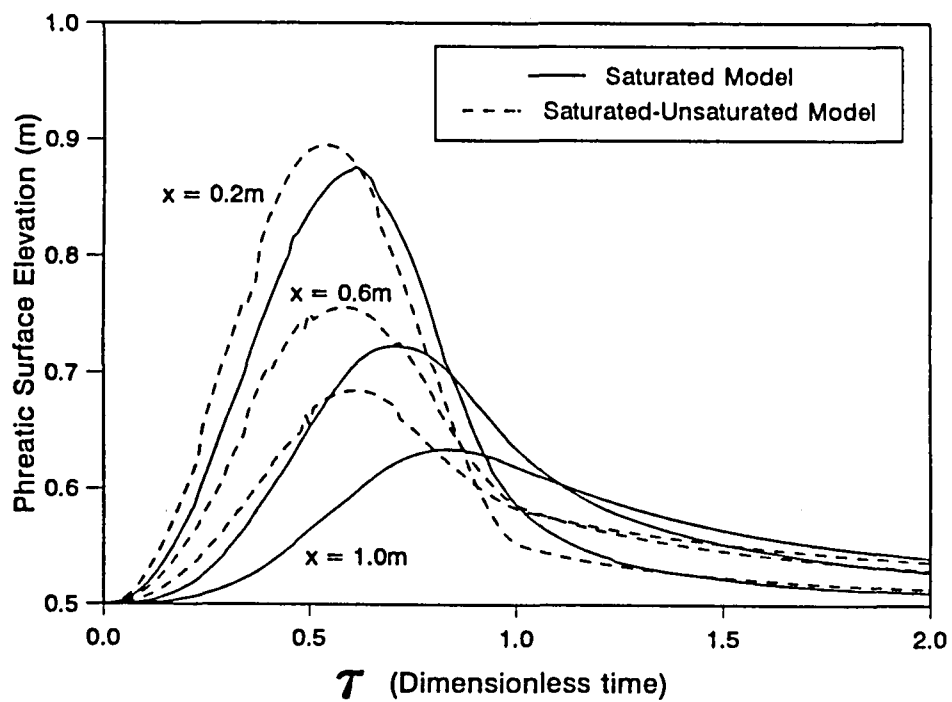


Figure 4.44 Phreatic surface responses predicted numerically.

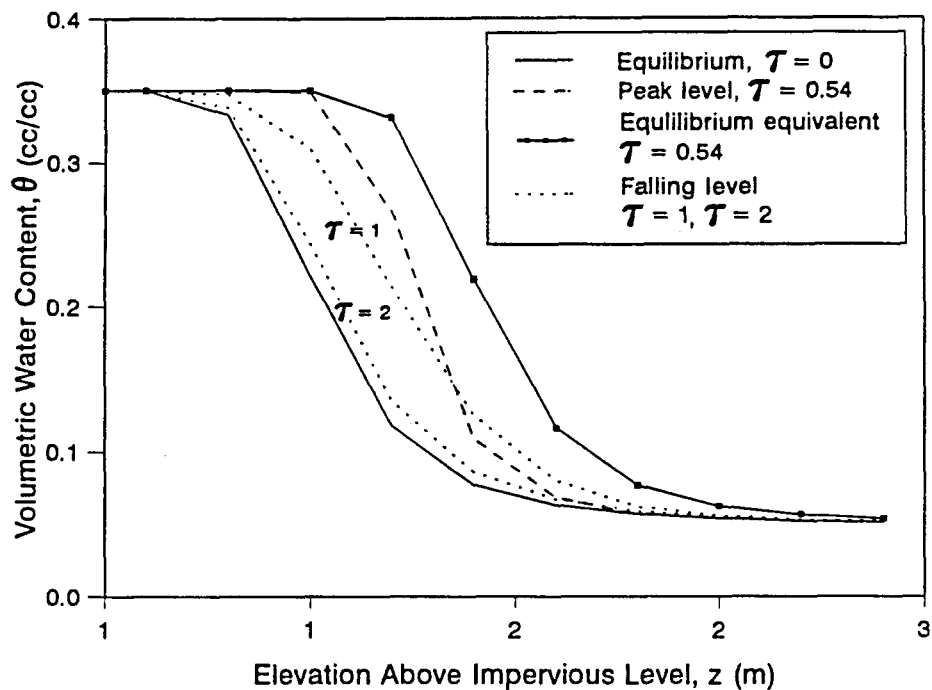


Figure 4.45 Water content profile responses predicted numerically.

compressed, as indicated by the profiles at  $\tau = 0$  and  $\tau = 0.54$ , and the phreatic surface rises more rapidly than for the saturated flow model. Capillarity continues to transmit soil moisture even after the phreatic surface has begun falling, as illustrated by the increased water contents for  $z > 1.8$  m and  $0.54 < \tau < 1.0$ . The water content profile therefore becomes extended, and the phreatic surface falls more rapidly than the saturated model equivalent. The non-equilibrium profiles result in decreased uptake and drainage of water, compared with translated equilibrium profiles, for rising and falling phreatic surface levels, respectively.

#### 4.2.4.2 Hulsart Well Data

Zucker *et al.* (1973) model the average annual phreatic surface response for the Hulsart well located near Old Bridge, New Jersey, using a one-dimensional saturated flow model. Pikul *et al.* (1974), apply a coupled quasi two-dimensional saturated-unsaturated (one-dimensional saturated horizontal model linked to one-dimensional unsaturated vertical models) model to the same problem and produce close correlation between modelled and measured hydrographs. The hydrograph is modelled here using the two-dimensional saturated vertical model, coupled to one-dimensional unsaturated vertical flow models.

The well is located 152.4 m from a stream in a 274.32 m wide watershed (Table 4.24). The stream stage is assumed constant (6.09 m), and the average monthly percolation (infiltration minus evapotranspiration) rates estimated by Pikul *et al.* (1974), are given in Table 4.25 and Fig. 4.46 (inset).

**Table 4.24** Hulsart watershed profile

Distance from Stream, $x$ (m)	Ground Level above Datum (m)
45.72	7.84
91.44	8.34
137.16	9.54
182.88	10.34
228.60	10.84
274.32	11.34

**Table 4.25** Percolation rates

Month	Percolation (cm/month)
November	5.77
December	9.30
January	9.88
February	7.62
March	9.09
April	5.11
May	0.86
June	0.00
July	0.00
August	0.00
September	0.00
October	0.00

The following soil-hydraulic models (adapted from Verma and Brutsaert (1970) are used in the analysis

$$\theta = (\theta_s - \theta_r) \left[ \frac{A}{A + \psi^B} \right] + \theta_r \quad 4.91$$

$$K = K_s \left[ \frac{A}{A + \psi^B} \right]^N$$

4.92

where  $A, B$  and  $N$  are soil specific parameters

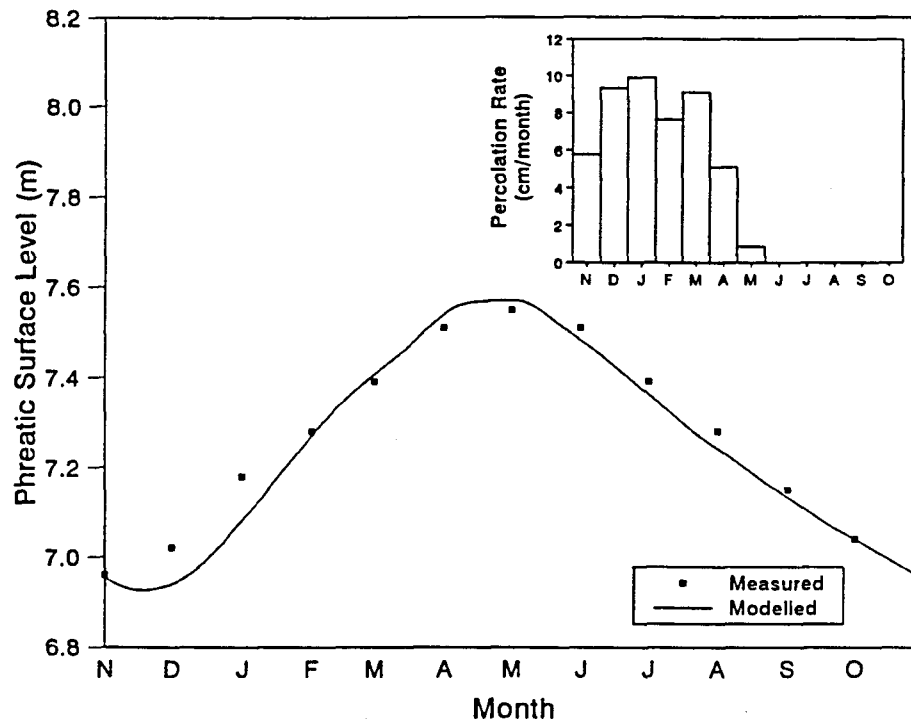


Figure 4.46 Measured and modelled phreatic surface responses at the Hulsart Well.

The soil-hydraulic data used by Zucker *et al.* (1973) and Pikul *et al.* (1974) to parameterise equation in 4.91 and 4.92 are given in Table 4.26. The finite-difference parameter values used in the analysis are given in Table 4.27.

Table 4.26 Soil-hydraulic data

$K_s = 0.349$ cm/min
$\theta_s = 0.451$
$\theta_r = 0.001$
$A = 40.0$ cm
$B = 1.00$
$N = 5.10$

**Table 4.27** Finite-difference parameter values

$\Delta t = 1$ day
$\Delta x = 45.72$ m
$\Delta z = 0.10$ m

The measured and modelled average annual hydrographs are plotted in Fig. 4.46. The quasi two-dimensional saturated-unsaturated modelled hydrograph correlates well with the measured data, but not as closely as the results of Pikul *et al.* (1974). Pikul *et al.* (1974) assume that the depth of the unsaturated zone is invariant, extending to the initially horizontal phreatic surface (6.09 m). This approximation is based on the low ratio of the total annual fluctuations (0.6 m at the Hulsart well) to the depth of the unsaturated zone (3.72 m at the Hulsart Well). The unsaturated drainage depths in the rigorously coupled model are significantly less (2.31 m to 2.91 m at the Hulsart well). It is then surprising that the rigorously coupled model presented here produces a lower minimum phreatic level with increased lag time, whereas the peak and timing are predicted equally well by both models. The differences between the model predictions may be attributed to the approximate saturated-unsaturated linkage applied in the model of Pikul *et al.* (1974).

### **4.3 Bank Storage Dynamics Model Verification**

#### **4.3.1 Scope**

The bank storage dynamics models developed in 4.1 are verified using field data collected at the site on the Sabie River, Kruger National Park (Chapter 2 Data Collection). Flows in the saturated and unsaturated zones are modelled separately. The justification for decoupling the models for this field verification arises from:

- The bank material at the study site is highly heterogeneous and stratified, and the spatial resolution of the data is not sufficient for spatially extensive unsaturated flow modelling. Adequate data was only collected at a single location (C3-4) to parameterise and verify the vertical unsaturated flow model.
- Vertical soil moisture movement in the unsaturated zone derived from infiltrated rainfall does not appear to influence the flow distribution in the saturated zone significantly. This is confirmed later in this chapter.

One-directional dependency between zones is assumed, with the saturated model providing the temporal variation of phreatic surface as boundary



condition to the unsaturated model.

#### **4.3.2 Saturated Flow**

The groundwater responses to fluctuations of river stage are modelled using the saturated flow models developed in 4.1.1. Extractions to support transpiration and percolation of infiltrated rainfall are not considered in the saturated flow analysis for the following reasons:

- The groundwater potential data show no measurable gradients arising from transpiration.
- Infiltrated rainfall over the period of data collection is shown to be extracted in the unsaturated zone by transpiration thereby preventing percolation to the saturated zone.

##### **4.3.2.1 Two-dimensional Vertical Model**

The use of a two-dimensional vertical model implies homogeneous conditions with distance downstream. This approximation may be acceptable for most situations, since longitudinal flows are likely to be less significant than lateral seepage arising from temporal river stage. The principal flow directions for surface-subsurface interaction are therefore considered to be in the lateral and vertical directions.

##### **4.3.2.1.1 Model Application**

The purpose of this application is to assess the performance of the two-dimensional saturated model when applied deterministically. The cross-sectional sediment surface and bedrock profiles are specified as pervious and impervious boundaries, respectively (Fig. 2.10). The bank zone is assumed to consist of uniform coarse textured sand, with  $K_s = 21.85$  m/hr and  $S_y = 0.34$  (Table 2.3 and Table 2.4). A sequence of river stage hydrographs are routed past the cross-section, and the response of groundwater potential is modelled using the finite-difference parameters values  $\Delta x = 6.25$  m;  $\Delta z = 0.20$  m and  $\Delta t = 1.0$  hr.

The modelled groundwater potential responses are compared with hydrographs monitored from 14 to 20 January 1995 at locations C1, C3L and C5L (Fig. 4.47). The general response (lag, attenuation and peak magnitudes) to the stage hydrograph sequence is satisfactorily predicted using the parameterisation data. The rate of rise and recession and peak levels, however, are underestimated at all monitored locations.

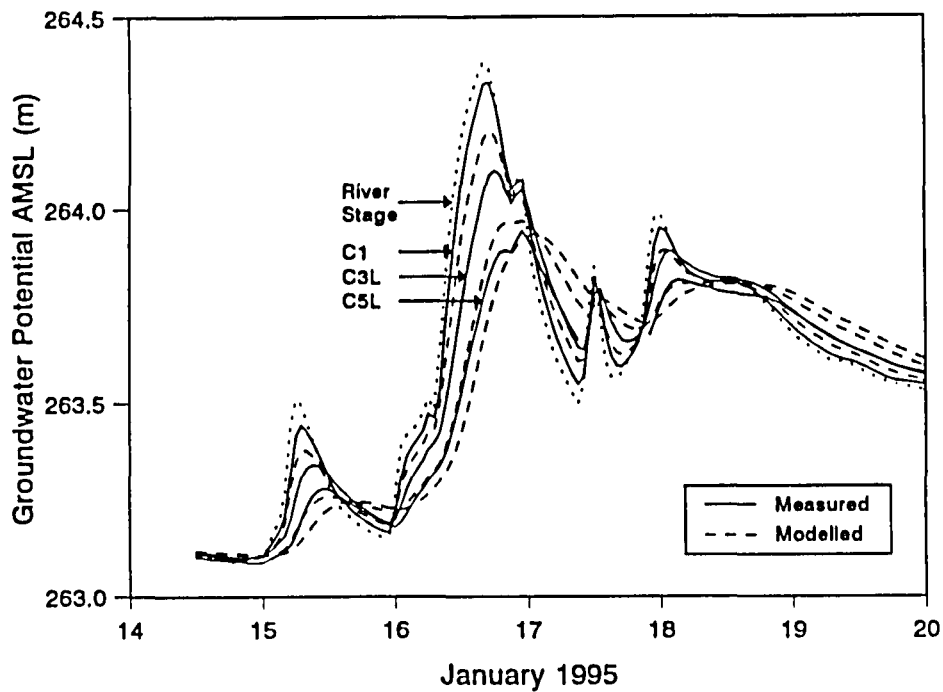


**Figure 4.47** Measured and modelled (two-dimensional deterministic) groundwater potential hydrographs.

#### 4.3.2.1.2 Model Calibration

The values and spatial distribution of alluvial-hydraulic parameters are calibrated to achieve improved response than that predicted assuming homogeneous conditions. The bank is divided into four uniform alluvial zones (refer to Fig. 2.10) with the parameter values in Table 4.28 obtained by trial and error.

**Table 4.28** Calibrated alluvial-hydraulic parameter values

$x$ (m)	$z$ (m)	$K_s$ (m/hr)	$S_y$
$x < 68$		40	0.34
$x > 68$	$z < 263$	8	0.34
$68 < x < 93$	$z > 263$	0.1	0.17
$x > 93$	$z > 263$	0.01	0.17

The improved groundwater potential responses achieved by calibrating the spatial distribution of alluvial-hydraulic conditions are illustrated in Fig. 4.48. The stratified deposit in the macro-channel infill provides a physical basis for reducing the bulk hydraulic conductivity and specific yield in this

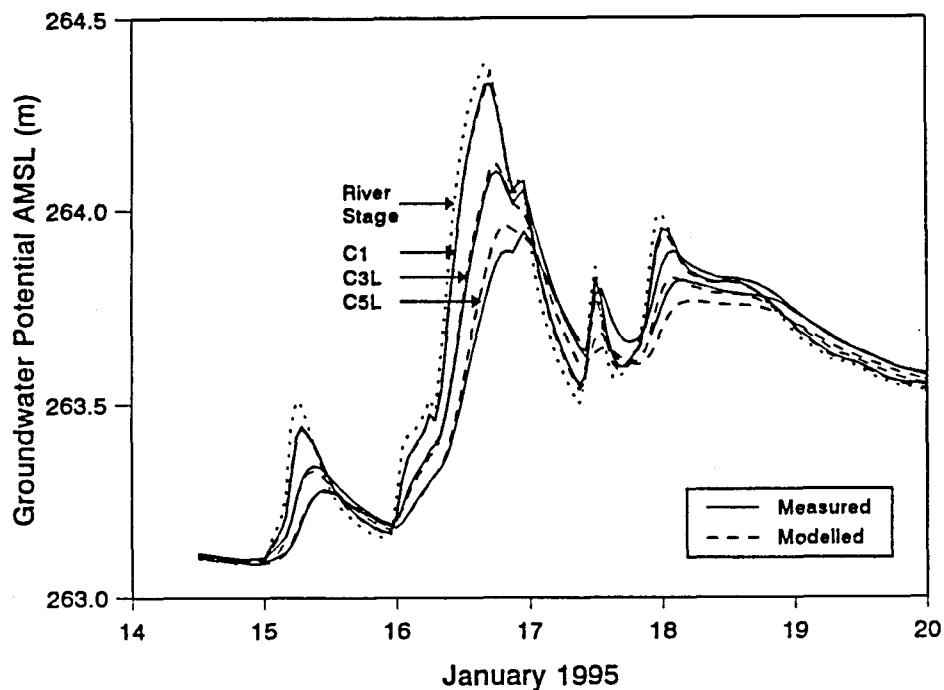


Figure 4.48 Measured and modelled (two-dimensional calibrated) groundwater potential hydrographs.

zone (Table 2.3 and Fig. 2.10). There is no physical justification, however, for specifying bulk hydraulic conductivities within this zone ( $x > 68$  m;  $z > 263$  m) that vary by one order of magnitude (Table 4.28). This is confirmed by comparison of grain-size distributions at locations C3 and C5 (Fig. 2.12).

#### 4.3.2.2 Quasi Three-dimensional Model

##### 4.3.2.2.1 Longitudinal Flows

Observed longitudinal gradients of recorded groundwater potential (such as can be inferred from the offsets between the upstream-central-downstream and central-downstream levels in Fig. 4.49b and Fig. 4.49c, respectively) indicate the existence of significant groundwater flow parallel to the river at the study site. Groundwater level data from a piezometer located 100 m downstream of the central monitoring line (Fig. 2.11) indicated a longitudinal gradient of 0.0025. The corresponding river stage slope is approximately 0.00028 (Table 3.5). The longitudinal flows arise from a combination of hydraulic controls (bedrock outcrops) in the active channel 118 m downstream of the central line, and uneven bedrock topography within the macro-channel infill. The drop in stage level at the hydraulic discontinuity (Fig. 2.11) increases with discharge from 0.249 m (2.05

m<sup>3</sup>/s) to 0.353 m (40.29 m<sup>3</sup>/s) (Table A3.4).

The occurrence of longitudinal flows at the study site resulted in the extension of the groundwater model to quasi three-dimensions. This was achieved by imbedding the two-dimensional vertical model within a two-dimensional horizontal model which extends over the macro-channel infill deposit. The two-dimensional horizontal model introduces fluxes perpendicular to the vertical modelling plane, resulting in more accurate representation of flow conditions at the site.

#### 4.3.2.2.2 Model Calibration

The additional boundary conditions required to model two-dimensional horizontal flow within the macro-channel infill deposit are illustrated in Fig. 2.11. The vertical and horizontal models intersect along the central line. The rating curves for cross-section 1 and cross-section 3 (Fig. 3.5) are specified downstream and upstream of the hydraulic discontinuity. The cross-section through the central line (Fig. 2.10) is divided into three uniform alluvial zones with the calibrated parameter values given in Table 4.29. The coarse alluvium underlying the macro-channel infill deposit was found to be spatially extensive, and therefore characterises the alluvial-hydraulic conditions in the horizontal model.

**Table 4.29** Calibrated alluvial-hydraulic parameter values

$x$ (m)	$z$ (m)	$K_s$ (m/hr)	$S_y$
$x < 68$	$z < 263$	50	0.34
$x > 68$	$z < 263$	25	0.34
$x > 68$	$z > 263$	0.5	0.17

The finite-difference parameter values are as previously used in the two-dimensional model, with the addition of  $\Delta y = 50$  m. The modelled and measured hydrographs along the central, third and fifth monitoring lines are plotted in Figs. 4.49a, 4.49b and 4.49c, respectively.

The alluvial-hydraulic parameter values are calibrated (Table 4.29) to replicate the measured responses (rate of rise and recession, and magnitudes) along the central line (Fig. 4.49a). Comparison of modelled and measured hydrographs along the third (Fig. 4.49b) and fifth (Fig. 4.49c) monitoring lines shows satisfactory correspondence. The less favourable agreement in the longitudinal flow direction results from a limited data set (alluvial-hydraulic and boundary conditions).

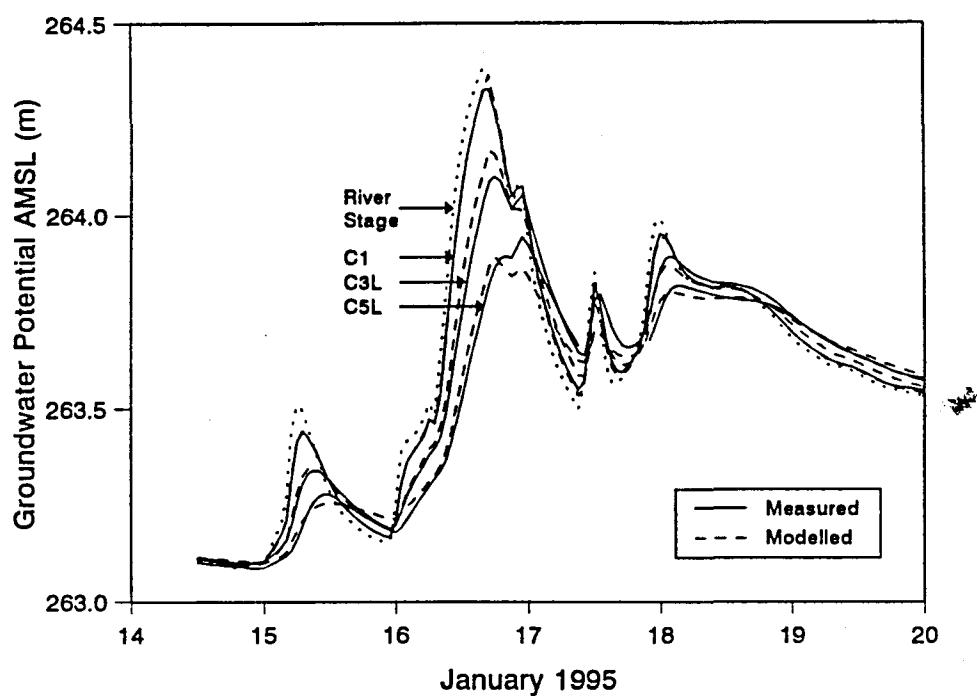


**Figure 4.49a** Measured and modelled (three-dimensional, calibrated) groundwater potential responses along the central line.

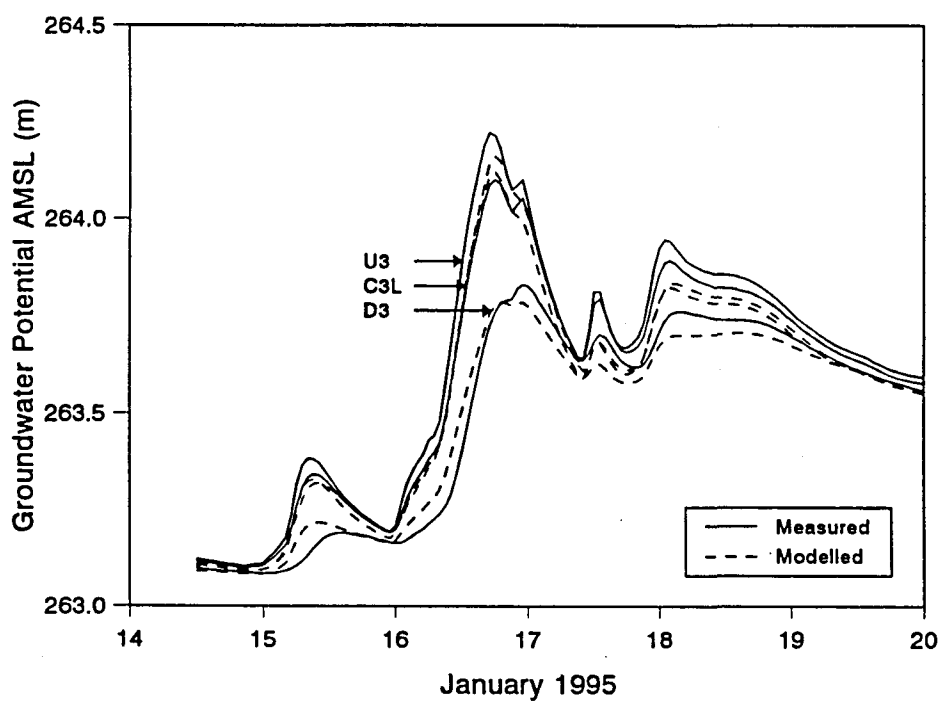


**Figure 4.49b** Measured and modelled (three-dimensional, calibrated) groundwater potential responses along monitoring line 3.

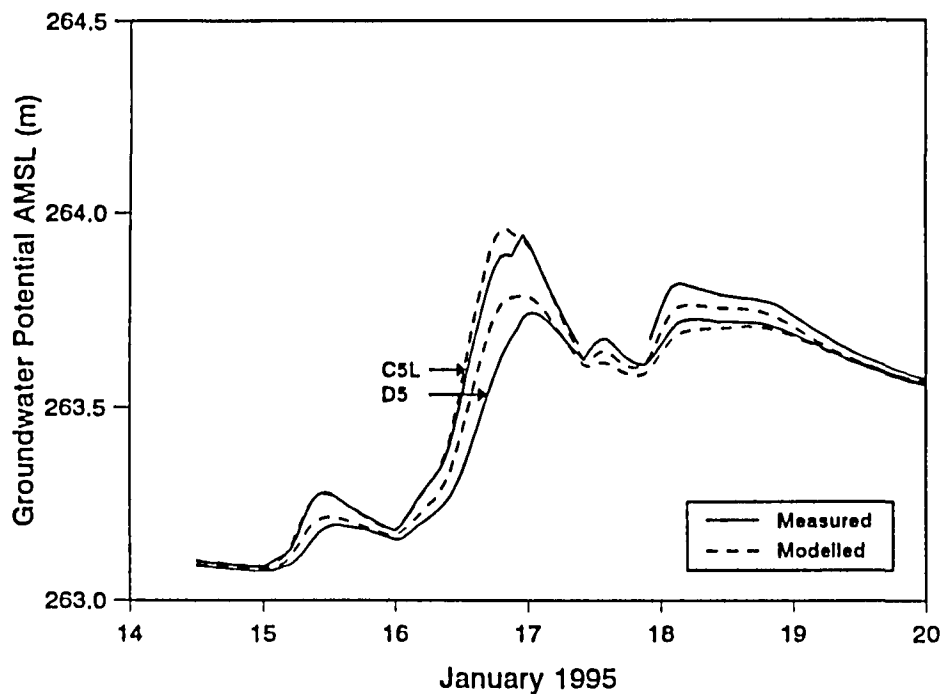


**Figure 4.49c** Measured and modelled (three-dimensional, calibrated) groundwater potential responses along monitoring line 5.

The relative importance of longitudinal seepage gradients is shown in Fig. 4.50, using data from locations C3L, C5L and D3 to compute lateral ( $i_x$ ) and longitudinal ( $i_y$ ) gradients. The gradients are similar for low magnitude fluctuations, with lateral seepage becoming more significant during higher magnitude events. The modelled negative lateral gradient (C3L-C5) implies seepage towards the river, which is not implied from the monitored variations in groundwater potential.

The modelled vertical losses in potential are small, as illustrated by the difference between the modelled groundwater potentials and phreatic surface levels (Fig. 4.51). Assuming that the calibrated model reasonably replicates the dynamics of bank storage at the site, the measured groundwater potentials may be used (rather than phreatic surface levels which are not available) to infer measured storage volumes. The modelled and measured temporal bank storage values along the central line are plotted in Fig. 4.52a. The modelled and observed responses correlate well, yielding a regression coefficient  $R^2 = 0.973$  (Fig. 4.52a, inset). The relative bank storage volumes (Fig. 4.52b) also provide excellent agreement.

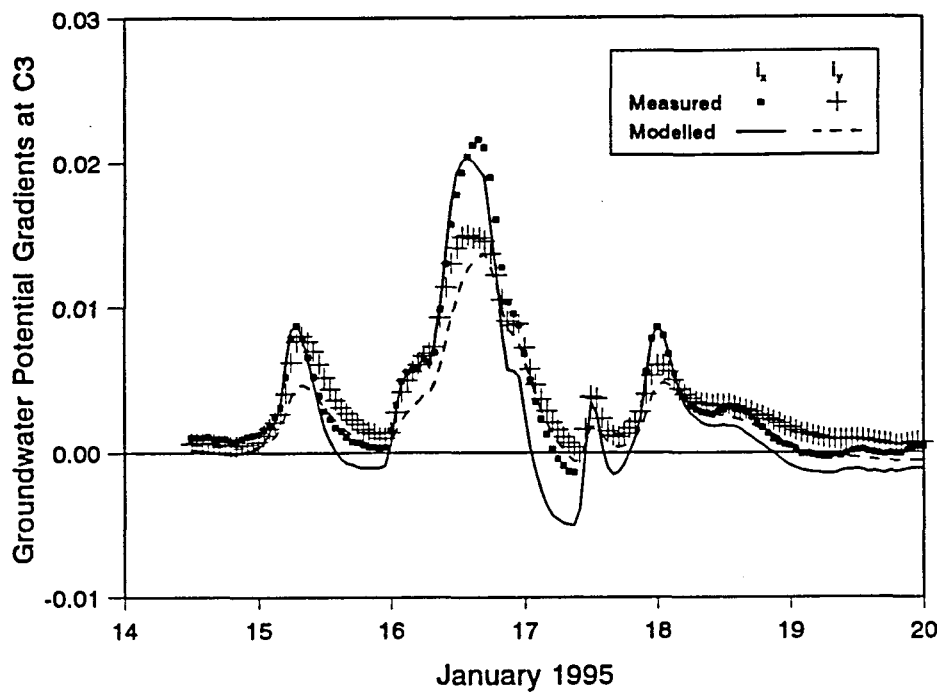


Figure 4.50 Measured and modelled lateral ( $i_x$ ) and longitudinal ( $i_y$ ) flow gradients.

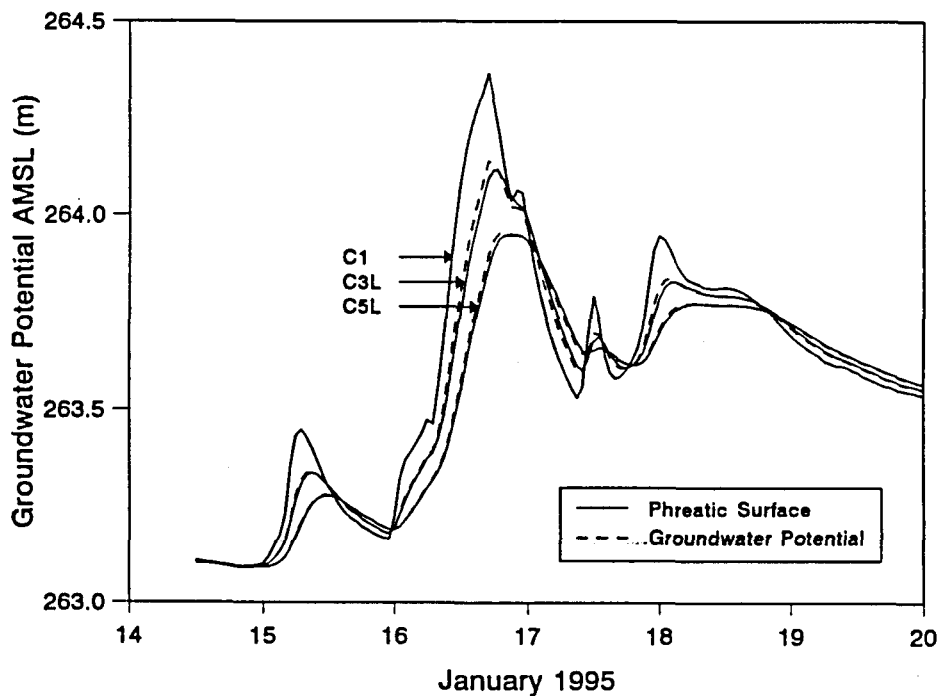
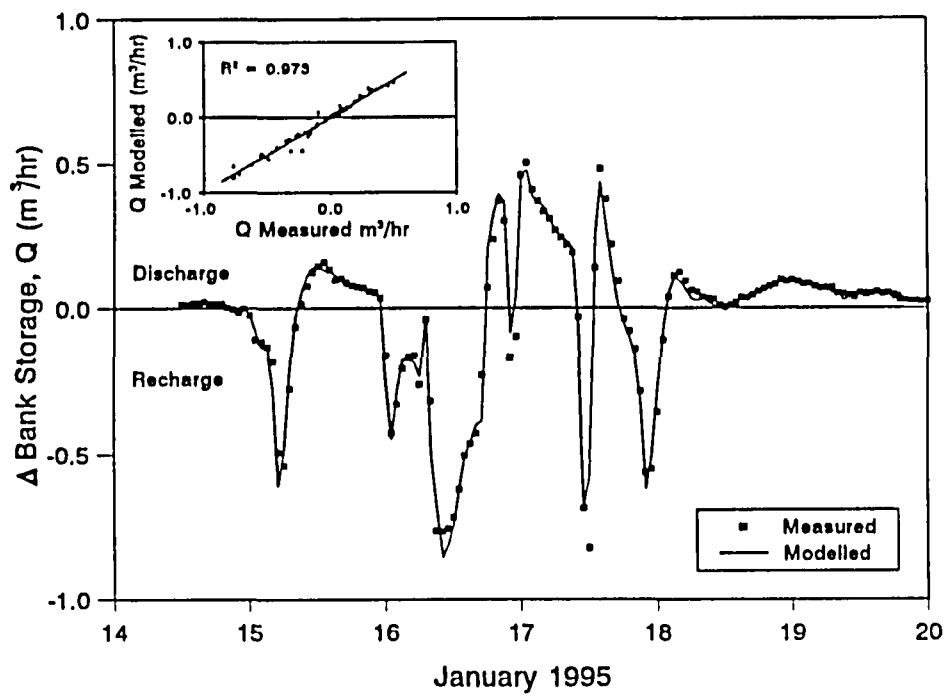
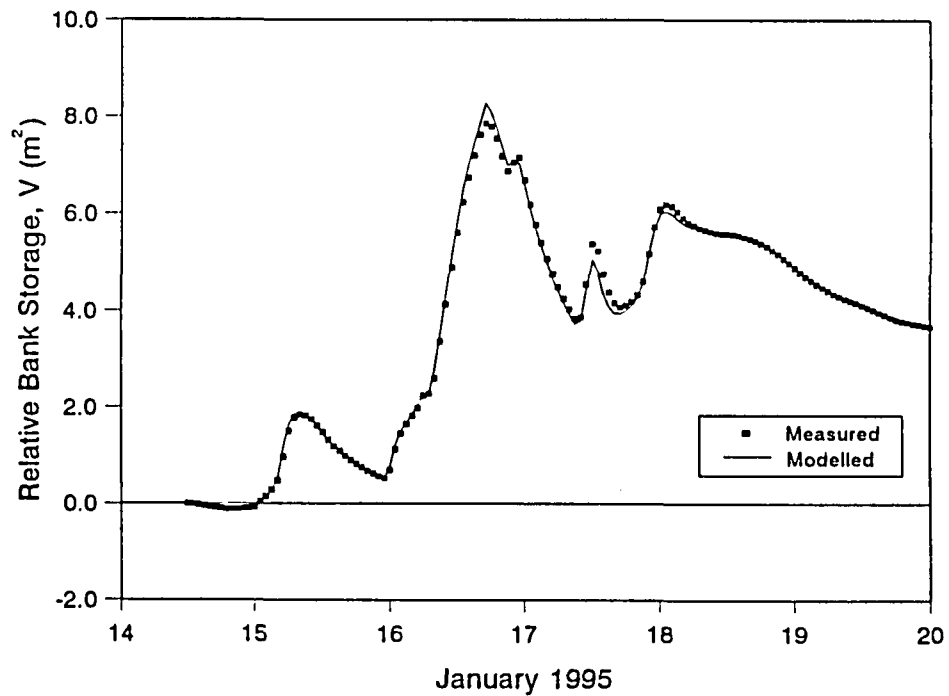


Figure 4.51 Modelled groundwater potential and phreatic surface responses along the central monitoring line.



**Figure 4.52a** Change in bank storage along a cross-section through the central monitoring line.



**Figure 4.52b** Relative bank storage within a cross-section through the central monitoring line.



#### 4.3.2.3 Justification for Three-dimensional Modelling

The modelled phreatic surface responses at locations 1, 3 and 5 along the central line are compared in Fig. 4.53 to the calibrated two-dimensional (4.3.2.1.2) and quasi three-dimensional (4.3.2.2.2) models. The models predict significantly different responses. The quasi three-dimensional model predicts small vertical gradients (Fig. 4.51), whereas large gradients, increasing with distance from the active channel, are predicted two-dimensionally. The large gradients result from the low hydraulic conductivities (Table 4.28) required to calibrate the groundwater potential responses (Fig. 4.48). Water levels in the upper nested piezometers (Fig. 2.3) were not reliably recorded. The upper nested piezometers were also positioned too low (263 m AMSL) to facilitate measurements of vertical flow gradients within the stratified deposit. The vertical variation in groundwater potential are therefore not available.

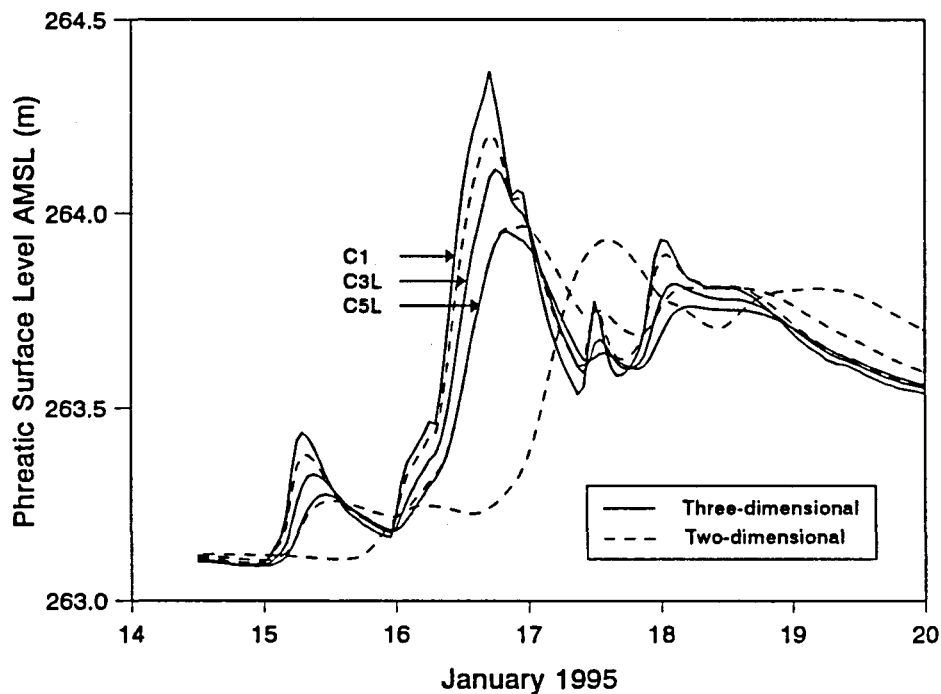


Figure 4.53 Modelled groundwater potential and phreatic surface responses along the central monitoring line.

The justification for implementing the quasi three-dimensional model rather than the two-dimensional model is based on the ability of the model to account for longitudinal flows. These are shown to compare satisfactorily with measured data. Furthermore, and a more realistic representation of observed alluvial characteristics at the study site is provided.

#### 4.3.2.4 Model Application : Quasi Three-dimensional Model

The calibrated model is used to simulate groundwater response to nine distinct hydrographs (2801 hourly recordings) monitored over the period December 1992 to January 1995. The groundwater potential responses at locations C1, C3L, C4L and C5 (Fig. 2.2) are plotted in Fig. 4.54. The measured and modelled peak levels correlate exceptionally well, yielding a regression coefficient  $R^2 = 0.996$ .

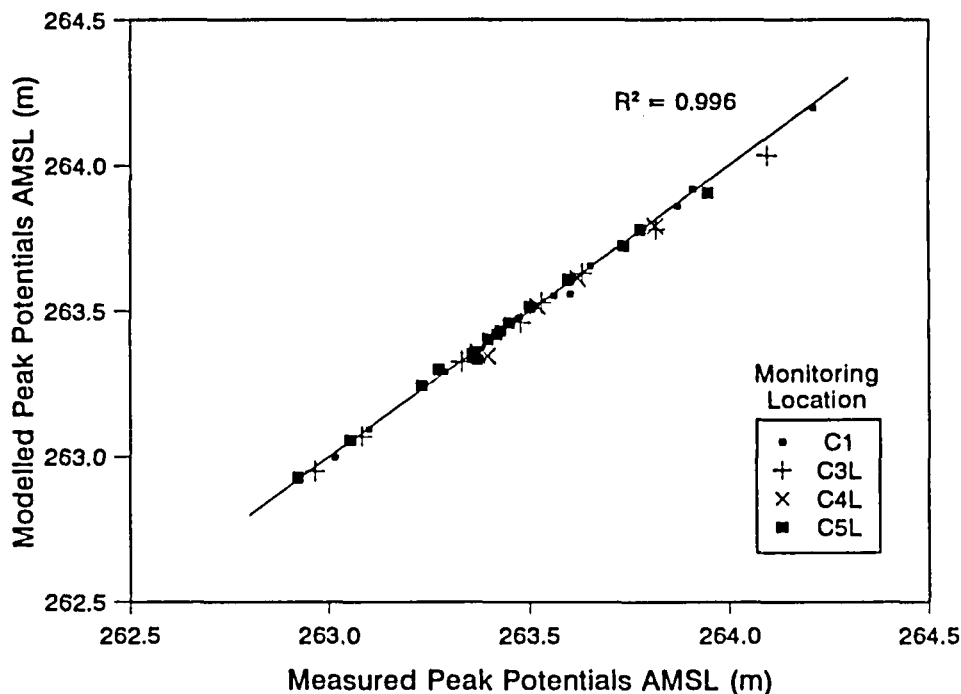


Figure 4.54 Correlation between measured and modelled peak groundwater potentials over the period December 1992 to January 1995.

#### 4.3.3 Unsaturated Flow

Changes in the moisture contents along a vertical profile at location C3-4 (Fig. 2.2), over the period October 1992 to July 1995, are modelled one-dimensionally. Phreatic surface fluctuations, rainfall and extractions to support transpiration are considered in the analysis. Monitoring location C3-4 is positioned below the canopy of a large *Ficus sycomorus* tree. Evaporation from the alluvial surface is therefore likely to be small relative to transpiration losses, and is consequently neglected.

#### **4.3.3.1 Model Input Data**

##### **4.3.3.1.1 Stratified Alluvial Profile**

Water retention relationships have been fitted to measured data (Fig. 2.14) and unsaturated hydraulic conductivities generated for the four (clay, silt, silty sand, coarse sand) characteristic sediment types. These materials cover the range of sediments observed at the study site (Fig. 2.12).

Augered samples were used to describe the stratified sediment profile, using the characteristic sediment types (Fig. 2.13). The stratified profile may be further divided into four alluvial zones: 0 cm to 75 cm (clay, silt and silty sand); 75 cm to 125 cm (coarse sand); 125 cm to 250 cm (silty sand, clay and silt); > 250 cm (coarse sand).

##### **4.3.3.1.2 Phreatic Surface Levels**

The calibrated saturated flow model (4.3.2.2.2) is used to predict phreatic surface response to daily fluctuations of river stage. The phreatic surface levels are specified as the lower boundary condition in the unsaturated model.

##### **4.3.3.1.3 Rainfall, Infiltration and Runoff**

Rainfall is being measured at the Skukuza weather station, located approximately 5 km from the study site. For this reason and foreseeing problems associated with measurement at the infrequently serviced weather station, rainfall was not recorded at the site.

The interception of rainfall by the canopy of the *Ficus sycomorus* is neglected. The leaf area density varies with season and climatic conditions and the effects of interception are considered small, particularly when compared with assumptions made in the analysis (e.g. Skukuza rainfall data, characterisation of alluvial heterogeneity and transpiration extraction patterns).

Infiltration at the soil surface is limited by the ability of the material to transport water. The actual infiltration is limited by the Darcian flux or daily rainfall. The surface topography across the macro-channel is irregular, varying from steep bank gradients to distributary channels. The surface slope at C3-4 is 0.08, and excess daily rainfall is assumed to provide runoff, with no allowance for ponding and subsequent infiltration.

#### 4.3.3.1.4 Transpiration

Daily transpiration rates determined from sap flow measurements on the *Ficus sycomorus* anchor tree (refer to Chapter 5) are expressed as consumption per unit plan area. The vertical distribution of plant roots is required to enable spatial extraction patterns to be determined. Vertical rooting densities for crops such as potatoes and maize have been measured and applied in crop growth models (e.g. Feddes *et al.*, 1988). Information on rooting densities for large trees is rare and non-existent for indigenous woody vegetation. In the absence of rooting data, a uniform distribution of root density is assumed.

Moisture in the unsaturated zone is not equally available for transpiration, with water becoming increasingly difficult to extract at larger soil suctions. The wilting point represents the suction (1.5 MPa) above which soil moisture extraction (to support transpiration) ceases. In the linked soil moisture - transpiration model, the actual extraction rate at a given depth is assumed to be a function of the relative soil suction, according to

$$qt_z = \frac{\psi_o - \psi}{\int_0^{z_r} (\psi_o - \psi)} qt \quad 4.93$$

where

$qt$  is the transpiration rate per unit plan area (m/day)

$qt_z$  is the extraction rate at depth  $z$  (m/day)

$\psi_o$  is the soil suction at the wilting point (m)

$\psi$  is the soil suction at depth  $z$  (m)

$z_r$  is the rooting depth (m)

Potential transpiration refers to the condition where the availability of subsurface water does not limit the rate of extraction. Potential transpiration may be reduced to give losses that are soil moisture dependant (e.g. Feddes *et al.*, 1988). At the study site, flow in the active channel maintains a zone of saturation within the macro-channel infill and active channel deposits (Fig. 2.10). Therefore, assuming no distinction between water availability to vegetation in the saturated and unsaturated zones, potential transpiration rates may be supported. In the model, the transpiration rate is not a function of soil suction (or water content), since the transpiration fluxes used are derived from field measurements. The rooting depth is assumed to extend over the extent of the fluvial deposit ( $z_r = 4$  m in equation 4.93).

#### 4.3.3.2 Model Application

The distribution of volumetric water content is modelled over the period August 1993 to July 1995 using daily input data (smaller time-steps are applied in the solution procedure to satisfy mass balance criteria), with  $\Delta z = 2.5$  cm. The results are presented from October 1993 to allow modelled field conditions to establish.

##### 4.3.3.2.1 Soil Water Contents

The modelled volumetric water contents and calibrated neutron probe data are plotted in Fig. 4.55a for the aggregated layers given in Fig. 2.13. The synthesized and calibrated neutron probe measurements compare remarkably well taking into account the approximations applied in the solution procedure as well as the inaccuracies in determining depth averaged water contents (Fig. 2.9) within the highly stratified deposit. Isolated Neutron probe measurements indicate water content underestimates in January 1994 (8%), February 1995 (8%) and February 1994 (5%) in the upper (0 to 75 cm), intermediate (75 to 125 cm) and lower (125 to 250 cm) layers, respectively. The modelled data reflects the measured seasonal variability that result from meteorological changes.

The water content fluctuations in the upper layer are caused by the combined effects of rainfall infiltration and transpirational water extractions. Following a rainfall event, the water content rapidly increases by infiltration, and thereafter reduces exponentially as transpiration depletes the replenished storage. The exponential decrease results from increasing soil suctions and hence reducing extractions as water contents reduce. The higher rainfall and extended duration during the period October 1994 to June 1995 than experienced the previous season is evident from the sustained higher water content of the upper layer. Depletion of the upper layer is noted to occur over relatively short periods for water contents greater than 20%. This is because soil moisture may be effectively extracted by transpiration at low soil suctions. This is not apparent from the monthly measurements, however, due to the temporal scale of data collection.

Sustained low water contents ( $\theta = 3\%$ ) at the wilting point for the intermediate layer (75 to 125 cm) are predicted over the period October 1993 to July 1995. This is confirmed by measurement, with the exception of an increase to 11% in February 1995. The low water contents infer a low hydraulic conductivity for the poorly graded sediment type. The modelled results confirm that no significant vertical flows were transmitted across this layer during the 1993/1994 wet season, as deduced by Birkhead *et al.* (1995) from periodic water content measurements.

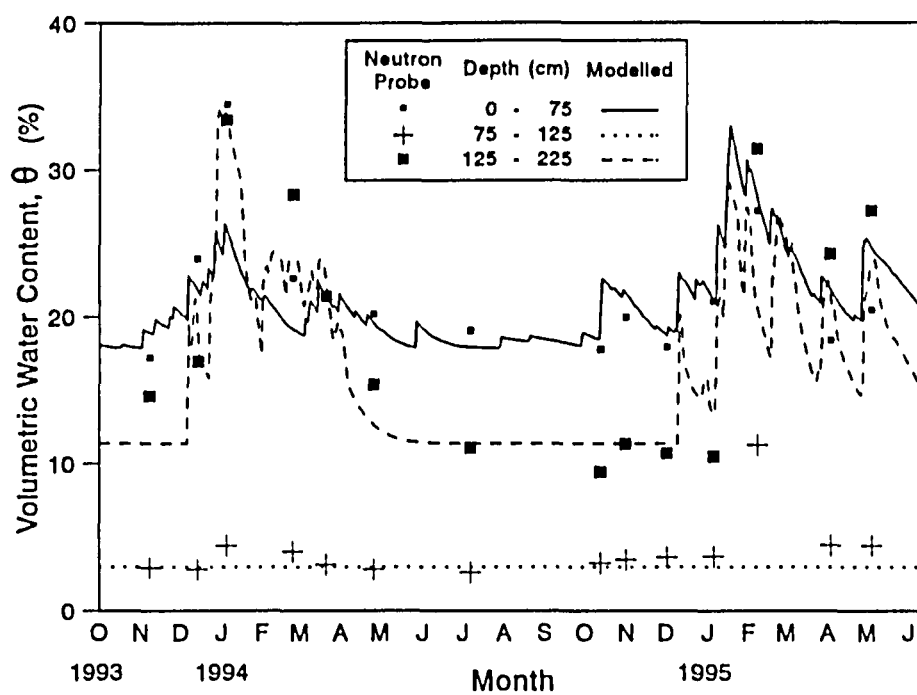


**Figure 4.55a** Measured and modelled changes in water content for upper, intermediate and lower layers in the unsaturated zone.

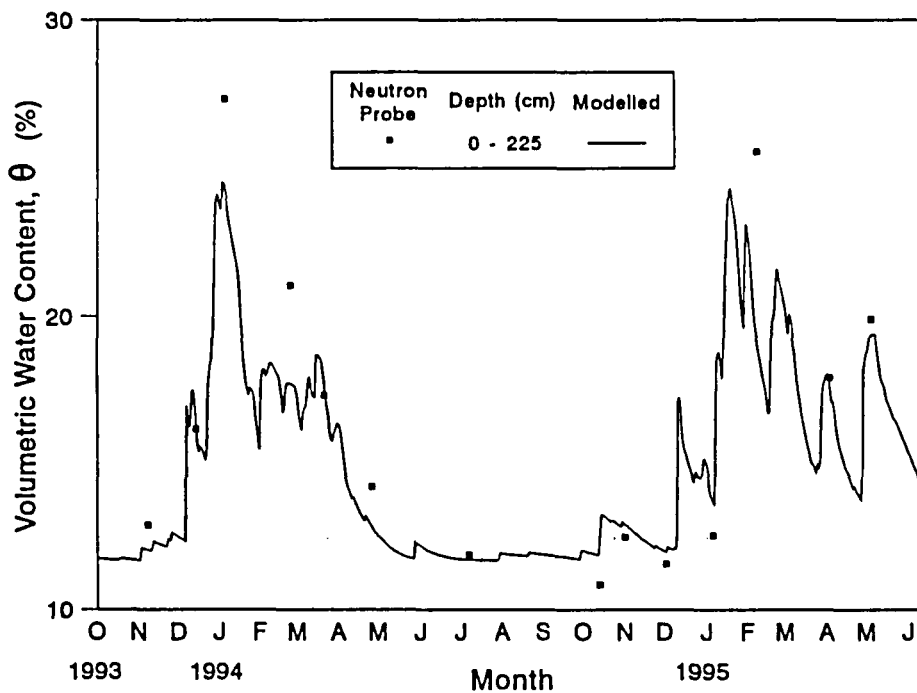


**Figure 4.55b** Measured and modelled changes in water content for the aggregated layers in Fig. 4.55a.

The large water content fluctuations in the lower layer are caused by the combined effects of phreatic surface response to stage levels, and transpirational losses. Significant variations in water content during the wet seasons result from saturation and drainage of the soil profile, and occur over short periods. The extent of the variations are not apparent from the less intensive neutron probe data. The modelled water contents and measured data indicate that moisture available for extraction in the lower layer, derived from elevated phreatic levels during the 1993/1994 wet season, were materially depleted by May 1994.

The averaged water contents over the three layers are plotted in Fig. 4.55b. The modelled and measured variations correlate well for the aggregated profile. The model underestimates the measured average water content for January 1994 and February 1994 by approximately 5%. The seasonal variation in water content between October 1993 and October 1994 is well described, as are the interseasonal variations.

#### **4.3.3.2.2 Water Balance within a Vertical Column at the Study Site**

The fluxes across the boundaries of a one-dimensional column define the water balance at location C34 at the study site (Fig. 4.56, inset). The modelled cumulative fluxes are plotted in Fig. 4.56. A moderate contribution of infiltrated rainfall to transpirational losses occurs over the period October 1993 to July 1995. The deficit is provided by seepage from the active channel.

The relative contributions to transpiration by the unsaturated and saturated zones are illustrated in Fig. 4.57. The unsaturated zone is divided into the layers illustrated in Fig. 4.55a, with the base of the lower layer modified to coincide with the transient phreatic surface. The considerable contribution of water derived from seepage is again apparent. Water in the upper layer accounted for 15% of the losses during February 1995, with only 4% derived from this layer over the period October 1993 to October 1994. Although the unsaturated zone is rapidly depleted of the storage derived from infiltration and recharge by river stage fluctuations, the lower layer of the unsaturated zone accounts for approximately 8% of the losses during winter months. This water is derived by capillary rise from saturated storage and transient river stages, and although extracted from the layer directly above the phreatic surface, the water is derived by seepage from surface flow in the river channel. This confirms the significance of seepage as the process for providing subsurface water to meet transpiration in hydraulically connected surface-subsurface systems, such as at the study site.

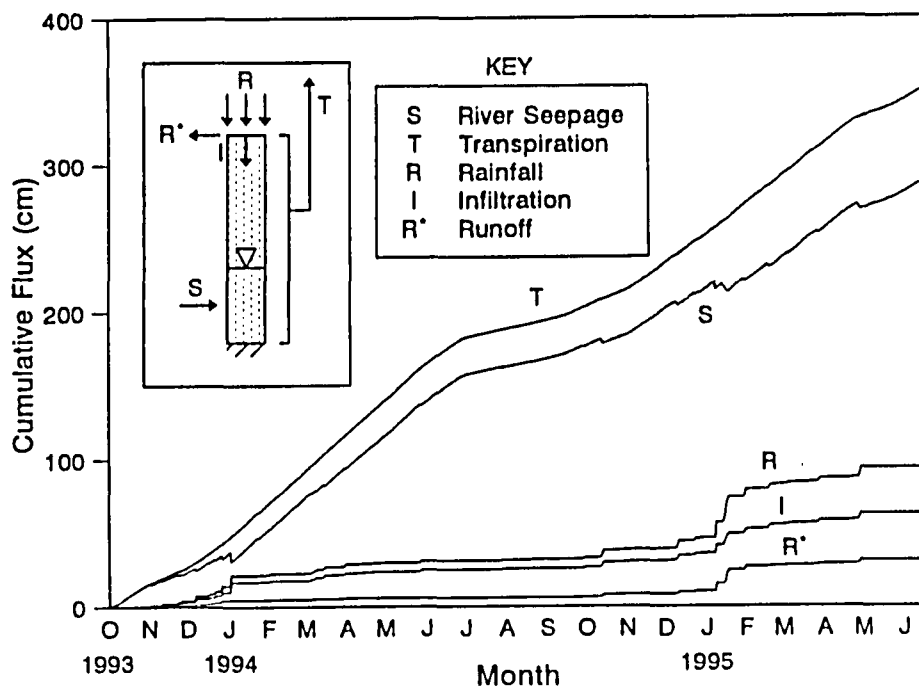


Figure 4.56 Cumulative fluxes defining the water balance for the soil column at location C3-4 from October 1993 to June 1995.

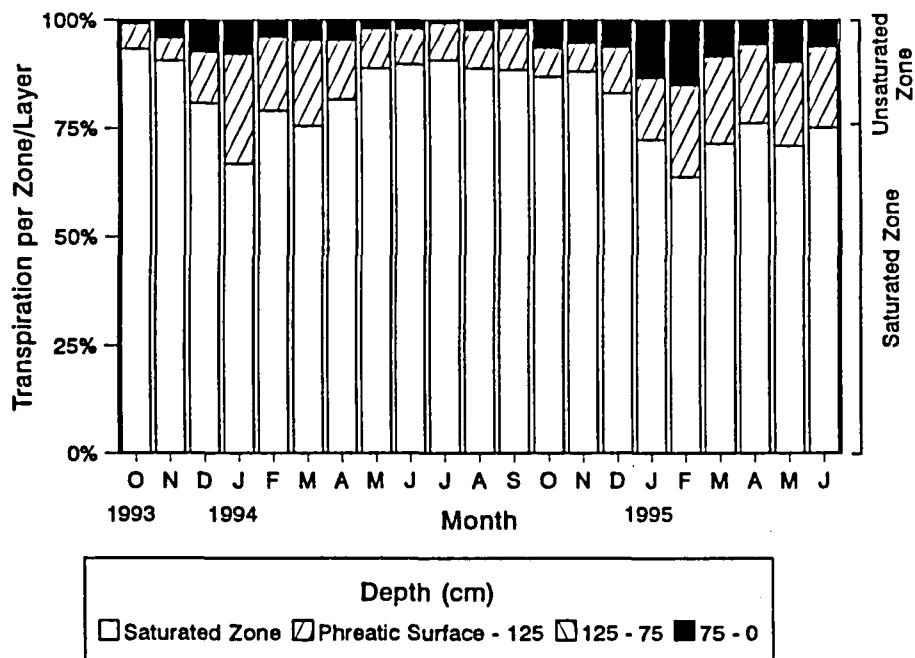


Figure 4.57 Contribution of the unsaturated and saturated zones to transpiration at location C3-4.



## **CHAPTER 5**

### **TRANSPIRATION MODELLING**

---

#### **5.1 Introduction**

##### **5.1.1 The data sets and time step of the transpiration models**

On conclusion of the study 711 days of hourly fig tree transpiration data were available together with the corresponding meteorological conditions. In the case of the reed transpiration data, measurements were made at 15 minutely intervals on a total of sixteen reeds for approximately ten days in each of three data collection periods. One obvious source of input data for both transpiration models would be the prevailing meteorological conditions. These data were available at an hourly time step from the automatic weather station located at the Narina site. The minimum time step the source data would allow would therefore have been an hourly time step. While, this would have been compatible with the time step of the groundwater monitoring programme at Narina, it would have provided data at a resolution beyond the level at which management would have found it useful. For this reason, a daily time step was decided on for the transpiration models. An immediate benefit is that it would be possible to run the model using data collected by manually serviced weather stations with a daily record. In addition, streamflow data records are generally also only available at a daily time step.

#### **5.2 Methodology**

The same process was followed in developing the models for both the fig tree transpiration rates and for the reed bed. In the case of the fig tree, the model predicts the transpiration from the selected branch, while the model for the reeds predicts the average transpiration rate for the reed bed. In both cases a simple regression procedure was adopted to infer relationships between the observed transpiration rates and the prevailing climatic conditions. This approach was adopted in favour of the more conventionally used Penman-Monteith-type evaporation modelling because of its simplicity, and because the aim of the project was to develop a model that is easily applied. The Penman-Monteith approach may have resulted in a model that requires input data that are difficult to meet, therefore limiting the usefulness of the predictive model.

The modelling process was done in broadly two phases: The first involved identifying potential outliers by repeatedly fitting models until the only cases retained in the modelling process were those that satisfied outlier and influential point diagnostic criteria. In the second phase, predictors with significantly non-zero coefficients were identified. It was also necessary to keep the number of predictors small in order to make the input data requirements

easy to meet. While it is necessary to develop so-called parsimonious models, only models with no evidence of collinearity were selected.

The models presented here were also subjected to other tests of statistical rigour, such as the distribution of residuals. To be seriously considered the selected models must also have residuals (the difference between the observed and predicted transpiration rates) that are randomly distributed about zero (when plotted against the predicted values), confirming that the structure in the data is wholly captured by the model. (What remains is random noise.) The residuals must be normally distributed. Lastly, to be useful as a predictive model, it must satisfy an adequacy criterion.

The model development and analysis was carried out using programs written in the SAS language. Outlying and/or influential cases, as well as collinear predictors were identified using the procedure REG. The PLOT procedure was used to produce residual and other diagnostic plots, and the UNIVARIATE procedure to check the normality assumption of the residuals. SAS Macro's were written to test the assumptions of random residuals and model adequacy.

#### **5.2.1 Identifying outliers/influential points**

The SAS procedure REG was used to calculate studentized residuals (the residual divided by its standard error), and the Cook's D statistic used as a measure of the influence of each case on the model. This test was used to determine which data should be excluded as outliers in the analyses. In the case of the reed data, data were retained in the analysis provided the studentized residuals were less than 2.65, and Cook's D was less than 0.802 (Cook and Weisberg 1982, p 114 - 118). For the fig tree study the corresponding values were 3.26 and 0.942 respectively.

#### **5.2.2 Model selection**

A stepwise regression procedure was used for model selection. As a result, the predictors most correlated with the response variable were included in the model first. The predictor with the highest partial correlation with the response is considered next and so on until no useful predictors can be included or excluded from the model. At each step it is necessary to examine whether the predictors already in the model are still useful predictors. Draper and Smith (1981) give further details of the procedure.

Because between seven and sixteen reeds were monitored on any given day a weighted regression was fitted to the daily Gastwirth medians, the weights being the numbers of reeds monitored. The fig data was divided into two groups, alternate values included in each group. The model was fitted to each

group. The one with the largest  $R^2$  is reported. The reported outliers were identified in fitting the model to the two data sets.

### **5.2.3 Random and normal residuals and regression adequacy**

In acceptable models the residuals, plotted against the predicted value should demonstrate no visible structure. The probability of rejecting the randomness assumption for each of the models was tested by comparing the number of runs of the same sign to the number of positive and negative residuals (Owen 1962, section 12.4). The normality test used by SAS for this study is the extension of the Shapiro Wilk W test for large samples developed by Royston (1982). The Shapiro Wilk test is the recommended test of the normality assumption for 50 or less cases, while Royston's modification applies to a maximum of 2000 cases.

The residuals for the first reeds model can be assumed normal at the 3% significance level, but not at the 5% level. The residuals for the second reed model and the fig models can be assumed normal at the 10% level.

Regression adequacy is discussed by Box, Hunter and Hunter (Box et al, 1978, p 524). The test statistic is a function of the difference between the maximum and minimum predicted values and the mean square error. Draper (1984) suggests that the statistic exceed 10, for the model to be useful for the purposes of prediction. This condition was met for both the Fig and the reed models.

### **5.2.4 Collinear predictors and significant coefficients**

Where two potential predictors are nearly perfectly correlated, for example evaporation demand (VPD) with relative humidity (Rh) (or temperature), the regression coefficients are rendered unstable, having large standard errors. Procedure REG computes the variance inflation factor (VIF) for every predictor in the model. Wetherill (1986, p 87) proposes that all VIF values be less than 10 for no predictor to be collinear with any other variable. In the case of the fig tree model four of the predictors have VIF values between 10 and 16. This is not considered a serious violation of the assumption.

In order to ensure parsimonious models the probability that a regression coefficient is equal to zero should be significantly small. For all three models this probability is less than 0.001.

### **5.3 Modelling Transpiration from the Fig Tree**

Once the transpiration data had been paired up with meteorological data the data set used to develop the fig tree transpiration model contained data from 11 February 1993 to 5 June 1995. No data was available from 20 June to 1 July 1993, 28 July to 12 August 1993, 14 December to 4 January 1994, 2 March to 25 April 1994, nor from 2 February to 13 February 1995.

The following variables were monitored per day:

- transpiration rate (in litres/day);
- wind speed ( $\text{m sec}^{-1}$ ), average;
- photosynthetically active radiation (PAR:  $\mu\text{mol m}^2 \text{sec}^{-1}$ ) average and maximum;
- relative humidity (%), average and minimum;
- temperature ( $^{\circ}\text{C}$ ), average, minimum and maximum;
- vapour pressure deficit (VPD - kPa) a combination of relative humidity and temperature, average and maximum;
- river level (metres above the minimum level recorded);
- rainfall (mm) - daily total.

The only tree parameter monitored was leaf area index (LAI).

#### **5.3.1 Monthly indicators and slope variables**

As the fig tree data was monitored over a sufficiently long period that seasonal factors can be expected to influence the expected transpiration rate, it was necessary to investigate possible monthly changes to the intercept and the slopes (regression coefficients) of the predictors of transpiration rate. Should a clear pattern in the regression coefficients or the intercept emerge for successive months, an attempt to define appropriate seasonal indicators would be considered. During the stepwise model fitting procedure, (Draper and Smith 1981, p 307), only monthly indicators and slopes that are essential for predicting transpiration rate were retained. This in turn may suggest possible season variables.

Eleven indicator variables were needed to represent the twelve months. As the month of May appeared most frequently in the data set, indicators were defined for the remaining months. This was achieved by introducing a further eleven columns of indicator values that could have a value of either zero or one. Opposite data collected during January, for example, the January indicator would have a value of one, while the remaining ten indicators would all be zero. As May has no indicator, observations for that month in the three years are zero for all eleven indicators.

The modelling exercise then identified potential predictors for possible entry into the model as "month variables". To do this eleven new variables were generated for each predictor by multiplying the predictor by each of the eleven indicator variables. The stepwise procedure then selected the month form of the predictor that significantly improved the model of water usage.

Month indicators for February and July were included in the model. The "leaf area indicator" (LAI) variable assumes different slopes for the months of January, February, July, October and November. The WATER variable assumes a different slope for December.

### **5.3.2 The predictive model for transpiration from the reference fig tree**

The best model for predicting transpiration from the fig tree is presented in Table 5.1. The model accounted for 78% of the observed variation in transpiration. The distribution of data in the scatter diagram of observed against predicted values (Figure 5.1) was encouraging for three reasons: Firstly, evaporation estimates covered a large range from 10.4 to 127.1 l per day. Secondly, there was a good fit between observed and predicted values with a slope close to one, and thirdly, the intercept was close to zero. This indicated that the model was unbiased, and that it could reliably be used over a wide range of evaporative conditions. It was also encouraging that in only four of the 711 data points were excluded from the analysis as being 'outliers'.

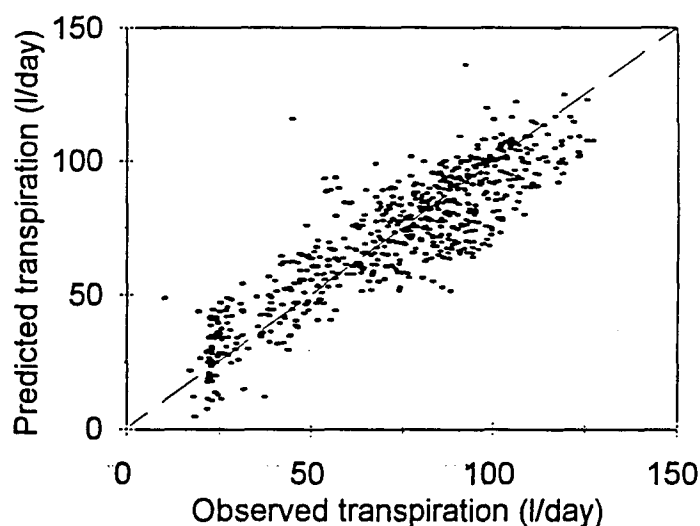


**Figure 5.1** A comparison of the observed transpiration rates recorded for the fig tree against those predicted by the model

Two equivalent forms of the model are presented, the model formulation in the first row should be used when predicting transpiration for an entire year. The remaining rows present a breakdown of the model into its monthly components.  $R^2$  achieved, by only including predictors that make a significant contribution to the model, was 0.779. The final model requires data on only the VPD, LAI, and the river level. It was desirable to develop a parsimonious model that required few parameters, and this model meets that requirement.

The coefficients in Table 5.1 illustrate changes in the modelled transpiration from month to month, relative to that level recorded during May. It is important to note that the coefficient for the VPD transform remains unchanged over the course of the year. The coefficient for all the months remains the same, but is only a third of its size during the month of December. This is possibly because the trees may derive significant amounts of water from rainfall during December, and may therefore be less affected by fluctuations in river level. The coefficient for leaf area index (LAI) changes from near zero for February to over 40 for July. The intercept changes accordingly with a positive value for February and large negative value for July.

An examination of the model and its fit to the data show that the model does not fit the entire data set equally well. The fit between the model and the observed data is really pleasing for the period November 1993 to October 1994 as a result of the clusters of data with residuals around zero (Figure 5.2). The fit in the prior and following periods was poorer with greater deviations from the zero residual line. This is clearly illustrated in the figure illustrating the distribution of residuals for the entire data set (Figure 5.2). The most disturbing feature of this figure is that ideally the distribution of residuals should show no pattern, and it is clear that in the period prior to November 1993 and after October 1994 there was a clear pattern in some of the deviations from the zero residual line.

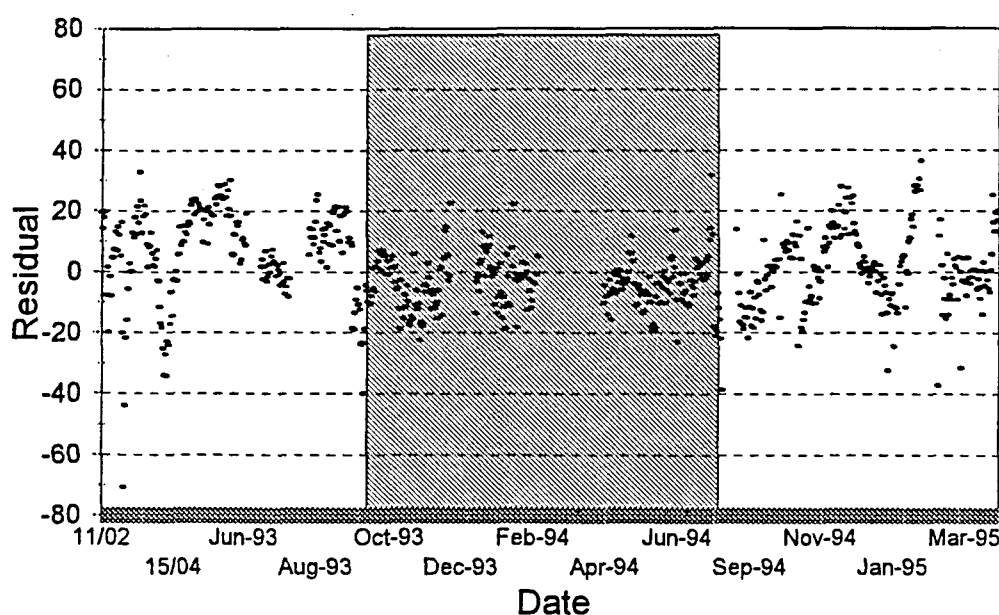


**Figure 5.2** The distribution of residuals for the model. The cross-hatched area represents that period where the model performs best (November 1993 to November 1994)

The pattern in the residuals is most clearly demonstrated in the subset of the data illustrated in Figure 5.3. For the bulk of the period, the residuals were retained in a band between +20 and -20, however on the 27 February the residuals became rapidly more negative. This only lasted for a period of only five days, whereafter they returned to the earlier levels. The large negative residual implies that according to the model, a larger evaporation rate was expected under the prevailing meteorological conditions than was recorded. This particular departure was apparently caused by the extremely high water levels recorded over this period. The water levels were so high that the base of the fig tree was under water. It is likely that this resulted in anaerobic conditions in the soil which, in turn, resulted in the low evaporation rates. This theory is supported by the recovery of transpiration rates recorded once the water level had dropped.

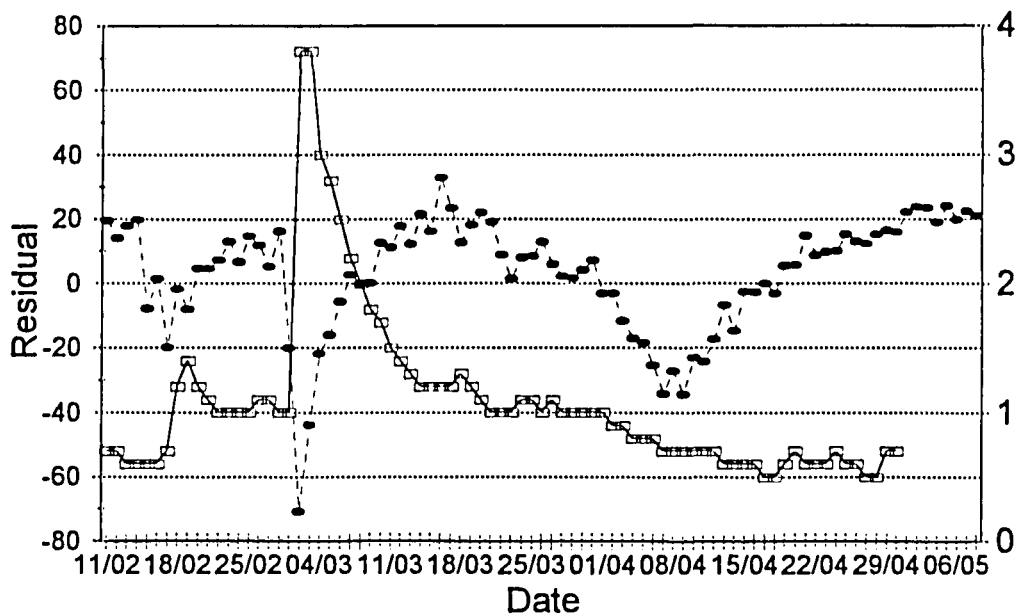


**Figure 5.3** The distribution of residuals (●), and the river level (□) expressed in metres above the minimum level recorded during the study, for the period 11 February to 8 May 1993.

Unfortunately not all the departures observed were caused by floods. For example, the gradual decline and subsequent increase in residuals observed during the first half of April (Figure 5.3) coincided with a period of steadily decreasing water levels. It was unfortunately, not possible to explain most of these gradual deviations from using the data to hand. However, the two most likely possible explanations are that the behaviour results from physiological changes in the tree that result in a sharp decline in transpiration followed by a rapid recovery. This may for example be caused by cavitation of the xylem (Tyree and Sperry, 1991). It is also possible that this results from a rapid decline in the leaf area index (through leaf drop) and a recovery following the flush of new leaves. Bear in mind that LAI readings were taken at the Narina site at monthly intervals and a linear interpolation method was used to predict the LAI for each day. It is therefore conceivable that the LAI may change quite rapidly in the interval between any two monthly surveys, and return to the original level without being detected during the monthly surveys. The cause of such a rapid change in LAI may once again be cavitation of the xylem, or the result of fungal disease on the leaves (this has been observed in commercial poplar trees), or it could merely reflect the natural canopy dynamic of fig trees.

It is largely because of the relatively poor residual distribution in the period prior to November 1993, and after October 1994 that the overall  $R^2$  accounts



for less than 80% of the observed variation. The model performs substantially better for the year-long period from November 1993 to November 1994 (Figure 5.4) and accounts for 88% of the observed variation. It is not entirely clear why this is the case. Our expectation was that the model would perform poorly over this period especially as the tree was affected by the severe frost event recorded on the 30th of June 1994. As a result of this event the tree displayed a very large range of evaporation rates during the course of the year ranging from a maximum of 119 l per day during January and February down to only 10 l per day recorded in July. While it is difficult to understand why the model performance was so good over this year, it was really encouraging to see such a good performance over a year which resulted in such a wide range in evaporative conditions.

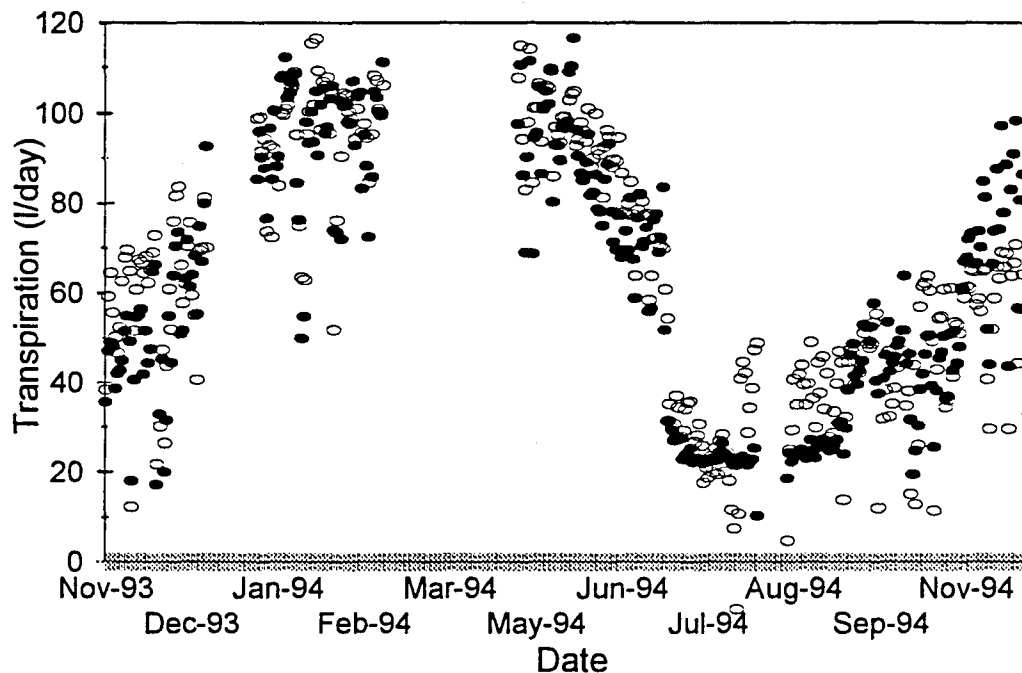


**Figure 5.4** A comparison of the observed transpiration recorded in the fig tree (●) and that predicted by the model (○) for the period November 1993 to November 1994.

The model suggests that there is no change in the behaviour of the fig tree for the months March to June, and August to September (Table 5.1), as these have the same coefficients and intercept. It is felt that the change in intercept recorded for the month of July was influenced by an uncommon occurrence, the severe frost event experienced at the end of June in 1994. Had this frost event not occurred, it is felt that July would also have been included in the above period. There is also no good reason why there should be such a

dramatic change in July as indicated by the large change in intercept, and the LAI coefficient (Table 5.1). For this reason it is recommended that the above model be applied as if July were included in the period March to September.

**Table 5.1**

The fig tree transpiration model ( $R^2=0.779$ ). This model was developed with a daily time sep and requires data on the leaf area index, river level at the Narina site, and vapour pressure deficit. The model predicts transpiration in litres per day.

Model	Intercept	Leaf Area Index LAI	$1 - e^{(-av\_vpd)}$	River level	Feb	Jul	LAI Jan	LAI Feb	LAI July	LAI Oct	LAI Nov	River level Dec
Main	-83.416	21.052	61.992	22.493	95.598	-60.357	-5.776	-22.523	-60.357	-4.606	-7.553	-14.471
Jan	-83.416	15.276	61.992	22.493								
Feb	12.182	-1.476	61.992	22.493								
M-J A-S	-83.416	21.052	61.992	22.493								
July	-143.773	40.566	61.992	22.493								
Oct	-83.416	16.446	61.992	22.493								
Nov	-83.416	13.499	61.992	22.493								
Dec	-83.416	21.052	61.992	8.022								

**NOTES:**

- i The equation given in the first row is reduced to "monthly" models in the following rows by adjusting the coefficients of the intercept and three predictors to accommodate coefficients six to thirteen.
- ii The "M-J A-S" row is the model for the months March to June and August to September.
- iii For February the LAI has virtually no impact on the water usage. However, the positive intercept compensates for this lack of influence.
- iv The influence of LAI is at its greatest for July when the intercept is at its lowest.
- v The influence of the river level is lowest for December.

## 5.4 Modelling transpiration from the reeds

The water use of up to sixteen reeds was simultaneously monitored over a period of 10 days in September 1993, 15 days in October 1994, 14 days in February and 9 days in March 1995, the latter was a continuous period of 23 days. Transpiration was adjusted for differences in leaf area between reeds, therefore the units of transpiration are  $\text{l day}^{-1} \text{m}^{-2}_{\text{foliage}}$ .

The following variables were recorded

- average daytime wind speed ( $\text{m sec}^{-1}$ );
- average and maximum photosynthetically active radiation (PAR,  $\mu\text{mol m}^{-2} \text{sec}^{-1}$ );
- average relative humidity (%);
- average, minimum and maximum temperature ( $^{\circ}\text{C}$ ),
- average and maximum vapour pressure deficit (VPD - kPa) a combination of relative humidity and temperature,;

As these variables monitor the environment influencing the transpiration rate they are referred to as environmental variables below.

### 5.4.1 Season/age indicators and slope variables

There were two alternate ways of examining the three periods of reed water use data. The first was to view the three data sets as representing a snapshot of water use from a reed bed that was getting progressively older. The September 1993 data set would then be regarded as representing water use from a 'young reed bed', while the data from October 1994 and February 1995 would be regarded as two replicate samples of data from an 'older' reed bed. The alternative was to regard the first data set collected as being typical of a young reed bed, while the second and third data sets present data typical of two distinct seasons. These would be the water use recorded under conditions of minimum flow (October) and that under high flow conditions (February/March). It was decided to develop models for both situations, the user would then be required to make a subjective decision as to which situation more accurately reflects the one which he is modelling.

Two assumptions are implicit in the above. In the first case one assumes that the primary factor influencing reed transpiration is age. The implication of the alternative is that one assumes the effect of reed age to override the effect of season while the reed bed is 'young'. Once the reed bed is older the effect of season becomes evident.

To cater for these two situations, dummy variables were created to represent each of the seasons and ages as described below:

**Model 1: Treating the three data sets as being representative of transpiration in a young and old reed bed**

An indicator variable was defined for each of the three data sets to indicate age. The indicator assumed the value zero for the September 1993 data set, and one for the October 1994 and February/March 1995 data sets.

**Model 2: Treating the three data sets as being representative of transpiration firstly from a young reed bed, and secondly from an older reed bed under low- and high-flow conditions respectively.**

In this case, two indicators were defined: SEASON2 and SEASON3. For the data of September 1993 both were set to zero. For the data of October 1994, SEASON2 was set to one, while SEASON3 was zero, and for the data from February/March 1995, SEASON3 was set to one while SEASON2 was set to zero.

**5.4.2 What is the most appropriate measure of the mean water use of the reed bed?**

It is desirable to use a robust measure of the mean behaviour of the reeds in the reed bed. As the data may be asymmetrically distributed around the mean, and as the conventional 'average' gives equal weight to all observations, this may result in a misleading value for the mean transpiration of the reed bed. As it is likely that symmetry may not be present in the reed water use data, it is advisable to use an estimate of location that is robust to outlying values. Using a robust measure of location removes any need to question the appropriateness of the estimate as measure of centrality.

In 1972, Princeton University published an exhaustive study, "Robust Estimates of Location" (SAS, 1986), of a large number of estimators of location. The book has become the standard reference on the subject.

Three estimates are recommended:

- the median (50th percentile that divides the data into two equal parts);
- a weighted mean of the 33rd percentile, the median and the 66th percentile, better known as the Gastwirth median (SAS, 1986 p 8);
- a "piecewise linear M-estimate" (SAS, 1986 p 14) referred to as "12A".

The Princeton study recommends the 12A estimate as the leader for all sample sizes (section 6L5 of SAS, 1986 p 216), with both the median and Gastwirth median as close followers (section 6K5 of SAS institute manuals, p 215).

Because a weighted mean of the 33rd, 50th and 66th percentiles of a distribution is clearly more informative about its location, than is the 50th percentile, and is easier to grasp than the 12A estimate, the Gastwirth median was used as the estimate of the reed bed water usage.

The Gastwirth median is defined as:

$$0.3*(33\text{rd percentile})+0.6*(50\text{th percentile})+0.3*(66\text{th percentile})$$

The models discussed below are developed using the Gastwirth median, rather than the average, of 7 to 16 replicate measures of daily water usage. The predicted water usage, from the model, is then the expected water usage (per leaf area) of a reed in the reed bed.

### **5.4.3 Transformation of vapour pressure deficit**

Given that a linear multiple regression approach was adopted to develop a predictive model for the reed bed, it was necessary to determine whether the relationship between the independent variables and the dependent variable is in fact linear. This was tested graphically by means of plotting scatter graphs of all possible independent variables against the mean transpiration rate from the reed bed. Plotting the daily average values (AVG\_VPD) against the corresponding Gastwirth median transpiration rate revealed a tendency towards an asymptote of approximately 5.5 litres/leaf area for September 1993, and 4 litres/leaf area for both October 1994 and February/March 1995. The data illustrated a negative exponential relationship with transpiration reaching an asymptote at high VPD. This non-linear relationship between transpiration and VPD is consistent with the expected physiology of plants.

To avoid the complexities of adopting a non-linear modelling, VPD was transformed to account for this non-linear behaviour. In this way, it was possible to accurately reflect the nature of the relationship between VPD and transpiration, and also still use a simple multiple regression approach to model development. The following transformation, a special case of the more general Richards growth curve model (Seber and Wild, 1989), was used:

$$\text{AVG\_VPDT} = 1 - e^{(-\text{AVG\_VPD})}$$

As a test of the appropriateness of the above transformation, AVG\_VPDT was used as a predictor of water use for each of the three periods (September 1993, October 1994 and February/March 1995). Significant models were obtained in all three cases (Table 5.2) indicating that the transformation was appropriate.

**Table 5.2** Predicting the mean water use of the reed bed with a model in which VPD has been transformed to reflect the nature of the relationship between transpiration and VPD.

Period	Intercept	Slope	Water use at asymptote (VPD=5 <sup>*</sup> )	R <sup>2</sup>
September 93	0.90	5.03	5.90	0.64
October 94	-0.39	3.68	3.26	0.85
February/March 95	1.12	3.06	4.16	0.77 <sup>**</sup>

<sup>\*</sup> For VPD=5, AVG\_VPDT ( $=1-e^{-5}$ ) = 0.9933

<sup>\*\*</sup> Two of the twenty three cases were rejected as outlying.

The possibility of developing a model that used a transformed maximum daytime VPD was also tested, but found to be non-significant and therefore excluded from further analysis.

#### **5.4.4 Models derived for the mean daily transpiration of the reed bed**

The stepwise procedure was used to select predictors from the eight environmental variables and the indicator variable(s). Two models were found that gave satisfactory predictions of average transpiration for the reed bed. The model parameters are presented in Table 5.3. These models met the criteria for statistical rigour discussed in the section on model selection above.

The first model was derived using the indicator for "old" reeds (those sampled in 1994 and 1995), while the second model was derived using the two season indicators for October 1994 and February/March 1995. The two models presented in Table 5.3 are split into "sub-models" using the coefficient(s) of the indicators.

**Table 5.3** The coefficients for the two best models developed to predict the median daily transpiration per unit leaf area from the reed bed at the Narina study site.

Model	Intercept	$1-e^{(-av\_vpd)}$	Oldreed	Season2	Season3	R <sup>2</sup>	Outlier (Case)
1	2.8223	2.2002	-1.9735			0.82	none
1a	2.8223	2.2002					
1b	0.8488	2.2002					
2	2.2231	3.4313		-2.4367	-1.3243	0.94	950303 (42) 950307 (46)
2a	2.2231	3.4313					
2b	-0.2136	3.4313					
2c	0.8988	3.4313					

Notice that models 1a and 2a, for the same period, have different slopes and intercepts. With the additional information about the increasing age of the reed bed, and change in season included in the overall model, the model for this period is better estimated (with larger R<sup>2</sup>), with a smaller intercept and steeper slope (Table 5.3). Notice also that for model 2a,  $av\_vpd > 5$  the transpiration rate for a young reed bed is  $> 5.6$  ( $0.99326 \times 3.4313 + 2.2231$ ,  $1 - e^{-5} = 0.99326$ ).

The corresponding transpiration rates for models 2b and 2c, for progressively older reeds, for  $av\_vpd > 5$ , are 3.2 and 4.3 respectively. Though both are smaller than 5.5, the difference in value probably reflects the effect of the seasons when data was collected. Notice how closely they compare to the results presented in (Table 5.2). The benefits of modelling all the data rather than each period separately is apparent. Notice further that for model 1a the transpiration rate threshold for  $av\_vpd > 5$  is 5.0. For model 1b it is 3.3.

#### 5.4.5 The Distribution of Residuals for the Reed Models

Figures 5.5 and 5.6 present the observed and predicted transpiration, the residuals, and an indicator of the cases that had to be excluded as outliers on the right-hand side of the figure. The residuals for model one were larger than those for model two confirming that model two fits the data better, and also reflecting the larger R<sup>2</sup> of model two.



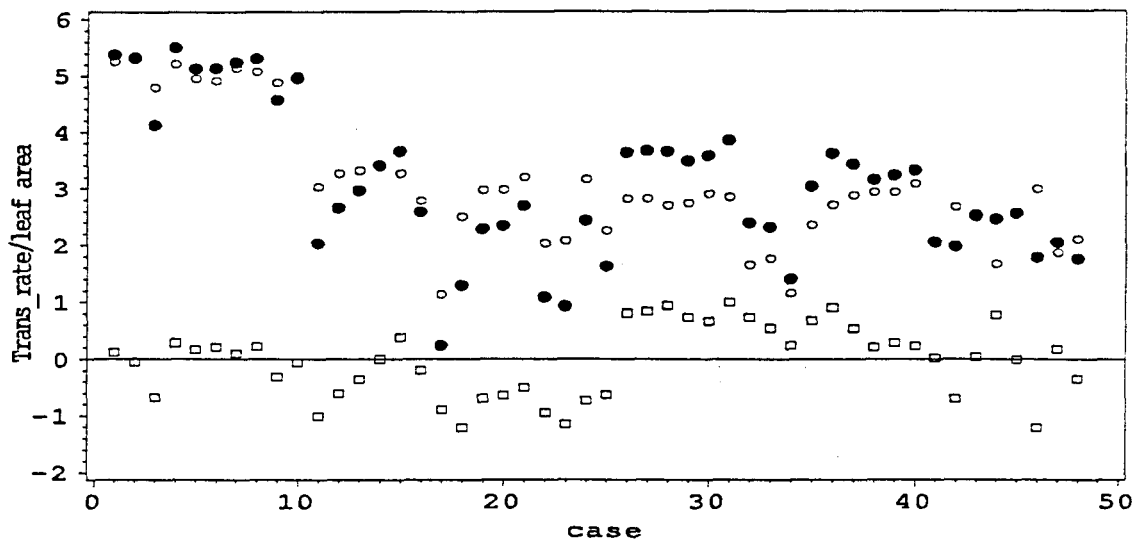


**Figure 5.5** A comparison of the observed mean daily transpiration per unit leaf area recorded for the reed bed (●) with that predicted by Model 1 (○), and the corresponding distribution of residuals(□).

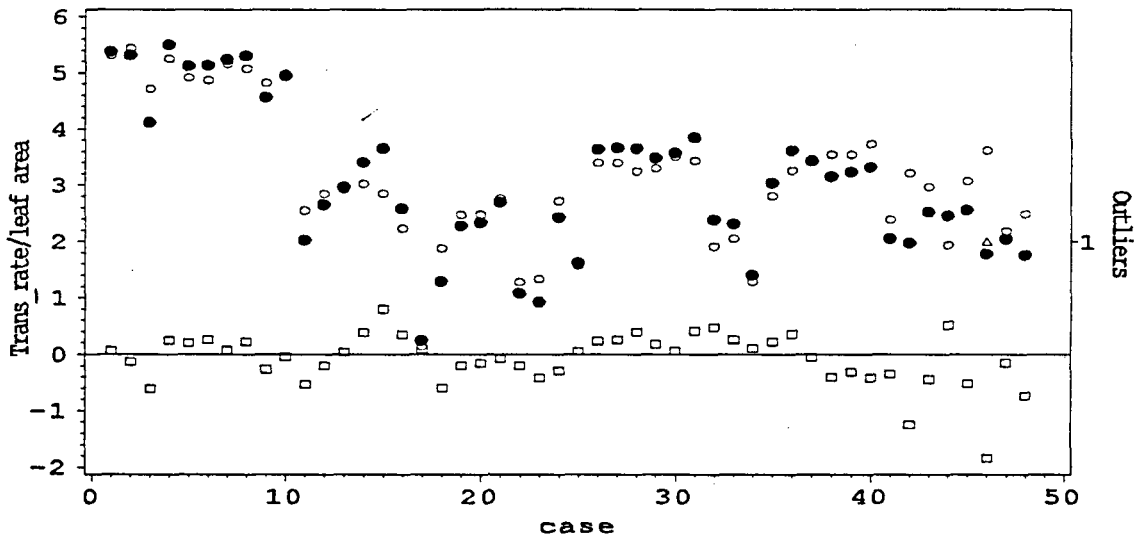


**Figure 5.6** A comparison of the observed mean daily transpiration per unit leaf area recorded for the reed bed (●) with that predicted by the Model 2 (○), and the corresponding distribution of residuals (□). The location of the two outliers (Δ) omitted from the analysis.

The above results indicate that it was possible to accurately model the water use per unit leaf area of a reed bed for three data sets requiring only three input variables. The first is an indication of the age of the reeds, and if they are 'old' then also the season is required. One meteorological variable is required, VPD. This should be transformed to a negative exponential form as above, to reflect the asymptote reached in transpiration with increasing evaporative demand. This would then give a result of the predicted transpiration per unit leaf area. In practice, the transpiration per unit ground area is of more interest, and therefore it would be necessary to multiply the above by leaf area index as has been done in Chapter 6 of this report.

While the above model does describe the data well, and it appears adequately parsimonious with regard to its demands for input data, it should be stressed that the model was developed on a limited data set. In addition, this data set was constituted of data collected from only 16 reeds (which is a very small sample relative to the population of reeds). Also the application of the model does require considerable subjective assessment with regard to whether the reeds are 'young', or old. In reality the differences that were observed may represent something other than age, such as changing nutrient status in the reed's root zone. The biologically significant point of this study, however, is that it was possible to estimate the median daily transpiration per unit leaf area from a reed bed using only one meteorological variable, VPD, which results in a very 'practical' model.

The heat balance technique was used in this study to measure transpiration from the reed bed. The strength of the technique is that it does not have severe constraints regarding the environment in which it can be applied, and that it was the only technique that would have been appropriate at the Narina site. Measurements of populations of reeds would, however, be better made using a 'top-down' technique, such as Bowen ratio. This would provide an integrated estimate of the water use of entire reed beds, but does have constraints with regard to the micro meteorological conditions under which it can be applied. As such, it would be better suited to application in large reed beds such as those in the Sabie River east of the Lower Sabie camp. The above study does however provide the first direct estimates of evaporation from reed beds in this country, and future work should aim to validate and refine the model predictions.

## **CHAPTER 6**

### **SABIE RIVER RIPARIAN WATER BALANCE**

---

#### **6.1 Potential Transpiration Losses**

The data presented in Chapter two of this report illustrated that there was no indication of water stress in any of the sample trees at the Narina study site even during the driest months of the year and when river flow was at its lowest. For this reason, this chapter heading is 'Potential transpiration losses' which indicates that we believe that the trees at Narina transpired at near potential rates over the course of this study. It is, however, important to emphasise that we do not believe that this is always the situation in the Sabie River system, rather it is only typical of forest established on alluvial deposits which are hydrologically well connected to the water flowing in the stream channel. Where this is not the case, for example in bed-rock controlled sections of the river, we expect transpiration to decline as the water supply to the riparian forest diminishes.

##### **6.1.1 Transpiration from the Narina Site**

###### **6.1.1.1 Transpiration from Trees**

The transpiration data collected from the Narina study site (presented In Chapter two) indicated that the transpiration rates of the reference fig tree did vary seasonally with generally higher rates recorded during summer than in the winter months. Also, there was a linear relationship between the reference tree and the other trees sampled at the site during the periods of intensive field sampling. It is therefore possible to scale up to the transpiration from the Narina site by multiplying the transpiration recorded by the reference tree by a factor which reflects the slope of the relationship between the reference tree and each respective species present at the site. As it was not possible to measure transpiration from all the trees at the site, it is also necessary to estimate the transpiration rate for the other trees present at the site. The most logical approach to this was to estimate transpiration on the basis of the cross-sectional area of the stem, as this is known to correlate with the leaf area of the tree and therefore is related to the total evaporative surface the stem supports. Transpiration from the trees at the Narina site was therefore determined by:

- i) calculating the transpiration rate per unit basal area for each of the sample trees
- ii) determining the relationship between the reference fig tree and the other trees sampled at the Narina site

- iii) measuring the basal area of all the trees rooted within the study site. The boundary of the site was taken to be the line of piezometers on the upstream and downstream side of the site, the river on the northern end, and the top of the macro-channel bank on the southern side. The site therefore had a total area of 2800m<sup>2</sup>, 1740m<sup>2</sup> of which was dominated by trees, and the remainder dominated by reeds.
- iv) The total transpiration from each species was then calculated by multiplying the transpiration rate recorded on the reference fig tree by the factor relating it to the relevant species, and by the total basal area of the species on the site. The aggregate for all the species present then represents the total transpiration for the site.

Transpiration from the reeds at the site was determined by applying the reed transpiration models to the historic meteorological data and multiplying by the measured leaf area indices in the reed bed at Narina.

i) *Basal area of trees rooted at the Narina site*

The total basal area (measured above the basal swelling) of trees at the Narina site was 5.33 m<sup>2</sup>. Three species, *F. sycomorus*, *T. emetica* and *D. mespiliformis* constituted 88.2% of the basal area of trees at the site (Figure 6.1). The most abundant tree species was *D. mespiliformis* with 62 of the 87 stems measured at the site. They were, however generally small, with a mean diameter of only 10 cm, and therefore contributed only 11.6% of the basal area. By contrast, the *T. emetica* and *F. sycomorus* trees were substantially larger with mean diameters of 32.7, and 66.4 cm respectively, and while they were fewer in number, they had significantly higher basal areas (Figure 6.1).

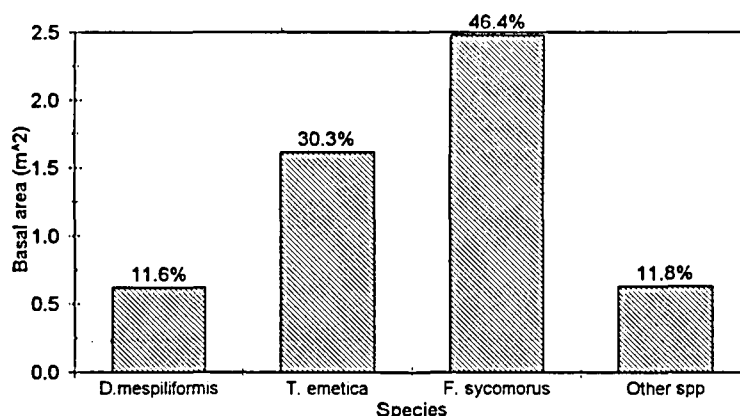


**Figure 6.1** The basal area recorded for the tree species at the Narina site, and relative proportion they contribute to the total.

ii) *Transpiration per unit basal area and the relationship between species*

The mean transpiration per unit sapwood area was calculated by dividing the mean transpiration rate recorded for each of the five species by the cross-sectional area of the stem at the time of measurement (Table 6.1). As was expected due to relatively large differences in the mean transpiration rate recorded at each of the surveys and the more stable cross-sectional area, the rates differed quite significantly over the course of the study. They were highest for the February 1993 survey, and lowest for the October 1994 survey. These data were then multiplied by the total cross-sectional areas measured for each of the respective species at the site (Figure 6.1). For those species (eg. *A. robusta*) not included in the HPV survey, but present at the site, the mean transpiration per cross-sectional of all the species listed in (Table 6.1) multiplied by the total cross-sectional area of 'other' species was used to estimate the daily transpiration. The sum of the above data represented the total daily water use from all tree species within the study area at the Narina study site.

**Table 6.1** The mean daily transpiration per unit sapwood area ( $l\ cm^{-2}\ day^{-1}$ ) calculated for each of trees sampled during the intensive HPV surveys carried out at the Narina study site.

Survey	<i>F. sycomorus</i>	<i>T. emetica</i> (river)	<i>T. emetica</i> (bank)	<i>B. zeyheri</i>	<i>D. mespiliformis</i>
Feb '93	0.163	0.102	0.149	0.034	0.158
Sep -'93	0.141	0.052	0.065	0.041	0.076
Oct-'94	0.045	0.035	0.029	0.021	0.035
Feb-'95	0.089	0.056	0.076	0.034	0.068

The above data were only available for selected periods over the course of the study. To estimate the total water use from all the species over the course of the year, a factor was calculated for each of the periods where there were data relating the total transpiration from the *F. sycomorus* tree to that of each of the other species present at the site. Therefore, for each species there were four factors, one for each intensive survey carried out. These factors were then used to calculate the total daily transpiration rates for the site for the periods in between the intensive HPV surveys. The factors were applied to the data as outlined in Table 6.2. This resulted in an estimate of transpiration in litres from all the trees at Narina per day.

**Table 6.2** The periods into which the transpiration simulation for the Narina site was divided up, and the relationships used to extrapolate from the reference tree data to the data for the whole Narina site.

Period			Relationship used
Year	Start	End	February 1993
1993	31 June	30 September	September 1993
1993	1 October	31 December	October 1994
1994	1 January	30 May	February 1993
1994	1 June	30 November	October 1994
1994	1 December	30 May	February 1995

As it was necessary to express the transpiration rate from the site in mm per day, the above value was converted to mm by dividing the transpiration rate by the total ground area occupied by the riparian forest between the two outer piezometer lines (1740 m<sup>2</sup>). This value was then transpiration averaged over the whole site in mm (as one litre per square metre is equivalent to one mm).

#### 6.1.1.2 Transpiration from Reeds

The transpiration models presented in Chapter five were applied to meteorological and LAI data collected over the course of the study to estimate yearlong transpiration rates from the reed bed. As the model predicted transpiration in l per square of foliage per day, it was necessary to multiply this with the recorded LAI data for the reeds, to derive an estimate in mm per day. The two reed transpiration models developed both had sub-models which were appropriate to different ages of reeds, and seasons. The way in which the sub-models were applied to the data is presented in Table 6.3.

**Table 6.3** The periods for which the various reed sub-models were applied in the simulation exercise to estimate yearlong transpiration rates from the reed bed. The model notation refers to the models presented in Chapter five.

Period	Which sub-model was applied	
	Model 1	Model 2
September 1993 - June 1994	1a	2a
July - November 1994	1b	2b
December 1994 - June 1995	1b	2c

The reed bed was estimated to occupy a total of 1260 m<sup>2</sup>. To calculate the total water use in litres per day the transpiration estimate in mm per day for the reed bed should be multiplied by 1260, and the mean transpiration estimate for the site as a whole was calculated as the area-weighted average of the two transpiration estimates (trees and reeds).

### 6.1.1.3 Results and Discussion

#### i) *Transpiration from reeds*

The daily transpiration estimates simulated using Model 2 for the reed bed shows a clear seasonal trend with peaks during the latter half of summer, and minimum values towards the end of the winter season (Figure 6.2). This basic pattern follows the trend in the LAI values for the reed bed, and is a consequence of LAI being one of the input variables into the model. The figure also indicates those periods where measurements are based on actual transpiration data collected at the field site, as opposed to the remaining period where the result is the output of the application of Model 2. It is felt that the simulated peak transpiration rates are unrealistically high, as peaks in excess of 15mm per day are considered questionable. The highest actual daily transpiration estimates was approximately 12 mm per day during February 1995, and at approximately 7 mm per day during September 1993 (Figure 6.2). While these rates are high, they are not so high as to be of real concern given the evaporative demand at the site and the free access to water. The very high values are in fact simulated values, indicating that while the models developed fitted the data on which they were developed well, they did not perform satisfactorily on the extended data set.

This raises the question of where the error lies. There are four likely sources of error: Firstly, the estimates of transpiration on the individual reeds derived using the heat balance technique may be inflated. The second is that the leaf area estimates of the sample reeds may have been erroneous. Thirdly, the leaf area index measurement used in the simulation may be inaccurate, and fourthly, it is possible that transpiration per unit leaf area may not increase linearly with increasing LAI.

a) Does the SSHEB technique measure transpiration accurately on reeds? The technique has yet to be tested specifically on reeds, but was found acceptable on a number of other small stemmed plants, such as soybean (*Glycine max*) and sunflower (*Helianthus annuus*) with accuracies of  $\pm 10\%$  (Sakuratani, 1981). It is, however, not clear whether the hollow stems of the reeds resulted a violation of the assumptions underlying the application of the technique. Attempts to test the technique on *P. mauritianus* were not successful as growing the reeds in small containers proved unsuccessful.

b) It is unlikely that the error lies in the measurement of the leaf area of the sample plants, as the leaf area metre was calibrated prior to use with a calibration disk, and each batch of leaves was passed through the leaf area metre twice.

The average daily transpiration rate per unit leaf area recorded for the reeds during the September 1993 data set was  $5.7 \text{ l m}^{-2} \text{ day}^{-1}$ . Although this is considerably higher than that recorded for plantation trees in which maximum rates of 2.0, and average rates over a series of age classes and seasons was  $1.45 \text{ l m}^{-2} \text{ day}^{-1}$  (Olbrich, 1994), it is none the less in the same order of magnitude. Also, once the faster-growing habit of the reeds, and the higher the evaporative conditions under which the reeds were growing are taken into account the rates in the reeds do not seem too unrealistic.

c) We feel that the most likely source of error was in the estimation of LAI with the Licor 2000 meter. As the stand of reeds aged, the stand became very dense, and the general impression gained was that there were progressively more stems relative to the total foliage. The LAI metre is unable to distinguish between foliage and stem, and it is likely that the high LAI's recorded during the summers of 1994 and 1995 may have been severely inflated. Destructive sampling should be carried out to test the accuracy of the metre in estimating the LAI of the reed beds.



d) It is also possible that transpiration per unit leaf area is not constant through the range of possible leaf areas. This is as a consequence of the increasing degree of self-shading that occurs with increasing LAI. While it is likely that this does contribute to an over-estimation when the LAI is high, it is unlikely that this is the main reason for the high estimates.

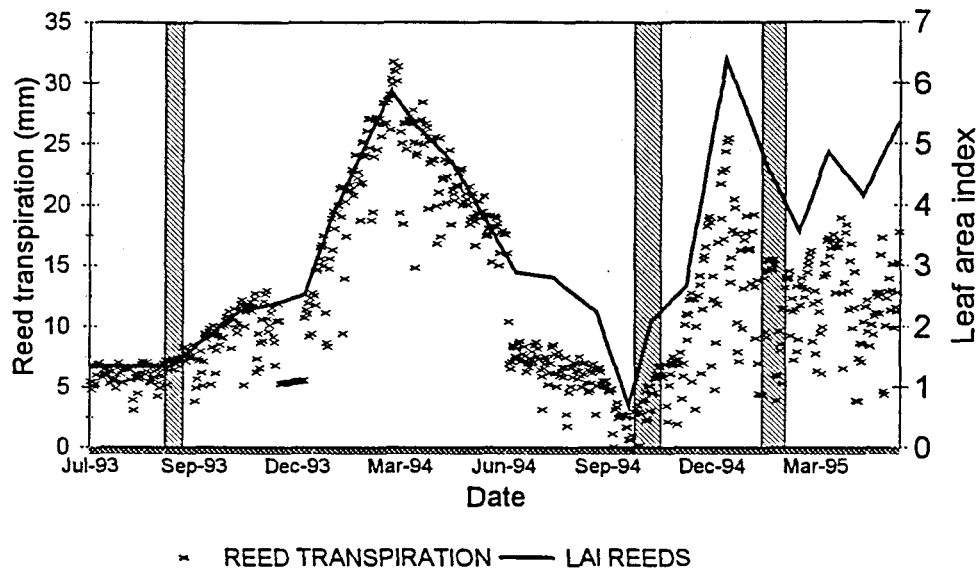


**Figure 6.2** Simulated daily transpiration rates from the reed bed at the Narina study site for the period 1 July 1993 to 5 June 1995. The vertical cross-hatched rectangles correspond to those periods where the estimates are based on actual field data.

ii) *The total water use of the trees at the Narina study site*

Predictions of the total transpiration from the tree canopy at Narina are presented in Figure 6.3. For ease of interpretation only the monthly mean data are presented. Peak transpiration rates at the site of 3.4 and 3.1 mm per day were predicted for the first two months of the study, in February and March 1993. The maximum daily transpiration rate predicted for this period was 4.02 mm day<sup>-1</sup>. This is considered to be a modest transpiration rate especially as the evaporative demand was at times extreme, and the trees were shown to have adequate access to water.

It is, however, important to bear several factors in mind. Firstly, the trees were not evenly distributed across the site. As a result, parts of the alluvial bank that were included in the 1740 m<sup>2</sup> area, did not have any trees on it. Also, especially during summer, there was a considerable annual herbaceous layer whose water use was not measured. This layer is likely to have transpired at least one millimetre of water per day. Thirdly, two multi-stemmed plants namely *Acacia schewinfurthii* and *Ficus capreifolia* were present at the site, but not

included in the estimate because it was not possible to measure the cross-sectional areas of the stems. Both these plants contributed significantly to the total foliage area on parts of the site. Clearly the inclusion of these plants would have raised the evaporation estimates, particularly in summer when the herbaceous layer was at its densest. Even if the above factors mentioned are taken into account, the transpiration rates recorded in the riparian forest are very conservative. The highest annual total transpiration predicted for the trees on the site was only 830 mm per year. Adjusting this value for the estimated error due to the vegetation not sampled, results in a possible estimate as high as 1079 mm per year. By comparison, transpiration from commercially planted *Eucalyptus grandis* in the Sabie region has been estimated to be 1170 mm per year (Dye, 1987). Given the higher evaporative demand in the Lowveld region, I would have expected the transpiration rates for the riparian forest to be higher.

An approximate relationship exists between the sapwood area of trees and their foliage area (Waring and Schlesinger 1985, Olbrich 1994), allowing an approximate estimate to be made for the trees at the Narina site. This analysis was done, and showed that the maximum transpiration rate per unit leaf area recorded for the fig tree was approximately 0.34 and the average  $0.17 \text{ l m}^{-2}_{\text{foliage}} \text{ day}^{-1}$ . By comparison, the maximum rate for *E. grandis* recorded was  $2.0 \text{ l m}^{-2}_{\text{foliage}} \text{ day}^{-1}$ , with an average for an age-sequence of trees at  $1.45 \text{ l m}^{-2}_{\text{foliage}} \text{ day}^{-1}$ . The estimated rate for the *T. emetica* was also low with an average of  $0.25 \text{ l m}^{-2}_{\text{foliage}} \text{ day}^{-1}$ .

There are two possible reasons for the relatively low transpiration rates from the trees at the Narina site. Firstly, unlike trees in commercial forest plantations, the trees at Narina were severely clumped resulting in a large degree of mutual shading. This would have the natural consequence of depressing transpiration. Secondly, the dominant trees at the Narina site were all very large and most probably old. It has been shown that the transpiration per unit leaf area declines with age (Olbrich 1994) as a consequence of the tortuous flow paths water must follow in passing from the root through long branches to the leaves (Cole *et al.* 1990). The result is that even though the LAI is reasonably high, and there is an adequate supply of water the transpiration rates can be depressed in large, old trees. The corollary, is that young trees will have significantly higher water requirements than those demonstrated here.

Despite the relatively low rates of transpiration in the riparian forest at Narina, rainfall at the site was inadequate to maintain the vegetation as the mean annual rainfall at the site over the three years of study was 447mm per year. The riparian trees are therefore heavily dependent on the water from the river to maintain transpiration rates for at least half of the year.

Despite the differences in the absolute transpiration estimates for trees and reeds, it was encouraging that there was a clear correspondence in the trend followed by the trees, and the simulated values from the reeds (Figure 6.3). This suggests that the behaviour of the reed model is acceptable, but the absolute prediction is unrealistic.

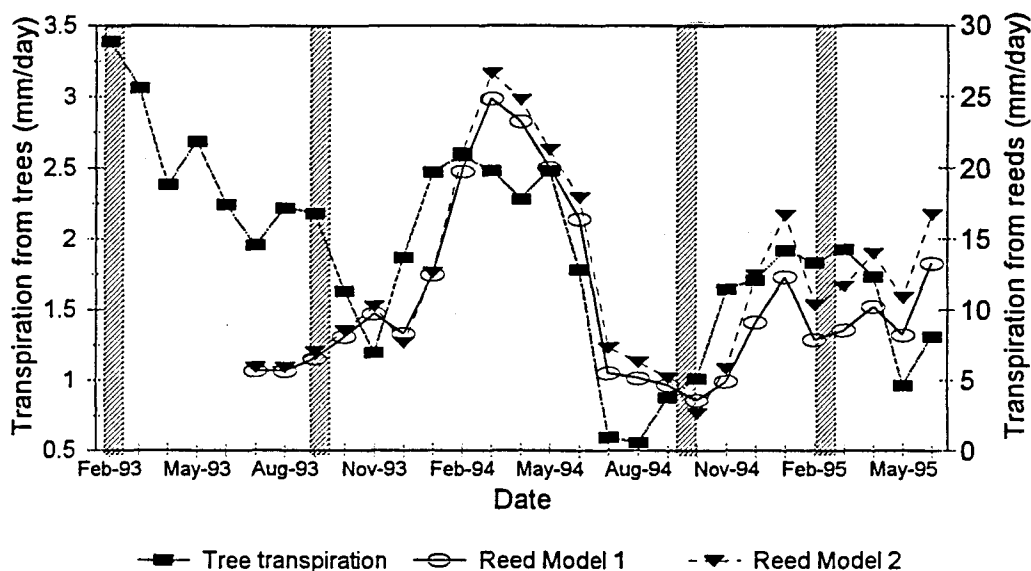


**Figure 6.3** Monthly mean daily transpiration rates estimated for all the trees at the Narina study site, and the output of the two reed model simulations from February 1993 to June 1995. The cross-hatched areas indicate those periods where intensive measurements were made of transpiration from the tree species.

### 6.1.2 Scaling the Transpiration Model from Narina to the Sabie River

One of the aims of this project was to estimate the water use of the riparian vegetation on the Sabie River through the Kruger National Park. It was initially hoped to estimate this by calculating the area under reeds and trees in the riverine system, and running simulations for each of the component vegetation types. As the reed transpiration model requires validation and possibly further development in view of its unrealistic predictions, it was no longer possible to run the simulations as planned. Also, it was hoped that better spatial and seasonal data on the variation in LAI would be available to scale the transpiration rates for the component vegetation communities. While it was possible to collect a limited data set during the low flow season, access to most of the sites was limited during the high-flow season resulting in an incomplete

LAI data set for the transects on the river system. However, the data to hand confirms the strong seasonal change in LAI in all vegetation types sampled on the river. This was reassuring as it indicated that there was a harmonious change in LAI (and therefore transpiration) in the riparian vegetation on the river system.

Despite the limitations cited above, it was possible to make a first guestimate of the consumptive water use of the riparian vegetation by making the assumption that the mean transpiration rate of the riparian vegetation approximates to that recorded for the Narina study site. Bredenkamp et al (1993) estimate the total area of the riparian vegetation on the Sabie River in the Kruger National Park to be 3844 hectares ( $3.844 \times 10^7 \text{ m}^2$ ). The product of this area and the mean monthly daytime transpiration estimates from Narina results in a estimated average consumptive water use of  $0.84 \text{ m}^3 \text{ sec}^{-1}$ , with an annual average ranging from  $1.01 \text{ m}^3 \text{ sec}^{-1}$  to  $0.60 \text{ m}^3 \text{ sec}^{-1}$  for the years with highest and lowest transpiration respectively. The maximum monthly mean rate estimated was for February 1993 (Figure 6.4), with a consumptive water use of  $1.51 \text{ m}^3 \text{ sec}^{-1}$ . The absolute minimum predicted was for September 1994 (following the severe frost), with a consumptive water use estimate of only  $0.25 \text{ m}^3 \text{ sec}^{-1}$ .

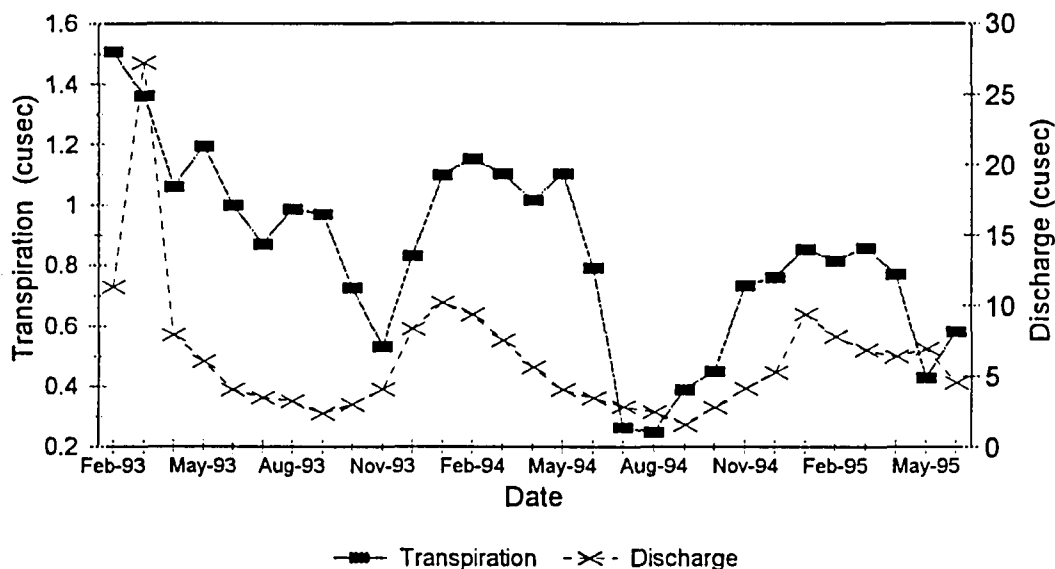


**Figure 6.4** Variation in the consumptive water use of riverine vegetation along the entire length of the Sabie River in the Kruger National Park in  $\text{m}^3 \text{ sec}^{-1}$ , and the discharge of the Sabie River measured at the Narina site.

As will be shown later in this chapter, the above estimates are similar to those calculated from a weir-gauging exercise conducted during winter, and slightly lower, but of the same order of magnitude as that derived from a Symon pan estimate. This result was pleasing, as it indicated that although the transpiration rates from the trees at Narina were felt to be conservative, they were realistic.

It is necessary to be critical of the application of transpiration data from trees to reeds, especially as reeds form a dominant component in 33 % of the riparian zone of the Sabie River (Bredenkamp 1993). The actual data collected from Narina shows that their transpiration is perhaps a little higher than that recorded for the trees, and this may reflect the situation in the tall reed beds which are common in the downstream sections of the Sabie. Other sections of the river, however, have dry open sparsely-vegetated reed beds classified by Bredenkamp et al (1993) as '*Vernonia glabrata*-*Grewia flavescens* Reed Scrub', and it is most likely that their water use is substantially lower than that recorded in the riparian forest. Also, even in the well-established reed beds, there are large open sandy patches with low leaf area indices, and therefore near zero water use. It is as a result of these compensating factors that the estimates derived from the trees at Narina are also realistic for the whole riparian system.

It is felt that the estimate presented above may be a little inflated because Bredenkamp et al (1993) include several vegetation communities such as the "*Acacia tortilis*-*Combretum imberbe* woodland", and the "*Spirostachys africana*-*Trichilia emetica* dry riparian forest" that are consistently associated with the riparian zone, but it is unlikely that they have consistent access to phreatic water. They are therefore not dependent on water supplied by the river, and for the purposes of this extrapolation exercise, these dry riparian woodlands and savannas should be excluded. This reduces the estimates of consumptive water use by approximately 20 %. The best estimate of the mean annual consumptive water use then decreases to the range 0.81 and 0.48 m<sup>3</sup> sec<sup>-1</sup>.

### **6.1.3 Seasonal and Long Term Trends in Transpiration**

As expected the trend in the predicted values follow those of the transpiration estimates for Narina with late summer peaks in transpiration, and late winter minima (Figure 6.4, and 6.5). The most interesting result is to examine the proportion of the discharge that is estimated as being required to support the consumptive water use of the riverine vegetation. The mean estimated consumptive water use of the vegetation relative to the discharge over the course of the study was 16.5% with a maximum and minimum of 40.8 and 5.0% respectively. Notably, despite the fact that transpiration decreases during the dry season (Figure 6.4), the proportion of discharge used in supporting

transpiration increases steadily during the dry season. This is clearest in 1993, where the consumptive water use reached a maximum of 41% of discharge in September of that year (Figure 6.5). This trend would have been repeated the following year had it not been for the severe frost which resulted in the decline in water use estimated for July and August 1994 (Figure 6.5).

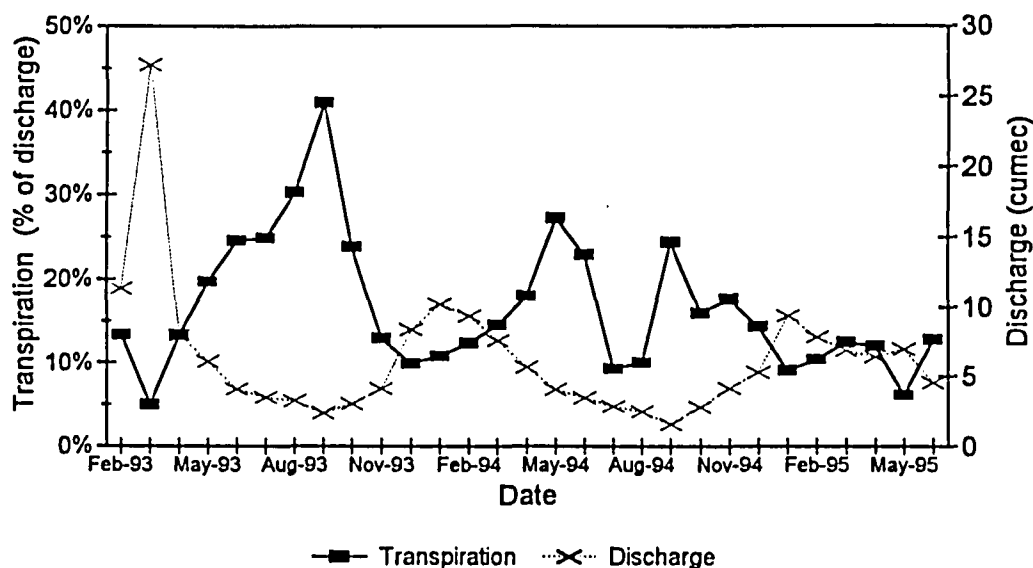


**Figure 6.5** Estimated consumptive water use from the riverine vegetation on the Sabie River as a percentage of the recorded discharge from February 1993 to June 1995.

It had been hoped to take this simulation one stage further and integrate the results of this study with that of Carter (1991) in which he predicts changes in vegetation cover as a result of changing flow regimes. Two of his cover classes were riparian forest and reeds, and it would have been interesting to use the transpiration models to predict the change in consumptive water use concomitant with the change in cover of the various vegetation types. Also, it would have been interesting to predict the historical consumptive water use of the riverine vegetation to determine whether there is still enough water in the system to support that vegetation mix. This simulation was not done for two reasons: firstly the reed models were not giving realistic estimates of water use, and secondly, it required the LAI of each of Carter's vegetation types to be classified properly. It is strongly suggested that this form the focus of a future project, as this data would be invaluable in determining whether the flow of the river in future can sustain the consumptive water requirement of the riverine vegetation, especially as Carter showed the vegetation is changing directionally towards an increasingly wooded state.

## 6.2 The Sabie River Riparian Water Balance in the Kruger National Park in Perspective

The 108 km Sabie River in the Kruger National Park extends from the Albasini trade site in the west, to the gorge through the Lebombo Mountains in the east where the Sabie enters Mozambique to ultimately discharge into the Indian Ocean. The principal consumptive water users along the river upstream from the KNP, and within the KNP, include:

### 1 *Abstractions for irrigation between Albasini and Kruger Gate*

This section incorporates Lisbon Estates, and large tracts of land bordering the KNP where subsistence type agriculture has traditionally been practised. Development of services is taking place in this region, providing the capability to significantly reduce instream flows from pumping on an *ad hoc* basis to larger scale abstractions.

### 2 *Abstractions for irrigation and domestic supply for communities within the KNP*

The volume of water abstracted for irrigation and domestic use at Skukuza, Pretoriuskop, Lower-Sabie and Mkhulu rest camps and Kruger Gate as at 1985 was estimated at  $10\,254\text{ m}^3\text{ day}^{-1}$  (Gertenbach, 1985).

### 3 *Animal consumption*

The consumptive allowance for animals in the vicinity of the Sabie River as determined by the 1985 census, is  $655\text{ m}^3\text{ day}^{-1}$  (Gertenbach, 1985)

### 4 *Evapotranspiration*

The Sabie River in the KNP has a well developed riparian zone up to 500 metres wide. As has been shown above, evapotranspiration contributes significantly to consumptive water use. The long-term (1960 to 1995) average Symon pan annual evaporation recorded at Skukuza is 1572 mm ( $4.3\text{ mm day}^{-1}$ ) (Birkhead *et al.*, 1996b). Assuming a riparian zone of 3114 hectares (Bredenkamp *et al* 1993, (this excludes non-phreatic forest)), and a transpiration rate equal to the pan evaporation (transpiration not limited by subsurface water availability) the consumptive use is  $134\,000\text{ m}^3\text{ day}^{-1}$  ( $1.54\text{ m}^3\text{ sec}^{-1}$ ), thirteen times the water abstracted for use within the KNP.

Bank seepage from active channels in laterally extensive fluvial deposits provides recharge of subsurface storage. Laterally extensive macro-channel deposits typically occur in single-thread, braided and isolated alluvial sections of the predominantly bedrock influenced pool-rapid and anastomosing channel types. In these hydraulically connected surface-subsurface systems, the consumptive water use by vegetation (potential transpiration) is limited only by plant physiology and climatic conditions, since groundwater is freely available provided adequate base-flow is assured. Transmission losses or the consumptive use of riparian vegetation during low-flow periods therefore accounts only for transpiration from vegetation hydraulically connected with surface flow. For this reason the vegetation types cited at the end of section 6.1.2 have been omitted from the above analysis.

### **6.3 Water Balance Between Gauging Stations**

#### **6.3.1 Transmission Losses**

Transmission losses along the Sabie River were estimated by applying a water balance between the gauging weirs located downstream of Kruger Gate (DWAF Gauging Station X3H021) and downstream of Lower Sabie rest camp (DWAF Gauging Station X3H015).

The accuracy of the water balance is compromised for the following reasons:

1. The flow contributions from tributaries to the Sabie River, particularly the Sand River, are difficult to assess with any confidence.
2. The inherent inaccuracies involved in calculating discharge rate from stage level for low discharges over gauging structures with wide crests.
3. Data on the consumptive water use (extractions minus return seepage from sewage treatment works and irrigation) at the Skukuza and Lower Sabie rest camps were not available.

To overcome the flow contributions of tributaries, the water balance is computed for the low-flow months of May to September. It is therefore possible to regard influent flow from the tributaries (which are seasonal and ephemeral) to be negligible. Mean monthly discharges are used to reduce the significance of travel time along the length of river. The flow discharge data was obtained from the Department of Water Affairs and Forestry. Gauging at the crump weir below Kruger Gate (X3H021) commenced in November 1990, providing only 16 months of low-flow data.



The mean monthly discharge rates at the gauging stations and mean transmission losses (difference between the mean monthly discharges) between the stations are plotted in Figure 6.6.

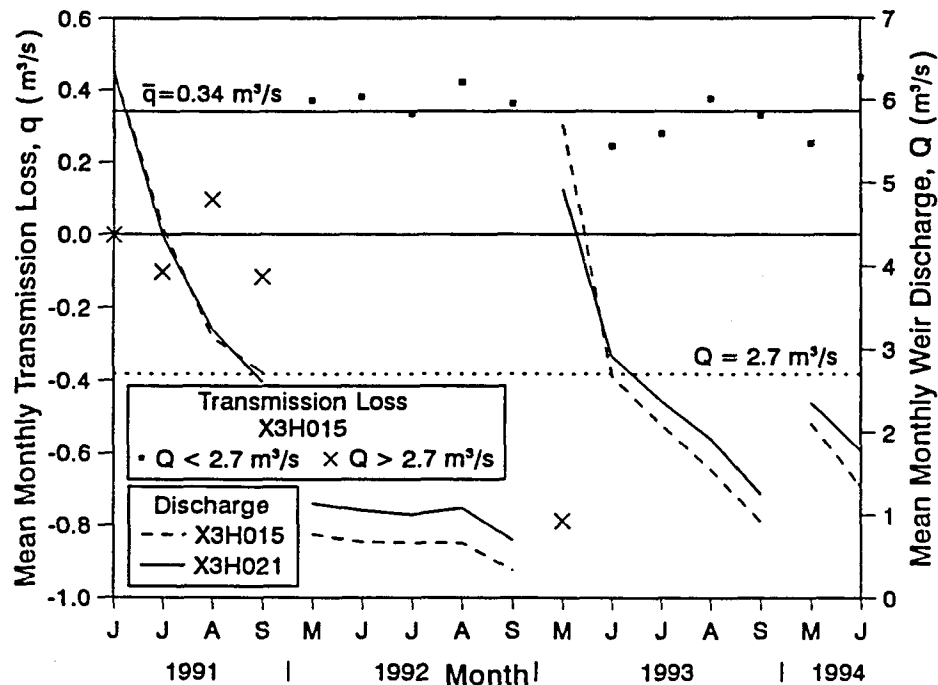


**Figure 6.6** Mean monthly transmission losses between gauging stations.

The transmission losses range from  $0.24 \text{ m}^3 \text{ s}^{-1}$  to  $0.43 \text{ m}^3 \text{ s}^{-1}$  with a mean of  $0.34 \text{ m}^3 \text{ s}^{-1}$  for mean monthly discharges less than  $2.7 \text{ m}^3 \text{ s}^{-1}$  measured at the downstream station. A discharge of approximately  $2.7 \text{ m}^3 \text{ s}^{-1}$  at station X3H015 is accompanied by a change in hydraulic behaviour as the flow level inundates a successive notch, compromising the accuracy of discharge computation from stage. The accuracy was assumed to be 5% and 10% error in discharge which is characteristic of the particular gauging structures at the upstream and downstream stations, respectively. The mean monthly transmission loss may consequently range from  $0.26$  to  $0.49 \text{ m}^3 \text{ s}^{-1}$ .

### 6.3.2 Water Supply to Rest Camps

The volume of water abstracted and water usage at Skukuza and Lower Sabie rest camps are provided by Gertenbach (1985). A summary of these estimates are provided in Table 6.4 and Table 6.5.

The estimated irrigation and domestic water use neglects rest rooms, workshops, and recharge of swimming pools, but nevertheless constitutes only 25% of the volume abstracted. The figures in Table 6.5, particularly irrigation which is widespread and seemingly uncontrolled, represent significant underestimates. The water supply to the rest camps (neglecting return flows) constitutes 29% of the calculated transmission losses.

**Table 6.4** Abstractions at pumping stations.

<b>Rest camp</b>	<b>Abstraction (<math>\text{m}^3 \text{s}^{-1}</math>)</b>
Skukuza	0.083
Lower Sabie	0.015
<b>Total</b>	<b>0.098</b>

**Table 6.5** Water usage at rest camps.

<b>Sector</b>	<b>Water Usage ( <math>\text{m}^3 \text{s}^{-1}</math> )</b>	
	Skukuza	Lower Sabie
Personnel & Tourists	0.005	0.001
Irrigation	0.017	0.003
<b>Total</b>	<b>0.022</b>	<b>0.004</b>

### 6.3.3 Losses to Evapotranspiration, Animal Consumption and Regional Aquifers

For the 60 km stretch of Sabie River considered in the water balance, the losses arising from evapotranspiration, animal consumption and seepage to regional aquifers is estimated at  $0.24 \text{ m}^3 \text{s}^{-1}$  or  $0.35 \text{ m}^3 \text{day}^{-1}$  per metre length of river. Since this is for low-flow periods, and applies to vegetation hydraulically connected to the active channel/s (such as occurring at the Narina site). For the 114 km stretch of river in the KNP the equivalent loss is  $0.46 \text{ m}^3 \text{s}^{-1}$ , compared with  $1.54 \text{ m}^3 \text{s}^{-1}$  estimated from Symon pan evaporation data.

#### **6.4 Water Balance in the Unsaturated Zone at the Narina Study Site from Neutron Probe Measurements**

The first change observed in the soil water content during the 1993/94 season, was an increase in water content in the surface layers in December 1993, as a result of the 102 mm of rainfall received. Six of the seven monitored locations, recorded in an increase in water content to a depth of 25 cm. Wetting of the profile to a depth of 1.25 m was noted at the foot of the macro-channel bank, attributed to increased runoff. A substantial increase in water content was observed in January 1994, resulting from a rise in the phreatic surface and further infiltration. By March of that year, however, the available water in the unsaturated zone had transpired. No further changes were noted in the unsaturated zone until the onset of the following wet season, demonstrating that soil moisture was only available in this zone for a period of about three months.

The pattern observed during the 1994/95 was somewhat different. The large increases in soil water content recorded the previous January were not repeated as a consequence of relatively late rainfall, and associated lower river stages. During February, however, the soil profile was at its wettest, resulting from the 323 mm of rainfall recorded during the previous month. The availability of soil moisture in the upper layers persisted to May, with increased soil moisture contents in the lower layers in this month resulting from phreatic surface response to rises in river stage.

These differences in soil water availability between the 1993/94 and 1994/95 summer seasons considered to be responsible for the higher leaf area index measured at the site and the extensive development in the herbaceous, sub-canopy layer during the latter season. This serves to illustrate the importance of the temporal distribution in soil water in effecting changes in the demographics and water use of the species on site.

#### **6.5 Diurnal River Stage Fluctuations**

The river stage fluctuates in response to evapotranspiration losses and upstream abstractions for agricultural, industrial and domestic water supply (Figure 6.7). The daily river stage fluctuations resulting from evapotranspiration are superimposed on the unsteady river discharges determined by the natural hydrology as modified by upstream abstractions and return flows. Analysis of daily river stage fluctuations during low-flows periods from 1992 to 1995 show that the stage generally falls between early morning (03:00 to 07:00) and late afternoon/early evening (15:00 to 20:00) (Figure 6.8). This appears to correspond with daytime extractions to support transpiration losses and

evaporation from the open water surface. A daily water extraction model was developed to assess whether the diurnal fluctuations can be used to infer evapotranspiration losses. The model results show, however, that the timing of stage peaks and troughs and the magnitude of fluctuations are a function of position along the river. These data can therefore not be used without additional data collection and analysis.

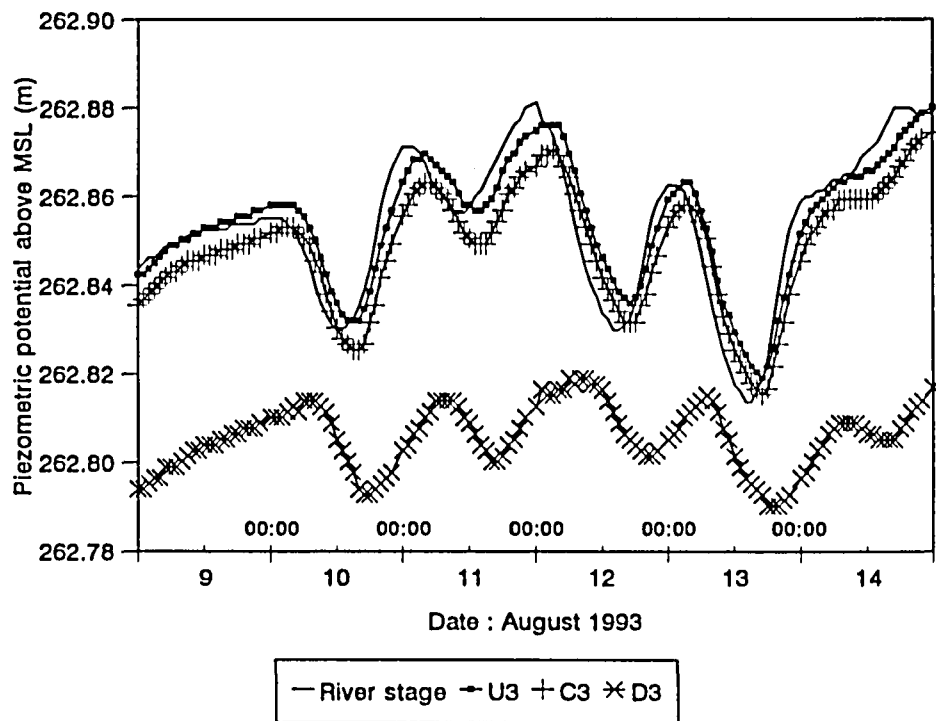


**Figure 6.7** Daily fluctuations of river stage and piezometric potentials.

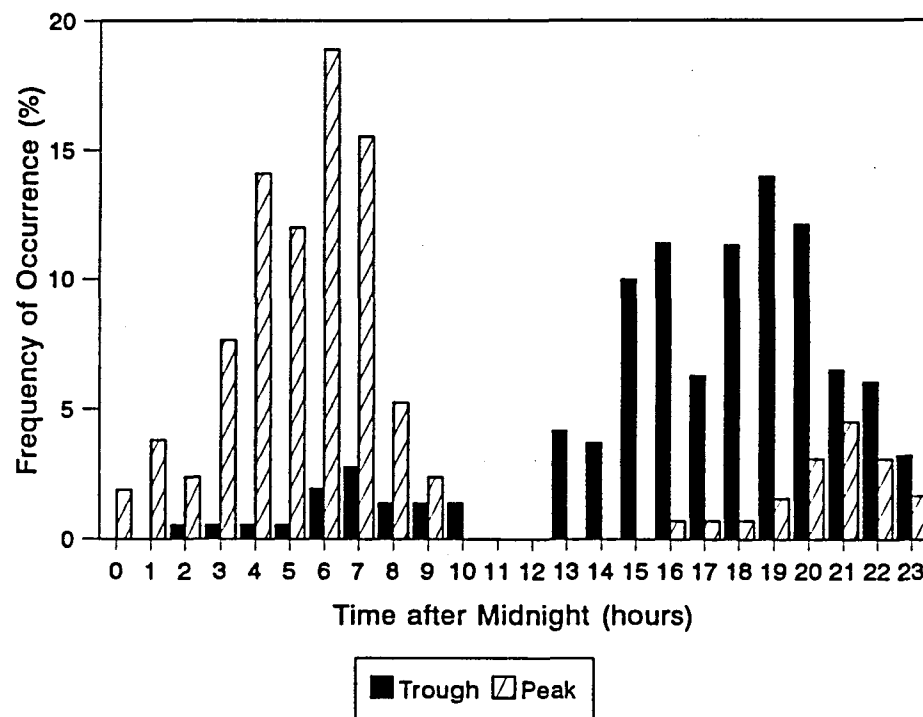


**Figure 6.8** Frequency distribution of river stage fluctuations arising from evapotranspiration.

## **CHAPTER 7**

### **DISCUSSION, CONCLUSIONS AND RECOMMENDATIONS**

---

#### **7.1 Scope**

Several models have been developed in the course of meeting the objectives of this project. These include models describing river hydraulics (Chapter 3 and Broadhurst *et al.*, in press); riparian bank storage dynamics (Chapter 4), and consumptive water use by common riparian tree species and reeds (Chapter 5). Discussion relating to the development, validation and verification of the component models has been presented in each of the relevant chapters. This chapter presents broader discussions and conclusions relating to the ability to integrate models of river flow, subsurface flow and transpiration, based on intensive and site specific data collection. We also address some of the broader implications of the results and limitations of this study.

#### **7.2 Intensive Data Collection and Integrated Modelling**

##### **7.2.1 The Need for an Integrated Modelling Approach in Semi-Arid River Systems**

The rationale for pursuing an integrated study of the riparian water balance is that all processes defining fluxes between surface water, subsurface storage and movement, and riparian transpiration are intrinsically linked in the riparian system under investigation. Rogers and van der Zel (1989) defined the riparian zone of a river as that region along the banks of the channels (and in places over the wider floodplain) in which water availability, determined by fluctuations in river stage, is the major determinant regulating plant growth and species distribution. On the Sabie River in the KNP, the riparian vegetation is well developed and sharply contrasted to the surrounding terrestrial vegetation. It is most prominent during the dry season when it is best likened to a ribbon of well hydrated vegetation meandering through the parched landscape of the semi-arid Lowveld region. This is a consequence of only 8% of the mean annual runoff being generated within the catchment occupied by KNP, coupled with the extreme flow variability characteristic of these semi-arid rivers. This emphasizes the need to include river hydraulics and dynamic bank storage when determining transmission losses due to transpiration.

##### **7.2.2 River Hydraulics**

The river hydraulics component of the riparian water balance (Fig. 1.1) provides the means to translate discharge into local hydraulic conditions such as river stage and flow velocity. The temporal variation of river stage

is the primary determinant governing the interaction between river and subsurface flows (Fig. 1.2). The required output from the river hydraulics model for this study is the ability to generate rating (stage-discharge) relationships.

#### **7.2.2.1 Flow Resistance**

The Manning's resistance coefficients determined by Broadhurst *et al.* (in press) for a typically braided river morphology are shown to compare well with those determined within the pilot study (Chapter 3.2). The comparison of synthesized against measured rating curves (Fig. 3.8), confirms their transferability within the braided channel type used in the analysis. Broadhurst *et al.* (in press) also quantified the roughness components (morphological, sedimentological and vegetational) for the five principal morphological channel types along the Sabie River as defined by Heritage *et al.* (in press). The resistance data and models developed are therefore transferable within the Sabie River, and also to river systems with similar resistance characteristics.

#### **7.2.2.2 Muskingum Routing**

The synthesis of the rating curve for a river section using local stage recordings and remote discharge monitoring is described in Chapter 3.3, as is its application to the study site. The modest data requirements include a short-term stage hydrograph and cross-sectional survey at the section, the corresponding discharge hydrograph at the remote location, and an estimate of the distance along the river between the section and discharge monitoring location. Three models are presented for optimising the parameters of the rating curve, expressed as a simple power function using the hydrograph data. Two of these are based on different nonlinear forms of the Muskingum storage function and can easily be applied to any flow sequence. The third does not depend on this function, and while it is easier to apply it requires a complete event hydrograph bounded by steady flows. All three methods have been verified by comparison with rigorous flood routing in a hypothetical channel. Results from the first two models are virtually indistinguishable and compare closely with those of the third. The application of these procedures to the reach upstream of the Narina study site showed that neglecting bank storage led to unrealistic estimates of the Muskingum storage weighting factor and unreliable rating curve parameter values. The procedure was successfully modified to account for bank storage by estimating the extent and the porosity of bank alluvium and assuming an instantaneous bank storage response. The synthesized rating curve at the site agrees closely with comparable point data collected over the duration of the project.

### **7.2.2.3 Flow Modification Resulting from Temporal Bank Storage**

Flow modification resulting from dynamic bank storage has not been the direct concern of this project. The significant contribution of bank storage to reach storage along the 4.6 km reach of the Sabie River upstream of the Narina site was demonstrated using the Muskingum routing, however (Chapter 3.3). River stage and groundwater potential monitoring at the study site (Chapter 2.2.1) has established the rapid response of bank storage to river flow. Similar rapid responses are likely to exist in hydraulically connected fluvial deposits along the Sabie River and other rivers in the KNP, due to the existence of coarse textured sediments which are characterised by high saturated hydraulic conductivities. The effects of dynamic alluvial storage on river flow may be important when specifying upstream discharges to satisfy downstream ecological criteria (e.g. Birkhead *et al.*, 1996b). The interaction between river and subsurface flow is likely to be of particular significance in seasonal and ephemeral river systems with extensive fluvial deposits (e.g. Letaba, Levuvhu and Limpopo Rivers in Fig. 2.1), where the alluvial water storage depleted during winter months must be recharged before surface flow can occur.

### **7.2.3 Bank Storage Dynamics**

The development, validation and verification of the bank storage dynamics model (Chapter 5) showed that a deterministic approach can successfully be used to quantify the interaction between river flow and subsurface water in the saturated and unsaturated zones, provided site specific data are available. These data include the temporal distribution of river stage; macro-channel surface and bedrock topography; spatial distribution of alluvial-hydraulic characteristics; and meteorological conditions (e.g. rainfall and evaporative demand). Incorporating vegetation water use in the model requires additional data, including actual transpiration (a function of evaporative demand, water availability and vegetation type); and the spatial distribution of plant roots. The drawback of the deterministic modelling approach is that the data requirements are relatively large and may be difficult to meet, particularly with regard to the flow boundaries and sediment hydraulic characteristics. Site-specific calibration may reduce the data requirements for model parameterisation, but requires additional site-specific monitoring of the groundwater response. The principal advantage is that the model is generally applicable because it is based on solutions of mathematical equations describing flow through porous media. The model can therefore be applied to any site with considerable fluvial deposits. The successful application of the bank storage dynamics models at the study site demonstrates the predictive capabilities of the deterministic approach.



#### 7.2.4 Transpiration by Riparian Vegetation

The strategy used to address the challenge of estimating the water use of the riparian vegetation on the Sabie River was first to concentrate on a single site, the Narina study site, with the aim of determining the consumptive water use of vegetation on that particular site. This was achieved by monitoring one tree (*F. sycomorus*) continuously over a two and a half year period, and comparing its transpiration rates to other dominant trees at the site during four intensive water-use sampling surveys. In addition, transpiration estimates were made for three discrete periods in the reed bed at the site. As a consequence of this strategy, the consumptive water use of the species at the site was estimated. Furthermore, by collating the transpiration data with meteorological data, LAI data, and phreatic surface level data as determined by the bank storage dynamics model, transpiration models were developed for the *F. sycomorus* tree and the reeds.

In both cases a simple regression modelling approach was used, since a more process-based approach requires data such as stomatal conductance, and aerodynamic roughness of the canopy. These data are often not available therefore limiting the applicability of the models. Statistically sound models were developed for both the reeds and the *F. sycomorus* tree. Both models required only one meteorological parameter, VPD, which was found to be non-linearly correlated with transpiration, and one vegetation parameter, LAI. In addition, the *F. sycomorus* tree model required phreatic surface level data, indicating that transpiration is a function of river stage as determined by bank storage dynamics. The parameter coefficient values were found to change over the course of the study, resulting in different coefficients corresponding to season in the case of the reeds, or months of the year for the *F. sycomorus* tree model.

Transpiration at the Narina site was found to vary with season and between the years of study. Peak transpiration rates were recorded in the latter half of summer, while the lowest transpiration rates were recorded prior to the onset of the summer rains in the latter part of winter. The variability in transpiration corresponded approximately with that recorded in LAI, but it is not clear to what extent the changes in LAI were causative, or merely indicated a change in the phenology of the plants. Importantly, none of the trees at the Narina site showed any symptoms of water stress, even at the end of the dry winter season. This suggests that the changing LAI at Narina was not a result of stress-induced leaf abscission, but rather reflected the natural phenology of the trees at the site. The importance of accurate LAI measurements (temporally and spatially) is also important because of its relationship with transpiration, and furthermore, because of its value in identifying sites which do not have continuous access to phreatic water.

The absence of water stress at the Narina site was a consequence of the structure of the alluvial substrate in which layers of coarse sand were interspersed with layers of finer sediment, including clay lenses. The sandy soil layers acted as a conduit rapidly transferring water from the active channel to the trees located some distance from the channel. This implied that even the trees located 70 m from the river had access to phreatic water provided there was surface flow in the active channel. The clay lenses in the stratified deposit exhibit high water retention capabilities, absorbing and retaining water, whether of rainfed origin or from subsurface seepage. The extent and depth of these fine sediments are probably central to the establishment and survival of seedlings, and the development of a herbaceous layer during the summer months.

Transpiration rates of the selected trees at the Narina site were found to be strongly correlated, simplifying the calculation of water use for those periods when all the trees at the site were not sampled. The correlation also indicated that all the trees were responding to the same environmental stimuli, and had ready access to water. The relative ranking in the daily transpiration of the trees sampled also remained relatively constant through the course of the study despite large changes in transpiration from one sample period to the next.

The fact that the trees at the Narina site had continual access to phreatic water implied that they were likely to be transpiring at near-potential rates. It is important to emphasise that this is not the case in the riverine vegetation throughout the Sabie River system, rather it is a characteristic of the vegetation growing in hydraulically connected alluvial zones. In the bedrock dominated sections of the river, it is likely that areas become hydraulically isolated when the river level drops below a certain stage. As a result, trees growing on the isolated alluvial deposits will experience water stress once the subsurface water storage has been depleted. Consequently, the frequency and magnitude of river stage fluctuations play a significant role in determining the extent and severity of water stress amongst the riverine trees growing in the bedrock influenced sections of the river. Analysis of drought stress and in many cases mortalities resulting from the severe drought experienced in 1991/92 shows that riparian tree mortality is strongly correlated with the degree of bedrock influence (Birkhead *et al.*, 1996b).

As part of the transpiration data collection exercise, it was necessary to determine whether there were significant differences in transpiration between tree species. If this was found to be the case, it would then be necessary to discriminate between species in making transpiration estimates. The study showed, however, that tree size was the dominant factor in regulating transpiration and there were no significant differences

between species. It was therefore possible to treat the riparian forest as a homogeneous element in the prediction of consumptive water use.

### 7.2.5 Extending the Integrated Modelling Approach

The component models (river hydraulics, bank storage and transpiration) have been applied using the following uni-directional linkages:

- 1 The hydraulic sediment characteristics were calibrated in the quasi three-dimensional saturated model to replicate the measured groundwater potential responses to a sequence of hydrographs (Fig. 4.49). The calibrated model was verified using field data collected over the period December 1992 to January 1995 that exclude the data used for calibration (Fig. 4.54). The model was used to predict daily phreatic surface response to changes in river stage at the Narina site from October 1994 to June 1995.
- 2 The phreatic surface levels from 1 above were used to determine the parameter values of this determinant in the empirical transpiration models.
- 3 The daily phreatic surface levels from 1 above and measured transpiration from a *F. sycomorus* tree were used to simulate the temporal daily variations in water content along a vertical profile through the unsaturated zone, below the canopy of the *F. sycomorus* tree (Fig. 4.55).

To extend the integrated modelling approach applied in this study, the dependence of transpiration on water availability in areas of variable subsurface water supply should be addressed. This relationship is illustrated in Fig. 1.2 by the reliance of the "biological system (water availability)" on the "bank storage dynamics (groundwater movement and soil moisture)" system.

It is interesting to note that water availability, as determined by phreatic surface levels at the Narina site, was found to be a determinant in the transpiration model, even though the riparian vegetation was considered to transpire at near potential rates.

Two factors possibly explain this linkage:

- Firstly, it is possible that the transpirational demand of the trees is strongly coupled to phreatic water, and fluctuations in phreatic surface level affect transpiration despite the fact that the trees do not suffer from water stress. Changes in LAI would form one mechanism whereby this self-regulating coupling could be effected.

- Secondly, it is possible that the trees do not suffer from water stress, but do experience nutrient shortages. Rising phreatic surface levels would hydrate a proportionally greater volume of soil increasing the availability of nutrients to trees.

The need to further investigate the relationship between transpiration and water availability arises from the profound influence of bedrock in areas of the Sabie River where subsurface water storage supporting transpiration is hydraulically disconnected from river flow due to irregular bedrock topography (refer to Birkhead *et al.*, 1996). Mapping temporal changes in LAI over the length of the river would help identify these patches as their change in LAI would be out of phase with that recorded in the well hydrated alluvial sections of the river.

### **7.3 Riparian Water Balance at the Study Site**

#### **7.3.1 Distribution of Subsurface Water in the Saturated and Unsaturated Zones**

Monitored groundwater potential data shows no measurable gradients arising from vegetation water use. This is a consequence of the underlying highly conductive fluvial deposit (Fig. 2.10). Similar alluvial conditions were observed to exist at a site located approximately 4.2 km downstream of Skukuza. The conductive layer in the saturated zone results in rapid groundwater response to changes in river stage observed at the study site. Poorly graded coarse sediments, unlike fine-textured material, exhibits poor water retention capacities in an unsaturated state, however. The spatial distribution of water content and associated water availability to riparian vegetation in the unsaturated zone therefore depends on the local sediments and stratification, as observed in Fig. 4.55a along a vertical profile at the Narina site. The neutron probe was found to provide an effective and reliable means of monitoring soil moisture variations within the macro-channel infill deposit providing a spatially averaged description of temporal water content in the unsaturated zone. These data also provided important information on the seasonal availability of water in the upper soil layers.

Integrated modelling and monitoring of river hydraulics, bank storage dynamics and transpiration losses (*F. sycomorus*) at the study site shows that seepage from the active channel accounted for 80% and 74% of the transpiration during the summer of 1993/94 and 1994/95, respectively, and 95% of the loss during the winter of 1994. This confirms the importance of bank seepage as the mechanism recharging subsurface storage in alluvial areas along the river where local vegetation is hydraulically connected with river flow through subsurface seepage.

### 7.3.2 Transpiration

Transpiration from the trees at the Narina site were found to be relatively conservative averaging 2.3 mm per day from February 1993 to January 1994, and only 1.34 mm per day for the 12 months July 1994 to June 1995. It was felt that these conservative rates were a consequence of the age of the trees, older trees having been shown to have reduced transpiration rates per unit leaf area as a consequence of an obstructed hydraulic architecture. Also, it was not possible to estimate transpiration for all the species on the site, as some were either structurally unsuitable (e.g. *A. shweinfurthii*), or too ephemeral as was the case for sub-canopy grasses and forbes.

Since the seasonal profile in transpiration was available from the Narina site, it was possible to use this result together with the total area of the riparian vegetation to estimate the total water use of the riverine vegetation on the Sabie in the Kruger National Park. The maximum estimate of the consumptive water use of the riverine vegetation was 1.51 m<sup>3</sup>/s recorded during February 1993, with a mean of 0.84 m<sup>3</sup>/s, and minimum levels of 0.5 m<sup>3</sup>/s and 0.25 m<sup>3</sup>/s in 1993 and 1994, respectively. These values compare most favourably with two independently derived estimates. The first was derived from a long-term average Symmons pan evaporation from which a mean annual evaporation of 1.54 m<sup>3</sup>/s was calculated. The second estimate was derived from a gauging based water balance for several low-flow months of the year. This resulted in a winter-time mean monthly estimate of 0.46 m<sup>3</sup>/s.

Actual transpiration estimates peaked at 12 mm per day for the reeds, but there is some question regarding the accuracy of this estimate. Simulated values were even higher casting serious doubt on the validity of the result.

It is not surprising that the Symmons pan estimates are higher than those recorded for the vegetation because the Symmon's pan estimates represent evaporation from an open water surface, and these therefore approximate maximum levels. While the riparian forest is largely constituted of trees and reeds with ready access to water, there are none-the less areas with sparse vegetation and relatively low LAI's from which evaporation rates will invariably be low.

An important finding was that although transpiration declines during winter, it reduced less than the river discharge rate. As a result, the transpiration loss constituted an increased proportion of the discharge through the winter months, reaching a maximum of 41% of the discharge in September 1993. The implication of this result is that the impact of trees on low flows is considerably more dramatic than that on high flows, and it is also important that low flows be kept at an adequate level to ensure that the

trees do not account for the entire low flow. Riparian trees therefore exacerbate the problem that exists elsewhere in the river system, in that they are most dependant on the water from the river when the discharge is at its lowest

By comparison to the consumptive water use of the riverine vegetation ( $1.5 \text{ m}^3/\text{s} = 129\,600 \text{ m}^3/\text{day}$ ), the water use of the tourist camps and facilities ( $10\,714 \text{ m}^3/\text{d}$ ) is small, as is the estimated consumptive water requirement of animals ( $655 \text{ m}^3/\text{d}$ ). This confirms the assertion made in the proposal that one of the major requirements of water in ecosystems is to meet the consumptive requirement of the riparian vegetation.

#### **7.4 Riparian Water Balance along the Sabie River in the KNP in Relation to Water Demands in the Catchment**

The water demands and land use in the Sabie River catchment are summarised in Table 7.1, and water demands are compared with those in the Olifants and Letaba River catchments (Fig. 7.1) to assess the status of the Sabie River in relation to other major rivers flowing through the KNP.

The total water demands in the catchments of the Sabie (1985), Olifants (1990) and Letaba Rivers (1985) upstream of the KNP accounted for 28%, 39% and 56% of the natural mean annual runoff (MAR), respectively (Fig. 7.1). The projected total increase in water demand in the Sabie River catchment is 84% at 2010 (Table 7.1). The projected increase in demand for domestic, industrial and municipal water use in the under-developed rural areas of the Sabie River catchment is 737% (6% of MAR at 2010). At present, only 30% to 40% of rural households have ready access to an adequate drinking water (Water and Sanitation 2000, 1991). The main purpose of the Injaka Dam, under construction on the Marite River tributary of the Sabie River is to supply water to rural communities, whilst also providing higher assurance water supplies for agriculture (Department of Water Affairs and Forestry, 1994). Trends towards more intensive agricultural land use can be expected with a higher assurance water supply as dry-land farming practises progress towards irrigation. The demands by afforestation in the Sabie and Letaba River catchments, and the demands by irrigation in all the catchments considered are significant (Fig. 7.1). Afforestation in the Sabie River catchment has resulted in an estimated 17% reduction in the MAR (Chunnet *et al.*, 1990a). The projected increase in water demand by irrigation in the Sabie River catchment (Fig. 7.1) will further reduce existing low base-flows, emphasizing the urgent need to effectively manage the water supplies for the maintenance of riparian ecosystems.

The water demands projected for 2010 from the Sabie River place abstractions at levels comparable to those experienced in 1985 on the impacted Letaba River. The Injaka Dam on the Marite River will provide the means to maintain winter base-flows. This will avoid the impending flow degradation of the Sabie River to a seasonal system, with potentially severe impacts to riparian vegetation in hydraulically connected river-subsurface alluvial zones such as the Narina site considered in this study.

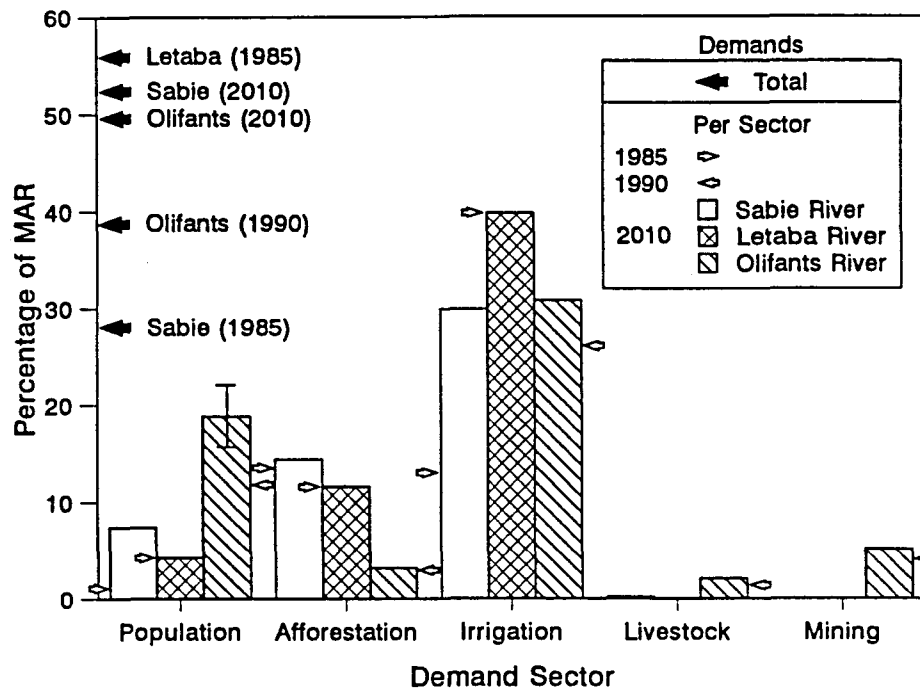


**Figure 7.1** Water demands at 1990 (Olifants River), 1985 (Sabie and Letaba Rivers) and 2010 (Sabie and Olifants Rivers) as a percentage of the MAR for the respective catchments.

## 7.5 Recommendations

### 7.5.1 Data Archiving

The river hydraulic, groundwater, soil-moisture, transpiration and climatic data (Chapter 2) collected over the duration of this project are saved on electronic media. The Centre for Water in the Environment (University of the Witwatersrand) is the custodian of these data, which are available on request from: The Director, Centre for Water in the Environment, University of the Witwatersrand, Private Bag 3, WITS 2050, Johannesburg, South Africa.

**Table 7.1** Projected water demands and land use for the Sabie River catchment  
(Chunnet *et al.*, 1990a, 1990b)

Catchment Area (km <sup>2</sup> )						7096
Natural MAR (10 <sup>6</sup> m <sup>3</sup> /a)						762
Percentage of population living in underdeveloped conditions						92
Demand Sector		1985		2010		% Growth in water demand
		km <sup>2</sup>	10 <sup>6</sup> m <sup>3</sup> /a	km <sup>2</sup>	10 <sup>6</sup> m <sup>3</sup> /a	
Population (Urban & Rural)	SA		1.1		3.5	218
	GLKV		6.3		52.7	737
Irrigation	SA	66	51.2	66	51.2	0
	GLKV	48	48.1	166	176.9	268
Livestock	SA	4230	0.4	4230	0.4	0
	GLKV	2207	1.4	2207	1.4	0
Afforestation	SA	624	92.7	740*	95.5	3
	GLKV	97	13.9	680*	14.5	0
Total	SA	145.4		150.6		4
	GLKV	69.7		245.5		252
	Combined	215.1		396.1		84

\* Total net afforestation potential

GLKV Former self-governing homelands of Gazankulu, Lebowa, KaNgwane and independent state of Venda



### 7.5.2 Technology Transfer and Research Priorities

The extensive influence of bedrock in the Sabie River system has important implications for estimating the consumptive water use of riparian vegetation, since irregular bedrock topography obstructs seepage from surface flow. Flow variability (resulting in surface flooding) is a fundamental process recharging subsurface storage and local riparian vegetation in variable source supply areas of the river. This is demonstrated by the extensive riparian tree mortalities observed in 1991/92, shown to be strongly correlated with bedrock influence (Birkhead *et al*, 1996). The areas with bedrock influence also coincide with the sections of the river where the riparian forest is best developed and at it's widest. It is therefore imperative that the flow regimes be tailored to suit the rehydration of the isolated alluvial deposits to ensure the survival of the forest that has developed in these areas.

The Injaka Dam may impact severely on the vegetation in bedrock dominated areas along the Sabie River by reducing flow variability and associated surface flooding. There is consequently an urgent need to determine the water use by riparian vegetation in bedrock dominated morphologies. These data can then be used to optimise the delivery of water to the river to ensure that at least the consumptive needs of the riparian forest in the anastomosing sections of the river are met. If this is achieved, the results of this study suggest that the needs of the trees situated on alluvial substrate such as that at Narina, will also automatically be met.

It is important to develop techniques that can be used to monitor the response of vegetation in these bedrock influenced sections of the river to the altered flow regimes and to develop methods that will serve as an early warning system so that unnecessary mortality can be prevented. This is particularly relevant given the future ability to regulate flows through releases from the Injaka Dam. Two techniques should be considered here, including, growth increment measurements, and the development of techniques to measure the spatial distribution of LAI. Since LAI reflects the integrated soil moisture status of the site, trees on sites experiencing water stress will drop leaves and therefore the change in LAI on these sites will be out of phase with those on parts of the system adequately supplied with water. This measurement is likely to be particularly useful as it will allow sections of the river most sensitive to changes in the flow regime to be identified. It may also be of value to establish long-term monitoring of tree growth, population density, and LAI.

The interaction between river and subsurface flow is important in seasonal and ephemeral river systems (e.g. Letaba River), where upstream flows must be specified to satisfy ecological requirements downstream. The

need to address the interaction between alluvial storage and flow activation in these infrequently active river systems has arisen in numerous workshops conducted to establish the ecological flow requirements of rivers across Southern Africa.

It is important to stress that further research should also focus on verifying the consumptive water use estimates produced by this study and validating the model outputs. It is suggested that accurate flow gauging would provide a suitable test of the transmission losses for low-flow periods determined in this study. In addition, further measurements need be made on the water use of reed beds, as the estimates based on results from the application of the heat balance technique on individual reeds in this study were not entirely satisfactory. It is also necessary to validate and verify the transpiration rates estimated by the two reed models presented in this study, especially as reeds are a dominant vegetation type in the Sabie River system. It is suggested that a more integrative technique such as the Bowen Ratio technique be used to derive independent estimates of transpiration to compare to those derived using the heat balance technique.

The Sabie River experiences natural diurnal fluctuations in river stage (Fig. 6.7 and Fig. 6.8). The interpretation of these fluctuations may provide a simple integrated value of the riparian water use. However, while this potential has been identified, further study and modelling is required to explore the potential of this technique.

Continued data collection (biotic and abiotic) along the Sabie River and meteorological data collection at the Narina site initiated within this project and other projects is required to improve the knowledge base, and provide data for future simulations and models generated by projects within the KNP Rivers Research Programme.

## CHAPTER 8

### REFERENCES

---

Abdulrazzak, M.J. and Morel-Seytoux, H.J., 1983. Recharge From an Ephemeral Stream Following Wetting Front Arrival to Water Table. *Water Resources Research*, Vol. 19 No. 1, 194-200.

Andrews D.F., Bickel P.J., Hampel F.R., Huber P.J., Rogers W.H. and Tukey J.W., 1972. Robust Estimates of Location, Princeton University Press, Princeton, New Jersey.

Babajimopoulos, C., 1991. A Douglas-Jones Predictor-Corrector Program for Simulating One-Dimensional Unsaturated Flow in Soil. *Ground Water*. Vol. 29 No. 2, 267-270.

Bamber, R.K. and Fukazawa, K., 1985. Sapwood and Heartwood: A Review. *Forestry Abstracts*, Vol. 46 No. 9, 567-580.

Barnes, H.H., 1967. Roughness Characteristics of Natural Channels. *U.S. Geol. Surv. Water Supply Paper 1849*, U.S. Geol. Surv., Washington, D.C.. pp. 1-9.

Bear, J. and Verruijt, A., 1992. *Modeling Groundwater Flow and Pollution*. Second Edition. D. Reidel Publishing Company, Dordrecht, England. 414 pp.

Belmans, C., Wesseling, J.G. and Feddes, R.A., 1983. Simulation Model of the Water Balance of a Cropped Soil : SWATRE. *Jour. of Hydrology*, 63, 217-286.

Binley, A. and Bevan, K., 1992. Three-dimensional Modelling of Hillslope Hydrology. *Hydrological Processes*, Vol. 6, 347-359.

Birkhead, A.L., James, C.S. and Olbrich, B.W., 1995. Monitoring the Bank Storage Dynamics Component of the Riparian Water Balance in the Sabie River, Kruger National Park. *Water SA*, Vol. 21 No. 3, 211-220.

Birkhead, A.L., Heritage, G.L., White, H. and van Niekerk, A.W., 1996a. Ground-penetrating Radar as a Tool for Mapping the Phreatic Surface, Bedrock Profile, and Alluvial Stratigraphy in the Sabie River, Kruger National Park. *Jour. Soil Water Cons.*, Vol. 51 No. 3, 234-241.

Birkhead, A.L., van Coller, A.L., James, C.S. and Heritage, G.L., 1996b. Modelling Water Availability to Riparian Vegetation in an Impacted River System. *Ecohydraulics 2000*, 2<sup>nd</sup> IAHR International Symposium on Hydraulics and Habitats. Quebec, Canada, 11-14 June 1996.

Boulton, N.S., 1963. Analysis of Data from Non-Equilibrium Pumping Tests Allowing for Delayed Yield from Storage. *Proc. Inst. Civ. Eng. (London)*, 26, 469-82.

Bouwer, H., 1969. Theory of Seepage from Open Channels. In Ven Ten Chow (ed.) *Advances in Hydrosience*, 5, 121-172. Academic Press, New York, NY.

Box, G.E.P, Hunter G.H. and Hunter J.S., 1978. Statistics for Experimenters. *An Introduction to Design, Data Analysis and Model Building*. John Wiley and Sons.

Bredenkamp, G.J., Van Rooyen, N. and Theron, G.K., 1991. A survey of the riparian vegetation of the Sabie River in the Kruger National Park.

Broadhurst, L.J., Heritage, G.L., van Niekerk, A.W., James, C.S. and Rogers, K.H., in press. Translating Hydrological Output into Local Hydraulic Conditions on the Sabie River, Kruger National Park. *Water Research Commission Report No. 474/2/96*, Volume 2. Water Research Commission, South Africa.

Bruch, J.C., Jr., 1973. Nonlinear Equation of Unsteady Ground-Water Flow. *Jour. Hyd. Div. Amer. Soc. Civil Eng.*, Vol. 99 No. HY3, 395-403.

Carter, A.J. and Rogers, K.H., 1991. Phragmites reed beds in the Kruger National Park: the complexity of changes in riverbed state. In: the proceedings of the 4<sup>th</sup> South African National Hydrology Symposium, Eds S. Kinzle and H. Maaren. 339-346.

Cernica, J.N., 1982. *Geotechnical Engineering*. CBS College Publishing, New York, NY. 488 pp.

Chadwick, A. and Morfett, M., 1993. *Hydraulics in Civil and Environmental Engineering*, Second Edition. Chapman and Hall, London. 557 pp.

Cheshire, P., 1994. Geology and Geomorphology of the Sabie River in the Kruger National Park and its Catchment Area. Report No. 1/1994, Centre for Water in the Environment, University of the Witwatersrand, South Africa.

Childs, E.C. and Poulouvassilis, A., 1962. The Moisture Profile above a Moving Water Table. *Jour. Soil Sci.*, Vol. 13 No. 2, 271-285.

Chunnet, Fourie and Partners, 1990a. Water resources planning of the Sabie River catchment, South Africa. Department of Water Affairs and Forestry Report No. P.X.300/00/0490, Vols. 1 to 10.

Chunnet, Fourie and Partners, 1990b. Kruger National Park Rivers Research Programme, Water for Nature, Hydrology, Sabie River Catchment, South Africa. Department of Water Affairs and Forestry Report No. P.X.300/00/0390.

Clark, L., 1988. *The Field Guide to Water Wells and Boreholes*. Geological Society of London Handbook Series, Open University and Halstead. 155 pp.

Cohen, Y., Fuchs, M. and Green, G.C., 1981. Improvement of the heat pulse method for determining sap flow in trees. *Plant, Cell and Environment*, 4, 391-397.

Cole, D.W., Ford, E.D. and Turner, J.H. 1990. Nutrients, Moisture and Productivity of Established Forests. *Forest Ecology and Management*, 30, 283-229.

Cook, D.R and Weisberg S., 1982. *Residuals and Influence in Regression*. Chapman and Hall.

Cooper, H.H., Jr. and Rorabaugh, M.I., 1963. Changes in Ground-Water Movement and Bank Storage Caused by Flood Waves in Surface Streams. *U.S. Geol. Surv. Prof. Pap.* 475-B, B192-B195.

Cuenca, R.H., 1988. Hydrologic Balance Model Using Neutron Probe Data. *Jour. Irrig. Drain. Eng.*, 114, 644-663.

Deacon, A.R., 1991. Kruger Park's rivers: Many Disciplines Involved in Research Programme. In: van der Merwe, S (ed.) *Custos* Vol. 20 No. 8, 14-19 (November 1991). The National Parks and wildlife magazine, National Parks Board of South Africa, Pretoria, South Africa.

Dillon, P.J., 1983. Boundary Integral Model of Stream-Aquifer Interaction. Hydrology and Water Resources Symposium, Hobart. 8 to 10 November 1983.

Doley, D. and Grieve, B.J., 1966. Measurement of Sap Flow in a Eucalypt by Thermo-electric Methods. *Australian Forest Research*, 2, 3-27.

Douglas, J., Jr. and Jones, B.F., 1963. On Predictor-Corrector Methods for Nonlinear Parabolic Differential Equations. *Jour. Soc. Ind. Appl. Math.*, 11, 195-204.

Draper, N.R. and Smith, H., 1981. *Applied Regression Analysis*. Second Edition. John Wiley and Sons.

Draper, N.R. 1984. The Box-Wetz Criterion Versus  $R^2$ . *Journal of the Royal Statistical Society, Series A* 1984, 100-103.

Dye, P.J., 1987. Predicting Transpiration from *Eucalyptus grandis* with the Penman-Monteith Equation. Proceedings of the IUFRO conference in Vancouver.

Dye, P.J. and Olbrich, B.W., 1992. Heat pulse observations of *Eucalyptus grandis* in South Africa. In: *Growth and water use of forest plantations*, Calder, I.R., Hall, R.L. and Allard, P.G. Eds. pp 216-225. Wiley, New York.

Dye, P.J. and Olbrich, B.W. 1993. Estimating transpiration from 6-year-old *Eucalyptus grandis* trees: development of a canopy conductance model and comparison with independent sap flux measurements. *Plant, cell and environment*, 16, 45-53.

Dye, P.J., MacDevette, M.G., and Olbrich, B.W., 1994. Third Phase Research into Differences in the Efficiency of Water Use and Drought Resistance shown by Eucalyptus Clones in Zululand. CSIR report commissioned by Mondi Forests, Kwambonambi, Zululand.

Feddes, R.A., Kabat, P., Van Bakel, P.J.T, Bronswijk, J.J.B. and Halbertsma, J., 1988. Modelling Soil Water Dynamics in the Unsaturated Zone - State of the Art. *Jour. of Hydrology*, 100, 69-111.

Fletcher, R. and Reeves, C.M., 1964. Function Minimisation by Conjugate Gradients. *Computer Jour.*, Vol. 7, 149 -154.

Fourie, A.B. and Strayton, G., 1996. Evaluation of a New Method for the Measurement of Permeability in the Field. *Jour. South Afr. Inst. Civil Eng.*, Vol. 38 No. 1, 10-14.

Freeze, R.A., 1969. The Mechanism of Natural Ground-Water Recharge and Discharge 1. One-dimensional, Vertical, Unsteady, Unsaturated Flow above a Recharging or Discharging Ground-Water Flow System. *Water Resources Research*, Vol. 5 No. 1, 153-171.

Freeze, R.A., 1972. Three-Dimensional Transient Saturated-Unsaturated Flow in a Recharging or Discharging Groundwater Flow System. *Water Resources Research*, Vol. 7 No. 2, 347-366.

- Gardener, W.R., 1958. Some Steady-State Solutions of the Unsaturated Moisture Flow equation with Application to Evaporation from a Water Table. *Soil Sci.*, **85**, 228-232.
- Gertenbach, W.P.D., 1985. Beplanning van Waterbehoefte van die NKW uit die Sabie Rivier. Internal Report No. NK/44, 1985.
- Gill, M.A., 1978. Flood Routing by the Muskingum Method. *Jour. of Hydrology*, **36**, 353-363.
- Gill, M.A., 1979. Flood Routing by Muskingum Method - Reply *Jour. of Hydrology*, **41**, 169-170.
- Grant, S.A., Jabro, J.D., Fritton, D.D. and Baker, D.E., 1991. A Stochastic Model of Infiltration which Simulates "Macropore" Soil Water Flow. *Water Resources Research*, Vol. **27** No. 7, 1439-1446.
- Gureghian, A.B., 1978. Solutions of Boussinesq's Equation for Seepage Flow. *Water Resources Research*, Vol. **14**, No. 2, 231-236.
- Hack-ten Broeke, M.J.D. and Kabat, P., 1988. Use of Agrohydrological Simulation Models in Quantitative Land Evaluation. *Proc. of the EC-workshop on Application of Computerised EC Soil Maps and Climate Data*. Van Lanen, H.A.J. and Bregt, A.K. (ed). 15-16 November 1988, Wageningen, Netherlands, 1988.
- Harr, M.E., 1962. *Groundwater Flow and Seepage*. McGraw-Hill, New York, NY.
- Haverkamp, R., Vauclin, M., Touma, J., Wierenga, P.J. and Vachaud, G., 1977. A Comparison of Numerical Simulation Models for One-dimensional Infiltration. *Soil Sci. Soc. of Amer. Jour.*, No. **41**, 285-294.
- Haverkamp, R. and Vauclin, M., 1979. A Note on Estimating Finite Difference Interblock Hydraulic Conductivity Values for Transient Unsaturated Flow Problems. *Water Resources Research*, Vol. **15**, No. 1, 181-187.
- Heritage, G.L., van Niekerk, A.W., Moon, B., Rogers, K.H. and James, C.S., in press. Geomorphological Responses of the Sabie and Letaba Rivers to Changing Flow and Sediment Regimes. *Water Research Commission Report No. 376/1/96*, Volume 1. Water Research Commission, South Africa.

Hornberger, G.M., Erbert, J. and Remson, I., 1970. Numerical Solution of the Boussinesq Equation for Aquifer-Stream Interaction. *Water Resources Research*, Vol. 6 No. 2, 601-608.

Huber, B. and Schmidt, E., 1937. Eine Kompensations Methode zur Thermoelektrischen Messung Langsamer Saftströme. *Die Berliner Deutsche Botanische Gesellschaft*, 55, 514-529.

Ibrahim, H.A. and Brutsaert, W., 1965. Inflow Hydrographs from Large Unconfined Aquifers. *Jour. Irrig. Drain. Div. Am. Soc. Civil Eng.*, Vol. 91 No. IR2, 21-38.

Kabat, P. and Neefjes, K., 1988. SWA-package, Version 1.0. The User-Friendly Version of the Simulation Model SWACROP with Auxiliary Programs to Generate Input and Model Parameters. ICW/Euroconsult Joint Report. 80 pp.

Kastanek, F., 1971. Numerical Simulation Technique for Vertical Drainage from a Soil Column. *Jour. of Hydrology*, 14, 213-232.

Kool, J.B. and Parker, J.C., 1987. Development and Evaluation of Closed-Form Expression for Hysteretic soil Hydraulic Properties. *Water Resources Research*, 23, 105-114.

Koutitas, C.G., 1983. *Elements of Computational Hydraulics*. Pentech Press, Plymouth.

Marshall, D. C., 1958. Measurement of Sap Flow in Conifers by Heat Transport. *Plant Physiology*, Vol. 33, No. 6, 385-396.

McCarthy, G.T., 1938. The Unit Hydrograph and Flood Routing, Unpublished Paper Presented at the Conference of North Atlantic Division, U.S. Army Corps of Engineers, New London, Conn. Printed by U.S. Engineering Office, Providence R.I.

Meehan, P.J., 1979. Flood Routing by the Muskingum Method. *Jour. of Hydr. Eng.*, Vol. 111 No. 12, 1447-1460.

Minoux, M., 1986. *Mathematical Programming - Theory and Algorithms*. John Wiley. 149 pp.

Moench, A.F., Sauer, V.B. and Jennings, M.E., 1974. Modification of Routed Streamflow by Channel Loss and Base Flow. *Water Resources Research*, Vol. 10 No. 5, 963-968.



Mualem, Y., 1976. A New Model for Predicting the Hydraulic Conductivity of Unsaturated Porous Media. *Water Resources Research*, Vol. 12, No. 3, 513-522.

Olbrich, B.W., Le Roux, D., Poulter, A.G., Bond, W.J. and Stock, W.D., 1993. Variation in Water Use Efficiency and  $\delta^{13}\text{C}$  levels in *Eucalyptus grandis* clones. *Jour. of Hydrology*, 150, 615-634.

Olbrich, B.W., 1994. The Application of the Heat Pulse Velocity Technique to the Study of Transpiration from *Eucalyptus grandis*. PhD Thesis. University of Natal, Durban.

Owen, D.B., 1962. *Handbook of Statistical Tables*. Addison-Wesley.

Papageorgiou, G., 1994. The Evaluation of Moisture Retention and Hydraulic Conductivity Characteristics of Unsaturated Soils. MSc Thesis. Faculty of Engineering, University of the Witwatersrand, Johannesburg.

Pikul, M.F., Street, R.L. and Remson, I., 1974. A Numerical Models Based on Coupled One-Dimensional Richards and Boussinesq Equations. *Water Resources Research*, Vol. 10 No. 2, 295-302.

Pinder, G.F. and Sauer, S.P., 1970. Numerical Simulation of Flood Wave Modification due to Bank Storage Effects. *Water Resources Research*, Vol. 7 No. 1, 63-70.

Press W.H., Flannery B.P., Teukolsky S.A. and Vetterling W.T., 1989. *Numerical Recipes: The Art of Scientific Computing* (FORTRAN Version). Cambridge University Press.

Prickett, T.A., 1975. Modeling Techniques for Groundwater Evaluation. *Advances in Hydroscience*. Vol. 10. Academic Press, New York. 143 pp.

Reading, H.G., 1986. *Sedimentary Environments and Facies*. Blackwell Scientific Publications, Oxford, England. 615 pp.

Reid, P., 1990. Specialists Prepare Framework for Water Study in Kruger National Park. In: van der Merwe, S (ed.) *Custos* Vol. 18 No. 10 14-17 (January 1990). The National Parks and Wildlife Magazine, National Parks Board of South Africa, Pretoria, South Africa.

Rogers, K.H., 1991. Developing an Integrated Approach to Predicting the Water Use of Riparian Vegetation. Research Proposal to the Water Research Commission, 1991.

Rogers, K.H. and van der Zel, D.W., 1989. Water Quantity Requirements of Riparian Vegetation and Floodplains. In: Ferrar, A.A, (ed.) Ecological flow requirements for South African Rivers. South African National Scientific Report No. 162, 94-109.

Royston, J.P., 1982. An Extension of Shapiro and Will's W Test for Normality to Large Samples, *Applied Statistics*, **31**, 115-124.

Rushton, K.R. and Redshaw, S.C., 1979. *Seepage and Groundwater Flow*. John Wiley and Sons. 339 pp.

Seber, G.A.F and Wild, C.J., 1989. *Nonlinear Regression*. John Wiley and Sons.

Sakuratani T., 1981. A Heat Balance Method for Measuring Water Flux in the Stem of Intact Plants. *Jour. Agr. Met.*, **37**, 9-17.

SAS Institute Inc., 1986. SAS Circle, Box 8000, Cary, NC 27512-8000.

Srivastava, R. and Yeh, T.-C.J., 1991. Analytical Solutions for One-Dimensional, Transient Infiltration Toward the Water Table in Homogeneous and Layered Soils. *Water Resources Research*, Vol. **27** No. 5, 753-762.

Swanson, R.H. and Whitfield, D.W.A., 1981. A Numerical Analysis of Heat pulse Velocity Theory and Practice. *Jour. of Experimental Botany*, Vol. **32** No. 126, 221-239.

Swanson, R.H., 1983. *Numerical and Experimental Analyses of Implanted Probe Heat Pulse Velocity Theory*. PhD Thesis. Department of Botany, University of Alberta, Edmonton, Canada.

Thomas, L.H., 1949. Elliptic Problems in Linear Difference Equations Over a Network. *Watson Sci. Comput. Lab. Rep.*, Columbia Univ., New York.

Tung, Y.K., 1985. River Flood Routing by Nonlinear Muskingum Method. *Jour. of Hydrology*, **41**, 187-168.

Tyree, M.T. and Sperry, J.S. 1991. Do Woody Plants Operate Near the Point of Catastrophic Xylem Dysfunction Caused by Dynamic Water Stress? *Plant physiology*, **88**, 574-580.

Urban Foundation, 1990. Population Trends: Demographic Projection Model. Part of the "Policies for a New Urban Future" Series.

van Genuchten, M.Th., 1978. Calculating the Unsaturated Hydraulic Conductivity with a New Closed-form Analytical Model. Research Rep. 78-WR-08. Water Resources Program, Princeton Univ., Princeton, NJ.

van Genuchten, M.Th., 1980. A Closed-form Equation for Predicting the Hydraulic Conductivity of Unsaturated Soils. *Soil Sci. Soc. of Amer. Jour.*, Vol. 44, 892-898.

van Niekerk, A.W and Heritage, G.L., 1994. The use of GIS techniques to evaluate sedimentation patterns in a bedrock controlled channel in a semi-arid region. *In Proc. International Conference on Integrated Basin Management*. Wallingford, England, U.K.. 13-16 September 1994. John Wiley, Chichester.

van Niekerk, A.W., Heritage, G.L. and Moon, B.P., 1995. River Classification for Management: The Geomorphology of the Sabie River in the Eastern Transvaal. *South African Geography Jour.*, Vol. 77 No. 2, 68-76.

Venter, F.J. and Deacon, A.R., 1994. The Letaba River in the Kruger National Park: Management Objectives of the National Parks Board and General Overview of Impacts on the River. Department of Water Affairs and Forestry (DWAF) 1994 workshop to identify the instream flow requirements of the Letaba River. DWAF, Pretoria, South Africa.

Verma, R.D. and Brutsaert, W., 1970. Unconfined Aquifer Seepage by Capillary Flow Theory. *Jour. Hyd. Div. Amer. Soc. Civil Eng.*, Vol. 96 No. HY6, 1331-1344.

Verma, R.D. and Brutsaert, W., 1971. Unsteady Free Surface Ground Water Seepage. *Jour. Hyd. Div. Amer. Soc. Civil Eng.*, Vol. 97 No. HY8, 1213-1229.

Vukorić, M. and Soro, A., 1992. Determination of Hydraulic Conductivity of porous media from Grain-Size Composition. Water Resources Publication, Colorado. 83 pp.

Waring, R.H. and Schlesinger, W.H., 1985. *Forest Ecosystems : Concepts and Management*. Academic Press, New York.

Warrick, A.W., Islas, A. and Lomen, D.O., 1991. An Analytical Solution to Richard's Equation for Time-Varying Infiltration. *Water Resources Research*, Vol. 27 No. 5, 763-766.

Water and Sanitation 2000. Strategies for Water Supply and Sanitation Provision. Proceeds of Workshop held in Johannesburg, South Africa. 1 August 1991.

Watson, K.K., 1967. Experimental and Numerical Study of Column Drainage. *Jour. Hyd. Div. Am. Soc. Civil Eng.*, Vol. 93, HY2, 1-15.

Wetherill, G.B., 1986. *Regression Analysis with Applications*. Chapman and Hall.

Wösten, J.H.M. and Van Genuchten, M.Th., 1988. Using Texture and Other Soil Properties to Predict the Unsaturated Soil Hydraulic Functions. *Soil Sci. Soc. of Amer. Jour.*, Vol. 52, 1762-1770.

Yoon, J. and Padmanabhan, G., 1993. Parameter estimation of liner and nonlinear Muskingum models. *Jour. of Water Resources Planning and Management.*, Vol. 119 No. 5, 600-610.

Zarandy, H., 1993. *Groundwater Flow in Saturated and Unsaturated Soil*. A.A. Balkema Publishers, Rotterdam, Netherlands. 279 pp.

Zhang, T. and Berndtsson, R., 1991. Analysis of Soil Water Dynamics in Time and Space by use of Pattern Recognition. *Water Resources Research*, Vol 7 No. 7, 1623-1636.

Zhang, W.Z., 1992. Transient Groundwater Flow in an Aquifer-Aquitard System in Response to Water Level Changes in Rivers or Canals. *Jour. of Hydrology*, 133, 233-257.

Zitta, V.L. and Wiggert, J.M., 1971. Flood Routing in Channels with Bank Seepage. *Water Resources Research*, Vol 7 No. 5, 1341-1345.

Zucker, M.B., Remson, I., Erbert, J. and Aguado, E., 1973. Hydrologic Studies Using the Boussinesq Equation with a Recharge Term. *Water Resources Research*, Vol. 9 No. 3, 586-592.

## CHAPTER 9

### APPENDICES

---

#### Chapter 2 Data Collection

Birkhead, A.L., Heritage, G.L., White, H. and van Niekerk, A.W., 1996. Ground-Penetrating Radar as a Tool for Mapping the Phreatic Surface, Bedrock Profile, Alluvial Stratigraphy in the Sabie River, Kruger National Park., *Jour. Soil Water Cons.*, Vol. 51 No. 3, 234-241.

# Ground-penetrating radar as a tool for mapping the phreatic surface, bedrock profile, and alluvial stratigraphy in the Sabie River, Kruger National Park

A.L. Birkhead, G.L. Heritage, H. White, and A.W. van Niekerk

**ABSTRACT:** This study evaluates the effectiveness of ground-penetrating radar (GPR) as a non-destructive, sedimentological tool for mapping the phreatic surface, bedrock profile, and alluvial stratification within a homogeneous, sand-gravel fluvial deposit in the Sabie River, Kruger National Park, South Africa. The bedrock topography was mapped using a 90 MHz center frequency antennae pair, and a 500 MHz center frequency antennae was used to achieve higher resolution for mapping the phreatic surface and alluvial sediments. The phreatic surface and bedrock profiles determined using GPR correlate well with ground-truthing data ( $R^2=0.97$  and  $R^2=0.85$ , respectively). A groundwater monitoring system and physical probing provided the independent estimates of the phreatic surface and bedrock depths, respectively. Dynamic cone penetration (DCP) tests were used to infer interfaces between sediments of different size and composition characteristics. The DCP interfaces assisted with the interpretation of the high-frequency radar imagery, enabling a detailed description of the alluvial stratigraphy.

Ground-penetrating radar (GPR) is well established as a technique for viewing the subsurface and has received widespread applications over the past decade in the fields of agricultural, environmental, construction, and mining engineering. GPR has been successfully used for evaluating soil properties and estimating the variability and composition of soils. In particular, GPR has been used to determine the lateral extent of soils (Puckett et al. 1990; Rebertus et al.

1989), depth to the phreatic surface and bedrock (Collins et al. 1989; Davis and Annan 1989), thickness of soil horizons (Boll et al. 1993; Fisher et al. 1992a; Truman et al. 1988), geologic and mineral formations (Annan et al. 1988), organic matter content in soils, and to assess soil compaction. In addition, GPR has been employed for investigating the integrity of pavements, location of subsurface structures such as pipes and drains (Vellidis et al. 1989), and for detecting the movement of groundwater and pollutants in soils (Davis and Annan 1989). The conventional sampling tools used in soft sediments are the spade and auger, which have been aided by backhoe and mechanical probing techniques. Conventional methods of observing soils are slow and tedious and produce incomplete data sets because of the limited

number of observation sites and the small area covered by the survey (Doolittle and Asmussen 1992).

The objective of this study is to assess the effectiveness of GPR using continuous reflection sounding in a homogeneous fluvial deposit consisting largely of medium sands to medium gravels. Physical probing data are used to provide an assessment of the accuracy of the radar and also to assist in the interpretation of detailed radar imagery showing structures within the fluvial sediments. This study forms part of the Kruger National Park Rivers Research Programme, which was initiated to evaluate the ecological water requirements of the rivers flowing through the Kruger National Park (KNP) in the Transvaal Lowveld, South Africa, so that they may be given due consideration in the planning and management of future resource development.

The escalating human and agricultural development in the upper catchments of the rivers has placed extreme pressure on land and water resources, resulting in reduced flows and increased sediment yields (van Niekerk and Heritage 1994). This is leading to morphological changes within the rivers and associated changes in habitat availability for riparian fauna and flora. It is useful to employ a non-destructive technique to evaluate subsurface conditions in sensitive environments, including the migration of potentially hazardous contaminants in groundwater and studies in ecologically sensitive areas. The ecological sensitivity of the KNP precludes the use of large-scale mechanized probing to obtain bedrock and sedimentary data resulting in the application of GPR as a non-destructive sedimentological tool for probing fluvial sediments.

The structure of fluvial sediments may be highly variable (Reading 1986), reflecting the ensuing processes of erosion and deposition that result from changes in the flow discharge and sediment regime in rivers. The sedimentation patterns in fluvial deposits represent a signature of past

A.L. Birkhead is a research officer in groundwater hydrology, G.L. Heritage is a senior research officer in fluvial geomorphology, and A.W. van Niekerk is a research officer in sedimentary processes with the Centre for Water in the Environment (CWE), Department of Civil Engineering, University of the Witwatersrand, Private Bag 3, WITS 2050, South Africa; H. White is the head of the Geophysical Imaging Department, ISS International Ltd., Private Bag 2083, Welkom, 9460, South Africa. Trade names have been supplied to provide specific information on the equipment used and do not constitute endorsement by the authors, their respective organizations, or funding agencies. This study forms part of a research project conducted under contract with the Water Research Commission (South Africa). The project is supported financially and materially by the Mazda Wildlife Fund and ISS International Ltd., and logistically by the National Parks Board. The field work support provided by G. Strydom, P. Mdlolvo, G. Mauleke, and J. Maboso of the Kruger National Park, D. Leskiewicz of ISS International Ltd., and P. Frost of Kings College (London University) is greatly appreciated.

J. Soil and Water Conserv. 51(3) 234-241

## Interpretive Summary

This study has shown that GPR is an effective sedimentological tool for use in coarse sediments to accurately delineate the phreatic surface and bedrock topography. DCP signature profiles characterize the textural variability along vertical sedimentary profiles and may be used to assist the interpretation of radar imagery of alluvial sediments in relatively homogeneous fluvial deposits. The network of GPR surveys conducted over the study site demonstrates the advantage of surveying continuous profiles of the subsurface. Continuous profiles facilitate the interpretation of radar data in vertical belts where reflectors are indistinct because of signal dissipation. The compromise between radar penetration depth and resolution is shown using 90 MHz and 500 MHz center frequency surveys.

**Key words:** ground-penetrating radar, fluvial sediments, phreatic surface, bedrock topography, dynamic cone penetration

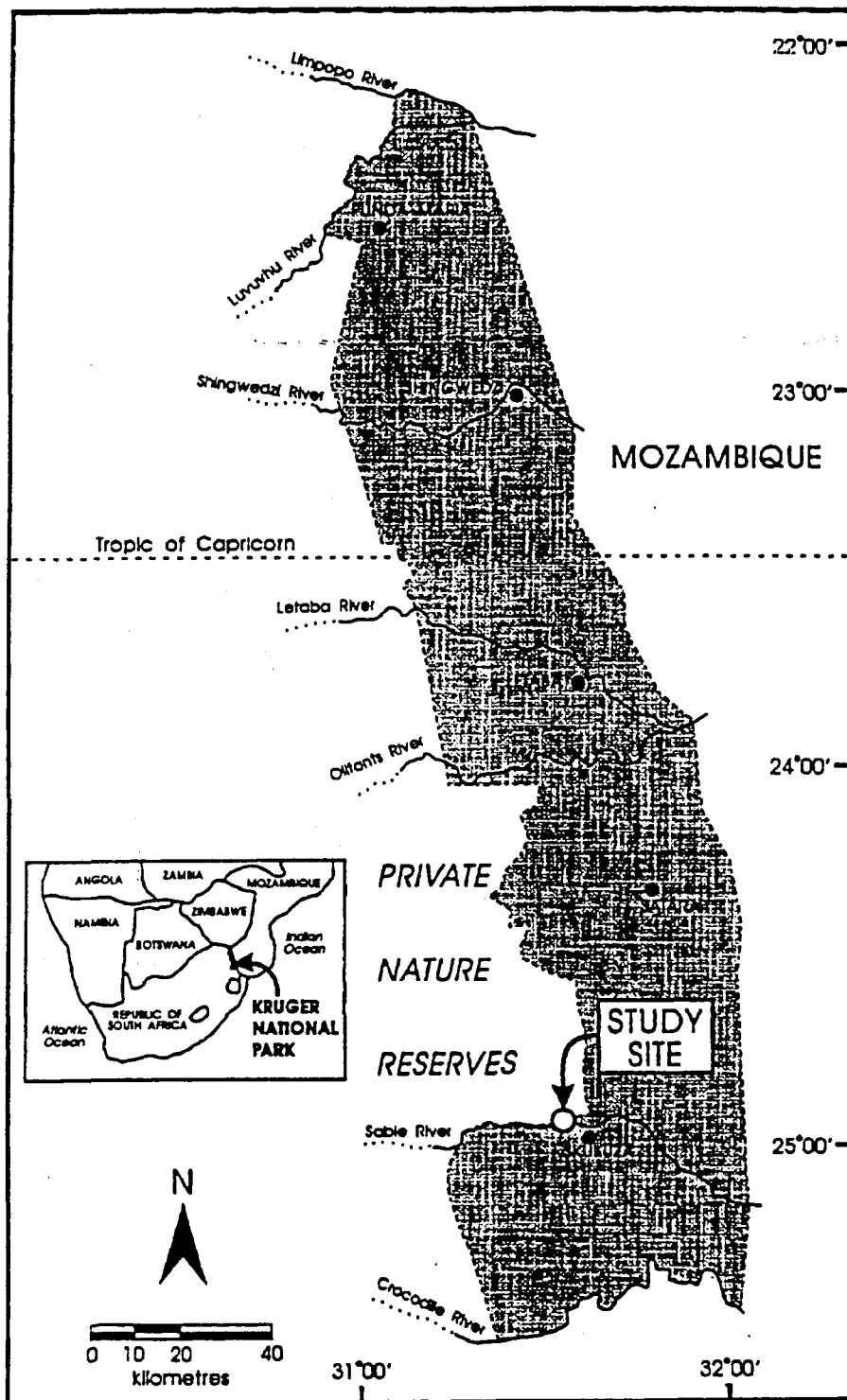


Figure 1. Location of the study site along the Sabie River in Kruger National Park

hydrological events and provide an insight into historical floods and the degree of denudation of the catchment drained by the river system. The composition and, thus, the hydraulic characteristics of fluvial sediments in riverbank deposits determine the interaction between surface flow and subsurface water. This in turn influences water availability to riparian vegetation and the stability of riverbanks.

GPR has been used previously in fluvial environments to map the depth to bedrock and position of the phreatic surface. A limited number of studies (Davis and Annan 1989; Fisher et al. 1992a; Fisher et al. 1992b) include an interpretation of the GPR data using sedimentary logs from observation holes. These studies involve depths to bedrock ranging from 5 m to 25 m (16.4 to 82 ft) and predomi-

nantly medium- to coarse-textured soils. GPR has been shown to be most effective in areas of coarse- or moderately coarse-textured soils containing limited fines, and in soils of low electrical conductivity (Boll et al. 1993; Doolittle 1987).

### Study site

The study site is located on the Sabie River in the KNP, which lies along South Africa's eastern border with Mozambique (Figure 1). The site was selected for a vegetation water-use study based on specific physical and biological criteria. The study location required alluvial sediments overlying the bedrock with a zone of saturation above bedrock level to facilitate groundwater data collection and modeling. These physical characteristics make it difficult to determine the bedrock profile, a knowledge of which is essential to understanding the surface-subsurface water interactions within the riparian zone. The biological characteristics of the study site included the presence of an assemblage of large woody riparian species commonly found along the Sabie River, as well as the reed species *Phragmites mauritianus*.

The Sabie River in the vicinity of the study area is incised into the underlying gneisses and granites of the basement complex, forming a 200-m (656-ft) wide macro-channel that is influenced by seasonal and infrequent higher-flow events. In the Sabie River, perennial flow is maintained in a smaller active channel displaying bedrock and alluvial geomorphological features (van Niekerk and Heritage 1993). Bedrock outcrops occur in the river channel in areas displaying local change in bedrock resistance as a result of lithological and structural variability (Cheshire 1994). Deposition of alluvial bars occurs upstream of such bedrock controls in the active channel because of the reduction in channel gradient, and thus, channel competence. The study site is located in one of these depositional areas, and transects were run through active channel lateral bar and macro-channel infill deposits (Figure 2).

### Methods

**Radar system.** The radar system used was the Subsurface Interface Radar (SIR) System-10 (Geophysical Survey Systems, Inc., North Salem, New Hampshire), which consists of transmitting and receiving antennae linked by a cable to the control and recording units. The transmitter radiates a short pulse of electromagnetic energy into the ground. Changes in the electrical properties in the ground at the interfaces between different media cause

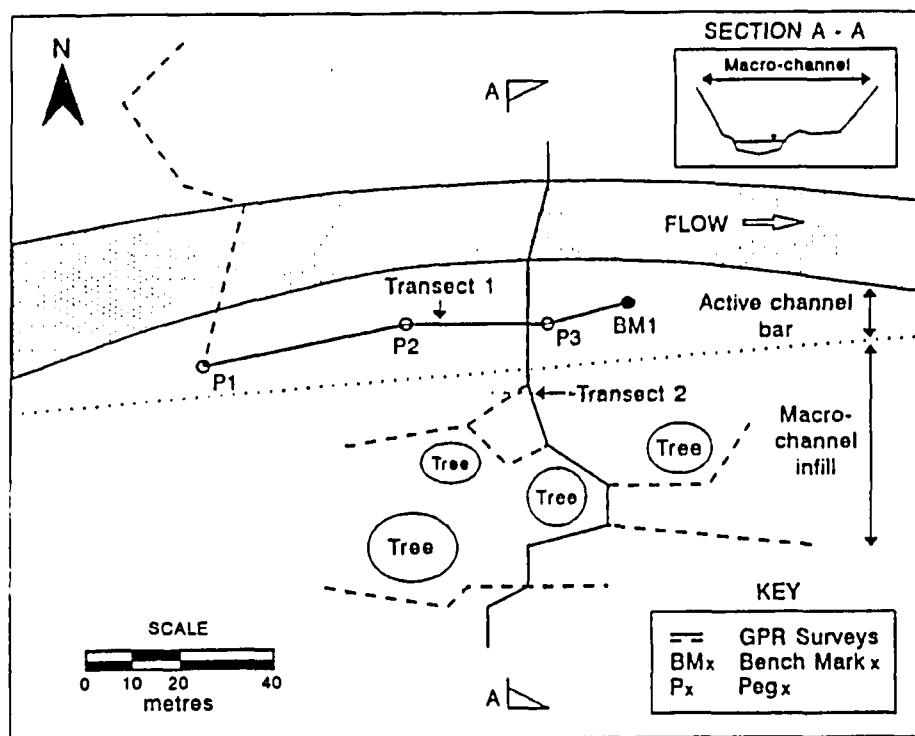


Figure 2. Network of GPR surveys traversing the study site within the Sabie River macro-channel

part of the transmitted signal to be reflected. The reflected signal is detected by the receiver, and after amplification, its amplitude and two-way travel time are stored on magnetic tape in a digital format for subsequent processing and playback.

There is a compromise between the range and resolution for GPR systems, with lower frequencies having increased penetration over higher frequencies but having reduced resolution capabilities. Radar systems with a center frequency of 100 MHz have been shown to offer the best range-resolution compromise in many geological environments (Davis and Annan 1989). The radar penetration to a reflective interface is measured by the travel time between the transmitter and receiver of the reflected wave. This two-way travel time is converted to a penetration depth by applying Equation 1:

$$d = \frac{ct}{2\sqrt{\epsilon}} \quad (1)$$

where

$d$  is the depth to the interface (m);

$c = 3 \times 10^8$  m/s ( $9.8 \times 10^8$  ft/s) is the propagation velocity of electromagnetic waves in a vacuum.

$t$  is the two-way transmitter-receiver travel time of the reflected waves (s).

$\epsilon$  is the dielectric constant relative to a vacuum.

**Radar surveys.** A network of survey

lines was run over the study area during the winter low-flow period (Figure 2). The seemingly random orientation of the lines results from the necessity to have vehicle and antennae access with minimal disturbance to the densely vegetated riverbank. The total length of the survey was 375 m (1,230 ft). Prior to the radar survey, augering was undertaken at four locations to establish depths to bedrock. This was unsuccessful due to collapsing coarse-textured sands below the phreatic surface. An estimate of the bedrock depth is useful for selecting the appropriate center frequency and associated penetration capability. Since an estimate of the range required by the GPR was not established prior to the radar study, the first GPR survey was performed using a single transmitter-receiver 90 MHz center frequency antennae.

The depth to bedrock and stratification of alluvial sediments along transects 1 and 2 were determined independently by physical probing, DCP tests, and sedimentary profiling using an auger. These data were collected after the original GPR survey was completed (June 1992), and resulted in the GPR surveys being repeated (June 1994) along the selected longitudinal and lateral transects (1 and 2) using both 90 MHz and 500 MHz center frequency antennae. The low frequency (90 MHz) survey was rerun with the transmitter and receiver antennae spaced 1.5 m

(4.9 ft) apart and linked by a fiber-optic transmitter cable to reduce the signal-to-noise ratio that was detected in the first survey. The high frequency (500 MHz) survey was undertaken to achieve an improved resolution of the alluvial sediments. The results of the subsurface explorations along transect 1 (P1-BM1) are presented.

#### Determination of dielectric constants.

The dielectric constant describes the electrical properties of the material influencing the propagation of waves in the range 10 MHz to 1,000 MHz (Davis and Annan 1989). The reflection of the radar signal coincides with changes in the dielectric constant, which is a function of the material type and volumetric water content (Table 1) (Davis and Annan 1989; Truman et al. 1988; von Hippel 1954). The dielectric constant may be determined by correlating reflectors with geological and sedimentological logs taken from test pits and auger holes. The phreatic surface and bedrock topography are used in this study to infer relative dielectric constants for the unsaturated and saturated zones, respectively.

**Conventional probing and sediment profiling.** Transect 1 is 90 m (295.3 ft) long and runs along an active lateral channel bar, the bulk of which consists of medium sands to medium gravels. Thin clay lenses are also present. The sediments are classified according to the Wentworth (1922) classification system. The depth to bedrock was estimated at 5-m (16.4-ft) intervals by successive probing through the soft sediments using a 20 mm (0.79-in) diameter, 6.5-m (21.3-ft.) long steel probe. The saturated zone inhibited the sediment recovery achieved by augering but markedly assisted the probing procedure by reducing soil-probe friction.

**Dynamic cone penetration (DCP) tests.** The DCP test provides a measure of the energy required to drive a cone through the sediments. The test involves dropping a free-falling mass through a fixed height to drive a rod with a cone-shaped tip into the ground. This provides an assessment of the relative sediment resistance to penetration of the probe. This measure of resistance has been used to infer properties such as relative density, stiffness, strength, and bearing capacity (Cernica 1982). In this study, a change in resistance to penetration offered by the medium is used to define interfaces between alluvial sediments of varying grain size and composition.

#### Results and discussion

**Graphic imagery.** The radar data are used to delineate the bedrock profile (Fig-



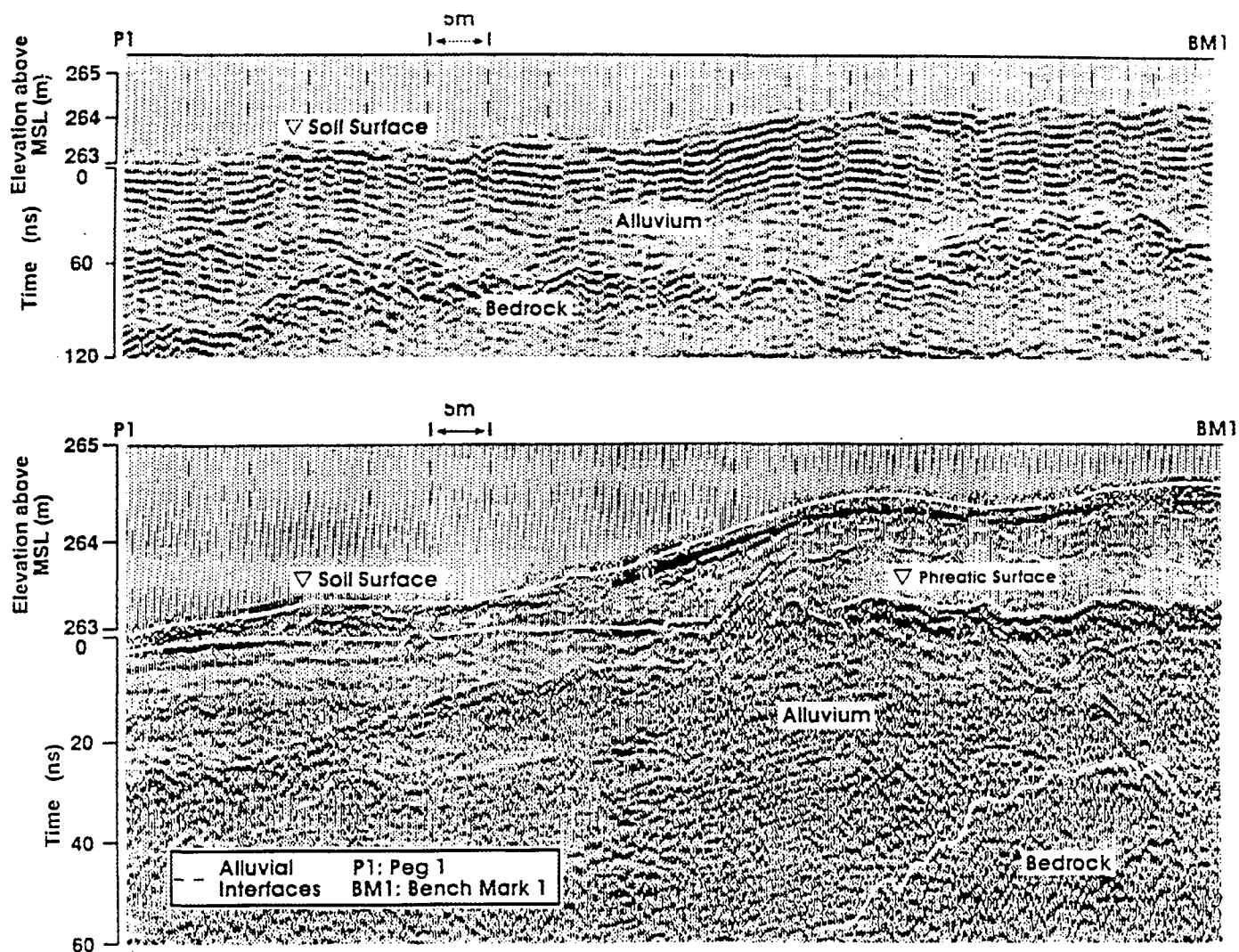


Figure 3a. (top) Radar data showing the bedrock topography below an active channel lateral bar along transect 1 using a 90 MHz survey  
Figure 3b. (bottom) Radar data showing the phreatic surface and alluvial stratification within an active channel lateral bar along transect 1 using a 500 MHz survey

ure 3a), depth to the phreatic surface (Figure 3b), and alluvial stratification within the fluvial deposit (Figure 3b). The vertical axes are expressed in terms of the two-way travel time, in nano-seconds, below the surface of the active channel lateral bar to the reflected wave. The bar surface is plotted relative to mean sea level (MSL). The compromise between penetration and resolution for the two different frequencies is evident. The radar image from the 90 MHz survey produces a strong reflector at the alluvium-bedrock interface with poor resolution above the bedrock interface; the 500 MHz survey provides detailed information within the alluvial sediments. The higher frequency signal, however, produces indistinct reflectors for defining the bedrock interface because of the dissipated radar signal beyond 40 ns penetration depth. The solid lines (Figures 3a and 3b) represent the phreatic surface and bedrock interfaces

Table 1. Typical relative dielectric constants for air, water, and various soft and hard sediments

Material	Relative dielectric constant, $\epsilon$			
	100 MHz*	100 MHz †	300 MHz ‡	3000 MHz ‡
air	1			
water	80	81	77.5	76.7
sand				
dry	3-5	5	2.55	2.55
16.8% moisture		20	20	
saturated	20-30	25		
silt	5-30			
loam				
dry		2.5	2.47	2.44
13.77% moisture		20	20	
saturated		15		
clay	5-40			
dry		2.6	2.38	2.27
20.09% moisture			20	11.3
saturated		15		
granite	4-6			
limestone	4-8			
shale	5-15			

\* Davis and Annan 1989.

† Truman et al. 1988.

‡ von Hippel 1954.

and are positioned directly above the reflectors. The dashed lines are stratigraphic delineations within the alluvial deposit, which generally trace weaker signals.

**Comparison of depths to the phreatic surface.** A groundwater monitoring system installed at the study site has shown that the phreatic surface within the lateral channel bar remains approximately horizontal. This is a consequence of both the orientation of transect 1 parallel to the active channel, and the high hydraulic conductivity of the coarse sediments. Figure 4a is a plot of the actual depth to the phreatic surface against the scaled depth to the phreatic surface using the radar data (Figure 3b). These data are fitted to the regression expression in Equation 2:

$$y = mx \quad (2)$$

The constant,  $m$ , in Equation 2 should ideally be unity. This is achieved by calibrating the relative dielectric constant (Equation 1) for sediments in the unsaturated zone above the phreatic surface. The relative dielectric constant obtained using this technique is 3.0, which compares well with the values of 2.55 to 5 for dry sands quoted in Table 1. The sensitivity of the dielectric constant to radar frequency is not significant (Table 1), allowing the comparison of the calibrated dielectric constant from the 500 MHz survey to the values in Table 1 for 300 MHz and 3,000 MHz. The phreatic surface data correlate well over the full range of data for transect 1, yielding a regression coefficient  $R^2 = 0.97$ . The average error between the actual depth to the phreatic surface and depth predicted using radar is 7.9%, which translates to 0.08 m (0.26 ft). The accuracy with which the radar maps the depth to the phreatic surface is attributed to the abrupt change in the dielectric constant at this interface, resulting from the sharp decline in the soil water content above the phreatic surface for the coarse-textured material. The region of missing data in the vicinity of a 1.5-m (4.9-ft) depth results from strong reflectors masking the phreatic surface reflector (Figure 3b). These more intense reflectors delineate alluvial interfaces within the deposit.

**Comparison of depths to bedrock.** Figure 4b is a plot of the probing depth to bedrock against the depth to bedrock predicted using the radar data (Figure 3a). The correlation procedure previously described for the unsaturated zone is used, with the relative dielectric constant for the unsaturated zone kept equal to 3.0. The calibrated relative dielectric constant obtained for the saturated zone is 20, with a

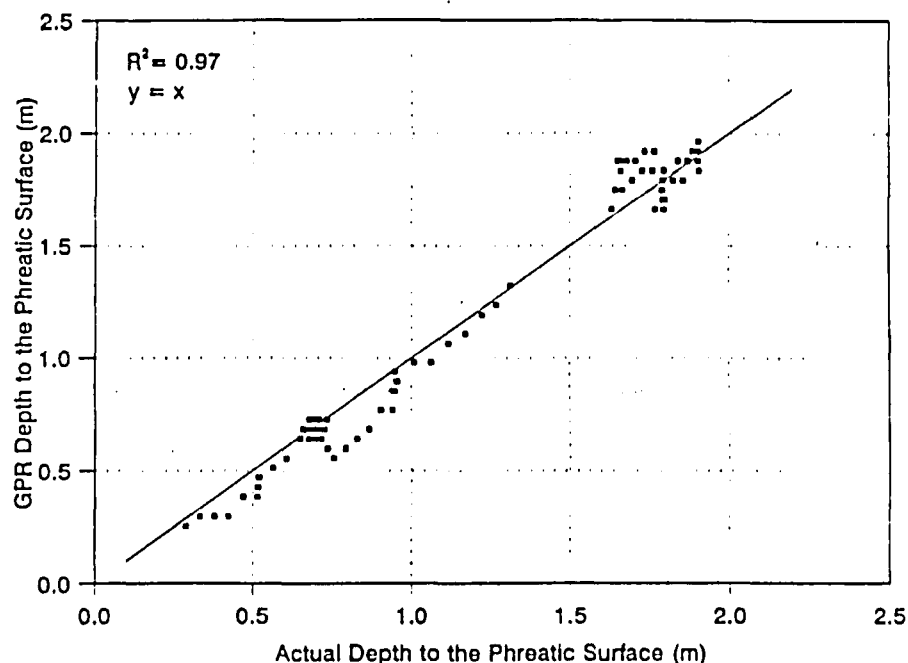


Figure 4a. Relationship between the actual depth to the phreatic surface versus depth determined by ground-penetrating radar, with a relative dielectric constant in the unsaturated zone of 3.0

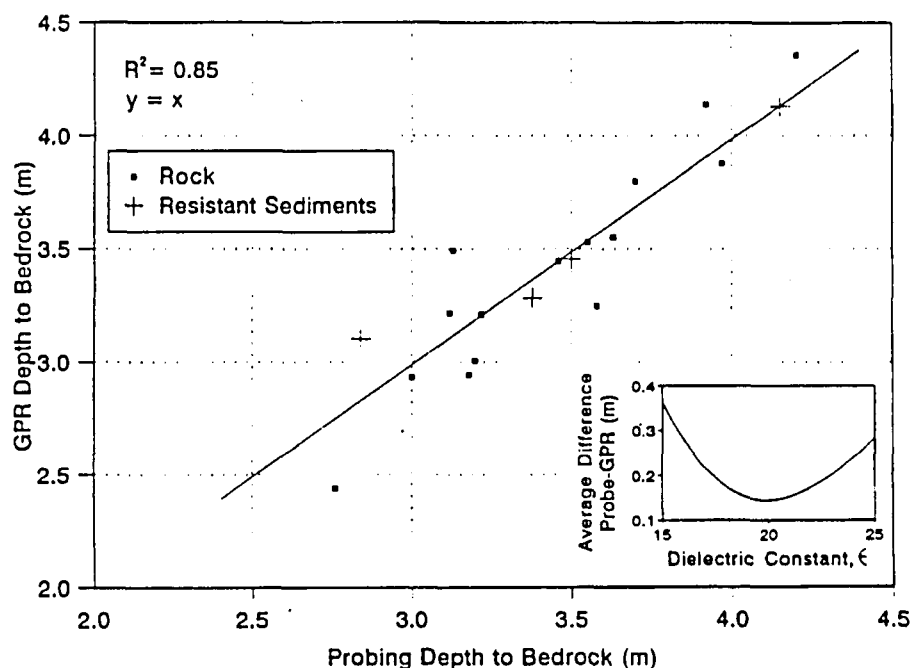


Figure 4b. Relationship between the probing depth to bedrock versus depth determined by ground-penetrating radar, with a calibrated relative dielectric constant in the saturated zone of 20

regression coefficient  $R^2 = 0.85$ . The average error between the probing and radar depth predictions is 4.4%, or 0.14 m (0.46 ft). The depth to a subsurface structure predicted using GPR is inversely proportional to the square-root of the dielectric constant (Equation 1), and is therefore relatively insensitive to the selec-

tion of this parameter. This is illustrated in Figure 4b (inset), where the average difference between the probing and GPR depth predictions is plotted against the dielectric constant over the range 15 to 25. A 25% change in the calibrated dielectric constant results in a maximum average difference of 0.36 m (1.2 ft) (10.5%

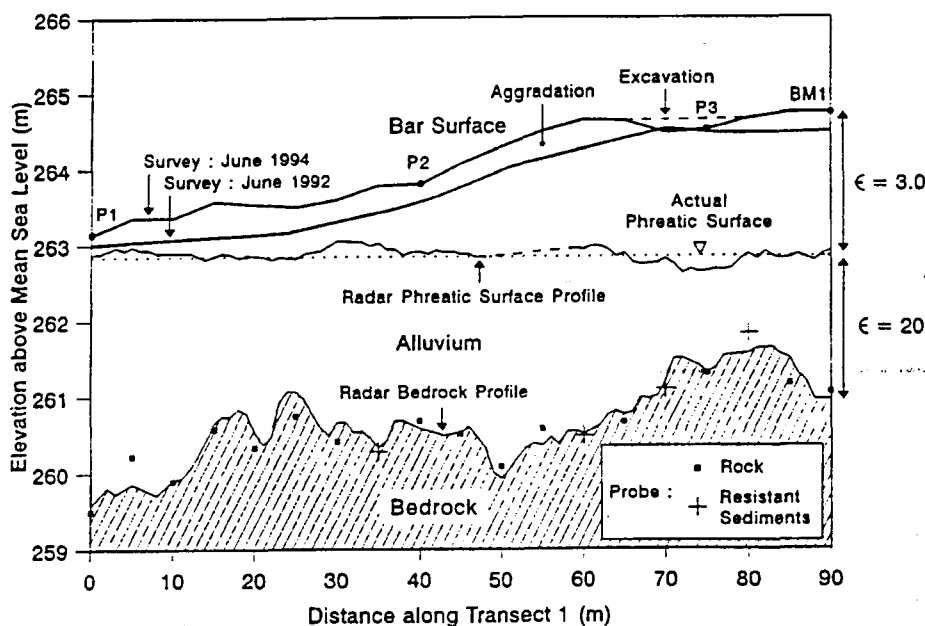


Figure 5. Comparison between actual phreatic surface and phreatic surface and bedrock profiles predicted by radar, plotted on a vertical cross-section along transect 1

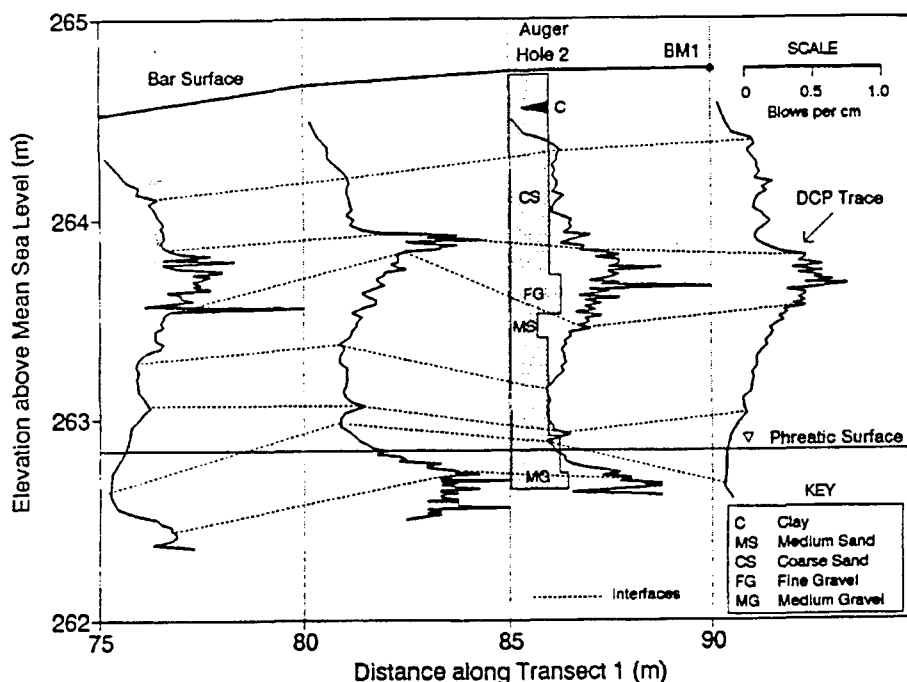


Figure 6. Dynamic cone penetration signatures at four profiles used to define interfaces between stratigraphic units

error) between the probing and GPR depth estimates. The optimum average difference of 0.14 m corresponds to the calibrated dielectric constant of 20.

The dielectric constant for the saturated sediments lies at the lower limit of the range for saturated sands (20 to 30) in Table 1 for 100 MHz center frequency. This may be due to a low porosity, reflect-

ing the presence of gravel lags embedded within the sand bar. These gravel layers are made up of mixed-grain-size materials with a lower porosity than that of uniform materials because of the decrease in the volume of voids (Terzaghi and Peck 1948). The low porosity decreases the dielectric constant in the saturated zone and not the unsaturated zone because of the reduced

influence of water (which has a high relative dielectric constant) on the average dielectric constant for the saturated medium.

The correlation between the bedrock depth predictions is significant ( $R^2 = 0.85$ ,  $p < 0.001$ ), although it is lower than that achieved for the phreatic surface depths ( $R^2 = 0.97$ ). The physical probing depth (independent variable) is susceptible to inaccuracies because of the non-vertical alignment of the probe, irregular bedrock topography, and the inability to distinguish bedrock from large clasts such as cobbles and boulders. The positive correlation achieved between the probing and radar imagery over the data range [2.5 m to 4.5 m (8.2 to 14.8 ft)] for transect 1 is attributed to the low clay content and the homogeneity of the sediments in the unconsolidated sand bar, which facilitated the use of both physical and radar probing.

Radar penetration could not be achieved beyond a layer of resistant sediments at particular locations along the transect (Figure 4b). The positions of these data points in Figure 4b do not signify any deviation below the fitted regression line, indicating that the resistant sediments lie directly above the bedrock topography.

The actual phreatic surface, and the phreatic surface and bedrock topography predicted by radar are plotted on a cross-section through the subsurface (Figure 5). The unsaturated and saturated zones are delineated at the phreatic surface, illustrating the abrupt change in the dielectric constant at this interface.

**Soft sediment differentiation.** An understanding of the subsurface stratification of the sediments deposited along transect 1 can be achieved by combining the textural variation information provided by spatially isolated DCP results with the interface patterns generated by the GPR survey.

The DCP data can be plotted to produce vertical sedimentary signatures that show changes in the textural characteristics of the sediment along the vertical profile. DCP tests were performed at 5-m (16.4-ft) intervals along transect 1, and the results of four profiles between 75 m (246 ft) and 90 m (295.3 ft) are presented (Figure 6). The number of blows required to drive the cone per centimeter penetration is plotted against penetration depth. The trace represents changes in the number of blows per unit penetration, and therefore reflects variations in the grain size and composition characteristics of the sediments, the peaks constituting units more resistant to penetration and vice-versa. The interfaces between the DCP sig-

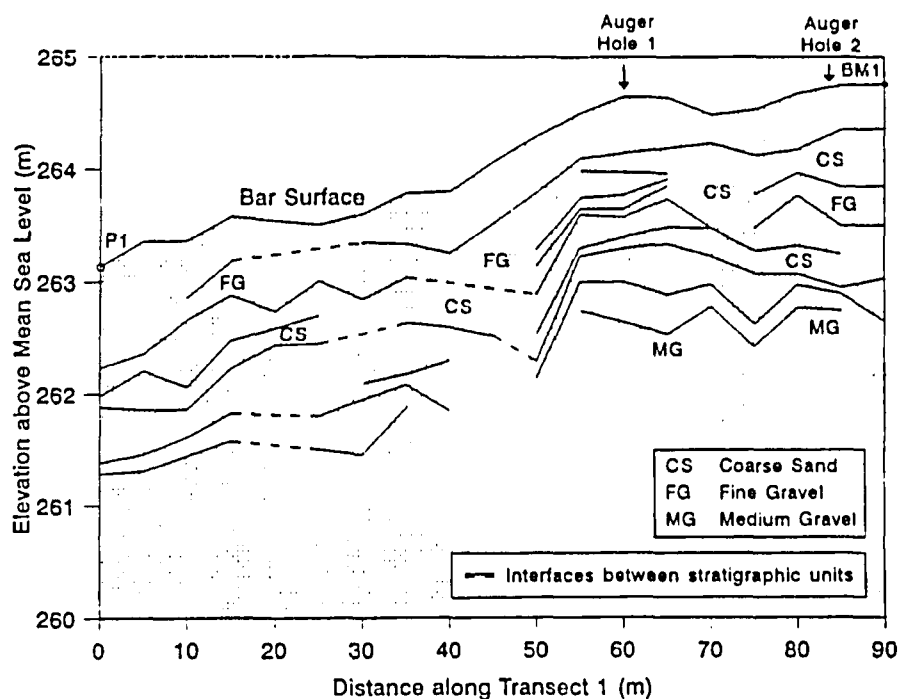


Figure 7a. Stratifications within the fluvial deposit along transect 1 inferred from DCP signatures

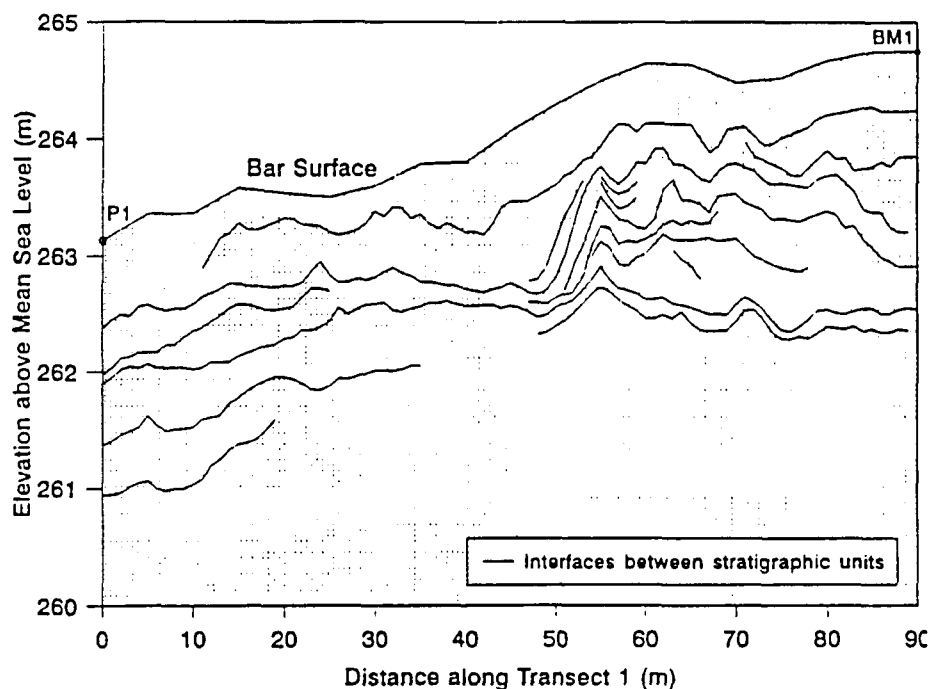


Figure 7b. Stratifications within the fluvial deposit along transect 1 using high-frequency GPR imagery and DCP results

natures of adjacent vertical profiles are inferred where similar patterns are present to produce discrete units of similar characteristics. The blow count increases with depth due to overburden pressures and with increasing coarseness of a cohesionless material (Cernica 1982). This is confirmed by

the location of fine and medium-sized gravels in the sedimentary profile at auger hole 2, which relates to the increased resistance to penetration and irregular patterns within the DCP signatures.

The DCP signatures provide detailed, spatially isolated information on the sedi-

ment variability with depth that was not easy to detect visually in the field from sediment size classifications. The DCP test also has the advantage of being able to provide information below the phreatic surface, while sediment profiling by augering in coarse sediments is restricted by sample recovery to the unsaturated zone.

The interfaces delineating sediments of different textural characteristics inferred from the DCP signatures are illustrated in Figure 7a. The DCP interfaces are used to assist in the interpretation of the high frequency GPR data (Figure 3b), enabling a more detailed description of the sedimentary stratification in the alluvium (Figure 7b). In particular, lateral continuation of stratigraphic units in the zone between 50 m and 55 m (164 and 180 ft) was difficult to infer from the isolated DCP traces. Reference to the radargram revealed the existence of dipping sediment interfaces and provided clarification of the sedimentation pattern. Similarly, stratigraphic continuity was enhanced in areas where the DCP signature was not clear.

Homogeneous units displaying distinctly different textural compositions are inferred from the DCP and sedimentary profile data (Figure 7a). Such units are associated with hydrological events or, less commonly, with changes in the hydraulic and sediment regimes within a particular event. The stratification within the alluvial sediments indicates that the lateral channel bar is aggrading, with preferential deposition having taken place on the upstream section of the bar. A resurvey of the bar surface in June 1994 (Figure 5) demonstrated that a flood in March 1993 lead to overall aggradation of the feature, and the apparent erosion close to Peg 3 reflects excavation of the recently deposited sediments to re-expose groundwater monitoring equipment. The aggradation pattern (Figure 7b) is similar to that expected given the local channel hydraulics. The upstream face of the bar represents a zone of reduced flow energy and increased form resistance, thus inducing deposition. Such a phenomenon is enhanced at the site by the rapid colonization by reeds, which introduces a vegetative resistance component, further increasing the form and frictional resistance of the bar and channel. In this way, the lateral bar is being enlarged longitudinally and migrating upstream.

#### REFERENCES CITED

- Annan, A.P., J.L. Davis, and D. Gendzwil. 1988. Radar sounding in potash mines, Saskatchewan, Canada. *Geophys.* 53(12):1556-1564.
- Boll, J., K.J.S. Kung, W.F. Ritter, J.M.H. Hendrickx, S.J. Herbert, J. Daliparthi, M.D. Tomer, and T.S. Streenhuis. 1993. Detection of textural inter-

- faces using ground-penetrating radar. In: H.J. Morel-Seytoux (ed.) *Hydrology Days. Proceedings of the Fourteenth Annual Geophysical Union*. 197-207.
- Cernica, J.N. 1982. *Geotechnical Engineering*. CBS College Publishing, New York, New York.
- Cheshire, P.E. 1994. *Geology and Geomorphology of the Sabie River in the Kruger National Park and its Catchment Area*. CWE Report No. 1/1994. Centre for Water in the Environment, University of the Witwatersrand, Johannesburg, South Africa.
- Collins, M.E., J.A. Doolittle, and R.V. Rourke. 1989. Mapping depth to bedrock on a glaciated landscape with ground-penetrating radar. *Soil Science Society of America Journal* 53:1806-1812.
- Davis, J.L., and A.P. Annan. 1989. Ground-penetrating radar for high-resolution mapping of soil and rock stratigraphy. *Geophys. Prospecting*. 37:531-551.
- Doolittle, J.A. 1987. Using ground-penetrating radar to increase the quality and efficiency of soil surveys. In: W.U. Reybold and G.W. Petersen (eds.) *Soil Survey Techniques*. Soil Science Society of America Special Publication 20:11-32.
- Fisher, E., G.A. McMechan, and A.P. Annan. 1992a. Acquisition and processing of wide-aperture ground-penetrating radar data. *Geophys.* 57(3):495-504.
- Fisher, E., G.A. McMechan, A.P. Annan, and S.W. Cosway. 1992b. Examples of reverse-time migration of single-channel, ground-penetrating radar profiles. *Geophys.* 57(4):577-586.
- Puckett, W.E., M.E. Collins, and G.W. Schellentrager. 1990. Design of soil map units on a Karst area in West Central Florida. *Soil Science Society of America Journal* 54:1068-1073.
- Reading, H.G. 1986. *Sedimentary Environments and Facies*. Blackwell Scientific Publications, Oxford, England.
- Rebertus, R.A., J.A. Doolittle, and R.L. Hall. 1989. Landform stratigraphic influences on variability of loess thickness in Northern Delaware. *Soil Science Society of America Journal* 53: 843-847.
- Terzaghi, K., and R.B. Peck. 1948. *Soil Mechanics in Engineering Practice*. John Wiley and Sons, London, England.
- Truman, C.C., H.F. Perkins, L.E. Asmussen, and H.D. Allison. 1988. Using ground-penetrating radar to investigate variability in selected soil properties. *Journal of Soil and Water Conservation* 43(4):341-345.
- USDA. 1992. Fourth International Conference on Ground Penetrating Radar, June 8-13, 1992, Rovaniemi, Finland. In: P. Hänninen and S. Autio (eds.) *Geological Survey of Finland, special paper* 16:139-147.
- van Niekerk, A.W., and G.L. Heritage. 1993. *Geomorphology of the Sabie River*. CWE Report No. 2/1993. Centre for Water in the Environment, University of the Witwatersrand, Johannesburg, South Africa.
- van Niekerk, A.W., and G.L. Heritage. 1994. The use of GIS techniques to evaluate sedimentation patterns in a bedrock controlled channel in a semi-arid region. In: *Proceedings of the International Conference on Integrated Basin Management*. Wallingford, England, 13-16 September 1994. 257-269. John Wiley and Sons, Chichester, England.
- Vellidis, G., M.C. Smith, D.L. Thomas, M.A. Breve, and C.D. Perry. 1989. Using ground penetrating radar (GPR) to detect soil water movement in sandy soil. *American Society of Agricultural Engineering, Paper No. 89-2520*. St. Joseph, Michigan.
- von Hippel, A.R. (ed.). 1954. *Dielectric Materials and Applications*. MIT Press, Cambridge, Massachusetts.
- Wentworth, C. 1922. A scale of grade and class terms for clastic sediments. *Journal of Geology*. 30: 377-392.

### Chapter 3 Modelling River Hydraulics

**Table A3.1** Cross-section chainage

Cross-section	Chainage (m)
1	0
2	111
3	229
4	526
5	742
6	802
7	940
8	1022
9	1182

**Table A3.3** Elevation of the top of the PFLR's,  
relative to MSL

Cross-section	Peak Flow Level Recorder Elevation AMSL (m)		
	PFLR1	PFLR2	PFLR3
1	266.733	268.468	268.287
2	265.992	267.789	
3	264.747	266.499	
4	264.963	267.054	
5	266.004	268.355	269.684
6	266.242	268.186	
7	266.159	268.347	270.159
8	266.978	268.755	

**Table A3.2 Elevations of cross-section bench marks relative to MSL**

Cross-section	Bench Mark (BM) Elevation AMSL (m)					
	Left Bank (LB)			Right Bank (RB)		
	LB3	LB2	LB1	RB1	RB2	RB3
1			268.793	265.678	272.878	
2			271.974	266.118	272.801	
3				BM4	Manhole Cover	C1 Cap
				266.543	264.815	264.416
4 5 6 7 8 9	LB3	LB2	LB1	RB1	RB2	RB3
	269.113	266.431	267.881	268.810	272.668	273.007
			267.518	266.615	271.780	
			274.311	266.388	272.630	
			274.263	266.862	273.407	
			274.185	267.161	273.315	
			274.156	267.038	274.005	

**Table A3.4** Discharge and stage levels recorded over the period June 1993 to January 1995

Date	Discharge m <sup>3</sup> /s	River Water Level AMSL (+ 260.000 m)								
		Cross-section								
		1	2	3	4	5	6	7	8	9
11\06\93	3.28	2.616	2.895	2.936	3.014	3.241	3.734	3.771	4.286	
05\08\93	2.05	2.504	2.753	2.798	2.906	3.067	3.637	3.672	4.189	4.191
11\10\93	2.49	2.565	2.885	2.905	2.965	3.143	3.722	3.757	4.266	4.288
08\11\93	3.80	2.595	2.941	2.985	3.028	3.167	3.775	3.817	4.324	4.339
29\12\93	44.51	4.008		4.345	4.533		4.542			
13\01\93	8.20				3.263	3.414				
02\03\93	6.31	2.783	3.093	3.111	3.133	3.304	3.880	3.926	4.445	
09\01\95	22.83	3.495		3.737	3.838	3.964	4.548	4.457		
09\01\95	13.73	3.448				3.674		4.218		
16\01\95	40.29	4.385	4.032		4.698	4.594		5.047		



**Table A3.5.1 Cross-section 1**

$Q$ (m <sup>3</sup> /s)	$v$ (m/s)	$D_{max}$ (m)	$A$ (m <sup>2</sup> )	$P$ (m)	$R$ (m)
2.05	0.162	0.888	12.68	28.32	0.45
2.49	0.174	0.949	14.32	29.29	0.49
3.28	0.286	1.000	15.73	20.04	0.52
3.80	0.251	0.979	15.14	29.73	0.51
6.31	0.308	1.167	20.51	32.34	0.63

**Table A3.5.2 Cross-section 2**

$Q$ (m <sup>3</sup> /s)	$v$ (m/s)	$D_{max}$ (m)	$A$ (m <sup>2</sup> )	$P$ (m)	$R$ (m)
2.05	0.161	1.256	12.77	21.44	0.60
2.49	0.159	1.388	15.69	25.40	0.62
3.28	0.206	1.398	15.93	25.82	0.62
3.80	0.231	1.444	16.45	26.75	0.62
6.31	0.302	1.596	20.86	34.06	0.61

**Table A3.5.4 Cross-section 4**

$Q$ (m <sup>3</sup> /s)	$v$ (m/s)	$D_{max}$ (m)	$A$ (m <sup>2</sup> )	$P$ (m)	$R$ (m)
2.05	0.62	0.387	3.33	23.29	0.14
2.49	0.49	0.446	5.07	40.60	0.12
3.28	0.47	0.495	6.95	56.35	0.12
3.80	0.49	0.509	7.78	62.24	0.12
6.31	0.70	0.614	9.04	38.39	0.23
8.20	0.57	0.744	14.27	43.37	0.33
22.83	0.59	1.319	38.55	44.88	0.86
44.51	0.63	2.014	70.61	55.20	1.28

**Table A3.5.5 Cross-section 5**

$Q$ (m <sup>3</sup> /s)	$v$ (m/s)	$D_{max}$ (m)	$A$ (m <sup>2</sup> )	$P$ (m)	$R$ (m)
2.05	0.32	0.450	6.40	20.06	0.32
2.49	0.31	0.526	7.95	22.92	0.35
3.28	0.34	0.624	9.72	24.31	0.48
3.80	0.45	0.550	8.50	24.48	0.34
6.31	0.56	0.687	11.23	25.48	0.44
8.20	0.58	0.797	14.02	27.52	0.51
22.83	0.77	1.347	29.47	32.05	0.92
40.29	0.80	1.977	50.22	38.28	1.31

Table A3.5.3 Cross-section 3

$Q$ (m <sup>3</sup> /s)	$v$ (m/s)	$D_{max}$ (m)	$A$ (m <sup>2</sup> )	$P$ (m)	$R$ (m)
0.63	0.05	0.01	12.34	21.32	0.58
1.04	0.07	0.11	14.49	22.10	0.66
1.28	0.08	0.14	15.13	22.32	0.68
1.52	0.09	0.18	16.13	22.67	0.71
3.39	0.17	0.37	20.45	23.99	0.85
3.63	0.18	0.35	20.03	23.91	0.84
4.28	0.21	0.38	20.55	24.01	0.86
5.47	0.25	0.43	21.78	24.20	0.90
6.74	0.31	0.43	21.93	24.22	0.91
6.84	0.28	0.54	24.52	24.61	1.00
7.35	0.29	0.56	25.01	24.68	1.01
7.87	0.31	0.56	25.01	24.68	1.01
9.00	0.32	0.70	28.33	25.17	1.13
12.11	0.40	0.77	30.11	25.43	1.18
12.25	0.39	0.84	31.79	25.67	1.24
13.35	0.42	0.84	31.79	25.67	1.24
13.73	0.43	0.84	31.86	25.68	1.24
16.39	0.50	0.87	32.66	25.80	1.27
16.79	0.46	1.03	36.68	26.37	1.39
18.46	0.52	0.99	35.63	26.22	1.36
20.97	0.56	1.07	37.68	26.51	1.42
22.10	0.51	1.27	43.02	27.24	1.58
25.10	0.56	1.33	44.53	27.45	1.62
25.91	0.57	1.38	45.81	27.62	1.66
33.05	0.63	1.64	52.79	28.61	1.84
36.91	0.65	1.77	56.55	30.30	1.87
39.57	0.71	1.73	55.48	29.82	1.86
83.87	0.91	2.52	91.99	80.74	1.14
103.97	0.92	2.82	113.63	82.61	1.38
172.65	0.89	3.71	194.08	106.73	1.82
644.72	1.55	5.66	415.50	123.89	3.35

**Table A3.5.6 Cross-section 6**

$Q$ (m <sup>3</sup> /s)	$v$ (m/s)	$D_{max}$ (m)	$A$ (m <sup>2</sup> )	$P$ (m)	$R$ (m)
2.05	0.13	1.181	16.17	34.91	0.46
2.49	0.13	1.266	19.10	35.15	0.54
3.28	0.17	1.278	19.51	35.19	0.55
3.80	0.18	1.319	20.93	35.31	0.59
6.31	0.26	1.424	24.57	35.61	0.69
22.83	0.45	2.092	50.82	44.45	1.44
40.29	0.57	2.536	70.28	46.59	1.51

**Table A3.5.7 Cross-section 7**

$Q$ (m <sup>3</sup> /s)	$v$ (m/s)	$D_{max}$ (m)	$A$ (m <sup>2</sup> )	$P$ (m)	$R$ (m)
2.05	0.11	1.674	18.61	37.88	0.49
2.49	0.13	1.759	18.85	29.77	0.63
3.28	0.17	1.773	19.25	30.88	0.62
3.80	0.18	1.819	20.66	34.54	0.60
6.31	0.27	1.928	23.81	37.69	0.63
40.29	0.58	3.049	69.51	53.01	1.31

**Table A3.5.8 Cross-section 8**

$Q$ (m <sup>3</sup> /s)	$v$ (m/s)	$D_{max}$ (m)	$A$ (m <sup>2</sup> )	$P$ (m)	$R$ (m)
2.05	0.16	0.576	12.53	37.25	0.34
2.49	0.16	0.653	15.43	41.18	0.37
3.28	0.20	0.673	16.26	41.37	0.39
3.80	0.21	0.711	17.83	41.73	0.43
6.31	0.27	0.832	23.41	52.28	0.45

## Chapter 4 Modelling Bank Storage Dynamics

### A4.1 Analytical Model of Cooper and Rorabaugh (1963)

#### A4.1.1 Groundwater Potentials

The groundwater potentials or phreatic surface elevation are given by

$$h_{t \leq \tau} = ND_o \left\{ e^{-\eta \beta \omega t} \left[ \frac{\cos[(L-x) \frac{\pi \sqrt{\eta}}{2L}]}{\cos \frac{\pi \sqrt{\eta}}{2}} - A \cos(\omega t + \theta) \right] + \frac{4}{\pi} \sum_{n=1}^{\infty} \sin[(2n-1) \frac{\pi x}{2L}] \frac{(2n-1) e^{-(2n-1)^2 \beta \omega t}}{[\eta - (2n-1)^2] + [\eta - (2n-1)^2]^3 \beta^2} \right\} \quad \text{A4.1a}$$

$$h_{t \geq \tau} = \frac{4ND_o}{\pi} \sum_{n=1}^{\infty} \sin[(2n-1) \frac{\pi x}{2L}] \frac{(2n-1) [1 - e^{-[\eta - (2n-1)^2] 2\pi \beta}] e^{-(2n-1)^2 \beta \omega t}}{[\eta - (2n-1)^2] + [\eta - (2n-1)^2]^3 \beta^2} \quad \text{A4.1b}$$

where

$$\beta = \frac{\pi T \tau}{8L^2 S}$$

$$\eta = \frac{\delta}{\beta \omega}$$

$$A = \left[ \frac{\cos^2 a \xi + \sinh^2 b \xi}{\cos^2 a + \sinh^2 b} \right]^{1/2}$$

$$\theta = \arctan \left[ \frac{f_s(a\xi, b\xi) f_c(a, b) - f_c(a\xi, b\xi) f_s(a, b)}{f_c(a\xi, b\xi) f_c(a, b) + f_s(a\xi, b\xi) f_s(a, b)} \right]$$

$$f_s = \sin u \sinh v$$

$$f_c = \cos u \cosh v$$

$$\xi = \frac{L-x}{x}$$

$$a = \pi \left[ \frac{(\eta^2 + \frac{1}{\beta^2})^{1/2} + \eta}{8} \right]$$

$$b = \pi \left[ \frac{(\eta^2 + \frac{1}{\beta^2})^{1/2} - \eta}{8} \right]$$

#### A4.1.2 Seepage Rates

The seepage rates per unit length of stream are given by

$$Q_{t \leq \tau} = ND_o \sqrt{\omega TS} \left\{ e^{-\eta \beta \omega t} \left[ \sqrt{\eta \beta} \tan \frac{\pi \sqrt{\eta}}{2} + B \cos(\omega t + \varphi) \right] + \frac{4\sqrt{\beta}}{\pi} \sum_{n=1}^{\infty} \frac{(2n-1)^2 e^{-(2n-1)^2 \beta \omega t}}{[\eta - (2n-1)^2] + [\eta - (2n-1)^2]^3 \beta^2} \right\} \quad \text{A4.2a}$$

$$Q_{t \geq \tau} = ND_o \sqrt{\omega TS} \cdot \frac{4\sqrt{\beta}}{\pi} \sum_{n=1}^{\infty} \frac{(2n-1)^2 [1 - e^{-\eta - (2n-1)^2 2n\beta}] e^{-(2n-1)^2 \beta \omega t}}{[\eta - (2n-1)^2] + [\eta - (2n-1)^2]^3 \beta^2} \quad \text{A4.2b}$$

where

$$B = (\eta^2 \beta^2 + 1)^{1/4} \left[ \frac{\cosh 2b - \cos 2a}{\cosh 2b + \cos 2a} \right]^{1/2}$$

$$\varphi = \arctan \left[ \frac{a \sinh 2b + b \sin 2a}{b \sinh 2b - a \sin 2a} \right]$$

and  $a$ ,  $b$ ,  $\beta$ , and  $\eta$  are as previously defined.

#### A4.1.3 Bank Storage

The bank storage volumes per unit length of stream are given by

$$V_{t \leq \tau} = ND_o \left( \frac{TS}{\omega} \right)^{1/2} \left\{ e^{-\eta\beta\omega t} \left[ \frac{1}{\sqrt{\eta\beta}} \tan \frac{\pi\sqrt{\eta}}{2} - \frac{\beta}{\sqrt{\eta^2\beta^2+1}} \sin(\omega t + \varphi - \arctan \eta\beta) \right] \right. \\ \left. + \frac{4\sqrt{\beta}}{\pi} \sum_{n=1}^{\infty} \frac{e^{-(2n-1)^2\beta\omega t}}{[\eta-(2n-1)^2]\beta + [\eta-(2n-1)^2]^3\beta^3} \right\} \quad A4.3a$$

$$V_{t \geq \tau} = ND_o \left( \frac{TS}{\omega} \right)^{1/2} \frac{4\sqrt{\beta}}{\pi} \sum_{n=1}^{\infty} \frac{[e^{-[\eta-(2n-1)^2]2\eta\beta-1}] e^{-(2n-1)^2\beta\omega t}}{[\eta-(2n-1)^2]\beta + [\eta-(2n-1)^2]^3\beta^3} \quad A4.3b$$

#### A4.2 Sand Flume Test Results

Table A4.1 Saturated hydraulic conductivities

Flume Test	Layer	Hydraulic Conductivity $K_s$ (m/hr)
1	1	7.24
2	1	5.33
	2	42.84
	3	5.33
	4	0.13
	5	5.33
	6	42.84
	7	5.33
3	1	2.27

#### A4.2.1 Flume Test 1

Table A4.2 Piezometric potentials

Piezometer	Piezometric Potential (mm)					
$h_1$	350.0	350.0	250.0	250.0	150.0	150.0
1	333.0	337.5	240.0	236.5	145.0	141.5
2	321.5	328.0	231.5	230.5	140.5	139.5
3	<del>307.5</del>	<del>316.5</del>	<del>222.0</del>	<del>223.0</del>	<del>135.0</del>	<del>136.5</del>
4	280.5	292.5	203.0	208.0	124.5	130.5
5	254.0	270.0	185.0	194.0	115.0	126.5
6	225.0	246.0	165.0	179.0	104.5	121.5
7	192.5	217.5	142.5	162.5	92.5	117.5
8	155.0	183.5	117.0	143.5	79.5	111.5
9	110.0	145.0	88.0	122.0	65.5	105.5
$h_2$	300.0	250.0	200.0	150.0	100.0	50.0

Table A4.3 Seepage rates

$h_1$ (mm)	$h_2$ (mm)	Seepage (ml/min)
350.0	50.0	1203
339.0	50.0	1154
320.0	50.0	1080
350.0	100.0	1061
304.0	50.0	1017
287.0	50.0	935
269.0	50.0	783
250.0	50.0	689
250.0	100.0	518
206.0	50.0	512
150.0	50.0	286
150.0	100.0	151

#### A4.2.2 Flume Test 2

Table A4.4 Piezometric potentials

Piezometer	Piezometric Potential (mm)			
$h_1$	300.0	250.0	200.0	150.0
1	290.0	240.0	194.0	148.5
2	280.0	233.5	188.5	145.0
3	269.5	223.5	181.0	140.5
4	250.0	208.5	170.5	134.5
5	229.0	190.5	157.0	128.0
6	207.0	173.0	145.0	122.0
7	182.5	153.5	132.0	115.0
8	154.5	134.5	120.5	109.5
9	128.5	117.0	109.5	104.0
$h_2$	100.0	100.0	100.0	100.0

Table A4.5 Seepage rates

$h_1$ (mm)	$h_2$ (mm)	Seepage (ml/min)
300.0	100.0	1592
250.0	100.0	1081
200.0	100.0	676
150.0	100.0	335



### A4.2.3 Flume Test 3

Table A4.6 Piezometric potentials

Piezometer	Piezometric Potential (mm)				
$h_1$	200.0	200.0	150.0	150.0	100.0
1	348.0	349.0	299.0	299.0	248.0
2	346.5	348.0	298.0	298.0	247.0
3	343.5	345.5	295.5	296.0	244.5
4	336.5	339.5	290.0	291.5	240.5
6	275.0	284.0	239.0	248.5	202.0
7	265.5	278.0	231.5	243.5	196.0
$h_2$	100.0	150.0	100.0	150.0	100.0

Table A4.7 Seepage rates

$h_1$ (mm)	$h_2$ (mm)	Seepage (ml/min)
200.0	100.0	350
200.0	150.0	275
150.0	100.0	262
150.0	150.0	182
100.0	100.0	139

### A4.3 Analytical Model of Srivastava and Yeh (1991)

#### A4.3.1 Hydraulic Conductivity

The hydraulic conductivity is given by

$$K_{z,t} = q_B - (q_B - e^{a\psi_0})e^{-z} - 4(q_B - q_A)e^{(L-z)/2}e^{-t/4} \sum_{n=1}^{\infty} \frac{\sin(\lambda_n z) \sin(\lambda_n L) e^{-\lambda_n^2 t}}{1 + \frac{L}{2} + 2\lambda_n^2 L} \quad \text{A4.4a}$$

#### A4.3.2 Outflow at the Phreatic Surface

The outflow at the phreatic surface is given by

$$q_t = K_s q_B - 4K_s (q_B - q_A) e^{L/2} e^{-t/4} \sum_{n=1}^{\infty} \frac{\lambda_n \sin(\lambda_n L) e^{-\lambda_n^2 t}}{1 + \frac{L}{2} + 2\lambda_n^2 L} \quad \text{A4.4b}$$